Dissertationsreihe am Institut für Hydromechanik
der Universität Karlsruhe (TH)
Heft 2005/2

Shallow Turbulent Wake Flows: Momentum and Mass Transfer due to Large-Scale Coherent Vortical Structures

Carl Friedrich v. Carmer

universitätsverlag karlsruhe

Carl Friedrich v. Carmer

Shallow Turbulent Wake Flows: Momentum and Mass Transfer due to Large-Scale Coherent Vortical Structures

Dissertationsreihe am Institut für Hydromechanik
der Universität Karlsruhe (TH)
Heft 2005/2

Figure on page 1:

Leonardo da Vinci, Depiction of whirlpools and a study of a musing old man, ca. 1513, Royal Library, Windsor (RL 12579)
The Royal Collection © 2005, Her Majesty Queen Elizabeth II

This document has been typeset using LaTeX2e.

Shallow Turbulent Wake Flows: Momentum and Mass Transfer due to Large-Scale Coherent Vortical Structures

von
Carl Friedrich v. Carmer

universitätsverlag karlsruhe

Dissertation, genehmigt von der
Fakultät für Bauingenieur-, Geo- und Umweltwissenschaften
der Universität Fridericiana zu Karlsruhe (TH), 2005
Referenten: Prof. Gerhard H. Jirka, Ph.D., Prof. Dr.-Ing. habil. Dr. h.c. Bodo Ruck,
Prof. Dr.-Ing. habil. Cameron Tropea

Impressum

Universitätsverlag Karlsruhe
c/o Universitätsbibliothek
Straße am Forum 2
D-76131 Karlsruhe
www.uvka.de

SOME RIGHTS RESERVED

Dieses Werk ist unter folgender Creative Commons-Lizenz
lizenziert: http://creativecommons.org/licenses/by-nc-nd/2.0/de/

Universitätsverlag Karlsruhe 2005
Print on Demand

ISSN 1439-4111
ISBN 3-937300-63-5

Shallow Turbulent Wake Flows:

Momentum and Mass Transfer due to Large-Scale Coherent Vortical Structures

Zur Erlangung des akademischen Grades eines

Doktor-Ingenieurs

von der Fakultät für
Bauingenieur- und Vermessungswesen
der Universität Fridericiana zu Karlsruhe (TH)

genehmigte

Dissertation

von

Dipl.-Ing Carl Friedrich Graf v. Carmer
aus Schwäbisch Hall

Tag der mündlichen Prüfung: 13.04.2005

Hauptreferent: Prof. Gerhard H. Jirka, Ph.D.,
Universität Karlsruhe (TH)

Korreferenten: Prof. Dr.-Ing. habil. Dr.h.c. Bodo Ruck,
Universität Karlsruhe (TH)

Prof. Dr.-Ing. habil. Cameron Tropea,
Technische Universität Darmstadt

Karlsruhe 2005

Shallow Turbulent Wake Flows — Momentum and Mass Transport due to Large-scale Coherent Vortical Structures

Abstract

Shallow turbulent flows are ubiquitous in nature. Many environmental flows can be characterized by horizontal length scales much greater than the flow depth. Such flows are encountered in wide rivers, in estuaries and in coastal seas, in stratified lakes and, on geophysical scale, in the stratified atmosphere or in the ocean. Due to a large single obstacle like a small island, a disturbance is introduced in the shallow near-equilibrium vertical shear flow. Large, predominantly two-dimensional eddies can alternately shed off from the obstacle and advect downstream. Although an unbounded plane lateral shear flow is inviscidly unstable, in shallow wakes due to the limited vertical extent, the large-scale eddies are not affected and disintegrated by three-dimensional vortex stretching mechanisms. By virtue of the bottom–induced vertical shear, firstly, the disturbance can be stabilized, and secondly, the kinetic energy of the large eddies can be dissipated.

The purpose of this project study is to characterize the mean flow and turbulence properties of shallow turbulent wakes induced by a single cylindrical obstacle. The mechanisms of generation and decay of 2D large-scale coherent vortical structures will be clarified, as well as their role in the transport of turbulent kinetic energy and of mass. The global and local stability of different classes of shallow turbulent wakes will be analyzed, and related to experimental data.

The experimental investigation of shallow turbulent wake flows necessitates specially adapted measurement devices and experimental techniques, described in Part I. Non-intrusive optical measurement techniques for flow velocity and mass concentration had to be applied to shallow flows maintained in a newly installed shallow flow facility. Shallow wake flows comprise a wide range of turbulence scales introduced both by the random turbulence of the vertical bottom–induced shear, and by the quasi-periodic motion of the transversely sheared wake flow. In order to satisfy this duality, two different optical flow measurement systems have been employed. A standard 2D Laser Doppler Velocimetry (LDV) system allowed to obtain point-wise horizontal flow velocities with high spatiotemporal resolution. This was complemented by an especially designed Laser Induced Fluorescence (LIF) system, which provided measurements of tracer mass concentrations. The dynamic range of the LIF system has been extended by a non-linear LIF attenuation model. Spatial correlation and temporal coincidence of both measurement volumes allowed to observe also the turbulent mass fluxes with the combined LDV-LIF system. Field-wise measurements with lower resolution provided insight in the spatial coherence

of the large-scale quasi-periodic flow. A Particle Image Velocimetry (PIV) system provided near-surface velocity fields. To observe depth–averaged dye tracer concentrations, a Planar Concentration Analysis (PCA) technique has been developed employing a hydro-optical model for light scattering and absorbtion. A specific measurement program provided a comprehensive data base for this study, which is also employed to validate numerical analysis and flow simulation tools.

The mean properties and the stochastic description of shallow wakes, as presented in Part II, reveal a strong duality induced by the lateral and vertical shear. The spectral energy distributions display the enstrophy cascade of 2D turbulence at large scales and the energy cascade of 3D isotropic turbulence at small scales; also the corresponding spectral transfer of mass variance follows the appropriate theoretical concepts of 2D and 3D isotropic turbulence. Using a phase–resolved averaging technique, the data are decomposed into their low-frequent quasi-periodic and high-frequent random parts, thus demonstrating the importance of the large-scale quasi-periodic motion for the balance of turbulent kinetic energy and of scalar fluctuations. An analytical wake model, including the influence of bottom friction, is derived from the integral conservation equations for momentum deficit, volume deficit, and mass. This allows to predict the development of the mean flow field in the self-similar far wake, where large-scale structures are no longer dominating. Evaluation of time-mean flow fields of laboratory flows show a near field, where shallow wakes behave similar to unbounded plane wakes. Contrarily, in the large eddy–dominated intermediate and in the passive far wake, the growth and decay rates diminish. Experimental data are related to the results of linear stability analysis, and local stability regions are identified. In contrast to unbounded plane wakes, shallow wakes stabilize after a short distance that is comparable to the length of the near field.

Part III elaborates the structure and dynamics of the periodic wake flow, and stresses the significance of the large-scale eddies. From the velocity and mass fields, provided by PIV and PCA measurements, the low-frequent quasi-periodic parts are extracted using an adaptive phase–resolved averaging procedure. By means of a structure identification scheme based on vorticity and shear strain, large-scale coherent vortices are educed from the quasi-periodic velocity fields. Coherent and incoherent parts of derived flow quantities are used to characterize the structure of vortex street-like periodic flows, and to identify regions of turbulence production and intense mixing. A numerical particle tracking is developed to predict the mass transport on the basis of coherent surface velocity fields. The incoherent fluctuations can be obtained from small-scale turbulence models. Tornado-like secondary motions of the large 2D vortices and its consequences on the lateral mass spreading are evidenced from the velocity fields and transport simulations.

Flache turbulente Nachlaufströmungen — Impuls- und Massentransport durch großräumige kohärente Wirbelstrukturen

Kurzfassung

Natürliche Strömungen können vielfach als flache turbulente Scherströmungen beschrieben werden, so in breiten Flüssen, Ästuaren, in geschichteten Seen und Küstengewässern. Solche Strömungen weisen gegenüber den horizontalen Ausdehnungen eine sehr geringe Tiefe auf. Durch ein großes Hindernis wie eine Insel wird in die flache Gleichgewichtsscherströmung eine Störung eingetragen, wodurch sich großräumige Wirbelstrukturen alternierend vom Störkörper ablösen können, die im Nachlauf eine Wirbelschleppe ausbilden. Obwohl unbegrenzte ebene Nachlaufströmungen grundsätzlich instabil sind, werden in flachen Strömungen die Instabilitätsmechanismen sowohl aus kinematischen als auch aus dynamischen Gründen abgeschwächt, was zu einem geänderten Stabiltätsverhalten flacher Nachlaufströmungen führt. Dies kann gravierende Auswirkungen auf das Austausch- und Ausbreitungsverhalten flacher Nachlaufströmungen haben.

Diese Studie soll dazu beitragen, flache Nachlaufströmungen genauer zu beschreiben und zu klassifizieren, und ihre Turbulenzeigenschaften zu erfassen. Die Mechanismen für die Entstehung und den Zerfall von großräumigen Wirbelstrukturen sollen ebenso untersucht werden wie der Einfluss solcher Strukturen auf den Energie und Stoffhaushalt der Strömung. Die globale und lokale Stabilität unterschiedlicher Arten von flachen Nachläufen soll analysiert und anhand von Laboruntersuchungen verifiziert werden.

Die experimentelle Untersuchung von flachen turbulenten Nachlaufströmungen erfordert speziell angepasste Messeinrichtungen und Analyseverfahren, die in Teil I behandelt werden. Berührungslose optische Messverfahren zur Erfassung der Strömungsgeschwindigkeiten und Stoffkonzentrationen werden auf flache Scherströmungen angewandt, die in einer neu errichteten Flachwasser-Versuchseinrichtung erzeugt werden. Da flache turbulente Nachläufe ein breites Turbulenzspektrum aufweisen, welches sowohl die 3D Turbulenz aufgrund der sohlinduzierten vertikalen Scherung als auch die großräumige periodische Bewegung aufgrund der horizontalen Scherung umfasst, werden zwei sich ergänzende optische Messverfahren eingesetzt. Mit einem gebräuchlichen 2D Laser Doppler Anemometrie (LDA) System werden die horizontalen Geschwindigkeitskomponenten punktweise mit hoher räumlicher und zeitlicher Auflösung erfasst. Um Konzentrationen eines Markierstoffes zu beobachten, kommt ergänzend ein speziell entwickeltes Laser Induzierte Fluoreszenz (LIF) System zum Einsatz, wobei der Messbereich durch ein nichtlineares LIF Strahlungsmodell deutlich erweitert wird. Räumliche Korrelation und zeitliche Koinzidenz der Messvolumen beider Lasermesssysteme erlauben die Erfassung auch der Mas-

senflüsse mit dem kombinierten LDA-LIF. Flächige Messungen mit geringerer Auflösung sind geeignet, die langsamen quasi-periodischen Strömungsbewegungen im Nachlauf in ihrem räumlichen Zusammenhang zu quantifizieren. Ein kommerzielles Particle Image Velocimetry (PIV) System wird adaptiert, um die Geschwindigkeitsfelder nahe der Wasseroberfläche zu erfassen. Tiefengemittelte Massenkonzentrationen werden mit einer Planaren Konzentrations Analyse (PCA) Technik unter Verwendung eines hydro-optischen Lichtabschwächungsmodells gemessen. Mit einem genau abgestimmten Versuchsprogramm wird eine umfassende Datenbasis für dieses Projekt bereitgestellt, welches aber auch zur Validierung von numerischen Analyse- und Simulationsverfahren verwendet wird.

Nach einer Betrachtung der theoretischen Konzepte sowohl der klassischen homogenen 3D Turbulenz als auch der 2D Turbulenz wird in Teil II mit Hilfe spektraler Verteilungen der Geschwindigkeits- und Massenfluktuationen die Dualität flacher turbulenter Nachlaufströmungen nachgewiesen. Die Zerlegung der Geschwindigkeiten und Konzentrationen in ihre niederfrequenten periodischen und hochfrequenten zufälligen Anteile verdeutlicht die besondere Bedeutung der langsamen kohärenten Strömungsbewegung flacher Nachläufe. Zur Beschreibung des zeitgemittelten Strömungsfeldes wird ein analytisches Nachlaufmodel, das auch den Einfluss der Bodenreibung berücksichtigt, aus den integralen Erhaltungsgleichungen für Impulsdefizit, Volumendefizit und für Masse hergeleitet. Dieses ermöglicht die Berechnung der longitudinalen Nachlaufentwicklung im selbstähnlichen Fernfeld, in dem die Dynamik großräumige Wirbel bereits deutlich gedämpft ist. Die Auswertungen der experimentell erfassten zeitgemittelten Strömungsfelder erlaubt die Identifizierung eines Nahfeldes, in dem das Ausbreitungsverhalten eines flachen Nachlaufs dem eines unbegrenzten 2D Nachlaufs gleicht. Dagegen sind die Wachstumsraten im von Großwirbeln dominierten Übergangsfeld und im passiven Fernfeld stark vermindert. Indem experimentelle Daten mit den Prognosen einer linearen Stabiltätsanalyse verglichen werden, können Bereiche unterschiedlicher lokaler Instabilität identifiziert werden. Im Vergleich zu unbegrenzten 2D Nachläufen ist der konvektiv instabile Bereich flacher Nachläufe stark verkürzt, der unterstromige Abstand bis zur Stabilisierung deckt sich in etwa mit der Länge des Nahfeldes.

Die Struktur und Dynamik des kohärenten quasi-periodischen Anteils der Nachlaufströmung wird in Teil III ebenso herausgearbeitet wie die Bedeutung der Großwirbel für die Strömungsentwicklung. Mit einer adaptiven phasenaufgelösten Mittelung werden die quasi-periodischen Geschwindigkeits- und Konzentrationsfelder aus PIV und PCA Messungen extrahiert, ein Verfahren zur Strukturerkennungsverfahren erlaubt es, darin die großräumig-kohärenten Wirbel genau abzugrenzen. Mit Hilfe der kohärenten und inkohärenten Anteile abgeleiteter Strömungsgrößen werden die Strömungsprozesse in flachen Wirbelstraßen-Nachläufen sowie die Rolle der großräumigen Wirbelstrukturen

erklärt. Ein Numerical Particle Tracking Verfahren wird realisiert, um aus gemessenen quasi-periodischen Oberflächen-Geschwindigkeitsfeldern auf die tiefengemittelten Massenkonzentrationen schließen zu können, wobei die kleinskaligen 3D Fluktuationen durch geeignete Turbulenzmodelle simuliert werden. Erneut zeigt sich der besondere Einfluss der Großwirbel, der nur durch die Berücksichtigung auch der Tornado-artigen Sekundärströmungen zu erfassen ist.

Acknowledgements

This doctoral thesis is based on research projects carried out by the author during his affiliation with the Institute for Hydromechanics, University of Karlsruhe. The financial support of the German Research Foundation under the DFG grants Ji 18/4, and Ji 18/8 is gratefully acknowledged.

Needless to say that a large number of people have vitally contributed to this project, and each of them surely deserves my gratitude. In a more or less erratic selection I want to name only few of those I am deeply indebted to.

First of all I want to express my deep gratitude to Prof. G.H. Jirka, Ph.D. for his continuous guidance and support. I have been strongly motivated by his thoroughgoing seriousness and enthusiasm about scientific research in environmental fluid mechanics. He not only provided a well–equipped working environment, but also a wide scope of a fascinating and challenging research topic. Hence,—much appreciated by me—I was granted to experience academic freedom in the classical sense.

I would like to express my appreciations to my co-supervisors Prof. Dr.–Ing. B. Ruck, and Prof. Dr.–Ing. C. Tropea for their willingness to accept a 'Korreferat' and for their patience when working through a rather voluminous document.

My sincerest appreciation goes to Prof. em. Dr.–Ing. E. Naudascher who not only taught me the basics of hydromechanics in 1988/89 but encouraged me since this time to keep on wondering and thinking about the various facets of life beyond hydromechanics.

I am very thankful for the kindness, the personal and professional support I received at the Institute for Hydromechanics, in particular to Dr.–Ing. C. Lang, H. Meyer, and Dr.–Ing. A. Richter for the administrative support, to M. Schröder for the mechanical support, to H. Deutsch for his photo and video artistry, to G. Kühn and Dr.–Ing. V. Weitbrecht for providing the PIV system, to P. Giraud for the electrical backing, and to H. Oppmann for the IT assistance.

Without many helping hands and heads of my student co-workers it would have been surely impossible to operate the shallow flow facility and to perform the experiments. Your work and your questions fostered the project a lot, and I enjoyed working with you, P. Dietz, K. Heinrich, K. Hickel, G. Kühn, M. Kurzke, D. Lehmann, A.C. Rummel, K. Schmidhäußler, D. Schoppmann, and J. Schröder.

I want to say "Hartelijk bedankt!" to the people of the hydromechanics section of the Delft University of Technology, The Netherlands for their kindness and hospitality during my stay in Delft. I also enjoyed many inspiring discussions particularly with dr. ir. B. van Prooijen, F. Maggi, and prof. dr. ir. W.S.J. Uijttewaal.

Special thanks go to A.C. Rummel for arduously carrying on the research topics, to M.E. Negretti for sharing my scientific enthusiasm, and to D. Schoppmann for having been a great office mate. My warmest thanks go to Dr.–Ing. Y.M. Lamour for the many miles of a socio-cultural and philosophical run. Much appreciated Dott. Ing. G. Lipari shared my musical passion helping to balance the scientific endeavor.

Finally I am deeply indebted and grateful to all those who accompanied me on my way—either for a while or for life. I am fortunate to have such family and friends still by my side. *You* are my solid ground, my lighthouse, my inspiration, my ever-full source.

Karlsruhe, May 2005

Carl F. Graf v. Carmer

Contents

1. Introduction 1

2. Phenomenology of Instability in Shallow Flow 7
2.1 Nature's repertoire of large vortical structures in shallow turbulent flow 7
2.2 Shallow shear flows 11
2.2.1 Definition of shallow shear flow 11
2.2.2 Large-scale vortical structures and quasi-2D turbulence . 14
2.2.3 Forcing mechanisms 15
2.2.4 Methods of investigation 17
2.3 Shallow turbulent wakes 19
2.3.1 Stability of shallow wakes 20

Part I. Non-Intrusive Flow Measurement Techniques for Coincident Data Acquisition of Velocity and Mass Concentration

Brief introduction to non-intrusive flow measurement techniques 29

3. Planar Measurement Systems 35
3.1 Particle Image Velocimetry 35
3.1.1 Introduction to PIV analysis 35
3.1.2 Technical equipment 37
3.2 Planar Concentration Analysis 39
3.2.1 Optical background and light attenuation 40
3.2.2 Data acquisition and pre-processing system for PCA 53
3.2.3 Data processing — transfer relation from light intensity to concentration 56
3.3 Synchronization of PIV and PCA measurements 66

4. Pointwise Measurement Systems 69
4.1 Laser Doppler Velocimetry 69
4.1.1 Introduction to optical background of LDV 70
4.1.2 Technical detail of the employed LDV system 75
4.2 Laser Induced Fluorescence 79
4.2.1 Introduction to fluorescence 80
4.2.2 Fluorescent tracer material 86
4.2.3 Analytical model for fluorescence intensity 92
4.2.4 Modelling various attenuation effects of a LIF signal 96
4.2.5 Verification and validation of an extended LIF model relation 104
4.3 Combined LDV-LIF system 114
4.3.1 Technical implementation of LIF to LDV 114
4.3.2 Equal interval re-sampling of LDV and LIF data 116

5. Experimental Set-up and Program 123
5.1 Shallow flow facility 123
5.2 Measurement program 126
5.2.1 Conducted measurement series 128
5.2.2 Classification of experimental observations 131
5.3 Characterization of base flow as plane turbulent shear flow . . . 134
5.3.1 Horizontal flow field 135
5.3.2 Vertical flow field 136
5.3.3 Spectral analysis in frequency domain 139
5.3.4 Mass transfer and mixing 141

Summary of Part I 144

Part II. Time-Mean Flow Characteristics of Shallow Turbulent Wakes

6. Theoretical Background of Turbulence and its Local Description 149
6.1 Introduction to time-series analysis 149
6.1.1 Correlation 149
6.1.2 Fourier analysis 151
6.1.3 Spectral Density 152
6.1.4 Discrete Spectral Analysis 153
6.2 Spectral description of turbulence 156
6.2.1 The energy cascade 156
6.2.2 Kolmogorov spectra of turbulent velocity fields 158

6.2.3 Spectra of passive scalar tracers 160
6.2.4 Spectra of 2D turbulent flows 162
6.3 Scales of turbulence 168
6.3.1 Macro scales of turbulence 168
6.3.2 Micro scales of turbulence 170
6.3.3 Micro scales of scalar fluctuations 174

7. Analysis of LDV-LIF Measurements in Wake Flows 177
7.1 Time series analysis of wake flow measurements 177
7.1.1 Time histories of LDV-LIF measurements 177
7.1.2 Correlation coefficients of measured data 180
7.1.3 Scales of turbulence 183
7.1.4 Downstream development of coherent and random transport of momentum and mass 190
7.2 Spectral density estimates in shallow wake flow 196
7.2.1 Spectral structure of turbulence in shallow wake flow . . . 198
7.2.2 Spectral density estimates for different shallow wake classes 202
7.2.3 Spectral density estimates for small- and large-scale turbulence 207

8. Integral Model for Shallow Wake Flow 211
8.1 Basic considerations 211
8.1.1 Transverse distribution of velocity and mass 211
8.1.2 Integral volume and momentum equations 213
8.1.3 Initial conditions for flux quantities 214
8.2 Conservation equations in far field of shallow wake 215
8.2.1 Momentum deficit flux equation 219
8.2.2 Flux equations for volume and tracer mass 221
8.3 Solution of the system of flux equations 223
8.3.1 Auxiliary relations for flux quantities 223
8.3.2 Set of flux equations 225
8.3.3 Non-dimensional set of conservation equations and their solutions 226
8.3.4 Model equations for velocity and mass fields in wake flow 227
8.3.5 Continuity equation in non-defect form 229
8.4 Application of integral far wake model 233
8.4.1 Sensitivity to variation of non-dimensional parameters . . 233
8.4.2 Comparison of prediction of momentum and volume deficit fluxes 238
8.4.3 Prediction of velocity and scalar fields 239
8.4.4 Discussion of model assumptions 245
8.4.5 Concluding remarks 251

9. Time-mean Description of Shallow Wake Flow 253
9.1 Time-mean evaluation of planar measurements 253
9.1.1 Transverse distribution of velocity and mass 253
9.1.2 Downstream development of velocity and mass 257
9.2 Linear stability analysis 262
9.2.1 Introduction to linear stability analysis 262
9.2.2 Stability regimes and flow classes 264
9.3 Local instability of shallow wake flows 268
9.3.1 Comparison of measurement and linear stability analysis 268
9.3.2 Control of wake instability 274

Summary of Part II 276

Part III. Large-Scale Coherent Vortical Structures in Shallow Wakes

10. Large-Scale Coherent Vortical Structures in Shallow Wakes 283
10.1 Identification of large coherent structures 284
10.1.1 Definition of coherent structures 284
10.1.2 Eduction scheme for LCS in shallow wake flow 285
10.2 Characteristic flow properties of large coherent structures 291
10.2.1 Topography of large coherent structures 291
10.2.2 Transient behavior of large coherent structures 304
10.2.3 Two–length–scale decomposition of velocity fields 309
10.2.4 Dynamics of shallow wakes — coherent and incoherent properties 313

11. Mass Transport due to Large Coherent Structures 331
11.1 Topography indicated by mass concentration 331
11.1.1 Coherent concentration fields 334
11.1.2 Incoherent concentration fields 336
11.1.3 Gradient of coherent concentration 340
11.1.4 Conceptual model for a vortex street-like shallow wake . . 342
11.2 Coherent mass transport 343
11.2.1 Experimental evaluation of coherent mass transport 343
11.2.2 Numerical Particle Tracking 347
11.3 Parametrization of large-scale coherent fluctuations 361
11.3.1 Mean scalar equation 362
11.3.2 Mean fields of coherent mass flux 364
11.3.3 Turbulent diffusivity and turbulent viscosity 364

Summary of Part III 368

12. Conclusions and Recommendations 371
12.1 Measurement techniques 371
12.2 Mean characteristics of shallow wakes 372
12.3 Large-scale coherent vortical structures in shallow wakes 374
12.4 Further perspectives 375

Appendix 377

A. Calculation procedure for spectral density estimates 377
A.1 Preparation of time series 377
A.2 Windowing and smoothing 378
A.2.1 Time domain weighting 378
A.2.2 Frequency domain smoothing 382

Bibliography 384

List of Figures

2.1 Atmospheric vortex street in the wake of Jan Mayen Island 8
2.2 Atmospheric vortex streets behind the Canary Islands and Guadalupe 9
2.3 Large-scale oceanic vortices 11
2.4 Forcing mechanisms for large vortical structures 16
2.5 VS and SB instability of shallow turbulent wake 24
3.1 Light matter interaction at molecular scale 32
3.2 Energy level diagrams of Raman and Rayleigh scattering 34

3.3 Concept of radiance L at a point 42
3.4 Absorption and scattering of pure water 45
3.5 Spectral sensitivity of human eye 49
3.6 Chromaticity diagram 51
3.7 Radiance field for shallow clear-water conditions 56
3.8 Photometric response of Amaranth E 123 solutions for different concentrations 57
3.9 Photometric response of *Tri-Active Red* solutions 59
3.10 Conceptual sketch of observed radiance components 63

4.1 Concept of Doppler effect for LDV 72
4.2 Measurement principle of LDV using a fringe model 73
4.3 General setup of the 2-component LDV system 76
4.4 Quantum-mechanical molecule model 82
4.5 Emission spectra of sulphorhodamine B 90
4.6 Characteristic fluorescence spectra of employed LIF tracers 91
4.7 Beam attenuation of incident light 106
4.8 Temperature sensitivity of quantum efficiency 108
4.9 Extended LIF model 111
4.10 Procedures for equal interval re-sampling of random data series . . . 120

5.1 View of shallow flow facility 123
5.2 Sketch of shallow flow facility 124
5.3 Examples of shallow wake flow stability classes 131

5.4 Stability number in Re_h–Re_D space 133
5.5 Stability diagram for shallow wakes 134
5.6 Vertical distribution of time-mean main velocity of base flow 138
5.7 Vertical distribution of standard deviations of base flow velocity . . 140
5.8 Typical 1D ESD estimates and auto-correlations of base flow 142
5.9 Spreading of passive tracer plumes in base flow 143

6.1 Schematic diagram of the energy cascade 158
6.2 Enstrophy and inverse energy cascades of forced 2D turbulence . . . 166
6.3 Inertial subranges of the kinetic energy and scalar cascades 168
6.4 Eulerian length scales of turbulence 172

7.1 Double-decomposition of time-resolved data 178
7.2 Auto-correlations of velocities and mass in VS wake 181
7.3 Auto-correlations of velocities and mass in SB wake 182
7.4 Integral time scales in VS wake 185
7.5 Variation of Strouhal number with wake stability parameter 187
7.6 Decay of TKE along axis of shallow wake flows 191
7.7 TKE and mass variance along axis of shallow VS wake 192
7.8 Coherent and random turbulence intensities in VS wake 193
7.9 Variance of coherent and random parts of mass transport 195
7.10 Example of 1-D power spectral distribution 197
7.11 Dual spectral turbulence structure of shallow shear flow 198
7.12 1D PSD estimates of velocity and mass in VS, UB, and SB wake . 203
7.13 1D PSD estimates in VS wake from triple-decomposed data 208
7.14 1D PSD estimates in VS wake from triple-decomposed data using linear scaling 209

8.1 Conceptual sketch for time-mean flow field of shallow wake 211
8.2 Longitudinal decay of normalized momentum and volume deficit fluxes 228
8.3 Approximation of normalized complete volume flux Q^* of far wake 232
8.4 Sensitivity of volume deficit flux Q_s to variation of bottom friction coefficient λ 235
8.5 Sensitivity of volume deficit flux Q_s to variation of wake strength R_m 236
8.6 Sensitivity of volume deficit flux Q_s to variation of entrainment coefficient α 237
8.7 Deficit fluxes for pure VS wake 240
8.8 Deficit fluxes for VS wake tending to UB 241
8.9 Characteristic flow properties for pure VS wake 243
8.10 Characteristic flow properties for VS wake tending to UB 244

8.11 Transverse distribution of normalized velocity deficit 246
8.12 Longitudinal development of entrainment coefficient 248
8.13 Transverse bottom shear in the transitional wake region 252

9.1 Transverse distribution of velocity deficit and mass concentration . 255
9.2 Transverse distribution of velocity deficit in near field of VS and UB wake 256
9.3 Comparison of wake spreading based on velocity deficit and mass . 258
9.4 Comparison of downstream development of flow in different wakes 259
9.4 Comparison of downstream development of flow in different wakes (con't) 260
9.5 Definition of local absolute and convective instability in shear flow 266
9.6 Absolutely and convectively unstable regions in wake flow 267
9.7 Experimental data compared to analysis of shallow wake stability . 270
9.7 Experimental data compared to analysis of shallow wake stability (con't) 271

10.1 Phase-resolved averaged flow fields for vortex street-like shallow wake 293
10.2 Phase-resolved downstream development of a vortex street-like shallow wake 296
10.3 Coherent streaklines in a phase–resolved averaged wake flow 298
10.4 Streamlines of a von Kaŕmaŕ vortex street 300
10.5 Coherent streamlines of a vortex street-like shallow turbulent wake flow 302
10.5 Coherent streamlines of a vortex street-like shallow turbulent wake flow (con't) 303
10.6 Evolution of a single LCS in a Lagrangian frame 305
10.7 Transient behavior of LCS 307
10.8 Coherent vorticity of vortex street-like shallow wake 313
10.9 Coherent shear strain rate of vortex street-like shallow wake 315
10.10 Divergence from horizontal coherent surface flow field 316
10.11 Visualization of the surface divergence field by particle floats 318
10.12 Turbulent kinetic energy from triple-decomposed surface flow field 321
10.13 Reynolds shear stresses from triple-decomposed surface flow field . 323
10.14 Coherent production of random turbulence for a distinct phase–interval 325
10.15 Turbulence production from triple-decomposed surface flow fields . 326
10.16 Longitudinal distribution of mean production of coherent and random turbulence 328

11.1 Phase-resolved averaged concentration fields for vortex street-like shallow wake 333
11.2 Streaklines observed in vortex street-like wake flows 337
11.3 Phase–resolved averaged rms concentration fields for vortex street-like shallow wake 339
11.4 Coherent distributions of mass concentration gradients 341
11.5 Conceptual sketch of coherent flow in shallow VS wakes 342
11.6 Phase-resolved averaged distributions of coherent mass flux 345
11.7 Total longitudinal coherent mass flux 346
11.8 Numerical particle tracking in coherent flow field 349
11.9 Distribution of floats from numerical particle tracking 355
11.10 Release of artificial floats for numerical particle tracking 356
11.11 Comparison of characteristic mean mass quantities of wake 358
11.11 Comparison of characteristic mean mass quantities of wake (con't) 359
11.12 Rates of mean and coherent transverse mass transfer 365
11.13 Transverse turbulent diffusivity and viscosity 366

A.1 Employed window functions and its FFTs 381

List of Tables

3.1 Employed non-intrusive measurement techniques 31

3.2 Instrumentation of the field-wise measurement systems for surface velocity fields (PIV) and for depth-averaged mass concentrations (PCA) 38

3.3 Approximate vacuum wavelength and frequency ranges for the various colors 49

4.1 Instrumentation of the point-wise measurement systems for flow velocity (LDV) and for mass concentration (LIF) 78

4.2 Inelastic molecular scattering processes 84

4.3 Fluorescent dye tracer employed for LDV-LIF measurements 89

4.4 Coefficients for extended LIF model 111

4.5 Error bounds of linear LIF model 113

5.1 The shallow flow facility—shallow flow basin, system control, and measurement equipment 127

5.2 Overview of conducted experiments 129

7.1 Macro and integral scales of time and length 186

7.2 Micro scales of time and length 189

7.3 Spectral density estimates in shallow turbulent wake flows 201

8.1 Conversion of commonly used definitions of wake half width 212

9.1 Downstream distances for transition among local stability regions . 274

List of Symbols

Latin

A_{opt}	aperture ratio of LDV receiving optics	–
D	diameter of cylindrical obstacle	m
D_m	molecular diffusivity of a mass species in a fluid	$m^2\ s^{-1}$
D_t	(large-scale) turbulent diffusivity of a species in the flow	$m^2\ s^{-1}$
E	irradiance (3.3)	$W\ m^{-2}$
Fr	Froude number $Fr = Q/A/\sqrt{gh}$	–
I	radiant intensity	$W\ sr^{-1}$
I_e	intensity of LIF excitation	$W\ sr^{-1}$
I_f	(observed) intensity of LIF fluorescence radiation	$W\ sr^{-1}$
K'	irradiance attenuation coefficient (3.10)	$\left(m\ kg\ m^{-3}\right)^{-1}$
L	radiance (3.1)	$W\ m^{-2}\ sr^{-1}$
$\mathcal{L}$	macro length scale of mean flow	m
M	specific momentum flux (8.6)	$m^4\ s^{-2}$
P	power spectral density distributed along frequency f, angular frequency ω, or wave number k_w	$a.u.$
$\mathcal{P}$	rate of turbulence production (6.18)	$m^2\ s^{-3}$
Q	volume flux (8.5)	$m^3\ s^{-1}$
Q	Weiss function (10.1)	s^{-2}
$R_{\phi\psi}(\tau)$	correlation function (6.2)	$a.u.$
Re_D	Reynolds number based on cylinder diameter D	–
Re_h	Reynolds number based on flow depth h	–
R_m	wake strength model–parameter (8.68a)	–
R_w	relative wake velocity difference (9.7b)	–
S	energy spectral density distributed along frequency f, angular frequency ω, or wave number k_w	$a.u.$
S	wake stability number (2.6)	–
S_0	bottom slope	–
S_f	energy (or friction) slope	–
S_g	gradient stability number (2.4)	–
S_{ij}	mean rate-of-strain (6.19)	s^{-1}
Sc	Schmidt number $Sc = \nu/D_m$	–

Sc_t	turbulent Schmidt number $Sc = \nu_t/D_t$	–
St	cylinder Strouhal number, $St = f\,D/U_a$	–
T	temperature	°C
$\mathcal{T}$	energy transfer rate along turbulence spectrum	$m^2\ s^{-3}$
T_P	periodicity of coherent flow field	s
TI	turbulence intensity	–
U	main component of time–mean flow velocity, $U = \langle u \rangle$	$m\ s^{-1}$
V	transverse component of time–mean flow, $V = \langle v \rangle$	$m\ s^{-1}$
a_m	entrainment model–parameter (8.68c)	–
b	length of LIF optical path in fluorophor solution	m
c	mass concentration	$kg\ m^{-3}$
c	light speed	$m\ s^{-1}$
c_f	bottom friction coefficient $c_f \equiv \frac{\lambda}{4}$	–
d_P	diameter of tracer particle	m
f	frequency	s^{-1}
g	gravitational acceleration (considered to be a constant)	$9.81\ m\ s^{-2}$
h	water depth	m
h	Planck's constant	$6.626\,10^{-34}\ Js$
k	turbulent kinetic energy (10.14)	$m^2\ s^{-2}$
k	specific logarithmic coefficient of absorbtion, cf. (4.9)	$\left(cm\ \mu g\ l^{-1}\right)^{-1}$
k_w	wave number $k_w = 2\pi/\lambda$	m^{-1}
ℓ	characteristic length scale of turbulence	m
ℓ_0	macro length scale of turbulence	m
ℓ_η	Kolmogorov's micro length scale of turbulence (6.57)	m
ℓ_{η_γ}	Batchelor's scalar micro scale (6.66)	m
ℓ_I	Eulerian integral length scale (6.42)	m
ℓ_λ	Taylor micro scale of turbulence (6.50)	m
ℓ_{λ_γ}	scalar micro scale of turbulence (6.64)	m
ℓ_M	integral wake length scale (9.1)	m
ℓ_{mv}	length of measurement volume of LDV-LIF system	m
m_T	temperature sensitivity coefficient, cf. (4.20)	–
n	index of refraction of a medium	–
n	width conversion factor for Gaussian profile, cf. Table 8.1	–
q_c	concentration quenching coefficient, cf. (4.21)	$m^3\ kg^{-1}$
r	(length of) optical path	m
r_γ	diffusion ratio based on wake half width, i.e. $r_\gamma = \delta_c/\delta_u$	–
$r_{\phi\psi}\,(\tau)$	correlation coefficient (6.3)	–
s_{ij}	fluctuating rate-of-strain (6.21)	s^{-1}
t	time	s
$\boldsymbol{u}$	velocity vector	$m\ s^{-1}$
u	main component of instantaneous flow velocity	$m\ s^{-1}$

$u_\star$	bed friction velocity (5.5)	$m\ s^{-1}$
u_s	deficit velocity of wake flow	$m\ s^{-1}$
v	transverse component of instantaneous flow velocity	$m\ s^{-1}$
w	vertical component of instantaneous flow velocity	$m\ s^{-1}$
x	longitudinal or main flow direction	–
y	lateral or spanwise direction (also called transverse)	–
z	vertical direction (not called transverse)	–
$z_\star$	viscous length, cf. (5.7)	m

Greek

Φ	radiant (i.e. photon) flux, cf. p. 41	W
Φ_f	quantum efficiency of fluorophor	–
α	entrainment coefficient (8.90), cf. (8.48)	–
α'	light absorbtion coefficient (3.6)	m^{-1}
β	velocity ratio with respect to light speed, cf. p. 71	–
β	enstrophy production rate, cf. (6.37)	s^{-3}
β'	light scattering coefficient (3.7)	m^{-1}
γ	specific weight $\gamma = \rho\, g$	$N\ m^{-3}$
γ'	light attenuation coefficient (3.8)	m^{-1}
δ	half-width of wake	m
ϵ	rate of viscous dissipation of TKE, (6.20)	$m^2\ s^{-3}$
ϵ_γ	dissipation rate of scalar variance (6.30)	$m^2\ s^{-3}$
ε	specific decadic extinction coefficient	$\left(cm\ \mu g\ l^{-1}\right)^{-1}$
ε_M	molar decadic extinction coefficient	$\left(cm\ M\ l^{-1}\right)^{-1}$
η_{opt}	transmissivity of LDV optical components in beam path	–
λ	Darcy-Weisbach friction coefficient given in Section 5.3.1	–
λ	wavelength of electro-magnetic radiation	m
ν	kinematic viscosity of a fluid	$m^2\ s^{-1}$
ν_t	turbulent (or eddy) viscosity of the flow, $\nu_t = \frac{\langle u'v' \rangle}{\partial U / \partial x}$	$m^2\ s^{-1}$
ρ	mass density	$kg\ m^{-3}$
σ_ϕ	root-mean-square (rms) value or standard deviation of quantity ϕ, e.g. for x velocity component $\sigma_u = \sqrt{\langle u^2 \rangle}$	$a.u.$
τ	time scale of turbulence	s
τ_0	macro time scale related to low-frequent coherent flow	s
τ_b	bottom shear stress (5.5)	$N\ m^{-2}$
τ_I	Eulerian integral time scale (6.45)	s
τ_η	Kolmogorov's micro time scale (6.57)	s
τ_λ	Taylor micro time scale (6.55)	s
τ_{ij}	shear stress (10.11)	$N\ m^{-2}$

ϕ	half angle of beam intersection in LDV measurement volume	$^\circ$
ϕ	phase angle of phase-correlated flow field	rad
ϕ_m	bottom friction model–parameter (8.68b)	–
ψ	streamfunction defined by (10.3)	$m^2\ s^{-1}$
ω_i	i-component of vorticity vector $\boldsymbol{\omega}$	s^{-1}
ω	angular frequency $\omega = 2\pi f$	$rad\ s^{-1}$

Subscripts

$_\eta$	Kolmogorov's micro-scales of turbulence
$_\gamma$	with respect to a passive scalar tracer
$_0$	initial (upstream, inflow) conditions
$_F$	quantity with respect to fluid
$_P$	quantity with respect to particle
$_a$	ambient (or undisturbed) flow field conditions
$_c$	value at the wake centerline (i.e. $y = 0$)
$_f$	regarding fluorescence
$_l$	longitudinal (or main) component of flow property
$_p$	phase–resolved averaged, periodic, coherent part of decomposed quantity using a double-decomposition (10.4), e.g. $u_p = u - u_r$, where $u_p = \{u\}$
$_{\overset{\star}{p}}$	coherent part of a quantity using a triple-decomposition (10.5)
$_r$	random or residual part of decomposed quantity, e.g. $u_r = u - u_p$
$_s$	deficit quantity of wake flow
$_t$	transverse (i.e. lateral or spanwise) component of flow quantity
$_x$	longitudinal or main component of quantity
$_y$	lateral or spanwise component of quantity (also called transverse)
$_z$	vertical component of quantity (not called transverse)

Superscripts

*	normalization of longitudinal profile by corresponding initial value, e.g. $u^*(x,y) = \frac{u(x,y)}{u(0,0)} = \frac{u(x,y)}{u_0}$
$^+$	normalization of transverse profile by corresponding centerline value, e.g. $u^+(x,y) = \frac{u(x,y)}{u(x,0)} = \frac{u(x,y)}{u_c(x)}$

Symbols

$\langle\ \rangle$	ensemble average (4.25)
$\langle\ \rangle_t$	time average (4.26)
$\{\ \}$	phase–resolved average, e.g. $u_p = \{u\}$
$\tilde{}$	phase–resolved averaged quantity, i.e. quantity derived from phase–resolved averaged velocity fields
$\bar{}$	spatially averaged quantity, e.g. the main velocity component averaged along s is $\bar{u} = \frac{1}{\ell}\int_0^\ell u\,(s)\,ds$
$'$	instantaneous deviation of a quantity from its ensemble mean value, e.g. for the fluctuating main velocity $u' = u - \langle u \rangle$

Abbreviations

2D	Two-Dimensional
3D	Three-Dimensional
DNS	Direct Numerical Simulation
ESD	Energy Spectral Density
LCS	Large-scale Coherent Structure
LES	Large Eddy Simulation
LDV	Laser Doppler Velocimetry
LIF	Laser Induced Fluorescence
PCA	Planar Concentration Analysis
PDF	Probability Density Function
PIV	Particle Image Velocimetry
PSD	Power Spectral Density
RANS	Reynolds-Averaged Navier-Stokes Equations
RGB	Red Green Blue color space
SWE	Shallow Water Equations
TKE	Turbulent Kinetic Energy

1. Introduction

Shallow shear flows. Free-surface flows and open waters in the natural environment can be regarded as shallow shear flows, such as wide rivers, estuaries, stratified lakes, and coastal seas. Shallow flows occur also on geophysical scale in the stratified atmosphere or in the upper ocean. Shallow flows are characterized by horizontal length scales much greater than the flow depth. In environmental shallow flows vertical shear is usually introduced by bottom friction along the fixed bed or by wind shear along the free surface, the vertical boundary layer extends over the full flow depth.

Boundary layer shear flows can be destabilized by a sudden change in the topography, but also by a horizontal velocity shear, or by global deceleration of the flow. Due to a large single obstacle a disturbance can be introduced in the shallow near-equilibrium vertical shear flow. Large, predominantly two-dimensional eddies can alternately shed off from the obstacle, and advect downstream. Although an unbounded plane lateral shear flow is inviscidly unstable, in shallow wakes due to the limited vertical extent, the large-scale eddies are not affected by three-dimensional vortex stretching mechanisms. By virtue of the bottom–induced vertical shear, the disturbance can be stabilized, and the kinetic energy of the large eddies can be dissipated.

In Chapter 2, we illustrate the different types of environmental shallow shear flows and the associated large-scale vortical structures from a compilation of laboratory and field observations. We also report major research contributions, and discuss the main concepts for the investigation of shallow wakes.

Shallow wake flows can be induced either by man-made obstacles (like groynes, discharge structures, working platforms, or pylons of wind turbines) or by natural changes in the bathymetry (like islands, headlands, or dunes). Due to the large-scale coherent vortices introduced by the obstacle, the transport and exchange processes in the base flow will be altered significantly. For the prediction and evaluation of the impacts of water resources management or structural engineering activities on the environmental water bodies, improved knowledge about the processes associated with shallow wake flow is needed.

Objectives. The main objectives of this project can be summarized in three categories.

Experimental methods: To investigate shallow turbulent wake flows in the laboratory, an experimental facility, measurement techniques and devices are needed, which are specifically adapted to the geometrical restrictions (large horizontal vs. small vertical extent) and the wide dynamic range of shallow shear flows. Whereas commercial optical measurement systems for flow velocities are easily adjustable to these needs, the quantification of mass concentrations requires the development or significant improvement of techniques based on the observation of irradiance from the concentration field and its evaluation with respect to the light attenuation due to various physicochemical and/or optical reasons. In order to access the mass fluxes, synoptic measurements have to be ensured, or synchronization of data has to be ascertained.

Mean characteristics of shallow wakes: The effects of shallowness and bottom friction significantly change the flow properties of shallow wakes with respect to unbounded 2D wake flows. The time-mean wake flow fields, the stochastic description of turbulence, and its flow stability will reflect the additional kinematic and dynamic effects.

Large-scale coherent vortical structures: Horizontal vortical structures with a lateral dimension much larger than the flow depth are regarded as key features in the understanding of the transport of kinetic energy and mass in shallow wakes. Its generation and decay mechanisms as well as the interaction of the large coherent structures with the small-scale shear–induced turbulence have to be clarified experimentally. Its influence on the transport of TKE and mass has to be quantified.

Contributions. Major contributions of this project can be related to the main objectives listed above. Regarding the experimental methods, a fully equipped and automated shallow flow facility has been designed and realized at the Institute for Hydromechanics, University of Karlsruhe. An on-axis backscatter LIF measurement system with an extended measurement range has been added to the 2D LDV system, hence both the flow velocities and the mass concentrations of a fluorescent dye tracer can be obtained simultaneously with high spatiotemporal resolution. A Planar Concentration Analysis (PCA) technique has been developed on the basis of a hydro-optical attenuation model to obtain field-wise depth–averaged mass concentrations. In the post-processing, an adaptive phase–resolved averaging technique has been established in order to decompose the velocity and mass data into low-frequent quasi-periodic motion and random turbulence parts of the flow. This allows to correlate the quasi-periodic coherent mass fields to the appropriate near-surface velocity fields, provided by a PIV measurement system.

The turbulence spectra reveal, at the low wave number scales, a spectral transfer of turbulent kinetic energy and mass variance toward higher wave numbers following a -3 enstrophy cascade of 2D turbulence. The complementary transfer toward lower wave numbers along an inverse energy cascade is absent, i.e no merging of vortices occurs at the large scales. At the high wave numbers, the spectral transfer in the inertial–convective subrange of 3D isotropic turbulence is observed. The scale duality of shallow turbulent wake flow, thus, is evidenced from the turbulence spectral distributions. An analytical far wake model, including the effect of bottom friction, has been deduced that predicts the downstream development of the time-mean flow field of shallow wakes. The comparison of experimental data to results of a linear stability analysis identifies local instability regions, and indicates a strong decrease of the convectively unstable region compared to unbounded 2D wake flows.

Decomposition of the field-wise velocities and mass concentrations into their large-scale coherent and small-scale random parts allowed to localize regions of kinetic energy production and of enhanced mixing and entrainment. Using a structure identification scheme based on vorticity and shear strain, the large-scale 2D vortical structures have been identified in the coherent flow fields. The structure and dynamic behavior of a wake flow organized in a vortex street have been illustrated as well as the generation and decay of the associated coherent vortical structures. These are also highly relevant in the production of TKE and in the mass transfer. To predict the depth–averaged mass concentrations from surface velocity fields, a numerical particle tracking procedure has been developed that makes use of given coherent velocity fields together with a small-scale 3D turbulence model. The importance of the secondary motion of the large-scale vortices for the lateral mass transfer has been demonstrated.

Outline. This study is organized into three main parts that discuss (I) non-intrusive flow measurement techniques for the coincident data acquisition of velocity and mass, (II) the time-mean flow characteristics of shallow turbulent wakes, and (III) large-scale coherent vortical structures in shallow wakes. Because of the wide range of topics and the resulting voluminous size of the report, the reader is encouraged to concentrate on the most interesting part of the report, and eventually follow some cross–references to related subjects in the other parts of this work. The author felt it desirable to give concise information also of the technical and physical background in order to improve the understandability of this report. Some readers may find it useful to obtain more detailed background information organized in textbook–like chapters and paragraphs throughout this book, although in turn the style and range of a technical report will be exceeded. The reader is encouraged to skip such textbook–like paragraphs, if no additional information is needed.

Preceding the main parts of the report, in Chapter 2 shallow shear flows and shallow wakes are introduced, major research contributions are reported, and the main concepts for the investigation of shallow wakes are discussed.

Part I is initialized by a short introduction to non-intrusive flow measurement techniques. The planar and point-wise optical measurement techniques, developed and employed for this projected, are described in detail in Chapters 3 and 4, respectively. Both for the LDV/LIF and the PIV/PCA systems, besides the technical information, emphasize is given to the conceptual and physical background for the development of the model equations for the fluorescence and for the hydro-optical light attenuation. In Chapter 5 the shallow flow facility is introduced, the measurement program is summarized, and the base flow—a plane near-equilibrium bottom friction–induced turbulent shear flow—is characterized by its mean flow and turbulence.

To open Part II, in Chapter 6 the theoretical concepts of homogeneous 3D turbulence and of 2D turbulence are reviewed with respect to the spectral distribution both of turbulent kinetic energy and of mass variance. Characteristic macro and micro scales of length and time are reported that reflect the ambiguity of 2D and 3D turbulence. In Chapter 7 the conclusions of the theoretical considerations are applied to the high resolution LDV/LIF data. Time scales and corresponding length scales of turbulence are calculated for the different wave number regimes. Spectral density estimates for TKE and mass variance are computed from the full data sets, but also from data, which have been decomposed into 2D quasi-periodic and 3D random turbulent parts. In order to describe and to predict the mean flow properties, in Chapter 8 an analytical wake model is derived from the integral conservation equations of momentum and volume deficit and of mass. Its range of applicability is confirmed from field-wise flow measurements. The results of a linear stability analysis are related to experimental observations of laboratory wake flows with different wake stability numbers. Thus, in Chapter 9 the local regions of absolute and convective instability have been identified in shallow wakes.

In Part III, devoted to large-scale coherent vortical structures in shallow wakes, Chapter 10 gives a definition for large coherent structures, and presents a phase–resolved averaging technique to extract the coherent quasi-periodic flow field as well as an identification scheme to educe the vortical structures. The generation of the large coherent structures, its organization and downstream decay are described as well as the dynamics of shallow wakes that are introduced by the interaction of the large coherent structures with the small-scale incoherent fluctuations. The mass transport due to these large-scale vortices is addressed in Chapter 11. The coherent and incoherent field-wise distributions of mass concentrations are obtained from a phase–resolved averaging, and are related to the coherent velocity fields and to the large-scale vortical structures. The coherent mass transport is evaluated and compared to results

of a numerical particle tracking that allows to predict the mass transport from a given set of coherent surface velocity fields.

In Chapter 12 we conclude with a brief summary of the main results. Further perspectives for future work are given that may help to elaborate and further develop the findings of this project as to meet the needs of applied science and engineering applications.

2. Phenomenology of Instability in Shallow Flow

Shallow turbulent flows are ubiquitous in nature. Many environmental flows can be characterized by horizontal length scales $\mathcal{L}$ much greater than the flow depth h, i.e. $h \ll \mathcal{L}$. Due to a large single obstacle like a small island, a disturbance is introduced in the shallow near-equilibrium vertical shear flow. Large, predominantly two-dimensional eddies can alternately shed off from the obstacle and advect downstream. Although an unbounded plane lateral shear flow is inviscidly unstable, in shallow wakes due to the limited vertical extent, the large-scale eddies are not affected and disintegrated by three-dimensional vortex stretching mechanisms. By virtue of the bottom–induced vertical shear, firstly, the disturbance can be stabilized, and secondly, the kinetic energy of the large eddies can be dissipated.

2.1 Nature's repertoire of large vortical structures in shallow turbulent flow

Observations of large-scale quasi-2D vortical structures in shallow turbulent flow are well-documented in the meteorological and geographical literature over the past 4 decades. Besides inland and coastal flows with a limited water depth due to the solid bottom, we encounter shallow flow conditions also in geometrically deep situations. In the deep oceans or the near-surface atmosphere we often observe density stratifications, which again restrict the vertical extent of the flow.

Atmospheric wake flows. For a number of isolated islands around the world, the appearance of large-scale eddy structures often arranged in a vortex street is reported occasionally. In general, the air flow in an atmospheric convective boundary layer (CBL) covered by a stably stratified layer is forced to flow around an isolated obstacle extending over the whole height of the lower CBL. In the lee of the island obstacle the flow is destabilized, and large eddy structures are generated, which are imprinted onto the cloud cover at the inversion on top of the CBL.

Berger & Wille (1972), as well as Chopra (1973), summarized the first analytical explanations and the early observations from satellite images. Fol-

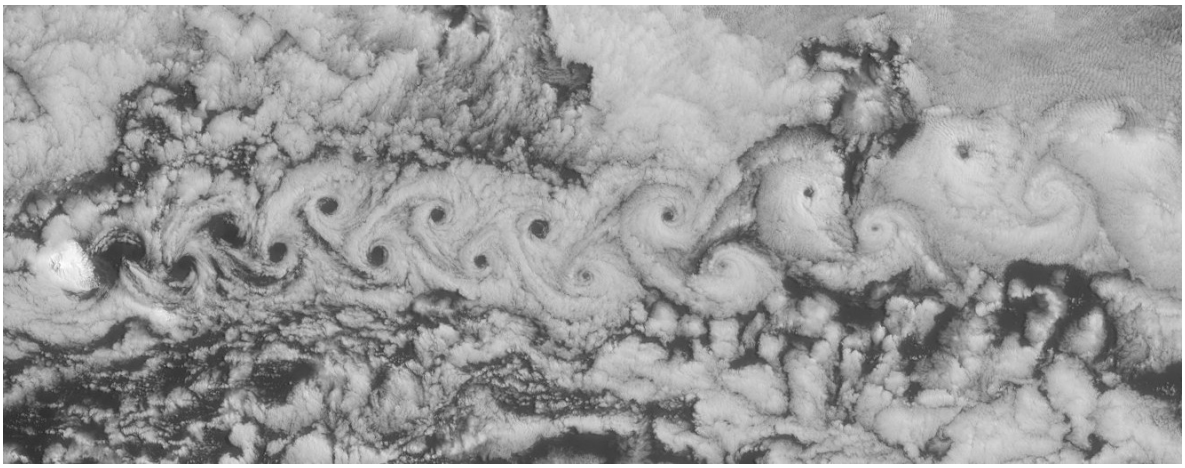

Figure 2.1. This over 300 km long atmospheric vortex street in the wake of Jan Mayen Island about 650 km northeast of Iceland in the North Atlantic Ocean was captured on June 6, 2001 from the "Terra" observer. The snow-covered Beerenberg volcano, which appears on the left of the image, rises about 2.2 km above sea-level, providing a significant impediment to the wind flow. (`http://photojounal.jpl.nasa.gov/tiff/PIA03448.tif`)

lowing Berger & Wille (1972) and Etling (1990), the first observations on periodic separation of horizontal vortices were made by the Norwegian meteorological station on the arctic island of *Jan Mayen* in the 1930s. Simply because of their large horizontal dimensions, atmospheric vortex streets are not accessible from terrestrial or airborne observations, thus they were frequently identified only since the 1960s from satellite images. Etling (1989, 1990) discussed recent concepts for the emergence of atmospheric vortex streets behind cone-shaped islands with a special focus on the so-called *dividing streamline concept*. As extracted from field data by Etling (1989), necessary preconditions for the generation of a vortex street pattern is (i) a stable stratification of the lower atmosphere always combined with a low elevated inversion, and (ii) the disturbance of the flow due to an isolated obstacle, that is significantly higher than the inversion height. Prominent examples are found in the trade-wind zones: the island of *Madeira* and the *Canary Islands* in the Atlantic Ocean (e.g. Chopra, 1973) (see Figure 2.2(a)), the island of *Guadalupe* near Baja California (Etling, 1990; Klingholz, 1997) (see Figure 2.2(b)), the *A. Selkirk Island* near the Robinson Crusoe Islands off the Chilean coast (DeFelice et al., 2000), and the *Hawaiian Islands* in the Pacific Ocean. On the other hand, CBLs can often be observed in the Polar regions, isolated islands here are *Jan Mayen* northeast of Iceland in the North Atlantic Ocean (Scorer, 1986; NASA, 2002; Spiegel Online, 2002) (see Figure 2.1), the *Aleutian Islands* near Alasca in the North Pacific Ocean (Thomson et al., 1977), or *Cheju* off the Korean coast.

Oceanic wake flows. Also in coastal waters obstructions of the shallow (evtl. tidal) flow due to islands or headlands induce wake flows of different stabil-

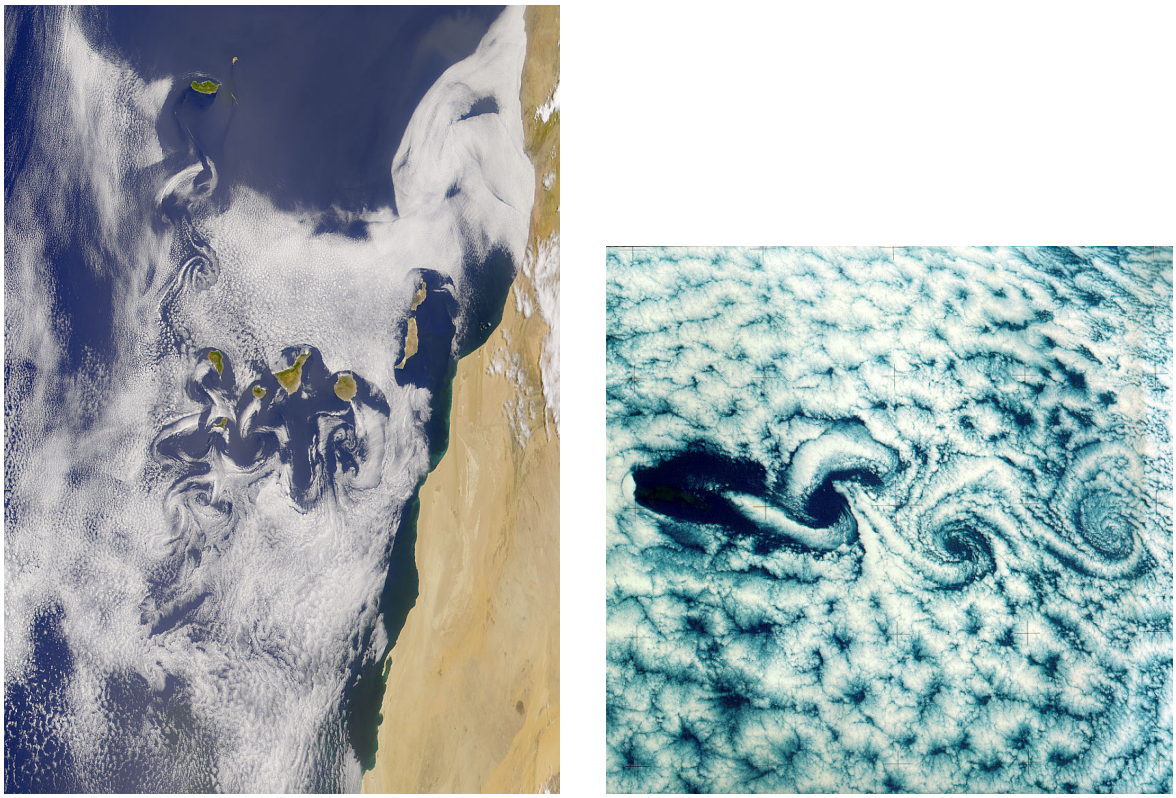

(a) Madeira and the Canary Islands (b) Island of Guadalupe near Baja California

Figure 2.2. (a) The vortex street patterns behind Madeira (located in the upper left corner of the image) and the Canary Islands show significant interaction and annihilate each other for the given air flow conditions. Contrarily, for an only slightly different wind direction parallel vortex streets emanating from the Canaries can be observed over long distances without cancellation. (`http://visibleearth.nasa.gov/data/ev25/ev2532_S2000156133525.png`) - (b) An atmospheric vortex street (length more than 250 km) in the lee of Guadalupe off the Mexican coast was observed on July 28, 1973 from a height of 435 km (Klingholz, 1997, p. 34).

ity regimes. Thus, also large-scale vortical structures can emerge from such obstacles under certain flow conditions. Qualitative information of the wake pattern in shallow coastal flows can be obtained from airborne and satellite infrared images, or from pattern recognition of satellite images of flows exhibiting a turbidity pattern due to suspended sediments or biological markers like phytoplankton.

Wolanski et al. (1984) reviewed the early field observations, but also analyzed the wakes of Australian coral reefs (esp. *Rattray Island*) from enhanced sediment turbidity images and radar, and employed more quantitative oceanographic methods like moored current meters and sea level, salinity and temperature surveys. Other field studies using airborne photographs were carried out e.g. by Ingram & Chu (1987) for islands in *Ruppert Bay*, Northern Ontario, by Cramp et al. (1991) for *Flat Holm* in the Severn Estuary of the

Bristol Channel, or by Ferrier et al. (1996) for a rocky island *The Battery* in the River Tay estuary. Another example for quantitative field studies are ADCP[1] measurements of tidal flows around a headland conducted by Geyer & Signell (1990); Geyer (1993) in the *Vineyard Sound*, Massachusetts.

Especially the works of Wolanski et al. (1984); Ingram & Chu (1987) also serve as test cases both for laboratory simulations (cf. e.g. Ingram & Chu, 1987; Wolanski et al., 1996) and for numerical models (e.g. Furukawa & Wolanski, 1998; Wolanski et al., 1996). The stability of the flow past headlands was studied in the field and laboratory e.g. by Pattiaratchi et al. (1986) and numerically by Davies et al. (1995).

Albeit in the majority of observed shallow wakes the ambient flow is destabilized by natural geometrical obstacles like islands or headlands, also anthropogenic alterations of the bathymetry due to technical structures can induce unstable wake flows and shallow vortex streets. A spectacular example is the wake of a grounded tanker presented by van Dyke (1982, p. 100). The crude oil spilled by the *Argo Merchant*, that went aground on the Nantucket shoals in 1976, formed a vortex street-like wake pattern, though the Reynolds number was $Re_D \approx 10^7$. On smaller scales the recent installations of off-shore wind farms with multiple generators will introduce wakes behind the pylons, which in the case of shallow flow conditions may be 2D and very persistent on the larger scales. They eventually will become unstable and arrange in vortex streets (Lass, 2002), and thus may influence also the coastal aquatic environment.

Large-scale vortical structures. In coastal seas large whirling flows with a vertical vorticity vector exist, which are primarily shed from solid obstacles disturbing the base flow. Large-scale vortices, so-called *tidal vortices* were observed all over the world since ancient times in narrow straits with high tidal flow velocities. As famous classical examples for tidal vortices that are advected by the base flow, Lugt (1979, pp. 366) mentioned the *Charybdis* of Homer's Odyssee in the Strait of Messina east of Sicily, and the *Maelstrom* in the Norwegian Lofoten Islands. The probably strongest tidal vortices are encountered in *Naruto Strait* connecting a large lagoon to the Japanese Sea, they shed from the southern headland into the tidal flow of the strait (maximum current speed 4.6 m/s, maximum difference of tidal sea levels across street: 1.5 m). Chanson (2002) reported of an freighter, which accidentally became caught in the vortices and got stranded during his visit (cf. Figure 2.3(a)). Very large vortices with a life time of several years can be observed in the Pacific Ocean off the coast of British Columbia and

[1] Acoustic Doppler Current Profiler

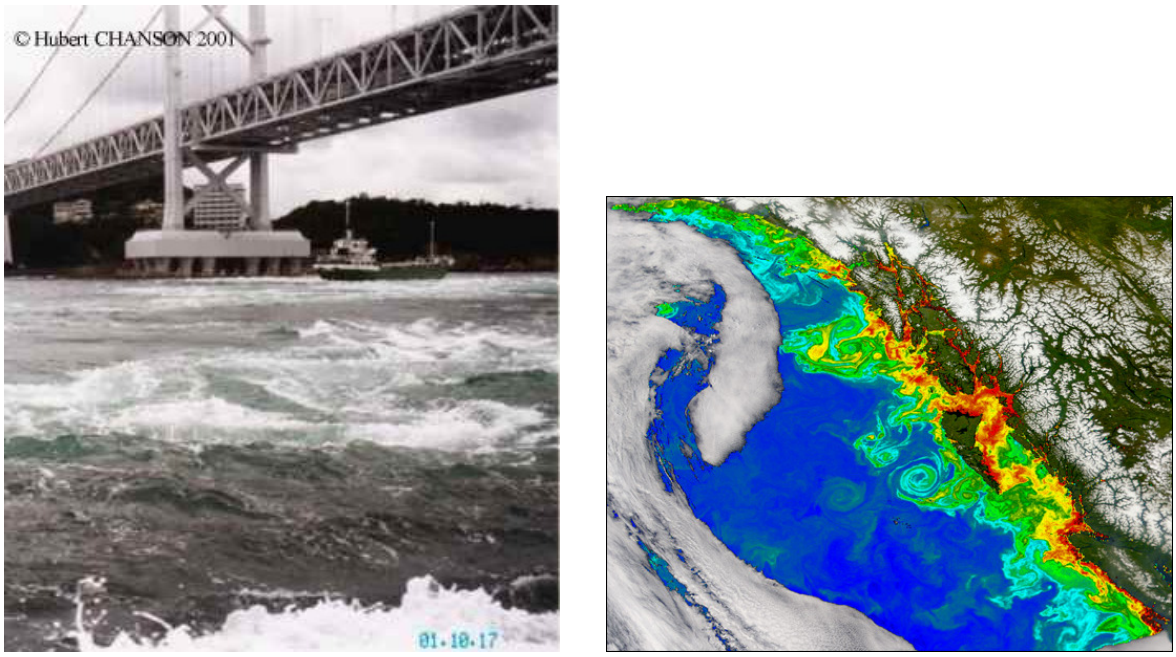

(a) Tidal vortices shedding into Naruto Strait

(b) Phytoplankton indicating large vortices off British Columbia

Figure 2.3. (a) The tidal whirlpools in the Naruto Strait, Japan, caught a freighter, that got grounded near the bridge pier. In the foreground of the image a large vortical structure (diameter up to 15 m) is visible. (`http://www.uq.edu.au/~e2hchans/whirlpl.html`) - (b) The bright red, green, and turquoise patches to the west of British Columbia's Queen Charlotte Islands and Alaska's Alexander Archipelago highlight the presence of biological activity in the ocean. These colors indicate high concentrations of chlorophyll, the primary pigment found in phytoplankton. Notice that there are a number of eddies visible in the Pacific Ocean in this pseudo-color scene. The eddies are formed by strong outflow currents from rivers along North America's west coast that are rich in nutrients from the springtime snowmelt running off the mountains. This nutrient-rich water helps stimulate the phytoplankton blooms within the eddies. (`http://visibleearth.nasa.gov/cgi-bin/viewrecord?13572`)

Alaska (cf. Figure 2.3(b)), they are subject of the TOPEX/Poseidon mission (`http://earthobservatory.nasa.gov/Study/Eddies/`).

2.2 Shallow shear flows

2.2.1 Definition of shallow shear flow

Shallow wake flows being the subject under consideration in this research report, belong to the class of shallow shear flows, which we can understand to result from the interaction of a turbulent *vertically sheared base flow* (vertically bounded frictional flow) and a *free horizontal shear flow* (unbounded plane flows like mixing layer, jet, or wake).

Flow classification. An *unbounded plane shear flow* is characterized in its time-mean flow field by a predominately uni-directional flow U_1, which is

sheared in the transverse direction $\partial U_1/\partial x_2$, whereas it is homogeneous in the third dimension, i.e. $\partial/\partial x_3 = 0$. Thus, it can be considered a free 2D flow in its time-averaged flow quantities, though its instantaneous turbulence behavior is of course clearly 3D in the higher order wave numbers. Plane mixing layer flows, plane jets, and plane wake flows are prominent examples discussed in many text-books of hydromechanics and turbulence, e.g. Pope (2000, Chapter 5) gives a thorough overview about these free shear flows. In their far field, i.e. farther away from an initial disturbance of the base flow, free shear flows turn out to be *self-sustaining* in terms of momentum conservation. Additionally, they reveal a *self-similar* behavior in their far fields, i.e. when non-dimensionalized by local characteristic scales, their behavior is independent of the downstream position.

The base flow (liquid) can be confined in its vertical extent either by a solid wall of a given roughness (liquid - solid), by a free surface (liquid - gaseous), or by a density stratification (liquid - liquid). The *influence of boundaries on turbulent free shear flows* is two-fold depending on the type of boundary interaction. Firstly and from purely kinematic reason, every fluid boundary will reduce or suppress the turbulent (Reynolds) normal stresses $\langle w'w' \rangle$ perpendicular to the boundary, consequently (due to continuity or conservation of momentum) the tangential normal stresses will be amplified. Secondly, if a "no-slip" condition has to be assigned to the boundary, i.e. viscosity induces a sheared flow near an interface, esp. near a solid rough wall, an additional dynamic damping of these turbulent fluctuations occurs.

Provided a sufficiently high Reynolds number, viscous *boundary layer flows* exhibit an "inertial subrange" of wavenumbers k_w in their turbulence spectrum, through which energy is transferred at a rate $\propto k_w^{-5/3}$ from the production range (TKE contained in large eddies with low k_w) to the dissipation range (where viscous effects dominate eddy motions down to the Kolmogorov length scale ℓ_η). According to Kolmogorov's first similarity hypothesis (Pope, 2000, pp. 185), the turbulence statistics in the "universal equilibrium range", consisting of the inertial subrange and the dissipation range, depend uniquely on dissipation rate ϵ and molecular viscosity ν regardless of the type of flow. On the contrary, the energy-containing large eddies of the production range, and thus the appropriate statistics, vary in different flow configurations.

In different *shallow shear flows* the large-scale vortical structures of the production range, therefore, have to be examined explicitly, whereas we expect the small-scale turbulent motion not to change for different types of shallow shear flow. Furthermore, because of the amplification of the horizontal normal stresses due to vertical boundaries, also the horizontal growth rates of shallow shear flows significantly exceed the growth rates of their unbounded relatives. Moreover, large-scale vortical structures with vorticity vectors orientated per-

pendicular to the interfaces may be introduced into a shallow flow and may grow following an "inverse energy cascade" and decay obeying the laws of "2D" turbulence.

Further restrictions. Throughout this work we will firstly neglect *geostrophic flows* by excluding the influence of the Coriolis force on the flow due to the earth's rotation Ω, i.e. we restrict this work to flows, for which the typical largest length-scale is significantly below the Rossby radius, i.e. $L_\Omega \gg \mathcal{L}$.[2] Secondly, we will restrict the base flow or inflow condition to nearly *uniform plane shallow flows*, thus we are excluding any effects due to variation in bathymetry and due to flow curvature, which implies any secondary currents e.g. in river bends or in corners of compact channel cross–sections. Though this assumption seems to be crude, there might be some justification due to the limited area of investigation, if we look at the flow variations only in those flow regions deviating significantly from the shallow base flow conditions, or even more strict, if we look at variations of the shallow base flow only over the travel distance of a large-scale eddy structure.

Since we want to understand real-world flows being highly *turbulent* in general, we examine flows with—as a characteristic non-dimensional quantity—a bulk Reynolds number $Re = U\,h/\nu$ of the magnitude $\mathcal{O}\left(10^3\right)$ or larger, where U is the bulk mean main-velocity component, and ν is the kinematic viscosity. It is not always easy to achieve such high Reynolds numbers in shallow flow in the laboratory.

The viscous fluid is subjected to shear stresses at the bottom equipped with a given geometrical roughness, which might be small, but finite. This results in a vertical variability of the flow velocity, which for the time-mean values of the main flow component is described by the theoretically and empirically well-founded logarithmic law of boundary layer flow. The structure of turbulence in such flow is dominated by the mechanisms of generation and decay of *small-scale 3D turbulence* in a turbulent boundary layer. For instance, Kelvin-Helmholz instabilities generated in the near wall viscous sublayer introduce vortical structures into the turbulent shear flow via vortex stretching mechanisms, where they are continuously stretched and disintegrate into smaller structures. Therefore, near the bottom energy is extracted from the mean flow due to production of turbulent kinetic energy (TKE), close to the surface the dissipation

[2] The *Rossby number Ro* relates the nonlinear convective acceleration to the Coriolis force, $Ro \sim \frac{U^2/L}{f_\Omega U} = \frac{U}{f_\Omega L}$, where U and L are characteristic flow scales and $f_\Omega = 2\Omega \sin\theta$ is the *Coriolis frequency*. For small $Ro \leq \mathcal{O}(1)$ the earth's rotation significantly influences or even dominates the flow. The *Rossby radius* being a length scale, where Coriolis forces become important to the flow, can thus be estimated to be $L_\Omega \geq \frac{U}{f_\Omega}$. For instance, for a latitude of $\theta = 50°$ and a typical riverine flow velocity of $U \approx 1.0\,m/s$, $L_\Omega \geq \frac{1.0\,m/s}{2\Omega \sin 50°} \approx 9\,km$ with $\Omega = 2\pi/24\,h = 7.29 \cdot 10^{-5}\,s^{-1}$.

rate exceeds the turbulence production. The re-organization and transfer of TKE in the spectral distribution of the turbulent fluctuations down to smaller wave numbers k_w (the so-called *"energy cascade"*) reveals the well-known $-5/3$ power law in the wave number spectrum $S(k_w) \propto k_w^{-5/3}$ of isotropic 3D turbulence, given a sufficiently high Re. For more detail on the structure of boundary layer turbulence the reader is referred to turbulence textbooks like Lesieur (1997) or Schlichting & Gersten (1997), the broad variety of turbulent features in rivers including also larger-scale structures is thoroughly discussed by Nezu & Nakagawa (1993).

2.2.2 Large-scale vortical structures and quasi-2D turbulence

This turbulent shallow base flow, which we want to regard as uniform or at least nearly uniform, may be disturbed locally at sudden changes of the boundary geometry, for instance by a blunt obstacle mounted on the channel floor. It can also be subjected to continuous disturbances distributed over a larger part of the flow domain, like dunes on a river bottom or a gradual change in the bathymetry, e.g. in depth. Besides this convective variations also local changes of the flow, like a decelerating tidal current, may induce disturbances to the base flow. These initial disturbances can sustain oscillations, that reorganize the kinetic energy of the flow and may grow into large-scale eddy structures. The horizontal extent $\mathcal{L}_{LCS}$ of these vortical structures is significantly larger than the water depth, i.e. $\mathcal{L}_{LCS} \gg h$. Obviously from kinematic reason, the vorticity vectors of such large vortical structures are orientated vertically, i.e. perpendicular to bottom and free surface.

Therefore, we can expect eddy structures to behave essentially two-dimensional on the larger scales, and not to show any depth-dependent flow variations despite in a thin viscous boundary sublayer close to the bottom. We address this large-scale behavior of turbulent fluctuations in shallow flows as quasi "*two-dimensional*" turbulence induced by large-scale *two-dimensional* vortical structures. Of course, also these large-scale 2D structures show the spectral behavior of 3D turbulence in the larger wave number range, i.e. higher frequency range, resulting from high-frequency fluctuations and small-scale coherent turbulence structures. Contrary to the mechanisms of 3D turbulence, vortex stretching mechanisms of the classical energy cascade are suppressed in the wave number range of large-scale 2D turbulence. Instead, vortex pairing or merging of eddies with the same sense of rotation may even lead to growth of the 2D vortical structures, thus spectral energy will even be transferred to lower frequencies or larger wave numbers via the so-called "*inverse energy cascade*".

2.2.3 Forcing mechanisms

Mean advective kinetic energy is extracted from the base flow by an initial transverse shear and is translated into turbulent kinetic energy at different wave number ranges depending on the type of shear. In shallow turbulent flow, a significant amount of TKE is incorporated into the large-scale vortical structures of the low-frequency 2D turbulence, that emerge into the flow from the initial shear. Within these large-scale eddies, the low-frequency turbulent fluctuations are represented by vertical vorticity ω_z.

According to Jirka (1998, 1999, 2001), one can define three types of *generation mechanisms* for large-scale vortical structures, listed in order of their strength:

> "Type A: Topographical forcing: This is the most severe generation mechanism in which topographic features (islands, headlands, jetties, groynes, etc.) lead to local flow separation, formation of an intense transverse shear layer and return velocities in the lee of the feature."

> "Type B: Internal transverse shear instabilities: Here velocity variations in the transverse directions that exist in the shallow flow domain give rise to the gradual growth of 2DCS [i.e. 2D Coherent Structures]. Such lateral velocity variations can be caused by a number of causes: due to source flows representing fluxes of momentum excess or deficit (shallow jets, shallow mixing layers, shallow wakes) or due to gradual topography changes or roughness distributions (e.g. flow in compound channels)."

> "Type C: Secondary instabilities of base flow: This is the weakest type of generating mechanism and experimental evidence is still limited. As remarked earlier, the nominal base flow is a uniform wide channel flow that is vertically sheared and contains a 3-D turbulence structure also with coherent features, i.e. the well-known 3-D burst events, controlled by the bottom boundary layer. Slight imbalances in this flow process can lead to a wholesale redistribution of the momentum exchange processes at the bottom boundary, including as an extreme case separation of the bottom boundary layer. The distortion of the vortex lines caused by these flow imbalances lead ultimately to 2DCS. Contributing factors may be localized roughness zones or geometrical elements (underwater obstacles). [...] Gradual decelerations in the base flow (spatial or temporal, viz. tidal oscillations) can also lead to a breakdown of the base flow into 2DCS. [...] In either instance, the transverse momentum exchange induced by these flow patterns may

(a) Type A: Vortex shedding from groin (b) Type B: Shallow mixing layer

Figure 2.4. (a) Groin fields on the River Rhine (Waal) in the Netherlands (Jirka & Uijttewaal, 2004). – (b) The Bavarian city of Passau is located at the confluence of the river Inn (light brown due to sediment load), the river Danube (dark brown) and the tributary river Ilz (black). Large vortical structures can be observed growing in the transverse shear layer especially for high discharges. [photograph by courtesy of F. Carmer]

> explain the perplexingly high friction factors (Darcy-Weisbach coefficients) that have been found necessary when hindcasting numerical model results for flows in very wide open channels."
>
> Jirka (2001, p. 568)

Various examples for the different forcing mechanisms can be found in natural shallow flows as well as in flows with an anthropogenicly altered bathymetry, as illustrated in Figure 2.4. The topographical forcing (type A) leads to the shedding of large-scale eddies directly from an obstacle, which rapidly changes the flow geometry along the flow direction. Locally well-defined regions of intense Reynolds shear stresses indicate the generation region of large vortices, and are essential for type A forcing. As an example Figure 2.4(a) shows the shedding of large eddies from the head of a groin.

For the type B forcing, a horizontal shear layer has to extend continuously over a significant downstream distance. Shallow jets and wakes characterized by their initial momentum excess, resp. deficit, which recovers due to the influence of bottom friction, may show long, but finite shear layers (e.g. shallow flow in the lee of islands). On the contrary, shear layers induced by changes in cross–sectional geometry may be virtually infinite (e.g. river reaches trained by series of groin fields). Such an elongated shear layer nourishes the gradual growth of large-scale vortical structures. Figure 2.4(b) exemplifies the growth of internal transverse shear instabilities for the confluence of the rivers Danube, Inn, and Ilz in Passau, Germany.

The type C forcing due to secondary instability of the base flow is not induced by localized (type A) or distributed (type B) transverse gradients

of the mean longitudinal flow, i.e. part of the horizontal mean rate of shear strain. Compared to the types A and B, is the weakest mechanism, and as such it is the least obvious one. But occasionally there are reports, which could be associated with this kind of forcing. For instance, so-called "boils", i.e. large-scale vortical structures, are frequently observed in rivers. Also in coastal waters such large eddies can occur in tidal creeks localized by scour holes (Lugt, 1979). In estuaries such instabilities might also be triggered by spatially distributed macro roughness elements (e.g. dunes) in decelerating tidal currents. This may lead to astonishing high friction coefficients, that are found to be necessary when calibrating a numerical model of an estuarine river (Khatibi et al., 2001).

2.2.4 Methods of investigation

As shown in Section 2.1,—mainly from airborne and satellite field observations—we have a good qualitative impression of the variety of shallow flow instabilities as well as of their general behavior. To understand the underlying physical mechanisms of the de- and re-stabilization of shallow shear flows in more detail, we also want to conduct quantitative measurements, which is not possible on the field scale with sufficient data density and accuracy. Thus, we have to reduce the geometrical scale of such flows down to laboratory size, which enables us to receive detailed information, that can be compared to analytical solutions and numerical simulations.

Laboratory experiments. If we want to experimentally explore plane shallow flows, i.e. flows which are confined vertically but laterally remain unbounded, we need a well furnished laboratory facility including a large[3] shallow water flume or basin. For such installations, high accuracy is needed in the bottom bathymetry and roughness as well as in the discharge control in order to establish a horizontally uniform and homogeneous base flow. Among few others, appropriate experimental facilities have been installed at the Delft University of Technology, The Netherlands, (Tukker, 1997) and at the University of Karlsruhe, Germany, (v. Carmer & Deutsch, 2001). Primary measuring systems, which are recommended for shallow flow investigations, employ non-intrusive optical techniques to observe the flow fields both of momentum and a

[3] To avoid influences due to surface tension, the water depth should be kept above 2 cm to 3 cm. E.g. for a shallow wake flow, using an aspect ratio for an obstacle of $D/h = 10$ to satisfy shallowness, and a blockage of the discharge area of below 5% to 10% to satisfy lateral unboundedness, we can estimate the lateral extent of a shallow flow basin to be around 3 m to 5 m. The shallow base flow in an installation of that dimension reaches depth-averaged Reynolds numbers $Re_h \geq \mathcal{O}(10^3)$, i.e. a turbulent base flow can be provided.

passive scalar, ideally in a synoptical way. These include both point-wise techniques like Laser Doppler Velocimetry (LDV) and Laser Induced Fluorescence (LIF), and planar techniques like Particle Image Velocimetry (PIV), Particle Tracking Velocimetry (PTV), Planar Laser Induced Fluorescence (PLIF) and Planar Concentration Analysis (PCA).

Other experimental facilities are dedicated to the examination of 2D vortical structures, as they also occur in shallow turbulent shear flow. Here, experimental research aims more at oceanic or atmospheric flows, the base flow condition is a non-turbulent or even quiescent fluid. For instance, the largest installation of that kind is the "Coriolis" turntable with a diameter of 13 m operated at the LEGI in Grenoble, France. At the Eindhoven University of Technology, The Netherlands, the re-organization of 2D vortical structures is investigated both resulting from an initial mechanical grid-forcing in a density-stratified tank (Maassen et al., 2002) and resulting from initial or continuous electromagnetic forcing. Another type of nominally 2D flows are thin film flows. Only recently new laboratory installations to generate soap-film flows were set up (cf. Rutgers et al. (2001) for an up-to-date overview), and employing LDV and PIV measurement techniques they now also provide quantitative inside into shallow wake flows.

Numerical simulations. With the rapidly increasing computational power at affordable expense (increasing cpu speed combined with construction of large cluster farms) methods to numerically simulate shallow turbulent shear flows become more and more promisingly. Especially Direct Numerical Simulation (DNS) greatly benefits from this development. Though not yet applied to shallow flows, DNS calculations are conducted for cylinder wake flows at cylinder Reynolds numbers close to those realized in laboratory experiments. For instance, Ma et al. (2000) report DNS results at $Re_D = 3900$ in comparison to laboratory measurements and to Large Eddy Simulation (LES) calculations. As in many shallow shear flows large-scale 2D vortical structures dominate the flow, 2D or 3D LES are expected to be suitable also for high Reynolds number flows, since in LES the low wave numbers are explicitly resolved, whereas for the higher wave numbers of the 3D turbulence a closure model has to be applied (Hinterberger, 2004). In order to solve the depth-averaged 3D SWE, a $k-\epsilon$ turbulence model has been applied to a shallow wake flow by Stansby (1997), which provided reasonable results in the near field dominated by small-scale 3D turbulence. Yet it remains questionable, whether a $k-\epsilon$ model is capable of representing the anisotropic turbulence in the wake far field, where quasi-2D turbulent structures prevail.

Stability analyses. Shallow shear flows are also examined theoretically using the methods of linear stability analysis, which are well suited to explore the stability of unbounded laminar plane shear flows disturbed by small-amplitude

perturbations.[4] Since shallow turbulent shear flows are horizontally bounded by a solid bottom and a free surface, Chu et al. (1983, 1991) and later Chen & Jirka (1997, 1998) implemented a bottom friction term in the depth-averaged shallow-water equations (2D SWE) and used an eddy viscosity formulation to cover the lateral shear stresses. Substituting small-amplitude 2D perturbations into the equations of motion, Chen & Jirka (1997) derived a modified form of the Orr-Sommerfeld equation with the added effect of bottom friction, and carried out linear stability analyses of plane wakes in shallow turbulent water flows. Albeit the stability problem is simplified due to linearization and due to the application of algebraic turbulence and shear models, linear stability analysis has proven to be a useful tool in order to understand and predict the evolution of perturbations also of a shallow turbulent shear flow.

2.3 Shallow turbulent wakes

This work is devoted to the examination of a special class of plane shear flows, namely to *shallow turbulent wakes*, which develop in plane shallow base flows, that receive additionally shear in the horizontal direction due to a large obstacle. Such an obstacle may be a circular cylinder vertically extending over the whole flow depth with a lateral dimension $D \gg h$. As mentioned above, in contrast to unbounded cylinder wakes the limited vertical dimension gives rise to the development of large-scale 2D structures—this is justified both from kinematic and dynamic reason—and to a quasi 2D mean flow field at least in the dominating low wave number scales of turbulence. Unbounded wakes have been the subject of research for decades[5] now. Consequently there exists a vast amount of literature concerning theoretical, numerical, and experimental aspects of this fundamental topic. We will refer to selected questions and details on unbounded wakes, as is necessary for comparison throughout this work on bounded turbulent wakes. The reader may want to study unbounded wakes in more detail and therefore may consult various review papers; instead we recommend the 'meta-review' of Zdravkovich (1997), that deals with the fundamentals of flow around circular cylinders in the first volume; the second volume on applications (esp. geometry variations, unsteady free stream, and flow induced oscillations) has been announced to be published in 2003.

[4] The well-known *Rayleigh* and *Orr-Sommerfeld equation* for inviscid and viscous plane shear flow will be briefly introduced in Chapter 9.

[5] Leonardo da Vinci, Italian universal genius of the Renaissance, was concerned also with hydrodynamic scientific and engineering questions (e.g. Gharib et al., 2002). He studied the turbulent motion of water also in the wake of an obstacle as early as in the beginning of the 16th century (see also Figure on page 1).

2.3.1 Stability of shallow wakes

A main focus of this work is on the global instability of shallow wake flows coupled with the generation and decay of large-scale 2D structures in (or as part of) the turbulent plane shear flow. Crucial for the generation of such large-scale 2D structures—at least for the two strong forcing mechanisms (type A and type B) encountered in wake flows—is the interaction of the vertical shear layer induced by bottom friction in the base flow and of the horizontal shear layers representing the transverse difference in longitudinal momentum transport. Since bottom friction slows down the vortical motion of the large-scale structures, it suppresses the development of turbulence due to lateral shear. Therefore, the spatiotemporal evolution of the 2D structures is controlled by the interaction of both shear mechanisms. On the one hand, kinetic energy is extracted from the mean advective flow and incorporated into the large-scale coherent motion by means of transverse shear, on the other hand within the bottom boundary layer large-scale turbulent kinetic energy is continuously extracted again from the coherent motions and dissipated either directly or via the energy cascade of small-scale 3D turbulence. Thus, bottom friction not only opposes the generation of large-scale structures near obstacles (type A forcing), but also dampens their development within the lateral shear layers (type B forcing). Regarding the wake flow dynamics, lateral shear may induce large-scale instabilities into the plane shear flow and maintain their growth, whereas bottom friction counteracts their generation and evolution. In conclusion, the mechanism of generation and decay of the large-scale 2D vortical structures is also crucial for the global stability of a turbulent wake flow.

Stability number. By comparison of the loss (dissipation) F_b of large-scale 2D kinetic energy due to bottom friction to the production P_c of large-scale 2D kinetic energy due to lateral shear, one can define a dimensionless stability number S_{flux}, called the *flux stability number* describing the transfer of large-scale TKE. S_{flux} characterizes the influence of bottom roughness on the generation and supply of large-scale 2D vortical motion, and thus characterizes the global stability of shallow shear flows. The *large-scale coherent production P_c of TKE* due to horizontal shear is given by the product of the Reynolds shear stress due to large-scale coherent fluctuations and of the transverse gradient of the time-mean main velocity component

$$P_c = -\langle u_p\, v_p \rangle \frac{\partial U}{\partial y}. \tag{2.1}$$

The large-scale coherent motions doing work against the bottom shear result in the loss F_b of TKE, which is dissipated directly at the high-frequency turbulent fluctuations without passing through the inertial subrange in a classic 3D energy cascade. As properly derived from the 2D SWE by Babarutsi

& Chu (1991)[6], if we assume for shallow shear flows that the time-averaged transverse velocity component V and the large-scale coherent fluctuations u_p and v_p are small compared to the mean longitudinal velocity component U, the *dissipation of large-scale TKE* can be approximated by

$$F_b = \frac{c_f}{2h} U \left(2 \langle u_c \, u_c \rangle + \langle v_c \, v_c \rangle\right), \tag{2.2}$$

where c_f denotes a quadratic law friction coefficient. Using a two-length-scale decomposition of the flow velocity $\boldsymbol{u}$, we will identify three flow components: the time-mean flow $\boldsymbol{U}$, the large-scale coherent flow $\boldsymbol{u_p}$, and the small-scale turbulent flow $\boldsymbol{u_r}$, as explained in more detail in Chapter 10.

Using the above expressions for P_c and F_b, the *flux stability number* becomes

$$S_{flux} \equiv \frac{F_b}{P_c} = \frac{c_f \, U}{2h \, \partial U/\partial y} \, \frac{2 \langle u_p u_p \rangle + \langle v_p v_p \rangle}{\langle u_p v_p \rangle}. \tag{2.3}$$

For values S_{flux} above unity, i.e. the dissipation of large-scale TKE exceeds the production of large-scale TKE, large-scale fluctuating motions will be damped away, the flow is stabilized in the low wave number range. The term $\left(2 \langle u_p u_p \rangle + \langle v_p v_p \rangle\right) / \langle u_p v_p \rangle$ represents the ratio between the large-scale Reynolds normal and shear stresses. For the evaluation of the stability criterion, in definition (2.3) also this stress ratio has to be obtained from 2D turbulence measurements, or has to be estimated e.g. from corresponding free shear flow values[7].

Chu et al. (1983) proposed a *gradient stability number* S_{grad} for a shallow turbulent shear flow with an inflection point in its transverse main velocity profile, where $\partial^2 u/\partial y^2 = 0$. S_{grad} can be obtained from (2.3) by neglecting the large-scale stress ratio as well as a factor 1/2. The transverse velocity gradient has to be evaluated locally (Chu et al. (1983) suggested to choose the inflection point) and could be replaced by finite differences, i.e. $\partial U/\partial y \approx \triangle U/\delta$, where $\triangle U = U_1 - U_2$ displays a characteristic velocity difference between both sides of a shear layer with the width δ. Thus, a *gradient stability number* can be defined as

$$S_{grad} \equiv \frac{c_f}{h} \left. \frac{U}{\partial U/\partial y} \right|_{IP} \approx c_f \frac{\delta}{h} \frac{U_{avg}}{\triangle U} = \frac{c_f}{2R} \frac{\delta}{h} \tag{2.4}$$

evaluated at the lateral position of the inflection point $y = IP$. Herein, the *relative velocity difference* R is given by

$$R \equiv \frac{U_{high} - U_{low}}{U_{high} + U_{low}} = \frac{\triangle U}{2U_{avg}}. \tag{2.5}$$

[6] cf. also Chu et al. (1991, pp. 1371)

[7] Babarutsi & Chu (1991); Chu et al. (1991) give a value of 0.1 following Bradshaw et al. (1967).

In order to analyze the stability of the wake flow behind an island, INGRAM & CHU (1987) applied (2.4) at the end of the recirculation bubble attached to the island, where the mean flow is $U_{low} = 0$ for the rear stagnation point, thus $R = 1$. The half-width of the wake being the width of each of both shear layers was estimated to be half the island diameter, $\delta = D/2$. The *wake stability parameter*

$$S \equiv c_f \frac{D}{h} \tag{2.6}$$

then is related to the gradient stability number by $S = 4\,S_{grad}$. Compared to the flux or gradient stability number, the wake stability number is a more geometric parameter, which is related to the origin of the shallow wake flow instead of varying with the downstream position. S can thus be regarded as a global stability parameter, S_{flux} and S_{grad} as local stability parameters. Therefore, the stability of shallow shear flows induced by a type A forcing mechanism can be addressed by the wake stability number S, whereas the gradient stability number S_{grad} is well suited to characterize a type B instability of shallow shear flow.

Stability classification. CHEN & JIRKA (1995) used the wake stability number S in an extensive visualization study to classify the stability of shallow turbulent wake flows induced by circular cylinders as well as by solid and porous flat plates. They observed the flow pattern in the wake of such local disturbances of a shallow plane equilibrium shear flow, which can contain (or consist of) large-scale 2D vortical structures. These wake instabilities can be associated with type A or B forcing mechanisms. With respect to the strength of the perturbation, one can distinguish three classes of instability, which in agreement with CHEN & JIRKA (1995) we address as *vortex street (VS)* instability, *unsteady bubble (UB)* instability, and *steady bubble (SB)* instability. The following explanations reflect the flow around axisymmetric (e.g. cylindrical) obstacles, but they can be extended to capture also further shapes of obstacles.

<u>VS - Vortex Street-like Wake</u>
In the case of a massive perturbation of the base flow (type A forcing) a large amount of kinetic energy is extracted from the mean flow and transferred to the fluctuating flow field, i.e. converted into TKE. In the VS case a significant part of the extracted mean-flow energy is incorporated into large-scale 2D vortical structures, which alternately shed from the shoulders of the obstacle, and, analogously to a v. Kármán vortex street, staggeredly arrange in both shear layers each containing vortices of opposite sense of rotation (i.e. eddies in left shear layer rotating clockwise, and vice versa).

<u>UB - Unsteady Bubble Wake</u>
If the mean momentum deficit due to the local disturbance is weaker,

the boundary layers separate simultaneously from both sides the obstacle, and delimit a recirculation bubble attached to the obstacle. At the downstream end of the recirculation zone, the separated shear layers merge and roll up into large eddies of alternately changing sense of rotation, which again alternately shed from the bubble end. Thus, firstly the length of the recirculation bubble varies with the shedding cycle, and secondly the feedback of the vortex shedding on the recirculation zone leads to a sinusoidal fluctuation of the lateral bubble shear layers. Therefore, this class of wake instability is characterized by unsteady motion of a recirculation zone. More downstream, the large-scale eddies arrange in a vortex street-like pattern similar to a VS case.

SB - Steady Bubble Wake

For a further decrease of the momentum deficit the recirculation bubble in the lee of the obstacle stays almost completely stable. The separation of large-scale vortices does not occur anymore. Nevertheless, smaller-scale eddies (which are still larger than the flow depth) may grow in the lateral shear layers, so the forcing mechanism is of type B for a SB wake.

Figure 2.5 shows typical flow pattern of shallow wake instabilities to exemplify the stability classes VS and SB. Contrary to the impressive photographs of v. Kármán vortex streets (cf. e.g. VAN DYKE, 1982), where streaklines can easily be visualized, the flow pattern in shallow turbulent flows is more blurred and fuzzy. This results from the modified transport mechanisms in shallow turbulent shear flow compared to unbounded laminar plane flows. The turbulent diffusive transport of tracer mass due to small-scale 3D fluctuations dominates the molecular diffusion of the laminar flow. Also dispersive effects due to the depth-average visualization and modelling of shallow turbulent flow play an important role in loosing visual clarity, especially the retardation of mass in the viscous boundary layer close to the bottom in combination with the depth-integrating optical access may obscure the detail of the 2D flow structures.

The characteristic properties of the different stability classes of shallow turbulent wake flows are discussed in Part II of this work. There, a special focus is on the near-field topography of the time-mean wake flow including the recirculation zone and the region of large-scale vortex generation. The wake flow is described by the development of its geometric (e.g. wake half width δ), kinematic (e.g. centerline velocity deficit u_{sc}), and dynamical properties (e.g. TKE, Reynolds stresses). We also quantify the momentum and mass transfer both along the wake centerline (employing LDV-LIF) and over the whole wake (employing PIV-PCA).

The damping effect of bottom friction on the growth of the wake and therefore on the evolution of the large-scale 2D vortical structures is illustrated in

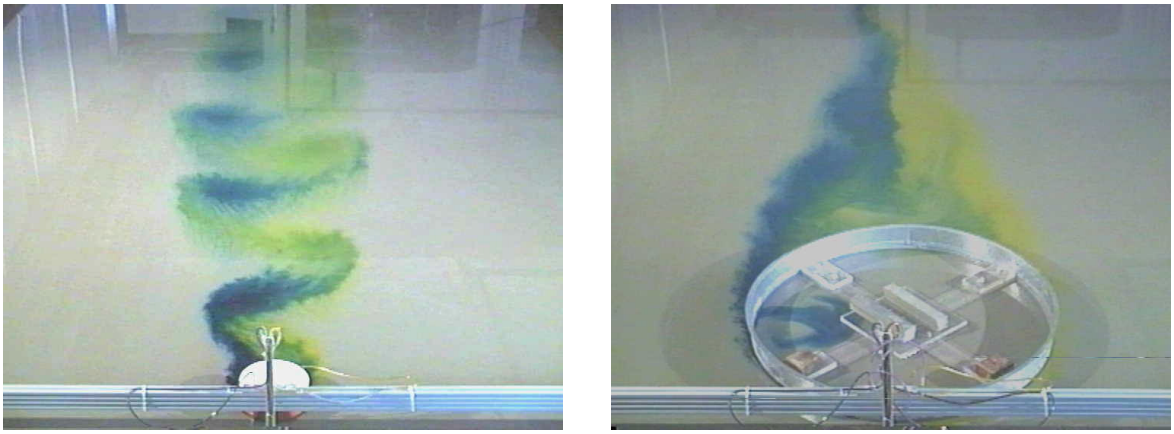

(a) VS - vortex street-like instability (b) SB - steady bubble instability

Figure 2.5. The instability of a shallow turbulent wake flow behind a circular cylinder is shown for a base flow with $h = 17mm$ and $Re_h = 2.100$. Viewed from an oblique angle, the flow direction is from the bottom to the top of the picture into the picture plane. For the classification we employ the wake stability number S given by (2.6). (a) Vortex street-like (VS) instability with $S = 0.15$ – (b) Steady bubble (SB) instability with $S = 0.69$

Figure 2.5(a) in the near and far field of a vortex street-like shallow wake, whereas Figure 2.5(b) shows the suppression of large-scale instabilities at all. The transfer of kinetic energy from the mean flow into the quasi 2D turbulent motion of the large-scale eddies, as well as the further transfer of TKE into larger wave numbers and its dissipation is mirrored in the turbulence structure of a shallow wake flow instability. The role of the large-scale 2D vortical structures and their interaction with the small-scale turbulent fluctuations can be clarified from the spectral distribution of turbulent kinetic energy over a wide range of wave numbers k_w (or frequencies f).

Flow separation. The strong initial instability mechanism of topographic forcing (type A) characterizes primarily the shallow-wake-flow class of vortex street-like instability (VS), but also plays an essential role for the class of unsteady bubble wakes (UB). Introduced by an obstacle disturbing the plane shallow base flow, large eddy structures are generated periodically, and while they are advected downstream in the wake, they are damped, since their kinetic energy is dissipated under the influence of bottom friction. In the UB case, the region, where such large-scale instabilities are generated, is located somewhat downstream in lee of the obstacle, thus opening a flow region attached to the obstacle, which shows a more stable motion. This region, consisting of the recirculation zone and its lateral shear layers, significantly differs from the convectively unstable region in the wake far field with respect to transport of mass and momentum; for instance, the mass exchange between recirculation bubble and ambient flow is reduced.

Leder (1992) distinguished two different types of flow separation in wakes of axisymmetric bodies, which we can associate with specific instability regimes and apply them to the different stability classes of shallow wake flows.

Separation of first kind denotes the classical separation of a *wall-bounded* shear layer; the separation will not necessarily lead to a roll-up of the boundary layer and the shedding of large-scale eddies. The occurrence of a boundary layer separation of first kind requires the following pre-conditions:

- adverse pressure gradient in flow direction, $\partial p/\partial s > 0$,
- viscous effects in the fluid are important, $\nu \neq 0$.

We will inevitably observe such separations of the wall-bounded shear layers in every turbulent wake flow with a recognizable initial momentum deficit. In the case of a vortex street-like shallow wake, the separated shear layers immediately roll-up to form the characteristic large-scale eddies, that alternately shed and advect downstream in a vortex street. Contrarily in the UB case, the boundary layers separated from the obstacle steadily demarcate both sides of a recirculation zone; these more stable shear layers also nourish smaller-scale 2D vortices, which eventually grow while advected in the shear layers. Both shear layers merge at the downstream end of the recirculation bubble, where in the UB case again large-scale structures are generated, whereas they are suppressed in the SB case.

The generation of large-scale vortical structures at the end of the recirculation zone, and their shedding and downstream advection is implied in the *separation of second kind*, which has to fulfill the requirements of a separation of first kind and additionally:

- two inflection points in the lateral velocity profile $u(y)$,
- interaction of the separated shear layers on both sides of the recirculation zone.

The occurrence of a second inflection point in the transverse velocity profile is a characteristic feature in the near field also of a shallow turbulent wake. In general, linear stability analyses of unbounded wake flows as well as the investigations of Chen & Jirka (1997, 1998) on shallow wake flows make use of the far field velocity distribution, which shows transverse profiles $u(y)$ with just one inflection point.

Part I

Non-Intrusive Flow Measurement Techniques for Coincident Data Acquisition of Velocity and Mass Concentration

Brief introduction to non-intrusive flow measurement techniques

Non-intrusive measurement techniques for velocity and scalar quantity in water flows. The examination of large-scale coherent vortical structures in a shallow turbulent near-equilibrium shear flow required elaborated measurement techniques. Since the coherent flow field is very sensitive to disturbances, only non-intrusive devices could be employed. Due to the multi-scale nature of the flow under examination, even using former leading-edge technology it was impossible to meet all necessities with respect to spatial and temporal resolution within a single measurement system. The turbulence characteristics of the bottom-induced shear flow (Kolmogorov or Taylor micro scales of length and time) demand to realize a high temporal and spatial resolution (cf. Sections 5.3.3 and 7.1.3). Since the time scale of the coherent flow field usually is several orders of magnitude larger than the micro scales of turbulence, high data rates over long periods of time have to be sampled to resolve the whole wave number range of the process. Similarly, due to the large horizontal dimension of the large-scale structures a large field of observation has to be resolved in great detail. The combination of a high temporal and spatial resolution and an extended window of observation both in time and space leads to a huge amount of information to be recorded, processed and analyzed. The need for coincident observation of velocity and mass fields leads to an even more complicated system.

Instead of tackling the measurement problem as a whole, a stepwise approach was considered to be more appropriate, as suggested by the spatial duality of small-scale turbulence and large-scale coherency of shallow turbulent wake flow fields. In order to obtain the horizontal flow velocities in high temporal resolution, as a single-point measuring technique a 2-channel Laser-Doppler Velocimetry system (LDV) was employed. The intersection of two focussed laser beams defines a very small measurement volume. Micro particles advected with the flow pass the interfering laser beams and reflect Doppler-shifted signals, which allow for calculating its velocity component. The same incident laser beams and the same receiving optics are used to obtain mass concentrations with a Laser Induced Fluorescence technique (LIF). A low-concentrated tracer dye is excited by absorbing monochromatic photons of the high-intensity laser light to emit part of the absorbed energy frequency-shifted

usually at longer wave-lengths. The mass concentration of the dye tracer in the measurement volume can be inferred from the intensity of the emitted fluorescent light. In Chapter 4 more detail will be given on the measurement techniques and the LDV and LIF systems employed to obtain pointwise information of the flow velocity and mass concentration, as well as on combining both systems for coincident measurements, which allow to compute mass fluxes.

In order to examine the large-scale vortical structures, that comprise the coherent flow field of a vortex street-like (VS) or unsteady bubble (UB) shallow wake, it was crucial to capture the spatial interrelation of the flow field. For this purpose, whole-field measuring systems were necessary, which did not need to provide a high resolution in time and space, but large windows of observation. To obtain the appropriate velocity fields of the shallow wake flows a Particle Image Velocimetry (PIV) system was employed. Also this measurement technique is based on the observation of small floating particles, which are illuminated in a plane which is usually defined by a laser light sheet. Images are recorded at a given resolution and frame rate depending on the camera and digitization. Using image analysis techniques the images are divided in smaller subregions. From correlating the same subregion in successive images the average velocity in each subregion can be calculated. By combining the individual subregions the flow velocity field can be obtained over the whole area of observation, in which obviously the spatial resolution now also depends on the algorithms of segmentation and correlation. Since we are interested in the mass transport related to the large-scale coherent structures, as a second whole-field measurement technique we apply another quantitative image processing technique, the Planar Concentration Analysis (PCA). Making use of the attenuation of incident light due to a dilute dye tracer injected to the flow, the mass distribution in the flow field can be evaluated with reasonably high spatial resolution in the horizontal plane. In Chapter 3 both measurement techniques will be explained in more detail. In Section 11.2 we describe analysis techniques to calculate the mass transport within the coherent flow both directly from the flow fields of velocity and mass obtained with PIV and PCA and from a numerical particle tracking based solely on the velocity fields.

Table 3.1 lists the non-intrusive measuring techniques applied in this research project. The pointwise and planar measuring systems for flow velocities, LDV and PIV respectively, are off-the-shelf systems, which are especially adapted to the shallow flow conditions. Both measuring techniques used to analyze the mass concentration within the flow are developed and designed to meet the special needs of laboratory examination of shallow flows.

Introductory optics for flow measurement techniques. Measurement and analysis techniques for the non-intrusive observation of flow quantities utilize detailed knowledge of various fields of *optics*. For some questions it

may suffice to rely on *geometrical optics*, for instance in order to represent the effects of reflection and refraction in the optical path of a LDV system. On the other hand, all applicable measurement systems involve the use of very small devices[1], which are vital for the specific techniques. To obtain flow velocities, LDV or ultrasonic systems need small tracer particles, for which Doppler-shifted frequency signals can be evaluated. It is therefore essential to capture the wave nature of light in the electromagnetic theory of classical *physical optics*. Furthermore, the quantum-mechanical treatment associating the wave nature to its particle behavior is needed especially for the evaluation of scalar concentrations, which both directly work on absorbtion and emission processes in LIF and necessitate to quantify the attenuation due to scattering by flow constituents and due to other photophysical and photochemical effects. Various spectroscopic methods are extensively used in chemistry to examine the structure of unknown molecular combinations; for more basic information the reader is referred to textbooks, for instance Hesse et al. (1995).

Concerning the interaction of light and matter we can distinguish an *elastic* behavior from an *inelastic* behavior. In the former case a light wave is redirected without otherwise altering it, whereas in the latter case also a change in frequency and wavelength occurs. The reader is referred to Figure 3.1 for a concise overview of selected light-matter interactions, as they are relevant within the measurement techniques employed throughout these studies.

If the quantized radiant energy hf_a of a photon[2] matches the energy necessary to bring an atom from its ground electronic state to one of the upper electronic states, the atom will "absorb" the light, making a quantum jump to that higher and less stable state. In a dense arrangement of atoms (esp. in solids and liquids) the excitation energy will be transferred via collisions of atoms into thermal energy almost instantly. This process is therefore called *dissipative absorbtion*. We will address this effect in the context of light at-

[1] The dimensions of these devices are smaller than or of the order of the wave length of the illuminating light $d_P \lesssim \mathcal{O}(\lambda)$, e.g. tracer particles for LDV with d_P of 1 µm to 10 µm.
[2] Here h is the Planck's constant.

Table 3.1. Flow velocities $\boldsymbol{u}$ and mass concentrations c in shallow turbulent free-surface water layers were observed throughout this study employing various non-intrusive measurement techniques. From coincident measurements of $\boldsymbol{u}$ and c or from appropriate post-processing of the data also mass fluxes were obtained.

	flow velocity	**mass concentration**
pointwise	LDV	LIF
planar	PIV	PCA

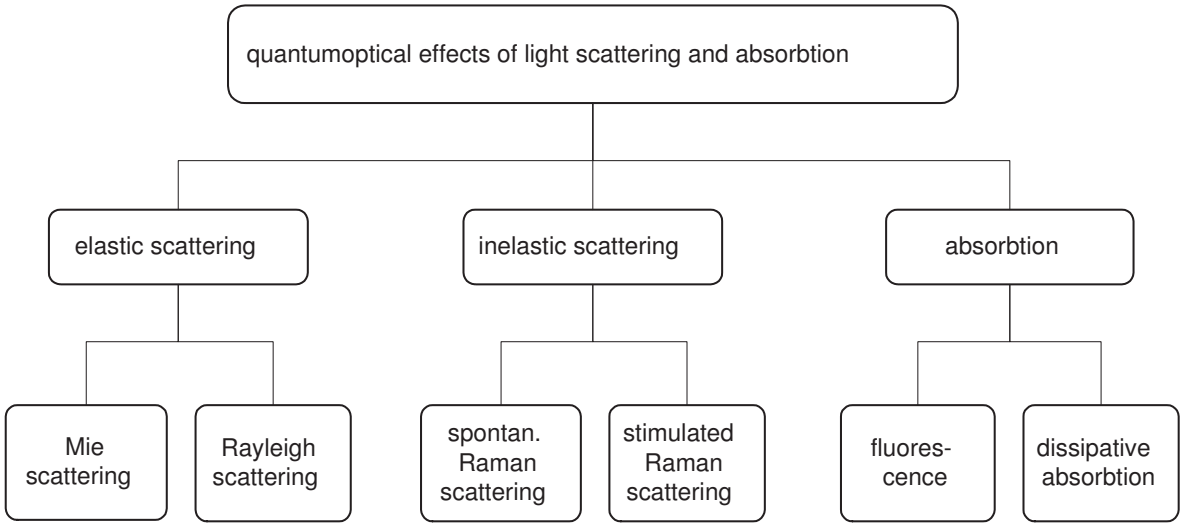

Figure 3.1. A schematic overview of light-matter interactions on the molecular scale presents quantum optical effects, which are relevant in the context of the non-intrusive measurement techniques for flow velocity and mass concentration throughout this work.

tenuation in Sections 3.2.1 and 4.2.3. In a less dense concentration an excited atom may transit to a lower state and thus re-emit part of the absorbed energy. If radiant energy hf_e is re-emitted in the visible frequency range, one speaks of *fluorescence*[3], which we use for high-resolution concentration measurements with LIF described in Section 4.2.

In contrast to the absorbtion and emission processes, which affect the *electronic states* of atoms, there are less energetic light-matter interactions, where the incoming radiation alters the *vibrational or rotational levels* of molecules. These are often referred to as *scattering* processes. A detailed presentation of the various quantum optical processes can be found in the classical textbooks on optics (e.g. Hecht, 2002; Born & Wolf, 1964), we suggest Bergmann & Schaefer (1987) for a thorough discussion. Referring to Figure 3.1 we will briefly mention the prime scattering processes with respect to the attenuation of light. For the *specular reflection* at optically smooth surfaces and *diffuse reflection* at a rough or wavy surface[4] the laws of geometric optics will apply as well as for the *refraction* of light due to variation of the optical density (i.e. variation of the refraction index n). The attenuation due to *diffraction* is not a macroscopic effect and, thus, can only be explained qualitatively using the classical electromagnetic wave theory of light. Furthermore, to quantitatively

[3] Whereas *fluorescence* involves the direct transition between two singlet states, *phosphorescence* describes a non-radiative intersystem crossing from an excited singlet state to a triplet state followed by a radiative transition to the ground state (e.g. Hesse et al., 1995). Consequently, the less energetic phosphorescent radiation consists of a lower frequency (near infra-red), longer wave length emission.

[4] The dimension of roughness has to be large compared to the wave length λ of the incident light. This is also applicable to large particles where $d_P \gg \lambda$.

predict the spectral distribution of energy we need a quantum mechanical approach.

If we assume a small particle to interact with a bundle of light waves[5], two cases of *elastic scattering* can be distinguished depending on the relative size of the particle with respect to the wave length. First, if the dimension of the particle is slightly larger than the wave length of the incident light or at least of the same order of magnitude ($d_P \gtrsim \mathcal{O}(\lambda)$), *Mie-scattering* occurs. The light diffracted at both sides of the particle can be assumed to interfere in an either constructive or destructive way. Thus, the scattered light is of the same frequency as the incident light, but the re-emitted light undergoes changes in phase, amplitude, and polarization. The intensity of the scattered light depends on the diffraction angle, the forward scattered portion may be 2 orders of magnitude more intense than the backward scattered light. This can be observed for particles with diameters up to 10 μm, e.g. for aerosols in the atmosphere or suspended colloids in water. If the dimension of the particle is small compared to the wave length of light, $d_P \ll \lambda$, *Rayleigh scattering* occurs. A very small particle in an oscillating electromagnetic field of incident light can be thought of as a small dipole stimulated to oscillate with same frequency and phase. It thereby emits electromagnetic waves perpendicular to the incoming waves.

Also *inelastic scattering* can occur on the molecular level. Similar to atoms, also molecules can absorb photons (in the visible or ultraviolet range) through the mechanism of electron transition. But molecules can also receive energy in the microwave and infrared wave lengths and convert it to kinetic energy via changing their rotational or vibrational motion. We may think of a monochromatic source and a photon of the energy $h\,f_0$ colliding with a molecule in its ground state. The molecule will temporarily absorb the photon and reach a virtual state (also called an intermediate state), but since this is a highly unstable state, it has to immediately transit to a stable state again. If the molecule returns to its initial ground state, it will emit the total absorbed energy in a photon of the same frequency f_0; again, this elastic process is called *Rayleigh scattering* (cf. Figure 3.2(a)). If the molecule returns to a more energetic vibrational or rotational level of the ground state $h\,f_M$, it will emit a photon of the energy $h\,(f_0 - f_M) = h\,f_S$, where f_S is the *Stokes shift*. If, on the other hand, the molecule has been in an excited state (e.g. heated) initially, it is also possible that it will return to a lower vibrational or rotational level from the virtual state emitting the energy $h\,(f_0 + f_M) = h\,f_{aS}$, this is called an anti-Stokes transition (cf. Figures 3.2(b) and 3.2(c)). The emission of frequency-shifted energy is called *spontaneous Raman scattering*. In Raman

[5] We assume a bundle of light waves of a given amplitude, frequency and phase, i.e. monochromatic and coherent light of a fixed intensity.

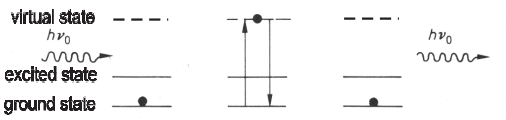

(a) Rayleigh scattering

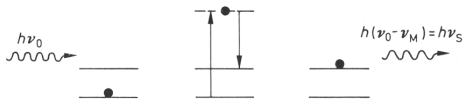

(b) Raman scattering with Stokes transition

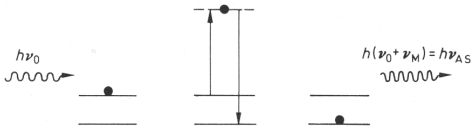

(c) Raman scattering with anti-Stokes transition

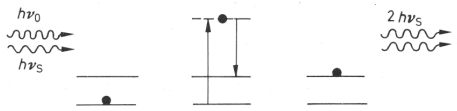

(d) Stimulated Raman Scattering

Figure 3.2. The energy-level diagrams of elastic Rayleigh scattering and different types of inelastic Raman scattering each show the initial energetic state of a molecule hit by a photon $h\,f_0$ (on the left), the temporary absorbtion of the photon and transition to a virtual state (in the middle part), and the return to a stable state accompanied by light emission (on the right). (a) *Rayleigh Scattering*: spontaneous elastic scattering of an incident photon with the same frequency f_0. – (b) and (c) *Spontaneous Raman Scattering* with Stokes and anti-Stokes transition, respectively. – (d) *Stimulated Raman Scattering*: a molecule is excited by a photon of $h\,f_0$, and while in the intermediate state, a second photon of $h\,f_S$ stimulates the *coherent* emission of two photons. (after Bergmann & Schaefer, 1987, p.854)

spectroscopy the differential frequencies f_M, which are characteristic for different materials, are obtained from the emission spectrum of a monochromatic excitation (usually by a laser source). Note, that Raman scattering by Stokes and anti-Stokes shifts is not characterized by a specific emission spectrum of wave lengths (as is fluorescence), but by a specific spectrum of frequency differences f_M (see also Section 4.2.1). Finally, at high incident intensities we can also encounter *stimulated Raman scattering* (cf. Figure 3.2(d)). We shall assume that a molecule has just absorbed a photon of the energy $h\,f_0$. While it is still in a virtual state, a second photon $h\,f_S$ hits the molecule and stimulates it to emit 2 photons $h\,f_S$ of the same phase, frequency and polarization. Thus, the emission of coherent light is stimulated. Stimulated Raman scattering is the core effect for setting up high-intensity coherent sources, namely LASERs[6], extending from IR to UV radiation.

[6] This is the abbreviation for "Light Amplification by Stimulated Emission of Radiation".

3. Planar Measurement Systems

Shallow turbulent wake flows cover a wide range of spatial and temporal scales ranging from the small turbulence scales of the plane bottom shear flow up to the large-scale coherent flow field induced by the obstacle or island. If we focus our interest on the development of quasi 2D large-scale eddies, then we need information with less temporal and spatial resolution compared to boundary layer turbulence, but with still reasonable resolution in a wide area of observation and over an extended duration. Field-wise measurement systems for flow velocity and mass concentration are employed, which are especially adapted or developed for the shallow water facility at the Institute for Hydromechanics, University of Karlsruhe, and take full advantage of the shallowness of the flow.

3.1 Particle Image Velocimetry

3.1.1 Introduction to PIV analysis

Both in basic research and engineering applications of fluid dynamics information is needed not only about the temporal development of a flow, but also on its spatial correlation. In order to address the spatial organization of a flow also in its temporal evolution, new measurement techniques have been developed in the past two decades. The availability and rapid increase of computer power facilitated the introduction and spreading of planar and even volumetric measurement systems applying image analysis techniques to obtain velocity distributions of the observed flow section. Nowadays, such measurement systems are widely used in aero- and hydrodynamic laboratories for academic research and industrial development. Turn-key systems providing a package of appropriate devices for image capturing and storing, light sheet generation, system control, and data processing are available from a variety of manufacturers.

The basic idea of such velocity measurement systems is as simple as its realization in measurement hardware and software code needs skill and endurance. In order to examine the motion of a flow, particulate or even soluble tracers are added to the flow. At successive instances in time of known interval images are taken and analyzed in order to obtain the displacement of the tracers in time, and thus, to obtain velocity vectors. Grossly, two main strategies can

be distinguished in the analyses. First, individual particles can be located and identified in different exposures, and thus tracked in their movement in the flow. This so-called *Particle Tracking Anemometry* (PTA) or *Particle Tracking Velocimetry* (PTV) demands a low particle density compared to the image resolution in order to trace each particle. The second approach is more probabilistic as it resolves the mean displacement of a structure of tracers (the "signature" of a small group of tracer particles) employing an auto- or cross-correlation algorithm on successive images fragmented into small interrogation areas. This general approach—known as *Particle Image Velocimetry* (PIV)—requires higher concentrations of particles and appropriate image resolutions. Combined techniques which employ a PIV algorithm on a course segmentation as an estimate for the following PTV algorithm lead to an expanded dynamic range and higher accuracy of PTV (cf. Cowen & Monismith, 1997). We will not reiterate issues of theory, measurement equipment, and analysis tools related to Particle Image Velocimetry in this work, since there is an extensive amount of high-quality literature available. Instead, the reader is referred to textbooks like Raffel et al. (1998), who also present a categorized bibliography, or to review articles like Adrian (1991).

Besides holographic 3D PIV techniques, planar velocimetry systems generally require a *light sheet* to establish a *measurement plane*, which nowadays is always generated by a laser tube operated either continuously or in a pulsed mode. Only those tracer particles are visible to the observer that are advected by the flow in the light sheet, which therefore defines the measurement plane[1]. Because of strong attenuation effects in water flows high laser power is needed to produce a light sheet of still varying intensity, moreover, also the thickness of the sheet will expand due to scattering in the water body. Therefore, in water flows the area of observation is restricted to a lateral extent of few 10th of centimeters, when employing a laser light sheet. Since for a number of reasons some classes of flows cannot be scaled down as to meet the dimensions of a laser light sheet, laboratory examinations of such flows in scale models exclude the application of a common PIV system featuring a laser sheet illumination. Obviously, shallow free-surface flows with a significant large-scale coherent motion belong to such flows.

Using *suspended* particles a measurement plane can be generated by a laser light sheet at an arbitrary position *in the flow volume*. Using particles *floating at or near the free surface* will limit the movement of the tracers to the water surface and therefore defines a measurement plane without employing a laser light sheet. The idea of applying a laser-free PIV measurement system to obtain

[1] A laser light sheet actually defines a measurement *volume* of finite thickness. Albeit the light sheet is thin compared to its lateral extent, scaled in diameters of the tracer particle it may still comprise a thickness of several orders of magnitude.

surface velocity fields is nicely straightforward, and has already been reviewed some years ago by Adrian (1991). Applications of surface PIV to large-scale laboratory flows have been reported recently e.g. by Fujita et al. (1998), Weitbrecht & Jirka (2001), v. Carmer et al. (2001), Müller et al. (2002), and Muste et al. (2004). The restrictions to the application of a surface PIV measurement system are twofold. From the hydrodynamical point of view they will focus on the question, if and to what extent the surface velocity field is adequate for characterizing the flow.[2] On the other hand, a variety of new technical problems will occur concerning for instance the proper illumination, control of exposure, kind of tracer, or data pre-processing. Some of these issues have been addressed by Kühn (2000) and Weitbrecht et al. (2002).

3.1.2 Technical equipment

In order to obtain large-scale surface velocity fields in the shallow wake flows under observation a turn-key PIV measurement system was employed that consisted of standard components—a PC, software for system control and image analysis, frame-grabber card, camera, and timing unit—provided and integrated by *LaVision*®. Further components have been added to allow for high-quality surface PIV measurements, namely flood-light illumination, tracer particles, and a particle dispenser. The whole PIV system was described in detail by Kühn (2000) and Weitbrecht et al. (2002). The left side of Table 3.2 summarizes the main components of the measurement system.

A 12 bit gray-scale, $1280 * 1024$ pixel digital camera (LaVision's *Imager 3*) was mounted directly above the water surface in a height of about 3 m. A flat-field, ultra wide angle ($f = 15$ mm) f-mount lens allowed for an area of observation of $1.2*1.4$ m. White-light photo flood-lights were carefully adjusted to provide a diffuse illumination of homogeneous luminance in the field of view without any reflections from the water surface. Upstream of the field of view the flow was evenly seeded with polypropylene beads over a width of 1.6 m using a specially developed particle dispenser capable of variable seeding rates to obtain an appropriate particle density at different base flow velocities. The floating PP tracer particles ($\rho = 0.9$ g/cm^3) had been specially coated with black lacquer to minimize its tendency to agglomerate. With a diameter of

[2] Contrary to laser sheets that can be positioned at different flow depths to obtain vertical distributions of horizontal flow fields and, thus, to calculate vertical averages, in surface PIV measurements the vertical distribution of flow properties has to be known a-priori. In equilibrium bottom shear flows the transverse distributions of the mean and rms velocity components are well described semi-empirically (cf. e.g. v. Carmer, 1998), but for large-scale coherent flows or for flows containing large-scale vortical structures additional efforts are often necessary (cf. e.g. v. Carmer et al., 2003).

Table 3.2. Instrumentation of the field-wise measurement systems for surface velocity fields (PIV) and for depth-averaged mass concentrations (PCA)

PIV camera *LaVision Imager 3* equivalent to *PCO SensiCam*	
type	cross-correlation camera
CCD chip	2/3", grade 0, gray-scale
size	$1280 * 1024$ pixel
dynamic range	12 bit
spectral range	300 - 800 nm
modes of operation	single-frame mode, double-frame mode
minimum time between frames	single-frame: 125 ms, double-frame: 300 ns
electronic shutter	exposure > 100 ns
Nikon lens	flat-field, ultrawide, f-mount
focal length	$f = 15$ mm
max. aperture	$f_{\#} = 3.5$
area of observation	$1.4 * 1.2$ m
frame rate	7 Hz

PC for system control, data storing, and data processing	
personal computer, dual-processor P-III 500 MHz, 1 GB RAM, two 18 GB SCSI hard disks, Ethernet card, RS 232 interface, frame-grabber card, programmable timing unit	
frames per run	300
OS	Windows NT
software	DaVis 5.4, LaVision

tracer particles	
material	polypropylene beads with black coating
diameter	3 mm
density	0.9 g/cm^3

illumination	
4 photo floodlights	1,000 watt each
spectrum	artificial day light

PCA camera *Siemens SiColor C810*	
type	PAL/SECAM video camera
CCD chip	1/2", color
size	$768 * 576$ pixel
dynamic range	$3 * 8$ bit
signal-to-noise	≥ 46 dB
lens	c-mount
focal length	$f = 10$ mm
aperture (applied)	$2 \leq f_{\#} \leq 8$
area of observation	$1.6 * 1.2$ m
frame rate	25 Hz

data storage	
digital video recorder	Mini DV-recorder Sony GV-D 900 E
tape	Mini DV
frames per run	limited by tape length

image transfer to PC
import via IEEE 1394 and digital video card "DV Studio 7" (Pinnacle Systems); save AVI–stream to hard disk, extract uncompressed TIFF–files with MainActor video editor

tracer	
colorant	Sicovit Amaranth 85 E123, BASF
C.I. 16185	Acid Red 27
maximum absorption	520 nm
solubility	80 g/l
maximum concentration	≤ 15 mg/l
molecular diffusivity	$\mathcal{O}\left(10^{-9} m^2/s\right)$

illumination	
4 photo floodlights	1,000 watt each
spectrum	artificial day light
diffused illumination	conical cotton cloth diff.

3 mm a particle occupied an area of 4 to 5 pixel in the image plane, which was sufficiently large to avoid jitter in the image analysis due to peak-locking effects. The camera was connected fiber-optically to the frame-grabber card of the PC. Images were taken in single-frame mode and streamed with a rate of 7 Hz to the RAM of the computer, up to 300 images could be stored in a single run allowing for sequences of up to 45 s, before the images had to be read out to hard disk. The software-package *DaVis* was able to control the camera settings and to trigger the camera via a programmable timing unit. Also the data processing was performed using the Davis software. An 'adaptive multi pass' cross-correlation algorithm—using a final size of 32 px $*$ 32 px for the cross-correlation window and an overlap of 50%—provided velocity fields on a regular 64 $*$ 80 grid with a physical spacing of about 18 mm. For further analysis and post-processing the vector fields containing the horizontal velocity components were exported as plain text files.

3.2 Planar Concentration Analysis

For the non-intrusive field-wise observation of mass concentrations in gaseous and liquid flows *planar laser induced fluorescence* (PLIF) techniques are applied. The broad variety of applications comprises laboratory and prototype flows in scientific and engineering research, where mixing or exchange processes are relevant, e.g. hydro- or aerodynamics, mechanical, chemical, or environmental engineering. Since the excitation of a fluorescent material requires high intensities of incident radiation in wave length close to the maximum absorption wave length, usually a laser light sheet will provide the necessary energy. In hydrodynamic research such laser sheets are restricted to small areas, as already mentioned in the previous section about PIV measurement systems. In general, PLIF will be not the first choice for large-scale laboratory investigations. However, if an increased thickness of the sheet, i.e. a reduced spatial resolution, and strong attenuation are acceptable, PLIF is capable also of large-scale flows, as was shown for instance by Nash et al. (1995) for a thermal plume discharge in shallow tidal flow, and by Chen & Jirka (1999) for a shallow plane jet.

In order to obtain depth-averaged scalar fields of mass concentration in shallow free-surface flows, we developed a Planar Concentration Analysis (PCA) system based on image analysis. An easy-to-use experimental setup allows for quick conduction of measurements. The fully automated analysis provides field-resolved conversation algorithms of color intensity to mass concentration also representing their non-linear relation.

Applications of the PCA system for the depth-averaged analysis of field-wise distributions of mass concentrations in shallow laboratory flows have been re-

ported by the Environmental Fluid Mechanics Group, University of Karlsruhe. v. Carmer et al. (2001) applied the PCA on the identification of large-scale vortical structures in shallow vortex street-like wake flows. Rummel (2002); Rummel et al. (2002) examined the plume spreading in a shallow equilibrium shear flow with different turbulence characteristics. Kurzke (2002); Kurzke et al. (2002) applied the same algorithms to analyze the retardation of suspended matter in groin fields.

3.2.1 Optical background and light attenuation

Remote sensing technologies opened up the promising opportunity of field-wise examination of earth's water bodies for oceanographers and limnologists. For the analysis and interpretation of remotely sensed optical data, detailed knowledge of *aquatic optics*, or hydro-optics, is essential. The photons of direct sun light and diffuse sky radiation propagating through natural water bodies firstly encounter elastic scattering and absorption by water molecules, resulting in light attenuation of pure water. Secondly, the diverse constituents of natural (or real-world) water bodies result in a variety of additional light-matter interactions, also leading to further attenuation. These interactions, and thus also the accompanying attenuation, are wave length-dependent in the visible wave spectrum. Therefore, the kind of constituents ultimately determines the water color and other optical properties of the water body. Since the organic and inorganic constituents, also called color producing agents, are indicators for the ecological status of the aquatic environment, strong efforts are currently made to infer the kind and concentration of the various constituents from remotely sensed images in order to qualitatively and quantitatively survey the changes in water quality.

The physical and thus optical complexity of natural aquatic environments strongly depends on terrestrial influences. Instead of distinguishing salty, fresh, and brackish waters, in aquatic optics water bodies are commonly divided into Case I and non-Case I waters. Far away from land masses in the offshore water bodies, in *Case I waters*, phytoplankton and subsequent products of its life cycle is the main constituent, that determines the optical properties of the water body. Modelling of the propagation of light only requires the knowledge of the phytoplankton concentration. The inverse modelling of the water constituents in Case I waters needs the calculation of the concentration, but not the identification of the kind of constituent (namely phytoplankton). On the contrary, *non-Case I waters* of coastal areas and lakes besides phytoplankton are also influenced by additional terrigenous (and anthropogenic) constituents, especially by inorganic suspended matter and by dissolved organic matter. Coastal and limnological optics has to deal with various kinds of constituents influencing the optical properties of the water body. Modelling of light propagation in

non-Case I waters has to represent a variety of optically relevant constituents as well as additional influences resulting e.g. from the bottom in optically shallow water. The identification and quantification of different constituents in coastal and fresh waters from remotely sensed data is a future challenge, for which there is an urgent demand, since coastal areas are crucial for social and economic development of mankind[3].

Among others, Kondratyev & Filatov (1999) and Pozdnyakov & Grassl (2003) provide further contemporary readings on the topic of remote sensing for the analysis of inland and coastal waters. In the remainder of this section, we will present a brief overview of some optical properties of natural water bodies and light propagation in the aquatic environment. We restrict this overview to conceptual basics, that are helpful in the context of laboratory shallow flow research projects. There is a broad variety of monographs and papers dealing with aspects of hydro-optics, we suggest for example to study Bukata et al. (1995) or recently Arst (2003) for a sound and scientific introduction to the field.

For the field-wise analysis of the mass concentration in laboratory shallow wake flows, presented here, we encounter difficulties similar to those of oceanographers and limnologists analyzing remotely sensed optical data. As in Case I waters we make use of just a single water constituent, which is optically relevant. But as in non-Case I waters the bottom may influence the propagation of light in the experimental setup.

Light attenuation in natural water bodies. The photon flux Φ propagating through the atmosphere and the aquatic environment can be quantitatively described using the term radiance and irradiance. The *radiance* L in a specific direction at a point in the radiation field is defined as the radiant (energy) flux[4] Φ at that point per unit solid angle $d\Omega$ and per unit area dA projected at right angles to the photon beam (cf. Figure 3.3),

$$L = \frac{d^2\Phi}{dA\, d\Omega} \quad \text{in } Wm^{-2}sr^{-1}, \tag{3.1}$$

where the radiant flux per unit solid angle is called *radiant intensity* $I = \frac{d\Phi}{d\Omega}$. The unit solid angle is given in steradian by $d\Omega = \sin\theta\, d\theta\, d\phi$, and the unit area by $dA = r^2\, \Omega$ in spherical polar coordinates (polar angle θ, azimuthal angle ϕ, radius vector $\boldsymbol{r}$). If the photon beam is impinging on or emanating from a unit surface dS tilted to the direction of the light propagation, i.e. $dS = dA/\cos\theta$, then the radiance of a light beam becomes

[3] For instance, about two thirds of the large cities of the world are located in coastal areas.

[4] The *radiant flux* Φ is defined as the time rate of flow of radiant energy, $\Phi = \frac{d\xi_T}{dt}$ in $J\, s^{-1}$ or W, where the total energy of the polychromatic photon beam is the photon energy times the number of photons in the beam $\xi_T = \sum_{i=1}^{N} h\, f_i$ in J.

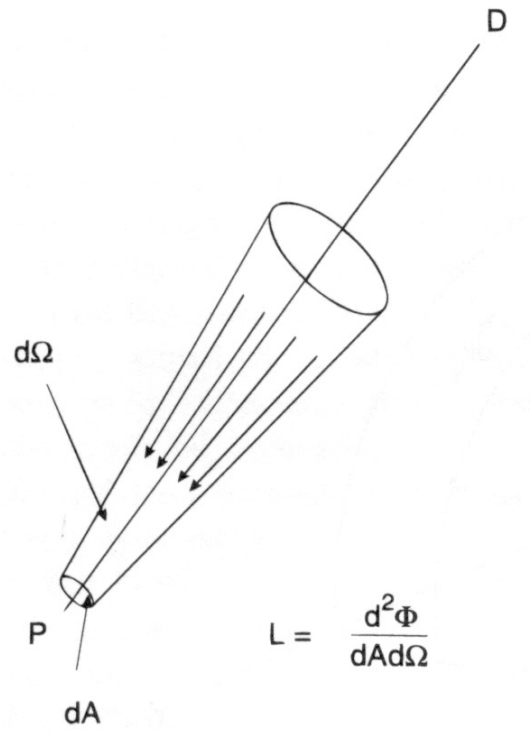

Figure 3.3. A conceptual sketch illustrates the radiance L at a point P, that results from a radiant flux Φ of radiant (energy) intensity $I = d\Phi/d\Omega$ from direction D (with solid angle $d\Omega$).

$$L(\theta, \phi) = \frac{d^2\Phi}{dS \, \sin\theta \, \cos\theta \, d\theta \, d\phi} \; . \tag{3.2}$$

The *irradiance* E refers to the radiant flux Φ per unit area at a point within the radiative field integrated over all directions of a hemisphere,

$$E = \frac{d\Phi}{dS} \quad \text{in } Wm^{-2}. \tag{3.3}$$

Thus, the radiant flux is the total irradiance on the whole surface area.

When passing through a mass-containing volume, i.e. a medium different from the vacuum, light is attenuated due to various kinds of light-matter interactions. An incident radiant flux Φ of photons will propagate through a water body of infinite thickness ∂r, thereby suffering from attenuation e.g. due to absorbtion of photons by matter, so that the emanating radiant flux is $\Phi_{em} = -(\partial\Phi - \Phi)$. To give an illustrative derivation we will assume a monochromatic light source, the water body to consist of pure water, and restrict the processes of attenuation to the absorbtion of photons. The radiant flux is reduced by $\partial\Phi$ due to the photon energy absorbed by water molecules. The absorbed radiant flux is expected to be proportional to the incident radiant flux and to the length of the optical path,

$$\partial\Phi = -\alpha' \, \Phi \, \partial r \; , \tag{3.4}$$

as was first proposed by J.H. Lambert (1728 - 1777). If we allow the optical medium to vary its density, then the probability of a photon of being absorbed

along ∂r increases with higher concentrations of the absorbing matter. It was A. Beer in 1852, who first reflected this dependency, and suggested an *absorbtion coefficient* $\alpha' = \alpha\, c$.

Integration of (3.4), keeping α and c as constants, then leads to the well-known *Lambert-Beer law of absorbtion*,

$$\Phi\,(r, c) = \Phi\,(0, c)\; e^{-\alpha\, c\, r}\;. \tag{3.5}$$

From (3.5) we see, that the attenuating effect of the water body depends on the product $c\,r$. For a given value of $c\,r$ the attenuation should be the same for a thick layer of a low-concentrated medium, or for a thin layer of a high-concentrated medium. This holds as long as inter-molecular exchange processes or matter-matter interactions can be excluded. For higher concentrations of matter we find significant deviations from the Lambert-Beer law, as will be demonstrated in Section 4.2 for the validation of the LIF measurement system. The linear approach of the Lambert-Beer law can, thus, be regarded to be valid only in the limit of low concentration (cf. also Bergmann & Schaefer, 1987, p. 263). We will discuss the restrictions of the Lambert-Beer law in more detail in Section 4.2, where we will also introduce a non-linear expansion to cope with the mutual influence of fluorescent dye molecules in higher concentrations.

Since *dissipative absorbtion* describes a process of energetic interaction of light and matter, the absorbtion coefficient α and thus the absorbance—i.e. the ability of molecules to absorb light quanta from the visible spectrum, to change its rotational or vibrational state, and to re-emit the acquired energy in the far-infrared spectrum—depends on the species. More precise, besides the material components it depends on the physico-chemical conditions of the state of matter (liquid or gaseous), which influence the moveability of molecules and thus the absorbance. To a given species of matter (and to a lesser instance to a given solution) a specific absorption coefficient can be associated, which is independent of the mass concentration as c is low enough to prevent the inter-molecular exchange processes to significantly influence the absorbtion of photon energy.

However, absorbtion still depends on the second partner in the light–matter interaction, on the light. The *absorbtion coefficient* of a given material is significantly dependent on the wavelength of the incident radiant flux, $\alpha'\,(\lambda)$. With the above remarks from (3.4) we obtain as a definition equation for a specific matter

$$\alpha\,(\lambda)\; c = -\frac{1}{\Phi_c(r,\lambda)}\;\frac{\partial \Phi_c(r,\lambda)_{abs}}{\partial r}\;, \tag{3.6}$$

where the subscript $_c$ denotes a medium described by a given mass concentration, and the subscript $_{abs}$ denotes the attenuation due to absorption. Figure 3.4 shows the absorbtion coefficient $\alpha'\,(\lambda)$ of pure water in the wavelength range of

visible light (390 nm $< \lambda <$ 740 nm). Characteristically for transparent media we observe a rapid increase of α' toward the near-ultraviolet (UV-A, -B, -C 390 nm $> \lambda >$ 280 nm) and near-infrared range (740 nm $< \lambda <$ 2.4 µm).[5]

On the other hand, the radiant flux is also subject to attenuation due to *scattering*, and similarly to the absorbtion coefficient (3.6), the *scattering coefficient* $\beta'(\lambda)$, defined as the fraction of radiant energy scattered from a beam per unit distance as it traverses an infinitesimal distance ∂r, is mathematically expressed as

$$\beta(\lambda)\ c = -\frac{1}{\Phi_c(r,\lambda)}\ \frac{\partial \Phi_c(r,\lambda)_{sc}}{\partial r}\ , \tag{3.7}$$

where the subscript $_{sc}$ denotes the attenuation due to scattering. In Figure 3.4 the spectral distribution of the scattering coefficient of pure water $\beta'(\lambda)$ is indicated by out-lined symbols. In pure water attenuation due to elastic Rayleigh scattering becomes important in the blue region of the visible spectrum.[6]

In general, both absorption and scattering processes are responsible for attenuation. The *beam attenuation coefficient* $\gamma'(\lambda)$ is defined as the fraction of radiant energy removed from an incident light beam per unit distance as it traverses an infinitesimal distance ∂r due to the combined processes of absorption and scattering,

$$\gamma(\lambda)\ c \equiv -\frac{1}{\Phi_c(r,\lambda)}\ \frac{(\partial \Phi_c(r,\lambda)_{abs} + \partial \Phi_c(r,\lambda)_{sc})}{\partial r}\ . \tag{3.8}$$

The beam attenuation coefficient, therefore, is given mathematically by the sum of the absorption and scattering coefficients,

$$\gamma'(\lambda) \equiv \alpha'(\lambda) + \beta'(\lambda)\ . \tag{3.9}$$

Besides the direct sun light also the diffuse sky light will attenuate when passing through a water body. To describe this process we can formally replace the radiant flux Φ by the irradiance E to obtain the *irradiance attenuation coefficient* from (3.8)

$$K'(r,\lambda) = -\frac{1}{E(r,\lambda)}\ \frac{\partial E(r,\lambda)}{\partial r}\ . \tag{3.10}$$

[5] It is seen that pure water strongly absorbs in the red wavelength region of the visible spectrum, an absorption band that is peripheral to stronger near-infrared absorbtion at $\lambda >$ 700 nm. Relative peak values correspond to higher harmonics of the water molecule valence vibration at 3 µm. The absorption in the ultraviolet spectral region is inherent to electronic transitions occurring within the water molecule. (Bukata et al., 1995, p. 118)

[6] Because of the dominance of attenuation by absorption in the red region of the visible spectrum and the balancing effects of Rayleigh scattering and absorption at small λ, pure water displays a blue hue.

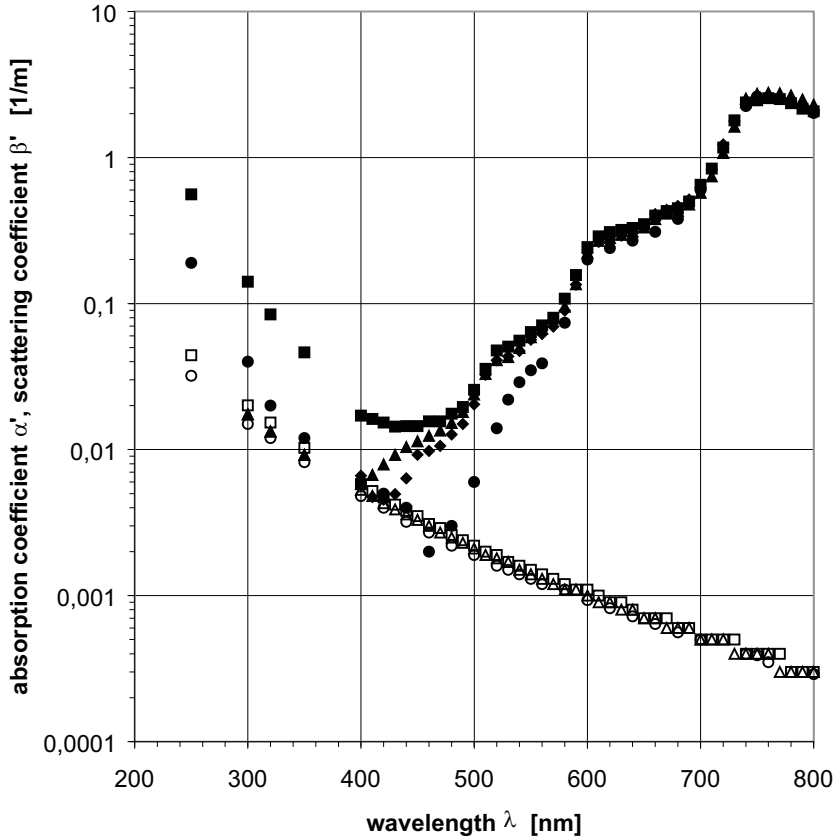

Figure 3.4. A comparison of absorbtion coefficients α' and scattering coefficients β' for pure water at $T = 20°C$ obtained by different authors: ■ (Smith and Baker, 1981), ● (Multi-Author, 1983), ▲ (Buiteveld et al., 1994), ◆ (Pope and Fry, 1997). Full symbols refer to α', out-lined symbols refer to β' (data compiled by Pozdnyakov & Grassl, 2003)

Again, we can decompose $K' = K\,c$, and assuming K and c to be depth-invariant, the Lambert-Beer law (3.5) applies to the irradiance,

$$E\,(r,\lambda) = E\,(0,\lambda)\;\; e^{-K(\lambda)\,c\,r}\;. \tag{3.11}$$

In general, the combined specular and diffuse illumination may show a directional preference, i.e. depend on the polar angle θ, which in turn may show a temporal dependency, so does the sun obscured by clouds possess a diurnal cycle. The irradiance attenuation coefficient therefore is also related to the direction of incident light, the directional dependency can be represented in $K_{spec}\,(\lambda,\theta)$ in contrast to $K_{diff}\,(\lambda)$. An average of K is obtained by weighting with the irradiance portions resulting from the specular and diffuse illumination. When including the directional aspects of the combined illumination in K, we can easily change from the path coordinate r to the vertical coordinate z. Employing *Snell's law of refraction*, $n_{inc}\,\sin\theta_{inc} = n_{refrac}\,\sin\theta_{refrac}$, the

depth is $z = r\,\cos\theta_{refrac}$.[7] The product $K\,c\,r = K'\,r$ in the exponent in (3.11) is called the *optical depth*.

In free-surface flows reflection of incident light at the air-water interface reduces the value of the *downwelling* irradiance E_d, i.e. the sum of the radiance propagation through the lower hemisphere, as it transits from the gaseous to the liquid medium. The (diffuse) *reflectance* at a (rough) boundary is defined as the relation between the upwelling and the downwelling irradiance,

$$R_{diff}(r) = \frac{E_u(r)}{E_d(r)} \ . \tag{3.12}$$

Obviously, the specular reflection of a light beam at a smooth surface is described by the Fresnel equation. The specular reflectance can then analogously be given as a radiance reflectance, $R_{spec}(r) = \frac{L_u(r,\theta_r,\phi_r)}{L_d(r,\theta_i,\phi_i)}$. Values of R_{diff} can be associated to the water body at any depth, at a boundary like the water surface it is often called *albedo*. In shallow flows the incident light may also impinge on the bottom. Its diffuse reflectance, or bottom albedo, mainly depends on the material, the bottom bathymetry, and the possible vegetation. If applicable, the bottom reflectance has to be taken into account in the computation of the light attenuation in water bodies.

To distinguish optically deep from optically shallow flows, the attenuation length can be compared to the flow depth. The *attenuation length* τ is the path distance in the attenuating medium that is required to reduce the radiant energy of a light beam by a factor of $1/e$, i.e. the optical depth equals 1. Thus, $\tau(\lambda, z)$ is defined as the inverse of the total attenuation coefficient $\gamma'(\lambda, z)$,

$$\tau\,(\lambda, z) = 1/\gamma'\,(\lambda, z) \ . \tag{3.13}$$

Inland and coastal waters show attenuation lengths of few meters to few centimeters, whereas mid-ocean waters are characterized by attenuation length of tenth of meters.

We have strongly emphasized the spectral characteristics of the attenuation processes. In the following we will omit λ in the notation for brevity. All properties and quantities can also be regarded as spectrally averaged values $\chi = (\lambda_{red} - \lambda_{blue})^{-1} \int \chi\,(\lambda)\,d\lambda$, that are usually obtained easier, and without the use of spectrometric methods.

One of the main objectives in aquatic sciences is often not to characterize pure water, but to examine its additional constituents. Also such scalar quantities like salinity or temperature, which often are of concern to hydrodynamicists, can be addressed as constituents to pure water. For the interpretation of remotely sensed optical data in marine research hydro-optical models have to

[7] Also the value of the *refraction index* n depends on the wavelength of the refracted light, which gives rise to chromatic aberrations in geometrical optics (e.g. beam splitting by a prism).

be employed, that are capable of representing the light attenuation processes due to water molecules and due to further constituents. In Case I waters there is only one optically relevant component besides the atmosphere and the water column, namely the phytoplankton population and its descendants. The chlorophyll-bearing biota are characterized by specific absorption and scattering coefficients, α'_{chl} and β'_{chl}, which strongly depend on the visible wavelength. In non-Case I waters, the situation becomes much more complex due to the various constituents, that may be found in inland and costal water bodies. In the visible and near-infrared spectrum also these constituents have individual spectral imprints. Since these constituents occur in different combinations of species and in different concentrations, it is basically impossible to identify individual species and concentrations solely from remotely sensed data. Hydro-optical models of non-Case I waters always group its constituents at least as a homogeneous combination of pure water, unique suspended organic material (represented by the chlorophyll-a concentration), unique suspended inorganic material (represented by the suspended mineral concentration SM), and dissolved organic material (represented by the dissolved organic carbon concentration DOC[8]). The *bulk* optical properties of a natural water body can then be considered as the additive result of the individual *specific* optical properties associated with the constituent groups present in the water column in addition to the pure water itself:

$$\alpha' = \sum_{i=1}^{n} \alpha_i \, c_i \qquad \text{and} \qquad \beta' = \sum_{i=1}^{n} \beta_i \, c_i \ . \tag{3.14}$$

Bukata et al. (1995) are generally not very confident about the applicability of remote sensing image analysis and hydro-optical modelling to the observation of non-Case I waters and to the control of environmental impacts.

> "The optically competitive organic and inorganic material comprising inland and coastal waters, therefore, prohibits the use of chromaticity as a single-component monitoring aid. Even if the spectral limitations of existing satellite imaging systems were overcome, chromaticity analyses of the upwelling radiance spectrum generally would be of little value to any but the least optically complex of natural waters."
>
> Bukata et al. (1995, p. 182)

Pozdnyakov & Grassl (2003) explain that there are other optical processes influencing the chromaticity of natural waters and its observable

[8] In the decomposition process of phytoplankton yellow and brown melanoids occur that are responsible for the yellow hue observed in inland and coastal waters. Though they are not the main portion of the DOM, the dissolved aquatic humus is generally referred to as *yellow substance*, historically also *Gelbstoff*, *gilvin*, and others.

derivatives like upwelling radiance L_u. Water color results, in addition to absorption and Rayleigh (elastic) scattering, also from Raman (inelastic) scattering of water, from fluorescence by phytoplankton and dissolved organic material, and in optically shallow waters from bottom reflectance as well. They point out that the contribution of these processes of photon interactions with the aquatic medium to water color is highly variable, since it depends on a variety of varying parameters like the concentrations c_i of the diverse constituents, surface topography of the air-water interface, intensity of illumination by direct solar and diffuse sky radiation, bottom topography and cover, or the variable spectral signatures of the color-producing constituents. Water color is therefore generally nonlinearly related to the mixture ratios and dilutions of water constituents, as they are ubiquitous in coastal and inland (non-Case I) waters. There still is a lack of analytical models to be implemented to the hydro-optical simulation of the aquatic environment. The inverse solution of such calculation will allow for the qualitative and quantitative description of the water constituents also under optically complex conditions. The mathematical and numerical tools as well as the computer capacity are available, though they could be improved.

The vertical inhomogeneity of the constituents and, thus, of the optical properties in the water column has to be taken into account, when evaluating the results of hydro-optical simulations and analyses. For clearer waters the vertical distribution of optical properties may play not a negligible role (cf. e.g. Frette et al., 2001), and thus should be given more attention to also in the hydro-optical simulation.

Color spaces. [9] In the visible spectrum electro-magnetic waves of a given wavelength can be associated with a specific color, Table 3.3 lists the main colors and their wavelength and frequency ranges. Thus, the radiometric concept is related to the psycho-physiological capability of the observer. The perception of color, and so its definition, depends on the individual impression and interpretation of light of a given spectral distribution perceived by a human eye. The perceptibility of the human retina is tri-chromatic, three different types of photopigments in the so-called "cones" of the retina with maximum sensitivities at 445 nm, 535 nm, and 575 nm make the cones responsive to different spectral regions. The spectral sensitivity bands of the 3 types of cones are unevenly weighted and overlap significantly (cf. Figure 3.5). The partitioning of light into tristimulus values usually of red, green, and blue—which was, though observed before by other scientists, first codified in the Young-Helmholtz

[9] For a thorough discussion on color theory the reader is referred to Bergmann & Schaefer (1987, chpt. 6). Chromaticity theory and its application to the color of natural waters is briefly introduced by Bukata et al. (1995, pp. 167). Definitions of different color spaces are presented by Jähne (2002, pp. 158).

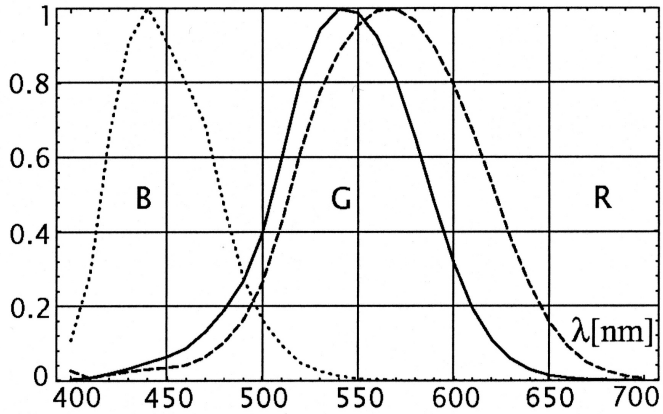

Figure 3.5. The three kinds of cones of the human retina show photosensitivity in different band of the visible spectrum (JÄHNE, 2002). Note, that especially the cones for the green (solid line) and red band (dashed line) are overlapping significantly. Also the absolute values for the peak sensitivity (used here to normalize cone sensitivity) are different for the various cones.

law—forms the basis for the definitions of various 3D color spaces which are employed to represent chromaticity information. Since image recording imaging systems usually are based on this concept, also the color analysis of such images has to process chromaticity information of this kind.

A given irradiance spectrum, $E(\lambda)$, can be related to human vision and the perception of color through color analyses that fold the sensitivity of the human eye with the irradiance spectrum impinging upon it. The tristimulus values X', Y', and Z' are obtained from this integration, and are employed to derive the chromaticity coordinates X, Y, and Z. Since chromaticity is understood as a additive mixture of the three *primary colors*, only those colors can be displayed in a color space that are linear combinations of orthogonal base colors.

Following the Commission Internationale de l'Éclairage (CIE) standard colorimetric system, the *tristimulus values* of an irradiance spectrum $E(\lambda)$ are given by:

$$X' = \int E(\lambda)\, x(\lambda)\, d\lambda \,, \tag{3.15a}$$

$$Y' = \int E(\lambda)\, y(\lambda)\, d\lambda \,, \tag{3.15b}$$

Table 3.3. Approximate vacuum wavelength and frequency ranges for the various colors

color	λ_0 **[nm]**	**f [THz]**
red	780 - 622	384 - 482
orange	622 - 597	482 - 503
yellow	597 - 577	503 - 520
green	577 - 492	520 - 610
blue	492 - 455	610 - 659
violet	455 - 390	659 - 769

$$Z' = \int E(\lambda)\ z(\lambda)\ d\lambda\ , \tag{3.15c}$$

where $x(\lambda)$, $y(\lambda)$, and $z(\lambda)$ represent CIE color mixture data for the red, green, and blue regions of the spectrum, respectively, and thus define a set of primary colors. These weighting functions reflect the perceptibility of the human eye with respect to the wavelengths of the visible spectrum.[10] Numerical values of $x(\lambda)$, $y(\lambda)$, and $z(\lambda)$ for an equal energy incident spectrum are quoted e.g. in Bukata et al. (1995, p. 172).

The *chromaticity coordinates* X, Y, and Z for the red, green, and blue components are then obtained from:

$$X = X' / \left(X' + Y' + Z'\right)\ , \tag{3.16a}$$

$$Y = Y' / \left(X' + Y' + Z'\right)\ , \tag{3.16b}$$

$$Z = Z' / \left(X' + Y' + Z'\right)\ , \tag{3.16c}$$

where $X + Y + Z = 1$, and $X' + Y' + Z'$ provides a measure for the luminous intensity.

Obviously, the photometric description of a visual sensation is given by a set of 3 parameters. It is defined either by the immediate set of tristimulus values X', Y', and Z' or by appropriate information in a color space. As can be seen from (3.16), since the sum of a chromaticity triplet per definitionem equals unity, two chromaticity coordinates define the chromaticity of a perceived light beam, a third parameter is needed to describe its luminous intensity.

As illustrated in Figure 3.6 a *chromaticity diagram* may be employed to represent the visible radiative spectrum. The color of monochromatic light of a given wavelength is uniquely represented in the color space by a pair of its chromaticity coordinates. Figure 3.6 shows the representation of a sequence of monochromatic light for 380 nm $\leq \lambda \leq$ 740 nm in the color plane of the X (red) and Y (green) chromaticity coordinates. The chromaticity triplets associated with the dominant wavelengths of all polychromatic lights fall within the enveloping monochromatic curve.

For a "white" irradiance spectrum, for which $E(\lambda)$ is wavelength-invariant, (3.16) yields $X = Y = Z = 0.333$. The triplet [1/3; 1/3; 1/3] defines the *white point* S or the *achromatic color* in a chromaticity diagram. A polychromatic light will consist of a given irradiance distribution $E(\lambda)$ in the visible spectrum peaked at a dominant wavelength[11]. The *dominant wavelength* is ob-

[10] The *standard luminosity function* provides a wavelength dependent conversion factor relating photometric quantities to radiometric quantities, e.g. the luminance $\mathcal{L}(\lambda)$ in lumen m^{-2} s^{-1} to the radiance $L(\lambda)$ in watt m^{-2} s^{-1}. For instance, for the maximum sensitivity at $\lambda = 555$ nm, 1 watt of radiant flux Φ corresponds to about 680 lumen of photometric flux. At 410 nm or 710 nm, however, 1 watt corresponds only to 1 lumen.

[11] If such a dominant wavelength does not exist, the irradiance spectrum has to be addressed as "white".

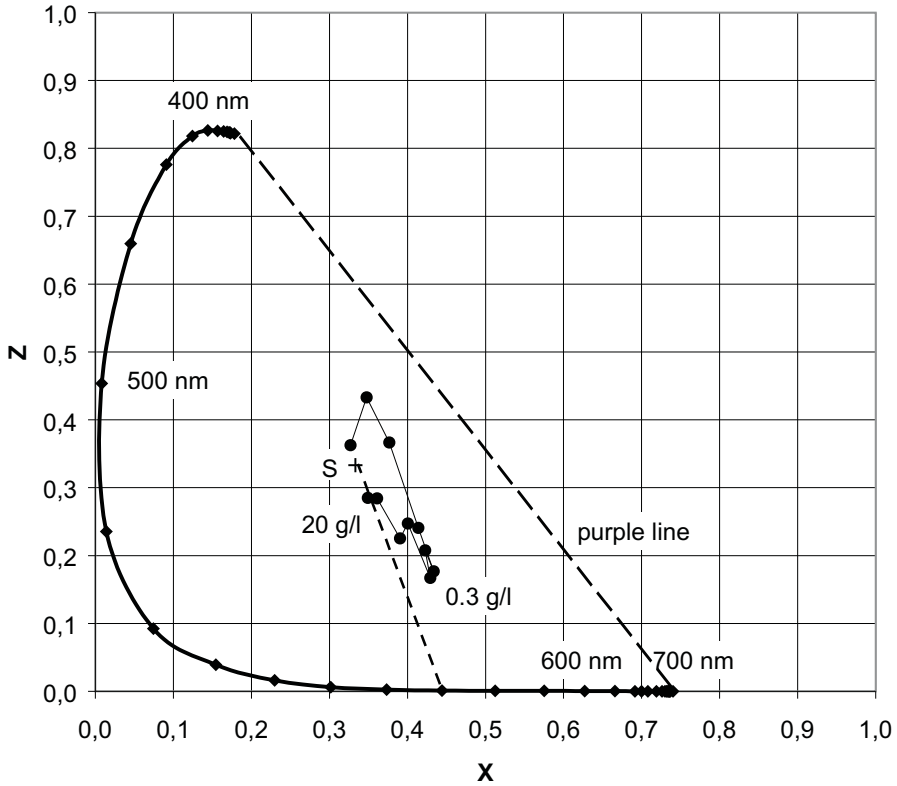

Figure 3.6. In a chromaticity diagram corresponding pairs of the chromaticity coordinates X, Y, and Z illustrate the dependency of color on some independent variable. To give an example for the XYZ color system, the chromaticity variation with the mass concentration of a dye tracer (*Tri-Active Red* from Tri-Tex Inc., RGB data reported by Balu et al. (2001)) diluted in water is plotted (thin line with circles) in the $X - Z$ plane. The thick line indicates the visible spectrum of monochromatic colors. The achromatic point S is marked as $+$.

tained graphically from the chromaticity diagram, when the connecting line between the achromatic point S and the chromaticity triplet C of the observed spectrum is elongated until it intersects the monochromatic perimeter. This is exemplified in Figure 3.6 by the dashed line for a specific observation.[12] The intersection point L indicates the strongest wavelength in the spectrum. Different spectral distributions of $E(\lambda)$ peaked at the same dominant wavelength will all lie on the same line $\overline{SL}$. Albeit they obtain the same dominant wavelength, the distribution along the wavelength is different nevertheless resulting e.g. in different peak-to-mean ratios. The *spectral purity* measures the importance of the dominant wavelength within an irradiance spectrum, a spectral purity value of 1 indicates monochromaticity, a value of 0 indicates achromatic

[12] A representation of a dye tracer (*Tri-Active Red* from Tri-Tex Inc., RGB data reported by Balu et al. (2001)) solved in water in different dilutions is given as a thin line, where circles indicate the different mass concentrations. For a mass concentration of 20 g/l the color hue corresponds to a monochromatic wavelength of about 570 nm.

light. Graphically, the aspect ratio of the lines $\overline{SC}$ and $\overline{SL}$ gives the spectral purity of an observed spectrum.

From the concept of the additive color mixture only those colors can be represented in a color space, that are given by linear combinations of 3 primary colors forming an orthogonal base. With respect to the significant overlap in the spectral perceptibility of the three photosensitive kinds of cones in the retina (especially in the green band, cf. Figure 3.5), it is obvious that no combination of 3 physical primary colors can cover the color spectrum. Thus, the range of colors displayable within a color space based on physical primary colors is always restricted to a region inside the monochromatic enveloping line of a chromaticity diagram. A common primary color system is given by the monochromatic colors red, blue, and green with wavelengths of 700 nm, 546.1 nm, and 435.8 nm, as recommended by the CIE in 1931. Nowadays, this *RGB colorimetric system* is the standard way (by European EBU norm) to digitally display color images. A *RGB* image of 24 bit color depth consists of the tristimulus triplets resolved in 8 bit in each of the 3 color channels for red, green, and blue.

In order to expand the range of displayable colors a new coordinate system based upon virtual primary colors, i.e. primary colors not related to any physical color, may be introduced. A commonly used system is the *XYZ color system* which represents the full range of monochromatic colors in the first quadrant, i.e. with all positive coordinates. It is related to the *RGB* color system by the following matrix transform:

$$\begin{bmatrix} X \\ Y \\ Z \end{bmatrix} = \begin{bmatrix} 0.490 & 0.310 & 0.200 \\ 0.177 & 0.812 & 0.011 \\ 0.000 & 0.010 & 0.990 \end{bmatrix} \begin{bmatrix} R \\ G \\ B \end{bmatrix} \tag{3.17}$$

The origin of a color system can be transferred into the white point to generate a *color difference system*. For digital video the *YCbCr* color system is widely used, for which the first channel features the luminance information, the next two channels contain color difference chromaticity coordinates.

When changing from a Cartesian to a polar coordinate system, the so-called *HSI* values are obtained (employed e.g. in the American NTSC norm). The *HSI or HSL color system* is given by *hue*, *saturation*, and *intensity* or *luminance* values. In the chromaticity diagram the monochromatic color indicated by point L gives the color hue, and is expressed by the polar angle of line $\overline{SL}$. The saturation of the color hue is represented by the spectral purity, and graphically by the aspect ratio $\overline{SC}/\overline{SL}$. The intensity or luminance directly gives the brightness of the irradiance.

Gray-scale images do not contain any chromaticity information, they can be described solely using the image brightness or luminous intensity. In the *HSI* or *YCbCr* colorimetric system this information is provided explicitly on a

separate channel. Since gray-scale images are achromatic, their *RGB* or *XYZ* values are always identical on the three channels. Instead of using a three-channel encoding, a single channel containing the intensity is sufficient.

3.2.2 Data acquisition and pre-processing system for PCA

The PCA measurement system is based on an image analysis technique, the measurement hardware therefore consists of a proper illumination of the field of observation, an optical system (i.e. a camera), and a storage device. Vital part of the measurement system is the software that was developed to process the raw images and to compute the planar distributions of tracer mass concentration. Various pre-processing and processing software modules that have been developed in order to extract fields of depth–averaged mass concentration $c(\boldsymbol{x})$ from PAL videos. In (Rummel et al., 2002) we gave a short overview of the established PCA system.

Measurement equipment. In order to obtain field-wise information on the transfer and mixing of a scalar quantity in laboratory turbulent shallow flows, the Planar Concentration Analysis System has been developed and installed at the Karlsruhe shallow flow facility. The PCA has been designed to be a very cost-efficient measurement system, the main objective was to get the necessary information from an easy-to-use, flexible, and inexpensive technique. The right side of Table 3.2 on page 38 gives an overview of the employed hardware components of the PCA system.

As an image of an object is received due to incident light reflected or scattered from the object, an essential component of the PCA system is the *illumination*. Target of observation is the water body and the bottom. Since reflections at the water surface would partially obscure the target, all reflections have to be omitted by a proper choice and adjustment of the illumination. Floodlights with a total power of 4,000 W emitting an artificial daylight spectrum were employed to continuously illuminate the area of about 6 m^2. Albeit it is practically impossible to obtain an exactly constant irradiance of such an area, the illumination should be as homogeneous as possible. Though not employed here, the PCA system receives significant improvement by employing an additional light diffusor, which results in an almost homogeneous light field (cf. Rummel, 2002, p. 29 and 79). The variation of the incident irradiance has to be taken into account in the development of an appropriate algorithm for the image analysis and processing done in the PCA software.

A *digital CCD camera*, *Sicolor C810* manufactured by Siemens, obtained color images in PAL resolution. This European video standard is characterized by a frame rate of 25 Hz, a spatial resolution of $768 * 576$ pixel, and a $3 * 8$ bit RGB color space. The signal-to-noise ratio of the camera is rather poor and has to be ascribed to the low-grade CCD chip. The $snr \geq 46$ dB results

in fluctuations with a standard deviation of about 2.5 gray units for a 8 bit intensity resolution independently of the intensity mean. The CCD camera was equipped with a 10 mm c-mount lens and was positioned vertically above the bottom of the flume at a height of 3.5 m. Thus, undistorted video images could be taken in an area of observation of approximately 1.2 m $*$ 1.4 m.

The video stream was stored by a Sony GV-D 900 E digital recorder on Mini-DV tapes. Using a frame-grabber card and the appropriate software, the video stream later was separated and converted into individual RGB images without any loss due to compression.

Tracer material. In order to simulate the mixing and transport of a scalar quantity in a turbulent shallow wake flow and observe the associated large-scale processes, the PCA system—as a non-intrusive, field-wise technique with strong operational and economic advantages—has been introduced. As an appropriate tracer material we chose *Sicovit® Amaranth 85 E 123*, a product of BASF with the INCI (CFTA) nomenclature C.I. 16185, Acid Red 27. This material is a widely used and inexpensive colorant for foods, drugs, and cosmetics. Therefore, the substance is well suited for laboratory use, since its handling bears no risk for the health of the lab personnel, and it does not mean a source of pollution for the lab water supply.

The maximum absorption of Amaranth E 123 occurs at 520 nm, its absorptivity is 440. Resulting from the subtractive color mixture, under white light illumination it displays a dark red hue. Amaranth E 123 is a very intense colorant with excellent solubility in water ($\approx$ 80 g/l), concentrations in the order of few mg/l are sufficient for conducting the PCA experiments. For such low concentrations the tracer material is regarded to be passive to the flow field, i.e. the flow field does not change due to variation of the fluid density. Amaranth E 123 provides good stability to pH, light, and heat. Under experimental conditions the tracer does not undergo any photochemical decomposition. Therefore, the tracer can be treated as conservative for the flows considered here. The molecular Schmidt number characterizing the diffusivity of the tracer mass in solution is of the order $Sc = \nu/D_m = \mathcal{O}\left(10^3\right)$. For more detail on the physical and chemical properties of this colorant the reader is referred to BASF (1996, 1997).

Pre-processing. The RGB or true color images were digitized in PAL resolution, i.e. the image plane is subdivided into 768 x 576 pixels with a color depth of 8 bit in the three primary color components for red, green, and blue. In the field-wise mass concentration measurement program for each individual run 3.000 images were digitized and had to be analyzed. It is, thus, of essential importance to identify the necessary information to meet the proposed research objectives, and to reduce the amount of data as much as possible. Before conducting a PCA analysis, in general three questions have to be answered:

- What is the *temporal resolution* and the *duration* necessary to capture the essential flow features?
- Which *spatial resolution* and which *dimension* is needed to depict the crucial processes?
- What kind of information is needed in the *color space*?

Spatio-temporal image transformation. Answers to these questions are always a trade-off between the scientific needs and the available means. As for this research project, the planar measurements focus on the large-scale processes in a shallow wake flow. This pre-defines the measurement duration and the dimensions of the field of observation. Regarding the measurement resolution, we decided not to restrain *temporal resolution* in the pre-processing, but to retain the available resolution of 25 Hz for the post-processing, esp. for the phase–resolved averaging procedures described in Section 10.1.2. The *spatial resolution* of the PCA measurements was chosen to be twice as high as for the PIV measurements. Two basic transformations were, thus, applied to the images containing the light intensity information. Firstly, the most outside lines and rows of pixels were cut off, since they were corrupted during the gathering and digitizing of the video frames. This image cropping reduced the area of observation by about 0.5% in each direction. Secondly, in a spatial averaging procedure—a binning with factor 4.5—the intensity information of about 20 neighboring grid points were consolidated and condensed to a single value. Due to binning and additional cropping of the PAL images the amount of information was reduced by a factor of 20, resulting in a 170 x 128 grid with a physical spacing of 9.5 mm. Additionally, the binning procedure provided a simple, but nevertheless effective filter algorithm to significantly reduce the measurement noise introduced by the CCD chip. Temporal filtering could not be applied for this purpose, since we wanted to fully retain the available resolution in the time domain.

Image transformation in color space. Chromaticity, or color, is primarily utilized to identify different constituents of the water body from their spectral properties. To evaluate the mass concentration of a given kind of mass we solely need the light intensity of its dominant color. Since in this examination the flow contains only a single and known kind of tracer material, the chromaticity bears not much additional information. It will therefore be discarded for the benefit of a reduction of data by a factor of 3 by converting the RGB images into gray-scale images.[13]

[13] Balu et al. (2001) also used the chromaticity information from RGB images for the evaluation of mass concentrations in a shallow wake flow. See the following section for a short discussion of their approach.

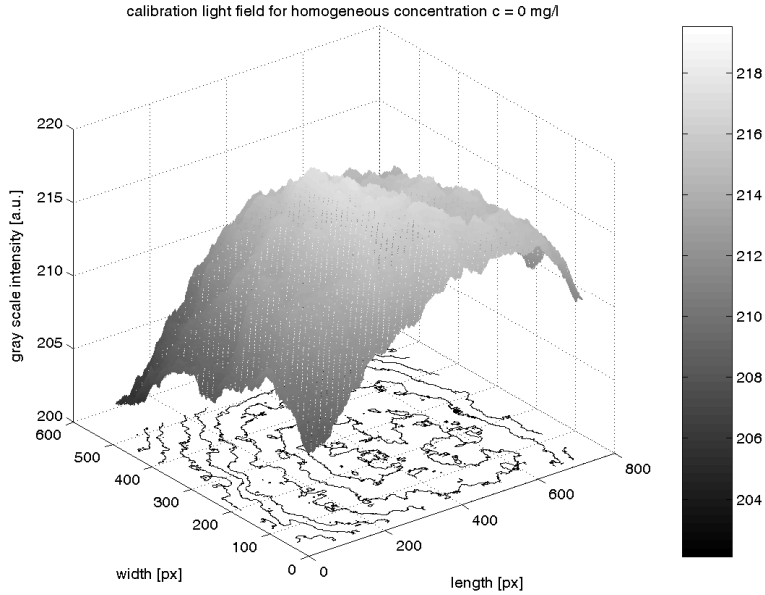

Figure 3.7. A significant spatial variation in the radiance field $L(\boldsymbol{x})$ is observed, though various measures have been taken to homogenize the illumination for the PCA measurements. Artificial day light of 4 photo flood lights is diffused using a special 'tepee' diffusor also preventing any surface reflection. The flow depth is 25 mm, the water body is tap water without additional dye tracer.

3.2.3 Data processing — transfer relation from light intensity to concentration

The PCA measuring technique as it has been developed in the framework of shallow laboratory flows is a non-intrusive methodology to evaluate depth-averaged mass concentrations by making use of light attenuation due to—generally nonlinear—absorption and scattering processes related to a tracer mass in aqueous solution. According to the main purpose of the measuring technique in the following we will focus on the pre-requisites and on the numerical procedures to convert the obtained light intensity distributions into fields of mass concentration. Furthermore, we intend to indicate, how the numerical solutions incorporate the underlying hydro-optical physics.

Aspects of illumination. For the sake of simplicity we decided to use a diffuse illumination with a polychromatic "white" spectrum instead of a more monochromatic light source. To our experience it is practically impossible—with a reasonable effort, in the shallow flow facility—to obtain a homogeneous radiative field with an incident radiative flux that is spatially constant over the whole area of observation. Both due to inhomogeneous illumination, and due to the employed optical components, the radiative fluxes impinging on the different photo-sensors of the CCD chip vary significantly with position. Moreover, under the prevailing optically shallow conditions the reflectance of the bottom has a significant influence on the upwelling irradiance observed by the camera. Imperfections of the bottom, i.e. slight color variations in the coating and minor variations of the bottom topography, could not be totally eliminated. The resulting deviations in the luminance distribution of the recorded images also depend on the value of the luminance itself. Figure 3.7 illustrates this behavior for an example calibration image (cf. Rummel (2002) for a detailed

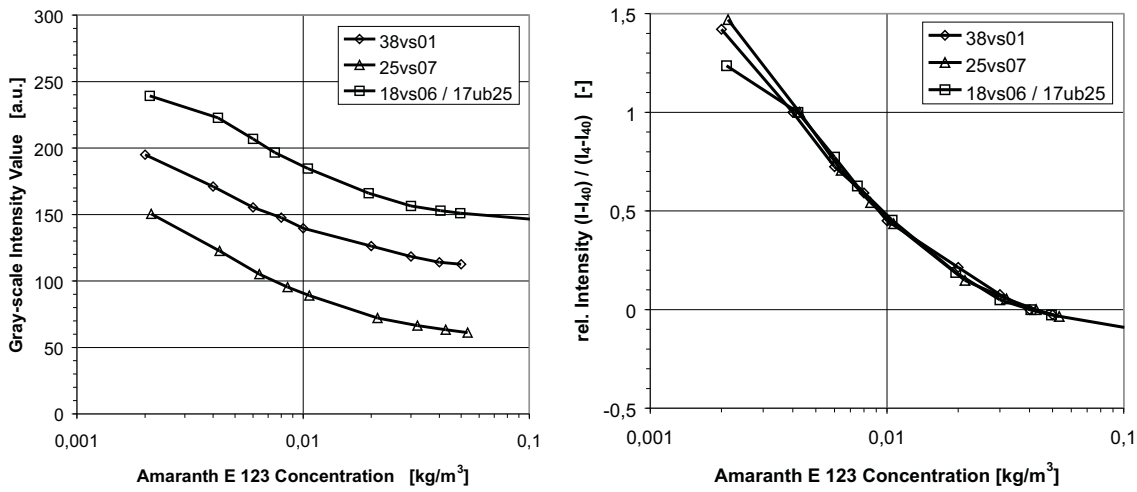

(a) gray-scale intensity values (b) normalized gray-scale intensity

Figure 3.8. The photometric response of aqueous *Amaranth E 123* solutions for different concentrations are shown for three sets of calibration images of the PCA system. (a) For each calibration set a different water depth is realized. Also the illumination and consequently the aperture and exposure time of the CCD camera differ between the sets. In terms of the mean gray-scale luminance $I(c)$ this results in a different response function for each set. — (b) When normalized by $[I(c = 4\ \text{mg/l}) - I(c)] / [I(c = 4\ \text{mg/l}) - I(c = 40\ \text{mg/l})]$ the three response functions show self-similarity. The optical attenuation can, thus, be described with the same optical model.

analysis). As an obligatory consequence of the unavoidable *inhomogeneity of the luminance field*, it is necessary to represent the spatial dependency of the photometric response in the transfer algorithm when computing the mass concentrations from the light intensity data.

Aspects of dye tracer. The food colorant *Amaranth E 123*, i.e. *Acid Red 27*, was found to be an appropriate tracer mass for the PCA measurements, as mentioned above. It provides a good detectability in the visual spectrum also in very dilute concentrations. Since we decided not to use the chromaticity information, gray-scale intensities of 8 bit depth provided the raw data for the concentration measurements. For concentrations spanning more than one order of magnitude a resolution of 6 to 7 bit could be obtained with the current instrumentation. Because of the photosensitive linear response of the CCD chip, the intensity resolution of the exponential attenuation process is also exponential, ranging from < 0.1 mg/l per unit brightness for concentrations < 4 mg/l up to > 5 mg/l per unit brightness for concentrations > 40 mg/l.

In Figure 3.8(a) the photometric response of aqueous Amaranth E 123 solutions for different concentrations are shown for three sets of calibration images of the PCA system. For each calibration set a different water depth is realized. Also the illumination differs between the sets, which in turn necessitated different apertures and exposure times of the CCD camera. In terms of the mean gray-scale luminance $I(c)$ this results in a different response function

for each set. When normalized by $\frac{I(c=4\ mg/l)-I(c)}{I(c=4\ mg/l)-I(c=40\ mg/l)}$, as illustrated in Figure 3.8(b), the response function shows self-similarity. The same optical effects are responsible for the attenuation for the different depths and illuminations. The optical attenuation can, thus, be described with the same optical model.

For concentrations up to 10 mg/l the exponential decay due to attenuation is essentially constant. For higher concentrations the light attenuation $\partial I/\partial c$ increases since non-linear effects (e.g. multiple scattering, direct molecular exchanges) are no longer negligible. The additional attenuation for higher concentrations leads to reduced resolution. The relative resolution per unit brightness is approximately constant with about 2% to 3% for solutions below 10 mg/l, but decreases rapidly for higher concentrations (e.g. $> 10\%$ for $c = 50$ mg/l). We therefore restricted all measurements to the low-concentration range (which also ensured the tracer to be passive to the flow).

The Canadian groups of V.H. Chu at McGill University, Montreal, and subsequently of R. Balachandar at the University of Saskatchewan, Saskatoon,—both active in experimental research in the field of shallow wake flows—also developed a methodology to compute dye concentrations from video image analysis, which dates back to the work of M.F. Tachie (cf. Balachandar et al., 1999).

It was Balu et al. (2001), who first used the chromaticity information of RGB images for the evaluation of mass concentrations. In doing so they could improve the concentration resolution by a factor of 2 or 3. With respect to evaluating only the luminance of the R-channel, using the information of the R-, G-, and B-channel one could expand the range of concentration by one order of magnitude without loss of resolution. Figure 3.9(a) shows the photometric response for the individual channels (broken lines) and for the gray-scale intensity (full line). The selected dye tracer (*Tri-Active Red*, produced by Tri-Tex Inc., St-Eustache, Quebeck) allows for taking full advantage of the channel splitting in the RGB color space. The three channels G, B, and R consecutively span a concentration range of 0.01 g/l to 0.04 g/l, 0.04 g/l to 0.3 g/l, and 0.3 g/l to 20 g/l, respectively, in total three orders of magnitude. Using also the chromaticity information improves the resolution by a factor of 3 compared to the 8 bit gray-scale intensity information, thus allowing 768 instead of 256 discrete concentration values. Contrarily to the assertions of Balu, Balachandar, & Wood in order to examine a single-component solution, firstly it is not possible to use the whole RGB color space resolving $256 * 256 * 256$ values. For different concentrations the variation in chromaticity (e.g. hue and saturation) follows a distinct line in the color space depending on the kind of the constituent instead of covering the whole space of possible chromaticity values. In Figure 3.6 the chromaticity variation of the colorant Tri-Active Red is indicated by a thin line. Secondly, a possible ambiguity in the gray-scale

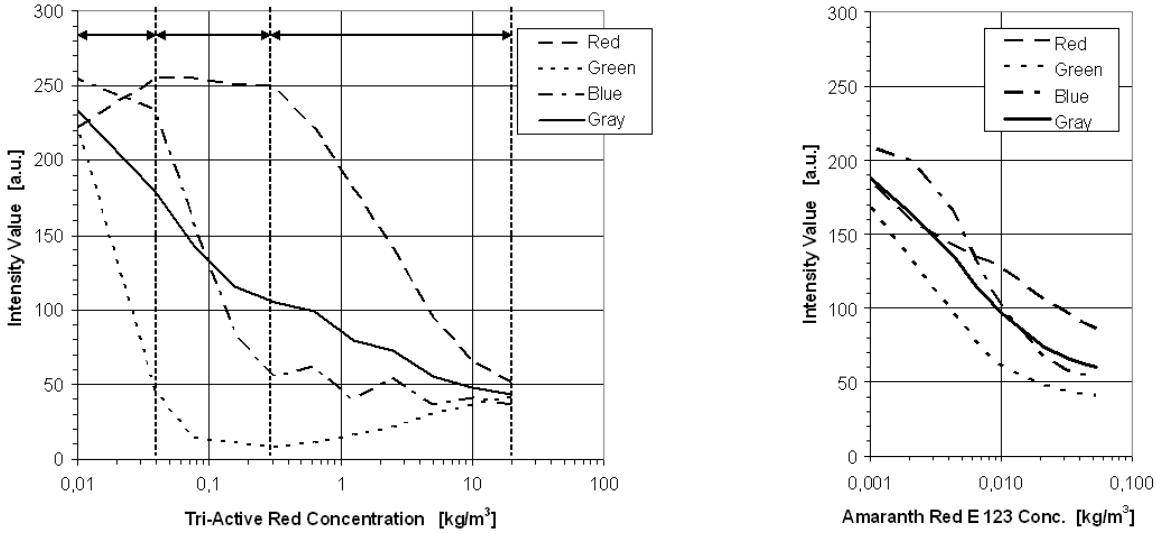

(a) Tri-Active Red (b) Amaranth Red E 123

Figure 3.9. (a) The brightness or luminance of aqueous Tri-Active Red solutions of different concentrations is displayed both for gray values (full line) and for the RGB color space. The luminance in the gray space is unambiguously related to the mass concentration. In the RGB space the consecutive responses of the G, B, and R channel for different concentration ranges make this dye well suited for a separate analysis of the color channels.
(*Tri-Active Red* from Tri-Tex Inc., RGB data reported by Balu et al. (2001))
(b) Amaranth Red E 123 shows a simultaneous decrease of the intensity values of the R, G, and B channel with increasing concentration. Its sensitivity is limited to about two orders of magnitude instead of three for Tri-Active Red.

intensity—as conjectured by Balu et al. (2001, p.123) [14]—does not necessitate a chromaticity evaluation in concentration analysis, since in general a single-componential solution will not lead to ambiguous readings. Also their own data, as plotted in Figure 3.9(a), show a definite relation between mass concentration and gray-scale luminance.

Ordinary Amaranth Red E 123 that is usually used with our PCA system in shallow flows reveals sensitivity to concentration over two orders of magnitude. Furthermore, as is also illustrated in Figure 3.9(b), the analysis of the intensity in the RGB color space does not improve the resolution compared to a gray scale analysis. Regarding the average resolutions, Tri-Active Red (3 channels for 3 decades) allows for a twice as deep analysis compared to Amaranth Red (1 channel for 2 decades). Unfortunately, the dye sensitivity is not distributed evenly among the three channels. The R color intensity of Tri-Active Red

[14] Different values of the color vector $[R, G, B]^T$ may lead to the same gray value $(R + G + B)/3$. For instance, $[200, 200, 200]^T$ and $[100, 250, 250]^T$ both correspond to a gray luminance value of 200.

spans 2 decades, resulting in the same resolution as for gray scale intensities of Amaranth Red.

To calculate the mass concentrations from the RGB values, Balu et al. employed a neural network technique, which consumes much processing time, and which is therefore not suitable to examine large sequences of images.[15] The advantage of an expanded range of observation, however, becomes questionable in the case of Balu et al. (2001), since due to the depth-averaged approach the applicability of the measurement technique is restricted to the mid- and far-field of the wake flow, where the dynamic range of the physical process under observation does not really necessitate this additional expansion of the concentration space. Furthermore, near the upper bound of the concentration range of 20 g/l one would have to ensure that the tracer would be still passive to a specific flow.

Calibration procedure. Preceding a set of PCA measurements, a calibration procedure has to be undergone in order to enable the proper initiation of the conversion algorithm to be employed. Though the individual calibration procedure may vary in some detail, some general guidelines can be stated. The following recommendations should be understood as a maximum requirement, since they apply to the most basic approach, namely the direct transformation algorithm. If one employs another algorithm, the procedure can be altered or reduced carefully. To briefly recapitulate, a calibration procedure before each set of measurements is necessary, because the experimental conditions change for each setup. Among these are changes in the illumination (direction and rate of radiant flux, spectrum of light), changes in optical equipment (lens, camera, aperture, exposure time), changes in tracer solution (kind of tracer material, pH of water), and changes in flow field (water depth, topography).

For the PCA measurements conducted in the framework of our research on shallow wake flows it was almost impossible to reproduce the re-emitted clear-water irradiance field because of changes in the illumination (photo floodlights, and/or neon tubes, and different kinds of light diffusor) and changes in the bottom reflectance. It has to be pointed out again that the re-emitted irradiance field provided significant spatial inhomogeneity, $L = f(\boldsymbol{x})$. Though we did not change the camera equipment, the aperture and exposure time had to be adjusted to the individual conditions of illumination.[16] Moreover, since

[15] Instead of using a neural network approach a more appropriate conversion strategy would take advantage of the segmented concentration range subdivided into the 3 color channels, and employ one of our PCA algorithms presented in the following.

[16] It is crucial for proper calibration of the conversion algorithm to ensure that the automatic exposure of the camera is disabled. Though an automatic exposure could be compensated to allow for correct measurement of homogeneous concentration fields, it definitely fails for the general case of laterally inhomogeneous mass distributions, as they occur in shallow wake flows.

the light attenuation depends on the water depth, the aperture and exposure time had to be properly adjusted for the individual flow conditions to retain a wide range of brightness levels. For clear-water conditions an image should be nearly over-exposed, whereas for the highest concentration expected to occur under the current flow conditions an image should nearly be underexposed. Within the PCA observations undertaken here the injection rate of tracer solution was adjusted as to restrict local maximum concentrations in the flow field to 10 mg/l to 15 mg/l. Also the changes in the topography necessitated to re-calibrate the conversion algorithm for the individual measurement series. A single cylindrical obstacle of different diameter, or a group of obstacles, was present or absent during the different measurement series and runs.

For actually obtaining the calibration images for each measurement series, a compartment containing the whole area of observation was hydraulically separated from the flume, after the water body had reached a constant temperature and the desired depth of flow, after the illumination had been installed, and after the camera exposure was set manually. Starting from clear-water conditions tracer mass was homogeneously distributed within the compartment, for increasing levels of mass concentration sequences of video images were recorded. The number of frames needed at each level of concentration depends mainly on the quality of the CCD chip of the camera (cf. Rummel (2002) for more detail using the *Sicolor C810* digital camera). The calibration images were digitized and pre-processed in the same way as the video images of the actual flow observations. For each concentration level c_i an appropriate set of images was then ensemble-averaged to obtain an individual photometric response $L_{cal}\left(c_i, \boldsymbol{x}\right)$ depending on the concentration level c_i and on the local position $\boldsymbol{x}$.

Direct transformation algorithm based on interpolation. A simple and straightforward approach to convert measured luminance values $L\left(\boldsymbol{x}\right)$ into depth-averaged mass concentrations $c\left(\boldsymbol{x}\right)$ is based on linear interpolation. Using the above mentioned calibration procedure a luminance matrix $L_{cal}\left(c_i, x, y\right)$ is obtained that contains the spatial brightness distribution for different discrete levels of concentration. A brightness value $L\left(x_i, y_i\right)$ at a specific pixel position will then be translated into a concentration value $c\left(x_i, y_i\right)$ by comparison with the luminance calibration matrix L_{cal}. Albeit we might not know anything about the hydro-optical processes that cause the light attenuation, we may still assume that the attenuation in the water column will continuously change with the concentration of the constituent, i.e. no jumps in $L = f(c)$. For the most basic transformation algorithm, which does not employ any hydro-optical model, we therefore utilize a *linear field-wise interpolation algorithm.*

In general the accuracy of this transformation algorithm is pre-defined by the quality of the approximation of the cumulative effect of the attenuation

processes. This approximation depends solely on the concentration of the solution for a specific set of boundary conditions for each experiment, as can be seen in Figures 3.8(a) and 3.9. The quality of the approximation by a numerical model to describe the physics of light attenuation will improve, if we increase the number of concentration levels and optimize their values. Obviously, for a given quality of approximation the necessary number of the concentration levels and its values will depend on the transformation algorithm, which will be applied on the luminance data. A—numerical and/or analytical—attenuation model, which captures the essential hydro-optical processes, will require less information for a proper calibration. Furthermore, such a model will allow to implement more efficient interpolation schemes. In the following section we present a rudimentary hydro-optical model, which is suitable for the PCA system, reduces the effort in calibration, and speeds up calculations.

Transformation algorithm applying a hydro-optical model. The optical device of the PCA system, the CCD camera, receives only a small fraction of the upwelling irradiance E_u, as each photo-sensor of the CCD chip can be associated with a small solid angle of observation depending on the employed optical lenses. Therefore, the camera rather receives upwelling radiance $L_u(\theta, \phi)$ under a given angle of view $[\theta, \phi]$, which is related to the total upwelling irradiance depending on the polar coordinates.

Generally, for the upwelling irradiance, and thus the radiance received by the camera, as many as four components can be distinguished:

L_a i.e. the portion of the received radiance resulting from backscattering of downwelling irradiance in the air, which therefore does not reach the air-water interface.

L_{aw} i.e. the portion of the received radiance resulting from reflection of downwelling irradiance at the air-water interface, which therefore will not intrude into the water body.

L_w i.e. the portion of the received radiance resulting from backscattering of incident irradiance in the water body, which therefore will not reach the bottom of the water body.

L_{wb} i.e. the portion of the received radiance resulting from reflection of downwelling irradiance at the water-bottom interface.

Because the path length of the incident irradiance in air is optically short in the PCA measurement setup, the portion L_a is essentially zero here. As indicated in Figure 3.10 the hydro-optical model, which we will derive for an improved transformation algorithm, will cover the remaining components of the received radiance, L_{aw}, L_w, and L_{wb}. For a given measurement setup (primarily characterized by illumination, and by view angle of observation, but also by the reflectances of the air-water and water-bottom interfaces, and by volume reflectance of water column) the received radiance L is regarded

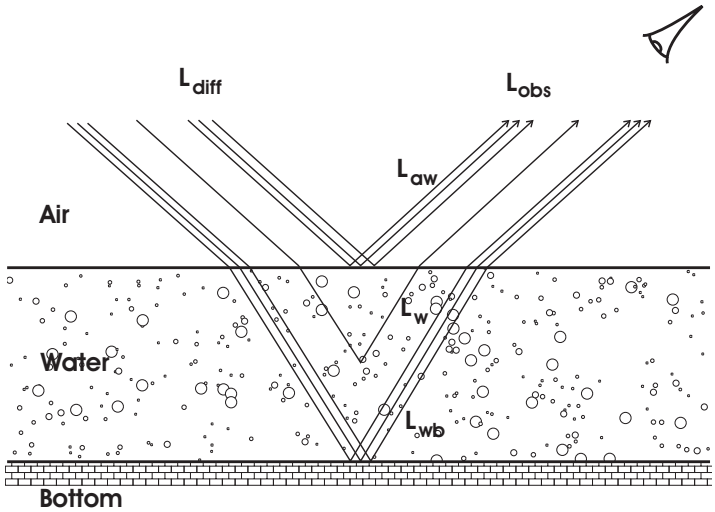

Figure 3.10. The components of the upwelling radiance captured by the PCA camera are illustrated conceptually. Neglecting backscattering in the air, three principal components are shown: L_{aw} due to reflectance at the air-water interface, L_w due to volume reflectance, i.e. backscattering, in the water body, and L_{wb} due to reflectance of the bottom.

as proportional to the total upwelling irradiance $E^+_{u,0}$ just above the water surface, i.e. $L = A_{opt}\, E^+_{u,0}$. The radiance received by the PCA camera can be described by

$$\begin{aligned} L &= L_{aw} + L_w + L_{wb} \\ A_{opt}\, E^+_{u,0} &= A_{opt}\, (E_{aw} + E_w + E_{wb}) \ . \end{aligned} \tag{3.18}$$

From the total irradiance $E^+_{d,0}$ impinging on the air-water interface a fraction R_{aw} will be reflected. The remaining portion $(1 - R_{aw})$ will be refracted while intruding into the water body. The incident radiation will attenuate within the water column, a fraction R_w will even be scattered back to the surface. The remaining portion $(1 - R_w)$ will be partly reflected (factor R_{wb}) at the water-bottom interface. All upwelling irradiance will suffer from further absorption and scattering along its optical path back into the air. These processes are represented in the following hydro-optical model equation:

$$\begin{aligned} L_{obs} = A_{opt}\, E^+_{u,0} = A_{opt} \big[& E^+_{d,0} R_{aw} \\ & + E^+_{d,0}\, (1 - R_{aw})\, e^{-K\,h/2\,c}\, R_w\, e^{-K\,h/2\,c}\, (1 - R_{wa}) \\ & + E^+_{d,0}\, (1 - R_{aw})\, (1 - R_w)\, e^{-K\,h\,c}\, R_{wb}\, e^{-K\,h\,c}\, (1 - R_{wa}) \big] \ . \end{aligned} \tag{3.19}$$

On the right hand side of (3.19) term I in the first line denotes the radiance portion *reflected at the air-water interface*, term II in the second line denotes the portion *backscattered in the water column*, and term III in the third line denotes that portion *reflected at the water bottom*. In a shorter notation Equation (3.19) reads:

$$\begin{aligned} L_{obs} = A_{opt}\, E^+_{d,0} \Big[& R_{aw} + (1 - R_{aw})\, (1 - R_{wa})\, e^{-K\,h\,c} \\ & \Big\{ R_w + (1 - R_w)\, R_{wb}\, e^{-K\,h\,c} \Big\} \Big] \ . \end{aligned} \tag{3.20}$$

Implementation of hydro-optical model in PCA. In optically very shallow waters the upwelling irradiance due to backscattering in the water body is expected to be small, the observed upwelling radiance component L_w might be negligible compared to L_{aw} and L_{wb}. As for small water depths h and low concentrations c the volume reflectance $R_w \to 0$, for the transformation algorithm of the PCA we let $R_w = 0$ in Equation (3.19) and (3.20). This leads to

$$L_{obs} = A_{opt}\, E^{+}_{d,0} \big[R_{aw} + (1 - R_{aw})\,(1 - R_{wa})\, R_{wb}\, e^{-K\,2h\,c} \big] \ . \tag{3.21}$$

Alternatively, we could include the volume backscattering term II in the surface reflection term I. Term I would then describe the *water surface albedo* A_{surf}, i.e. all the irradiance emanating from the surface regardless, whether it might result from reflected downwelling irradiance $E^{+}_{d,0}$, or from refracted upwelling irradiance $E^{-}_{u,0}$. Formally, in (3.21) A_{surf} would replace R_{aw} in term I.

The reflectances of the air-water interface, R_{aw} and R_{wa}, will be dependent on the surface topography (roughness or waviness) and on the mass concentration c in the water body. This dependency can be captured in a linear decrease with c as a first approximation, thus implementing $R_{aw} = R_{aw,0} - m_{aw}\, c$ and $R_{wa} = R_{wa,0} - m_{wa}\, c$ in (3.21). Since the decrease with c is only weak, we will neglect the quadratic term $m_{aw}\, m_{wa}$ in the bottom reflection term III.

Besides the variables h and c the resulting equation contains 8 unknown parameters $A_{opt}, E^{+}_{d,0}, R_{aw,0}, R_{wa,0}, m_{aw}, m_{wa}, R_{wb}$, and K, which are statistically correlated in some cases. In order to calibrate the hydro-optical model we will combine these parameters resulting in a model equation

$$I_{obs}\,(\boldsymbol{x}) = I_R\,(\boldsymbol{x}) + m_R\, c\,(\boldsymbol{x}) + \big(I_A\,(\boldsymbol{x}) + m_a\, c\,(\boldsymbol{x}) \big) e^{-K\,2h\,c(\boldsymbol{x})} \ . \tag{3.22}$$

This model equation relates the received luminance I_{obs} to the mass concentration c in the water body. Since the parameters I_R and I_A are related to the incident irradiance $E^{+}_{d,0}\,(\boldsymbol{x})$, they also depend on the local position. The parameters m_R and m_A represent the variation of the surface reflectance with c, and are themselves not sensitive to the local position, as is the attenuation coefficient K.

Details on the sensitivity of the model parameters, and on the solution of the model equation (3.22) implemented in the transformation algorithm of the PCA can be found in Rummel (2002), as well as recommendations for an appropriate calibration procedure.

Furthermore, it turned out in PCA measurements on passive plume spreading in shallow shear flow conducted by Rummel (2002) that $m_A \to 0$. This leads to a further simplified model equation

$$I_{obs}\,(\boldsymbol{x}) = I_R\,(\boldsymbol{x}) + m_R\, c\,(\boldsymbol{x}) + I_A\,(\boldsymbol{x})\, e^{-K\,2h\,c(\boldsymbol{x})} \ , \tag{3.23}$$

which could also be derived from the hydro-optical model (3.21). Instead of the surface reflectance R_{aw} we would use the albedo $A_{surf}\,(\boldsymbol{x})$ of the air-water

interface as a bulk property depending on the mass concentration. For the interfacial reflectances R_{aw} and R_{wa}—still occurring in term III to describe the transmissivity of the interface—we should then assume no significant relation with c.

Further processing of PCA data. In the data processing of the PCA system further software modules are involved that are optional, their application ranging from 'nice-to-have' to 'strongly-recommended'. An essential feature for the efficient performance of measurement series in the shallow flow facility is the possibility to evaluate and subtract a *background concentration* reading from individual fields of concentration. The Karlsruhe shallow flow facility is operated in a closed circuit configuration without an additional storage tank resulting in a circulation time in the order of minutes depending on water depth and flow speed. Instead of changing the water after each measurement run, which is a time-consuming procedure that as a consequence requires a new setup and calibration of the PCA system, it is preferable to conduct series of different measurement runs with the same fluid that is being loaded more and more with tracer mass from the previous runs. For this purpose a short sequence of images should be recorded from the flow before the injection of the tracer dye is started. A time-mean background concentration field $c_{bg}(\boldsymbol{x})$ can be calculated and subtracted from the individual concentration fields $c(\boldsymbol{x}, t)$ of the measurement run. Note that c_{bg} can be regarded a constant only if the duration of the dye injection, i.e. of the measurement run, is shorter than the recirculation time of the shallow flow facility.

Furthermore, from the ensemble of images (both of the calibration and background frames and of the individual frames) *statistical information* like the ensemble-rms distribution of the concentration fields can be extracted. A phase–aligned averaging procedure can be performed in order to allow for a later synchronization of PCA and PIV data. Temporal or spatial *filters* can be employed to improve the quality of the data and of the graphical output. Also an additional *binning in the time-domain* as well as data processing with *reduced temporal resolution* have been implemented in order to reduce the processing time and the amount of data if necessary. The level of detail in the data output can be adjusted to the requirements of the intended post-processing. In order to visualize the data and to produce improved video sequences, the gray scale intensity frames can be enhanced, and false-color images can be computed from the concentration fields.

Data handling and storage is not a trivial task when processing the PCA data. Since for each measurement run (with a duration of up to 5 min) 1,500 frames per minute have been recorded and digitized, all the information of a full run can be stored in computer RAM neither in graphical nor even in numerical form. Effort has been made to sequentially process and evaluate the images

and concentration data also in their ensemble averaged and phase–resolved averaged statistics. This also minimizes the computational time for the data input/output. The sequential structure of the pre-processing and processing of the PCA data has been organized as to meet the necessities of an optimized data handling.

3.3 Synchronization of PIV and PCA measurements

In order to access the horizontal mass transport in a flow field the instantaneous values of uc and vc have to be determined from synchronous field-wise measurements of velocity and mass concentration. If standard technologies of laser-based PIV and PLIF are available, simultaneous measurements can be conducted. Instead of a thorough discussion at this point we will give some references to exemplify the application of combined PIV-PLIF systems in hydrodynamic research. Firstly, PIV and PLIF have been set up as individual systems—each consisting of a stand-alone system with its own camera and laser light sheet—that were triggered simultaneously by a timing unit. Fukushima et al. (2000) investigated the mixing process in an axisymmetric turbulent jet employing such a measurement system. A set-up with two cameras observing the same laser sheet—which still requires the temporal and spatial coincidence of the two cameras, and thus, a proper synchronization and adjustment of the cameras—was employed by Meyer et al. (2000) on a jet in cross-flow, and by Webster et al. (2001) on the far field of a co-flowing turbulent jet. Cowen et al. (2001) employed a single camera and two individual laser sheets—a Nd: YAG laser for a PTV system and a scanned Ar^+ laser for the PLIF system—where the PLIF image was taken in between the two PTV images. They validated this technique by examining a turbulent round jet in stagnant ambient water.

In the framework of our research in shallow wake flows we employed a surface PIV system to obtain large-scale horizontal surface velocity fields and a PCA technique to obtain large-scale depth-averaged horizontal distributions of mass concentration. Both measurement systems were not operated simultaneously to observe identical flow fields, because the low-tech equipment of the PCA did not allow for coupling the two systems via a trigger board like the programmable timing unit of the PIV system. Nevertheless, coincident PIV-PCA measurements could be achieved by using a different PCA camera and data storage device, or by employing the PIV camera also for the PCA measurements—which will add some difficulty in choosing the appropriate exposure to satisfy the needs both of PIV and PCA. However, the presence of thousands of PIV tracer particles in the PCA images will involve additional

efforts to the data processing of the PCA (e.g. removal of tracer particles, possible disturbance due to their diffuse shadows, etc.).

Since in the present project planar measurement systems were employed to observe the large-scale, slowly-varying, and approximately periodic flow fields of shallow wakes of VS and UB classes, we chose a different approach that made use of the special quasi-periodic flow characteristics. A conditional re-sampling technique was used in the post-processing of the PIV and PCA data. As will be presented in depth in Part III, Sections 10.1.2 and 11.1.1, we extracted the large-scale quasi-periodic flow both from the velocity and mass fields applying a phase–resolved averaging technique to the instantaneous measurements. Briefly anticipating, from auto-correlations of the time-histories of the instantaneous flow fields obtained from PIV or PCA measurements the duration of each individual flow cycle was determined. The instantaneous data sets were then associated to the corresponding phase time, finally all data sets of a given phase time segment were averaged. The *phase–resolved averaged* fields for $\{\boldsymbol{u}\} = u_P$ and $\{c\} = c_P$ could now be cross-correlated. This procedure enabled us to calculate the large-scale quasi-periodic horizontal mass fluxes $\{u_P c_P\}$ and $\{v_P c_P\}$. A detailed discussion of this procedure will be given in Part III. An overview about the coupling of PIV and PCA measurements from their phase–resolved averaged data is presented in v. Carmer et al. (2002), where also the application to vortex street-like shallow wakes is introduced. v. Carmer et al. (2003) clarified some restrictions of surface PIV measurements from the analysis of combined PIV-PCA data.

4. Pointwise Measurement Systems

4.1 Laser Doppler Velocimetry

Compared to other measurement techniques for flow velocities *Laser Doppler Velocimetry* (LDV) offers some strong advantages. LDV is a non-intrusive technique, i.e. the flow in the fluid volume under observation will not be altered significantly by a probe, no disturbance will be imposed to the flow, only microscopic particles have to be added to the fluid as tracers. In general, provided a transparent fluid and an optical access to the measurement volume, a LDV technique is applicable to liquid and gaseous flows. Moreover, LDV systems allow for data acquisition of 3D velocity vectors covering a wide dynamic range with high temporal and spatial resolution.

Numerous textbooks and introductory texts on laser doppler velocimetry techniques have been published over the years, comprehensive introductions to LDV have been provided e.g. by Durst et al. (1981); Ruck (1987, 1990a,b); Leder (1990); Tropea (1993); Albrecht et al. (2003). Publications describing LDV applications (for instance in turbulent flows like jets, wakes, or boundary layer flows) are ubiquitous in the scientific hydrodynamic journals. Nevertheless, combined single-point measurements of the flow velocity and a scalar have been reported only scarcely (see e.g. Papanicolaou & List (1988), and Lemoine et al. (1996, 1997) for combined LDV-LIF systems).

Albeit the detailed hardware components may differ for various commercial LDV systems, three main groups usually can be distinguished according to their functionality:

- the *light source* or source of electro-magnetic radiation (usually provided by a laser source to meet the necessary intensity, chromaticity, and coherency of the radiation),
- the *transmitting and receiving optics* (to manipulate the source radiation as needed in the measurement volume for the specific LDV technique, and to manipulate the received optical signal),
- the *conversion and analysis* of the optical signal (to convert an optical signal into an electrical signal, to digitize and to analyze the signal).

Regarding their optical configuration, LDV systems can be subdivided into *dual beam* or differential Doppler, *reference beam*, and *two scattered beam* interferometer systems with the dual beam technique being the most common technique used in commercial systems.

4.1.1 Introduction to optical background of LDV

The optical *Doppler effect*, i.e. the frequency shift of light scattered by a moving particle, constitutes the basic principle of LDV measurement techniques. A particle moving in a coherent monochromatic light field of frequency f_0 will experience a frequency-shifted light field. Scattered light emitted by the particle will again be Doppler shifted when observed by a fixed receiver. Thus, the small frequency shift $(f_D - f_0)$ of the received scattered radiation f_D represents the velocity information of the moving particle. Since the velocity $|\boldsymbol{u}|$ of the moving particle is small with respect to the light speed c for all flow measurement applications, i.e. $\beta = |\boldsymbol{u}|/c \ll 1$, the relativistic optical Doppler effect can be treated in a non-relativistic way known as the acoustic Doppler effect (cf. e.g. Bergmann & Schaefer (1987) or Donges & Noll (1993)).[1]

The LDV system employed in the framework of this study was set up in a dual beam technique. For this technique, the coherent monochromatic laser beam is divided in two partial beams of equal intensity. The two partial beams are brought to a common focus by a lens. Due to the Gaussian cross-sectional intensity distribution of the partial beams, the two beams intersecting at a

[1] An observer moving in the direction of light propagation will receive a reduced frequency of the radiation emitted from a fixed source, as will experience a fixed observer with a light source moving away from him. If a fixed source emits radiation with a frequency f_0 and phase velocity c in the direction $\boldsymbol{e_i}$, the frequency recorded by an observer moving at $\boldsymbol{u}$ will be

$$f' = f_0 \left(1 - \boldsymbol{u}\boldsymbol{e_i}/c\right) \ .$$

Analogously, if a fixed receiver will detect a radiation of frequency f_D from the direction $\boldsymbol{e_D}$, the frequency emitted by a source moving at $\boldsymbol{u}$ will be

$$f' = f_D \left(1 - \boldsymbol{u}\boldsymbol{e_D}/c\right) \ .$$

Hence, if radiation is emitted with f_0 from a fixed source, received and re-emitted by a particle moving with $\boldsymbol{u}$, the frequency f_D detected by a fixed observer will be

$$\begin{aligned} f_D &= f_0 \frac{1 - \boldsymbol{u}\boldsymbol{e_i}/c}{1 - \boldsymbol{u}\boldsymbol{e_D}/c} \\ &= f_0 \frac{1 - \beta \cos\alpha_i}{1 - \beta \cos\alpha_D} \ . \end{aligned}$$

Since $\beta \ll 1$, by neglecting terms containing β^2 the above equation can be linearized to obtain

$$f_D = f_0 \left(1 - \beta \cos\alpha_i + \beta \cos\alpha_D\right) \ .$$

More details can be found, for instance, in Durst et al. (1981) or Ruck (1987).

small angle span an ellipsoidal volume, which constitutes the *measurement volume*. A particle, crossing the measurement volume at an arbitrary angle ψ_P with respect to the optical axis, will scatter the light of the two incident beams. Hence, the scattered light observed by the receiving optics consists of two frequency-shifted signals. Since the two beams are inclined with twice the intersection half angle ϕ, both scattered signals display slightly different shifted frequencies, f_{D_1} and f_{D_2} given by

$$f_{D_{1,2}} = f_0 \frac{1 - \beta \cos(\psi_P \mp \phi)}{1 - \beta \cos(\psi_P + \psi_D)} \ . \tag{4.1}$$

The frequencies of the emitted laser light and of the detected light are of the same order of magnitude, $f_{D_{1,2}} = \mathcal{O}(f_0) = \mathcal{O}\left(10^{15}\ \text{Hz}\right)$. It is neither possible to discretize these frequencies, nor are the frequency modulations due to the Doppler shift resolvable with any kind of light detector. Following scalar wave theory the electro-magnetic fields of both reflected beams can be superposed to yield a high-frequency wave field modulated by a much lower beat frequency, as illustrated in Figure 4.1. Contrary to the frequencies $f_{D_{1,2}}$ of the individual reflected beams, the beat frequency can be resolved using electro-optical transmitters.[2] Using (4.1) the beat frequency is given by the frequency difference

$$\Delta f = f_{D_2} - f_{D_1} = f_0\, \beta \frac{\cos(\psi_P - \phi) - \cos(\psi_P + \phi)}{1 - \beta \cos(\psi_P + \psi_D)} \ . \tag{4.2}$$

Since $\beta \ll 1$, (4.2) can be linearized using a Taylor series expansion around $\beta_0 = 0$ and neglecting terms of order 2 and above (i.e. Mac Laurin polynom of order 1), hence

$$\begin{aligned} \Delta f &\approx f_0\, \beta \left[\cos(\psi_P - \phi) - \cos(\psi_P + \phi)\right] \\ &= f_0\, \beta\, 2 \sin\psi_P \sin\phi \ . \end{aligned} \tag{4.3}$$

With the wave length $\lambda_0 = c/f_0$ in a fluid, the velocity ratio β is given by $\beta = |\boldsymbol{u}| / (\lambda_0\, f_0)$. Moreover, the velocity component obtained from an LDV measurement, i.e. the velocity component perpendicular to the optical axis of the scattering particle, is given by $u_n = |\boldsymbol{u}| \sin\psi_P$. Thus, (4.3) yields the defining equation for LDV measurements,

$$\Delta f = \frac{2}{\lambda_0} u_n \sin\phi \ , \tag{4.4a}$$

which is equivalent to

$$u_n = \frac{\lambda_0}{2\,\sin\phi}\, \Delta f \ . \tag{4.4b}$$

[2] In hydrodynamic measurement applications the beat frequency is of order $\Delta f = \mathcal{O}\left(10^5\ \text{Hz}\right)$.

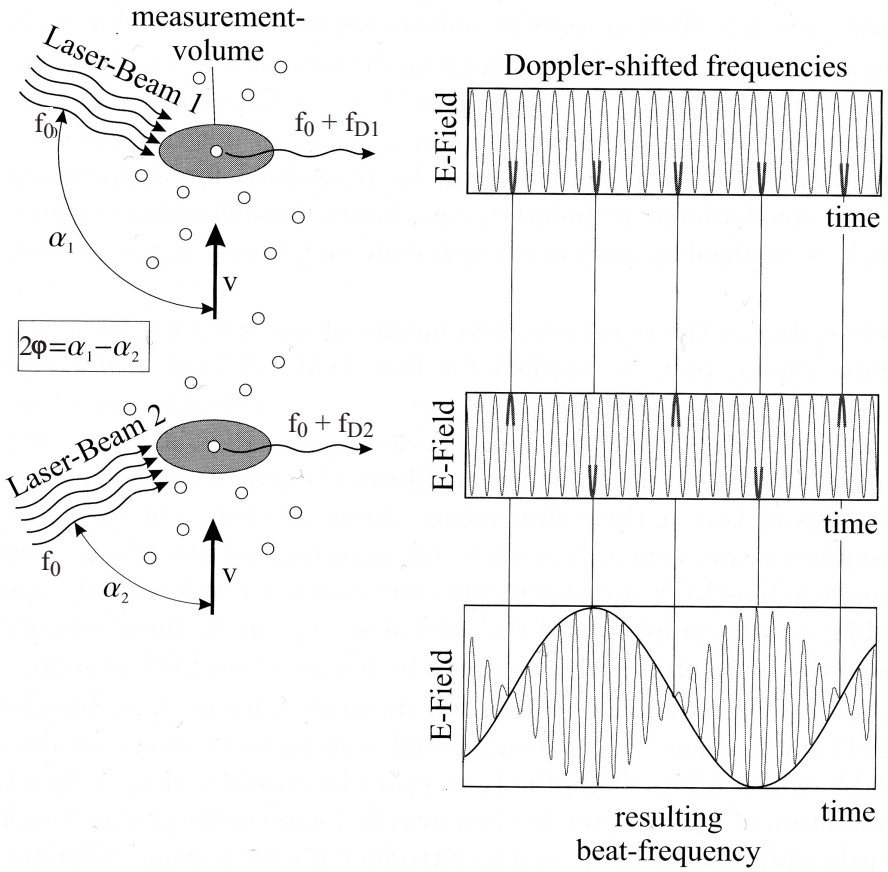

Figure 4.1. The measuring principle of the LDV technique is sketched for a dual-beam setup (adapted from EDER ET AL., 2001). Two coherent laser beams intersect with an half angle ϕ, and, thus, span the measurement volume. A particle, advected with the flow, crosses the measurement volume normally to the optical axis. The incident light scattered by the particle is frequency-shifted due to the *Doppler effect*. The Doppler-shifted signals $f_{D_{1,2}}$ of both incident beams are not resolvable by any opto-electronic means. The superposition of both signals results in a modulation with a much lower beat frequency Δf, which contains the velocity information and can be accessed and analyzed by electronic devices.

The above equation describes the beat frequency of the two Doppler-shifted signals from the incident laser beams scattered by a particle passing the measurement volume. Δf is often—though not very accurately—called the "*Doppler frequency*" of the particle. Equation (4.4) is valid in the limit of $\beta \to 0$, then the following characteristic properties of LDV techniques will apply. The velocity measurement is independent of the orientation of the receiving optics (forward-scattering, back-scattering, or inclined arrangements). The particle velocity component u_n, which is assumed to be an equivalent of the flow velocity component, is directly proportional to the beat frequency Δf. The measurements are sensitive to the intersection half angle ϕ as the only instrumental parameter to be accounted for.[3]

[3] Nevertheless, one has to make sure about the value of ϕ in order not to introduce a systematic error to a LDV measurement. Note, that ϕ has to be evaluated with respect to the same medium as λ_0, usually both values are given for vacuum or air.

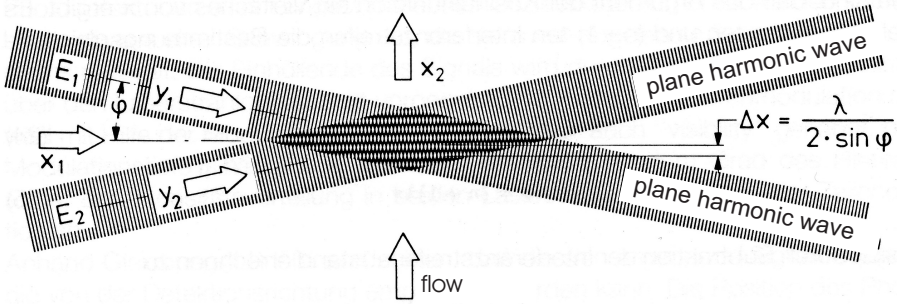

Figure 4.2. The optical principle of LDV measurements can also be derived by considering the interference of two coherent plane waves (following Ruck, 1990a). Constructive and destructive superposition result in a fringe pattern parallel to the optical axis with a spacing Δx filling the measurement volume. A particle passing through it will reflect light at the signal frequency $\Delta f = u_n/\Delta x$, which corresponds to the beat frequency (4.4).

It should be stressed that the defining equation (4.4) for the velocity measurements does not depend on the fluid in terms of the index of refraction n, albeit the intersection half angle ϕ changes with n.[4] We will briefly clarify this point using a simplified optical model based on light interference of the incident laser beams in the measurement volume, as indicated in Figure 4.2. The interference of the plane harmonic waves of two coherent beams (wave length λ) results in a fringe pattern which is directed with the optical axis. The *spacing of the fringes* is given by

$$\Delta x = \frac{\lambda}{2\,\sin\phi}\ . \tag{4.5}$$

Snellius' law says for the refraction of a light beam at a plane surface that $n_1\,\sin\phi_1 = n_2\,\sin\phi_2$. From $c = \lambda\,f$, and from the local light speed $n_1\,c_1 = n_2\,c_2$ the local wave length is $n_1\,\lambda_1 = n_2\,\lambda_2$, since f does not change when entering a different medium. Substitution into (4.5) shows that the indices of refraction cancel. The fringe spacing will remain a constant regardless of the fluid, in which the measurement takes place. Furthermore, as a particle passes the fringe pattern of the measurement volume with a velocity component u_n normal to the optical axis, i.e. normal to the fringes, it will scatter light pulses with a frequency $\Delta f = u_n/\Delta x$. Inserting (4.5) results in the defining equation (4.4a) once again.

Dynamics of tracer particles. From velocity measurements employing LDV systems (applies to PIV systems as well) we do not observe the motion of the fluid flow itself, but the motion of particles (or structures) advected by the flow. Therefore, the proper choice of tracer particles ideally suited for the given measurement task and flow configuration is crucial for a high quality of the

[4] In an arbitrary fluid (4.4b) becomes $u_n = n_{fl}\lambda_{fl}\,\Delta f/\,(2\,n_{fl}\sin\phi_{fl})$ using Snellius' law $n_1\sin\phi_1 = n_2\sin\phi_2$ and the local light speed $n_1\lambda_1 f = n_2\lambda_2 f$.

experimental examination. Concerning optical flow measurements, particles have to satisfy two general requirements. Firstly, tracer particles should have a good *scattering capability* to light in order to ensure their detectibility by optical devices. Secondly, the tracer particles have to be able to *represent the fluid motion* as much as possible (and necessary).

The first preposition requires a significant difference in the refraction indices of scattering particles and advecting fluid, which corresponds to a density difference ρ_P/ρ_F. Usually, tracers and fluid have a different state, i.e. solid tracers are transferred by a liquid flow, and solid or liquid tracers by a gaseous flow. The density difference ρ_P/ρ_F is of order $\mathcal{O}\left(10^0\right)$ in liquid flows, and of order $\mathcal{O}\left(10^3\right)$ in gaseous flows.

The second requirement—the ability of the tracer particle to follow the flow as close as possible—depends on the minimum wave number to be resolved in order to obtain the necessary information to answer the questions under consideration. Especially for turbulence measurements, for which the wave number range has to be resolved down to the smallest scales with high accuracy, a proper selection and handling of the seeding particles determines the quality of the results. From kinematic reasons particles have to be sufficiently small, and from dynamic reasons their mass to be accelerated has to be small. Compared to gaseous flows these restrictions are much less demanding in liquid flows, since on the one hand the Kolmogorov scale ℓ_η is usually much larger allowing for larger particles with better scattering ability. On the other hand, in liquid flows the density of the tracer particles can be adjusted to obtain $\rho_P/\rho_F \to 1$.

Under certain assumptions the flow behavior of suspended particles can be described analytically. For the *movement of a spherical particle in a viscous fluid* the following equation of motion has been derived based on the analysis of an individual particle settling in an infinite stagnant fluid by Basset in 1888.

$$\begin{aligned}\frac{\pi}{6}\, d_P^3\, \rho_p \frac{d\, u_P}{dt} &= 3\pi\, \nu_F\, \rho_F\, d_P\, (u_F - u_P) + \frac{\pi}{6} d_P^3\, \rho_F \frac{d\, u_F}{dt} \\ &\quad + \frac{\pi}{12}\, d_P^3\, \rho_F \frac{d}{dt}\, (u_F - u_P) \\ &\quad + \frac{3}{2}\, d_P^2\, \sqrt{\pi \nu_F} \int_{t_0}^{t} \frac{1}{t-T} \frac{d}{dT}\, (u_F - u_P)\, dT\end{aligned} \tag{4.6}$$

The force to accelerate the particle on the left-hand side of (4.6) is balanced by the terms on the right-hand side. The first term denotes the viscous drag force due to the *relative* or *slip velocity* $(u_F - u_P)$ according to Stoke's law. The second term represents the pressure gradient force due to local acceleration of the fluid around the sphere. The third term is the resistance of an inviscid

fluid to acceleration of the sphere following potential flow theory. The last term—the 'Basset history integral'—represents the drag force, which arises from the previous unsteadiness of the flow and, thus, covers the particle and fluid dynamics over the memory time T. The following assumptions have been made to obtain the above balance of forces for a settling spherical particle:

- homogeneous, time invariant turbulence,
- particles smaller than turbulence microscale,
- Stoke's drag law applies, i.e. spherical shape of particles, and
- relative Reynolds number ≤ 1 (i.e. relative velocity $(u_F - u_P)$ is small, $u_P/u_F \to 1$),
- low particle density and infinite flow domain, i.e. no interaction of particles and no change of fluid flow,
- no external forces (e.g. gravity, buoyancy, electromagnetic fields).

Assuming that the temporal derivative of the slip velocity, i.e. the relative acceleration of the particle $\frac{d}{dt}(u_F - u_P)$, is given by $\frac{d\,u_F}{dt} - \frac{d\,u_P}{dt}$, the *Basset-Boussinesq-Osseen (BBO) Equation* can be obtained.

$$\frac{d\,u_P}{dt} = \frac{18\,\nu_F}{\left(\frac{\rho_P}{\rho_F} + \frac{1}{2}\right) d_P^2}\,(u_F - u_P) + \frac{3}{2\left(\frac{\rho_P}{\rho_F} + \frac{1}{2}\right)}\frac{d\,u_F}{dt} + \frac{9}{\left(\frac{\rho_P}{\rho_F} + \frac{1}{2}\right) d_P\,\rho_F}\sqrt{\frac{\nu_F}{\pi}}\int_{t_0}^{t}\frac{1}{t-T}\left(\frac{d\,u_F}{dT} - \frac{d\,u_P}{dT}\right)dT \tag{4.7}$$

A more detailed discussion of the derivation of the BBO Equation (4.7) and its solution can be found in Durst et al. (1981), in Ruck (1987, 1990a), or in Albrecht et al. (2003). Moreover, consequences of the particle dynamics approximated by the BBO Equation with respect to optical flow measurement systems are introduced in the readings mentioned above—and are also discussed in literature dealing with field-wise optical measurement techniques (cf. e.g. Raffel et al. (1998) for PIV applications). For instance, if the magnitude of the particle velocity is restricted to deviate by less than 1% on average from the fluid velocity, depending on the frequency of the velocity fluctuation a maximum spherical diameter d_P can be computed. In a liquid flow with a density ratio $\rho_P/\rho_F = 1.5$ particles with a diameter of 16 µm are able to represent turbulent fluctuations of 1 kHz, particles of $d_P = 5$ µm will even follow 10 kHz fluctuations within 1% deviation in velocity amplitudes.

4.1.2 Technical detail of the employed LDV system

In order to obtain the horizontal velocity components of turbulent shallow wake flows an 'off-the-shelf' 2-channel LDV system was employed. This LDV

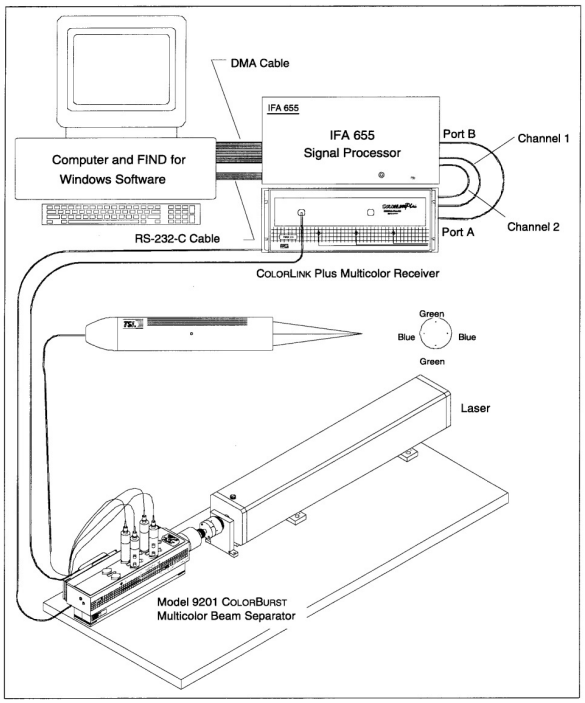

Figure 4.3. General setup of the off-the-shelf 2-component LDV system (TSI, 1996)

system was completed by a third channel to meet the needs of a LIF measurement technique, which will be introduced in Section 4.2. Optically, the LDV system used a dual-beam differential technique, and a backscatter mode for the receiving optics.

The configuration of the LDV measuring system is illustrated in Figure 4.3, a tabular overview is given in Table 4.1. The LDV system comprises a laser source, a two component beam separator (containing a 40 MHz Bragg-cell), emitting and receiving optics, a three component receiver (containing the photomultipliers), a burst signal analyzer, and a PC. Despite of the laser, the whole system was assembled and provided by TSI® Inc.

As a *laser light source* a water-cooled gas laser filled with the noble gas argon to be ionized—a 5 Watt Innova 70/5E provided by Coherent®—was operated in the continuous-wave mode. Because of a broadband reflector the laser tube emitted a polychromatic spectrum of light characteristic for argon-ion. The most energetic lines in the emitted Ar^+ spectrum are the green, blue-green, and blue lines (wave lengths $\lambda = 514.5$ nm, 488 nm, and 476 nm, respectively). Within the *multi-color beam separator* the two most intense lines $\lambda_g = 514.5$ nm and $\lambda_{bg} = 488$ nm—containing about 70% of the energy of the Ar^+ emission spectrum—were extracted from the collimated beam, for each wave length two partial beams were generated, and one partial beam of each color was frequency-shifted by a 40 MHz Bragg-cell. Finally, each beam was fed into an individual optical fiber and, thus, was directed over a distance of 10 m to the optical probe. The emitting optics focussed each beam, and directed

each pair of beams to intersect at the same point to build the measurement volume. The employed *optical probe* (model 9251-102, submersible) had a vacuum focal length of 101.1 mm, and an intersection half angle of approximately $\phi = 3.9°$. The ellipsoidal measurement volume had a length of approximately 1.0 mm and a diameter of 70 µm. The light intensity in the measurement volume was adjusted as to minimize the signal-to-noise ratio, or as needed for the LIF measurements. The long-term stability of the light intensity is of minor importance for LDV measurements, it will be addressed in Section 4.3. The Doppler-shifted light of each of the four beams scattered by a tracer particle crossing the measurement volume was observed with the receiving optics implemented in the probe. As the receiving optics—with an optical aperture of 0.091—were located exactly at the system's optical axis between the emission lenses of the four beams, the LDV was operated in a true backscatter mode. Together with the modulated wave lengths λ_g and λ_{bg} the full light spectrum was received and launched to the multi-line fiber.

Via the multi-line fiber the signals were passed to the *multi-color receiver*. The wave lengths of the predominant spectral lines λ_g and λ_{bg}, each of which contained a velocity information in the signal modulation by the beat frequency Δf, were separated by narrow band-pass filters yielding the signal channels 1 and 2. An additional band-pass filter isolated the fluorescence signal of the LIF system on a third channel. The optical signals were converted into electrical signals and amplified by means of photomultiplier tubes.

The voltage signals of the channels 1 and 2 have then been processed by the *burst signal analyzer* (Signal Processor IFA 655 Digital Burst Correlator) with respect to frequency, phase, burst initial time and transit duration. The evaluation of the signals utilized a patented technique based on auto-correlation for real-time burst detection and for digital frequency analysis. More detailed information about the burst signal evaluation technique is provided by TSI (1996). The obtained data was passed over a DMA interface on to the PC and was further processed and stored by the analysis and control *software package* FIND for windows, versions 1.2 and 1.3. The FIND software also enabled the user to control the LDV system via a RS 232 interface (e.g. frequency shift of Bragg-cell, voltage of photomultipliers, range of signal filters, parameters for BSA).

The optical probe, connected with the emitting and receiving devices by a 10 m optical fiber, could be positioned at an arbitrary location above the shallow flow under examination by means of a fully-automated 3D traversing system. The optical axis was exactly aligned vertically downwards, i.e. perpendicular to the bottom and to the stagnant water surface. By vertically traversing the optical probe with an accuracy of ≤ 20 µm the probe and, thus, the measurement volume could be placed accurately with respect to the bottom. Moreover, adjustment algorithms implemented in the control software

Table 4.1. Instrumentation of the point-wise measurement systems for flow velocity (LDV) and for mass concentration (LIF)

light source	
laser	argon-ion, continuous-wave
type	Innova 70/5E, Coherent®
power output	max. 3.5 W in polychromatic beam
LDV system *TSI®*	
beam separator	ColorBurst Multicolor Beam Separator (model 9201) with 40 MHz Bragg-cell, wave lengths $\lambda_g = 514.5$ nm, $\lambda_{bg} = 488$ nm
transmitting and receiving optics	2D probe (model 9251-102), submersible, backscatter, focal length 101.1 mm, intersection half angle $\phi \approx 3.9°$, aperture 0.091, length of fiber optic cable 10 m
measurement volume	ellipsoid, length 1.0 mm, diameter 70 µm, typical power during operation 150 mW to 200 mW
receiver	ColorLink Plus Multicolor Receiver (model 9230), 2 + 1 channels, photomultipliers for wavelengths 514.5 nm, 488 nm, and 590 nm (LIF)
burst signal analyzer	Signal processor IFA 655 Digital Burst Correlator, 2 components
LIF system *add-on for TSI® LDV system*	
receiver	ColorLink Plus Multicolor Receiver, bandpass-filter 590 ± 5 nm, photomultiplier, 1 kHz low-pass filter
LDV-LIF coupling	DataLink Multichannel Interface DL100 with 12 bit A/D card
PC for system control, data storing, and data processing	
personal computer, Intel processor P-I 90 MHz, 32 MB RAM, hard disk, Ethernet card, RS 232 interface, DMA interface card to IFA 655	
OS	Windows 3.11 and Windows NT
software	FIND for windows, versions 1.2 and 1.3
tracer particles	
LDV	low-concentrated latex particles (white emulsion paint)
LIF	Sulpho-Rhodamine, Acid Red 52, C.I. 45100 Rhodamine B, Basic Violet 10, C.I. 45170

FLAMES (cf. Dietz et al., 2002) allowed for positioning the measurement volume at a constant height above the bottom during a measurement run regardless of the horizontal coordinates of the probe. As the probe was placed above the free surface of the flow, both the incident laser beams and the scattered light signals had to cross the air-water interface. Since the laser beams were inclined only by the small intersecting half angle ϕ against the normal vector $\boldsymbol{n}$ of the surface plane, and the receiving optics were aligned exactly parallel to $\boldsymbol{n}$, following geometrical optics the air-water transition could be handled easily for a smooth plane interface. Although the shallow plane bottom shear flows under consideration were always restrained to Froude numbers $Fr = U/\sqrt{g\,h} \leq 0.3$, and additional measures were taken to minimize surface waves, small surface distortions remained. The introduction of a cylindrical obstacle into the base flow to generate lateral shear layers led to further distortion of the plane water surface. In order to improve the optical access to the measurement volume, an optical glass disk (diameter 2 in, thickness 0.25 in, crown glass with refraction index 1.52) was inserted into the optical path at the water surface.[5] The use of the optical disk ensured that fluctuations of the water surface did not influence the LDV-LIF measurements. Otherwise, a lower signal-to-noise ratio could reduce the signal quality and, thus, the data rate of valid bursts. Also, artificial turbulence due to movement of the measurement volume could be introduced. Furthermore, stronger inclination or curvature of the air-water interface could lead to a temporal reduction and even loss of the measurement volume, because the laser beams would not intersect properly. As a safety precaution the optical glass disk prevented laser light reflected by the wavy surface to randomly cross the laboratory.

4.2 Laser Induced Fluorescence

Laser Induced Fluorescence (LIF) is another non-intrusive flow measurement technique, which has been applied in experimental fluid dynamics research for almost 20 years now. Though its main field of applications is aerodynamics and combustion technology, LIF techniques are also used in hydrodynamics. LIF allows for qualitative flow visualization, and for one- or two-dimensional quantitative observation of mass concentration or temperature with high temporal and spatial resolution (but also LIF-based measurements of pressure or velocity have been reported in aerodynamics).

[5] Since the optical glass only touched the water surface, no significant disturbance of the flow could be observed in the water column below the disk. Because of its limited diameter and its smooth surface, the thickness of the developing boundary layer was much smaller than the length of the measurement volume. The LDV-LIF measurements can therefore still be called 'non-intrusive'.

LIF has become a common tool in gaseous flow studies both in fundamental research and in engineering applications. Andresen (2001) provides a comprehensive introduction to LIF together with some typical experimental set-ups and applications to examine combustion processes. In the field of basic hydrodynamic research also a large number of publications can be found, some papers concerning the measurement techniques will be referred to in the remainder of this chapter. Single-point LIF techniques have been applied to various turbulent shear flows. Lemoine et al. (1996) reported synoptic LDV-LIF measurements in a turbulent jet flow. Crimaldi & Koseff (2001) compared point-wise LIF measurements with high temporal resolution and field-wise PLIF measurements in a chemical plume tracing investigation. In unbounded wake flows Rehab et al. (2001) used LIF to access the concentration of a tracer mass, and Seuntiëns et al. (2001) utilized the temperature sensitivity of a fluorophor to observe the thermal transport with a PLIF system. v. Carmer & Jirka (2001) reported point-wise co-incident LDV-LIF measurements to obtain the mass transport in different kinds of shallow turbulent wake flows.

Technical detail also on the equipment of the employed LIF measurement system has already been presented in Section 4.1, since for the present application the LDV and LIF systems mainly feature the same hardware devices. Additional information on how to combine both systems into a synoptic LDV-LIF technique will be given in Section 4.3. The present implementation of a LIF technique to a LDV measurement system was first described by v. Carmer et al. (2000) regarding hardware, data analysis, and application to turbulent shallow wake flows. An overview of the LDV-LIF system and the extended LIF model has been published by v. Carmer (2000).

4.2.1 Introduction to fluorescence

LIF techniques are based on the natural fluorescence of molecules and atoms, i.e. the ability to absorb quantized electromagnetic energy hf, and to re-emit part of the absorbed energy at specific frequencies f_F in the visible spectrum. Since the electromagnetic radiation is emitted due to electron transitions from excited electronic states back to the ground electronic state, the intensity of the radiation is directly related to the population density in the upper electronic states, which naturally are only weakly populated. Due to induction by laser light a considerable number of molecules can be promoted from the densely populated ground state to an excited electronic state. The subsequent transition back to the ground state associated with emission of fluorescent light is, thus, induced or strongly enforced by the laser stimulation. Absolute values of the mass concentration of a considered molecular species in a measurement volume can be computed from the intensity of the fluorescence signal.

Quantum-mechanical molecule model. In order to illustrate the light–matter interactions involved in the inelastic Raman scattering and in fluorescence a simplified quantum-mechanical molecule model can be employed: BOHR's classical *model of electronic shells*. Briefly recapitulating the model concept, the protons and neutrons form the nucleus of an atom, electrons are encircling the nucleus along orbits—so-called 'shells'—with certain distinct radii. The energy of an electron depends on its orbital radius, i.e. on its distance from the nucleus; the quantization of the total energy of an atom is represented in BOHR's model by the assumption, that only discrete orbits or shells are allowed. In the least energetic state of an atom—the ground electronic state X—each electron occupies an orbit as close to the nucleus as possible. An atom can absorb an additional quantum of energy provided e.g. by collision with other atoms, electrons, or photons by lifting an electron from an inner shell to a free outer shell. This configuration is called an *excited* or *upper electronic state* denoted by A, B, C, etc. Since the excited states are inherently unstable, the electron tends to spontaneously relax back to a lower excited state or preferably to the ground state, thereby emitting an appropriate amount of energy.

Molecular inelastic scattering processes. For a molecule consisting of two or more atoms, besides the electronic state, two additional mechanisms exist to store energy: *vibration* and *rotation*. The atoms in the molecule can vibrate against their common center of mass; the forces controlling this vibration result from the bonded electrons of the atoms. Additionally, the molecule may rotate around its center of mass. Similar to the electronic orbits of atoms, only distinct levels are possible both for vibration and rotation. The energy difference of adjacent rotational energy levels J is much lower than the energy difference of adjacent vibrational levels v, which in turn is significantly lower than the energy difference between neighboring electronic states. Various vibrational levels exist for each electronic state of a molecule, and for each vibrational level different rotational levels may occur. Figure 4.4 illustrates this quantum-mechanical model. The total energy content E_{tot} of a molecule in the electronic state e (X, A, B, ...), with the vibrational level v, and with the rotational level J can be approximated by the sum of the term energy, the vibrational and rotational energy, $E_{tot} = E_e + E_v + E_J$.

As illustrated on the left of Figure 4.4, in Rayleigh and Raman scattering of light an incident photon of the energy hf_0 may provide an amount of energy to the molecule, which is too large to change the rotational or even vibrational level of the molecule, but which on the other hand is not sufficiently large to lift the molecule to an excited electronic state. Therefore, the molecule is lifted to a highly unstable intermediate, *virtual state*, and immediately—after a time of $\mathcal{O}\left(10^{-15}\text{ s to }10^{-14}\text{ s}\right)$ (cf. GUILBAULT, 1973; STRUBE, 2001)—drops back

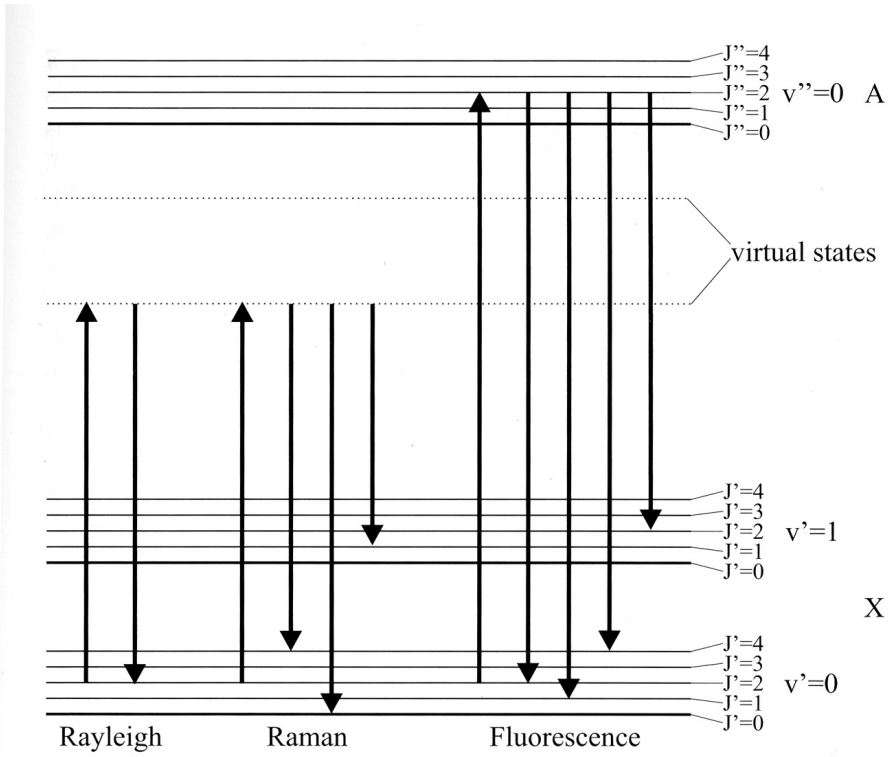

Figure 4.4. The processes of Rayleigh scattering, rotational and vibrational Raman scattering as well as fluorescence can be illustrated employing a simplified quantum-mechanical molecule model. Concerning the energetic states of molecules, three basic parameters are used to describe the energy associated with a molecule: the electronic state *X, A, B*, etc., the vibrational level v, and the rotational level J. Ro-vibrational levels of the ground electronic state X are denoted (v', J'), those of the first excited state A are denoted (v'', J''). (Kruppa et al., 2001)

to the ground electronic state emitting an appropriate amount of energy.[6] If the molecule relaxes back again to the same ro-vibrational level of the ground electronic state, the re-emitted energy quantum equals the absorbed quantum hf_0, i.e. the frequency of the scattered light remains the same as the frequency of the incident light. This inelastic scattering process is called *Rayleigh scattering*. If the excited molecule relaxes back to a vibrational or rotational level of the ground electronic state differing by hf_M from the initial level, it will emit an energy quantum $h(f_0 \pm f_M)$ deviating from the absorbed quantum hf_0, thus emitting radiation of a different wave length $c/(f_0 \pm f_M)$. This elastic scattering process is called *Raman scattering*. The frequency difference between the incident and the emitted photon corresponds to the difference in

[6] Note that the virtual state is not related to a specific energetic level, i.e. the excitation does not require a specific energy quantum hf. Thus, photons of arbitrary wave lengths c/f can participate in Rayleigh and Raman scattering.

the ro-vibrational levels, and is called Stokes shift $f_S = \mp f_M$.[7] It should be stressed again that Raman scattering does not depend on a specific frequency of excitation, therefore light of different wave length can be applied in Raman spectroscopy.

The radiative process of *fluorescence* involves a transition back to the ground electronic state from an excited electronic state—instead of a transition from a virtual state as for Rayleigh and Raman scattering processes. This is visualized on the right hand side of Figure 4.4. Depending on the amount of absorbed quantized energy a molecule is lifted to an appropriate ro-vibrational level of an excited electronic state. It then will undergo a transition without visible radiation to a lower—preferably the lowest—ro-vibrational level in the upper electronic state, followed by a transition involving visible radiation back to the ground electronic state. Since the absorbed additional energy is reduced due to the transition to a lower ro-vibrational level, less energy is emitted in the fluorescent relaxation back to the ground electronic state. Thus, the emitted fluorescent radiation displays longer wave lengths than the absorbed light, the emission spectrum is red–shifted to lower frequencies. Due to the additional ro-vibrational transition the temporal delay of the fluorescence response is much longer than the response time of Raman scattering (cf. also Table 4.2).[8]

Most species show the ability to fluoresce, i.e. to emit radiation of characteristic frequencies. Contrary to Raman spectroscopy in spectroscopic fluorescence the emission spectrum itself characterizes a molecular species. Depending mainly on the temperature, generally only a small fraction of a molecular species is in excited electronic states, since the upper electronic states are meta-stable, typical lifetimes in the excited states are in the order of $\mathcal{O}\left(10^{-10}\text{ s to } 10^{-5}\text{ s}\right)$ (cf. Kruppa et al., 2001). Therefore, the natural fluorescence process results in emission of very low intensity. In order to promote a larger number of molecules into their upper electronic states, additional energy has to be provided e.g. by high-intensity (laser) illumination. Since the given molecule, which is initially in a specific level of its ground state $X(v', J')$, has to be excited to a specific level of an upper electronic state, say $A(v'', J'')$, a

[7] Note that the Stokes shift is independent of the actual frequency f_0 of the incident photon. The Stokes shift denotes the frequency difference $f_S = f_0 - (f_0 \pm f_M)$. It indicates specific ro-vibrational energetic levels that are characteristic for a molecular species.

[8] Fluorescent radiation is emitted in the immediate transition from an upper electronic singlet state, i.e. a state with a multiplicity of 1, in which all electrons occur with paired spins. When the spin of one electron changes so that the spins of two electrons are the same or unpaired, a triplet electronic state with a multiplicity of 3 is achieved. We speak of *phosphorescence*, if the relaxation from the excited electronic singlet state involves a non-radiative inter-system crossing to an excited triplet state of a lower energy level, followed by a radiative transition back to the ground electronic state. The additional internal conversion from a singlet to a triplet state in phosphorescence leads to excitation lifetimes of $\mathcal{O}(10^{-4}\text{ s to } 10^{1}\text{ s})$. (cf. Guilbault, 1973; Wolfbeis, 1993)

specific quantum of energy hf_0 has to be provided. Thus, the stimulating laser light has to be tuned to a specific frequency f_0 in order to excite a desired transition of a given species. Hence, the absorbtion spectrum with the main excitation frequencies spectroscopically characterizes a fluorescent substance, as does the emission spectrum with the main extinction frequencies. Since in laser induced fluorescence the excitation of molecules into their upper electronic states lead to the absorbtion to larger energy quanta compared to Rayleigh and Raman scattering, also the re-emission of radiative energy is much stronger—5 to 15 orders of magnitude (Kruppa et al., 2001)—in fluorescence.

Table 4.2 summarizes some of the main differences of the inelastic light scattering processes discussed above.

Once a molecule is in a meta-stable excited electronic state, there are a number of possibilities to change into a different more stable state. Primarily, excited molecules will transit back to a ro-vibrational level of the stable ground electronic state, and will radiatively re-emit part of the additional quantized energy in the visible spectrum. Basically, the following transitions from an upper electronic state may occur:

- The molecule may undergo a *spontaneous fluorescence transition* to the ground electronic state involving light emission. Depending on which vibrational and rotational level of the ground state is reached, the fluorescent radiation may either be inelastic or elastic. Obviously, atoms may solely fluoresce elastically. The fluorescence rate is denoted by the first Einstein coefficient A_{21}, which equals the reciprocal of the mean lifetime in the appropriate excited electronic state.
- The molecule may relax back to the ground electronic state by a *laser-stimulated transition* emitting a photon at the laser frequency in the direction of the laser beam (analogously to Stimulated Raman Scattering). This process is represented by the second Einstein coefficient B_{21} directly proportional to A_{21} and to ${\lambda_0}^3 = (c/f_0)^3$. The rate of stimulated transitions is obtained by multiplication with the laser light intensity. Also the excitation rate of a molecule, i.e. the stimulated transition from the ground state to an

Table 4.2. Comparison of inelastic scattering of light by Raman scattering and fluorescence (data compiled from Mayinger & Feldmann, 2001)

scattering process	**scatterer**	**excited state**	**excitation lifetime** [s]	**frequency shift** $\Delta f/f$
Raman	molecules	virtual	$\mathcal{O}\left(10^{-14}\right)$	$\mathcal{O}\left(0 \div 10^{-1}\right)$
fluorescence	atoms, molecules	electronic	$\mathcal{O}\left(10^{-10} \div 10^{-5}\right)$	$\mathcal{O}\left(0 \div 10^{-2}\right)$

upper electronic state, is expressed by the product of an Einstein coefficient B_{12} and the intensity of the incident light.

- The molecule may absorb an additional quantum of incident light and transit to an even higher energetic state (including eventual ionization). The *photo-ionization* rate is usually negligibly small.
- For instance collisions of the molecule with other molecules may result in a non-radiative transition to a lower electronic state. This effect is referred to as '*collisional quenching*' or '*concentration quenching*'. The quenching rate denoted by Q_{21} usually is unknown for given system conditions (e.g. temperature, pressure, concentration).
- Collisions with other molecules may also cause *vibrational and rotational transitions* within the excited state, and a subsequent fluorescent transition.
- Interactions within the molecule may lead to *dissociation*; if the dissociation is caused by a shift from a stable configuration to an unstable electronic configuration, the process is called 'predissociation'.

In this work we want to emphasize on the main outcomes of the physico-chemical processes, as they are of interest for the practical implementation of a LIF measuring system. For a more thorough summary of the background of LIF the reader is referred for instance to Guilbault (1973); Andresen (2001); Deusch et al. (1996).

The fluorescence rate generally depends on the various rates of transitions and on the intensity of the excitation. Hence, the fluorescent light intensity and, thus, the signal strength I_f of a LIF measurement obtained from a fluid containing a specific fluorescent species is proportional to the absolute number of species molecules in the measurement volume,—i.e. to their number (or mass) concentration c—and to the intensity I_e of the exciting laser light,

$$I_f \propto I_e\, c\ . \tag{4.8}$$

Because of its direct proportionality to I_e in (4.8) this standard laser induced fluorescence technique featuring moderate excitation intensities is also called *linear LIF*. Apart from c, the signal strength I_f is also proportional to the excitation rate $B_{12}\, I_e$ and to an approximated *Stern–Vollmer factor* $A_{21}/(A_{21} + Q_{21})$, which is essentially the *fluorescence quantum efficiency* Φ_f. The a priori unknown quenching rate Q_{21} requires a detailed and extensive calibration procedure of the individual set-up in linear LIF.

For a high incident laser intensity, the signal strength I_f becomes independent of I_e, as the population density of molecules in the excited electronic state reaches its maximum value. This measurement technique is called *laser induced saturated fluorescence LI(S)F*. As demonstrated e.g. by Andresen (2001), the signal strength then becomes proportional solely to $A_{21}/(B_{12} + B_{21})$ and to the species concentration c. Note that in LI(S)F I_f does not depend on Q_{21}.

Hence, if a high excitation intensity can be realized for a specific measurement technique and set-up, LI(S)F is generally favorable since both calibration and control and stabilization of incident light intensity would be much easier. However, in the present set-up of a combined LDV-LIF measurement system a high light intensity in the measurement volume, firstly, is technically difficult to achieve and to maintain over the duration of a full measurement run due to the sensitive fiber optics and couplers. Secondly, it will lead to a loss of accuracy of the LDV measurements resulting in reduced data rates and temporal resolution. Thirdly, additional attenuation effects due to photo-decomposition may occur depending on the fluctuating transit times through the measurement volume, which could only be taken into account in a combined LDV-LIF system providing also the instantaneous flow velocity.

4.2.2 Fluorescent tracer material

Since the ability of molecules to fluoresce is utilized in different scientific fields and in various measurement techniques, much information can be found about specific fluorescent compounds. For hydrodynamic applications some useful readings may be suggested. Fluorophors employed as flow markers in field examinations were presented for instance by Smart & Laidlaw (1977) for free-surface flows, and by Käss (1992) for groundwater flows. For more fundamental information on fluorescent compounds we recommend for instance Green (1990) or Slavik (1994).

General considerations. For the different kinds of application of laser induced fluorescence like qualitative flow visualization, or point-wise or field-wise quantitative measurement of scalar flow properties a selection of few fluorescent tracer materials are commonly employed, among them most prominently *fluorescein sodium*[9] and *rhodamine B*. Among the basic constraints for a proper selection of a fluorescent tracer for liquid–flow applications is the solubility in water; water should be the primary solvent for the fluorophor. Since the transparency of the water body must not be reduced significantly in order to apply optical non-intrusive measuring techniques, the concentration of the fluorophor should be kept low. Therefore, the absorbtion or extinction coefficient ε of the tracer material as well as its fluorescent quantum efficiency Φ_f should display high values. Though numerous molecular species and compounds show the ability to fluoresce—and are subjected to fluorescence spectroscopy—, only few groups of organic substances meet the needs mentioned above, primarily the group of xanthene dyes.

[9] *Fluorescein sodium*—also known as *uranin*—is the disodium salt of fluorescein ($C_{20}H_{12}O_5$). In contrast to uranin, *fluorescein* has a poor solubility and fluorescence in water. Nevertheless, native English-speaking authors often misleadingly use 'fluorescein' for its disodium salt 'uranin'.

More specific criteria for the selection of a well-suited fluorescent tracer for the use in a LIF measuring system can be summarized as follows:

- good solubility in water,
- high specific decadic extinction coefficient ε to allow low concentrations in order to maintain transparency,
- high fluorescent quantum efficiency Φ_f to obtain sufficiently strong signals and high signal–to–noise ratio also for low concentrations of fluorophor,
- absorbtion spectrum should meet the incident laser light or vice versa,
- emission spectrum should meet the detector sensitivity or vice versa,
- large Stokes-shift—difference between maxima in wave length spectra of absorbtion and emission—to ensure good separability of LIF signal, and to avoid re-absorbtion of emitted radiation,
- high photo–stability,
- slowly reacting to avoid quenching by other molecular components of water body,
- low toxicity and secure disposability,
- good availability and price.

Since the LIF system was intended to be coupled to the 2-component LDV system powered by a cw Ar^+ laser, the wave lengths of the exiting laser light at $\lambda_{bg} = 488$ nm and $\lambda_g = 514.5$ nm as well as the comparably low intensity were predefined.

As a first choice *fluorescein sodium* could have been employed for the current LDV-LIF application, because it is well detectable, non-toxic, lowly sorptive, widely available, and inexpensive. The maximum absorbtion wave length $\lambda_{max} = 491$ nm meets the blue-green emission line λ_{bg} of an Ar^+ laser. Unfortunately, the maximum wave length of the emission spectrum of fluorescein sodium at $\lambda_{max} = 512$ nm coincides with the green—and strongest—emission line $\lambda_g = 514.5$ nm used for the LDV system. Thus, the major part of the fluorescence spectrum would be lost for the LIF concentration measurements, but would lead to poor signal quality of the first LDV channel. To avoid this problem the blue Ar^+ emission line at $\lambda_b = 476$ nm could have been used for the LDV instead of λ_g, the accompanying reduction of light intensity in the measurement volume would have been of relevance only for the LDV system, and could have been accepted. Since a major drawback of fluorescein sodium is its reduced photo–stability, instead of changing the LDV wave length we preferred to select a different fluorophor. For the same reason—poor photo–stability—another xanthene dye, the *eosin*, was excluded, albeit its extinction maxima at $\lambda = 516$ nm and 480 nm ideally suit the strongest Ar^+ emission lines. Some species of the family of rhodamine dyes, though generally well suited for Ar^+ laser excitation, also had to be rejected. *Rhodamine WT* is available primarily in the US. *Rhodamine 6G* shows high sorptivity, and is said to be

toxic and cancerogenic. *Amidorhodamine G* or *sulphorhodamine G* displays properties similar to sulphorhodamine B at a 25 nm blue-shift of the absorbtion and emission spectra, which would make it a preferable fluorophor for the Ar^+ excitation. However, the commercial-grade dye often can be obtained only in a reduced purity, which may lead to unexpected quenching effects. From the family of the rhodamines the *rhodamine B* and *sulphorhodamine B* are best suited for the designed synoptic LDV-LIF measurement system. Compared to rhodamine B the sulphorhodamine B is less sorptive, and shows a higher resistance to photo-bleaching and pH-variation. Table 4.3 summarizes the main characteristics of the fluorescent dyes employed in the framework of this research, i.e. sulphorhodamine B and rhodamine B, in comparison to the widely-used fluorescein sodium.

The time scale of the fluorescence processes can be characterized by the *mean excitation lifetime*, i.e. the average time between absorbtion and elastic re-emission of a light quantum, and is of order $\mathcal{O}(10^{-9}$ s) for most organic molecules. For instance, Guilbault (1973) reported a fluorescence lifetime of 5.8 ns for rhodamine 6G in water.

Sulphorhodamine B. The first of two different dye tracers that we employed for the non-intrusive point-wise combined measurements of velocity and mass by means of a synoptic LDV-LIF system was sulphorhodamine B (C.I. 45100, acid red 52) provided by Hoechst under the product name "Duasyn Säurerhodamin B 01". Using water as a solvent its wave length spectrum of extinction (or absorption or excitation) peaks around $\lambda_{max} = 564$ nm, with secondary maxima at 525 nm and 342 nm. The molar decadic extinction coefficient for λ_{max} is $\varepsilon_M = 89,900$ (cm M/l)$^{-1}$. The emission spectrum of the fluorescent radiation shows a maximum at a wave length of 583 nm, and hence a significant Stokes-shift of 19 nm.

The laser light in the measurement volume exciting the fluorescent dye was composed of four beams of the two distinct wave lengths 488 nm and 514.5 nm, adjusted as to obtain equal light intensity for both pairs of beams. Figure 4.5 shows the emission spectra of sulphorhodamine B solutions of different concentrations in tap water, as they were obtained from fluorescence spectroscopy using an equal intensity excitation with $\lambda_{bg} = 488$ nm or $\lambda_g = 514.5$ nm separately. Obviously, the absorbtion or extinction coefficient, $\varepsilon(\lambda)$, is much higher for the green light than for the blue-green light resulting in significantly more energetic emission spectra for excitation with $\lambda_g = 514.5$ nm.

The polychromatic light scattered by LDV tracer particles and by the LIF dye tracer was divided by beam splitters in the ColorLink multi-color receiver into three partial beams. Each partial beam was subjected to a narrow optical band-pass filter, then transformed and amplified by a photo-multiplier. Figure 4.6 (a) shows the extinction spectrum of sulphorhodamine B as well as

the emission spectrum when excited at $\lambda = 514.5$ nm, i.e. at the wave length λ_g of green LDV beams. Additionally, the characteristic line of the optical band-pass filter $\lambda = 590 \pm 5$ nm indicates, which portion of the fluorescence signal was separated from the emission spectrum to be processed and analyzed by the LIF measurement technique.

Rhodamine B. As a second xanthene dye tracer *rhodamine B* (C.I. 45170, basic violet 10) was employed for the synoptic LDV-LIF measurement technique adapted for measurements in shallow turbulent wake flows. The tracer material was produced by MERCK under the product number 7599. The absorption spectrum reaches its maximum at a wave length $\lambda_{max} = 554$ nm with secondary maxima at 520 nm, 355 nm, and 300 nm. The molar decadic extinction coefficient at λ_{max} approximately equals $\varepsilon_M = 108,000$ (cm M/l)$^{-1}$. The

Table 4.3. The organic molecular tracer materials employed for combined LDV-LIF measurement in the framework of shallow turbulent wake flows are *rhodamine B* and *sulpho rhodamine B* solved in tap water. Its characteristic values as relevant here are compared to *fluorescein sodium*, which is often employed in LIF applications. [data: GREEN (1990); KÄSS (1992) unless indicated otherwise]

	rhodamine B	**sulpho-rhodamine B**	**fluorescein sodium**
C.I. constitution no.	45 170	45 100	45 350
C.I. generic name	basic violet 10	acid red 52	acid yellow 73
producer & product name	MERCK, Merck index no. 7599	HOECHST, "Duasyn Säurerhodamin B 01"	
chemical structure	$C_{28}H_{31}N_2O_3Cl$	$C_{27}H_{29}O_7N_2S_2Na$	$C_{20}H_{10}O_5Na_2$
molar mass $[g/M]$	479.02	580.65	376.28
λ_{max} of extinction spectrum $[nm]$	554 520; 355; 300	564 525; 342	491 322
λ_{max} of emission spectrum $[nm]$	576	583	512
specific decadic extinction coefficient ε at λ_{max} $[(m\,kg/m^3)^{-1}]$	22,700	15,500	20,000
molar decadic extinction coefficient ε_M at λ_{max} $[(m\,M/m^3)^{-1}]$	10,800	8,990	6,813
molecular diffusivity D $[m^2/s]$	n. a. ($8 \cdot 10^{-10}$ for rhod. 6G (CRIMALDI & KOSEFF, 2001))		$5.2 \cdot 10^{-10}$ (WALKER, 1987)
molecular Schmidt no. $Sc = \nu/D$ $[-]$	n. a. (1,250 for rhod. 6G)		1,930
fluorescence quantum efficiency Φ_f $[-]$	0.60 (DEUSCH ET AL., 1996)	n. a.	0.92 (DEUSCH ET AL., 1996)

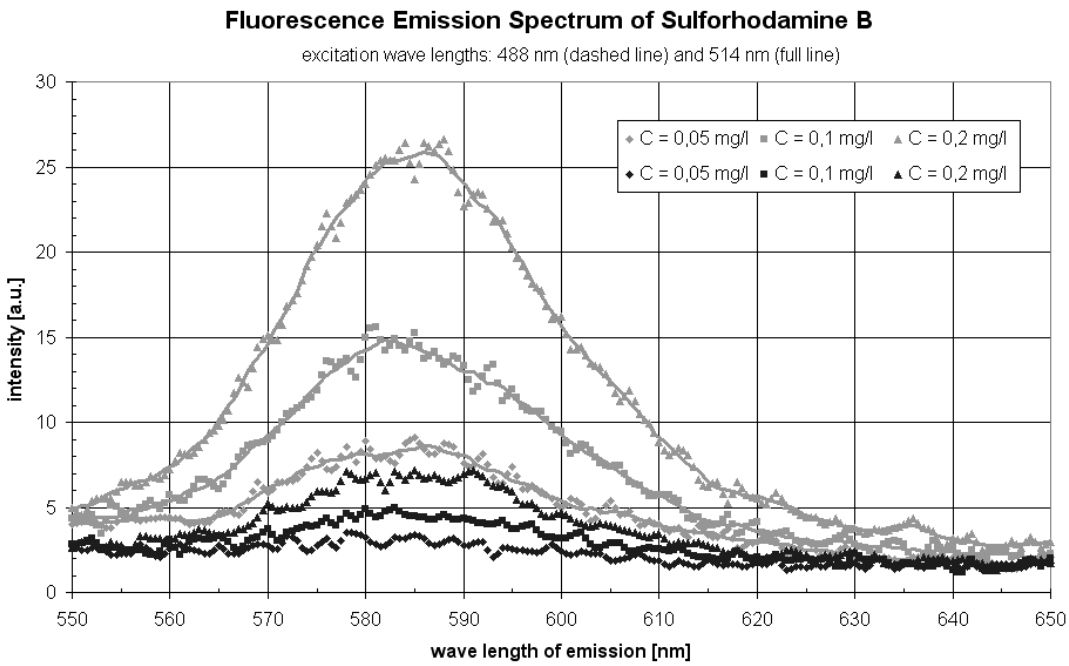

Figure 4.5. Sulphorhodamine B solutions in tap water of the mass concentrations $c = 50, 100, 200$ µg/l were analyzed using fluorescence spectroscopy. Light gray symbols indicate excitation with wave length $\lambda_g = 514.5$ nm, black symbols indicate excitation with $\lambda_{bg} = 488$ nm. The light intensity has been kept constant for all emission spectra.

fluorescence emission spectrum peaks at 576 nm revealing a high Stokes-shift of 22 nm and a fluorescence quantum efficiency of about 0.60.

A solution of 500 µg/l rhodamine B in tap water as analyzed by fluorescence spectroscopy reveals the absorption spectrum shown in Figure 4.6 (b). The emission spectrum obtained from an excitation with a wave length of 514.5 nm is displayed together with the characteristic line of the optical band-pass filter employed to isolate the fluorescence signal for the LIF analyzes.

From the absorbtion spectra in Figure 4.6 we can see that—compared to the reference values listed in Table 4.3—the wave length of maximum excitation is red-shifted significantly for both dye compounds. For sulphorhodamine B the absorption peaks at $\lambda_{max} = 572$ nm instead of 564 nm as reported in literature, for rhodamine B we obtained $\lambda_{max} = 561$ nm instead of 554 nm. Hence, the specific extinction coefficients $\varepsilon(\lambda_g)$ at the Ar^+ wave lengths were even lower than expected, i.e. the excitation was even less effective, but this could be accounted for by using a sufficiently high incident laser intensity. However, the maxima in the emission spectra for an excitation at λ_g occur with only a marginal red-shift (584 nm instead of 583 nm for sulphorhodamine B, and 577 nm instead of 576 nm for rhodamine B). The red-shift mainly of the absorption spectra results in a reduction of the Stokes shift from 19 nm to 12 nm for sulphorhodamine B, and from 22 nm to 16 nm for rhodamine B. A reduced Stokes shift means a higher rate of re-absorbtion of the emitted fluo-

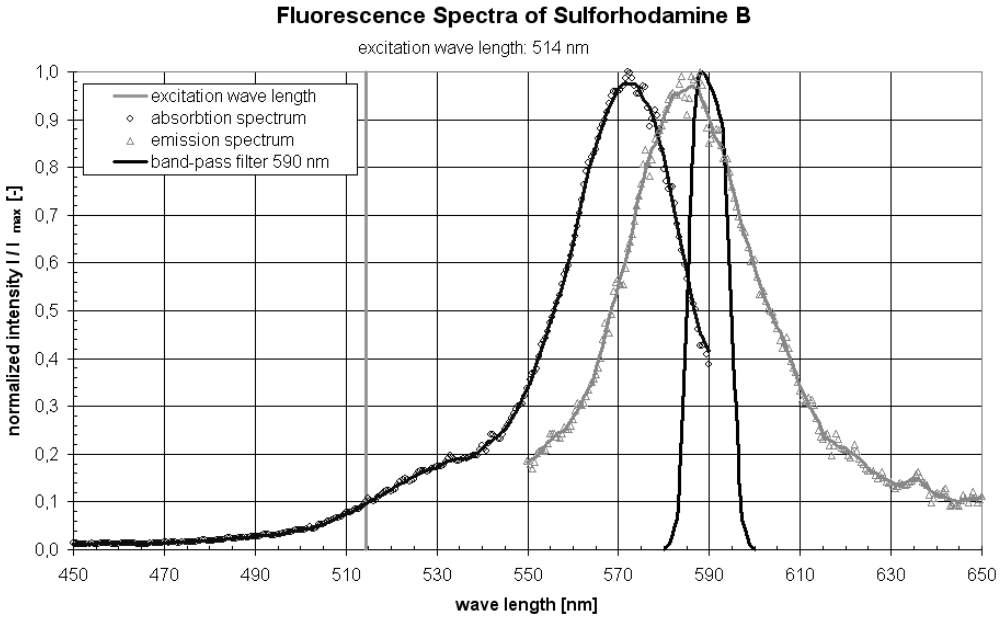

(a) Fluorescence spectra of sulphorhodamine B

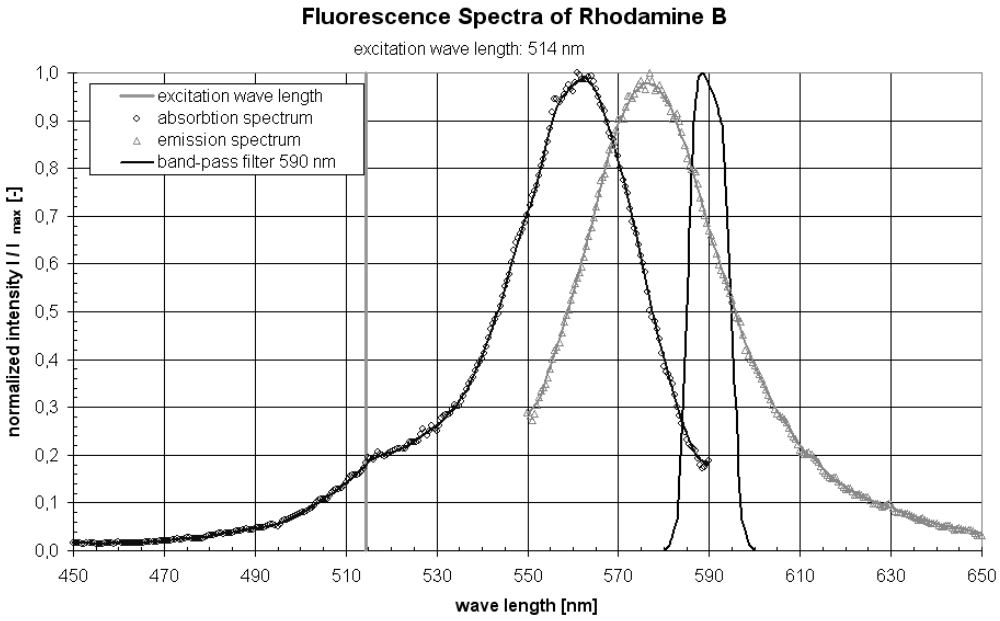

(b) Fluorescence spectra of rhodamine B

Figure 4.6. For the xanthene dyes sulphorhodamine B and rhodamine B—employed as fluorescent tracers for the combined LDV-LIF measurements—extinction spectra were recorded from 0.5 mg/l solutions in unbuffered tap water (dark full lines). For the emission spectra (light full lines) the excitation was tuned to the wave length $\lambda_g = 514.5$ nm of the strongest Ar^+ line, which obviously did not meet the wave length of maximum extinction very well. The characteristic line of the optical band-pass filter (dashed line) indicates, which part of the emitted fluorescence signal had been amplified by the photomultiplier tube.

rescent radiation. For the present LDV-LIF measurement set-up the emitted fluorescent light could suffer from additional attenuation, when scattered out of the receiving beam path. This attenuating effect could be addressed by a modified absorbtion coefficient $\tilde{\varepsilon}$, as will be discussed in the following section.

When directly comparing the non-normalized spectra of the two selected fluorescent dye tracers (cf. v. Carmer et al., 2000, Figure 3.8), our own fluoro-spectroscopic measurements showed—for a 500 µg/l solution in tap water—that for the specific decadic extinction coefficients the proportionality $\varepsilon\,(\lambda_{max} = 564\,nm)_{SRhB} \simeq 0.58\,\varepsilon\,(\lambda_{max} = 554\,nm)_{RhB}$ holds, whereas Käss (1992) reported a ratio of 0.68. When excited at the primary Ar^+ wave length $\lambda_g = 514.5$ nm, the specific absorbance of sulphorhodamine B only reached a value of 39% of rhodamine B, since the absorbtion wave lengths of sulphorhodamine B are generally longer—it actually displays the farthermost red absorbtion spectrum of all rhodamines. As the cw Ar^+ laser was able to provide up to approximately 2.1 W in the strongest emission lines λ_g and λ_{bg}, the rather low efficiency in the excitation of sulphorhodamine B could be easily compensated for by tuning up the incident laser radiation, if only the signal–to–noise ratio was kept at a sufficiently high level.

4.2.3 Analytical model for fluorescence intensity

Basic equation. The intensity of an incident light beam, exciting the fluorescent dye compound in the measurement volume, will attenuate along its beam path due to scattering and absorbtion by various reasons. When traversing an optically dense volume of thickness ds, the incident beam intensity is attenuated by dI_e (cf. also Section 3.2 for a general discussion). In a very dilute aqueous solution of fluorescent tracer mass, light is attenuated primarily by absorbtion. The decrease of the light intensity over an infinitesimal short path of length ds can be described by a homogeneous linear first-order differential equation, offering a solution similar to the Lambert-Beer law,

$$dI_e\,(s) = -k\,(s)\;\; c\,(s)\;\; I_e\,(s)\;\; ds\;, \tag{4.9}$$

where k a logarithmic coefficient of absorbtion,
$c\,(s)$ the mass concentration of the fluorophor at location s, and
$I_e\,(s)$ the intensity of exciting laser light at location s.

The light intensity I_e at a location s of an incident laser beam that attenuates while passing through a fluid along an optical path of length b is obtained from (4.9) as

$$I_e\,(s) = I_0\; e^{-\int_{s-b}^{s} k(\hat{s})\; c(\hat{s})\; d\hat{s}} \tag{4.10a}$$

$$\Leftrightarrow I_e\,(s) = I_0\; 10^{-\int_{s-b}^{s} \varepsilon(\hat{s})\; c(\hat{s})\; d\hat{s}}\;, \tag{4.10b}$$

where $I_0 = I_e\,(s = 0)$ the initial intensity of the incident laser light beam, and with ε the decadic extinction coefficient, given by $k = \ln\,(10^{\varepsilon}) = \varepsilon\ \ln\,(10)$.

As for most LIF applications also for the present case of a monochromatic light source the absorbtion coefficient is considered to be independent of the length of the beam path in the water body, i.e. solely depending on the wave lengths of the incident light predefined by the laser source of the LDV system. Therefore, $k\,(s) = k$, and $\varepsilon\,(s) = \varepsilon$.

As mentioned in Section 4.2.1 the irradiance of the fluorescent light, emitted isotropically by the fluorescent compound at a location s, is found to be proportional to the intensity of the exciting light $I_e\,(s)$, and to the fluorophor concentration $c\,(s)$ at this location (cf. also Equation (4.8)). The fluorescent light intensity I_f, which is emitted in the direction of the receiving optics, can be described by

$$I_f\,(s) = A_{opt}\ \Phi_f\ I_e\,(s)\,k\ \ell_{mv}\ c\,(s)\ \ . \tag{4.11}$$

Only a small fraction of the total fluorescent irradiance can be observed by the receiving optics covering a small solid angle Ω. For the collecting optics of the LDV-LIF system focussed on the measurement volume, the aperture ratio $A_{opt} = \frac{\Omega}{4\pi}$ is approximated by $A_{opt} = \frac{\pi r_l^2}{4\pi l_f^2}$, where r_l is the radius of the limiting aperture of the collecting lens, and l_f is the focal length of the lens, i.e. the distance to the measurement volume. The product $k\ \ell_{mv}\ c\,(s)\,I_e\,(s)$ is the total energy absorbed by the fluorescent mass of concentration c along the optical path under observation, i.e. along the measurement volume of a short length ℓ_{mv}.[10]

The *quantum efficiency* Φ_f represents the ratio of energy emitted as fluorescent radiation to the total absorbed energy. The total energy required to lift molecules from a ground electronic state to an upper excited electronic state will be re-emitted to a bigger part as visible radiation and to a lesser part in competing non-radiative transitions, in so-called quenching processes. Φ_f can be described by a kind of Stern–Vollmer factor $\frac{A_{21}}{A_{21}+Q_{21}}$ using the fluorescence rate A_{21} and a bulk quenching rate Q_{21}. As Q_{21} heavily depends on the specific conditions of the fluorescence process, the quantum efficiency for a given experimental setup is a priori unknown and far from being constant. In the following section we will identify the most important variables influencing Φ_f under the present LDV-LIF working conditions, and we will derive a model function to represent the variability of Φ_f, in order to finally infer the mass

[10] More common single–beam LIF systems in off-axis arrangement use optics with infinite focal depth and a very narrow field of observation of width ℓ_{mv}. In contrast, the present on-axis backscatter arrangement—emitting and receiving optics are aligned with the same optical axis—needs a very low depth–of–field focussed exactly on the LDV measurement volume to ensure a short path length ℓ_{mv} also for the LIF measurements.

concentration c of the fluorophor from the received fluorescent light intensity I_f.

Equation (4.11) would also describe the intensity of fluorescent light collected by the receiving optics, if light attenuation along the receiving path would be negligible. For the given measurement system and setup, attenuating effects due to various optical components (lenses, filters, optical fiber) will be included in a bulk optical efficiency η_{opt}. On the other hand, scattering and absorbtion of the re-emitted fluorescent light in the water body are usually neglected. As argued for instance by WALKER (1987, p. 218), "at λ_f [wave length spectrum of fluorescence] the extinction coefficient is much smaller than at λ_a [absorbtion wave length], so attenuation can be neglected along the receiving path." However, Figure 4.6 demonstrates that the extinction and emission spectra both of Rhodamine B and Sulphorhodamine B greatly overlap. Therefore, the re-absorbtion of fluorescent light especially of shorter wave lengths along the receiving path should not be excluded in general. If a low-pass filter—transmitting only the low-frequent red part of the emission spectrum that is not affected by re-absorbtion—would be employed, shorter wave lengths susceptible to attenuation due to re-absorbtion could be blocked. Unfortunately, the light intensity and, thus, the signal strength would also be reduced significantly. The narrow band-pass filter centered on the red side of the spectrum close to the maximum emission wave length, as was employed for the present LIF system, can be regarded a trade-off between omitting an attenuation effect and keeping sufficient signal strength and quality. If one is not willing to follow the above arguments, the attenuation of fluorescent light along the receiving path can also be represented—analogously to (4.10)—by an exponential factor $e^{-k_e \int_0^b c(s)\, ds}$. We will address this issue again in the next section in the context of the calibration of the LIF model equation.[11]

Light attenuation along the beam paths of the incident laser beams has to be taken into account according to (4.10a). Thus, the intensity of the fluorescent light emitted into the direction of the receiving optics can be directly related to the initial intensity I_0 of the exciting laser beams. Equation (4.11) thus becomes

$$I_f\,(s) = A_{opt}\; I_0\; \Phi_f\; k\; \ell_{mv}\; c\,(s)\;\; e^{-k \int_{s-b}^{s} c(\hat{s})\, d\hat{s}}\;. \tag{4.12}$$

[11] Note that the attenuation of the fluorescent light due to re-absorbtion, as discussed in the above paragraph, also involves the issue of secondary excitation not by the incident laser beams, but by the emitted fluorescent light. It is often argued that the density of the fluorophor molecules is low enough to neglect this effect. Otherwise, secondary excitation within or close to the measurement volume would introduce additional non-linearity to the LIF model equation. Since the fluorescent light is emitted in spherical waves, its intensity, i.e. the power per unit area, follows an inverse square law. The intensity of the fluorescent light emitted from the measurement volume will decrease with r^{-2}, thus, re-excitation along the receiving path might well be neglected.

If the concentration of the fluorescent compound can be regarded constant along the optical path within the water body, i.e. $c\,(s) = c$, then the intensity I_e of the exciting laser beams in the measurement volume according to (4.10a), and the intensity I_f of the fluorescent radiation toward the receiving optics according to (4.12) will become, respectively,

$$I_e\,(s) = I_0\; e^{-k\; b(s)\; c}\;, \tag{4.13a}$$

$$I_f\,(s) = A_{opt}\; I_0\; \Phi_f\; k\; \ell_{mv}\; c\; e^{-k\; b(s)\; c}\;. \tag{4.13b}$$

Note that in general the attenuation length b of the optical path within the water body will vary with the position s of the measurement volume, i.e. $b = b\,(s)$.

The supposition of a constant value of the concentration along the optical beam path is certainly justified, if the LIF measurements will be restricted to shallow flows and to flow parameters of appropriate length and time scales. In the framework of shallow wake flows considered in this study, for which the water depth h is significantly smaller than the large horizontal scales of the flow, for the attenuation length we always have $b < h$, since the on–axis backscatter LIF system is aligned vertically from above the water surface.

If the concentration of the attenuating compound in the optical path is low, i.e. if the constant value c or the spatially averaged value $\bar{c}$ tends toward zero, then the attenuation due to absorbtion becomes negligibly small, i.e.

$$\lim_{c \to 0} e^{-k\; b(s)\; c} = 1\;. \tag{4.14}$$

Note that obviously in this situation also spatial variations in c along the optical path will be of vanishing influence to the attenuation of incident light. Therefore, it is not necessary to postulate a homogeneous concentration, if concentrations are sufficiently low. In order to compute the intensities of the exciting and fluorescent radiation, Equations (4.13) (or (4.10a) and (4.12) directly) can be further simplified, i.e.

$$\lim_{c \to 0} I_e\,(s) = I_0\;, \tag{4.15a}$$

$$\lim_{c \to 0} I_f\,(s) = A_{opt}\; I_0\; \Phi_f\; k\; \ell_{mv}\; c\;. \tag{4.15b}$$

Equations (4.15) describe the linear correlation between the intensity of the emitted fluorescent radiation and the fluorophor concentration, and form the basis of *linear LIF techniques*, which are applicable in the limit of small c only. As an upper bound of c for the applicability of linear LIF most experimentalists adhere to a recommendation of Guilbault (1973). In order to ensure the linearity of (4.15), less than 5% of the incident light should be absorbed by the fluorescent compound along the optical beam path of length b in the fluid, i.e.

$$\frac{I_e\,(s)}{I_0} = \frac{I_0\; e^{-k \int_{s-b}^{s} c(\hat{s})\, d\hat{s}}}{I_0} \leq 0.95\;.$$

Thus, the tolerable spatial-mean concentration of the fluorophor along the optical path should not exceed

$$\bar{c}_{max} = \frac{\ln 0.95}{-k\ b} \tag{4.16}$$

in order to evaluate LIF data employing a linear model equation of the form (4.15).

Walker (1987) suggested for a fluorescein disodium solution to keep the concentration below 10^{-7} M/l to avoid significant beam attenuation along a 10 mm beam path, which corresponds to a more stringent value of 1.6% for the tolerable incident light attenuation. Finally, the accuracy in an experimental investigation necessary to answer the question under consideration, will predefine the level of precision of the applied LIF model equation.

In conclusion, for the experimental examination of shallow wake flows we employed an LDV-LIF measurement system in order to obtain correlated velocity and mass concentration data with high temporal and spatial resolution. The non-intrusive optical access with an on-axis backscatter probe aligned vertically from above the surface ensured a short attenuation length b. As the time–mean vertical gradient of the concentration distribution $\partial \langle c \rangle / \partial z$ was small in the free–surface layer of the shallow wake shear flow, the fluorophor concentration was assumed to be distributed homogeneously in the vertical direction along the optical beam path. This allowed for the implementation of a LIF model equation of the form (4.13).

If vertical homogeneity of c would turn out to be a too restrictive assumption for some kinds of flows, then an improved model equation could be implemented. Equation (4.13a) can be improved for a known mass distribution $c\,(s)$ along the optical path. Then, instead of c we can use a spatially averaged value

$$\bar{c} = \frac{1}{b} \int_{s-b}^{s} c\,(\hat{s})\ d\hat{s}\ .$$

The averaged concentration $\bar{c}$ can be related to the local concentration in the measurement volume by $\bar{c} \propto c\,(s)$. For a known spatial distribution a constant of proportionality $\alpha_c\,(s)$ can easily be calculated depending on the vertical position of the measurement volume. The intensity of fluorescent light emitted toward the receiving optics then would become

$$I_f\,(s) = A_{opt}\ I_0\ \Phi_f\ k\ \ell_{mv}\ c\,(s)\ e^{-k\ b(s)\ \alpha_c(s)\ \bar{c}}\ , \tag{4.17}$$

which would be a model equation closely related to (4.13b).

4.2.4 Modelling various attenuation effects of a LIF signal

The signal strength of the fluorescent radiation, as received by the LDV-LIF measurement system, will be influenced by a multitude of effects, which in gen-

eral reduce the signal quantitatively, but in some cases also qualitatively. The signal analysis with respect to the concentration of a fluorophor will have to represent these effects and processes, as needed and applicable. The influences on the fluorescence signal can be subdivided grossly into four categories:

- *Attenuation of the exciting and emitted light*
  due to scattering and absorbtion along the optical path (e.g. transmissivity of optical components, absorbtion by fluorescent compound in water body, scattering by particulate matter suspended in water body),
- *Variability of the quantum efficiency*
  of the fluorescent compound (for a given fluorophor Φ_f in general depends on e.g. temperature, pH-value, and wave length of excitation),
- *Quenching effects*
  of the fluorescence process (e.g. collisional/concentration quenching, oxygen quenching, impurity quenching),
- *Further aspects*
  of laser induced fluorescence (e.g. photo–decomposition of the fluorophor, saturation of fluorescence process in linear LIF application, optical arrangement, and definition of measurement volume).

Possible aspects of the four categories, as exemplified above, have to be considered carefully for their influence on the application of a specific LIF measurement technique in a given experimental set-up. If applicable, they have to be included in a model equation, e.g. in (4.13), in order to compute the mass concentration of a fluorescent tracer from the fluorescence signal data obtained from the LIF measurement system.

Attenuation of incident and emitted light. Both the incident laser light beams and the emitted fluorescent light are subjected to various light attenuation processes, which—regarding their spatial extent—can be divided into local and continuous effects. *Local attenuation* occurs if a sudden change in the optical properties of the transmitting medium is encountered by the propagating light. Primarily, the classical transition processes of reflection, refraction, and diffraction at optical boundaries will result in attenuation of a passing light wave. But also attenuation occurring along a short beam path in an optically dense medium may be spatially concentrated or 'localized', for instance to the center of an optical lens. Individual local attenuation processes can be quantified using a transmissivity $\eta_{opt,i}$, the transmissivity values of different local attenuation effects can be combined by multiplication to obtain a bulk local attenuation value $\eta_{opt} = \prod_i \eta_{opt,i}$.

In contrast, *spatially continuous attenuation* denotes scattering and absorbtion processes that occur if light propagates steadily within a transmitting medium, for instance sun light attenuating while travelling downward in the water column of a lake or ocean. We addressed this kind of attenuation from

the oceanographic or limnological point-of-view in Chapter 3. As mentioned in Section 4.2.3 continuous attenuation processes show an exponential decay which can be described using a model equation corresponding to (4.10). We can also use a discretized model for the description of spatially continuous attenuation processes along the optical path as

$$e^{-k \int_{s-b}^{s} c(\hat{s})\, d\hat{s}} = \prod_i \left(e^{-k_i \int_{s-b_i}^{s} c_i(\hat{s})\, d\hat{s}} \right)$$

in order to represent varying boundary conditions along the optical path.

For the present LIF measurement setup *attenuation due to absorbtion* will reduce the intensity of the incident laser beams as well as the intensity of the emitted fluorescent radiation, and should not be neglected. Assuming a homogeneous concentration of the fluorophor along the optical path, and with the path length of the incident and emitted light having the same length $b_i \approx b_e = b$ (because of a small beam-crossing half-angle ϕ), the effect of continuous absorbtion can be expressed as

$$e^{k_i\, b\, c}\, e^{k_e\, b\, c} = e^{(k_i + k_e)\, b\, c} \ . \tag{4.18}$$

Spatially continuous attenuation may also occur due to scattering of light by particulate matter. For the present measurement setup of a combined LDV-LIF system it is crucial for the velocity measurements that scattering tracer particles are advected through the measurement volume at an adequate rate. Since these LDV scattering particles have to be added homogeneously to the flow, they may lead to continuous attenuation all along the optical path in the liquid medium. Additional attenuation due to scattering may arise from the contamination due to organic or inorganic suspended material. Analogously to absorbtion, the *attenuating effect of spatially continuous scattering* due to various scattering materials along the optical path can be captured in exponential terms. For the present boundary conditions of experimental setup and measurement equipment the scattering by LDV seeding dominated further scattering effects due to contamination of the water body. The attenuating influence of the LDV seeding on the LIF signal—both on the incident laser light and the emitted fluorescence radiation—could have been represented by $e^{(k_{sct,i} + k_{sct,e}) b\, c_{sct}}$ similar to (4.18). However, as the concentration of the LDV tracer particles was kept low in order to maintain a good signal quality for the LDV measurements, the light attenuation due to scattering turned out to be negligible compared to the attenuation due to absorbtion by the LIF tracer material.

Variability of quantum efficiency. In order to describe the ability of a molecule to fluoresce, as a characteristic value the quantum yield, or quantum efficiency, Φ_f is commonly used. Following a general definition given by Guilbault (1973), the *fluorescence quantum efficiency*

> "is the ratio of the total energy emitted per quantum of energy absorbed:
>
> $$\Phi_f = \frac{\text{number of quanta emitted}}{\text{number of quanta absorbed}} = \text{quantum yield}$$
>
> The higher the value of Φ_f, the greater the fluorescence of a compound. A non-fluorescent molecule is one whose quantum efficiency is zero [...] All energy absorbed by such a molecule is rapidly lost by collisional deactivation."
>
> Guilbault (1973, p. 11-12)

The fluorescence quantum efficiency denotes which percentage of the energy absorbed by a molecule (at a given concentration of solution, temperature, and pressure) will be re-emitted in visible radiation instead of competing non-radiative deactivating processes. Here, non-radiative transitions include all changes in the ro-vibrational electronic states of activated molecules, and various kinds of 'quenching' processes. Φ_f can be described by a Stern–Vollmer factor comparing the spontaneous fluorescence rate and the bulk quenching rate, as mentioned in Section 4.2.1.

Because of the chemical nature of the processes involved in fluorescence, its quantum efficiency depends on the conditions of state of the fluorophor solution, i.e. on temperature, pressure, and concentration, which pre-define the level of activity of the molecules. Since changes of the *pressure* will lead to variations in Φ_f mainly in gaseous flows, we are allowed to neglect this effect for liquid solutions—especially in shallow free-surface flows. Contrarily, *temperature* changes affect the quantum efficiency also in liquid flows, as stressed by various authors (cf. e.g. Guilbault (1973); Smart & Laidlaw (1977); Walker (1987); Coppeta & Rogers (1998)). The temperature sensitivity $\Phi_f(T)$ of some fluorescent compounds allowed for the development of LIF-based measurement techniques for the temperature in flows. Lemoine et al. (1999) realized a point-wise LDV-LIF system for coincident measurements of temperature and velocity, which they applied to a turbulent jet in co-flow. Planar LIF systems for temperature measurements were implemented by Seuntiëns et al. (2001) for the investigation of a vortex street in a cylinder wake flow, and by Sakakibara & Adrian (1999) for thermal convection over a heated plate. Both techniques were using slightly different model equations to represent the temperature dependence of fluorescence for their data evaluation algorithms.

The *concentration* of the fluorescent compound also influences the quantum efficiency of the fluorescence process. For a higher number density of fluorophor molecules, obviously, the probability will increase to collide with each other while in an excited electronic state. We will address this competing 'collisional quenching' effect explicitly below. For the evaluation of Φ_f of

a given compound, usually a very dilute solution of a known molar concentration is probed in comparison to a well known fluorophor (for more detail cf. Guilbault, 1973, pp. 12). Most solutions are at 10^{-3} M/l, and at room temperature.

Also the kind of solvent will play a role for the efficiency of the fluorescence process. We will disregard the effect of viscosity here, as we were not allowed to change the flow medium. More important, the *pH value* of the solution strongly affects not the quantum efficiency, but the absorbtion coefficient ε or k of many fluorophor compounds. Smart & Laidlaw (1977) reviewed the early literature also on the pH dependance of fluorescence in their useful survey of fluorescent dyes for water tracing. A strong pH sensitivity of fluorescein disodium—a commonly used fluorescent dye—has been reported frequently (e.g. Walker, 1987). Coppeta & Rogers (1998) reported a LIF-based planar measurement technique for pH and temperature to examine mixing processes in turbulent shear flows. They also presented pH and temperature sensitivities for a substantial selection of possible LIF dyes. Within the framework of our study on shallow wake flows rhodamine B and sulphorhodamine B were regarded the most suitable dye tracers for the LIF measurements. Smart & Laidlaw (1977) as well as Coppeta & Rogers (1998) stated that no pH dependance of the molar absorbtivity had been observed for both rhodamine B (in a pH range above 6 pH) and sulphorhodamine B (in a range between 3 pH and 10 pH). In return, both dyes show the strongest temperature sensitivities compared to other fluorophor compounds used for laser induced fluorescence.

Finally, recall that the fluorescence process also depends on the *wave length spectrum* of the exciting and emitted light. Firstly, the molar absorbtivity of a fluorescent compound, and thus its extinction coefficient, strongly varies with the wave length of the incident radiation, i.e. $\varepsilon = \varepsilon(\lambda)$ or $k = k(\lambda)$. The wavelength dependance of the light absorbtivity has already been illustrated from the extinction spectra of the fluorophors employed in our LIF measurements, as shown in Figure 4.6. The fluorescence emission spectra are usually obtained from a monochromatic excitation at the maximum absorbtion wave length λ_{max}. If, secondly, the fluorophor will be excited at a different wave length than λ_{max}, as is the case for most LIF applications, the emission spectrum will differ in shape e.g. in the peak fluorescence emission wave length, since the kind and extent of the deactivating molecular transitions that are involved in the fluorescence process significantly depend on the amount of absorbed quantized energy. Thirdly as an additional technical aspect, the receiving optics usually do not allow for monitoring the full fluorescence emission spectrum. Therefore, the value of the quantum efficiency has to be reduced according to the width of the spectral window established by the employed receiving optics. For instance, in the present experimental setup we used a narrow band-pass filter at 590 nm,

hence only a small part of the radiant energy distributed along the whole emission spectrum was received.

Quenching effects. In fluorescence spectroscopy any process which reduces the intensity of the fluorescence radiation is called *fluorescence quenching* (Slavik, 1994, pp. 246). One can distinguish different types of quenching mechanisms, among them:

Static quenching results from a reaction of the fluorophor A in its ground–state with a quencher Q to form non-fluorescent complexes AQ. This process reduces only the number density of free fluorophors A, i.e. the extinction coefficient ε of the solution, and effectively, the concentration c. The lifetime of the exited fluorophors A^* remains the same, since the remaining uncomplexed fluorophors are not affected by the quencher.

Dynamic quenching describes the interaction of the quencher Q with the excited fluorophor A^*. This mechanism—also called *collisional or concentration quenching*—results in a decrease of the lifetime of A^*, because the excited fluorophors may be deactivated non-radiatively via collisions prior to re-emitting the absorbed energy as fluorescent light.

Note that for both static and dynamic quenching the fluorophor itself may act as a quencher. Also the mechanisms reducing the quantum efficiency, as discussed in the previous paragraph, could be regarded static or dynamic quenching, or at least to influence the quenching processes. Since the attenuation of the incident and emitted light reduces the fluorescence intensity from a holistic point–of–view, this is sometimes denoted 'trivial quenching'.

More rigidly, in this work the term 'quenching' describes only the *dynamic quenching* processes. The iodide ion and the molecular oxygen belong to the best fluorescence quenchers. The quenching capability of O_2 led to the implementation of LIF–based measurement techniques to measure the oxygen concentration in fluid flows. Münsterer & Jähne (1998) used HCl to replace the gas molecule by an ion in order to investigate the gas exchange in the air–water boundary layer.

Care always has to be exercised when conducting LIF experiments, since also unexpected and unwanted influences may easily and irreversibly be introduced to the measurements. These erroneous processes are specially termed *impurity quenching*, i.e. the quenching due to the presence of an additional unnoticed compound competing with the fluorophor in the fluorescence process. For instance, Sakakibara & Adrian (1999) reported the use of a fluoropolymer stirring bar, which significantly reduced the quantum efficiency of an aqueous Rhodamine B solution immediately after its preparation, though later the fluorescence radiation recovered asymptotically toward a reference value of a glass–stirred solution.

In the present LDV-LIF measurement setup the only quenching compound with variable concentration was the fluorescent dye itself. Concentration quenching of the fluorophor led to further concentration-dependent deviation from a linear LIF relation, and thus had to be implemented in an extended LIF model equation. We made no attempt to prevent oxygen quenching by de-gassing the fluid, since the shallow flow setup using a 80 m^2 free surface and flow depths of 17 mm to 38 mm would ensure a rapid re-aeration. Instead we assumed the tap water solution to be saturated showing a constant O_2 concentration in the longitudinal and lateral flow direction. As stated by Guilbault (1973, p. 25), oxygen—present in solutions at a concentration of about 10^{-3} M—normally reduces the fluorescence of a typical compound by approximately 20%. The decrease of the fluorescence intensity due to oxygen quenching therefore was incorporated in the extended LIF model equation, and in the calibration procedures of the LIF system.

Further photo-optical aspects. The received fluorescence intensity, available from a given incident radiation, can be further reduced by additional chemical and optical phenomena.

Photo-chemical decomposition of the fluorophor, or *photobleaching*, is a well-known process that has been reported frequently also in the context of fluorescent flow markers e.g. by Smart & Laidlaw (1977); Walker (1987); Arcoumanis et al. (1990); Crimaldi (1997); Wang & Fiedler (2000a,b). Due to the high-intensity incident radiation of LIF photo-chemical processes may render the fluorophor incapable of fluorescing even after a short exposure time. The capability of photobleaching may depend on kind and concentration of the fluorescent compound, on the solvent, on the exposure time and on the incident light intensity. Nevertheless, the proper representation of photobleaching in LIF measurement techniques only recently entered scientific discussion, and is still ambiguous, Crimaldi (1997) and Wang & Fiedler (2000a) proposed different model equations to describe the process of photobleaching. But there is general agreement that, contrarily to fluorescein sodium, the rhodamine dyes display a good photo-stability. If we would employ rhodamine 6G in the present experimental setup, from Crimaldi (1997) a flow velocity of $U > 1$ cm/s would restrict the decrease of the fluorescence intensity to less than 1% for an arbitrary concentration. Since for all flow configurations considered here U always was well above 10 cm/s, we assumed the effect of photo-decomposition to be of minor influence in the present measurement setup and flow configuration, and thus, to be negligible compared to light attenuation, concentration quenching, and temperature dependance.

Light passing through media of different optical density is subjected to reflection and refraction. Rapid changes in the indices of refraction at distinct interfaces of different media lead to rapid changes in the direction of light prop-

agation. But also gradual changes of the index of refraction within a fluid due to density gradients, e.g. due to changes in temperature, salinity, or concentration of suspended matter, will alter the light path. This phenomenon—sometimes denoted as *thermal blooming or wobbling*—may result in a partly or total loss of the measurement plane or measurement volume. In general, optical measurements of turbulent mixing processes are susceptible to thermal wobbling because of their strongly varying density gradients. Thermal wobbling surely has to be taken into account, if light is passing through fluid of variable density over a long distance compared to the spatial resolution of the measurement system. Such problems were reported in thermally driven flows by Nash et al. (1995) for large–scale planar-LIF with beam paths up to 5 m, and by Wang & Fiedler (2000a,b) for high–resolution point-LIF with a diameter of the measurement volume of 4 μm. Similar problems may occur, when investigating the mixing of fresh- and saltwater. In the present application the lengths of the beam paths were comparably short, and the density gradients were rather weak due to the generally low concentration of the fluorophor. Therefore, beam wobbling was not expected to become a severe problem in the present LDV-LIF measurement setup.

The *alignment of the emitting and receiving optics* can also influence the fluorescence signal. The usual arrangement of a pointwise LIF system employs a single well-collimated laser light beam for the excitation of the fluorophor. The receiving optics, masked by narrow pinholes, are aligned perpendicular to the incident beam as a 90° off-axis arrangement, which ensures an approximately spherical measurement volume.[12] The present on-axis backscatter arrangement is well-suited for the intended non-intrusive synoptical LDV-LIF measurements in a shallow plane shear flow. Since the fluorescence radiation is diffusely emitted in the full solid angle, the intensity of the received fluorescent light does not depend on the direction of observation. As a trade-off, the measurement volume of the LIF consists not only of the intersection of the 4 laser beams, but of the 4 individual beams. It is delineated by the blocking masks and collecting lenses of the receiving optics, but still it might exceed the LDV measurement volume to a certain amount. In order to check the size of the LIF measurement volume, one has to evaluate to what extent the fluorescence emission excited by a single beam outside the LDV measurement volume contributes to the LIF signal.

Firstly, it has been verified experimentally that the depth of the fluid volume below the LDV measurement volume, traversed by the diverging four laser

[12] Analogously, for planar LIF measurements a thin light sheet is generated to stimulate the fluorescence radiation, which is observed using a camera device in an out-of-plane arrangement. The measurement volume for a PLIF system is defined by the thickness of the light sheet and by the spatial resolution of the recorded image.

beams, did not change the reading of the received fluorescence intensity noticeably, i.e. that the LIF measurement volume was congruent with the LDV measurement volume in the downward direction. For a proper alignment of the laser beams this applied also to the measurement volume in the upward direction. Hence, the length of the LIF measurement volume should correspond to that of the LDV system. Secondly, it has been ascertained also for the LDV measurements that the 4 laser beams overlapped almost perfectly at the intersection of the measurement volume, i.e. that in the focal point the 4 beams were congruent. Therefore, the width of the LIF measurement volume was equal to the width of the LDV measurement volume. Albeit the shape of the LIF measurement volume was surely not a perfect ellipsoid, and the measurement volumes both of LDV and LIF therefore could not be identical, at least the dimensions of both volumes were the same. We therefore concluded that the alignment of the emitting and receiving optics would meet the requirements of combined LDV-LIF measurements.

4.2.5 Verification and validation of an extended LIF model relation

Shallow turbulent wake flows, and especially vortex street-like wakes, may reveal a strong variability of scalar concentrations c in the flow field. In the near-field of the wake we may find high-concentration fluid enclosed in stable vortex cores surrounded by regions of intense mixing and high intermittency showing also parcels of entrained unmixed ambient fluid. In the far-field scalar differences may largely be equalized due to turbulent mixing, the turbulent scalar field now being characterized by small-scale high-frequency fluctuations. To access the scalar pattern and the scalar transport we need a measuring technique capable of resolving strong scalar gradients over a wide measurement range with a high resolution.

Instead of simply calibrating an evaluation algorithm for the LIF system in order to apply a linear LIF technique according to (4.15), we will derive and calibrate an appropriate LIF model equation to describe also non-linear relations between I_f and c. This allows to extend the measurement range of mass concentrations toward higher c well beyond the linear range, and thus to maintain a strong fluorescence signal for a given moderate incident light intensity I_0.

From the linear LIF equation (4.15) we have $I_f \propto I_0\, c$ for a given measurement system and setup (i.e. for predefined values of $\Phi_f, k, A_{opt}, l_{mv}$). In order to increase the intensity of the fluorescence radiation, instead of increasing c beyond the linear regime, one could also keep c low, and increase the incident light intensity I_0. This would increase the sensitivity of the LIF system, and allow to access even lower concentrations. Nevertheless, the application of a linear LIF evaluation algorithm would imply further consequences which prevent

such an approach in the present setup. With respect to a combined LDV-LIF system, the LDV measurements do not benefit from higher I_0, but disadvantages (e.g. poor signal-to-noise ratio) have to be dealt with. Regarding the LIF measurements, chances increase that photo-decomposition of the fluorophor would become a serious problem that would have to be parameterized and calibrated in an appropriate LIF model equation. The temperature dependance of fluorescence—being a characteristic property of the fluorescent compound—still has to be incorporated into such a model equation. Increased I_0 may lead to unwanted transition to saturated LIF also involving non-linearity during transition. Finally and crucially, in the present setup LIF measurement runs need stable I_0 for the time of each run (up to 120 min). This is impossible to guarantee for high laser power, instead chances are high to destroy the optic fibers or optical components in the couplers of the beam-separator.

For the present experimental boundary conditions a non-linear LIF measurement technique has therefore been applied, which necessitated the implementation of an extended non-linear LIF model equation in order to represent the relevant influences of beam attenuation of the incident light, concentration quenching, and temperature dependance of the fluorescence.

Beam attenuation. For the present LDV-LIF measurement setup all attenuation effects will be related to an initial light intensity I_0 given by the total radiation of the four beams immediately in front of the probe optics.[13] Along the optical path the light is attenuated both locally at optical discontinuities and continuously within the optical media. On the receiving side of the LDV-LIF system *local losses* result from the splitting and filtering of the polychromatic signal prior to the opto-electric conversion by the photomultipliers—these are incorporated into a bulk optical system parameter A_{opt}. Additionally, we usually introduced a small disk made of crown glass into the incident and receiving beam paths. The disk (thickness 6.35 mm) was positioned as to touch the free water surface in order to improve and control the transition of the beams between air and flowing water (see Section 4.1 for more detail), its transmissivity η_{disk} was evaluated to be 92% to 93% slightly depending on the light intensity.

Regarding the *spatially continuous attenuation* the absorbtion of incident light along the beam paths in the flow due to the fluorescent compound is the most dominant effect. Assuming a vertically homogeneous distribution of the fluorophor the continuous decrease of the incident light intensity I_e can be described using (4.13a). The logarithmic extinction or absorbtion coefficient $k(\lambda)$ in the exponential term has to be evaluated for a given solution and wave

[13] The losses of light power between the laser tube and the probe are about 60% to 70% at best, mainly located in the beam–separator. Almost 40% of the laser power is contained in the blocked frequencies of the Ar^+ spectrum, but also the feeding of the monochromatic light into the individual optical fibers is a lossy process.

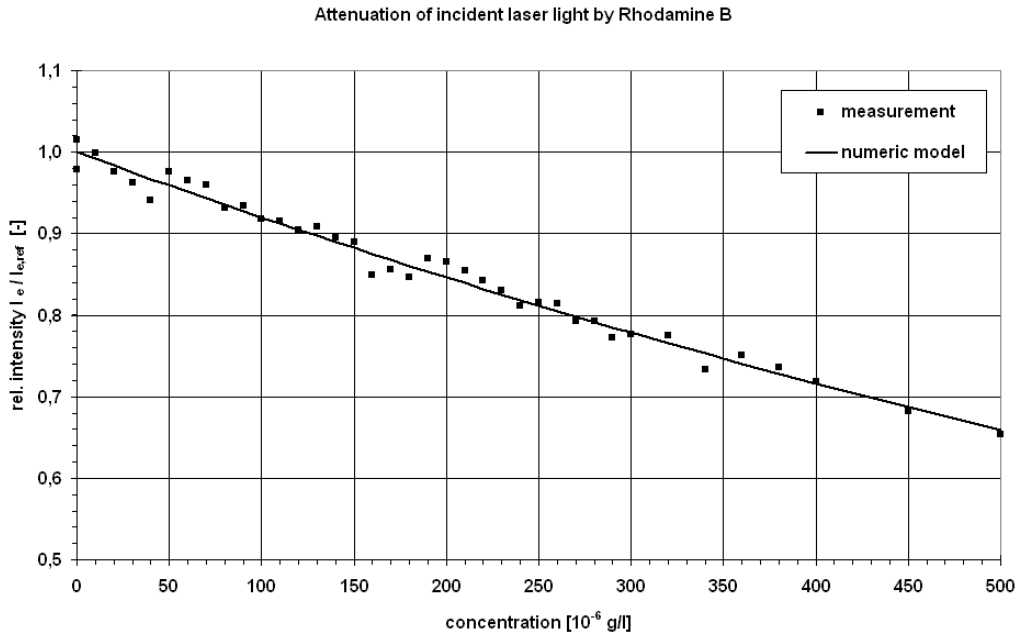

Figure 4.7. Laser light beams λ_g and λ_{bg} of equal strength were attenuated while passing through homogeneous rhodamine B solutions along an optical path of length 75 mm. The concentration of the solution ranged up to 500 µg/l. The light intensity I_e is normalized by it's zero-concentration reference value $I_{e,ref}$ according to (4.19). The bulk extinction coefficient was evaluated to be $k\left(\lambda_g, \lambda_{bg}\right) = 1.11 \cdot 10^4 \ \left(m\ kg/m^3\right)^{-1} = 6.46 \cdot 10^3 \ \left(m\ M/m^3\right)^{-1}$.

length spectrum of excitation. For the 2D LDV measurements equally strong beams of $\lambda_{bg} = 488$ nm and $\lambda_g = 514.5$ nm were employed. For both fluorescent dyes light was significantly more susceptible to absorption at λ_g, as is evident from Figure 4.6. Bulk extinction coefficients $\tilde{k} = k\left(\lambda_g, \lambda_{bg}\right)$ were evaluated by observing the attenuation of $I_e\left(c\right)$ along a 75 mm long optical path in a fluorophor solution of various concentrations. The temperature of the solution was kept constant to exclude influences on k. Figure 4.7 exemplifies the calibration of a bulk k for rhodamine B. The intensity of the attenuated incident light is normalized using a reference value $I_{e,ref}$ at a given concentration—here $c_{ref} = 0$, i.e. $I_{e,ref} = I_0$ in case of no further sources of attenuation. By fitting (4.13a) in non-dimensional form yielding

$$\frac{I_e\left(c\right)}{I_{e,ref}} = e^{-b\,k\,c} \ , \tag{4.19}$$

the logarithmic extinction coefficient for rhodamine B is obtained, $\tilde{k} = k\left(\lambda_g, \lambda_{bg}\right) = 1.11 \cdot 10^4 \ \left(m\ kg/m^3\right)^{-1} = 5.32 \cdot 10^3 \ \left(m\ M/m^3\right)^{-1}$. The corresponding decadic extinction coefficients $\tilde{\varepsilon} = \tilde{k}/\ln\left(10\right) = 0.48 \cdot 10^4 \ \left(m\ kg/m^3\right)^{-1} = 2.31 \cdot 10^3 \ \left(m\ M/m^3\right)^{-1}$ are significantly lower than the values at the maximum extinction wave length λ_{max} reported in literature (cf. Table 4.3).

For sulphorhodamine B the bulk logarithmic extinction coefficient was found to be $\tilde{k} = k(\lambda_g, \lambda_{bg}) = 5.12 \cdot 10^3 \left(m\, kg/m^3\right)^{-1} = 2.97 \cdot 10^3 \left(m\, M/m^3\right)^{-1}$. The logarithmic and molar values are lower compared to rhodamine B.

As demonstrated in (4.18) also the attenuation of the re-emitted fluorescent radiation could be taken into account. Then, additionally the extinction coefficients for the fluorescence spectrum would have to be evaluated, or a bulk coefficient also including attenuation along the receiving optical path has to be obtained. This has been done using a similar calibration setup to verify that attenuation of the fluorescent radiation was negligible compared to the attenuation of the incident light.

Temperature dependance. Most organic fluorescent dyes display a pronounced sensitivity of their quantum efficiency Φ_f to temperature variations (see for instance Guilbault (1973, p. 14, pp. 24)). Within the framework of our study on shallow wake flows rhodamine B and sulphorhodamine B were regarded the most suitable dye tracers for the LIF measurements. Both dyes show the strongest temperature sensitivities compared to other fluorophor compounds used for laser induced fluorescence (approximately -1.55% per K (Coppeta & Rogers, 1998), others report up to -2% K^{-1} for rhodamine B). On the contrary, the extinction coefficient ε usually is insensitive to changes in temperature, for rhodamine B the temperature sensitivity of ε was reported to be 0.05% per Kelvin (Sakakibara & Adrian, 1999). Hence, for the employed LIF tracer dyes the temperature dependance of the fluorescence radiation is solely ascribed to their quantum efficiency, their extinction coefficients are regarded effectively temperature–invariant.

In order to represent the decrease of the quantum efficiency Φ_f, and thus, the decrease of the fluorescence intensity with increasing temperature T, we use an exponential expression

$$\Phi_f(T) = \Phi_{f,0}\, e^{m_T\,(1-T/T_0)} \tag{4.20}$$

that relates the quantum efficiency to a reference value $\Phi_{f,0}$ at a reference temperature T_0. A similar exponential approach was reported by Smart & Laidlaw (1977), other authors (e.g. Sakakibara & Adrian, 1999) avoid to parameterize a relationship, though also from their data an exponential decay is evident.[14]

Figure 4.8 shows the variation of the normalized fluorescence intensity depending on the temperature for a homogeneous rhodamine B solution of

[14] Planar LIF measurements are sometimes employed to obtain temperature distributions in a flow field. In order to restrict the processing time, the evaluation of T usually is based on a simplistic linear decay model (e.g. Dantec's FlowMap software for PIV/PLIF measurements), which drastically reduces the measurement accuracy for larger temperature differences.

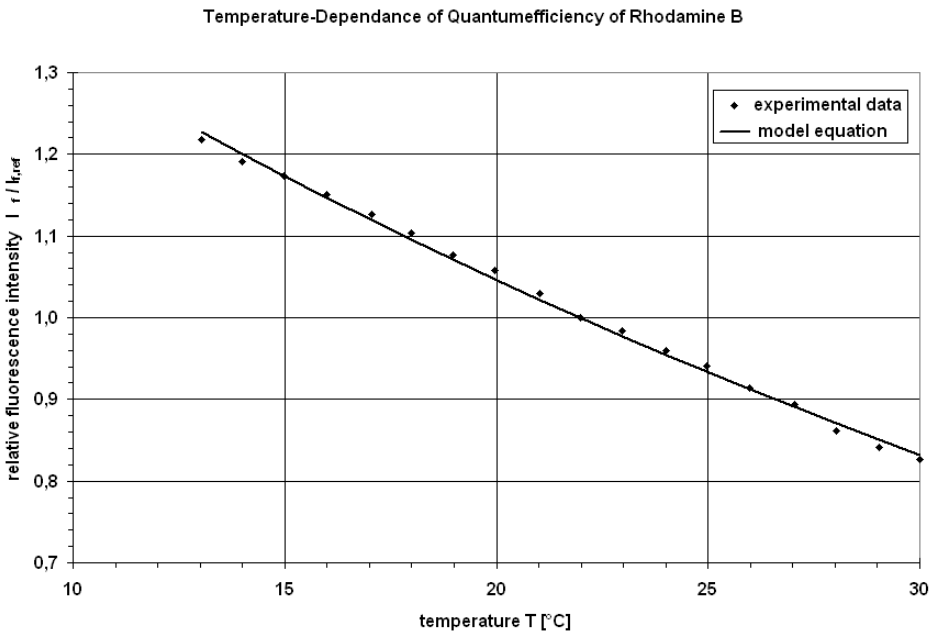

Figure 4.8. The temperature–sensitivity of the quantum efficiency Φ_f is illustrated from the normalized fluorescence intensity of a 50 µg/l rhodamine B solution. Over a temperature range of 13°C to 30°C a temperature sensitivity coefficient of $m_T = 0.4578$ is calibrated for the model equation (4.20) using $T_0 = 20$°C.

$c = 50$ µg/l. For a constant concentration the relative fluorescence intensity described by (4.13b) reduces to $I_f/I_{f,ref} = \Phi(T)/\Phi(T_{ref})$. For temperatures ranging from 13°C to 30°C a temperature sensitivity coefficient $m_T = 0.4578$ is obtained from (4.20) with a reference temperature of $T_0 = 20$°C. This represents a linearized decrease of 2.3% K^{-1} at T_0. From Smart & Laidlaw (1977) a higher value of the sensitivity coefficient of about 0.54 can be inferred.

For a sulphorhodamine B solution the temperature sensitivity coefficient is $m_T = 0.4834$ for $T_0 = 20$°C, i.e. its quantum efficiency is slightly more temperature–sensitive than rhodamine B, in agreement with Smart & Laidlaw (1977).

Concentration quenching. The variation of the fluorophor concentration in the measurement volume influences the amount of emitted fluorescence radiation. Contrary to attenuation of the laser light along the incident beam path, due to concentration quenching in the measurement volume the intensity of fluorescence emission, stimulated by a given absorbed amount of light energy, is reduced—by non-radiative inter-molecular energy transitions. For higher concentrations of a fluorophor the fluorescence (quantum) efficiency of a solution is reduced with increasing concentration due to self-quenching. The effect of concentration quenching can be represented in a LIF model equation using an exponential damping of the form $e^{(-q_c\, c)}$. In order to quantify the concentration quenching coefficient q_c, calibration measurements at known high fluorophor

concentrations have been conducted at a flow boundary, i.e. no attenuation along the optical path in the flow had to be considered, since $b = 0$. The flow temperature was monitored and represented in the quantum efficiency according to (4.20). To avoid any implication of photo-decomposition a sufficiently high flow velocity was maintained. The fluorescence intensity I_f, normalized by a reference intensity $I_{f,ref}$ usually at $c = 50$ µg/l, is given by

$$\frac{I_f\,(c,T)}{I_{f,ref}} = \frac{c}{c_{ref}} e^{-q_c\left(c-c_{ref}\right)}\; e^{-k\,b\left(c-c_{ref}\right)}\; e^{m_T\left(\frac{T_{ref}-T}{T_0}\right)}\;. \tag{4.21}$$

The concentration quenching coefficients q_c for rhodamine B and sulphorhodamine B have been evaluated to be 241.8 m^3/kg and 451 m^3/kg, respectively.

Neglecting the effect of concentration quenching when inferring the concentration from the measured fluorescence will result in an error of 1% for a 40 µg/l rhodamine B solution, and in an error of 9.2% for a 400 µg/l solution.

Extended LIF model equation. The descriptive model equation for the intensity I_f of the fluorescence radiation—emitted in the direction of the receiving optics of the present LDV-LIF measurement system—will cover the following attenuation effects, as presented above:

- reduction of the incident and emitted light intensity due into optical components introduced to the optical path outside the measurement system using a transmissivity η_{opt},
- attenuation of the incident light intensity I_e with respect to I_0 along the optical path in the fluorophor solution using an exponential decay law (4.19) and a specific extinction coefficient $\tilde{k}$ adapted to the wave number spectrum of the excitation,
- temperature sensitivity of the quantum efficiency Φ_f employing a model approach (4.20) with a temperature sensitivity coefficient m_T,
- decrease of the fluorescence intensity I_f due to concentration quenching in the measurement volume described by an exponential equation (4.21) with a quenching coefficient q_c.

An *extended LIF model equation*, based on (4.13) for homogeneous concentration distribution along the optical path, relates the observed intensity I_f of the fluorescence to the mass concentration c of the fluorescent compound in the solution. In conclusion,

$$I_f = \eta_{opt}\; A_{opt}\; \ell_{mv}\; \Phi_f\; I_0\; \tilde{k}\; c\; e^{-\tilde{k}\,b\,c}\; e^{-q_c\,c}\; e^{m_T(1-T/T_0)}\;, \tag{4.22}$$

where	I_0	[W]	light intensity at probe optics
	η_{opt}	[-]	transmissivity of optical components in optical path
	A_{opt}	[-]	aperture ratio of receiving optics,

		i.e. ratio of received to emitted radiance
ℓ_{mv}	[m]	length of the measurement volume
$\Phi_{f,0}$	[-]	quantum efficiency of fluorophor at T_0
$\tilde{k}$	[m^2/kg]	specific extinction coefficient
c	[kg/m^3]	mass concentration of fluorophor
b	[m]	optical path length in fluorophor solution
q_c	[m^3/kg]	concentration quenching coefficient
m_T	[-]	temperature sensitivity coefficient
T_0	[°C]	temperature of reference solution for quantum efficiency

For the present LDV-LIF measurement system a voltage signal U_f of the third photomultiplier provides the information on the fluorescence intensity I_f received by the probe optics. For further analysis of the concentration data using the extended LIF model equation (4.22), U_f first has to be converted into I_f applying a conversion factor. Because of the statistical mutual dependence of such a device-specific conversion coefficient and the—still unknown[15]—quantum efficiency in (4.22), only the product of both quantities can be calibrated. For clarity we will also incorporate A_{opt} and ℓ_{mv}, defined by the probe optics of the employed system, into a conversion coefficient P_0, which is specified by the given measurement system and setup. The amplification of the photomultiplier has to be adjusted before each measurement run according to I_0 and to the maximum concentration to be resolved. In order to represent this effect an amplification coefficient f_{pm} has to be calculated before each measurement—being the only parameter to be calibrated repeatedly. From (4.22) we obtain the *device-specific conversion equation* for the LIF system

$$U_f = \eta_{opt}\, f_{pm}\, P_0\, I_0\, \tilde{k}\, c\, e^{-c\,(\tilde{k}\,b+q_c)}\, e^{m_T(1-T/T_0)}\ , \tag{4.23}$$

where	U_f	[V]	voltage signal of LIF photomultiplier
	f_{pm}	[-]	measurement-specific amplification coefficient
	P_0	[Vm/W]	device-specific conversion coefficient incorporating also $\Phi_{f,0}$, A_{opt}, and ℓ_{mv}

Details on the procedures and results of the calibration and verification of the extended LIF model equation are presented in v. Carmer et al. (2000). Table 4.4 summarizes the necessary coefficients for the application of (4.23) calibrated for the present LDV-LIF measurement system using a two-color

[15] The quantum efficiency of the fluorophor solutions can be accessed by spectrofluorometric means using a reference measurement of a fluorophor solution of known Φ_f, as mentioned by Guilbault (1973).

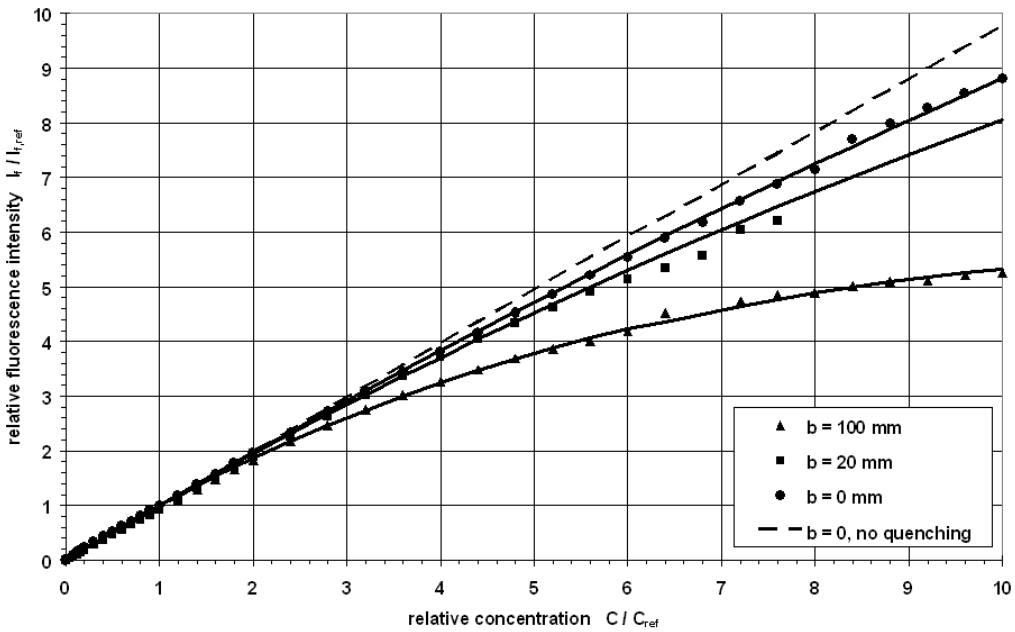

Figure 4.9. Normalized fluorescence intensities of rhodamine B solutions up to 500 µg/l are displayed for optical path lengths of $b = 0$ mm, 20 mm, and 100 mm indicated by ●, ■, and ▲, respectively. Normalization is done by the value at reference concentration $c_{ref} = 50$ µg/l. Full lines indicate the corresponding results of the extended LIF model equation in the device-specific formulation (4.23). The dashed line shows the model simulation of the $b = 0$ mm data without representing the effect of concentration quenching. It represents a near-linear LIF equation for low concentrations including only the temperature–sensitivity of Φ_f due to an increase of temperature by 1.3°C.

excitation with the fluorophors rhodamine B or sulphorhodamine B solved in tap water.

Figure 4.9 illustrates the applicability of the extended LIF model equation (4.22) for rhodamine B solutions—using the device-specific formulation of the

Table 4.4. Coefficients for the extended LIF model equation in device-specific form (4.23) calibrated for a two-color Ar^+ excitation of rhodamine B and sulphorhodamine B solutions in tap water

coefficient	**units**	**description**	**rhodamine B**	**sulpho-rhodamine B**
P_0	[Vm/W]	conversion coefficient	0.0191	0.0262
$\tilde{k}$	[m^2/kg]	specific logarithmic absorbtion coefficient	11,098	5,115
q_c	[m^3/kg]	concentration quenching coefficient	241.8	451.0
m_T	[-]	temperature sensitivity of Φ_f	0.4578	0.4834
T_0	[°C]	reference temperature for Φ_f	20	20

conversion equation, (4.23). Measured values of the fluorescence intensity are given for homogeneous mass concentrations up to 500 µg/l, and for three different attenuation path lengths $b = 0$ mm, 20 mm, and 100 mm indicated by ●, ■, and ▲, respectively. Full lines indicate the corresponding model results. The dashed line represents a model simulation for $b = 0$ mm without the effect of concentration quenching. Hence, it visualizes the results of the nearly linear model adapted to the low-concentration measurements with $c \leq 50$ µg/l, neglecting all non-linear fluorescence attenuation effects but the temperature sensitivity of Φ_f. The fluorescence intensities of each sequence have been normalized by their corresponding reference value $I_{f,ref}$ at a mass concentration $c_{ref} = 50$ µg/l, which—for $b = 100$ mm and $\tilde{k}$—constitutes the 5% attenuation limit (4.16) proposed by Guilbault (1973). The normalized intensity $I_f/I_{f,ref}$ is given by (4.21), the same relation is achieved from normalizing the conversion equation (4.23). Temperature was allowed to increase by 1°C to 1.5°C during each measurement sequence, hence the temperature-dependent decrease of the quantum efficiency had to be included in the model calculations. For $b = 0$ mm beam attenuation did not occur, the dashed line indicates the non-linearity solely due to a temperature increase by 1.26°C from the measurement at c = 0 µg/l to the measurement at c = 500 µg/l. The isolated effect of concentration quenching in the measurement volume can be obtained from the difference between the $b = 0$ mm full and dashed lines.

To assess the necessity for application of the extended non-linear LIF model instead of the linear approach, we can extend the Guilbault criterion (4.16) that not more than 5% of the incident light should be lost due to beam attenuation. Now, the total deviation of the observed fluorescence intensity from the value predicted using the linear LIF equation (4.15) should not exceed 5%. Then, the non-linear deviation is compiled from the effects of light attenuation along the optical path, concentration quenching of the fluorescence process, and temperature-sensitivity of the quantum efficiency,

$$\frac{I_f}{I_{f,lin}} = e^{-c\left(\tilde{k}\,b+q_c\right)}\; e^{m_T(1-T/T_0)} \overset{!}{\geq} 0.95\ . \tag{4.24}$$

If we assume that the temperature T does not deviate from the reference temperature T_0, i.e. that the quantum efficiency Φ_f does not deviate from its reference value $\Phi_{f,0}$, then we can calculate the allowable maximum concentrations for the present measurement setup. Table 4.5 lists c_{max} of rhodamine B for a deviation of linear LIF in fluorescence of 5% (Guilbault, 1973), and of 1.6% (Walker, 1987) for optical path length of $b = 0$ mm, i.e. concentration quenching only, $b = 20$ mm, and $b = 100$ mm. Obviously, both non-linear effects, beam attenuation and concentration quenching, will significantly reduce the emitted fluorescence intensity. Applying a linear LIF model to such data

will therefore result in considerable underestimation of the mass concentrations to be examined.

The analog voltage reading of the LIF photomultiplier with a signal range of 10 V was digitized with a depth of 12 bit resulting in an digitization interval of 2.44 mV. Employing a 1kHz low-pass filter the signal noise could be reduced to approximately 5 mV. The accuracy of the signal was expected to be of the order $\mathcal{O}(\Delta U_f) = 0.01$ V, i.e. the effective resolution of the signal range was about 10 bit. Assuming a linear proportionality of the fluorescence and the concentration, i.e. the applicability of a linear LIF model, over a range of 500 µg/l thus resulted in a maximum resolution of $\Delta c = 0.5$ µg/l. However, due to non-linear attenuation effects which had to be included in the extended LIF model the resolution could decrease significantly at higher concentrations near the saturation of the fluorescence process. In the example of Figure 4.9 for an attenuation length of 100 mm near 500 µg/l the signal resolution of 10 mV corresponded to a concentration resolution of 4.3 µg/l only, the accuracy was reduced by almost a full order of magnitude due to non-linear attenuation.

Implementation of an extended LIF model. From the extended LIF model equation (4.22) the radiance of a laser induced fluorescence process can be predicted. The device-specific conversion equation (4.23) can be used to directly predict the voltage reading of the LIF measurement system for known c and given experimental boundary conditions. Obviously, the inverse problem has to be solved with the LIF setup, i.e. to infer the mass concentration c in high spatio-temporal resolution from the measurement data U_f. Therefore, a procedure to solve (4.23) for given U_f and unknown c has been implemented in the LIF data processing program.

For a given LIF system and experimental setup the device-specific conversion equation has been discretized with respect to c with high resolution (e.g. 12 bit), as to obtain a lookup-table $\hat{c} - U_f(\hat{c})$. Each data point $U_f(t)$ of the voltage signal time series then was interpolated linearly to the discretized con-

Table 4.5. Largest tolerable mass concentrations are calculated using (4.24) for different allowable deviations of the fluorescence from the linear LIF model equation, and for different optical path lengths. The present LIF measurement setup is applied to rhodamine B solutions of temperature $T = T_0$.

optical path length	**maximum concentration** [µg/l]	
b [mm]	$\frac{I_f}{I_{f,lin}} \geq 0.95$	$\frac{I_f}{I_{f,lin}} \geq 0.984$
0	212	65
20	111	34
100	38	12

version equation $U_f(\hat{c})$. Hence, effectively, an inverse solution was obtained from a high-resolution piecewise linearization of (4.23).

4.3 Combined LDV-LIF system

Combined LDV-LIF measurement systems that allow for the simultaneous acquisition of both flow velocities and a scalar quantity have been accomplished only rarely compared to the ubiquitous application of individual LDV systems. Thus, turbulent mass fluxes $\langle \boldsymbol{u}'c' \rangle$ received much less attention than the turbulent momentum fluxes $\langle \boldsymbol{u}'\boldsymbol{u}' \rangle$.

Being one of the pioneers of combined non-intrusive measurements for flow and scalar, Papanicolaou & List (1988) realized a combined setup using independent measurement systems of LDV and LIF in order to investigate a turbulent vertical buoyant jet flow. They employed a forward-scattering two-reference-beam LDV to obtain two velocity components, and an off-axis LIF with an incident laser beam perpendicular to the LDV measurement volume. The dye tracer rhodamine 6G was excited with a monoline Ar^+ laser.

Lemoine et al. (1996, 1997) used a combined LDV-LIF system powered again by a monochromatic Ar^+ laser at $\lambda_g = 514.5$ nm. The receiving optics were oriented in an off-axis forward-scattering alignment, and collected the polychromatic scattered and fluorescent light, which was passed through a fibre-optical cable and then split for further processing as needed for LDV or LIF. Advantageously, their system guaranteed for spatial coincidence since only one measurement volume had to be employed. But it comprised only 1D velocity measurements, and the forward-scattering arrangement again required transparent measurement sections in the flow facility.

4.3.1 Technical implementation of LIF to LDV

The energy for the LIF measurements was also provided by the laser source of the LDV system, the continuous-wave Ar^+ laser. The polychromatic light emitted from the laser tube was set to a total intensity integrated along the Ar^+ spectrum of about 0.5 W. Then, a total power of 150 mW to 200 mW was obtained in the measurement volume, that was equally distributed between the four green and blue-green beams of wave-lengths $\lambda_g = 514.5$ nm and $\lambda_{bg} = 488$ nm, each color with shifted and un-shifted frequency. The laser tube was operated in a light-stabilized mode ensuring a variation of the power output below 1.0%. In order to omit any drifting of the light intensity during a longer LIF measurement, it was necessary to run the laser tube for about 6 h in advance to get all optical components along the whole optical path under working conditions. Especially the coupling devices needed extra care, as they usually

run out of focus during warm-up. Applying this pre-run allowed for excellent stability of the light power in the measurement volume, as was ascertained for each LIF measurement run.

The measurement volume of the LDV system was defined by four intersecting laser beams, small tracer particles crossing the illuminated fluid volume scattered light with Doppler-shifted frequencies. Together with the LDV tracer particles the fluid carried a soluble fluorescent dye of low concentration, that was excited by absorption of laser light and re-emitted the absorbed energy as fluorescent radiation of a spectral distribution characteristically for the employed dye. The *measurement volume* of an LIF system is therefore restricted by the volume illuminated by a laser light beam, but it is not restricted to the volume of two intersecting and interfering laser beams as for LDV systems. Hence, a specific alignment and optical instrumentation of the receiving optics is necessary to further limit the LIF measurement volume. More common single–beam pure LIF systems, as well as few combined LDV-LIF systems, use optics in off-axis arrangement with infinite focal depth, and a very narrow field of observation. In contrast, the present on-axis backscatter arrangement (emitting and receiving optics are aligned with the same optical axis) needs a very low depth–of–field focussed exactly on the LDV measurement volume to reduce the vertical extent of the LIF measurement volume. It has been verified experimentally that the length of the fluid volume beyond the measurement volume, traversed by the diverging four laser beams, does not contribute noticeably to the fluorescence intensity emerging from the measurement volume. The lateral extent of the LIF measurement volume is additionally restricted by blockage of most of the fluorescence radiation using pinhole masks.

The radiation received by the optical probe, thus, consisted of a portion elastically scattered—despite the Doppler effect—from the tracer particles traversing the measurement volume (i.e. the solid phase of the flow), and another portion inelastically scattered from the fluorescent dye in the fluid volume (i.e. the liquid phase of the flow). The time for the excitation and extinction of a fluorescent dye usually is of the order of few nanoseconds (e.g. approximately 3 ns to 5 ns for rhodamine dyes (Guilbault, 1973)), whereas it takes some microseconds for a particle to cross the measurement volume (for the current low-speed application $\gtrapprox$ 100 μs, and even $\gtrapprox$ 20 μs for a valid burst signal). Therefore, the polychromatic signal passed by the multi-componential receiving fiber to the ColorLink multi-color receiver contained *synoptical information about the motion of small tracer particles and about the concentration of a solute tracer mass in the same fluid volume.* The synchronous LDV and LIF signals then underwent time-consuming processes of transformation, amplification and analysis, during which the synchronicity had to be maintained.

The received light was divided into three parts, each of which was subjected to a narrow optical band-pass filter—of $\lambda = 590 \pm 5$ nm for the LIF

signal on the third channel—to separate the frequencies carrying the LDV and LIF signals. Using photomultipliers the optical signals were then transformed into electrical signals of 0 V to 10 V DC. The electrical LIF signal was low-pass filtered with 1 kHz, then passed over to the DataLink Multichannel Interface. There, the signal was digitized with a depth of 12 bit, and provided with an initial time code. For every valid burst event the LDV burst signal analyzer requested the corresponding LIF signal value from the DataLink.[16] Thus, the velocity information was related to the synoptical mass concentration data, and transferred via the DMA interface to the PC. Albeit the velocity information was computed from the beat frequency Δf of the Doppler-shifted signals using (4.4b) without any further calibration, the voltage signal of the mass concentration measurement required a proper calibration of the LIF transfer function (4.23) prior to each LIF measurement run.

4.3.2 Equal interval re-sampling of LDV and LIF data

During the LDV-LIF measurements for this project, the velocity data were sampled *randomly* as they were observed, i.e. not at equal time intervals. Additionally, the coincidence time window between the two LDV channels was chosen relatively wide, so that no burst on either channel was rejected because of a missing burst on the other channel. Otherwise, a (temporally) lower data rate on one of the channels would automatically restrict also the data rate on the other channel. Therefore, the data for both horizontal velocity components were not acquired co-incidentally. i.e. the instantaneous shear stresses uv are not cross-correlated a priori. By avoiding both the equal-interval sampling and the forced coincidence of bursts, it was ensured, that all valid bursts were used, and thus the maximum amount of the available velocity information was stored for further analysis. As mentioned above, the fluorescent light intensity was captured synchronously to each velocity burst, i.e. the data pairs uc and vc can be regarded as in fact co-incident information.

The data sets, acquired randomly with only a loose coincidence interval, assure the highest possible amount of information. Furthermore, every single observation (or burst event) was stored together with a so-called "time stamp" to keep track of the time sequence with respect to the start of the LDV measurement and with a time resolution of 10^{-6} s. This provides the opportunity to apply post-processing algorithms, which are adjusted and optimized for the given data quality and for the particular objectives of a data analysis.

The objectives of the LDV-LIF measurements in this project are two-fold. Firstly, we are interested in the *mass transfer rates* $\langle u_i c \rangle$ as well as in the

[16] The DataLink usually is employed to associate the LDV signals with corresponding system information like a rotor angle in turbo machinery, or the time after ignition or after fuel injection in combustion technology.

momentum fluxes $\langle u_i u_j \rangle$. The mass transfer rates are obtained from the random data without further review of the coincidence intervals, since the coupling of the LIF to the LDV ensures the synoptic measurement of a mass concentration to each velocity observation. Contrarily, the cross momentum flux $\langle uv \rangle$ can only be evaluated, if we assure that the particular observations of the two velocity components were obtained from the same event, i.e. from the same tracer particle passing the measurement volume. Therefore, to measure the Reynolds shear stress we have to conduct a coincidence re-sampling, i.e. we have to apply an appropriate[17] coincidence window on the sampled data. Note, that for the access of the Reynolds shear stress it is not inevitably necessary to use data, which is equally distributed in time.

Secondly, we want to gain more insight to the structure of turbulence. Therefore, we compute *auto- and cross-correlation functions* $R_{\phi\psi}(\tau)$ and *one-dimensional power density spectra* $S_{\phi\phi}(f)$ from the velocity and mass concentration data. For this purpose, the discrete data has to be re-arranged in equal time steps $\triangle t$, since the evaluation of $R_{\phi\psi}(\tau)$ necessitates equally spaced data, as does the evaluation of $S_{\phi\phi}(f)$, since it involves a discrete Fourier transform either of the data itself or of its correlation function. Note, that both the auto-correlations and the 1D power spectral densities do not require the coincidence of u and v velocity observations.

Turbulence statistics always imply the calculation of averages, for example the 0th to 3rd central moments of a given data series are its mean, variance, skewness, and flatness. If the time sequence of the data is not equally spaced with $\triangle t$, then the averages of the whole data ensemble are not identically equal to its time averages. The *ensemble average* of a series of N data points ϕ_i is given by

$$\langle \phi \rangle = \frac{1}{N} \sum_{i=1}^{N} \phi_i. \tag{4.25}$$

Its *time average* over the time interval T on the contrary is defined as

$$\langle \phi \rangle_t = \frac{1}{T} \sum_{i=1}^{N} \phi_i \ \triangle t_i, \text{ where } \quad T = \sum_{i=1}^{N} \triangle t_i. \tag{4.26}$$

Replacing the time averages by ensemble averages in a data analysis usually gives rise to a so-called *biasing error*. Obviously, if we assume the flow under consideration to be volumetrically homogeneous seeded with tracer particles, i.e. if we assume the volumetric density of tracer particles to be a constant, then a purely random sampled data series will contain a comparatively larger

[17] More information on how to estimate the length of an appropriate coincidence time interval for the specific flow under consideration, can be found for instance in TSI (1996).

amount of high-velocity observations, since high speed fluid parcels are passing the measurement volume faster than low speed parcels. Therefore, an ensemble average of a time series can be biased toward higher velocity. A large number of papers during the 70s and 80s were concerned with the theoretical analysis and correction of such biasing errors. Ruck (1990a) reported, that from experimental examinations the biasing error is less severe than expected theoretically and amounts to approximately 2% to 4% at its maximum deviations. For an equal interval time series with $\triangle t_i = \triangle t$ the time average of ϕ_i becomes

$$\begin{aligned}\langle\phi\rangle_t &= \frac{1}{T}\sum_{i=1}^{N}\phi_i\ \triangle t_i \\ &= \frac{\triangle t}{N\ \triangle t}\sum_{i=1}^{N}\phi_i = \langle\phi\rangle\,.\end{aligned}$$

That is, the time average and the ensemble average are the same in case of a constant $\triangle t_i$. Thus, theoretically, an effective way to avoid any biasing error would be to sample or re-sample the data with equal time steps from continuous velocity information $\boldsymbol{u}\,(t)$. Since, practically, from a tracer-based measurement technique velocity information can only be obtained at discrete instances in time $\boldsymbol{u}\,(t_i)$ depending on the presence of a tracer particle in the measurement volume, the 'particle-rate/velocity correlation' is inherent to LDV measurements. It can not a priori be omitted in the data collection, but only compensated for during the post-processing of the data.

Albeit not necessary for the evaluation of the mass and momentum fluxes, prior to any further data analysis all LDV-LIF measurement series were equal-interval re-sampled to allow further analysis of the data. With a software written for this task we first applied a low-pass filter on the still randomly distributed velocity data to reduce the noise due to erroneous LDV measurements, which reduced the amount of raw data by usually less than 0.5%. After splitting the data of the two velocity channels, which were originally stored in a sample & hold fashion, in order to reconstruct again the individual time histories of burst events for each channel, the separated data series of the velocity channels then were re-sampled with equal time intervals.

For the data re-sampling, we have to determine a constant re-sampling interval $\triangle t$. The *re-sampling frequency* $f_{res} = 1/\triangle t$ should be selected lower than the average data rate f_{raw}, at which the LDV data was obtained. It is possible to use different f_{res} for the re-sampling of the main and transverse velocity components. This implies that the data of both channels then can not be cross-correlated. Throughout this work we usually used a re-sampling frequency $f_{res} = 100$ Hz, the data rates f_{raw} were monitored and, ranging up to 1 kHz, always exceeded f_{res}. Instead of applying different re-sampling fre-

quencies, both channels were usually re-sampled using the same time sequence $t_i = t_0 + i\ \Delta t$ (i.e. the same initial moment in time and the same time step).

For the implementation of the actual re-sampling algorithm we have to use a certain interpolation or averaging scheme. Though also higher order interpolation schemes can be applied, for instance linear, cubic or spline interpolations, 0th order schemes guarantee the best representation of the randomly acquired data, whereas higher order schemes are more speculative ones. Since we want to examine the structures of turbulence, we should not apply an interpolation scheme, which a priori needs an assumption about the temporal development of the flow, i.e. about exactly the target of the examination. For example, if we would know that a turbulent signal could be approximated by just a sine function of a certain frequency and amplitude, we could easily employ a curve fitting algorithm to reconstruct the flow and to find the best-fit-interpolated data points. But turbulence is, at least for higher frequencies of 3D turbulence that we want to interpolate, a process demanding a stochastic description, which exactly is under investigation by this kind of measurements, i.e. not known a priori.[18]

In general, interpolation schemes do not evaluate all available information when down-sampling a data-set. When re-sampling with a frequency significantly lower than the mean sampling frequency, then part of the information content is lost depending on the order of interpolation, on the sampling frequency variability, and on the re-sampling frequency ratio. This is also illustrated in Figure 4.10 for two 0th order interpolation schemes. So-called *slotting techniques* are used to include all information of the available data within a data-set re-sampled at a lower frequency. Therefore, slotting techniques always smooth out high-frequent fluctuations and, thus, may dampen e.g. the noise, but also the turbulent kinetic energy, they effectively operate as low-pass filters. Basically using a rectangular window function of width Δt along the equally-spaced time line $t_i = t_0 + i\ \ \Delta t$ each measured data point is associated with its appropriate time slot. All data points in each time slot are then arithmetically averaged. Instead of a rectangular weighting function also advanced window shapes can be applied (cf. also Section A). Other weighting functions especially adapted to LDV measurements make use of the transit time or the inter-arrival time. An introduction to various slotting techniques and their application to LDV measurements and its analyses has been presented by Albrecht et al. (2003).

[18] Imagine for instance a time series $\phi(t)$ of a random turbulent process with a constant sampling interval Δt, whose fluctuation is characterized by its variance σ_ϕ. We could now re-sample the data using the same time step Δt, but shift the whole time series by adding an additional off-set of $\Delta t/2$. Obviously, if we would linearly interpolate the data, then this would result in a dampening of the fluctuations and in a reduction of σ_ϕ, which is not covered by the physical observations.

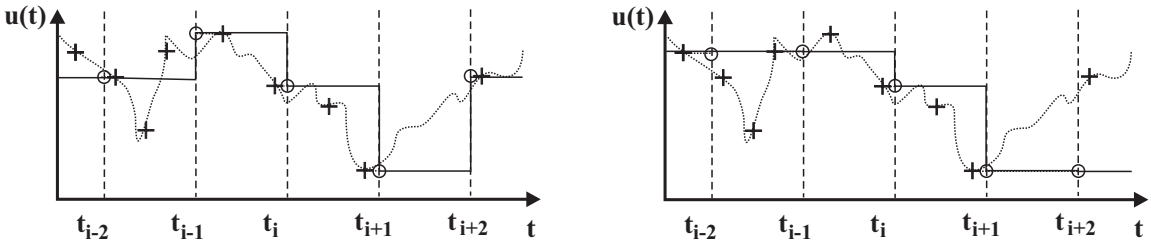

(a) Nearest neighbor re-sampling (b) Sample & hold re-sampling

Figure 4.10. The LDV-LIF system randomly acquires the velocity and concentration data at discrete times, i.e. information is unevenly distributed in time. In order to avoid biasing effects in the turbulence statistics and also to perform a Discrete Fourier Transform on the time series, the data has to be re-sampled with equal time intervals $\triangle t$. (a) Using a *nearest neighbor* algorithm minimizes the sum of the necessary time shifts $t_k - i\ \triangle t$. - (b) The *sample & hold* algorithm identifies the latest predecessor at a given time step, and thus imitates a hardware re-sampling technique, which was realized by measurement devices in the pre-computer era.

Two 0th order interpolation schemes are visualized in Figure 4.10. The best estimate is obtained from a *nearest neighbor* interpolation. As illustrated in Figure 4.10(a), with this scheme we approximate the unknown value of a turbulent process for a given instance in time by its the nearest observed value, looking both backward and forward in time. On the contrary, with a commonly used *sample & hold* interpolation we assign the youngest measured predecessor to the unknown value at a given time, i.e. we are looking only backward in time then (cf. Figure 4.10(b)). Using this method we can obtain estimates at a particular time "on the fly" during the data acquisition or temporal analysis. The sample & hold interpolation scheme thus imitates the hardware equal-interval sampling technique (using so-called buffer devices to temporarily store a signal), which was employed in the pre-computer era.

0th order re-sampling algorithms should preferably applied to measurements with a low variability of their data rate $\dot{N}$. Adrian & Yao (1987) recommended a mean data rate of about 20-times the highest frequency intended to be resolved in the power spectrum, if a sample & hold algorithm is employed. Due to the 0th order interpolation of the "true" velocity signal a so-called *step noise* will be introduced with the reconstructed signal that obscures the high frequency part of the PSD estimate. Since compared to the sample & hold algorithm with the nearest neighbor re-sampling the average width of the time step is only half as wide, i.e. the re-sampling accuracy is twice as high, the recommended data rate will be about 10-times the maximum PSD frequency. Hence, the nearest neighbor reconstruction of the flow velocity will be the preferred interpolation scheme with respect to further evaluation of the data (see Section 7 for the computation of auto-correlation functions and power spectral estimates).

In order to cross-correlate the two velocity components (e.g. for the evaluation of the Reynolds shear stress or of the cross-correlation function), we additionally applied a co-incidence window on the low-pass filtered data, prior to conducting the equal-interval re-sampling.

5. Experimental Set-up and Program

5.1 Shallow flow facility

In order to investigate the momentum and mass transport in various kinds of shallow turbulent plane shear flow the 'Karlsruhe shallow flow facility' has been established at the Institute for Hydromechanics, University of Karlsruhe. The flexible and fully equipped research installation offers precise and efficient measurements in a large-scale laboratory environment. Figure 5.1 gives a visual impression of the shallow flow facility looking from the outflow against the flow direction over the basin.

The shallow flow basin covers a total free-surface area of about 80 m^2, the basin has a width of 5.48 m and—due to the compact in- and outlet constructions—a usable length of about 13.5 m. Water depths up to 25 cm can

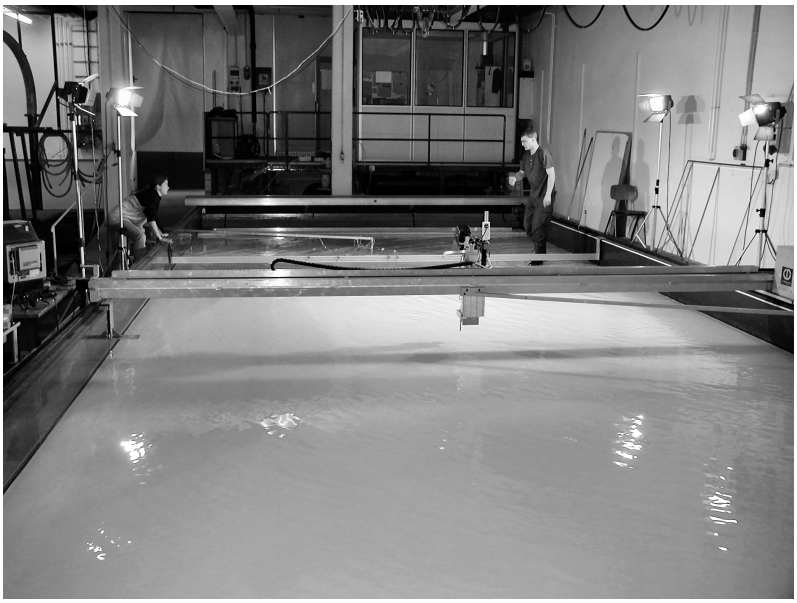

Figure 5.1. A view of the shallow flow facility against the flow direction. During the preparation of PCA measurements two co-workers arranged the carrier beam for the dye injection. In the foreground the 3D positioning system, carrying the LDV probe head and an ultrasonic distance sensor, is visible. In the upper part of the basin the inflow, consisting of diffusor trench and the flow conditioners, is located. In the background outside of the basin the control platform and the control cabin are visible. To the left outside the basin part of the LDV-LIF system can be found. (Photo by courtesy of H. Deutsch)

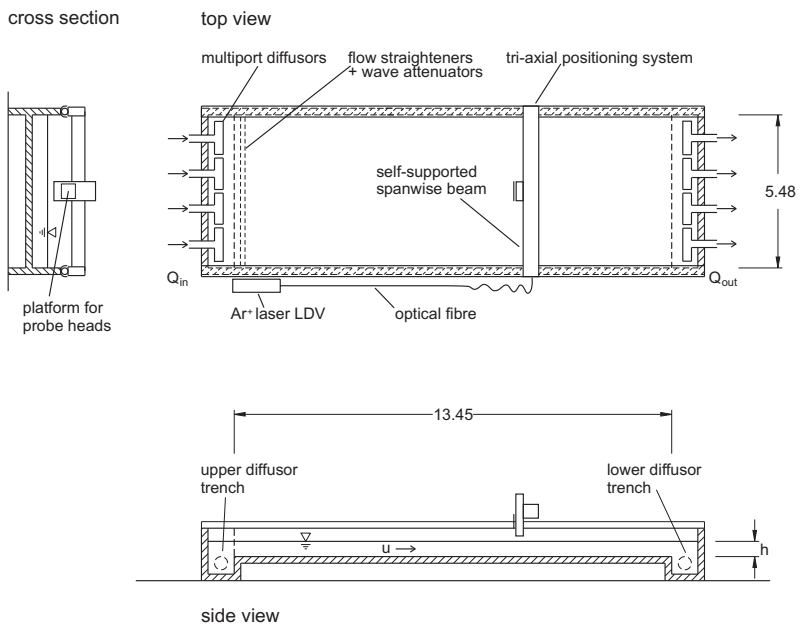

Figure 5.2. Sketch of the shallow flow facility (not to scale)

be adjusted and maintained with about 0.5 mm accuracy. Much effort has been made to obtain a plane and smooth bottom. The horizontal bottom of the basin is plane with a standard deviation of $\sigma_z = 0.7$ mm and a maximum deviation of ± 1.5 mm from the mean bottom level. The bottom slope is fixed horizontally ($S_0 = 0$)), and cannot be adjusted in order to obtain equilibrium shear flows for different discharge rates. The polyurethane-elastomer coating of the concrete bottom can be regarded nominally smooth, for the effective hydraulic roughness an equivalent sand roughness of $k_s = 0.05$ mm to $k_s = 0.1$ mm has been determined (cf. v. Carmer et al. (2000) for more detail). Figure 5.2 presents a schematic sketch of the shallow flow basin.

The shallow water basin is operated in a closed circuit, i.e. the water supply is independent from other test flumes in the hydraulics laboratory. Hence, pressure variations that might be induced by the operation of neighboring flumes have been omitted. Also external influences on the water quality could be excluded, a closed-loop arrangement allows to control and stabilize the experimental conditions with respect to fluid properties like temperature, turbidity, pH value, or chemical compounds, which is a crucial pre-requisite for the LIF and PCA measurements of mass concentrations of a minority species. In turn, also the contamination of other test rigs due to tracer material, especially due to fluorescent dye, is prevented. For a water depth of 3 cm (a typical value in the framework of the present work) the fluid volume circulating in the shallow flow facility is about 6 m^3, about 60% of the fluid is stored in the pipe system, and about 40% in the basin itself. Note that no additional fluid reservoir and no constant-head tank is provided making the control of the flow a delicate issue. The discharge is established by a 30 kW low-head radial pump ETA-R 250-300 provided by KSB. Its rotation speed is controlled by a frequency converter

(Danfoss, VLT 3500 HVAC) allowing for a continuously variable regulation of the discharge rate up to approximately 200 l/s. Since the frequency converter is provided with a serial bus RS 485 interface, the flow rate can be controlled remotely. For the examination of flow reversals (e.g. in tidal currents) the flow direction in the conduit can be inverted by operating 4 butterfly valves.

In order to obtain homogeneous inflow conditions without any lateral variation of the mean flow $\boldsymbol{U}_a$ the water is fed into the upper diffusor trench of the basin through a line of 4 multiport diffusors (cf. Figure 5.2). The discharge in each diffusor can be controlled by a gate valve, the openings of its multiple ports can be further adjusted by sheet metal sliders. Filter mat layers are used to completely equalize the outflow from the diffusor trench into the basin. For final conditioning of the flow multiple screens are employed as flow straighteners and initial turbulence generators, floating boards damp away the high-frequency surface waves introduced by the screens. After passing the basin the water is drained in the lower diffusor trench. Apart from the flow straighteners the outflow configuration is identical to the inflow configuration which allows to reverse the flow direction without otherwise significantly changing the flow field.

In the 16 m long straight part of the 200 mm return water conduit a magnetic-inductive discharge meter (Fischer & Porter, Mag XM) has been installed, which is supplied with a serial bus RS 485 interface. Hence, the flow rate can be obtained continuously with an accuracy of 0.5%.

A fully-automated three-axial traversing system (cf. Figure 5.2) which spans the full width of the basin allows to position various measurement probe heads at arbitrary places in the shallow flow basin. Video observations and measurements can also be conducted 'on–the–fly'. The repeat accuracy of the positioning system is below 1 mm in the horizontal directions, and about 0.03 mm in the vertical. The maximum positioning speed is 1.0 m/s, 0.5 m/s, and 0.1 m/s in the longitudinal, spanwise and vertical direction, respectively. Due to its compact self-supported construction the positioning system can be parked over the front or rear diffusor trench to provide a free field of observation over the full basin area. Communication with and control by the facility control computer was established using a hand-shake procedure via a serial RS 232 interface. The positioning system was constructed and assembled by Drescher Systemtechnik using stepper motors and controllers provided by Parker/Hannifin and linear positioning units provided by Isel.

In addition, the shallow flow facility is equipped with 2 PT 100 temperature sensors to survey the water- and air temperature with an accuracy of 0.1°C. Continuous measurements of the water level are obtained from ultrasonic distance sensors (Honeywell, 945 F4Y) with a repeat accuracy of 0.3 mm. 2 probes are installed in small external gauge tanks connected to the bottom of the basin at different longitudinal positions in order to observe the long-term

water level development. Another probe is mounted on the device platform of the positioning system in order to obtain the local water level at the measurement position. Both the temperature and distance sensors are connected to an A/D data acquisition card that is read out by the control software. A 12-channel peristaltic pump (Ismatec, IPC-12) is employed for the metered injection of dye tracer solution (for LIF, PCA, and visualization) into the flow at a fixed or variable rate of 0.002 ml/min to 44 ml/min with low pulsation. The dye can be introduced at arbitrary locations with negligible disturbance of the flow using thin tubes (diameter 1.0 mm) fixed to a self-supported aluminium carrier beam.

The communication of the facility control PC with the LDV-LIF measurement system is realized with a hand-shake protocol using a net-work connection with the LDV-LIF control PC. Thus, a sequence of data points can be measured as quick as possible. This is important especially for LIF measurements, as the duration of the fluorophor injection is limited due to increasing background concentration of the fluorophor in the flow.

The shallow flow facility including all the above mentioned equipment is supervised and controlled using a PC-based software FLAMES / STUMTRA. This software supports the precise calibration of the basin and its technical installations, and enables the signal acquisition, conversation, and data storage. It allows to prepare and to conduct extended measurement series. The execution of measurement series is fully automated, all requested operational data and experimental conditions are preprocessed and stored in reports. Hence, experimental investigations can be undertaken with best precision, efficiency, and reproductivity. Though the design and development of the software under LabView® was dedicated to this facility, it has also been migrated to another test flume. More details on the use and programming of the control software can be found in Dietz et al. (2002) as well as additional information about properties and calibration procedures of the technical equipment.

Table 5.1 summarizes the main features of the basin and its associated technical equipment. A visual impression of the Karlsruhe shallow flow facility is given in an introductory video-presentation by v. Carmer & Deutsch (2001, 2002).

5.2 Measurement program

In the framework of the present research project quantitative observations have been conducted using different measurement techniques in order to access the momentum and mass transport in shallow turbulent wakes both at the small and large temporal and spatial flow scales.

Table 5.1. The shallow flow facility—shallow flow basin, system control, and measurement equipment

shallow flow basin	
basin	total length 14.65 m, width 5.48 m, water depth up to 0.25 m
bottom	length 13.45 m, horizontal ($S_0 = 0$), plane ($\sigma_z = 0.7$ mm), smooth ($k_s = 0.05$ mm)
inflow	4 multiport diffusors, filter mats, screens, floating boards
water conduit	closed–loop, total volume approx. 6 m^3 under working conditions
main pump	radial pump (KSB, ETA-R 250-300), 30 kW, discharge in conduit continuously variable up to 200 l/s, frequency converter (Danfoss, VLT 3500 HVAC), RS 485 interface
primary measurement techniques	
LDV-LIF	2 component LDV for horizontal flow velocity synchronized with LIF for mass concentration, hand-shake via windows-network (cf. Chapter 4)
PIV	adapted to obtain surface velocity fields (cf. Section 3.1)
PCA	depth-averaged distribution of mass concentration (cf. Section 3.2)
supplementary measurement equipment	
flow meter	magnetic–inductive (Fischer & Porter, Mag XM), RS 485 interface
positioning system	3D positioning system from Drescher Systemtechnik (controllers and stepper motors by Parker/Hannifin, linear units by Isel), self-supported (spanning full width of basin), accuracy of position: horizontally 1.0 mm, vertically 0.03 mm, fully automated control, RS 232 interface
temperature sensor	2 PT100 sensors for water and air temperature, analog out to A/D card
distance sensor	3 ultrasonic distance sensors (Honeywell, 945 F4Y), repeat accuracy 0.3 mm, analog out to A/D card, 2 fixed probes installed in gauge tanks, 1 flying probe mounted on measurement platform of positioning system
dye tracer injection	peristaltic pump (Ismatec, IPC-12), 12 channels, flow rate per channel 0.002 up to 44 ml/min, RS 232 interface, injection into flow with 1 mm diameter tubes fixed to self-supported carrier beam
PC for system control	
personal computer, Intel processor P-II 200 MHz, 256 MB RAM, hard disk, data acquisition card (National Instruments, PCI-1200), multi-serial RS 232 interface, ethernet card	
OS	Windows NT 4.0
software	Flames/Stumtra, LabView 5

5.2.1 Conducted measurement series

For 10 different flow configurations detailed experimental investigations of a shallow turbulent flow in the wake of a single circular cylinder have been conducted. The smooth circular curvature, made of plastics or sheet metal providing a smooth surface, was attached perpendicularly to the bottom of the basin, its diameter varied as 63 mm, 125 mm, 250 mm, 500 mm, or 1120 mm. The ambient—i.e. undisturbed—plane shear flow was characterized by a bulk mean flow velocity U_a of 0.09 m/s up to 0.16 m/s, and by a water depth h of 17 mm up to 80 mm. The friction coefficient c_f was calculated to fall between $5.6 \cdot 10^{-3}$ and $9.4 \cdot 10^{-3}$, using an equivalent sand roughness $k_s = 0.05$ mm for the bottom roughness (cf. Section 5.3.1). The Froude number $Fr = U_a/\sqrt{gh}$ was kept below 0.33 in order to suppress surface waves in the base flow. The bulk mean Reynolds number $Re_h = U_a\, h/\nu$ ranged from 1,500 to 11,300. Hence, the base flow always was a fully turbulent boundary layer flow, since Re_h significantly exceeded the critical value of about 500 for the laminar–turbulent transition.

In order to link the geometry of the obstacle and the base flow, the aspect ratio of cylinder diameter and water depth, i.e. the shallowness of the flow, could be given as $1.7 \leq D/h \leq 66$. The cylinder Reynolds number $Re_D = U_a D/\nu$ ranged from 9,000 up to 146,000. For the stability parameter $S = c_f\, D/h$ (cf. Section 2.3) a maximum value of 0.55 was obtained. Table 5.2 summarizes the characteristic parameters of the different flow configurations. A wake flow stability classification of the conducted experiments will be presented in Section 5.2.2, Figure 5.5 illustrates the stability of the conducted measurement series together with data reported by Chen & Jirka (1995).

Besides qualitative flow visualization one or more of the non-intrusive optical measurement techniques of combined laser Doppler velocimetry and laser induced fluorescence (LDV-LIF), particle image velocimetry (PIV), and planar concentration analysis (PCA) have been applied. For the *flow visualizations* the following food and cosmetics colorants (BASF, Sicovit®) were used (BASF, 1996, 1997):

Amaranth 85 E 123	C.I. 16185, Acid Red 27
Indigotine 85 E 132	C.I. 73015, Acid Blue 74
Quinoline Yellow 70 E 104	C.I. 47005, Acid Yellow 3

Usually red and blue dye solutions were introduced at mid-depth into the right and left cylinder boundary layers, respectively. From overhead still and video cameras images and image sequences were obtained for real-time assessment of the flow, and stored for later analysis. Example photographs of the visualization arrangement are presented in Figure 5.3 for different shallow wake stability classes.

Point-wise measurements of the horizontal flow components and of a mass concentration have been obtained with high spatiotemporal resolution using a

Table 5.2. Summary of hydraulic conditions of shallow wake flow experiments behind a single circular cylinder employing various measurement techniques.

series name	description	D [mm]	h [mm]	Q [l/s]	c_f $[10^{-3}]$	Re_h	Re_D	D/h	c_f D/h	LDV-LIF	PIV	PCA
38_vs01	vortex street	63	38	29.8	6.7	5,438	9,016	1.66	0.01	-	x	x
80_vs01	vortex street	125	80	62.1	5.6	11,332	17,706	1.56	0.01	-	x	-
38_vs03	vortex street	125	38	29.8	6.7	5,438	17,888	3.29	0.02	-	x	-
18_vs06	vortex street	125	18	12.8	8.2	2,336	16,221	6.94	0.06	x	x	x
25_vs07a	vortex street	250	24.7	21.7	7.2	4,507	40,006	10.1	0.07	x	-	-
25_vs07b	vortex street	250	25	22.3	7.1	3,953	40,693	10.0	0.07	x	x	x
18_vs13	vortex street	250	17.5	8.2	9.4	1,487	21,246	14.3	0.13	x	-	-
17_ub25	unsteady bubble	500	17	11.4	8.4	2,080	61,185	29.4	0.25	x	x	x
25_ub33	unsteady bubble	1120	24.8	20.2	7.3	3,692	166,718	45.2	0.33	x	-	-
18_sb51	steady bubble	1120	18	12.8	8.2	2,336	145,337	62.2	0.51	x	(x)[a]	(x)[a]
17_sb55	steady bubble	1120	17	12.2	8.4	2,226	146,672	65.9	0.55	x	-	-
18_vs06_dz	double cylinder	125	18	12.8	8.2	2,336	16,221	6.94	0.06	-	x	-
25_vs07_row	cylinder row	63	23.3	21.9	7.1	3,996	10,806	2.70	0.02	(x)[b]	-	x

[a] restricted field of observation due to large size of obstacle
[b] LDV measurements only

combined 2D LDV-LIF measurement system (cf. Chapter 4). For the purpose of LIF measurements a fluorescent dye solution was introduced approximately iso-kinetically into the right cylinder boundary layer at mid-depth. For each experimental run a series of point-measurements were taken at various locations along the wake center line. The measurement volume was adjusted at each point to about two thirds of the water depth. The measurement duration in general was 120 s, selected points were observed for 600 s. Before each measurement a reference measurement has been conducted for 30 s well outside the wake in the ambient shear flow to obtain the background mass concentration in the ambient flow. The total duration of a measurement run was limited to 90 min to 120 min in order to restrict the background concentration of the fluorophor. Thus, a LDV-LIF measurement run could contain about 12 to 16 measurement points. Thereafter, the shallow flow basin had to be emptied, cleaned and refilled—a procedure that took a full day. For the LIF measurements it is crucial to know the exciting light intensity in the measurement volume, and to keep it constant during a full measurement run. This required to pre-warm the couplers, and to carefully feed the laser light into the optical fibres—again a time-consuming procedure of 6 hours pre-warming and at best 2 hours adjusting the LDV-LIF. Contrarily, LDV measurements without coupled LIF were much easier to conduct, since both background concentration and light stabilization were of no relevance. Nevertheless, despite the highly automated measurement sequence LDV measurements always need special care and attention.

In order to observe the horizontal wake flow field in its spatial context, an especially-adapted *surface PIV technique* (cf. Section 3.1) has been employed. Here, small beads floating at the water surface were laterally homogeneously distributed and advected through the field of observation. 300 frames could be obtained at 7 Hz for about 45 s with a single measurement run from a field of observation of 1.2 m x 1.4 m. Therefore, each measurement run had to be repeated some times, then the field of observation was moved downstream to the next measurement position.

Depth-averaged fields of mass concentration have been obtained employing a special *PCA measurement technique* (cf. Section 3.2). A food colorant solution was introduced into one or both cylinder boundary layers or into the wake of the cylinder at mid-depth. The field of observation of 1.6 m x 1.2 m was centered to the wake flow. For an individual measurement run images were recorded with a digital video camera at a frame rate of 25 Hz for more than 120 s, and later digitized and analyzed. Since changing the camera position to a new field of observation required to re-adjust the illumination and to re-calibrate the PCA algorithms, the optical arrangement was kept in place. Instead, the obstacle was moved upstream in order to obtain complete measurement series along the wake centerline.

(a) VS - vortex street-like wake (b) UB - unsteady bubble wake (c) SB - steady bubble wake

Figure 5.3. Flow visualizations, observed with an overhead camera, of typical flow configurations illustrate the three stability classes VS, UB, and SB in Figures (a), (b), and (c). The stability numbers were $S = 0.13$, 0.23, and 0.55, respectively at water depths $h = 30$ mm, 20 mm, and 11 mm. The bulk mean Reynolds numbers were $Re_h = 3100$, 1600, and 640, respectively, and the cylinder Reynolds numbers were $Re_D = 44,000$, $35,000$, and $25,000$.

Simultaneous data sets (u, v, c) were obtained directly from the combined LDV-LIF measurements (cf. Section 4.3) allowing to instantaneously correlate the horizontal flow velocity and mass, $u_i\, c = f\,(t)$. Also the planar measurements of surface velocity and depth-averaged concentration have been correlated after a phase–resolved averaging procedure to obtain the large-scale coherent mass fluxes $\{u_i\}\,\{c\} = f\,(\phi)$. More detail will be given in Part III of this work.

5.2.2 Classification of experimental observations

According to Chen & Jirka (1995) circular cylinder wakes in shallow turbulent plane shear flow can be subdivided into three flow classes regarding their overall stability behavior. In Section 2.3 the characteristic flow phenomena have been introduced, and the Stability number, given by $S = c_f \frac{D}{h}$, has been identified as a characteristic parameter to classify the wake flow. The following delimitations were recommended by Chen & Jirka (1995) in order to classify shallow wake flows.

$S < 0.2$	vortex street-like wake (VS)
$0.2 < S < 0.5$	unsteady bubble wake (UB)
$S > 0.5$	steady bubble wake (SB)

The different stability classes in shallow wake flows, VS, UB, and SB, are illustrated in Figure 5.3 for typical experimental flow conditions. Here, the stability numbers were $S = 0.13$, 0.23, and 0.55, respectively. The bulk mean Reynolds numbers were $Re_h = 3100$, 1600, and 640, respectively, and the cylinder Reynolds numbers were $Re_D = 44,000$, $35,000$, and $25,000$. The dye for the flow visualization was continuously introduced in flow direction into the upstream left and right cylinder boundary layers.

The delimitating critical values $S_{ca} \approx 0.2$ and $S_{cc} \approx 0.5$ were proposed to be invariant to the ambient Reynolds number $Re_h = U_a\, 4h/\nu$ for fully turbulent ambient shear flow, i.e. in the high Reynolds number regime of $Re_h \geq 6,000$. The critical values should not be regarded as stringent, but should be allowed to vary within $\pm 10\%$. The error bounds in the critical values are said to be mainly due to uncertainties in the estimation of the bottom friction coefficient c_f.

In general, the skin friction coefficient that is related to the Darcy-Weisbach friction coefficient by $c_f = \lambda/4$ depends on the bulk ambient Reynolds number and on the relative roughness, ie. $c_f = f\,(Re_h,\ k_s/4h)$ (cf. Section 5.3.1). The functional dependance of the stability parameter $S = c_f\, D/h$ then becomes $S = f\,(k_s/4h,\ Re_h,\ Re_D)$ including the cylinder Reynolds number $Re_D = U_a D/\nu$. Chen & Jirka (1995) used the approximation of a hydraulically smooth bottom, for which $c_f = f\,(Re_h)$ only, and thus $S = f\,(Re_h,\ Re_D)$. If S would be Re_h-invariant, then it would only depend on Re_D. This is applicable for unbounded wake flows, but it clearly contradicts the stability concept for shallow wakes that are based on the spanwise boundedness of the flow with depth h and on the vertical shear due the a bottom roughness with c_f. $S = f\,(Re_D)$ would require that D/h should depend on Re_h reciprocally compared to c_f. This is obviously wrong, since $D/h \propto Re_h^{-1}$ and $c_f \propto \left[\lg\left(Re_h^{-0.9}\right)\right]^{-2}$.

Hence, for shallow flow conditions the influence of the bulk ambient Reynolds number Re_h should be retained. Gray-scale iso-contours of S depending on Re_D and Re_h are represented in Figure 5.4 obtained from own flow visualizations (full symbols), and from data presented by Chen & Jirka (1995) (outlined symbols). The observed wake flows are classified into VS, UB, or SB wake stability types denoted by ■, ●, and ▲, respectively. Bold full lines indicate critical values of S for transitions between stability classes. Thin lines denote iso-contours of S calculated for $Re_h \leq 30,000$ and for $Re_D \leq 450,000$ as

$$S = c_f \frac{D}{h} = \frac{\lambda}{4}\, 4 \frac{Re_D}{Re_h}\ , \tag{5.1}$$

where $Re_D = U_a\, D/\nu$ is the cylinder Reynolds number, and is $Re_h = U_a\, 4h/\nu$ the bulk ambient Reynolds number based on the hydraulic flow diameter. Here, for the Darcy-Weisbach friction coefficient the explicit approximation of Swamee & Jain (1976) for the Colebrook-White equation is used in the limit of hydraulically smooth conditions, i.e.

$$c_f = \frac{\lambda}{4} = \left(\frac{0.25}{\lg\left(\dfrac{5.74}{Re_h^{0.9}}\right)} \right)^2 . \tag{5.2}$$

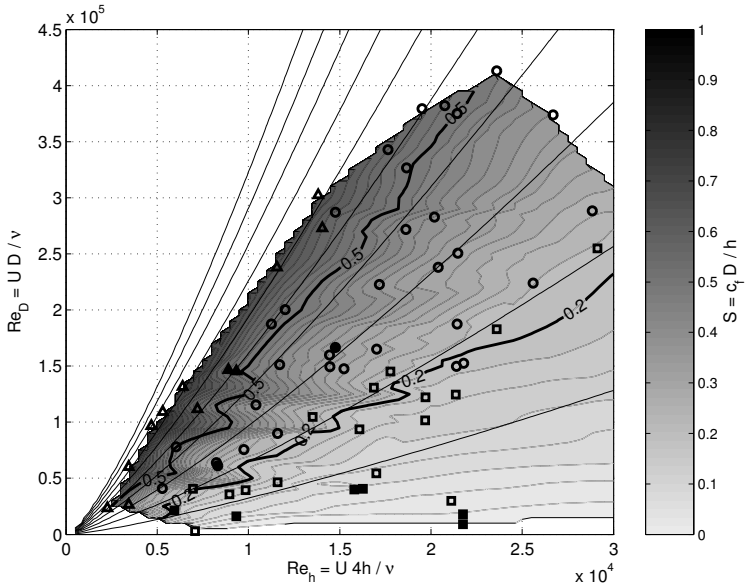

Figure 5.4. The shallow wake stability parameter S is presented in the Re_h–Re_D space. ■, ●, and ▲ denote own laboratory wake flows classified as VS, UB, or SB, respectively. □, ○, and △ indicate data of Chen & Jirka (1995) (re-computed employing improved values of c_f). Iso-contours of S, observed experimentally, are represented as gray-scale information, thick full lines indicate the transitions VS–UB and UB–SB. Thin lines show iso-contours of the stability parameter as calculated from (5.1) using (5.2). For $S \to 0$, i.e. for unbounded wakes, the stability parameter is invariant of Re_h. For increasing S its dependance on Re_h becomes significant, and should not be neglected.

To exemplify the dependance of $S = f\,(Re_h,\ Re_D)$, for a cylinder Reynolds number $Re_D = 1.5 \cdot 10^5$ a vortex street-like wake will be encountered for $Re_h = 2.2 \cdot 10^4$, an unsteady bubble wake for $Re_h = 1.5 \cdot 10^4$, or a steady bubble wake for $Re_h = 0.7 \cdot 10^4$. Although for $S \to 0$, i.e. for unbounded wake flows, the stability parameter is invariant of Re_h, for the general case of $S > 0$ its dependance on Re_h becomes significant. $S = f\,(Re_h)$ should not be neglected, especially not for higher values of D/h indicating a pronounced shallowness of the wake flow.

Additionally, the bottom roughness $k_s/4h$ should be represented in the friction coefficient c_f, as it will become relevant for small water depths. Therefore, the friction coefficients and, consequently, the stability parameters of the data from Chen & Jirka (1995) have been re-calculated using an equivalent sand roughness of $k_s = 0.1$ mm. For the predominant water depths of $h \lesssim 30$ mm this resulted in an increase of c_f and S of approximately 10%. The corrected data is depicted in Figure 5.5 together with own measurements. Of course, the error bounds of ±10% in the delimitation of the flow classes by S_{ca} and S_{cc} remain. But they should not be ascribed to uncertainties in the evaluation of c_f. More likely, they can be associated with the Re_h-variance of S (mainly for the

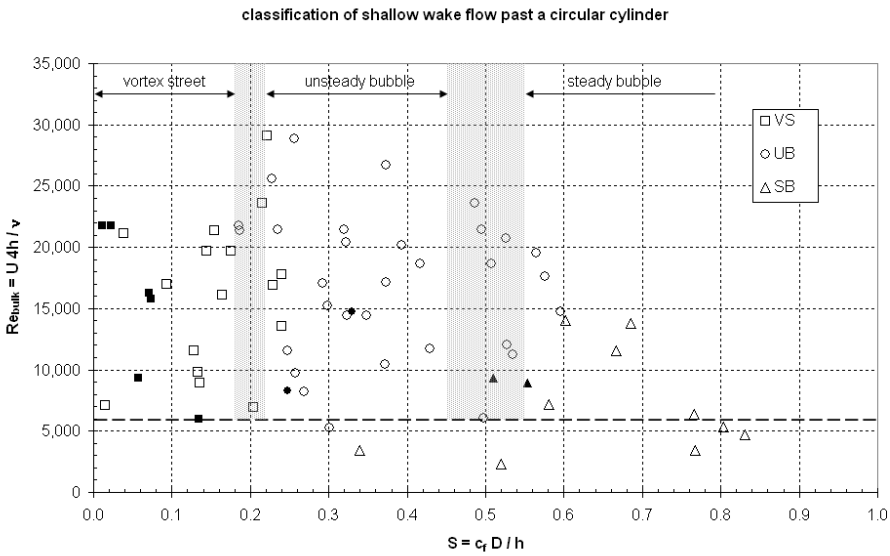

Figure 5.5. Laboratory shallow wake flows have been organized in three stability classes (VS) vortex street-like wake, (UB) unsteady bubble wake, and (SB) steady bubble wake denoted by ■, ●, and ▲, respectively. The data of Chen & Jirka (1995) (outlined symbols) has been re-calculated using improved friction coefficients c_f. Own measurements are indicated by filled symbols. Delimitations and error bounds of the shallow wake stability parameter S, as proposed by Chen & Jirka (1995), are included. The constant S-values for the transitions between the stability classes have to be re-adjusted and have to be allowed to vary with Re_h.

transition UB–SB), and to uncertainties in the flow classification (especially for the transition VS–UB).

5.3 Characterization of base flow as plane turbulent shear flow

The objective of this work is to clarify the effects of a horizontal shear—introduced by a large cylindrical obstacle—on a shallow turbulent base flow, and to examine the genesis and fate of large-scale convective instabilities in shallow wake flows. In the following section we will give a short description of the flow characteristics of the *ambient base flow*, a more thorough discussion has been presented by v. Carmer et al. (2000).

Ideally, the base flow will be a *plane turbulent free-surface equilibrium shear flow*. Then, the vertical gradients of the flow velocity components $\partial u_i/\partial z$, ranging from the bottom along the water column up to the free surface, reflect a shear stress distribution with its maximum at the bottom that will vertically decrease toward zero within the bottom boundary layer. A plane flow is characterized by horizontally homogeneous flow fields, i.e. the flow is invariant to lateral and longitudinal changes of position. This in particular will require the absence of any secondary motions of the flow. Since in the present experimental

set-up the flow can be characterized as a shallow straight rectangular open-channel flow, secondary flow due to a compact cross-sectional bathymetry as well as due to curvature of the bathymetry in the main flow direction can be excluded. Because of the high bulk ambient Reynolds number $Re_a = U_a h/\nu$ of the flow, viscous effects will be limited to a thin layer—the viscous sub-layer of the boundary layer—close to the bottom. In a 'near-equilibrium' shear flow the vertical distribution of the flow quantities still displays self-similarity in the longitudinal direction.

5.3.1 Horizontal flow field

Transverse velocity distribution. The presupposition of a plane base flow requires a uniform transverse distribution of the time-mean longitudinal velocity component, i.e. $\langle u \rangle \neq f(y)$. This has been ascertained by a proper discharge adjustment of the individual multi-port diffusors, and by a selection of flow straighteners and turbulence generators in the inflow of the shallow flow facility. With LDV measurements it has been verified for various discharges that the mean ambient flow as well as the turbulence intensities did not depend on the lateral and longitudinal measurement position. Also flow visualizations did not indicate any undesirable secondary motions of the base flow, as is visible for instance from the straight courses of the multiple dye plumes in Figure 5.9.

Longitudinal velocity distribution. Using the shallow water assumptions and the boundary layer approximation the 3D Reynolds-averaged Navier-Stokes equations can be simplified to result in *1D equations of motion* for continuity,

$$\frac{d\bar{U}}{dx} + \frac{\bar{U}}{h}\frac{dh}{dx} = 0 \quad , \tag{5.3a}$$

and for momentum,

$$\bar{U}\frac{d\bar{U}}{dx} = -g\frac{dh}{dx} + g\sin\vartheta - c_f\frac{\bar{U}^2}{2h} \quad , \tag{5.3b}$$

where $\bar{U}$ the depth- and time-averaged main flow component, and $\sin\vartheta$ the bed slope, $S_0 = \tan\vartheta \approx \sin\vartheta$. Inserting (5.3a) into (5.3b) results in the well-known expression for the 1D calculation of the *water surface level in open-channel flow*,

$$\frac{dh}{dx} = \frac{g\sin\vartheta - c_f\frac{\bar{U}^2}{2h}}{g - \frac{\bar{U}^2}{h}} = \frac{S_0 - S_f}{1 - Fr^2} \ . \tag{5.4}$$

As is evident from Equation (5.4), a longitudinally uniform flow can not be established in a viscous open-channel flow over a horizontal bottom, i.e. $\vartheta = 0$, without the driving force of gravity. Then, the loss of momentum due to bottom

friction can only be replenished from an existing longitudinal pressure gradient $\frac{dh}{dx}$. For Froude numbers decreasing toward 0 the changes in h diminish, and the flow tends to uniformity. For the experimental program of the present study, the Froude number has been limited to $Fr < 0.3$.

The effect of bottom friction is usually described by the *bed shear stress* τ_b that is related to the bed friction velocity $U_\star$ and to a bed friction coefficient c_f as

$$\frac{\tau_b}{\rho} \equiv U_\star^{\,2} \equiv c_f \, \frac{\bar{U}^2}{2} \; . \tag{5.5}$$

The *bed friction coefficient* c_f is related by $c_f = \lambda/4$ to the DARCY-WEISBACH friction coefficient λ that is used to describe the influence of the surface roughness in pipe and channel flows. λ represents the effects of both 'external' surface friction and of 'internal' viscous friction. It thus, firstly depends on the relative height of the roughness elements k_s/D_{hy}, where k_s is the equivalent NIKURADSE sand roughness, and $D_{hy} = 4R_{hy} = 4A/P_{hy}$ is the hydraulic diameter. Secondly, λ is dependent on the bulk Reynolds number $Re_{D_{hy}} = \bar{U} D_{hy}/\nu$. Whereas for 'hydraulically rough' flows λ becomes independent of $Re_{D_{hy}}$, i.e. $\lambda = f\left(k_s/D_{hy}\right)$ only, and for 'hydraulically smooth' flows $\lambda = f\left(Re_{D_{hy}}\right)$ only, the general case of $\lambda = f\left(k_s/D_{hy},\ Re_{D_{hy}}\right)$ can be solved implicitly by the COLEBROOK-WHITE equation. SWAMEE & JAIN (1976) presented an explicit approximation of the COLEBROOK-WHITE equation that provides reasonable accuracy[1],

$$\lambda = 0.25 \left[\lg \left(\frac{k_s/D_{hy}}{3.71} + \frac{5.74}{Re_{D_{hy}}^{0.9}} \right) \right]^{-2} \; . \tag{5.6}$$

Although the bottom of the shallow flow facility has been furnished with a smooth coating, it is not hydraulically smooth. For different steady low-Fr flow conditions the water depth h has been measured at multiple downstream positions (V. CARMER ET AL., 2000). The measured water surface elevations were also predicted with good agreement using Equations (5.4) and (5.6), which have been calibrated by adjusting k_s. Thus, from a best-fit the equivalent sand roughness of the bottom has been obtained as $k_s = 0.05$ mm to 0.1 mm.

5.3.2 Vertical flow field

In uniform plane boundary layer flow the flow fields are horizontally homogeneous, i.e. they do not change in the horizontal directions. Nevertheless, since

[1] The accuracy of Equation (5.6) compared to the implicit COLEBROOK-WHITE equation has been evaluated by SWAMEE & JAIN (1976) to fall within 1% over a wide range of k_s/D_{hy} and $Re_{D_{hy}}$. Since from the range of k_s/D_{hy} and $Re_{D_{hy}}$ occurring in the present study this deviation was well within the 1% error bound, λ has been determined here from (5.6) instead of iteratively solving the COLEBROOK-WHITE equation.

the shallow flow is confined between the solid bottom (no-slip condition) and the free surface, rapid changes and steep gradients occur in the vertical direction. Speaking of a uniform channel flow implies that vertical gradients exist, but do not depend on the horizontal position.

Hence, a fully developed open-channel flow should have established at the beginning of the test section of the shallow flow facility, i.e. the bottom-induced shear layer should have fully developed. Depending on the inflow conditions the length of the boundary layer development can range up to $L_x/h = 200$. For smooth open-channel flow KIRKGÖZ & ARDIÇLIOĞLU (1997) validated an estimate for the developing distance as $L_x/h = 76 - 10^{-4}\,\frac{Re_h}{Fr_h}$.

Time-mean vertical velocity distribution. In order to describe the vertical distribution of the time-averaged main velocity component $U(z)$ in a fully developed turbulent open-channel flow, usually a logarithmic law is employed analogously to boundary layer theory. Within the free boundary layer—for z/h between 0.15 and 0.6 approximately—the log-law provides a sound analytical solution for the vertical turbulent momentum exchange (cf. e.g. SCHLICHTING & GERSTEN, 1997). Closer to the bottom also viscous effects become important, thus the log-law has to be modified by a damping function (e.g. VAN DRIEST), and finally has to be replaced by a linear relation $U(z)$ in the viscous sub-layer immediately above the smooth bottom. When the free surface is approached ($z/h > 0.6$) the main velocity component U additionally increases due to the damping of the vertical component. Hence, an extra term—a *wake function*—is added to the log-law, usually employing a solution given by COLES (1956). Then, for a wide range of distances from the bottom (approximately $0.15 < z/h < 0.9$) the vertical distribution of the average main flow velocity over a smooth bottom is well described by a *log-wake law* given as

$$\frac{U}{U_\star} = \frac{1}{\kappa}\ln\frac{z}{z_\star} + B_z + \frac{2\Pi}{\kappa}\sin^2\left(\frac{\pi}{2}\frac{z}{h}\right) \ , \tag{5.7}$$

where $U_\star$ shear stress velocity given by (5.5),
$z_\star$ viscous length, $z_\star = \nu/U_\star$,
κ v. Kármán constant, here $\kappa = 0.412$,
B_z constant of integration,
here $B_z = 5.29$ for smooth bottom,
Π Coles' wake parameter, $\Pi = f(Re_h)$.

More detail on the log-wake law in open-channel flow is provided e.g. by NEZU & RODI (1986); NEZU & NAKAGAWA (1993). Some recommendations for an effective prediction of $U(z)$ and $U_\star$ from velocity measurements in open-channel flows are provided by V. CARMER (1998).

Figure 5.6 exemplifies the vertical distribution $U(z)$ for a shallow base flow characterized as a plane near-equilibrium shear flow with $Re_h = 12,075$ and

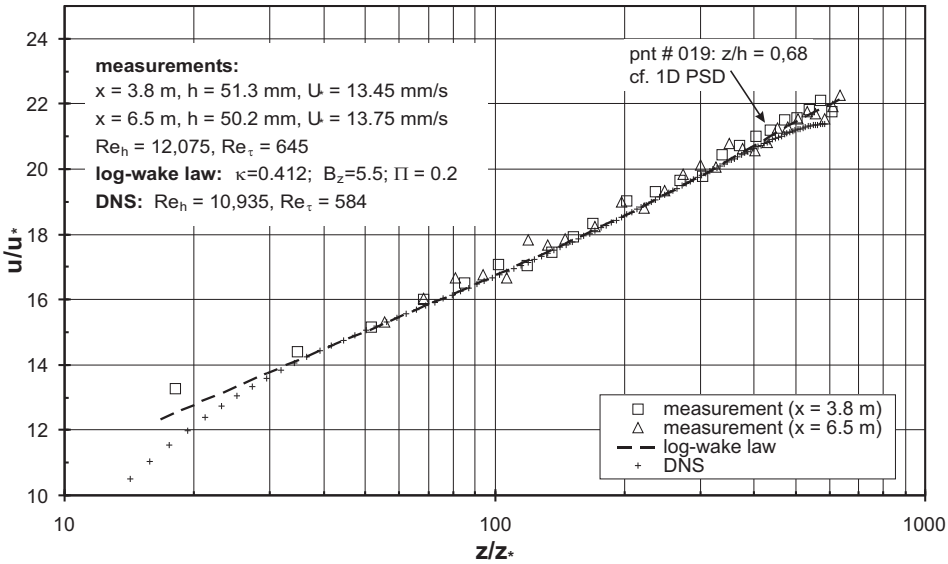

Figure 5.6. The vertical distribution of the time-averaged main velocity component has been obtained from LDV measurements at two downstream positions (□ and Δ symbols) in a longitudinally slightly non-uniform base flow with $Re_h = 12,075$ and $Re_\tau = 645$ (series 000419). The data is compared to a DNS of a turbulent channel flow at $Re_h = 10,935$ and $Re_\tau = 584$ (+ symbols, data provided by Moser et al. (1999)), and to a prediction using the log-wake law (5.7) with $B_z = 5.5$ and $\Pi = 0.2$.

$Re_\tau = U_\star h/\nu = 645$. The velocity data (denoted by □ and Δ symbols) have been obtained from LDV measurements at two different downstream positions of the gradually varying flow. The reader is referred to v. Carmer et al. (2000) for more information about the shortcomings of the employed LDV arrangement in order to obtain $\boldsymbol{u}(z)$ measurements with an appropriate spatial resolution. The measurements at both locations agree well with each other and with results obtained by Moser et al. (1999) from a DNS of a smooth channel flow with $Re_h = 10,935$ and $Re_\tau = 584$ (denoted by + symbols). This indicates that the slight non-uniformity of the base flow has hardly any effect on $U(z)$, and may also not affect a shallow wake flow and its 2D LCS. For the prediction of $U(z)$ from the log-wake law (5.7) (dashed line) $B_z = 5.5$ was employed together with a wake parameter $\Pi = 0.2$, though earlier measurements (Nezu & Rodi, 1986; v. Carmer, 1998) suggested a value of $\Pi = 0$ for uniform open-channel flows with $Re_h < 5 \cdot 10^4$. Also the prediction by the log-wake law correlates with the data demonstrating that $U_\star$ is computed correctly from Equations (5.5) and (5.6), and thus verifying the calibration of the equivalent sand roughness $k_s \simeq 0.1$ mm.[2]

Vertical distribution of turbulent velocity fluctuation. The mean turbulence field is commonly expressed in terms of a *turbulence intensity TI* that

[2] For the present flow conditions the sedimentological Reynolds number $Re_\star = U_\star k_s/\nu = k_s/z_\star = k_s^+$, characterizing the frictional effect of the bottom roughness, is of order $\mathcal{O}(1)$.

is defined by the standard deviation of the turbulent velocity fluctuations $\sigma_{u_i} = \langle u_i'^{\,2} \rangle^{1/2}$ normalized by its ensemble-mean value, i.e. $TI_{u_i} = \sigma_{u_i}/U_i$. In Section 7.1.4 downstream distributions of the horizontal turbulence intensities will be given along the centerline of various wake flows as well as for the corresponding base flows.

In order to characterize the mean vertical distribution of the turbulent velocity fluctuations in a plane boundary layer flow, the standard deviation is non-dimensionalized with the shear stress velocity $U_\star$. In the free shear region (approximately for $0.15 \leq z/h \leq 0.6$) of a smooth turbulent plane open-channel flow the standard deviations of the velocity components σ_{u_i} can be described by a semi-empirical exponential decay equation, which can also be related to the components of the turbulence intensity via (5.5),

$$\frac{\sigma_{u_i}}{U_\star} = \frac{TI_{u_i}}{\sqrt{c_f/2}} = D_{u_i}\, e^{c_k\, z/h} \ . \tag{5.8}$$

The empirical constants are $D_u = 2.30$, $D_v = 1.63$, $D_w = 1.27$, and $c_k = -1.0$ according to Nezu & Rodi (1986); Nezu & Nakagawa (1993).

The progression of the normalized horizontal velocity standard deviations $\sigma_u/U_\star$ and $\sigma_v/U_\star$ in the vertical direction is depicted in Figure 5.7 for base flow conditions already reported for Figure 5.6. The data obtained from LDV measurements is compared to DNS results of Moser et al. (1999) and to predictions using Equation (5.8). The measured turbulence distributions at both downstream positions coincide in the limits of the measurement accuracy. They also agree well with the smooth channel simulation of Moser et al. (1999). The prediction using (5.8) seems to be applicable in the free shear region, but also well into the free surface region, i.e. for $0.15 \lesssim z/h \lesssim 0.9$.

Hence, from the vertical turbulence intensity distribution as well as from the vertical distribution of the mean horizontal velocity components we conclude that the base flow can be described as a fully developed turbulent plane open-channel flow using the characteristics of equilibrium shear flows. The turbulent open-channel flow can be regarded as fully developed at the beginning of the test section after $x/h = 75$ in agreement with the smooth channel observation of Kirkgöz & Ardiçlioğlu (1997).

5.3.3 Spectral analysis in frequency domain

Turbulent flow fields show fluctuations of a wide range of frequencies, resp. wave lengths, that can be understood as eddies of various sizes. In a plane boundary layer the primary transverse 'Tollmien-Schlichting instabilities' are subject to secondary 3D instabilities in the laminar–turbulent transition, resulting in stretched 'Λ–structures'. As these decay, from their remains 'turbulent spots' develop, which occur more randomly, and grow rapidly in space and

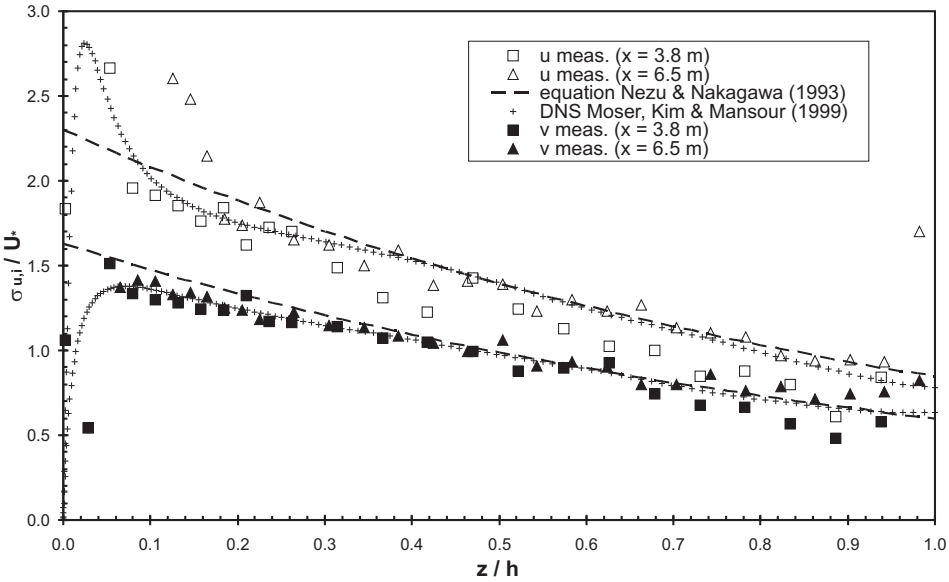

Figure 5.7. The vertical distribution of the standard deviations of the horizontal velocity components is normalized by the bottom shear velocity $U_\star$. Standard deviations of main and transverse flow components, $\sigma_u/U_\star$ and $\sigma_v/U_\star$, are denoted by □ and Δ symbols, and by ■ and ▲ symbols, respectively. Dashed lines indicate corresponding predictions using Equation (5.8). See also caption of Figure 5.6.

time, until finally a self-preserving turbulent state is reached. Of course, also in a fully turbulent boundary layer structures exist, e.g. spatially organized in longitudinal 'streaks' and temporarily in 'burst cycles'. (See e.g. Schlichting & Gersten, 1997; Oertel Jr. & Delfs, 1996)

Shear-induced mechanisms of vortex stretching are the main cause for the decay of turbulent structures in the full range of wave lengths. The energetic large vortical structures may be stretched along the gradient $\partial \boldsymbol{U}/\partial \boldsymbol{x}$ of the mean flow field. Thus, large eddies give rise to permanent anisotropy of the turbulence at low wave numbers. As the large eddies locally introduce shear stresses due to local velocity gradients, further vortex stretching and generation of smaller vortices occur. Such randomly occurring small-scale shear stresses of non-permanent character of course lead to anisotropy of the instantaneous turbulence field, but on average the random distribution results in isotropic turbulence in the higher wave number range.

As will be discussed later in Section 6.2, *energy spectral density* (ESD) estimates characterize the distribution of turbulent kinetic energy along the wave number range. In the *inertial subrange* of wave numbers, being a part of the universal equilibrium range of locally isotropic turbulence, the ESD distribution follows a -5/3 power law (cf. Equation (6.26)). Also the 1D ESD of the horizontal velocity components of the base flow—a uniform turbulent open-channel flow—display a distinct inertial subrange of 3D isotropic turbulence, i.e. identical distribution of S_{uu} and S_{vv} decaying to the power of -5/3. The ESD estimates shown in Figure 5.8(a)—computed from LDV data obtained at

a depth $z/h = 0.68$ in the same flow conditions as described for Figure 5.6—suggest local isotropy of an inertial subrange of homogeneous turbulence for frequencies $f \geq 5$ Hz.[3] However, in the lower frequency range the 1D ESD estimates reveal the characteristic anisotropy, for $f \to 0$ the ESD estimates for both components differ significantly.

Also in the *auto-correlation coefficients* of the horizontal velocity components, $r_{uu}(\tau)$ and $r_{vv}(\tau)$ (cf. Equations (6.5) and (6.46)), the large-scale turbulence anisotropy is present, as illustrated in Figure 5.8(b). *Integral time scales* T_I can be computed from $r_{\phi\phi}$ of the longitudinal and transverse components (cf. Equation (6.45)). For the velocity data presented in Figure 5.8 the integral time scales are $T_{I,u} = 0.204$ s and $T_{I,v} = 0.034$ s, i.e. $T_{I,v} \approx 1/6\ T_{I,u}$, which corresponds to the 1D ESD values in the low-frequency range.[4] Hence, concerning the large-scale anisotropy of the turbulent free-surface shear layer flow, the ESD estimates are consistent with the auto-correlation coefficients and the integral length scales.

5.3.4 Mass transfer and mixing

The spreading of a mass tracer in a plane shear layer flow can be used to check the existence of a nearly uniform turbulent open-channel flow. Figure 5.9 illustrates both the uniformity of the base flow without any secondary currents. Here, the flow is characterized by an average depth $h = 17.5$ mm, a bulk main velocity of $\bar{U}_a = 8.3$ cm/s, a friction coefficient $\lambda = 0.039$, and bulk Reynolds and Froude numbers $Re_h = 1,450$ and $Fr = 0.2$. A tracer dye was continuously injected iso-kinetically from 5 point sources at mid-depth. The spacing of the grid painted on the bottom was 20 cm. The video camera, supplied with a wide-angle lens, was oriented vertically downwards.

In order to characterize the lateral turbulent exchange of a passive conservative tracer plume introduced from a continuous point source into a shallow uniform open-channel flow, according to Fischer et al. (1979) the *transverse turbulent diffusivity* $D_{t,y}$ can be estimated by

$$\frac{D_{t,y}}{U_\star\, h} = 0.15 \pm 50\% \ . \tag{5.9a}$$

Rutherford (1994) summarized the results from a number of studies, and concluded a lower-bound estimate

[3] The Kolmogorov *micro length scale* of turbulence, here, can be estimated to $\ell_\eta \approx 0.28$ mm using the relation (6.60b), together with a macro length $\ell_0 \approx h$, and k predicted from σ_u^2 using (5.8). Employing Taylor's frozen-turbulence hypothesis the corresponding *micro time scale* becomes $\tau_\eta \approx 1.12$ ms.

[4] For $k_w \to 0$ the ESD is related to the integral scale as $\ell_{I,i} = \frac{\pi S_{ii}(0)}{2\left\langle u_i'^{\,2}\right\rangle}$.

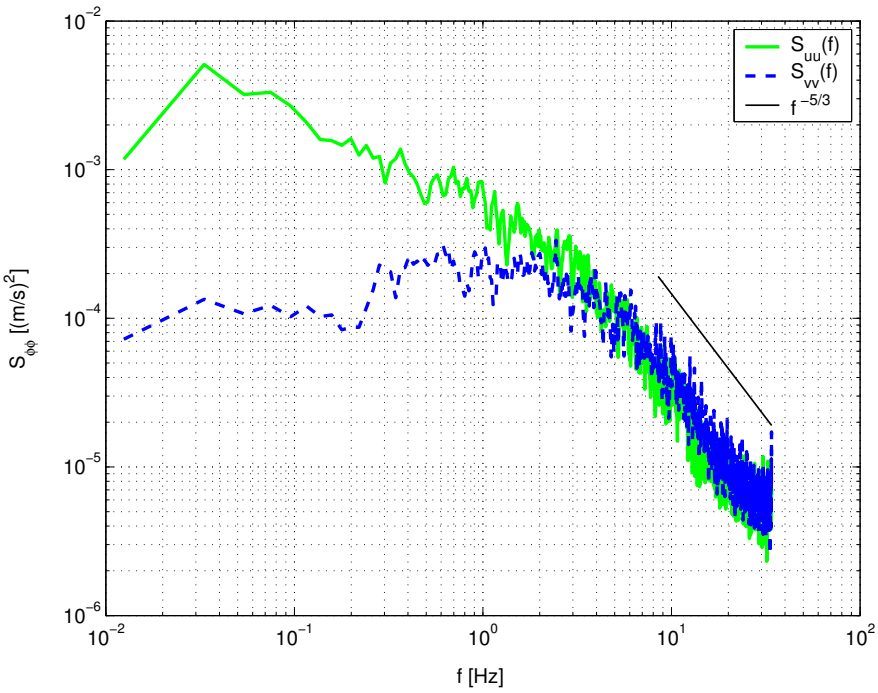

(a) 1D energy spectral density estimates of horizontal velocity components

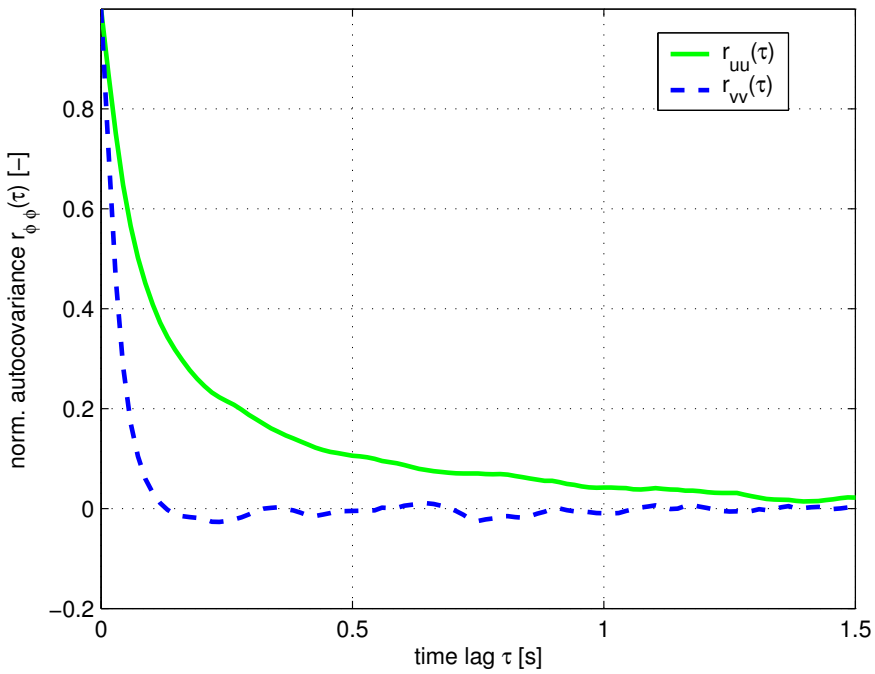

(b) Auto-correlation coefficients of horizontal velocity components

Figure 5.8. From LDV data obtained at $z/h = 0.68$ in a turbulent near-equilibrium free-surface shear flow (see caption of Figure 5.6) (a) 1D energy spectral density estimates $S_{\phi\phi}(f)$ and (b) auto-correlation coefficients $r_{\phi\phi}(\tau)$ have been computed. Full lines denote quantities employing the longitudinal velocity component, dashed lines denote transverse quantities.

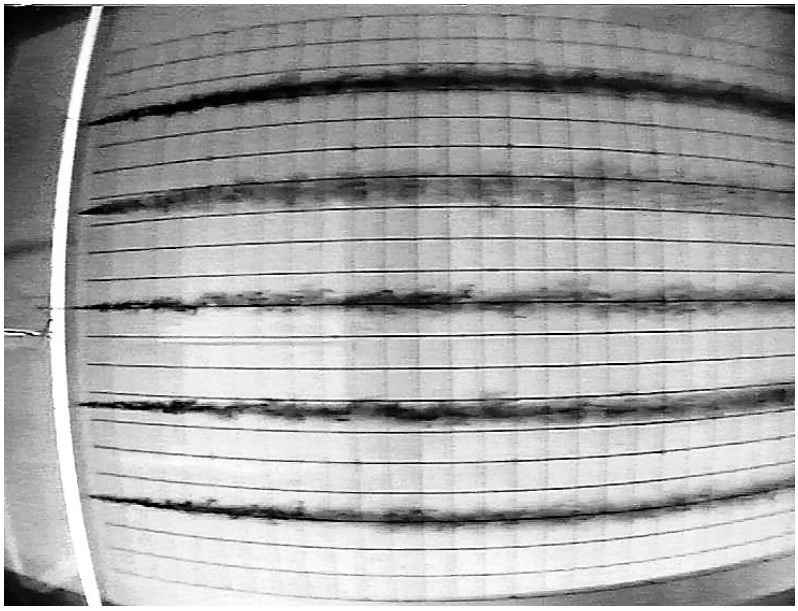

Figure 5.9. The top-view on a shallow base flow ($h = 17.5$ mm, $\bar{U}_a = 8.3$ cm/s, $\lambda = 0.039$, $Re_h = 1,450$, $Fr = 0.2$) with 5 continuous point sources illustrates the mass transport in a uniform open-channel flow. The flow is turbulent and free of secondary currents, the transverse mass spreading is consistent with predictions for equilibrium free-surface shear flows.

$$\frac{D_{t,y}}{U_\star\, h} = 0.13 \qquad \text{with} \qquad 0.10 < \frac{D_{t,y}}{U_\star\, h} < 0.26\ . \tag{5.9b}$$

These estimates have been verified also quantitatively in the shallow flow facility from detailed mass concentration measurements employing the PCA measurement technique (cf. Section 3.2), Rummel (2002) obtained $D_{t,y}/\left(U_\star\, h\right) = 0.16$ for similar base flow conditions.

The lateral spreading of the plume is indicated by the downstream increase of the *plume width* w_p, approximated on both sides as a distance from the centerline of twice the standard deviation of a Gaussian tracer distribution $c(y)/c(0) = \exp\left(-1/2\left(y/\sqrt{2D_{t,y}t}\,\right)^2\right)$, thus

$$w_p\left(x\right) = 4\sigma_{c,y}\left(x\right) = 4\sqrt{2D_{t,y}x/\bar{U}_a}\ . \tag{5.10}$$

The growth of a tracer plume, i.e. $w_p \propto x^{1/2}$ has been found quantitatively to be in agreement with (5.10). Also from flow visualizations the Equations (5.9) and (5.10) can be evidenced. For the flow conditions of Figure 5.9 the plume width can be estimated to about $w_p = 0.12$ m after a distance from the source of 5.0 m at the end of the area of observation.

Summary of Part I

Experimental set-up. To experimentally investigate shallow turbulent wake flows a new *shallow flow facility* has been installed at the Institute for Hydromechanics, University of Karlsruhe. Plane near-equilibrium bottom friction–induced shear flows can be realized with a horizontal extent of 5.5 m times 13.5 m and with a flow depth of about 20 mm to 30 mm. Fully automated flow controls and a 3-axial traversing system ensured the necessary accuracy, stability, and repeatability for the experimental programs. Table 5.1 provided an overview about the shallow flow facility and its instrumentation.

Due to the large horizontal and small vertical dimensions of the shallow flow field non-invasive measurements of flow velocities and mass concentrations could only be conducted from above the flow facility through the free water surface. Shallow wake flows are multi–scale flows with length scales ranging from the dissipative scales of random turbulence induced by vertical bottom shear up to the large scales of quasi-periodic motion of the horizontal wake flow. In order to satisfy this duality two different optical flow measurement systems have been employed. The measurement devices for the flow velocities were commonly available scientific systems, whereas the mass concentrations were obtained by specially designed or developed systems.

Point-wise measurement systems. A two-dimensional *Laser Doppler Velocimetry* (LDV) system has been employed to observe the horizontal flow velocity components point-wise with high spatial and temporal resolution as to access also the small-scale 3D turbulent fluctuations. Table 4.1 listed the point-wise flow measurement equipment.

The monochromatic LDV laser light also excited a fluorescent dye tracer in order to allow for additional *Laser Induced Fluorescence* (LIF) measurements. The optical probe head of the LDV system also received the fluorescent radiation, thus, the LIF was operated in an on–axis mode, which has never been reported before. A LIF attenuation model, given by Equation (4.22), extended the measurement range well into the non-linear concentration–irradiance dependency, and has been parameterized in order to capture the wide and dynamic spectrum of concentrations occurring in the wake near– and far–field. The optical arrangement guaranteed for a spatial correlation of the LDV and LIF measurements, the temporal coincidence was ensured by an additional data linking device.

The *combined LDV-LIF* system allowed for the synchronous measurement of velocity and mass, and hence, made available also the horizontal mass transport. Chapter 7 will present turbulence characteristics of shallow wake flows obtained from analyses of LDV-LIF data.

Field-wise measurement systems. The spatial correlation of the low-frequent quasi-periodic wake flow had to be observed by field-wise optical flow

measurements. A standard *Particle Image Velocimetry* (PIV) system has been adapted to obtain horizontal velocity fields close to the free surface (Weitbrecht et al., 2002) with a spatial and temporal resolution that allowed to access the large-scale motion, but not the inertial range of small-scale turbulent fluctuations. The equipment of the field-wise measurement systems was listed in Table 3.2. In Chapters 8 and 9 time-mean evaluations of PIV data will be used to characterize shallow wakes, and to verify an analytical wake model and linear stability analyses. The coherent flow field is extracted from surface velocity fields obtained by PIV measurements in Chapter 10 for the structural analysis of shallow vortex street-like wakes.

In order to observe the field-wise concentrations of a tracer mass a *Planar Concentration Analysis* (PCA) has been realized. A hydro–optical model for the light scattering and absorption has been formulated in Equation (3.22), and has been translated into a conversion algorithm to obtain depth–averaged mass concentrations from irradiance distributions observed with a digital video camera. Though PIV and PCA could not be operated simultaneously, a *phase–resolved averaging* technique has been implemented which allowed to observe the mass transport in the low-frequent periodic flow field associated with the large-scale vortical structures. Chapter 11 will present coherent quasi-periodic and small-scale fluctuating mass fields obtained by PCA in vortex street-like wake flows, and will correlate them to flow quantities derived from the PIV surface velocity fields. In Chapter 9 time–mean distributions of the depth–averaged concentrations will be given.

A set of complementary measurement series provided detailed information of a variety of shallow wake flows of the vortex street (VS), unsteady bubble (UB), and steady bubble (SB) shallow wake stability classes. Hence, a data base has been provided that can be employed for further data analyses, but also to validate numerical analysis tools and simulation models. The flow conditions of the examined shallow wake flows were listed in Table 5.2.

Part II

Time-Mean Flow Characteristics of Shallow Turbulent Wakes

6. Theoretical Background of Turbulence and its Local Description

Due to our human perceptive and cognitive abilities, we build up a four-dimensional image of our surrounding environment. We interpret and rate all our experiences with respect to the spatiotemporal space, the so-called 'physical space'. Despite our better spatiotemporal intuition it is sometimes useful to find a more suitable frame to describe and analyze processes. For instance, it might be easier to find a solution to a set of equations, if we leave the spatiotemporal domain and transform the equations to view and solve them in another domain.

6.1 Introduction to time-series analysis

A turbulent process can be characterized as a *continuous* random change of a quantity in time or in space. However, from experimental observation or from numerical simulation we only have incomplete, namely *discrete*, information of these processes depending on the temporal or spatial resolution of our tools. Owing to this fact, but also for brevity, we summarize aspects of time-series analysis in this section primarily with the help of discrete representations using summations, and avoid continuous representations using integrals. Furthermore, we restrict this short introduction to the description and analysis only of the temporal evolution of a turbulent process at a given point fixed in space. The same techniques analogously apply to the spacial analysis at a specific time.

6.1.1 Correlation

Let $\phi(t)$ be a statistically stationary and ergodic process, as it evolves in time at a fixed place in space. Information of this process is only available at certain times, e.g. since we observe the process with a sampling device. Thus, we only have a discrete representation of the process discretized at equal time intervals $\triangle t$

$$\phi(t_k) = \phi_k, \qquad \text{where} \qquad t_k = t_0 + k\,\triangle t, \qquad k \in \mathbb{N}_0 \tag{6.1}$$

We now use ϕ_k to describe the turbulent behavior of a steady flow by the *central moments* (of the time-series itself instead of its probability density function). The process can be characterized by its *mean* (or *expectation*) $m_\phi = \langle \phi_k \rangle$,[1] and by its 2nd central moment, i.e. the *variance* $\sigma_\phi^2 = \left\langle (\phi_k - \langle \phi_k \rangle)^2 \right\rangle = \langle \phi_k^2 \rangle - m_\phi^2$. Also the *probability density function* $p(\phi)$ can be evaluated to describe fluctuations of the process variable; a natural random process often shows a *normal* or *Gaussian* probability distribution $p(\phi)$. *Skewness* and *flatness* or *kurtosis*, the 3rd and 4th central moments, express the shape of a probability density function (PDF) with respect to the degree of asymmetry about its mean, and to the peakedness of the PDF, respectively. A Gaussian PDF reveals a skewness of 0, i.e. symmetry about its mean, and a flatness of $3\,\sigma_\phi^4$.

Unfortunately, the central moments do not contain any characteristics about the sequence or evolution of the time-history. In order to avoid this loss of information about the temporal interrelation of a turbulent process, *correlations* provide the appropriate statistical means. The *correlation function* of two random process variables ϕ and ψ, which are sampled with a time lag τ at times t and $t+\tau$, is defined as

$$R_{\phi\psi}(\tau) = \langle \phi(t)\ \psi(t+\tau) \rangle . \tag{6.2}$$

The *correlation coefficient* or *normalized covariance* is written as

$$r_{\phi\psi}(\tau) = \frac{\langle (\phi(t) - m_\phi)(\psi(t+\tau) - m_\psi) \rangle}{\sigma_\phi\,\sigma_\psi}. \tag{6.3}$$

Consequently, the *auto-correlation function* and the *auto-correlation coefficient* of a single random process variable are, respectively,

$$R_{\phi\phi}(\tau) = \langle \phi(t)\ \phi(t+\tau) \rangle \tag{6.4}$$

and

$$r_{\phi\phi}(\tau) = \frac{\langle (\phi(t) - m_\phi)(\phi(t+\tau) - m_\phi) \rangle}{\sigma_\phi\,\sigma_\phi} = \frac{R_{\phi\phi}(\tau) - m_\phi^2}{\sigma_\phi^2}. \tag{6.5}$$

For a continuous infinite process the time average $\langle\ \rangle$ is given by

$$\langle\ \rangle = \lim_{T\to\infty} \frac{1}{T} \int_{t=0}^{T} dt. \tag{6.6}$$

Some basic features of $R_{\phi\phi}$ have to be mentioned briefly. For a time lag $\tau = 0$ the auto-correlation function becomes

$$R_{\phi\phi}(0) = m_\phi^2 + \sigma_\phi^2 = \left\langle \phi^2 \right\rangle ,$$

and the autocorrelation coefficient $r_{\phi\phi}(0) = 1$ indicates a perfect correlation, since both representations of the process are identical. For the general case of

[1] The 1st central moment, thus, yields $\left\langle (\phi_k - \langle \phi_k \rangle)^1 \right\rangle = 0$.

an aperiodic process the autocorrelation approaches the mean value for large time lags,

$$\lim_{\tau\to\infty} R_{\phi\phi}(\tau) = m_\phi^2.$$

Finally, since the process is statistically stationary,

$$R_{\phi\phi}(\tau) = R_{\phi\phi}(-\tau).$$

Under real-world conditions, we are almost always concerned with a *finite* sequence (or an ensemble of finite sequences) of the discretized representation ϕ_k of the continuous infinite random process $\phi(t)$. From Equation (6.1) the finite, equal-interval discretized function is given by

$$\phi(t_k) = \phi_k, \qquad \text{where} \qquad t_k = t_0 + k\,\Delta t, \qquad k = 0, 1, 2, \ldots, N.$$

By applying a finite discrete averaging procedure the auto-correlation function $R_{\phi\phi}$ defined by (6.4) yields

$$\begin{aligned} R_{\phi\phi}(\tau = s\,\Delta t) &= \frac{1}{N-s}\sum_{i=1}^{N-s}\left(\phi(t_i)\;\phi(t_i + s\,\Delta t)\right) \\ &= \frac{1}{N-s}\sum_{i=1}^{N-s}\left(\phi_i\,\phi_{i+s}\right), \end{aligned} \tag{6.7}$$

where the length of the discrete time lag $\tau = s\,\Delta t$ should not exceed a reasonably small[2] percentage of the total length, i.e. $s/N \ll 1$.

6.1.2 Fourier analysis

A periodic function can be split into an infinite series of its harmonic components (a *Fourier series*)

$$\phi(t) = a_0 + \sum_{k=1}^{\infty}\left(a_k\,\cos\frac{2\pi kt}{T} + b_k\,\sin\frac{2\pi kt}{T}\right) \tag{6.8}$$

where a_0 and the a_k and b_k are constant Fourier coefficients given by

$$\begin{aligned} a_0 &= \frac{1}{T}\int_{-T/2}^{T/2}\phi(t)\,dt \\ a_k &= \frac{2}{T}\int_{-T/2}^{T/2}\phi(t)\cos\frac{2\pi kt}{T}dt \qquad k\in\mathbb{N} \\ b_k &= \frac{2}{T}\int_{-T/2}^{T/2}\phi(t)\sin\frac{2\pi kt}{T}dt \qquad k\in\mathbb{N}. \end{aligned} \tag{6.9}$$

[2] Emery & Thomson (1998, p. 376) recommend not to push the time lag beyond 10-20% of the length of a data series.

T denotes the main time period of the fluctuating function, $\omega_k = 2\pi k/T$ defines the angular frequency of the kth harmonic, the spacing between adjacent discrete harmonics is $\triangle\omega = 2\pi/T$. As $T \to \infty$ approaching the aperiodic case, the discrete Fourier series becomes the continuous Fourier integral and the Fourier coefficients become continuous functions of the frequency ω, called the *Fourier transform.*

For this classical approach of Fourier analysis to turn a discrete Fourier series representation into a Fourier integral to be true, a necessary condition can be expressed in the form

$$\int_{-\infty}^{\infty} |\phi(t)| < \infty, \tag{6.10}$$

i.e. the random function ϕ has to be absolute-integrable over the time domain. This condition holds only for ϕ, which decays to zero for $t \to \pm\infty$. Contrarily, aperiodic functions, which are not damped in time, can not be treated with the classical Fourier theory.

It has become customary to use the complex notation of the Fourier transform pair. $\Phi(\omega)$ is the (complex) Fourier transform of $\phi(t)$,

$$\Phi(\omega) = \frac{1}{2\pi}\int_{-\infty}^{\infty} \phi(t)\, e^{-i\omega t} dt \tag{6.11a}$$

$$\phi(t) = \int_{-\infty}^{\infty} \Phi(\omega)\, e^{i\omega t} d\omega. \tag{6.11b}$$

6.1.3 Spectral Density

If $\phi(t)$ is absolute-integrable over the entire domain, then also its transform pair defined by (6.11a) exists. The total energy E of the function is finite, and it is given by

$$E = \int_{-\infty}^{\infty} |\phi(t)|^2\, dt < \infty.$$

The *energy spectral density* (ESD) of $\phi(t)$ in the frequency domain is then defined as the square of the modulus of its Fourier transform $\Phi(\omega)$ for all frequencies

$$S_{\phi\phi}(\omega) = |\Phi(\omega)|^2 = \Phi(\omega)\, \Phi^*(\omega), \tag{6.12}$$

where the superscript asterisk denotes the complex conjugate.[3]

[3] We can employ Parseval's theorem to show that $dE/d\omega = S_{\phi\phi}(\omega)$ denotes the energy per unit angular frequency centered around ω. *Parseval's theorem* states, that the total energy E of $\phi(t)$ in the time domain is equal to the total energy $\int S_{\phi\phi}\, d\omega$ in the frequency domain,

Since in the general case of an undamped aperiodic random function, neither $\phi(t)$ nor its discrete representation $\phi(t_k)$ are absolute-integrable, and therefore its total energy is not bounded, it is not possible to directly compute its spectral density (ESD). However, the auto-correlation function $R_{\phi\phi}(\tau)$, which can be understood as the power (i.e. energy per time) of the process function, still is absolute-integrable[4], thus its Fourier transform exists. We can then define the *spectral density* of the process ϕ by

$$S_{\phi\phi}(\omega) = \frac{1}{2\pi}\int_{-\infty}^{\infty} R_{\phi\phi}(\tau)\; e^{-i\omega\tau} d\tau, \tag{6.13}$$

and its inverse transform by

$$R_{\phi\phi}(\tau) = \int_{-\infty}^{\infty} S_{\phi\phi}(\omega)\; e^{i\omega\tau} d\omega. \tag{6.14}$$

Since the auto-correlation function of a process signal can be understood as its signal power (i.e. energy per time, cf. Section 6.1.1), from the above definition (6.13) $S_{\phi\phi}(\omega)$ is called *power spectral density* (PSD). The distinction between energy and power spectral density is quite subtle, and in the practically interesting case of a *finite* discrete representation (or an ensemble thereof) of a random process, it can be shown for a periodic process that both expressions are equal, and how to estimate the spectral density of an aperiodic random process (cf. e.g. Newland (1993, pp. 120), Marple Jr. (1987, chpt. 4)).

From the previous subsection we know, that $R_{\phi\phi}(\tau = 0) = \left\langle \phi(t)^2 \right\rangle$, which for a zero mean process is the average energy of the process fluctuations. For $\tau = 0$, (6.14) then yields

$$\int_{-\infty}^{\infty} S_{\phi\phi}(\omega)\; d\omega = \left\langle \phi(t)^2 \right\rangle \tag{6.15}$$

6.1.4 Discrete Spectral Analysis

In most experimental measurements or numerical simulations of random processes the sample data sets are finite and discrete representations ϕ_k of the continuous process, which can be described using (6.1) for data series sampled with equal intervals $\triangle t$. Time series analysis aims to estimate the statistical characteristics of the true process from its finite discrete representation, and to specify the necessary length and density of ϕ_k in order to satisfy certain confidence criteria of the estimates.

$$\int_{-\infty}^{\infty} |\phi(t)|^2\, dt = \int_{-\infty}^{\infty} |\Phi(\omega)|^2\, d\omega\ .$$

[4] Provided that ϕ is a zero mean process $\langle\phi\rangle = 0$, which ϕ can easily be adjusted for.

The obvious and classical method to estimate spectra from measured data is to first make an estimate of its correlation function and then to apply a Discrete Fourier Transform (DFT) to this function to obtain the required spectrum. For this classical approach only a single Fourier transform has to be performed. The development of the *Fast Fourier Transform* (FFT) in the 1960s provided fast and efficient algorithms to perform a discrete Fourier transform of a time series, an introduction to FFT is found for instance in Brigham (1995). It is now quicker and more accurate to calculate spectral estimates *directly* from the original times series ϕ_k, instead of estimating spectra by first determining $R_{\phi\phi}$ and then Fourier transforming these as to *indirectly* get the spectra.

We finish this section by giving a short overview on calculating a reliable estimate for the spectral density of a random process $\phi(t)$ by making use of a set of M finite representations ϕ_k.[5] A reader, whose interest in time series analysis may reach beyond the limits of this recipe-like summary, is referred to a broad variety of textbooks, for instance Marple Jr. (1987); Newland (1993); Emery & Thomson (1998). As needed in the framework of this study, we will give more detail in Chapter 7, where we apply the methods of time series analysis to LDV-LIF measurements in shallow turbulent wake flow.

The *procedure of calculating an estimate for the spectral density of a random process* $\phi(t)$ is as follows:

1. *Prepare evaluation of the spectra.*
   a) Estimate the frequency range of interest $f \in [f_{low}\ f_{high}]$.
   b) Choose an appropriate re-sampling interval $\triangle t$ so that the *Nyquist frequency* $f_N = 1/2\ \Delta t$ exceeds the maximum frequency present and is at least e.g. twice the highest frequency of interest.
   c) Calculate the required length T of each re-sampled data series (excluding any padded zeros) using the lowest frequency of interest to be (say)
   $$T = (0.25 \div 0.5)\ 1/f_{low}.$$
   d) Verify the necessary resolution of the PDF.
      - Decide the required accuracy $\sigma_\phi / \langle\phi\rangle$.
      - Estimate the required frequency resolution, i.e. specify the maximum effective bandwidth B_e of the PSD.
      - Calculate the required length T_{res} of each re-sampled data series (excluding any padded zeros) from the estimate
      $$\frac{\sigma_\phi}{\langle\phi\rangle} \simeq \frac{1}{\sqrt{B_e T_{res}}},$$
      and verify $T_{res} < T$.

[5] Though we demonstrate the time series analysis for an auto-spectral density $S_{\phi\phi}$ only, it can easily be expanded also to a cross-spectral density $S_{\phi\psi}$.

e) Determine the number of data points $N = T/\ \triangle t$ which must be contained in each re-sampled time series.

f) Find the number of added zeros L needed to increase the length of each re-sampled series of data points to the next integer power of 2, i.e. $N + L = 2^n$, $n \in \mathbb{N}$.

g) Determine the odd number $(2n + 1)$ of adjacent spectral estimates, which have to be band-averaged to give the required bandwidth of the PSD, using the equation

$$(2n+1)\,\frac{N}{N+L} = B_e T$$

2. *Extract ensembles of blocked time series.* Remove the mean and trend from the full time series of length T'. Conduct an equal interval re-sampling of the de-trended time series using the re-sampling interval $\triangle t$ to obtain N' data points.

   a) Calculate the number $M = (1+p_{ol})N'/N$ (round down) of data blocks using a factor $p_{ol} \lesssim 0.25$ for overlapping blocks. Divide the full time series into M blocks to obtain data series ϕ_r, $r = 0, 1, 2, \ldots (N-1)$ each with N data points and length T.

   b) Taper each time series with a window function $w(t)$ to reduce effects due to end discontinuities.

   c) Pad each data series with L zeros in order to apply the FFT to 2^n data points.

3. *Calculate the DFT of each series* ϕ_r given by

$$\Phi_k = \frac{1}{N+L}\sum_{r=0}^{N+L-1} \phi_r e^{-i2\pi kr/N+L}\ , \qquad (6.16)$$
$$k = 0, 1, 2, \ldots N + L - 1\ ,$$

   and re-scale the spectra, since due to the applied window part of the spectral energy is lost. This has to be adjusted by multiplying Φ_k with a constant factor a_{wndw} depending on the window function $w(t)$.

4. *Calculate the spectral density* for the full time series.

   a) Calculate the required series of spectral coefficients S_k by forming the products

$$S_{\phi\phi_k} = \Phi_k\, \Phi_k^*, \qquad k = 0, 1, 2, \ldots, (N + L - 1).$$

   b) Calculate estimates of the continuous spectrum from the formula

$$\tilde{S}\,(\omega_k) \simeq \frac{T_L}{2\pi} S_k,$$

   where $\omega_k = \frac{2\pi k}{T_L}$ and $T_L = (N + T)\ \triangle t$.

   c) For block-segmented data, block-average the spectral density estimates S_k from the M blocks frequency-band per frequency-band to obtain a smoothed spectral estimate.

d) Modify these estimates to correct for the added zeros by multiplying by correction factor $(N+L)/N$ to give

$$\tilde{S}'(\omega_k) \simeq \frac{N+L}{N}\frac{T_L}{2\pi}S_k,$$

where $|k| \leq (N+L)/2$ and $k \in \mathbb{Z}$. Conduct final smoothing of $\tilde{S}'(\omega_k)$ by calculating the band-average of adjacent spectral estimates according to

$$\hat{S}(\omega_k) = \frac{1}{2n+1}\sum_{m=-n}^{n}\tilde{S}'(\omega_{k+m}). \tag{6.17}$$

6.2 Spectral description of turbulence

In the common understanding, a turbulent flow is a flow which is disordered in time and space. As for most fundamental phenomena, also for turbulence we lack a more accurate mathematical definition. Instead, the following properties will serve as a more precise characterization of turbulence (following Lesieur, 1997, p. 2):

- *unpredictability of flow realization* in the sense of amplification of small perturbations;
- *increased mixing ability* for transported quantities like heat, pollutants, or tracers;
- *interaction of a wide range of eddy scales* (spatial complexity), which implies high Reynolds numbers and excludes chaos of low-dimensional dynamical systems;
- *fluid continuum flow*, governed by the equations of fluid mechanics, which excludes for instance Brownian motion);

Two additional properties are often considered in defining turbulence (see for instance Tennekes & Lumley, 1977): the existence of *strong vorticity fluctuations* and *strong energy dissipation.*

6.2.1 The energy cascade

As already mentioned in Section 2.2 the production of turbulent kinetic energy is associated with large-scale turbulent motions in a low wave number range, the so-called *energy-containing range.* Usually, the rate–of–turbulence production is defined as

$$\mathcal{P} \equiv -\left\langle u_i' \, u_j' \right\rangle S_{ij}. \tag{6.18}$$

Forced by a mean shear strain rate

$$S_{ij} \equiv \frac{1}{2}\left(\frac{\partial\langle u_i\rangle}{\partial x_j} + \frac{\partial\langle u_j\rangle}{\partial x_i}\right), \tag{6.19}$$

TKE is extracted from the mean flow, and is incorporated into large-scale 2D vortices.[6] If ℓ_0 is the characteristic length scale of the mean flow, it is convenient to introduce a length scale $\ell_{EI} \approx 1/6\ \ell_0$ to demarcate the energy-containing range of large-scale anisotropic turbulence with scales $\ell > \ell_{EI}$. Due to the mean rate-of-strain S_{ij} vorticity is generated continuously perpendicular to the mean shear plane, so the anisotropy of the large-scale turbulence is maintained. The TKE contained in the large scales is transferred to smaller scales of turbulence at a transfer rate $\mathcal{T}(\ell)$, as the large scale eddies (and so their vorticity) are subjected to a strain field, which is time-dependent and more and more isotropic at smaller scales. Provided a sufficiently high Reynolds number, according to *Kolmogorov's hypothesis of local isotropy*, the small-scale turbulent motions are statistically isotropic, and—the first similarity hypothesis—its statistics have an universal form, which uniquely depends on the energy transfer rate $\mathcal{T}(\ell)$ and on the viscosity ν. The *universal equilibrium range* of turbulence scales $\ell < \ell_{EI}$ again can be split into an *inertial subrange*, where the flow behaves essentially inviscid, followed by the *dissipation range* for $\ell < \ell_{DI} \approx 60\ \ell_\eta$. Since the turbulence statistics depend solely on $\mathcal{T}(\ell)$ in the inertial subrange—the second similarity hypothesis—, TKE produced in the energy-containing range at large turbulence scales is just transferred along the scales of the inertial subrange ($\ell_{EI} > \ell > \ell_{DI}$) without any change of $\mathcal{T}(\ell)$ into the dissipation range. There, near the Kolmogorov length scale ℓ_η the velocity gradient between adjacent vortices is steep enough to allow the viscous stresses to become important. Here, energy is dissipated at a rate ϵ. The rate of viscous dissipation of turbulent kinetic energy is usually given by

$$\epsilon \equiv 2\nu \left\langle s_{ij}\, s_{ij} \right\rangle \ , \tag{6.20}$$

where the fluctuating rate of shear strain is given by

$$s_{ij} \equiv \frac{1}{2}\left(\frac{\partial u_i'}{\partial x_j} + \frac{\partial u_j'}{\partial x_i}\right) \ . \tag{6.21}$$

As shown by Hinze (1975, chpt. 3) in locally isotropic turbulence the various squared velocity gradient terms may be combined in such a way, that the mean dissipation rate can be approximated by

$$\epsilon = 15\nu \left\langle \left(\partial u'/\partial x\right)^2 \right\rangle \ . \tag{6.22}$$

The dissipation rate is of the same size as the energy production rate and the energy transfer rate,[7] i.e.

[6] See also the decomposition of the coherent flow field into large-scale and small-scale parts for vorticity, Equation (10.8), and for TKE, Equation (10.9).

[7] In the mean turbulent kinetic energy budget, production exactly balances dissipation only in a steady, homogeneous shear flow (in which all averaged quantities except U_i are independent of position and in which S_{ij} is a constant). Note, that though in most shear flows $\mathcal{P}$ and ϵ do not balance, they are of the same order of magnitude in most cases.

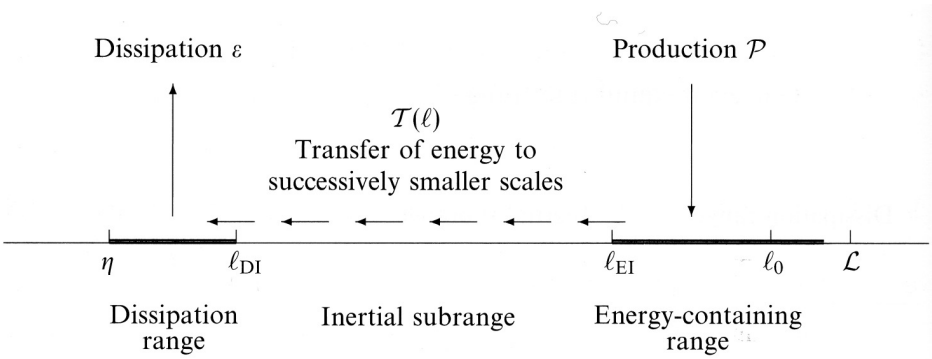

Figure 6.1. A schematic diagram of the energy cascade, its scales and ranges at very high Reynolds numbers (Pope, 2000, p. 188)

$$\mathcal{P} = \mathcal{T}(\ell) = \epsilon \ . \tag{6.23}$$

Figure 6.1 sketches the spectral picture of Kolmogorov's energy cascade in turbulent shear flows.

6.2.2 Kolmogorov spectra of turbulent velocity fields

The spectrum in the universal equilibrium range. Following Kolmogorov's concept of *local isotropy* at smaller scales of turbulence no permanent anisotropy can prevail, since eddies of a given size are continuously stretched mainly by somewhat larger (but still 3D) eddies, which themselves maintain a strain-field constantly shifting in direction and magnitude. Thus, though *locally* at smaller scales $\ell < \ell_{EI}$ the instantaneous strain-field is still anisotropic, the time-average of the the strain-field $\langle s_{ij} \rangle$ becomes isotropic, and so do all the turbulence properties. Since in the equilibrium range the scales are small compared to the energy-containing range, i.e. $\ell \ll \ell_0$, the conditions of the production of TKE do not influence the further re-distribution of energy along the smaller scales. The spectral energy distribution $S(k_w)$[8] may only depend on the transfer and dissipation of TKE. Since near ℓ_η energy is dissipated due to viscosity ν at a rate ϵ, and the transfer rate equals the dissipation rate ϵ (cf. Equation (6.23)), according to Kolmogorov's first similarity hypothesis we can characterize these processes solely by ϵ and ν. Therefore, the energy spectral distribution is $S = S\left(k_w, \epsilon, \nu\right)$. In non-dimensional form, *Kolmogorov's scaling law* reads

$$\frac{S\left(k_w\right)}{\nu^{5/4}\,\epsilon^{1/4}} = \frac{S\left(k_w\right)}{u_\eta^2\,\ell_\eta} = f_\eta\left(k_w\,\ell_\eta\right), \tag{6.24}$$

[8] As usual S is evaluated in the wave number domain, which is related to the spatial domain by $k_w = 2\pi/\ell$.

where $\ell_\eta = \left(\nu^3/\epsilon\right)^{1/4}$ and $u_\eta = (\epsilon\nu)^{1/4}$ are the *Kolmogorov micro scales of turbulence* for length and velocity, respectively. $f_\eta\left(k_w\,\ell_\eta\right)$ is a universal non-dimensional function called the Kolmogorov spectral function. If we choose ϵ and k_w to normalize $S(k_w)$, Equation (6.24) reads in alternative form

$$\frac{S\left(k_w\right)}{\epsilon^{2/3}\,k_w^{-5/3}} = \tilde{f}_\eta\left(k_w\,\ell_\eta\right). \tag{6.25}$$

The spectrum in the inertial subrange. In the low wave number part of the universal equilibrium range viscous dissipation is negligible, thus—Kolmogorov's second similarity hypothesis—in the *inertial subrange* the viscosity ν does not influence the re-distribution of TKE. In Equation (6.25) ν enters only through the micro length scale ℓ_η via the spectrum function $\tilde{f}_\eta$. For low wave numbers $(k_w\,\ell_\eta) \ll 1$, the spectrum function becomes independent of its argument $(k_w\,\ell_\eta)$, and thus $\tilde{f}_\eta$ becomes a constant. Within the inertial subrange we thus have $\tilde{f}_\eta\left((k_w\,\ell_\eta)\right) = C$. Equation (6.25) then results in the famous Kolmogorov $-5/3$ power law for the energy spectral density distribution,

$$S\left(k_w\right) = C\,\epsilon^{2/3}\,k_w^{-5/3}. \tag{6.26}$$

The universal Kolmogorov constant C is experimentally evaluated to be $C = 1.5$. For isotropic conditions and with $S(k_w)$ being a power-law spectrum (cf. Pope, 2000, pp. 228), the one-dimensional spectra are given by

$$S_{11}\left(k_{w1}\right) = C_1\,\epsilon^{2/3}\,k_{w1}^{-5/3} \tag{6.27a}$$

$$S_{22}\left(k_{w1}\right) = C_2\,\epsilon^{2/3}\,k_{w1}^{-5/3} \tag{6.27b}$$

where $C_1 \approx 0.49$ and $C_2 \approx 0.65$.

The spectrum in the energy-containing range. Also for very low wave numbers $k_w \to 0$ in the *energy-containing range* the viscosity ν is of no relevance, as we already stated for the inertial subrange. The distribution of energy along the turbulence scales now depends on the production of TKE extracted at lowest frequencies from the mean flow, which we characterize by its mean shear strain rate S_{ij}. At smaller turbulence length scales $\ell \approx \ell_{EI}$ the energy is transferred at a rate $\mathcal{T} = \epsilon$ toward the universal equilibrium layer. Therefore, the large-scale or inertial scaling in the energy-containing range will be based on S_{ij} and ϵ, the large-scale spectrum is only dependent on $S = S\left(k_w, S_{ij}, \epsilon\right)$. If we employ the characteristic large scales ℓ and u of the mean flow, S_{ij} and ϵ scale as $S_{ij} = u/\ell$ and $\epsilon = u^3/\ell$. The large-scale distribution of the energy spectral density then becomes

$$\frac{S\left(k_w\right)}{\epsilon^{3/2}\,S_{ij}^{-5/2}} = \frac{S\left(k_w\right)}{u^2\,\ell} = f_\ell\left(k_w\,\ell\right) \tag{6.28}$$

Compared to the universal spectrum function f_η in the equilibrium range, the large-scale spectrum function f_ℓ depends on the characteristic geometric

property ℓ of the mean flow, i.e. it is not universal for all turbulent shear flows, but varies for different classes of shear flows.

6.2.3 Spectra of passive scalar tracers

The cascade in the passive scalar tracer field. If the Reynolds number is large enough for an equilibrium range to exist in the kinetic energy spectrum, then there is also an equilibrium range, exhibiting local isotropy, in the spectrum of a passive scalar variance, because it is the turbulent motion, that is mixing the scalar field (cf. Tennekes & Lumley, 1977, p. 281). The dilute concentration c of a tracer mass, as used throughout this work, is a scalar passive to the flow; to give another prominent example for a scalar fluid property also a small temperature difference θ can be regarded as a passive scalar fields in the flow.[9] An estimate for the transfer of scalar variance along the wave number k_w, i.e. an estimate for its spectral flux, is given by

$$\mathcal{T}_\gamma\left(k_w\right) = C\, k_w^{5/2}\, S_\gamma\, S^{1/2}. \tag{6.29}$$

Spectra in the equilibrium range. Within the equilibrium range, $S_\gamma\left(k_w\right)$ should scale with the same parameters as $S\left(k_w\right)$, i.e. ϵ and ν, together with the corresponding parameters for the scalar field. The *dissipation rate of scalar variance* (i.e. the scalar flux) will be defined as

$$\epsilon_\gamma = D_m \left\langle \frac{\partial c}{\partial x_i}\, \frac{\partial c}{\partial x_i} \right\rangle, \tag{6.30}$$

where D_m is the *molecular diffusivity* (or thermal conductivity, respectively). Therefore, the *spectral distribution of scalar variance* will depend on $S_\gamma = f\left(k_w, \epsilon, \nu, \epsilon_\gamma, D_m\right)$. Non-dimensionalization for instance results in

$$S_\gamma\left(k_w\right) = \epsilon_\gamma\, \epsilon^{-1/3}\, k_w^{-5/3}\, f\left(k_w\, \ell_\eta, Sc\right),$$

where $Sc = \frac{\nu}{D_m}$ is the *Schmidt number* (or the Prandtl number, respectively). Thus, the non-dimensional spectrum function f varies for different fluids.

The inertial-convective subrange. At high Reynolds numbers an inertial subrange exists, i.e. $\ell_0 \gg \ell \gg \ell_\eta$. If D_m is small enough, so that there is a part of the (quasi-inviscid) inertial subrange, where also molecular diffusion is unimportant, we obtain an *inertial-convective subrange*, where scalar fluctuations are simply convected. Thus, the spectral distributions of energy and scalar fluctuation should be independent of ν, resp. D_m, i.e. $S_\gamma = S_\gamma\left(k_w, \epsilon_\gamma, \epsilon\right)$ resulting in

$$S_\gamma\left(k_w\right) = \beta\, \epsilon_\gamma\, \epsilon^{-1/3}\, k_w^{-5/3}\ , \tag{6.31}$$

[9] On the molecular scale, the diffusivity D_m of the solution or the conductivity D_ϑ of the fluid characterize the scalar field.

as first postulated by Corrsin (1951) and Oboukhov (1949). From experimental evidence, the proportionality constant can be estimated to be $\beta \approx 0.5$.

In the spectrum of velocity fluctuations the viscous dissipation dominates the energy cascade for length scales ℓ of order of the Kolmogorov micro length, $\mathcal{O}(\ell) = \ell_\eta$. If the molecular diffusivity $D_m < \nu$ is small compared to the kinematic viscosity, i.e. $Sc = Pr = \frac{\nu}{D_m} > 1$, then the scalar field is affected only by D_m at scales smaller than ℓ_η. In the *dissipative-convective subrange* for $\ell_\eta > \ell > \ell_{\eta_\gamma}$ [10], the velocity fluctuations have already been damped due to viscous dissipation, whereas the scalar fluctuations are still unaffected by molecular diffusion. At even smaller scales $\ell < \ell_{\eta_\gamma}$ in the *dissipative-diffusive subrange*, also the scalar fluctuations are damped.

On the contrary, for low Schmidt numbers $Sc < 1$, i.e. $\nu < D_m$ and $\ell_\eta < \ell_{\eta_\gamma}$, the scalar fluctuations can be dominated by the molecular diffusion, whereas the kinetic energy is not yet influenced by molecular effects. This is called the *inertial-diffusive subrange* of the scalar variance spectrum.

Inertial-diffusive subrange. In fluids with low Schmidt/Prandtl number $Sc < 1$ with $D_m > \nu$ and $\ell_{\eta_\gamma} > \ell_\eta$ we can observe a range of wave numbers k_w indicated by $(k_w\, \ell_\eta) \ll 1$, in which on the one side the transfer $\mathcal{T}(k_w)$ of kinetic energy is constant and equal to $\mathcal{P}$ and ϵ. On the other side, since $\left(k_w\, \ell_{\eta_\gamma}\right) \geq 1$, the spectral flux of scalar variance $\mathcal{T}_\gamma(k_w)$ is not constant as in the inertial-convective subrange, but decreases due to local dissipation by molecular diffusion. Therefore, we call the range of turbulence length scales within $\ell_{\eta_\gamma} > \ell > \ell_\eta$ the *inertial-diffusive subrange.* As recalled by Lesieur (1997, pp. 202), the scalar fluctuation spectrum, predicted by Batchelor (1959), obeys

$$S_\gamma(k_w) \propto \epsilon_\gamma\, D_m^{-3}\, k_w^{-4}\, S(k_w)\,, \tag{6.32}$$

which yields using the assumption of a $k_w^{-5/3}$ energy spectrum

$$S_\gamma(k_w) \propto \epsilon_\gamma\, D_m^{-3}\, \epsilon^{2/3}\, k_w^{-17/3}. \tag{6.33}$$

The scalar micro scale ℓ_{η_γ} is defined by Equation (6.67) for low Sc. It demarcates the lower limit of the inertial-convective subrange $\ell > \ell_{\eta_\gamma}$, and thus the beginning of the inertial-diffusive subrange with $\ell < \ell_{\eta_\gamma}$.

The dissipative-convective subrange. Considering fluids with high Schmidt numbers $Sc \geq 1$, there exists a range of wave numbers $k_\eta < k_w < k_{\eta_\gamma}$, in which the strain-rate field of order $\mathcal{O}\left(\left(\frac{\epsilon}{\nu}\right)^{1/2}\right)$ further reduces the scales of scalar fluctuations, but in which molecular diffusion is not yet effective, i.e. the spectral scalar flux is on constant rate ϵ_γ. We thus expect the spectral distribution of scalar fluctuation S_γ in this subrange to depend on

[10] ℓ_{η_γ} is the *Batchelor micro scale*, a diffusive micro scale defined by Equation (6.66).

$S_\gamma = f\left(k_w, \epsilon_\gamma, \left(\frac{\epsilon}{\nu}\right)^{1/2}\right)$ as proposed by BATCHELOR (1959). Thus, in the *dissipative-convective subrange* the spectral distribution of scalar variance follows a k_w^{-1} law

$$S_\gamma = C_B\, \epsilon_\gamma \left(\frac{\nu}{\epsilon}\right)^{1/2} k_w^{-1}, \tag{6.34}$$

where C_B is called *Batchelor's constant.*

The dissipative-diffusive subrange. In such high Schmidt number (or Prandtl number) fluids molecular diffusivity (or conductivity, respectively) becomes important for eddy sizes smaller than the Batchelor's micro scale ℓ_{η_γ} given by Equation (6.66). Then also $\frac{\ell_{\eta_\gamma}}{\ell_\eta} = Sc^{-1/2}$ is valid. It has been shown by BATCHELOR (1959), that the scalar spectrum decreases exponentially for $k_w > k_{\eta_\gamma}$. As argued by TENNEKES & LUMLEY (1977, p. 285) for wave numbers k_w near k_{η_γ}, where $\mathcal{T}_\gamma(k_w)$ is not too different from ϵ_γ, the scalar variance spectrum can be approximated by

$$S_\gamma(k_w) = C_B\, \epsilon_\gamma \left(\frac{\nu}{\epsilon}\right)^{1/2} k_w^{-1}\, e^{-C_B\,(k_w\,\ell_{\eta_\gamma})^2}. \tag{6.35}$$

6.2.4 Spectra of 2D turbulent flows

With respect to the turbulence characteristics given on page 156, a 2D turbulent flow can be defined as a turbulent flow depending only on two spatial dimensions. The flow field $\boldsymbol{u}(x, y, t)$, and so its turbulence properties, does not depend on a third spatial dimension z, which does not include, that there is no velocity component w in the third direction. The Navier-Stokes equations describing such a flow field show that this velocity component obeys a 2D passive scalar equation,

$$\frac{D_H\, w}{dt} = \frac{\partial w}{\partial t} + u\frac{\partial w}{\partial x} + v\frac{\partial w}{\partial y} = \nu \nabla_H^2 w\ , \tag{6.36}$$

where $\frac{D_H}{dt}$ and ∇_H^2 are the horizontal substantial derivative and the horizontal Laplacian, respectively.

In particular, the independence of the third dimension z characterizes flows which (by definition) are unstable, when they become turbulent (cf. Section 9.2), and develop 3D instabilities. Following the well-known concept of the *return to three-dimensionality* (cf. e.g. HERRING, 1974), a purely 2D flow in an infinite domain will become 3D if there is no external force acting to maintain the two-dimensionality. It therefore seems to be unrealistic to expect 2D flows to belong to the physical world; KRAICHNAN & MONTGOMERY (1980) stated in their classical review-paper:

> "Two-dimensional turbulence has the special distinction that it is nowhere realised in nature or in the laboratory but only in computer simulations."
>
> Kraichnan & Montgomery (1980, p. 549)

Nevertheless, since then 2D turbulent flows have been examined both in nature (e.g. planetary atmospheric and oceanic flows) and in the laboratory (e.g. thin-film flows, liquid-metal flows, flows under strong rotation, M.H.D. flows).[11] For instance, a simple possibility is to consider a flow with a limited extent in the vertical dimension, for instance constrained by two parallel plates of a distance D. At scales much larger than D, the flow is expected to be horizontal and 2D. Along the plates boundary layers will develop, interact, and generate 3D turbulence at scales smaller than D, which can effectively dissipate the kinetic energy of the large-scale 2D fluid motion. It is therefore necessary to restrict the growth of these boundary layers. This may be achieved for example with the help of a rapid[12] rotation $\boldsymbol{\Omega}$ perpendicular to the boundaries.

2D turbulent flows include the tendency to build up large coherent vortical structures, as will be shown below. Eventually and especially for externally forced turbulence, such eddy structures may organize and develop into a steady coherent flow, loosing its unpredictability, which is a general characteristic for both for 3D and 2D turbulence.

It can be shown that also the vertical vorticity $\omega_z = -\nabla_H^2 \psi = -\left(\frac{\partial u}{\partial y} - \frac{\partial v}{\partial x}\right)$, which is the vorticity of the horizontal velocity $\boldsymbol{u}_H$, obeys an equation similar to (6.36) for $w\,(x, y, t)$. However, the vertical vorticity is not a passive quantity to the horizontal flow field, since small deviations imposed on ω_z would influence the horizontal velocity $\boldsymbol{u}_H$. Nevertheless, a passive scalar advected in a flow of a Schmidt number of unity, in which the molecular diffusivity of the tracer is equal to the kinematic viscosity of the flow, would behave exactly like ω_z in 2D turbulence.[13]

As a consequence of the conservation of vertical vorticity, unlike in 3D turbulence a cascade of kinetic energy toward the small scales due to vortex stretching mechanisms does not exist. Instead, the early theoretical studies in 2D turbulence (e.g. Batchelor, 1967) showed that (for low but non-zero viscosity) kinetic energy is conserved, as is vorticity. The enstrophy, i.e. the variance of vorticity, decreases due to the absence of vortex stretching in con-

[11] Of course the ideal case of pure 2D turbulence will never occur in reality. But in the above mentioned systems the nearly 2D flows can be described and predicted surprisingly well using a 2D turbulence approach.

[12] i.e. with low Rossby number

[13] Unfortunately, in real-world flows we often encounter transport processes with $Sc \gg 1$, and shallow flows can be regarded as 2D only in the large scales. Thus, the diffusive mechanisms can not be covered by the 2D equations of motion without further subgrid-scale modelling.

trast to 3D turbulence, where enstrophy increases as smaller turbulence scales become involved due to the cascading process.

In the following subsections the central concepts of purely 2D isotropic turbulence are briefly reviewed. The essential statistical characteristics of such turbulence are described for instance by Kraichnan & Montgomery (1980) in more detail. A more complete discussion also of the contemporary developments is presented by Lesieur (1997) or Sommeria (2002).

Fjortoft's theorem. The redistribution of kinetic energy and enstrophy in a double cascade in 2D turbulence was given a first fundamental impulse by Fjortoft (1953), as mentioned by Kraichnan & Montgomery (1980) or Lesieur (1997). *Fjortoft's theorem*, which has no relation with the inviscid instability criterion in linear-instability theory, requests the conservation of kinetic energy and enstrophy to hold. Given an initial distribution of kinetic energy in Fourier space peaked around a wave number k_{wi}, with time the kinetic energy distribution will spread out and cover a wider wave number range, and will consequently decrease in its peak value at k_{wi}. The theorem then says that in order to conserve both energy and enstrophy, more kinetic energy will be transferred toward lower wave numbers than toward higher wave numbers, and in turn more enstrophy will go down to smaller scales than to larger scales. We will elucidate the spectral transport both of enstrophy and kinetic energy in the next paragraphs.

The enstrophy cascade of 2D turbulence. In the wave number domain we assume a forced 2D turbulence maintained by a stationary kinetic energy forcing $F(k_w)$ centered at k_{wi}. Kinetic energy and enstrophy are injected at the rates $\epsilon = \int_0^\infty F(k_w)\,dk_w$ and $\beta = \int_0^\infty k_w^2 F(k_w)\,dk_w \approx k_{wi}^2\epsilon$, respectively. The conservation equation for the enstrophy spectrum is

$$\left(\frac{\partial}{\partial t} + 2\nu k_w^2\right) k_w^2 S(k_w,t) = k_w^2 \mathcal{T}(k_w,t) + k_w^2 F(k_w)\,, \tag{6.37}$$

where $\mathcal{T}(k_w,t)$ is the transfer rate of TKE. The enstrophy flux across k_w may thus be given by $Z(k_w) \equiv \int_{k_w}^\infty k_w^2 \mathcal{T}(k_w)\,dk_w$. Assuming a steady energy spectrum, from Equation (6.37) we obtain $\beta = 2\nu \int_0^\infty k_w^4 S(k_w)\,dk_w$. For high Reynolds numbers there exists a wave number range $k_{wi} < k_w \ll k_{wd}$ above an enstrophy-dissipation wave number k_{wd}, where the enstrophy dynamics are not affected by viscosity. With a reasoning analogously to 3D turbulence we find that $Z(k_w) \equiv \beta$.

It was first proposed by Kraichnan (1967) that the kinetic energy spectrum in this range of wave numbers solely depends on the enstrophy production rate β and the wave number k_w. From dimensional grounds then the following proportionality arises

$$S(k_w) \propto \beta^{2/3} k_w^{-3}. \tag{6.38}$$

The same k_w^{-3} *enstrophy cascade* was proposed by Batchelor (1969) for freely-decaying 2D turbulence.

For high wave numbers $k_w > k_{wd}$ molecular viscosity dissipates the enstrophy, if local vorticity gradients are sufficiently steep. The enstrophy dissipation wave number k_{wd} only depends on β and ν. Analogously to the energy-dissipative wave number demarcating the dissipative subrange of Kolmogorov's kinetic energy spectrum of isotropic 3D turbulence, we obtain

$$k_{wd} = \left(\frac{\beta}{\nu^3}\right)^{1/6}.$$

To sketch a simplified picture of the enstrophy cascade we could imagine a fluid parcel in a mean strained velocity field. The fluid parcel will be deformed in the strain field and increase its characteristic longitudinal scale while shortening its transverse scale. As for 2D turbulence vorticity is conserved within each parcel, this results in a transverse steepening of the vorticity gradient across neighboring fluid parcels; in the spectral domain this means a flux of vorticity toward higher wave numbers.

The inverse energy cascade of forced turbulence. Given a forcing at a specific wave number k_{wi}, which continuously injects kinetic energy at a rate ϵ. Without any spectral truncation, neither at low k_w due to boundaries nor at high k_w due to numerical cutoff, an energy cascade can freely develop. As for the Kolmogorov spectrum in 3D isotropic turbulence, also in 2D turbulence dimensional analysis leads to the same inertial subrange with a spectral energy distribution (cf. (6.26))

$$S\left(k_w\right) = C\,\epsilon^{2/3} k_w^{-5/3}.$$

Since kinetic energy is conserved in 2D turbulence, a direct cascade toward a dissipative range of high wave numbers cannot occur. Kraichnan (1967) therefore suggested an inverse energy cascade toward low wave numbers and large scales. Also Fjortoft's theorem had shown that energy could be transferred to low k_w more easily. Both from numerical and laboratory experiments the theoretical concept of the *inverse energy cascade in forced 2D turbulence* has been confirmed thoroughly.

In the ideal case of an unbounded fluid domain there is no need for energy dissipation at low k_w, since energy can be transferred to larger and larger scales. At the same time, enstrophy is injected at k_{wi} at a rate $\beta = k_{wi}^2\epsilon$, and a k^{-3} enstrophy cascade transfers energy toward high wave numbers. However, as stressed by Kraichnan, the cascade should not be viewed as a carrying belt to simultaneously transport the energy $S\left(k_w\right)$ and its related enstrophy $k_w^2 S\left(k_w\right)$. The two cascades are mutually exclusive, as the rate of enstrophy transfer vanishes in the energy cascade and vice versa. The classical concept

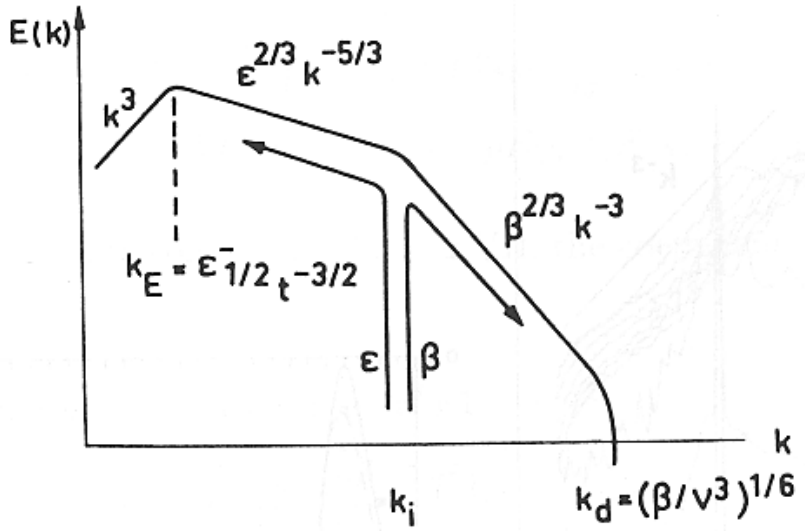

Figure 6.2. Conceptual sketch of the double cascade in forced 2D turbulence with a continuous forcing of production rates for kinetic energy ϵ and enstrophy β at k_{wi} in the inertial subrange (adapted from Lesieur, 1997).

of the double cascading energy spectrum in forced 2D turbulence is illustrated in Figure 6.2.

As predicted by Batchelor (1969) in freely evolving 2D turbulence the inverse energy cascade does not hold, but as indicated by recent numerical simulations starting at k_w^{-3} the cascade continuously becomes steeper due to the development and growth of LCS.

Diffusion of a passive scalar in 2D turbulence. The transport of a passive scalar in a 2D turbulent flow receives the special attention of the group of M. Lesieur, because

> "2D passive scalar diffusion is a significant problem when one is interested in the large-scale diffusion of tracers or pollutants in the atmosphere or the ocean [...] Since the vorticity and the passive scalar both obey [a conservation equation of the form (6.36)], they have close analogies. However, the scalar, whose variance is an inviscid invariant, is not constrained to the double energy-[vorticity] conservation like the velocity field. This will rule out the possibility of strong inverse scalar transport, inverse scalar cascades and negative eddy-diffusivity[14]."
>
> Lesieur (1997, p. 308)

[14] Contrary to 3D turbulence, negative values of the turbulent viscosity ν_t will and have to occur in 2D turbulence for a spectral energy distribution steeper than k_w^{-1}, as obtained from numerical simulations with an appropriate turbulence model. (cf. Lesieur, 1997, p. 303)

Given a scalar $c(\boldsymbol{x}, t)$, its spectrum $S_\gamma(k_w, t)$ with

$$\frac{1}{2}\langle c(\boldsymbol{x}, t)^2\rangle = \int_0^\infty S_\gamma(k_w, t)\, dk_w,$$

the scalar dissipation rate $\epsilon_\gamma = \int_0^\infty k_w^2 S_\gamma(k_w, t)\, dk_w$ and the scalar diffusivity D_m. According to Lesieur & Herring (1985) the scalar dissipation wave number is then

$$k_{wc} = \left(\frac{\epsilon_\gamma}{D_m^3}\right)^{1/6}.$$

The scalar quantity shall be introduced into the 2D turbulent flow in the spectral domain at a given wave number $k_{wi,\gamma}$. We will first assume that the scalar is injected into the enstrophy cascading range of wave numbers, i.e. $k_{wi} < k_{wi,\gamma}$. The corresponding inertial-convective, inertial-diffusive, and viscous-convective subranges are indicated in Figure 6.3.

In the *inertial-convective range* (i.e. for $k_{wi,\gamma} < k_w < k_{wc}$) following an analysis similar to Oboukhov's analysis for scalar transfer in 3D turbulence, the scalar spectrum is proportional to the spectrum of the cascading quantity, namely the enstrophy β, and thus

$$S_\gamma(k_w, t) \propto \frac{\epsilon_\gamma}{\beta}\, k_w^2\, S(k_w, t) \propto \epsilon_\gamma\, \beta^{-1/3}\, k_w^{-1} \tag{6.39}$$

The physics of this spectral distribution of the scalar are covered by a scalar gradient equation (see Lesieur, 1997, pp. 309, 292, 41 for more detail). The scalar gradient will be steepened normal to the direction of deformation along its second principal axis, perpendicular to the weak vorticity braids reconnecting the large coherent vortices. Thus, these braids will form local scalar 'fronts' with high $\frac{\partial c}{\partial n}$. This, in turn, may induce high scalar Laplacians $\approx \frac{\partial^2 c}{\partial n^2}$, and hence high scalar molecular diffusion. This scalar-front formation with high molecular mixing at the interface may be crucial to the large-scale transport and diffusion in shallow flows.

In the *viscous-convective range*, where $k_{wd} < k_w < k_{wc}$ for $Sc > 1$, Equation (6.39) is still valid.

In the *inertial-diffusive range* for low Schmidt numbers $Sc < 1$ and $k_{wc} < k_w < k_{wd}$ the scalar spectrum shows a k_w^{-7} cascade. Equation (6.32) already given for the case of 3D isotropic turbulence, also holds in 2D turbulence. If we employ an appropriate k_w^{-3} enstrophy spectrum, the scalar spectrum results as

$$S_\gamma(k_w) \propto \epsilon_\gamma\, D_m^{-3}\, k_w^{-4}\, S(k_w) \propto \epsilon_\gamma\, D_m^{-3}\, \beta^{2/3}\, k_w^{-7}. \tag{6.40}$$

Secondly, we will assume that the scalar will be forced into the $k_w^{-5/3}$ *inverse* kinetic energy cascade, for the injection wave numbers we thus have $k_{wi,\gamma} < k_{wi}$. The scalar will now cascade to higher wave numbers along a *direct* $k_w^{-5/3}$ spectral distribution in the inertial-convective range, as shown by Lesieur & Herring (1985).

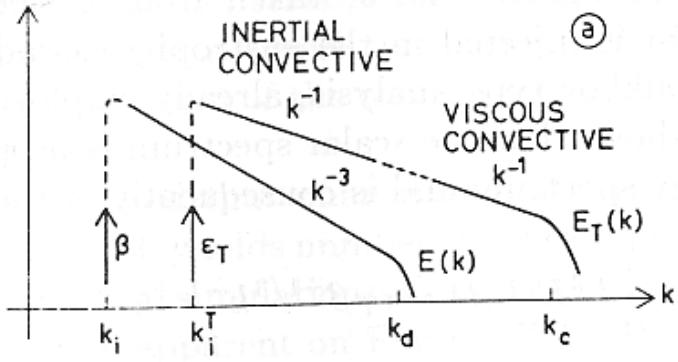

(a) $Sc > 1$

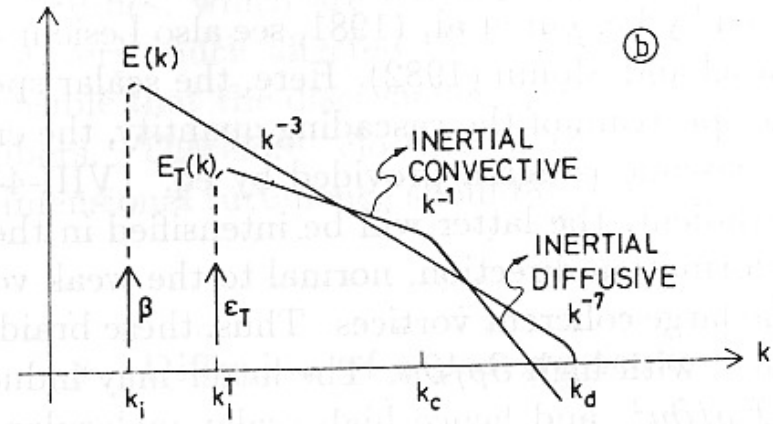

(b) $Sc < 1$

Figure 6.3. Conceptual sketch of the inertial subranges of the kinetic energy and scalar spectra in the enstrophy cascade of 2D turbulence (Lesieur & Herring, 1985). The enstrophy is injected at k_{wi} with a rate β, and the scalar at $k_{wi,\gamma} > k_{wi}$ at a rate ϵ_γ. (a) high Schmidt number $Sc > 1$, i.e. $D_m < \nu$ - (b) low Schmidt number $Sc < 1$

6.3 Scales of turbulence

In order to characterize the large-scale low-frequent fluctuations of a turbulent flow different macro scales of the turbulence field can be imagined.

6.3.1 Macro scales of turbulence

The *macro length scale* can be understood as the size range ℓ_0 of the largest eddies occurring in the flow, and is comparable to the flow scale $\mathcal{L}$. The characteristic velocity of the largest eddies, i.e. the *macro scale of velocity*, is $u_0 = u(\ell_0)$, which is of the order of the r.m.s velocity fluctuations $\sigma_u = \langle u'^2 \rangle$. The associated *macro time scale* follows as $\tau_0 = \ell_0 / u_0$.

A macro length scale associated with the large eddy sizes in the productive subrange can be defined as (cf. Pope, 2000)

$$\ell_0 \equiv \frac{k^{3/2}}{\epsilon} \ . \tag{6.41}$$

Here, the large eddy range is characterized by the TKE k contained in the high wave numbers, and by its transfer rate, which has to be of order of the dissipation rate ϵ (cf. Equation (6.23)). Consequently, the velocity macro scale is defined as $u_0 \equiv \sigma_u$. The macro time scale is then given by $\tau_0 \equiv k^{3/2} / (\epsilon \, \sigma_u)$.

Using Eulerian two-point correlations of flow measurements at fixed locations separated by a distance s we may expect that the correlation between the measurements will decrease with increasing distance, and finally vanish for distances larger than a longest distance, s_{max}. This Eulerian measure could be derived from the correlation coefficient r_{ii} given in Section 6.1.1. As another macro scale related to $r_{ii}(\boldsymbol{x}, \boldsymbol{s}, t, \tau)$ the Eulerian *integral length scale*, however, is not taken equal to the de-correlation length s_{max}, but is defined as

$$\ell_{I,l}(t) \equiv \int_0^\infty r_{11}(\boldsymbol{x}, \boldsymbol{s}, t, 0) \, ds \tag{6.42a}$$

in the longitudinal or main flow direction, and

$$\ell_{I,t}(t) \equiv \int_0^\infty r_{22}(\boldsymbol{x}, \boldsymbol{s}, t, 0) \, ds \tag{6.42b}$$

in the transverse direction. Presuming an unidirectional separation $\boldsymbol{s} = [s_1, 0, 0]$ the corresponding spatial velocity correlation coefficients are

$$r_{11}(\boldsymbol{x}, s_1, t, 0) = \frac{\langle u'(\boldsymbol{x}, 0) \, u'(\boldsymbol{x} + s_1, 0) \rangle}{\left\langle u'(\boldsymbol{x}, 0)^2 \right\rangle} \text{ , and} \tag{6.43a}$$

$$r_{22}(\boldsymbol{x}, s_1, t, 0) = \frac{\langle v'(\boldsymbol{x}, 0) \, v'(\boldsymbol{x} + s_1, 0) \rangle}{\left\langle v'(\boldsymbol{x}, 0)^2 \right\rangle} \tag{6.43b}$$

in the longitudinal and transverse flow direction, respectively. $\ell_{I,l}$ and $\ell_{I,t}$ are equivalent to the areas under the curves of the velocity correlation coefficients r_{11} and r_{22}. As illustrated in Figure 6.4 a rectangular of equal size is spanned by $r_{11}(0) \cdot \ell_{I,l}$ or by $r_{22}(0) \cdot \ell_{I,t}$, where $r_{ii}(0) = 1$. The integral length scales may deviate significantly from s_{max}, especially if for large values of s the velocity correlation coefficients become negative before tending to zero. This is the case for a periodically fluctuating flow (e.g. for a vortex street-like wake flow), but the transverse correlation coefficient r_{22} will also become negative for large s in isotropic turbulence or in 2D channel flow (Hinze, 1975). Although in general, the decrease of $r_{ii}(\boldsymbol{x}, s, t, 0)$ for large s can be approximated by an exponential function $r_{ii} \approx \exp(-c \, s / \ell_{I,i})$, fluctuating or negative values of r_{ii} cannot be reproduced this way.

In isotropic turbulence the relation between the longitudinal and the transverse integral length scale was found to be (cf. HINZE, 1975, eqs. (3-74),(3-75))

$$\ell_{I,l}\,(t) = 2\,\ell_{I,t}\,(t) \quad . \tag{6.44}$$

In the core of a shallow vortex street-like wake flow this relation will increase, as is obvious e.g. from the auto-correlation coefficients presented in Figures 7.2. Compare also the longitudinal and transverse integral time scales given in Table 7.1.

Analogously to the Eulerian integral length scales (6.42), the Eulerian *integral time scale*

$$\tau_{I,l}\,(\boldsymbol{x}) \equiv \int_0^\infty r_{11}\,(\boldsymbol{x}, 0, t, \tau)\,d\tau \tag{6.45}$$

can be regarded as a rough approximation for the de-correlation time of the longitudinal velocity component in the turbulent flow. Here, the Eulerian auto- or time correlation coefficient of the longitudinal velocity is

$$r_{11}\,(\boldsymbol{x}, 0, t, \tau) = \frac{\langle u'\,(\boldsymbol{x}, t)\,u'\,(\boldsymbol{x}, t+\tau)\rangle}{\left\langle u'\,(\boldsymbol{x}, t)^2\right\rangle} \quad . \tag{6.46}$$

For a homogeneous turbulence field with a constant mean velocity $\langle u\,(\boldsymbol{x}, t)\rangle = U$ in the longitudinal direction, where $U \gg \left\langle u'\,(\boldsymbol{x}, t)^2\right\rangle^{1/2} = \sigma_u$, we can assume (i.e. Taylor's "frozen cloud" hypothesis) that $x = U\,t$ and e.g.

$$\frac{\partial}{\partial t} = -\,U\frac{\partial}{\partial x} \quad . \tag{6.47}$$

If (6.47) holds[15], then a simple relation between the longitudinal integral time and length scales can be given as (cf. HINZE, 1975, pp. 46)

$$\ell_{I,l} = U\,\tau_{I,l} \quad . \tag{6.48}$$

6.3.2 Micro scales of turbulence

From the Eulerian velocity correlation coefficients also small length scales have been derived in order to characterize the size of the small eddies in the turbulence field. The definition of micro-length scales based on correlation coefficients of the turbulent flow was first presented by TAYLOR (1935), to his honor

[15] It still has to be clarified, for which conditions Taylor's hypothesis is valid in double shear flows like shallow wakes. Obviously (e.g. from turbulence intensity, TKE, or simply variance of fluctuation ${\sigma_u}^2 = f\,(x)$), the horizontal turbulence field in the near–field ($x/D \leq 30$) of a shallow wake flow is neither homogeneous nor isotropic. Hence, the Eulerian correlation coefficient $r_{ii}\,(\boldsymbol{x}, s, t, 0)$ between two points located along the wake centerline can not simply be translated into an auto-correlation coefficient $r_{ii}\,(\boldsymbol{x}, 0, t, \tau)$ at a single point. We will address this aspect in more detail in Chapter 7.

such scales are called *Taylor micro scales of turbulence*. A consistent theoretical review was presented, for instance, by HINZE (1975).

The longitudinal velocity correlation coefficient $r_{11}(\boldsymbol{x}, s, t, 0)$ can be expanded in a Taylor series about $s = 0$ as

$$r_{11}(\boldsymbol{x}, s, 0) = 1 + \frac{1}{2!} s^2 \left[\frac{\partial^2 r_{11}}{\partial s^2}\right]_{s=0} + \frac{1}{4!} s^4 \left[\frac{\partial^4 r_{11}}{\partial s^4}\right]_{s=0} + \cdots$$

For very small values of s r_{11} approaches a parabolic function $f_p(s)$ with its vertex at $s = 0$, thus

$$\lim_{s \to 0} (r_{11}) \approx f_p(s) = 1 - \frac{s^2}{{\ell_{\lambda l}}^2} \ . \tag{6.49}$$

Similar to the Eulerian time correlation shown in Figure 6.4, the osculating parabola intersects the s–axis at $s = \ell_{\lambda l}$.

Hence, the *longitudinal Taylor micro-scale* is given by

$$\frac{1}{\ell_{\lambda l}^2} = -\frac{1}{2} \left[\frac{\partial^2 r_{11}}{\partial s^2}\right]_{s=0} \ . \tag{6.50a}$$

$\ell_{\lambda l}$ is also related to velocity derivatives (cf. HINZE, 1975; POPE, 2000) as

$$\frac{1}{\ell_{\lambda l}^2} = \frac{1}{2\,\sigma_u^2} \left\langle \left[\frac{\partial u'}{\partial s}\right]_{s=0}^2 \right\rangle \ . \tag{6.50b}$$

Similarly, the *transverse Taylor micro-scale* is given by

$$\frac{1}{\ell_{\lambda t}^2} = -\frac{1}{2} \left[\frac{\partial^2 r_{22}}{\partial s^2}\right]_{s=0} \text{, and} \tag{6.51a}$$

$$\frac{1}{\ell_{\lambda t}^2} = \frac{1}{2\,\sigma_v^2} \left\langle \left[\frac{\partial v'}{\partial s}\right]_{s=0}^2 \right\rangle \ . \tag{6.51b}$$

Concerning the physical meaning of the Taylor micro length scale HINZE (1975) argued in agreement with TAYLOR (1935) that ℓ_λ should be regarded as the average size of the energy dissipating eddies, and he therefore called ℓ_λ the *dissipation scale*. However, TENNEKES & LUMLEY (1977) objected

> "that the length scale [$\ell_{\lambda l}$] was found by taking [σ_u] as a velocity scale. [...] The Taylor microscale is thus not a characteristic length of the strain-rate field and does not represent any group of eddy sizes in which dissipative effects are strong. It is not a dissipative scale, because it is defined with the assistance of a velocity scale [namely σ_u] which is not relevant for the dissipative eddies. Even though, [$\ell_{\lambda l}$] is used frequently because the estimate [$s_{ij} \sim \sigma_u / \ell_{\lambda l}$] is often convenient."
>
> TENNEKES & LUMLEY (1977, pp. 67-68)

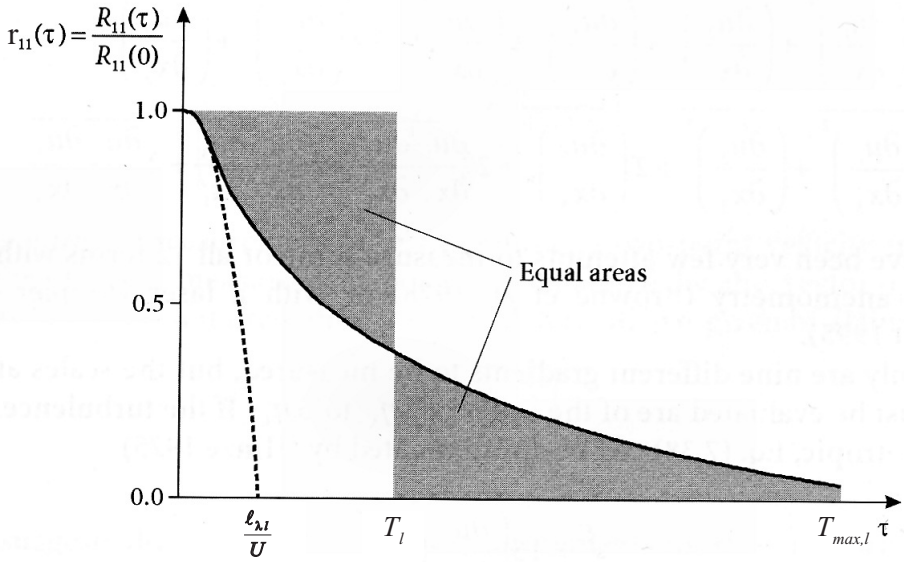

Figure 6.4. From the Eulerian velocity correlation coefficients r_{ii} characteristic scales of turbulence have been derived. The *Taylor micro timescale* τ_λ, the *integral time scale* $\tau_{I,l}$, and the *de-correlation time scale* $T_{max,l}$ are sketched conceptually with the longitudinal velocity auto-correlation coefficient $r_{11}(\boldsymbol{x}, 0, t, \tau)$. Corresponding length scales may be calculated from the velocity correlation coefficients $r_{ii}(\boldsymbol{x}, s, t, 0)$. (after ALBRECHT ET AL., 2003)

In isotropic turbulence the relation between the longitudinal and the transverse Taylor length scales is (HINZE, 1975, eq. 3-16)

$$\ell_{\lambda l} = \sqrt{2}\,\ell_{\lambda t} \ . \tag{6.52}$$

Using the approximation of the dissipation rate in isotropic turbulence $\epsilon = 15\nu \left\langle (\partial u'/\partial x)^2 \right\rangle$ (Equation (6.22)) together with (6.50b) and (6.52), the dissipation rate can be related to the transverse Taylor length scale and to the variance of the turbulent velocity fluctuations as

$$\epsilon = 15\nu \frac{\sigma_u^2}{\ell_{\lambda l}} \ . \tag{6.53}$$

Employing the Eulerian time correlation coefficient (6.46) the *Taylor micro timescale* τ_λ has been defined analogously to the Taylor micro length scales by

$$\lim_{\tau \to 0} (r_{11}) \approx f_p(\tau) = 1 - \frac{\tau^2}{{\tau_\lambda}^2} \ . \tag{6.54}$$

approximating a parabola $p(\tau)$ to $r_{11}(\boldsymbol{x}, 0, t, \tau)$ with its vertex at $\tau = 0$, as illustrated in Figure 6.4.

$$\frac{1}{{\tau_\lambda}^2} = -\frac{1}{2}\left[\frac{\partial^2 r_{11}(\tau)}{\partial \tau^2}\right]_{\tau=0} = \frac{1}{2\,\sigma_u^2}\left\langle \left[\frac{\partial u'}{\partial t}\right]_{\tau=0}^2 \right\rangle \ . \tag{6.55}$$

The Eulerian time scale τ_λ may be regarded a measure of the most rapid changes that occur in the fluctuating longitudinal velocity component $u'(t)$.

Hence, τ_λ is not a dissipative time scale, since the definition of τ_λ involves σ_u as a velocity scale that is not characteristic for the smallest eddies in the flow.

With the assistance of Taylor's "frozen turbulence" hypothesis, and thus with all restrictions associated with this hypothesis, a simple relation between the Taylor micro scales of length and time is given as

$$\ell_{\lambda l} = U\,\tau_\lambda \ . \tag{6.56}$$

The argument is similar to that for the relation of the integral scales of length and time (Equation (6.48)). However, for the Taylor micro scales, which may fall into the wave number range of local isotropic turbulence, the "frozen turbulence" hypothesis might well be applicable also in shallow shear flows that are inhomogeneous at larger flow scales.

In 1941 A. N. Kolmogorov identified the smallest scales of turbulence describing the range of eddies which are affected by viscosity leading to dissipation of the turbulent kinetic energy introduced at the largest scales to the flow. The *Kolmogorov scales of turbulence* have already been used in Section 6.2.2 to describe the processes of the energy cascade. Since in the range of the smallest eddies, in the dissipation range, TKE is dissipated at a rate ϵ due to viscosity ν, the dissipative scales of turbulence will solely depend on these two quantities. From dimensional reasons the dissipative micro scales, the *Kolmogorov scales of length, velocity, and time*, result as

$$\ell_\eta \equiv \left(\frac{\nu^3}{\epsilon}\right)^{1/4} \ , \tag{6.57a}$$

$$u_\eta \equiv (\epsilon\nu)^{1/4} \ , \tag{6.57b}$$

$$\tau_\eta \equiv \left(\frac{\nu}{\epsilon}\right)^{1/2} \ , \tag{6.57c}$$

respectively. The Reynolds number composed of the Kolmogorov micro scales is unity, $Re_\eta = u_\eta\,\ell_\eta/\nu = 1$. In the wave number range in which $Re_\eta = \mathcal{O}(1)$ viscosity prevails leading to dissipation. Also the velocity gradient for the dissipative eddies is consistently given by $\frac{u_\eta}{\ell_\eta} = \left(\frac{\epsilon\,\nu}{\nu^3/\epsilon}\right)^{1/4} = \frac{1}{\tau_\eta}$.

Briefly recapitulating the concept of the *energy cascade* says that TKE is produced by eddies of the largest scale at a production rate $\mathcal{P}(\ell_0)$, transferred inviscidly to smaller and smaller eddies at a transfer rate $\mathcal{T}(\ell)$, and finally dissipated by viscous effects at the smallest eddy scale with a dissipation rate $\epsilon(\ell_\eta)$, thus (Equation (6.23))

$$\mathcal{P}(\ell_0) \approx \mathcal{T}(\ell) \approx \epsilon(\ell_\eta) \ .$$

The largest eddies carry TKE of order u_0^2 and have a time scale of $\tau_0 = \ell_0/u_0$. Hence, energy is passed by the largest eddies to smaller ones at a rate $\mathcal{T} \propto u_0^2/\tau_0 = u_0^3/\ell_0$. From (6.23) the dissipation rate scales as $\epsilon \propto u_0^3/\ell_0$,

and is independent of ν. Defining a Reynolds number as $Re_{\ell_0} = u_0\,\ell_0/\nu$ using characteristic macro turbulence scales, the scale relations between the Kolmogorov micro scales and the macro scales of turbulence are found to be (e.g. Tennekes & Lumley, 1977)

$$\ell_\eta/\ell_0 \sim Re_{\ell_0}^{-3/4} \ , \tag{6.58a}$$

$$u_\eta/u_0 \sim Re_{\ell_0}^{-1/4} \ , \tag{6.58b}$$

$$\tau_\eta/\tau_0 \sim Re_{\ell_0}^{-1/2} \ . \tag{6.58c}$$

Evidently, for increasing Re_{ℓ_0} the range of the energy cascade will widen, e.g. given fixed macro scales like constant integral scales, the Kolmogorov micro scales will decrease.

In order to compare the Kolmogorov, Taylor, and macro length scales we can define a macro–scale turbulence Reynolds number using the macro length scale ℓ_0 (Equation (6.41)) as

$$Re_{\ell_0} \equiv \frac{k^{1/2}\ell_0}{\nu} = \frac{k^2}{\epsilon\,\nu} \ , \tag{6.59a}$$

and a Taylor–scale turbulence Reynolds number

$$Re_{\lambda l} \equiv \frac{\sigma_u\,\ell_{\lambda l}}{\nu} \ . \tag{6.59b}$$

The relations between the micro and macro length scales then become

$$\frac{\ell_{\lambda l}}{\ell_0} = \sqrt{10}\ Re_{\ell_0}^{-1/2} = \frac{15}{(3/2)^{3/2}}\ Re_{\lambda l}^{-1} \ , \tag{6.60a}$$

$$\frac{\ell_\eta}{\ell_0} = Re_{\ell_0}^{-3/4} \ , \text{ and} \tag{6.60b}$$

$$\frac{\ell_{\lambda l}}{\ell_\eta} = \sqrt{10}\ Re_{\ell_0}^{1/4} = \sqrt[4]{15}\ Re_{\lambda l}^{1/2} \ . \tag{6.60c}$$

Finally, it should be noticed that—using (6.53)—the Taylor time scale correctly represents the time scale of the dissipative eddies described by Kolmogorov's micro time scale,

$$\tau_\lambda = \frac{\ell_{\lambda l}}{\sigma_u} = \left(15\,\frac{\nu}{\epsilon}\right)^{1/2} = \sqrt{15}\ \tau_\eta \ . \tag{6.61}$$

6.3.3 Micro scales of scalar fluctuations

In a steady homogeneous shear flow, the equation governing the dynamics of the scalar (e.g. a small excess temperature) variance $\langle \vartheta'^{\,2} \rangle$ reduces to

$$-\left\langle \vartheta'\ u_i \right\rangle \frac{\partial \Theta}{\partial x_i} = D_m \left\langle \frac{\partial \vartheta'}{\partial x_i} \cdot \frac{\partial \vartheta'}{\partial x_i} \right\rangle , \tag{6.62}$$

which expresses that the gradient production of $\langle \vartheta'^2 \rangle$ is balanced by the molecular diffusion (cf. Tennekes & Lumley, 1977, p. 95). The *Taylor micro scale for the scalar fluctuations* ℓ_{λ_γ} can now be defined as

$$\left\langle \frac{\partial \vartheta'}{\partial x_1} \cdot \frac{\partial \vartheta'}{\partial x_1} \right\rangle \equiv 2\, \frac{\langle \vartheta'^2 \rangle}{\ell_{\lambda_\gamma}^2}. \tag{6.63}$$

Assuming that in steady flow the production and dissipation are of the same order of magnitude (cf. Equation (6.62)), we can estimate ℓ_{λ_γ} following an order-of-magnitude argument. This leads to the relation

$$\frac{\ell_{\lambda_\gamma}}{\ell_\lambda} \equiv C \left(\frac{D_m}{\nu} \right)^{1/2} = \frac{C}{\sqrt{Sc}}, \tag{6.64}$$

where C is a constant[16]. Just like ℓ_λ, also ℓ_{λ_γ} is an artificial scale without an exact physical equivalent.

Analogously to *Kolmogorov's micro length scale* ℓ_η for velocity fluctuations, a micro length scale ℓ_{η_γ} can be introduced to define the typical eddy size, at which molecular diffusion begins to predominate the convective transport of scalar variance along the wave number space. In the common case of $Sc > 1$ or $Pr > 1$, i.e. $\nu > D_m$, the *scalar micro scale* λ_{η_γ} is given with respect to Kolmogorov's length scale by (cf. Batchelor, 1959)

$$\frac{\ell_{\eta_\gamma}}{\ell_\eta} = \left(\frac{D_m}{\nu} \right)^{1/2} = Sc^{-1/2}. \tag{6.65}$$

Since for the Kolmogorov length scale $\ell_\eta = \left(\frac{\nu^3}{\epsilon} \right)^{1/4}$, the *Batchelor scale of scalar fluctuation* becomes

$$\ell_{\eta_\gamma} = D_m^{1/2} \left(\frac{\nu}{\epsilon} \right)^{1/4}. \tag{6.66}$$

If on the contrary $Sc \ll 1$, $\nu < D_m$ and $\ell_\eta < \ell_{\eta_\gamma}$, the molecular diffusivity dissipates the scalar fluctuations at eddy sizes $\ell_{\eta_\gamma} > \ell > \ell_\eta$, where the energy cascade still exhibits an inviscid behavior. Thus, ℓ_{η_γ} is independent of ν. The scalar micro scale then becomes (cf. Corrsin, 1951)

$$\ell_{\eta_\gamma} = \left(\frac{D_m^3}{\epsilon} \right)^{1/4} \text{ and formally } \frac{\ell_{\eta_\gamma}}{\ell_\eta} = \left(\frac{D_m}{\nu} \right)^{3/4} = Sc^{-3/4}. \tag{6.67}$$

[16] $\mathcal{O}(C) = 1$, cf. Corrsin (1951)

7. Analysis of LDV-LIF Measurements in Wake Flows

7.1 Time series analysis of wake flow measurements

7.1.1 Time histories of LDV-LIF measurements

Shallow turbulent flows are often characterized by a velocity field that reveals a significant low-frequent periodically fluctuating part. Instead of a *Reynolds decomposition* (7.1a) it is often more appropriate to use a "two–length–scale decomposition". Either a *double decomposition* (7.1b) into a low-frequent periodic and a random turbulent flow field, or a *triple decomposition* (7.1c) into mean, periodic, and random components can be defined that for the longitudinal velocity component are given by (cf. also Equations (10.4), (10.5))

$$u\,(t) = U + u' = \langle u \rangle + (u - \langle u \rangle) \tag{7.1a}$$

$$= u_p + u_r = \{u\} + (u - \{u\}) \tag{7.1b}$$

$$= U + u_p^\star + u_r = \langle u \rangle + \{u - \langle u \rangle\} + (u - \langle u \rangle - \{u - \langle u \rangle\}) \ . \tag{7.1c}$$

Here, angle brackets $\langle\ \rangle$ denote time or ensemble averages. Curly brackets $\{\ \}$ denote different kinds of filters employed to distinguish the low-frequent part of a signal. In Section 10.2.3 we will discuss aspects of a "two–length–scale decomposition" of wake flow fields in more detail, as we will also employ double- and triple-decomposed fields of velocity and mass extensively throughout Part III of this study.

The double–decomposition of LDV and LIF data is illustrated in Figure 7.1 by time histories of the horizontal velocity components u and v and of the mass concentration c, measured at the centerline of wake flows at about two thirds of the water depth. Figure 7.1(a) shows data obtained at $x/D = 4$ downstream of a cylindrical obstacle in a vortex street-like wake (measurement series 27_vs07). The passage of counter-rotating large-scale vortices alternatingly shed from both sides of the cylinder can be observed in distinct low-frequent fluctuations of the velocity and mass signals that reveal a strong periodicity with an almost constant cycle period. Such a prominent periodicity is a characteristic feature of the VS stability class of shallow wakes. In order to extract the strongly periodic part of the signals the data is conditionally re-sampled

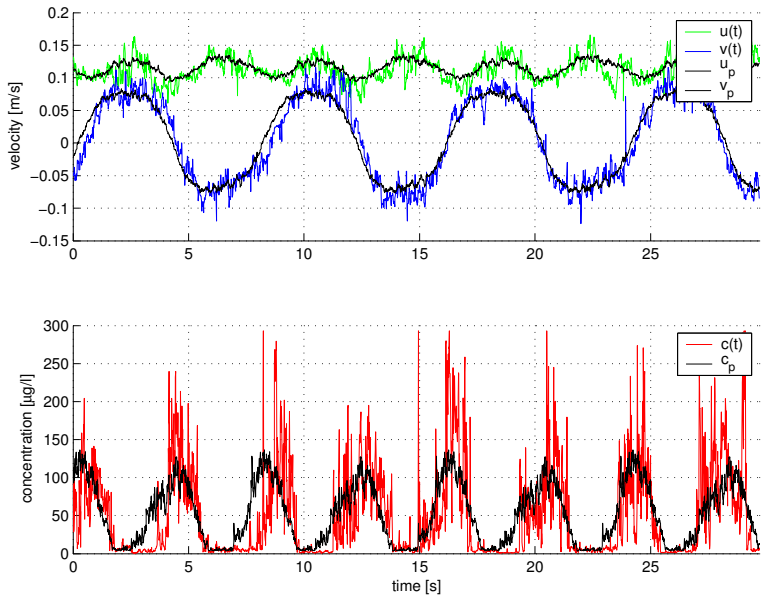

(a) Vortex street-like wake flow ($S = 0.07$)

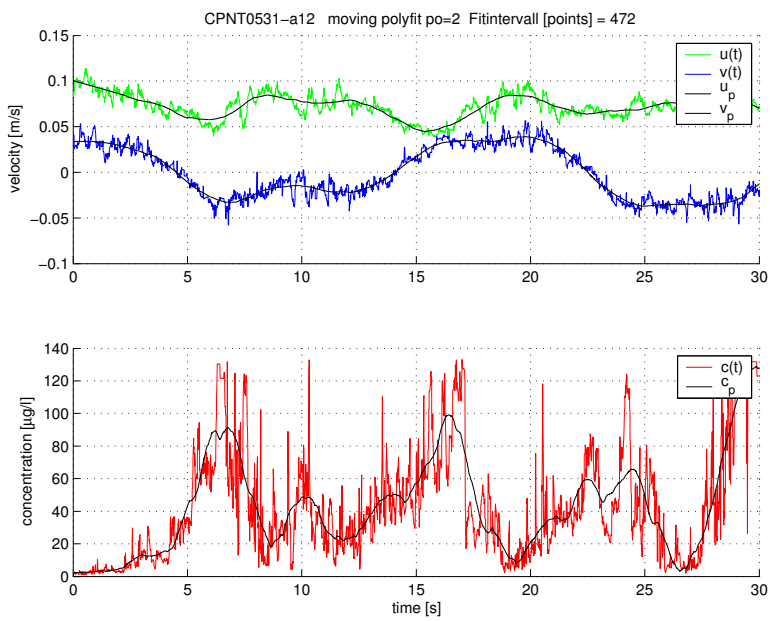

(b) Unsteady bubble wake flow ($S = 0.25$)

Figure 7.1. Time-resolved histories of measured u and v components of the flow velocity (upper plot) and of the mass concentration (lower plot) have been obtained at the centerline of shallow wake flows of the stability classes VS (Figure (a), series 27_vs07, $x/D = 4$) and UB (Figure (b), series 17_ub25, $x/D = 3$). In order to double-decompose the data into its large-scale coherent and small-scale random flow fields different strategies have been applied. (a) Making use of the strong periodicity of VS wakes a phase-resolve averaging procedure based on a mean cycle period has been performed. – (b) The slowly fluctuating parts of the time-resolved data have been identified from fitting a polynomial of order 2 in a moving window that was approximately a quarter cycle period wide.

employing a *phase–resolved averaging* procedure. Based on the mean cycle period T_P of the process the individual measurements are associated to their appropriate intervals or 'slots' ϕ_i of the phase time. The mean cycle period of the vortex street-like wake flow—spanning a full shedding cycle of two counter-rotating vortices—is obtained from the auto-correlation coefficient $R_{vv}(\tau)$ of the transverse velocity component, as discussed in Section 7.1.2. In order to represent slight variations in the cycle period that will occur for increasing values of the wake stability parameter S, the phase–resolved average can also be based on the individual cycle periods of the flow (cf. Section 10.1.2).

A different approach to extract the large-scale flow field from the time-resolved data is illustrated in Figure 7.1(b) taken from an unsteady bubble wake (measurement series 17_ub25) at $x/D = 3$. In contrast to vortex street-like shallow wake flows, in UB wakes the periodicity of the large-scale motion is weaker regarding both variability and significance of the periodicity. Though large-scale vortical structures are present also in wake flows of UB stability class, theses structures separate more irregularly, and they are less significant, e.g. they contain less kinetic energy and vorticity (both in total and in maximum values). Albeit there is a wealth of sophisticated filtering techniques available, we decided to employ an *interpolation scheme* to identify the low-frequent part of the signal. To the velocity measurement data, already re-sampled with equal time intervals, a moving time window with a width of approximately $T_P/4$—and half as wide for the mass concentration signal—was applied.[1] A second order polynomial was centrally fitted to the time-resolved data in the window, the interpolated low-frequent data can be regarded as an estimate for the large-scale motion of the flow field.

Irrespective of the mode of double-decomposition, some properties of the decomposed flow fields have to be ascertained. As for a Reynolds-decomposition, for the average of the fluctuations

$$\langle u_{r,i} \rangle = 0 \tag{7.2a}$$

has to hold. This also applies to the large-scale fluctuations for a triple-decomposition,

$$\left\langle u^*_{p,i} \right\rangle = 0 \ . \tag{7.2b}$$

Consequently, for double-decomposed data, we must have

$$\langle u_{p,i} \rangle = U + \left\langle u^*_{p,i} \right\rangle = U \ . \tag{7.2c}$$

[1] Lacking a distinct cycle period, a characteristic macro time scale $T = 1/f_0$ has been estimated from an initial wake Strouhal number $St = D\,f_0/U \approx 0.2$, though St slightly depends on S.

Since we assume the large-scale coherent and the small-scale turbulent flow fields to be completely de-correlated, thus

$$\left\langle u^*_{p,i}\, u_{r,i} \right\rangle = 0 \ . \tag{7.2d}$$

Whereas the presuppositions (7.2a), (7.2b), and (7.2c) for flow field decomposition are inherently met for interpolation algorithms of arbitrary order—also of 0th and of 2nd order—as well as for phase–resolved averages, the assumption of complete de-correlation (7.2d) has to be evidenced separately. For the schemes, employed for the decomposition of the point-wise measurement data in this study, the inter-scale cross-variances are always much smaller than the appropriate whole-scale variances, i.e.

$$\frac{\left\langle u^*_{p,i}\, u_{r,i} \right\rangle}{\left\langle {u_i}^2 \right\rangle} = \mathcal{O}\left(10^{-3}\right) \ , \qquad \text{and} \qquad \frac{\left\langle c^*_p\, c_r \right\rangle}{\left\langle c^2 \right\rangle} = \mathcal{O}\left(10^{-3}\right) \ .$$

In order for Taylor's hypothesis of 'frozen turbulence' to hold also if large-scale quasi-2D vortical structures are present, we should have

$$\left\langle u^2_{r,i} \right\rangle / \left\langle u^2_{p,i} \right\rangle \ll 1 \ . \tag{7.3}$$

Thus, the TKE of the small-scale turbulent fluctuation should be much smaller than the kinetic energy contained in the large-scale coherent flow field. Since, obviously, this in general will not be valid for the large-scale 2D motions with respect to the mean flow, $\left\langle {u^*_{p,i}}^2 \right\rangle / U_i^2$, the applicability of Taylor's hypothesis to quasi-2D turbulence can not be approved a priori.

In the present decomposed measurements the variance of the small-scale fluctuations amount to less than 3% of the variance of the coherent fluctuations for the transverse velocity component of a VS wake, $\left\langle v^2_r \right\rangle / \left\langle v^2_p \right\rangle < 0.03$, but are ten times larger for $\left\langle u^2_r \right\rangle / \left\langle u^2_p \right\rangle$ and for $\left\langle c^2_r \right\rangle / \left\langle c^2_p \right\rangle$. As the large-scale vortical structures become less pronounced in UB and SB wakes, the 3D random fluctuations are of level or dominating importance in these cases of wake instability.

7.1.2 Correlation coefficients of measured data

From the LDV-LIF data the Eulerian *auto- and cross-correlation coefficients* $r_{\phi\phi}(\tau)$ have been calculated for the horizontal velocity components u and v and for the mass concentration c. An appropriate discretized formulation $r_{\phi\phi}(s\ \Delta t)$, given by Equation (6.7) normalized by $R_{\phi\phi}(0) = \sigma^2_{\phi\phi}$, was applied to the discrete data—re-sampled at equal time intervals.

Point-wise measurements have been conducted along the centerline of shallow wakes of different stability classes. Vortex street-like cylinder wakes show a definite periodicity in the correlation coefficients of all measured flow components. Figure 7.2 illustrates this for data from a VS wake with an initial stability

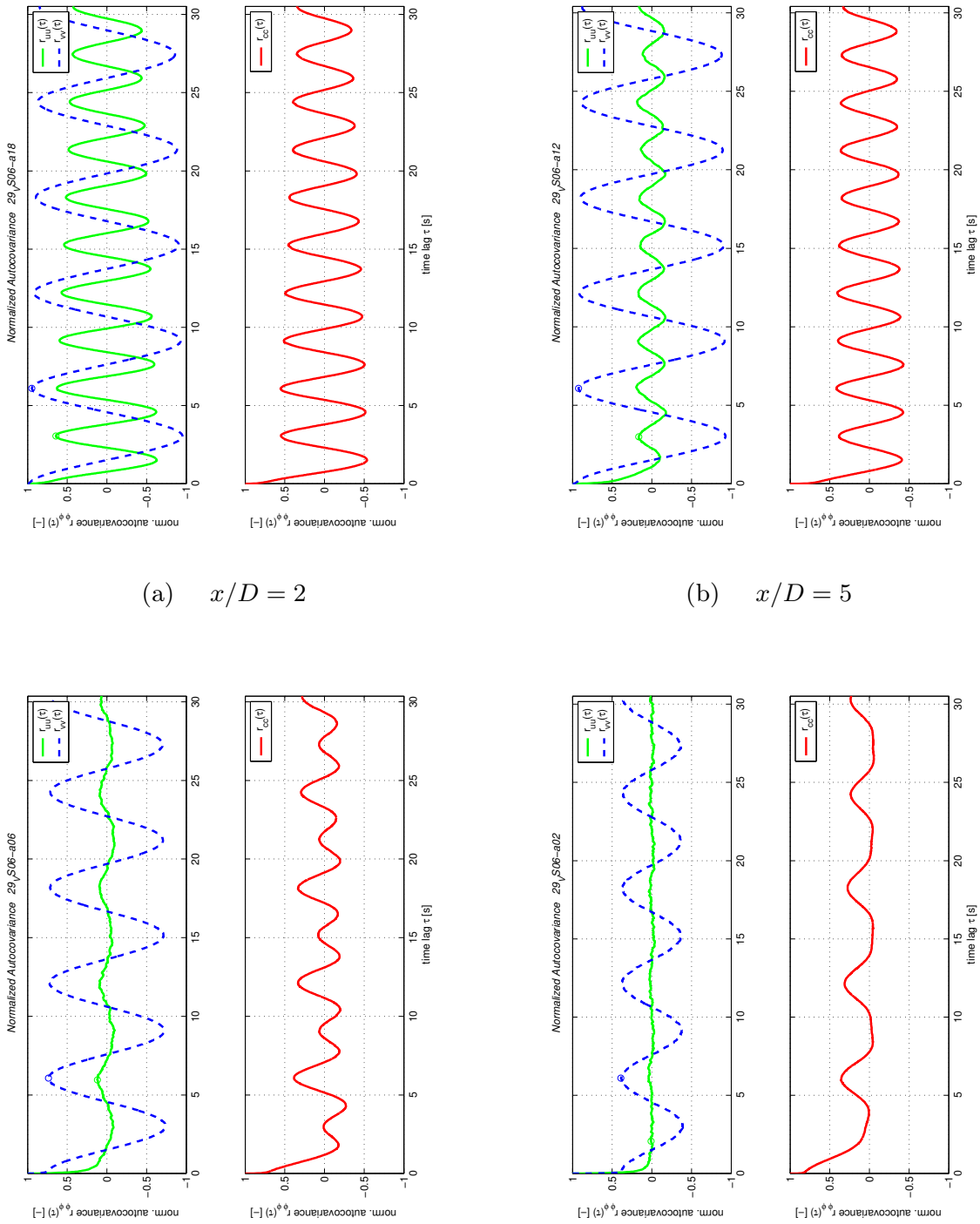

(a) $x/D = 2$ (b) $x/D = 5$

(c) $x/D = 15$ (d) $x/D = 25$

Figure 7.2. Correlation coefficients $R_{\phi\phi}(\tau_i)$ of the horizontal velocity components u and v (full and dashed lines, upper plots) and of the mass concentration c (lower plots) have been computed using the discrete formulation (6.7), as illustrated for a VS wake flow (series 25_vs07). Measurements were taken along the wake centerline at $x/D = 2$, 5, 15, and 25. The time lag was limited to $\tau/T \leq 0.3$.

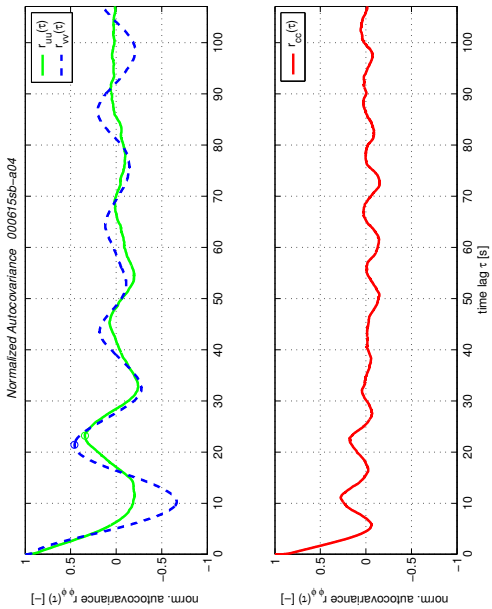

Figure 7.3. For a stabilized wake (series 18_sb51) the correlation coefficients $R_{\phi\phi}(\tau_i)$ of the horizontal velocity components u and v (upper plot) and of the mass concentration c (lower plot) have been computed from measurement data obtained at $x/D = 2.5$ ($S = 0.51$ indicating a lower–limit steady bubble (SB) stability class close to the UB class).

parameter $S = 0.07$ (measurement series 25_vs07). The data was obtained at the downstream positions $x/D = 2$, 5, 15, and 25 (or equivalently $x/h = 20$, 50, 150, and 250) along the centerline of the wake, corresponding to Figures 7.2(a) to 7.2(d). Correlation coefficients have been calculated for time lags $\tau/T \leq 0.3$ to visualize the periodicity in $r_{\phi\phi}(\tau)$. The correlation coefficients depicted in the upper plots show very strong correlation in the transverse velocity (dashed lines) for time lags corresponding to full cycle periods $\tau = nT_P$—reaching from almost 1 near the obstacle to about 0.4 far downstream—, but lower and rapidly dampened values of $r_{uu}(\tau)$ in the longitudinal flow direction (full lines). For $x/D = 2$ and 5 the doubled frequency of r_{uu} indicates the existence of the counter-rotating vortices (cf. Figures 7.2(a) and 7.2(b)). As the large-scale eddies decay, the wake stabilizes towards a purely meandering movement with the same frequencies in r_{uu} and r_{vv}, finally without significant periodic longitudinal velocity fluctuations (cf. Figures 7.2(c) and 7.2(d)).[2] The same behavior is evident more clearly in Figure 7.3 displaying the correlation of the velocity components in a steady bubble wake (series 18_sb51, $x/D = 2.5$). This meandering movement indicates that for a stability parameter of $S = 0.51$ the wake is not yet fully stabilized, but shows fluctuations in the flow field induced by the recirculation bubble attached to the obstacle.

[2] A description of the field-wise topography of vortex street-like shallow wakes will be given in Part III of this work. At this point, we want to state without prove that the meandering flow is not restricted to the core of the wake (e.g. by 'widening the gap' between the two rows of vortices) but is the result and remains of the complete disintegration of the coherent vortical motion.

Since tracer mass was introduced into both the left and right cylinder boundary layers, vortices shed from both sides get mass-loaded. As the eddies were advected downstream forming the rows of counter-rotating eddies in a VS wake, mass was laterally mixed and symmetrically distributed with respect to the wake axis. Hence, the correlation coefficient of the mass concentration $r_{cc}(\tau)$ (depicted in the lower plots) is related to r_{vv} of the transverse velocity component which represent the development of the individual large-scale eddies, and thus—combining two eddies—is related also to the full shedding cycle of a vortex street. As the individual LCS decay away, and the wake becomes more stable exhibiting a large-scale meandering motion, also the large-scale variations of the longitudinal velocity component cease, and r_{uu} remains uncorrelated. Because of the high Schmidt number $Sc \gg 1$, at this stage the injected mass remains organized into patches resulting from the former LCS development, and is subjected to mainly small-scale turbulence while advected downstream. As a consequence of the higher momentum diffusivity ν compared to the mass diffusivity D_m in these flow configurations, c remains correlated much farther downstream than u. Note that the periodicity of r_{cc} shifts toward the cycle period of the full shedding cycle captured by r_{vv} as a result of the straining processes in the wake far-field (cf. Part III, esp. Section 10.2). Again, the stabilized behavior of a transitional wake between the stability classes UB and SB is illustrated in Figure 7.3 from data taken at $x/D = 2.5$ immediately downstream of the recirculation bubble.

7.1.3 Scales of turbulence

Integral scales of time and length. The *Eulerian integral time scale* τ_I has been defined (Equation 6.45) using the longitudinal Eulerian auto-correlation coefficient $r_{uu}(\boldsymbol{x}, 0, t, \tau)$ (Equation (6.46)) as

$$\tau_I(t) \equiv \lim_{\tau' \to \infty} \int_0^{\tau'} r_{uu}(t, \tau)\, d\tau \ .$$

τ_I can be calculated directly from time series data, e.g. from LDV measurements of $u(t)$, without the assistance of Taylor's 'frozen turbulence' hypothesis. Thus, the presupposition of homogeneous turbulence is not required in order to obtain the integral time scale.

In the shallow wake of a single obstacle the time scales of the periodic–coherent and of the random–turbulent flow field differ by several orders of magnitude (v. Carmer et al., 2000; v. Carmer & Jirka, 2001). Hence, a triple decomposition (7.1c) can be applied to the time series of the velocity data. Since the periodic and the random fluctuations are completely de-correlated, as shown in Section 7.1.1, i.e. $\langle u_p^\star u_r \rangle = 0$, the Eulerian auto-correlation coefficient (6.46) becomes

$$
\begin{aligned}
r_{uu}(t,\tau) &= \frac{\langle u'(t)\ u'(t+\tau)\rangle}{\langle u'^2\rangle} \\
&= \frac{\left\langle \left[u_p^\star(t)+u_r(t)\right]\cdot\left[u_p^\star(t+\tau)+u_r(t+\tau)\right]\right\rangle}{\left\langle \left[u_p^\star+u_r\right]^2\right\rangle} \\
&= \frac{\left\langle u_p^\star(t)\ u_p^\star(t+\tau)\right\rangle + \langle u_r(t)\ u_r(t+\tau)\rangle}{\left\langle u_p^{\star 2}\right\rangle + \langle u_r^2\rangle}
\end{aligned}
\tag{7.4}
$$

Inserting (7.4) into (6.45) results in a decomposition of the integral time scale into coherent and incoherent parts,

$$
\begin{aligned}
\tau_I(t) = &\lim_{\tau'\to\infty}\int_0^{\tau'} \frac{\left\langle u_p^\star(t)\, u_p^\star(t+\tau)\right\rangle}{\langle u'^2\rangle} d\tau \\
&+ \lim_{\tau'\to\infty}\int_0^{\tau'} \frac{\langle u_r(t)\, u_r(t+\tau)\rangle}{\langle u'^2\rangle} d\tau\ .
\end{aligned}
\tag{7.5}
$$

Since the correlation coefficient of the periodic velocity component $\left\langle u_p^\star(t)\, u_p^\star(t+\tau)\right\rangle / \left\langle u'^2\right\rangle$ does not converge, but oscillates around 0 in the interval $\left[-\sigma_{u_p}^2/\sigma_u^2; +\sigma_{u_p}^2/\sigma_u^2\right]$, the integral time scale of the periodic component vanishes (first term on the right-hand-side of (7.5)). Hence, τ_I per definitionem contains the randomly fluctuating part of the velocity field only, and is therefore not suited to characterize the coherent velocity field. The cycle period T_P of the coherent motion of the flow field appears to be an appropriate macro time scale for the low-frequent periodic fluctuations. As a characteristic feature of shallow quasi-2D turbulent flows the scale duality is very prominent also in the different macro time scales, i.e. $\tau_I/T_P \ll 1$. This has recently been reported by Rummel et al. (2004) also for grid-generated quasi-2D turbulence.

Consequently, periodic motions that are a vital part of most shallow 2D shear flows will not be represented with the Eulerian integral time scale τ_I. Only the random 3D turbulence field can be characterized by τ_I, as can also be seen from the data presented in Table 7.1, page 186.

In order to compute the longitudinal integral time scale, which is given by the semi-infinite integral of r_{uu}, $\tau_{I,l}$ can by split into an finite integral up to an upper limit of $\tau = T_P$ and into an remaining semi-infinite integral. Hence, Equation (6.45) becomes

$$
\tau_{I,l} = \int_0^{T_P} r_{uu}(\tau)\, d\tau + \lim_{\tau'\to\infty}\int_{T_P}^{\tau'} r_{uu}(\tau)\, d\tau\ .
\tag{7.6}
$$

Because of the strong periodicity of unstable shallow wake flows, and thus of the appropriate r_{uu}, the unbounded integral will not converge. As a further consequence of the de-correlation of the large-scale coherent and the small-scale random flow fields, the second integral term of (7.6) does not contribute

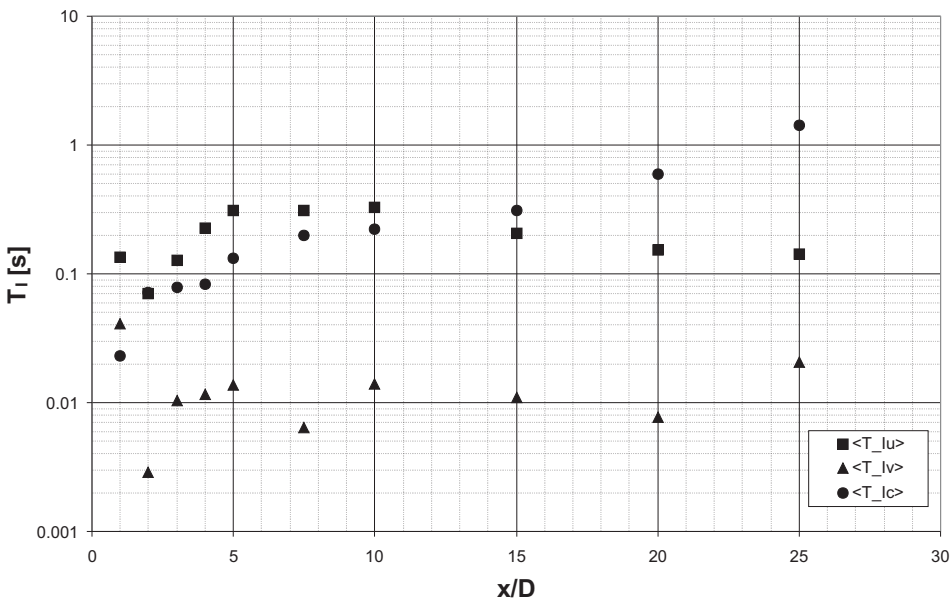

Figure 7.4. Eulerian integral time scales have been computed from the u, v, and c data obtained in a vortex street-like shallow wake (series 25_vs07) at different downstream positions along the wake centerline. The resulting longitudinal, transverse, and diffusive integral time scales $\tau_{I,l}$, $\tau_{I,t}$, and $\tau_{I,c}$ are denoted by ■, ▲, and ●, respectively. Whereas $\tau_{I,l}$ increases in the near-wake, then gradually decreases toward the 3D random turbulent integral time scale, the transverse integral time scale remains a constant with a surprisingly small value. Contrarily, the diffusive integral time scale $\tau_{I,c}$ exponentially grows even in the wake far-field.

to $\tau_{I,l}$, but varies around 0. This is due to the fact that the large-scale coherent motion will not contribute to the integral time scale (cf. Equation (7.5)) and the semi-infinite integral term solely represents correlation coefficients obtained from the coherent flow field. Only time lags $\tau < T_P$ up to the full cycle period, contained in the first integral term, have to be evaluated for the computation of the integral time scale, since the 3D random turbulent fluctuations are limited to time scales much smaller than the time scale T_P of the quasi-2D coherent motion.

The downstream development of the integral time scales is illustrated in Figure 7.4. The *longitudinal, transverse, and diffusive integral time scales* $\tau_{I,l}$, $\tau_{I,t}$, and $\tau_{I,c}$—denoted by ■, ▲, and ●, respectively—have been computed from the u, v, and c data obtained in a vortex street-like shallow wake (series 25_vs07) at different downstream positions along the wake centerline. In general, values for $\tau_{I,l}$ are slightly higher than the corresponding values of the ambient bottom-shear flow, values of $\tau_{I,t}$ are lower[3] than the corresponding ambient values. Both, $\tau_{I,l}$ and $\tau_{I,t}$, can be regarded as roughly independent of x/D. On the contrary, the diffusive integral time scale $\tau_{I,c}$ shows a continuous

[3] The transverse integral time scale $\tau_{I,t}$ obtained from our measurements in shallow wake flows is of the order of the data re-sampling time interval of 0.01 s. For a thorough discussion of $\tau_{I,t}$ it is necessary to evaluate data histories with higher temporal resolution.

exponential growth law with downstream distance. The increase of $\tau_{I,c}$, ranging over two orders of magnitude, approaches values of the order of the cycle period T_P. Because of the high Schmidt number of the mass solution, the mass will still advect and diffuse in the equilibrium shear flow, even when the TKE of large-scale eddies will have already been dissipated, and the LCS will have already disintegrated.

The *integral time scales of the ambient shear flow*, as averaged over all measurements at the corresponding downstream positions outside the wake, are $\tau_{I,l} \approx 0.12$ s, and $\tau_{I,t} \approx 0.08$ s for measurement series 25_vs07 presented in Figure 7.4. Since there is substantial variability in the averaged τ_I, the general relation of $\tau_{I,l} = 2\,\tau_{I,t}$ (cf. also the relation (6.44) of the integral length scales) in homogeneous turbulence is not contradicted. Assuming local homogeneity in the range of small-scale 3D turbulence, Taylor's hypothesis can be employed to obtain an *Eulerian integral length scale for the 3D turbulence*, $\ell_{I,l} = U\,\tau_{I,l} =$ 20 mm. The longitudinal integral length scale is of the order of the water depth, $\ell_{I,l} = \mathcal{O}(h)$. Hence, the integral scales of time and length, $\tau_{I,l}$ and $\ell_{I,l}$, consistently represent the range of the large eddies of the bottom–induced turbulence.

Macro scales of time and length. An appropriate *macro time scale* τ_0 which also covers the periodic part of the flow field is given by the low-frequent periodicity T_P of the flow. From the longitudinal auto-correlation coefficient $r_{uu}(\tau)$ the longitudinal macro time scale $\tau_{0,l}$ is obtained as the time of its first local maximum correlation, or as the inverse of its oscillation frequency (cf. e.g. Figure 7.2). Averaged values of the macro time scale, as evaluated

Table 7.1. Macro and integral flow scales have been evaluated from LDV data in flows of different wake instability classes. Values of the macro time scale τ_0 have been evaluated from the periodicity of r_{vv}, the appropriate length scale values ℓ_0 have been obtained with a coordinate transformation $t = U_a\,x$. Integral time scales τ_I were computed using (6.45), the corresponding ℓ_I were deduced employing Taylor's hypothesis.

series	macro scales		integral scales					
	time	length	time			length		
	$\tau_{0,l}$ [s]	$\ell_{0,l}$ [mm]	$\tau_{I,l}$ [s]	$\tau_{I,t}$ [s]	$\tau_{I,c}$ [s]	$\ell_{I,l}$ [mm]	$\ell_{I,t}$ [mm]	$\ell_{I,c}$ [mm]
18_vs06	4.99	812	0.202	0.05	0.023	32.9	8.1	3.7
25_vs07b	6.08	990	0.201	0.014	0.078	32.7	2.3	12.7
25_vs07c	7.96	1296	0.117	0.042	0.033	19.0	6.8	5.4
17_ub25	17.23	2805	0.241	0.049	0.032	39.2	8.0	5.2
18_sb51	21.4	3483	0.176	0.03	0.012	28.6	4.9	2.0

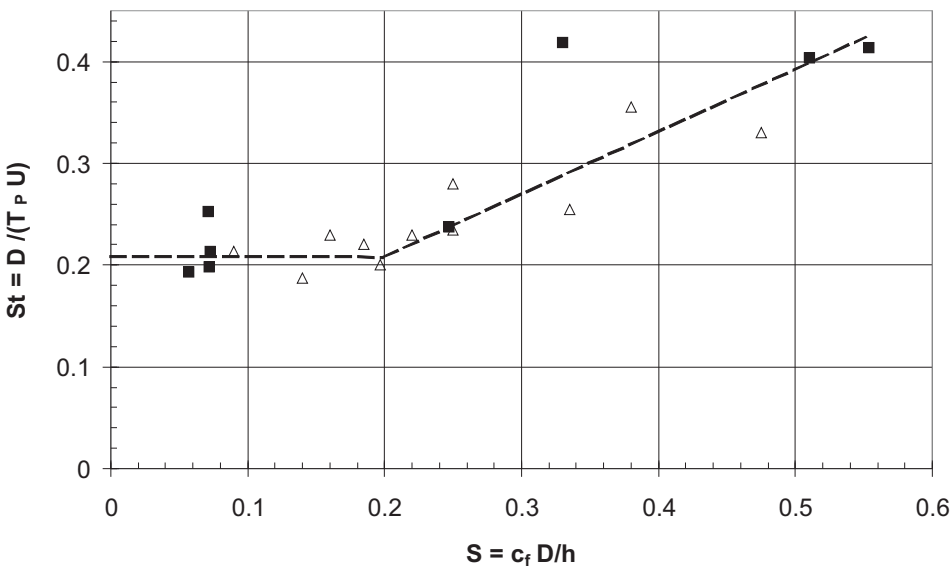

Figure 7.5. The macro time scale $\tau_0 = T_P$ of cyclic wake flows is usually normalized using the upstream flow velocity U_{amb} and the cylinder diameter D resulting in the Strouhal number $St = D/(T_P\, U_{amb})$. St depends on the typology of the wake, which in shallow wake flows is primarily related to the stability parameter $S = c_f\, D/h$. Values of T_P have been obtained from r_{vv} of our LDV measurements (full symbols), and from flow visualizations (empty symbols, Chen & Jirka, 1995). A linear approximation proposed by Chen & Jirka (1995) is indicated by the dashed line. If the macro length scale of the flow can be given as $\ell_0 = \tau_0\, U_{amb}$, then St^{-1} represents the non-dimensional macro length scale ℓ_0/D.

from each series of LDV measurements, are presented in Table 7.1 together with the integral time scales for selected measurement series. Note that also $\tau_{0,l}$ does not vary with the downstream position for the unstable wake classes suggesting that the size of the largest vortical structures in the flow will not grow while advected with the flow. Hence, merging processes characteristically associated with 2D turbulence do not occur in shallow wake flows, as will also be evidenced from the energy spectral distributions. In Part III we will explain this behavior from the topography of shallow wake flows.

The non-dimensional flow number characterizing the shedding process also from single cylindrical obstacles is the *Strouhal number* given by $St = D/(T_P\, U)$. In unbounded cylinder wake flows the Strouhal number is usually depending on the cylinder Reynolds number Re_D, which in turn has been associated to the detail of the flow phenomenon. For instance, the v. Kármán vortex street emerging from laminar wake boundary layers is related to $80 < Re_D < 200,000$. For more detail on unbounded cylinder wakes the reader is referred to various fluid-mechanical text books, to the monograph of Zdravkovich (1997), or to a review paper like Chen (1973). Also for cylinder wakes in shallow shear flow the frequency of the global instability depends on the specific typology of the wake. In contrast to unbounded wakes, the main parameter characterizing the flow behavior of a shallow wake is the wake stability number $S = c_f\, D/h$ that can be used to categorize the different shallow

wake instability classes (VS, UB, and SB). The stability parameter in turn depends both on Re_D and Re_h, i.e. $S = f\,(Re_D, Re_h)$ (see Section 5.2.2, esp. Figure 5.4 on page 133). For a vortex street-like shallow wake, $S \to 0$, the stability parameter becomes Re_h–invariant, i.e. the wake typology approaches that of unbounded wakes depending solely on Re_D.

Figure 7.5 displays the Strouhal number of shallow wake flows of different wake instability, and thus, of different S. The data was evaluated from our LDV measurements (full symbols), and from visualizations as reported by Chen & Jirka (1995)(empty symbols). A dashed line indicates a linear approximation proposed by Chen & Jirka (1995) that is roughly a constant $St \approx 0.21$ for VS wakes with $S < 0.2$, and linearly increases in the range of UB wakes up to $St\,(S = 0.55) \approx 0.42$. Note that we observe a large variability of St even for similar S which can not be accredited to measurement uncertainties, but may be considered the result of small initial perturbations up-stream of or immediately at the cylinder, or addressed to a Re_D–dependence.

In order to obtain the corresponding *macro length scale* ℓ_0 we can employ a coordinate transformation from a Eulerian frame to a Lagrangian frame moving with the mean advection speed of the largest structures comprising the coherent flow field.[4] Here, we use the ambient flow velocity U_{amb} as an advection speed—an assumption that is asymptotically correct for the wake far-field. The values of ℓ_0 are much larger than the water depth and even larger than the cylinder diameter (i.e. the initial wake width), thus $\ell_0 > D > h$. The relative macro length scale ℓ_0/D ranges from about 5 in vortex street-like shallow wakes down to about 2.5 in SB wakes. Since $\ell_0/D = U\,\tau_0/D = St^{-1}$, the remarks on the Strouhal number given above also apply to the macro length scale. If we would use the local mean flow velocity $\langle u \rangle$ instead of the ambient flow velocity as a characteristic velocity, then the resulting macro length could be regarded as the 'wave' length of the periodic flow field.

Micro scales of turbulence. In Section 6.3 also well-established micro scales of turbulence have been introduced. Though, in general, they are hardly capable of measurement in 3D turbulent flow, good estimates have been given for homogeneous turbulence. These estimates relate the micro length scales to a macro length scale ℓ_0 of the flow using a macro scale turbulence Reynolds number $Re_{\ell_0} = k^{1/2}\,\ell_0/\nu$, (6.59a). Then, the *Taylor micro length* $\ell_{\lambda l}$, and the *Kolmogorov micro length* ℓ_η are given by Equations (6.60a) and (6.60b), respectively. In the case of a shallow wake flow, susceptible to a two–length–scale decomposition, we considered the small-scale random turbulent flow to be crucial for the estimation of Re_{ℓ_0} assuming locally isotropic turbulence in the high wave-number range. Then, the macro turbulence scales of length and velocity

[4] Changing from a fixed to a moving reference frame just means a transition from a temporal to a spatial domain. This does not involve Taylor's hypothesis of 'frozen turbulence'.

became $\ell_0 = h$ and $k = 1/2\left((2.3 + 1.63 + 1.27)/2.3\right)^2 \left\langle u_r^2 \right\rangle = 2.56 \left\langle u_r^2 \right\rangle$ (cf. Equation (5.8)). Additionally, we employed an estimate for the turbulence intensity of $TI = \sqrt{\langle u_r^2 \rangle}/U = 0.05$.[5] The *Batchelor micro length scale of scalar fluctuations* ℓ_{η_γ} delineating the smallest diffusive structures of the flow has been defined by (6.66) for high Schmidt-number flows, i.e. $\nu \gg D_m$. Then, ℓ_{η_γ} is related to the Kolmogorov micro length scale through the Schmidt number $Sc = \nu/D_m$ as $\ell_{\eta_\gamma} = \ell_\eta \, Sc^{-1/2}$, (6.65). Assuming $Sc \approx 1,500$ for the flows under consideration, ℓ_{η_γ} is given in Table 7.2 for various wake flows together with the corresponding micro length scales of velocity fluctuations. While the diffusive micro length ℓ_{η_γ} is of the order of 10 µm, the Kolmogorov scale ranges at about 0.6 mm, whereas the Taylor micro scale amounts to 20% to 25% of the water depth.

In order to obtain *micro time scales* Taylor's 'frozen turbulence' hypothesis has been applied to the appropriate micro length scales. Table 7.2 lists the appropriate values of $\tau_{\gamma l}$, τ_η, and τ_{η_γ}. The Taylor micro time is in the range of 40 ms to 50 ms, the Kolmogorov time scale is a full order of magnitude smaller, and Batchelor's diffusive time scale is estimated to about 100 µs. With respect to both the temporal and the spatial resolution the Batchelor scales of mass fluctuations are not capable of measurement using the present LIF equipment (cf. also Section 4.2). The dissipative micro scales could have been resolved by

[5] If the macro turbulence scales would be obtained from the full flow field, they would predominantly represent the large-scale coherent motion, e.g. $\ell_0 = U T_P$ and $k = 1/2 \left\langle u^2 + v^2 \right\rangle$. Using $\sigma_u \approx 0.25\,U$ the order of magnitude of the micro length scale estimates would remain the same, though values of $\ell_{\lambda l}$ then would extend the water depth.

Table 7.2. Estimates of micro scales of time and length were calculated for different wake flow conditions using homogeneous turbulence approximations. The Taylor length scale $\ell_{\lambda l}$ and the Kolmogorov dissipative length scale ℓ_η were evaluated from (6.60a) and (6.60b), respectively, using macro turbulence scales characterizing the 3D random turbulent flow. Batchelor's diffusive length scale $\ell_{\eta\gamma}$ was obtained from the high–Schmidt–number approximation (6.65). All corresponding micro time scales were estimated employing Taylor's hypothesis of 'frozen turbulence'.

series	**micro scales**					
	time			**length**		
	τ_λ [s]	τ_η [s]	$\tau_{\eta\gamma}$ [s]	ℓ_λ [mm]	ℓ_η [mm]	$\ell_{\eta\gamma}$ [mm]
18_vs06	0.047	4.8E-03	1.2E-04	6.1	0.63	0.016
25_vs07b	0.039	3.5E-03	9.1E-05	6.4	0.57	0.015
25_vs07c	0.039	3.5E-03	9.1E-05	6.4	0.57	0.015
17_ub25	0.050	5.3E-03	1.4E-04	6.1	0.65	0.017
18_sb51	0.047	4.8E-03	1.2E-04	6.1	0.63	0.016

the employed 2D LDV system (cf. Section 4.1 for a spatial definition of the measurement volume), if a mean sampling rate of twice the highest fluctuation frequency (i.e. about 400 Hz to 550 Hz) would have been achieved. In the present study detailed examinations of the dissipative and diffusive ranges were not intended, hence, for all measurements a mean sampling rate of 100 Hz was guaranteed, and the data were re-sampled at this rate. Reliable power spectral estimates were obtained up to 25 Hz. Finally, albeit not conducted in this study, using the present LDV data the Taylor micro time scale could be evaluated by fitting the defining parabola (6.55) to the correlation coefficient r_{uu} for time lags $\tau \to 0$.

7.1.4 Downstream development of coherent and random transport of momentum and mass

Due to the immense transverse shear at the cylinder a considerable amount of kinetic energy is extracted from the shallow base flow and transferred to the fluctuating motion of the wake flow. As the flow advects downstream in the cylinder wake, the TKE produced at the obstacle is dissipated due to the bottom-induced vertical shear. In Figure 7.6 the longitudinal development of the TKE is presented for the different wake stability classes, as reported by v. Carmer et al. (2001). Following common practice, the *horizontal part of the mean TKE* has been non-dimensionalized by the corresponding local mean kinetic energy, i.e. $k^+ = \left(\langle u'^2\rangle + \langle v'^2\rangle\right) / \left(\langle u\rangle^2 + \langle v\rangle^2\right)$. Note that k^+ will represent also the *total TKE* in shallow wake flows dominated by large-scale horizontal quasi-periodic motion in good approximation, since in such flows $\mathcal{O}\left(w'^2\right) \ll \mathcal{O}\left(u'^2\right) \leq \mathcal{O}\left(v'^2\right)$ (cf. also Figure 7.8) and $\langle w\rangle = 0$. Large symbols denote values obtained at the wake centerline, small symbols denote ambient flow values outside the wake. The +, ◊, and Δ symbols indicate shallow wake flows of the stability classes VS, UB, and SB, respectively.

Compared to the ambient flow the k^+ shows significantly higher values within the different wakes. The dissipation of TKE follows a power-law decay, i.e. $k^+ \propto x^{-n}$. The level of the ambient TKE is reached after approximately $x_e = 20$ cylinder diameters in the case of VS instability ($S = 0.07$), which is significantly faster than for unbounded cylinder wakes. For an UB class wake ($S = 0.25$) the re-stabilization of the flow occurs after about $x_e = 10D$, and for $S = 0.51$ (UB-SB transition of wake instability class) at $x/D = 5.5$ the additional TKE of the flow is dissipated almost completely. Following Chen & Jirka (1995), the *momentum recovery distance* x_e may be defined as the distance for which the momentum deficit M_s of the mean flow has decreased to $1/e$ of the initial momentum deficit M_{s0}. The decrease of the additional TKE at the wake center line due to bottom friction–induced dissipation is then con-

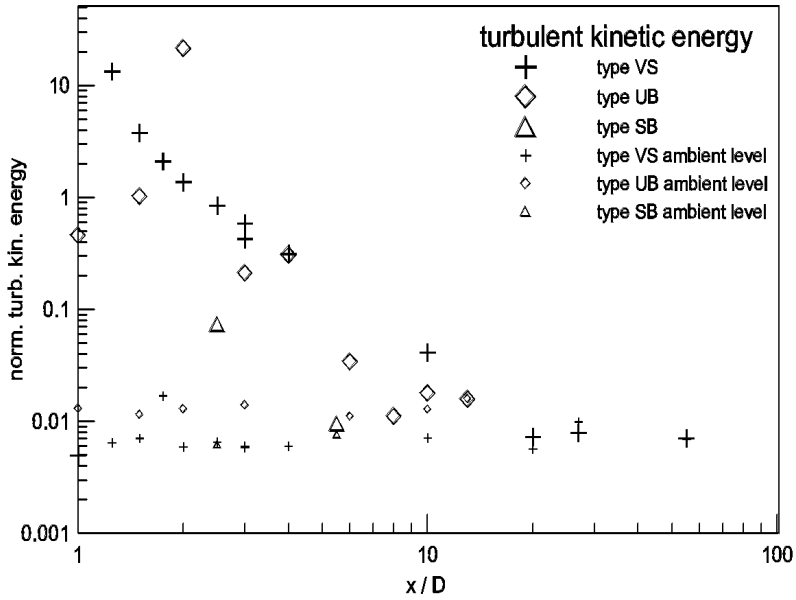

Figure 7.6. Production and decay of normalized turbulent kinetic energy along the centerline of shallow wakes with different instability classes. (v. Carmer et al., 2001)

sistent with the estimate[6] $x_e/D \approx 2/S = 2h/(c_f\, D)$ for the recovery distance of the momentum deficit. Obviously, a *friction length scaling* $x^* = c_f\, x/\,(2h)$, as applied for the analytical description of wake flows in Section 8.3.3, will be more appropriate to describe the dissipation of the energy-containing large-scale structures via bottom roughness-induced small-scale turbulence.

Normalization of k by local mean values results in $k^+ \to \infty$ for local mean longitudinal velocity component $U \to 0$, since also $V = 0$ at the wake centerline. Thus, very high values of k^+ in Figure 7.6 indicate a downstream stagnation point, which is found at the cylinder perimeter ($x/D = 0.5$), and for UB and SB wakes at the end of the recirculation zone. For instance, the UB wake instability shows its maximum value $k^+ \approx 20$ at $x/D = 2$. The decrease of k^+ has to be addressed partly to the increase of the center line velocity especially in the vicinity of the cylinder. Therefore, in order to represent the TKE decay within the wake rather than the asymptotical far-wake behavior, k will be non-dimensionalized by the appropriate mean values of the ambient flow.

In order to examine the role of the large-scale organized flow field for the transport or momentum and mass, the TKE and the mass variance can be computed from the triple-decomposed velocity components and mass concentrations. For the *normalized mass variance* $\left\langle c'^{\,2}\right\rangle^+$ we obtain

$$\frac{\left\langle c'^{\,2}\right\rangle}{\langle c\rangle^2} = \frac{\left\langle c_p^{*2}\right\rangle + \left\langle c_r^2\right\rangle + 2\left\langle c_p^*\, c_r\right\rangle}{C^2}\ . \tag{7.7}$$

Similar decompositions apply to other squared quantities like mass fluxes or TKE.

[6] x_e is easily obtained from Equation (8.65) for $M_s^* = e^{-1}$.

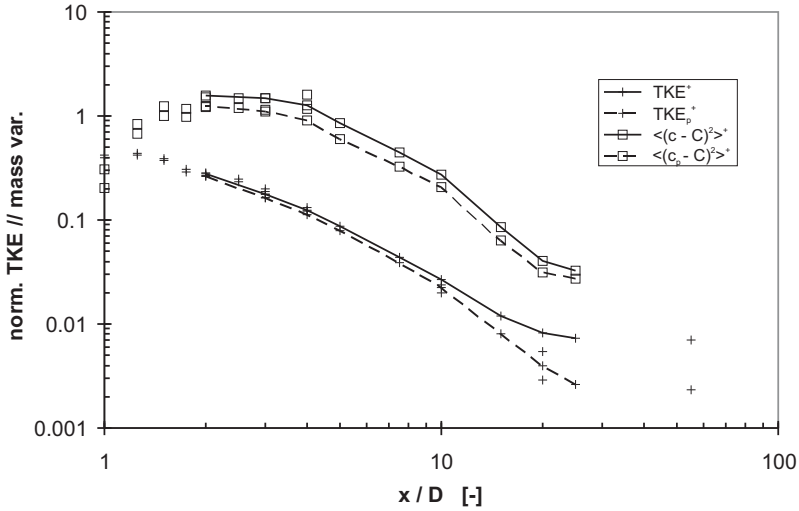

Figure 7.7. Production and decay of normalized turbulent kinetic energy and of mass variance along the centerline of vortex street-like shallow wakes (series 25_vs07b, 25_vs07c, 18_vs06).

In Figure 7.7 total values of the TKE and of the mass variance are compared to the appropriate large-scale periodic values of a vortex street-like wake flow (series 25_vs07b and 25_vs07c). + and □ symbols indicate k^+ (here normalized by mean ambient values) and the mass variance ${\sigma_c^2}^+$ given by (7.7). Full lines denote total values, dashed lines denote large-scale coherent parts only. The turbulent kinetic energy k^+ in the near-field of the wake amounts to more than 40% of the mean advective kinetic energy of the ambient flow. The coherent part of k^+ decreases from 94% to 85% at $x/D = 10$ in the near wake. The cross-band term amounts to generally $2\left\langle u_{p,i}^* \, u_{r,i}\right\rangle / U_i < 0.01$. The coherent part of k^+ therefore decays slightly faster than the total TKE. The dissipation of the total k^+ follows a power law dependency, $k^+ \propto x^{-n}$, where $n = 1.55$ for this wake flow. The decrease starts almost immediately at $x/D = 1.25$. In decaying grid-generated turbulence usually decay exponents $1 \leq n \leq 1.4$ have been observed, recently $n = 1.33$ has been reported by Zhou et al. (2000). For grid turbulence in shallow water flow Uijttewaal & Jirka (2003) confirmed a decay exponent of $n \approx 1.3$ to 1.5 in agreement also with experiments on grid-generated turbulence in soap-film flows.

In contrast, the *mass variance* $\left\langle c^2\right\rangle^+$ does not display a predominant power-law decay, though in decaying grid turbulence such a decay has been observed (e.g. $m = 1.36$ for temperature in air (Zhou et al., 2000)). From the total mass variance we could obtain $m = 1.71$ for $4 \leq x/D \leq 10$. Note also that, compared to k^+, the decay of the mass variance starts later, beyond $x/D = 3$. Values are generally larger by an order of magnitude, the maximum value is about 150% of the local mean value. The portion of the coherent variance is 75% of the total variance, the cross-band variance (third term on right-hand-side of (7.7)) is always less than 1.5%. At $x/D = 20$ the turbulent kinetic energy is already completely extracted from the large-scale structures, still the normalized mass variance amounts to about 0.4. Further mixing of mass in the

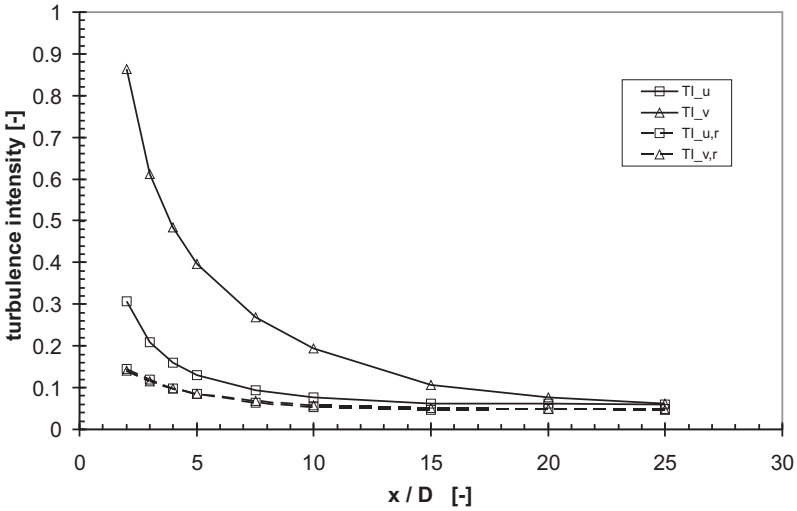

Figure 7.8. Coherent and random turbulence intensities in VS wake (series 25_vs07c).

wake flow field takes place only with the mechanisms of small-scale turbulent and molecular diffusion.

A widely-used measure for the strength of the fluctuating activity of the flow is the *turbulence intensity TI* defined as the standard deviation of a flow component normalized by its mean value, i.e. for instance for the main velocity component $TI_u = \left\langle u'^{\,2} \right\rangle^{1/2} / \langle u \rangle = \sigma_u / U$. Obviously, in shallow wakes the additional TKE induced locally at an obstacle will re-organize and dissipate again, as the flow advects downstream. The longitudinal *inhomogeneity* is drastically illustrated in Figure 7.8 from the distribution of the total turbulence intensities of the horizontal velocity components indicated by full lines. The inhomogeneity in x-direction which is very pronounced in the wake near-field vanishes in the wake far-field. Similarly, the transverse inhomogeneity in the y-direction initially will be very strong, but will equalize as the ambient flow is approached outside and downstream of the wake.

The values of TI_u and TI_v, denoted by $\square$ and Δ symbols, respectively, indicate a strong *anisotropy* of the horizontal turbulence field. In the near-wake the transverse intensity amounts to three times the longitudinal intensity, e.g. at $x/D = 2$ $TI_u = 0.3$ and $TI_v = 0.9$. The level of the ambient equilibrium shear flow of $TI = 0.06$ is reached at $x/D = 15$ and $x/D = 25$ by the longitudinal and transverse intensities, respectively.

From the decomposed velocity components the small-scale random and large-scale coherent turbulence intensities have been computed. It is found that the small-scale random turbulence (dashed lines in Figure 7.8) is horizontally isotropic, i.e. $TI_{u_r} = TI_{v_r}$. The level of background turbulence is reached after $x/D = 10$.[7] Hence, the anisotropy is introduced solely by the strong large-scale coherent turbulence fields. The intense mixing and exchange

[7] The downstream asymptotic value of $TI_{u,r} = TI_{v,r} \approx 0.05$ is slightly lower than the total value of the base flow turbulence. This results from the method of decomposition

processes in the wake of a cylinder, that are induced by the large-scale coherent flow field, tend to homogenize the small-scale random turbulence, as to prevent the anisotropy of plane equilibrium shear flows (cf. also Section 5.3.2). Also in shallow grid-generated turbulence, examined at similar flow conditions in the shallow–flow–facility, the horizontal anisotropy has been observed in the immediate near-field of the grid ($x/D < 5$), where 2D-LCS did not jet interact (Uijttewaal & Jirka, 2003).

At the end of the shallow wake flow—at about $x/D = 25$ for series 25_vs07—the turbulence field can be regarded as homogeneous and isotropic, which results from the intense shear induced by the large-scale quasi-periodic motion of the flow leading to re-distribution of the TKE along the wave number range and dissipation at high wave numbers. The vertical turbulence intensity comprising only the small-scale random part is expected to be of the order of the horizontal random intensities within the wake flow, i.e. $\mathcal{O}\left(\langle w^2\rangle\right) = \mathcal{O}\left(\langle u_r^2\rangle\right) = \mathcal{O}\left(\langle v_r^2\rangle\right)$. Further downstream an undisturbed plane equilibrium shear flow establishes again, revealing also the characteristic anisotropy of the turbulence intensities. For series 25_vs07 at $x/D = 55$ the transverse turbulence intensity is $TI_v = 0.76\, TI_u$, whereas the intensity ratios of plane equilibrium shear flow are $TI_v/TI_u = 0.71$ and $TI_w/TI_u = 0.55$ (Nezu & Nakagawa, 1993).

In order to access the *mean mass flux* in longitudinal flow direction besides a Reynolds decomposition $\langle uc\rangle = UC + \langle u'c'\rangle$ also a triple-decomposition can be applied, i.e.

$$\langle uc\rangle = UC + \left\langle u_p^* c_p^*\right\rangle + \langle u_r c_r\rangle + \left\langle u_p^* c_r\right\rangle + \left\langle u_r c_p^*\right\rangle \ . \tag{7.8}$$

It is found that in shallow cylinder wakes the dominating part of the mean longitudinal mass flux is associated with the total of the steady-advective and large-scale coherent parts (first two terms on right-hand-side of (7.8)). The small-scale random part (third term) is insignificant (of order $\mathcal{O}\left(10^{-3}\right)$ with respect to the total flux). Both cross-correlated 'inter-regime' fluctuation terms are again orders of magnitude smaller than the small-scale turbulent flux (of orders $\mathcal{O}\left(10^{-5}\right)$ and $\mathcal{O}\left(10^{-4}\right)$), and therefore completely irrelevant for the total mass flux.

The dynamics of the mean mass fluxes are of interest especially in the transverse direction, since because of symmetry $\langle vc\rangle = 0$ along the wake centerline. The *mass flux variance* in the longitudinal direction is given by

$$\begin{aligned}\left\langle (uc)'^2\right\rangle &= \left\langle (uc)^2\right\rangle - \langle uc\rangle^2 \\ &= 2\,UC\left\langle u'c'\right\rangle + U^2\left\langle c'^2\right\rangle + C^2\left\langle u'^2\right\rangle\end{aligned}$$

(polynomial fit in moving window) used to obtain the data of Figure 7.8. A different parametrization or a more advanced filtering technique will avoid this effect.

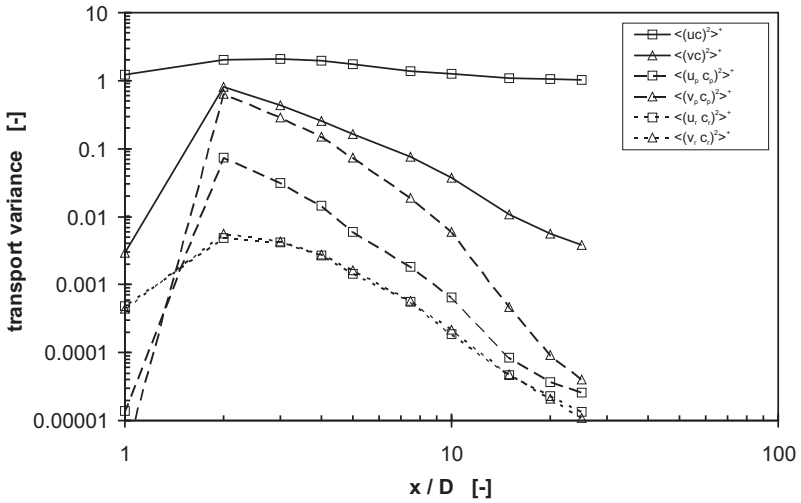

Figure 7.9. Variance of the horizontal mass transport at different downstream positions along the centerline of a shallow VS wake (series 25_vs07c). □ and Δ symbols denote the longitudinal and transverse mass transport, respectively. Full, dashed, and dotted lines indicate the variances of total, coherent, and random values. All variances are non-dimensionalized by the squared longitudinal mean–advective mass flux.

$$+2\,U\left\langle u'c'^2\right\rangle + 2\,C\left\langle u'^2c'\right\rangle + \left\langle u'^2c'^2\right\rangle - \left\langle u'c'\right\rangle^2 \quad . \tag{7.9}$$

In the transverse direction because of $V = 0$ only one double-correlation term, one triple-correlation term, and the quadruple-correlation terms will remain. In Figure 7.9 full lines and □ and Δ symbols indicate the mean mass flux variances in the longitudinal and transverse direction, respectively. All displayed variances have been non-dimensionalized by the squared mean-advective mass flux, $(UC)^2$. The dynamics of the longitudinal mass flux is slightly higher than that of the transverse flux. Note that—corresponding to the velocity and mass fields—in the wake near-field the mass transport is of significant variability in both horizontal directions.

Inherent to the mathematical definition of a variance—a Reynolds decomposition is employed on the velocity and mass components comprising the mass flux given by (7.9). Of course, the mean mass flux variance can also be expressed in terms of triple-decomposed fluctuations, i.e. e.g. $u' = u_p^* + u_r$. The variances resulting from coherent and random parts, i.e. $\left\langle \left(u_p^* c_p^*\right)^2 \right\rangle$ and $\left\langle (u_r c_r)^2 \right\rangle$ respectively in the longitudinal direction, are denoted by dashed and dotted lines in Figure 7.9. In the transverse direction the coherent mass flux variance is greater than in the longitudinal direction indicating the anisotropy of the large-scale fluxes, and prominently contributes to the full mass flux variance $\left\langle (vc)'^2 \right\rangle$. On the contrary the random flux variance is horizontally isotropic, and can be neglected for the representation of the mass flux variances.

Shallow wake flows—as a prominent class of *double shear flows*—have to be characterized not by a single but by two length scales ℓ_0 representing the

transverse and the vertical shear, namely D and h. Although different strategies can be employed to separate the large-scale coherent quasi-periodic flow field from the small-scale random turbulent fluctuations, some general remarks will commonly apply to the analysis of turbulence in shallow wake flows.

- The large-scale coherent and the small-scale random regimes of fluctuations can be separated both in the velocity fields and in the scalar fields. The cross-correlated 'inter-regime' part of compound mean quantities, i.e. $\langle c_p^* \, c_r \rangle$, is generally negligibly small compared to the 'inner-regime' parts.
- For predominating large-scale coherent structures in the flow these are crucial for the energy and mass balance and re-distribution of the flow. They may comprise almost the total amount of a quantity distributed over the two wave-number regimes.
- The small-scale random part of the wake flow fields are of the order of magnitude of the ambient equilibrium shear flow. In the wake far-field these values will be approached asymptotically.
- The anisotropy is due to the large-scale periodic fluctuations only. The intense mixing processes in the wake flow homogenize the small-scale random turbulence field that reveals perfect isotropy.

7.2 Spectral density estimates in shallow wake flow

Employing the filtering and averaging techniques described in Appendix A, reliable estimates of the 1D spectral density distributions of the velocity and mass concentration data have been calculated, as is exemplified in Figure 7.10 for a VS wake (series 25_vs07c) at a downstream centerline position of $x/D = 5$. The data has been separated into 5 shorter data blocks using an overlap of 50%. A *Kaiser-Bessel window*—Equation (A.3) with $\alpha = 3.0$—has been applied to minimize noise introduced by discontinuities at the ends of the data blocks. Thus, a *block-averaging* over 5 blocks has been conducted in order to improve the quality of the spectral estimates in the desired frequency range. To further smooth the PSD estimates, *band-averages* over 7 neighboring frequency bands have been calculated at the expense of frequency resolution.

Also spectral density estimates can be presented in non-dimensional form to allow for better comparison between different realizations. Hence, the spectral estimates may be normalized by characteristic length and time scales of the flow under consideration. In the present case of shallow wake flows multiple scales are of relevance. Different macro length scales describe, for instance, the production of kinetic energy by large-scale 2D coherent fluctuation ($\mathcal{L} = D$) and by 3D random turbulence ($\ell_0 = h$), micro length scales like ℓ_η characterize the transport and dissipation in the inertial and viscous subranges of isotropic turbulence. While illuminating phenomena in one part of the frequency range,

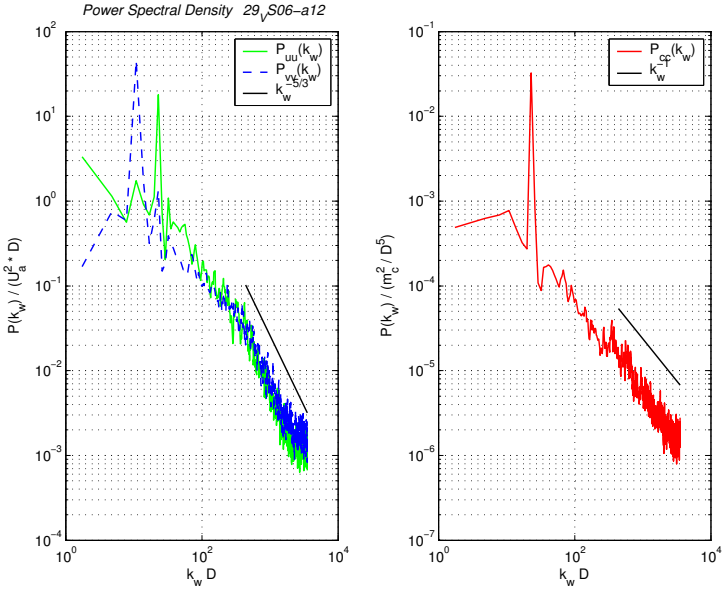

(a) Normalized 1D auto-PSD $P_{u_i u_i}(k_w)$ and $P_{cc}(k_w)$

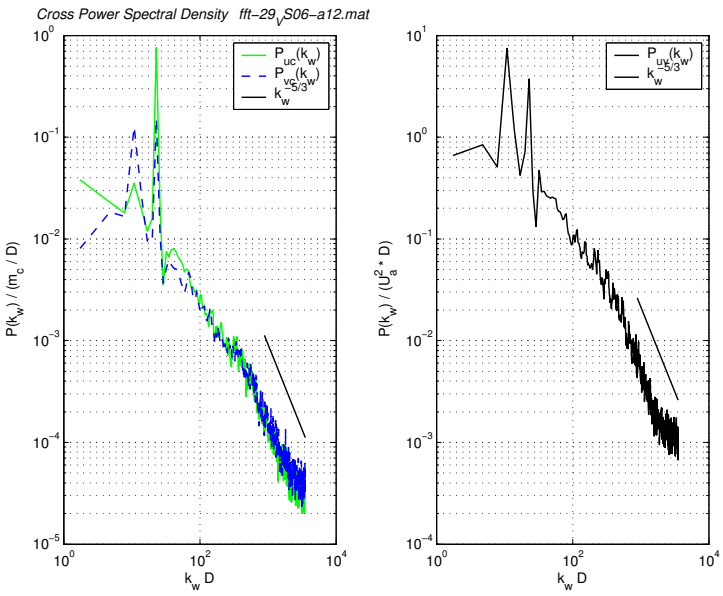

(b) Normalized 1D cross-PSD $P_{u_i c}(k_w)$ and $P_{u_i u_j}(k_w)$

Figure 7.10. The 1D power spectral density distributions of a vortex street-like shallow wake flow (series 25_vs07c) are calculated from a combined LDV-LIF measurement (duration $T = 600$ s, re-sampling frequency $f = 100$ Hz) at the downstream position $x/D = 5$ on the wake centerline ($y/D = 0$). The normalized PSDs were computed by using shorter data blocks extracted from the data set by a Kaiser-Bessel filter window (A.3) with $\alpha = 3.0$ and with an overlap of 50%. Thus, a block-averaging over 5 blocks has been conducted in order to improve the reliability of the spectral estimates. To further improve the PSD estimates, a band-averaging over 7 bands was applied. Figure (a) illustrates the auto power spectra of the measured quantities, whereas Figure (b) shows the corresponding cross power spectral distributions. The upper left plot shows the PSD estimates of the measured velocity components in the main direction u (full green line) and in the transverse direction v (dashed blue line), the upper right plot shows the PSD of the mass concentration fluctuations c (full red line). For the normalization we used characteristic large scales of the mean flow.

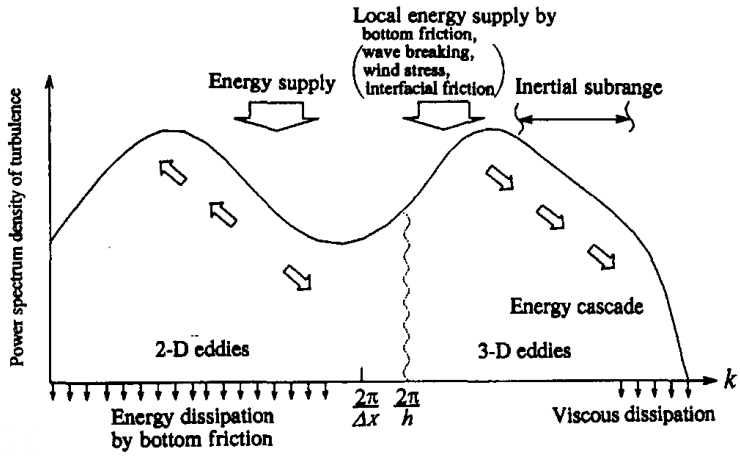

Figure 7.11. The duality of large-scale coherent fluctuation and small-scale random turbulence in shallow free–surface shear flows is clearly reflected in the spectral density estimates. It can be captured conceptually in a dual spectral structure of turbulence (Nadaoka & Yagi, 1998, Fig. 2).

another part may be obscured. In Figure 7.10 we used a normalization by macro flow scales, D and U_a. Then, the wave number scales as a Strouhal number, $k_w D = 2\pi D/\lambda = 2\pi f D/\bar{U}$. This kind of normalization is well suited to compare the 2D coherent flow part, but will be of no use in the higher wave number range.

In Figure 7.10(a) the *1D auto-power spectral density* estimates of the horizontal velocity components u and v are indicated in the left-hand plot by a green full line and a blue dashed line, respectively. The right-hand plot depicts the auto-PSD of the mass concentration, P_{cc}. Furthermore, also *1D cross-power spectral density* estimates can be computed, as shown in Figure 7.10(b). The left-sided plot displays the cross-spectra between velocity components and mass, P_{uc} and P_{vc}, the right-side plot shows the velocity cross-spectrum, P_{uv}.[8]

7.2.1 Spectral structure of turbulence in shallow wake flow

The duality of large-scale 2D coherent fluctuations and 3D random turbulent motion in the turbulence fields of shallow shear flows is reflected also in the spectral domain. The concept of a *dual spectral structure of turbulence* (cf. Figure 7.11) has been incorporated in two-length-scale turbulence models for 2D LES in order to numerically simulate the dynamics of large-scale vortical structures in shallow shear flows (e.g. Nadaoka & Yagi, 1998; Babarutsi & Chu, 1998). In the present case of turbulent shallow wake flows induced by a single obstacle, a distinct spectral distribution of turbulent fluctuations of velocity and mass may be observed, as discussed below and summarized in Table 7.3.

[8] The physical meaning of the cross-spectral density estimates is unclear in the context of turbulence and transfer of TKE and mass. Thus, we will refrain from showing cross-spectra in the present study.

Spectral range of large-scale coherent fluctuation. In the range of low frequencies for $f < U/h$ the turbulence field is dominated by large horizontal eddies ($\ell > h$) shedding off quasi-periodically from the obstacle, and constituting the low-frequent coherent part of the flow. This coherent motion and its associated transport of energy and mass can be described using concepts of 2D isotropic turbulence. Though in general, turbulence is far from being isotropic, 'locally' in the low wave number range, where vertical fluctuations are absent, the motion can be regarded as *horizontally isotropic*.

In the most unstable case of a vortex street-like wake instability (VS) kinetic energy is extracted from the mean flow, and introduced to the fluctuating flow field at a frequency or at a wave number predefined by the cylinder Strouhal number, i.e. $f_i = St\,U_a/D$, and with Taylor's hypothesis, $k_{w,i} = 2\pi\,St/D$, respectively. Though in an Eulerian frame the *energy forcing* is continuous (located at the obstacle), the coherent motion of the large horizontal eddies should rather be regarded as decaying turbulence in a Lagrangian frame as the LCS advect downstream with the mean flow. Of course, the LCS will not decay 'freely' due to viscous dissipation, but dissipation is induced by bottom friction. As the LCS advect downstream in the wake of the cylinder they may be considered to experience also an additional—continuous, but decreasing—forcing due to the weak mean transverse shear of the wake flow.

Turning from the topographic forcing at the obstacle for VS wakes to the internal transverse shear forcing of the steady bubble (SB) wakes—and to a minor degree also of unsteady bubble (UB) wakes—, the characteristics of the large-scale eddies growing in the wake shear layers and thus the large-scale 2D turbulence are quite different. In the lateral bubble boundary layers the forcing is more continuous, and not restricted to a fixed wave number. Still, the LCS are subjected to continuous dissipation due to bottom friction, but do not decay freely.

In quasi-2D turbulence, where energy, but also enstrophy are conserved quantities, a double spectral cascade of turbulence may be encountered (cf. Section 6.2.4). For wave numbers $k_w > k_{w,i}$ energy is transferred toward higher k_w following a k_w^{-3} *enstrophy cascade*, Equation (6.38). This represents the influence of the smaller vortical filaments connecting the LCS of alternate sign of vorticity across the vortex street (cf. also Part III). An energy transfer toward higher wave numbers following a k_w^{-3} spectral distribution has already been reported for shallow plane jets (Dracos et al., 1992) and for shallow mixing layers (Uijttewaal & Tukker, 1998; Uijttewaal & Booij, 2000)—representing continuously forced 2D turbulence due to a pronounced mean transverse shear—as well as for shallow grid–turbulence (Uijttewaal & Jirka, 2003)—representing decaying 2D turbulence.

According to *Fjortoft's theorem*, the conservation of energy and enstrophy requires a *double cascade* of 2D turbulence, through which energy will spread

from the forcing wave number $k_{w,i}$ both to lower and higher wave numbers. Consequently, this requires for wave numbers $k_w < k_{w,i}$ that energy will be transferred toward even lower wave numbers along an *inverse energy cascade* (cf. p. 165). This effect would necessitate a mechanism like the merging of eddies of the same sense of rotation to even larger vortices. Since on the one hand in a vortex street co-rotating eddies are permanently separated by shear-dominated regions due to the staggered arrangement (cf. also Part III), and since on the other hand the shear layers of UB and SB wakes are too short to allow significant merging processes, an inverse energy cascade will be missing in shallow wake flows.

In contrast to isotropic purely 2D turbulence, either continuously forced or freely decaying, in bounded 2D turbulence the bottom friction acting as a direct sink of energy may allow for such a 'truncated' double cascade consisting only of an enstrophy cascade into the higher wave number range. By means of the negative work done by the large-scale coherent motion against the bottom friction forces a significant part of the energy associated with the large-scale turbulence is transferred directly to the small-scale bed-generated turbulence without cascading through the 'spectral pipeline' of the intermediate length scales (Babarutsi & Chu, 1991). As indicated in Figure 7.11, the energy extracted from the 2D coherent fluctuations is also regarded as a source of small-scale 3D turbulence (Nadaoka & Yagi, 1998), though the major part of the small-scale TKE is produced directly due to the vertical bottom–induced shear of the mean flow (Babarutsi & Chu, 1998). As will be obvious from the PSD estimates of the decomposed fluctuations (cf. Figure 7.13), the amount of TKE contained in the large-scale coherent motion can easily reach the same order of magnitude compared to the amount contained in the 3D random turbulence. Of course, as the LCS fade away when advected downstream, also the TKE stored in the low-frequent spectral range decreases.

For the diffusion of a passive scalar in 2D turbulence the variance of a scalar quantity has been analyzed in the spectral domain (cf. pp. 166). For high Schmidt number flows ($Sc \gg 1$) the mass variance—contained in forced fluctuations with wave numbers $k_{wi,\gamma} > k_{wi}$ in the range of the enstrophy cascade of TKE—will pass through the *inertial-convective* and *viscous-convective subranges*. The spectral density distribution of mass concentration, $S_{cc}(k_w)$, can be described by Equation (6.40), and follows a k_w^{-1} cascade up to the smallest dissipative length scales.

Spectral range of small-scale random turbulent fluctuation. In shallow turbulent free–surface flows for sufficiently high bulk Reynolds numbers Re_h there exist a range of small length scales $\ell \ll h$, for which fluctuations of velocity and scalar may be approximated by Kolmogorov's concept of *locally isotropic 3D turbulence* in the universal equilibrium range, as introduced in

Section 6.2.2. This requires that—though the instantaneous strain field s_{ij} is anisotropic also at the small scales—, the time-averaged strain field $\langle s_{ij} \rangle$ shows isotropy. In the vicinity of flow boundaries at the bottom and the water surface obviously permanent anisotropy prevails (Uijttewaal & Jirka, 2003), but anisotropy may also be introduced by secondary currents of permanent (or periodic) character.

The spectral density distribution of the kinetic energy in the *inertial subrange* of locally isotropic 3D turbulence is characterized by an energy cascade $S(k_w) \propto k_w^{-5/3}$. Equation (6.26) represents the famous *Kolmogorov -5/3 power law.*

In highly turbulent flows with an universal equilibrium range of local isotropic turbulence also for the scalar fluctuations a wave number range of local isotropy will exist (cf. Section 6.2.3). For high Schmidt number flows the 3D random scalar variance will be re-distributed toward smaller length scales at first in the *inertial–convective subrange*, where both dissipation of TKE and diffusion of scalar variance are still negligible. Then, also the spectral density distribution of the scalar variance follows a $k_w^{-5/3}$ decay, Equation (6.31) describes the proportionality $S_{cc}(k_w) \propto k_w^{-5/3}$. In the *dissipative–convective subrange* at very small scales $\ell_\eta > \ell > \ell_{\eta_\gamma}$, where dissipation by viscosity dom-

Table 7.3. 1D spectral density estimates of horizontal velocity and mass concentration in shallow turbulent wake flows

	1D spectral density estimates	
	of horizontal velocity components, S_{uu}, S_{vv}	of mass concentration, S_{cc}
$D > \ell > h$	**quasi 2D turbulence forced at $k_{w,i}$**	
	inverse energy cascade ($k_w < k_{w,i}$) $S \propto k_w^{-5/3}$ (truncated)	direct scalar cascade $S_\gamma \propto k_w^{-5/3}$ (truncated)
	enstrophy cascade ($k_w > k_{w,i}$) $S \propto k_w^{-3}$	inertial–convective subrange ($\ell > \ell_\eta > \ell_{\eta,\gamma}$) $S_\gamma \propto k_w^{-1}$ dissipative–convective subrange ($\ell_\eta > \ell > \ell_{\eta,\gamma}$) $S_\gamma \propto k_w^{-1}$ (not applicable)
$\ell \ll h$	**3D isotropic turbulence**	
	inertial subrange $S \propto k_w^{-5/3}$	inertial–convective subrange ($h \gg \ell \gg \ell_\eta$) $S_\gamma \propto k_w^{-5/3}$
	dissipative subrange eq. (6.25) (not resolved)	dissipative–convective subrange ($\ell_\eta > \ell > \ell_{\eta,\gamma}$) $S_\gamma \propto k_w^{-1}$ (not resolved)

inates the TKE spectrum but scalar variance is still unaffected by molecular diffusion, the spectral transfer of scalar variance becomes less rapid. It then follows a $S_{cc}(k_w) \propto k_w^{-1}$ re-distribution given by Equation (6.34). As mentioned previously, the spatiotemporal resolution of the LDV-LIF measurement system and setup does not allow to access length scales $\ell \leq \mathcal{O}(\ell_\eta)$.

7.2.2 Spectral density estimates for different shallow wake classes

Shallow turbulent wake flows of the different classes of stability will show a common duality of the structure of turbulence, characterized on the large scales by the quasi-2D behavior of the coherent flow motion generated by the mean horizontal shear and on the small scales by the 3D isotropic behavior of the random turbulence field generated by the bottom–induced vertical shear. As will be elucidated from the plots of Figure 7.12, this duality is reflected in the spectral density distributions of energy and mass observed for the different wake stability classes. As on the small scales all wake flows are subjected to the same mechanisms of 3D turbulence, their PSD estimates will follow the same laws, regardless of the actual wake stability class. However, as the predominating forcing mechanisms for the VS and SB wakes differ, which are responsible for the stability of the large-scale coherent flow field, these are expected also to influence the structure of turbulence on the large scales in different ways.

Spectral density estimates of 3D turbulent fluctuations. For length scales $\ell \lesssim h$ the mean vertical strain of the shallow channel flow, bounded by the bottom and the free surface, will act as a source of TKE. The turbulent energy produced in the lower 3D scale range, then, is spectrally transferred through the inertial subrange of locally isotropic turbulence to be affected by viscosity and dissipated at even smaller scales of the viscous subrange. Consequently, we can identify a transitional wave number or frequency between the 2D and 3D turbulence ranges, i.e. at the low–frequency end of the 3D turbulence range, that will be of the order of $k_{w,h} = 2\pi/h$, or $f_h = \bar{U}/h$, respectively. In the wave number or frequency range $k_w > \mathcal{O}(k_{w,h})$ or $f > \mathcal{O}(f_h)$ the cascades of energy and scalar variance will follow the power laws of locally isotropic turbulence, provided that a sufficiently high bulk Reynolds number Re_h allows for the establishment of a significant inertial subrange. In the framework of this study all laboratory shallow turbulent wake flows displayed transitional frequencies of the order of $f_h = \mathcal{O}(1) \leq U_a/h \approx 7$ Hz.

Figure 7.12 presents 1D power spectral density estimates of the transverse velocity component (left-hand plots) and of the mass concentration (right-hand plots) for wake flows of different stability classes at selected downstream positions along the centerlines of the wakes. Dashed lines indicate power laws of the cascades of 2D and 3D turbulence, as discussed in Section 7.2.1 (cf. also

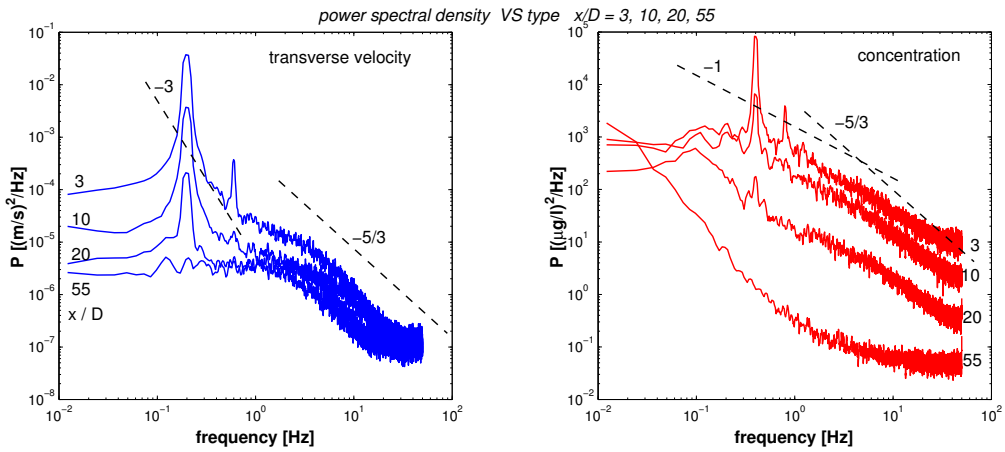

(a) $P_{vv}(k_w)$ and $P_{cc}(k_w)$ of VS wake

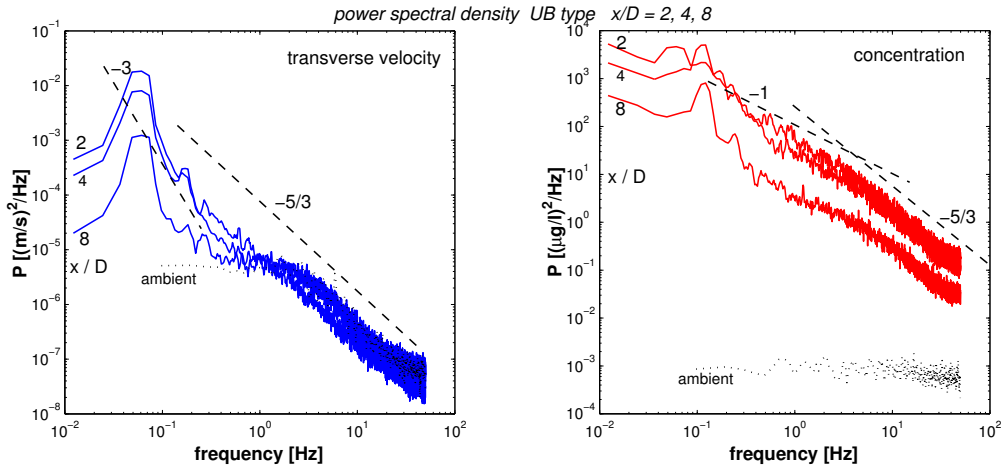

(b) $P_{vv}(k_w)$ and $P_{cc}(k_w)$ of UB wake

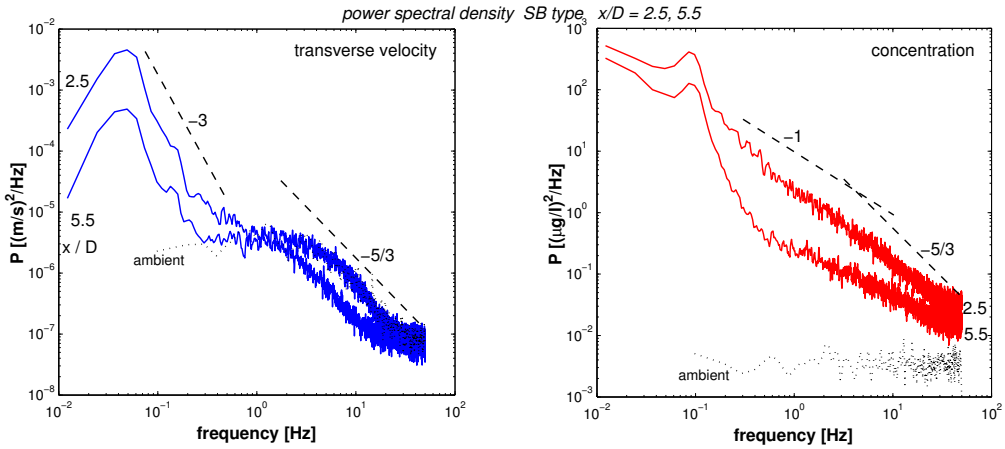

(c) $P_{vv}(k_w)$ and $P_{cc}(k_w)$ of SB wake

Figure 7.12. 1D power spectral density estimates of the transverse velocity component (left-hand plots) and of the mass concentration (right-hand plots) are presented for wake flows of different stability classes. The data has been obtained at selected downstream positions along the centerlines of the wakes. Dashed lines indicate power laws of the cascades of 2D and 3D turbulence (cf. Table 7.3). — (a) Vortex street-like wake (series 18_vs06) at $x/D = 3$, 10, 20, and 55. (b) Unsteady bubble wake (series 17_ub25) at $x/D = 2$, 4, and 8. (c) Steady bubble wake (series 18_sb51) at $x/D = 2.5$, and 5.5.

Table 7.3). Figures 7.12(a), (b), and (c) display PSD estimates for a vortex street-like wake (series 18_vs06) at $x/D = 3$, 10, 20, and 55, for an unsteady bubble wake (series 17_ub25) at $x/D = 2$, 4, and 8, and for a steady bubble wake (series 18_sb51) at $x/D = 2.5$, and 5.5, respectively.

Regardless of the stability class all shallow turbulent wake flows display an energy cascade in the 1D PSD estimates of the transverse velocity component that follows the Kolmogorov -5/3 power law, Equation (6.26), and indicates the existence of an inertial subrange. This also applies to the 1D PSD estimates of the longitudinal velocity component, as can be seen, for instance, from the example VS wake data presented in Figure 7.10. Consequently, all examined wake flows encounter an inertial–convective subrange of scalar transport and mixing, in which the mass variance also cascades toward higher wave numbers following a -5/3 power law, Equation (6.31). Due to the restrictions in the spatiotemporal resolution of the LDV-LIF measurements the dissipative subrange, delineated by the Kolmogorov scales of length and time, ℓ_η and τ_η, cannot be inferred from the calculated PSD estimates P_{vv}. Moreover, albeit due to the high Schmidt number an viscous–convective subrange will exist, also its more gradual -1 power law decay is not resolved in the spectral estimates of the mass variance.

Spectral density estimates of low-frequent fluctuations. The low-frequent coherent motion of the wake flow is generated by the mean horizontal strain field induced by a single blunt obstacle, that immediately becomes unstable on the large scales. Regarding the forcing of the *large-scale* or *global instability* of a shallow shear flow, different mechanisms have been distinguished by Jirka (1998, 1999, 2001) (cf. Section 2.2.3). As introduced in Section 2.3, in shallow wake flows, on the one hand, we observe a *topographic forcing* with only small regions of *absolute instability* located immediately at the cylinder perimeter, which result in alternate shedding of large vortices directly from the obstacle that form a vortex street when advected downstream—constituting a large region of *convective instability*—. On the other hand, for more stable shallow wakes the region of absolute instability develops into a recirculation zone which is attached to the cylinder. Due to *internal transverse shear forcing* vortical structures then grow in the lateral shear layers of the recirculation bubble, and in the case of an UB wake they roll-up engulfing part of the bubble and separate from the downstream bubble end to form the convectively unstable vortex street-like wake. If in the case of a SB wake the internal shear forcing is weak compared to the damping by bottom friction, the LCS in the bubble shear layers will not contain enough energy to roll-up and merge at the end of the bubble, so that the wake remains stable at the large scales. The roll-up mechanisms of UB wakes as well as the stabilization due to bottom

friction has been visualized by Negretti (2003b). More detail on the global instability of shallow wake flows will be given in Section 9.2.

As has been reported by v. Carmer & Jirka (2001), the spectral structure of shallow turbulent wakes on the large scales reflects some aspects of 2D turbulence. However, other structural aspects of 2D turbulence are missing in the spectral imprint of shallow wakes, as argued in Section 7.2.1. Since shallow wake flows differ significantly regarding their large-scale coherent flow fields—because of different kinds and strengths of the forcing mechanism and different strengths of the dampening, resulting even in a different global stability regime—, we will surely expect also the spectral structure of turbulence to be affected in the low frequency range, and to reflect such differences.

The forcing of the large-scale coherent motion of the wake flow is introduced at a frequency f_i given by the Strouhal number of the global wake instability, i.e. $f_i = St\,U_a/D$ the shedding frequency of the LCS. Due to the organization of the LCS in a vortex street-like arrangement further growth of the eddies due to merging is effectively prevented, as has been discussed in the previous section and will be illustrated in Part III also from the field-wise observations. Hence, no *inverse energy cascade* occurs in shallow VS and UB wakes. As in SB wakes the transverse shear forcing is weak compared to the stabilizing influence of the bottom friction–induced viscous dissipation, also in the PSD estimates of SB wakes no inverse cascading of energy toward lower wave numbers can take place.

On the other hand, for a frequency range larger than the excitation frequency, but still smaller than the transition frequency toward 3D turbulence, i.e. $f_i < f < f_h$, TKE can be spectrally transferred following a -3 *enstrophy cascade* given by Equation (6.38). This represents the effect of smaller vortical filaments connecting the primary LCS. Vortex street-like wakes are characterized by a very narrow spectral peak with steep edges indicating very pronounced LCS with rather weak connecting vortical filaments, which can be understood rather as isolated LCS living in an enhanced background turbulence field. As the coherent flow field is advected downstream, its energy is dissipated due to bottom friction, with the weak filaments disintegrating quickly. Hence, an enstrophy cascade is hardly encountered in VS wakes. On the contrary, in unsteady and steady bubble wakes LCS are evolving continuously in the detached bubble shear layers, which results in a broader variety of sizes of large-scale eddies. This also allows for a more significant enstrophy cascade in UB and SB wakes (cf. Figures 7.12(b) and (c)).

The transition between the the spectral ranges of 2D and 3D turbulence takes place following a very gentle decline, which approaches the constant 1D spectral energy distribution of 3D turbulence at low wave numbers, $S_{vv}(k_w) \propto k_w^0$. This may be regarded as a strong indication that the coherent TKE contained in the low wave number range of the PSD estimates is dissi-

pated directly due to bottom friction instead of cascading down the 'spectral pipeline' into the viscous subrange.

The spectral density estimates of the mass variance of the coherent flow field clearly show the two-dimensional structure at the large scales. In shallow wakes of all stability classes the spectral mass transfer follows a -1 power law decay given by Equation (6.40). A significant amount of mass variance is concentrated at the frequency of the primary LCS as long as they exist. Remarkably and in contrast to the velocity spectral density estimates, the mass fluctuations are cascading steadily toward higher wave numbers through the 2D and 3D spectral ranges until they finally will be diffused molecularly. In the PSD estimates we observe a continuous transition from the -1 power law of 2D turbulence to the -5/3 power law in the inertial–convective subrange. Finally there is some evidence that the mass variance concentrated at f_i may also inversely cascade toward lower wave numbers, or that low-frequent fluctuations are less susceptible to molecular diffusion. This may hint at a fundamental difference between the TKE of the coherent flow field, which is to a certain part directly dissipated by bottom friction, and the mass, which is not sensitive to the existence of a rigid bottom. Obviously, there is no mass concentration equivalent to the steep vertical velocity gradient near the bottom.

Spectral peak of forcing. The periodicity T_P of the large-scale coherent motion of the vortex street-like wake flow will not change with increasing downstream position, as has already been demonstrated from the evaluation of the auto-correlation coefficients $R_{vv}(\tau)$. In the spectral density distributions the periodicity corresponds to the *forcing frequency* $f_P = T_P^{-1}$ of the pronounced PSD peak representing the turbulence forcing. Along the wake centerline we may obtain the time of a full shedding cycle either from the transverse velocity component or from the longitudinal velocity component as $T_P = T_{P,v} = 2\,T_{P,u}$ (cf. Section 7.1.3). Thus, the peak of forced turbulence is located at $f_P = f_{P,v} = 1/2\,f_{P,u}$, as can be seen, for instance, in Figure 7.10. Since tracer mass is continuously introduced into both the right and left cylinder boundary layers, the cycle period of the concentration measurements is $T_{P,c} = 1/2\,T_p$, thus $f_{P,c} = 2\,f_P = 2\,f_{P,v}$. From the PSD estimates both of the transverse velocity and of the concentration, presented in Figures 7.12(a) to (c), no shift in the peak frequency f_P can be recognized. Also from PSD estimates, calculated with higher spectral resolution for this purpose, f_P remained constant for all downstream positions. This indicates the absence of vortex pairing or merging events on the large coherent flow scale.

The *peak amplitude* of the PSD estimate represents the strength of the turbulence forcing. Of course, VS class wakes show a higher amplitude of up to 3 orders of magnitude above the 3D turbulence level compared to SB class wakes. This reflects the more rigorous topographic forcing of VS wakes com-

pared to the rather internal shear forcing of SB wakes. As the LCS containing the low-frequent TKE advect downstream, their energy is dissipated due to bottom friction. Hence, the peak amplitude and the magnitude decrease with downstream position as does the TKE in the full spectral range (cf. Figures 7.6 and 7.7).

7.2.3 Spectral density estimates for small- and large-scale turbulence

The 1D spectral density distribution among the scales of turbulence led to a kind of dual spectral structure of turbulence in shallow wake flows. In order to demarcate the part of TKE contained in the large-scale coherent motion from the part contained in the small-scale random turbulent fluctuation, the techniques of spectral analysis may also be applied to data sets that have previously been triple-decomposed.

In Section 7.1.1 we introduced different methods to discriminate the low- and high-frequency parts of sampled velocity and concentration data using the cycle period of the vortex shedding process as a characteristic time scale for the coherent flow. A *phase–resolved averaging* procedure (cf. also Sections 3.3 and 10.1.2) can be employed to re-sample the phase–aligned data. Note that phase–resolved averages can be based either on the average cycle period T_P or on the individual cycle periods $T_{P,i}$. The latter has been preferably employed for shallow wake flows, since this technique is unaffected by slight variations of $T_{P,i}$. It turned out that using the average T_P tended to blur the phase–resolved averages especially over long time histories comprising many cycles. The phase–resolved averaging procedure effectively operates as a narrow band-pass filter centered about f_i. As a second technique to access the large-scale motion a *moving average* has been calculated using a low–order polynomial that was fitted in a time window of roughly $2\pi\, D/U_a$, i.e. roughly $T_P/4$ if a global wake instability would exist. Since this method works as a low-pass filter, it is well suited to extract the low-frequent part of an aperiodic flow field as encountered in shallow wake flows of SB stability class.

Both averaging techniques have been applied to the same velocity and mass concentration data in order to separate the large and small scale fluctuations of a vortex street-like shallow wake flow (series 25_vs07b) at a downstream centerline position of $x/D = 2$. The resulting 1D PSD estimates are presented in Figure 7.13. Here, full lines indicate the PSD estimates obtained from the small-scale random fluctuations only, whereas dash-dotted lines indicate the superposition of both—random and coherent—parts. Using the phase–resolved averaged data the spectral peak containing solely the coherent motion can be extracted from the turbulence spectral distribution, as exemplified in Figure 7.13(a). The spectral density distribution associated with the random tur-

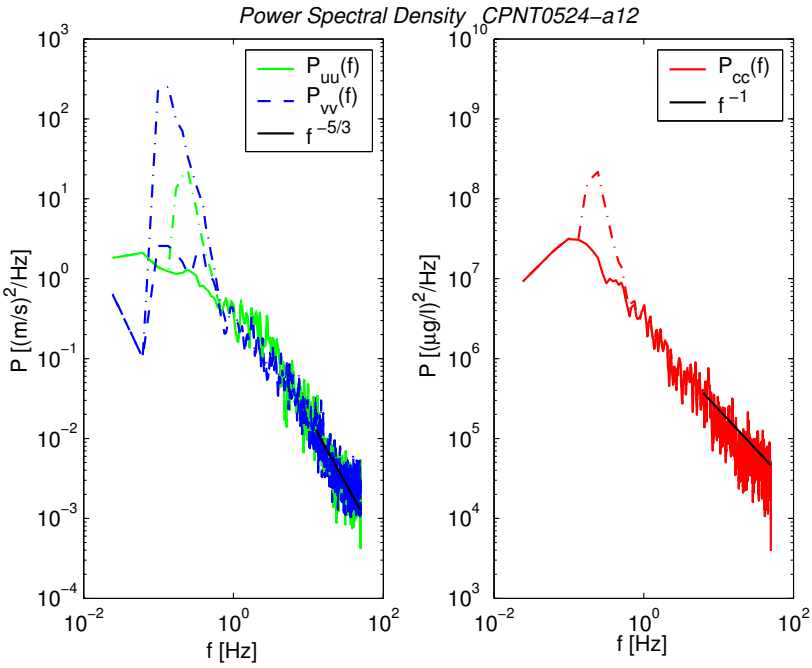

(a) Decomposition using a phase–resolved averaging procedure

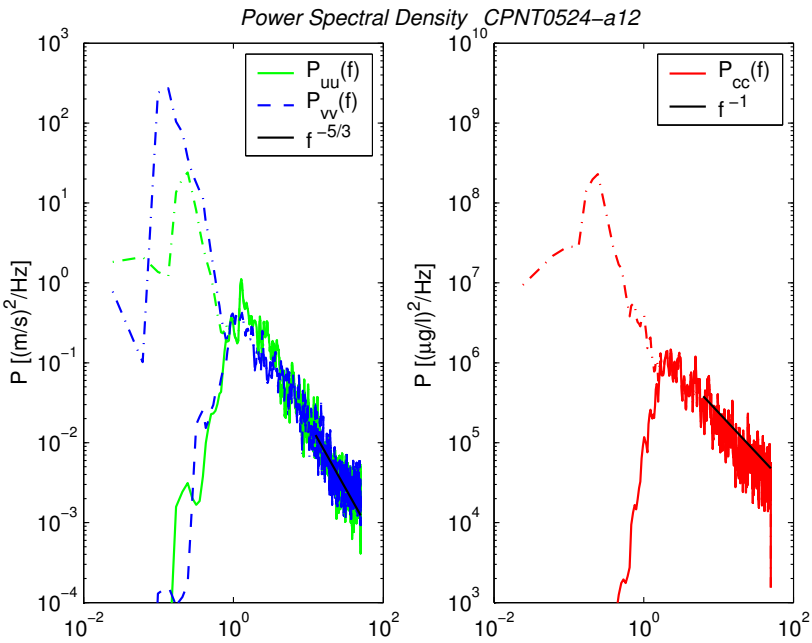

(b) Decomposition using a low–order polynomial fitted to the data in a moving time window

Figure 7.13. 1D PSD estimates in shallow turbulent wakes have been calculated also from triple-decomposed data separately for 2D coherent and 3D random flow fields. Different averaging techniques have been applied to the same velocity and mass concentration data of a vortex street-like shallow wake flow (series 25_vs07b) at a downstream centerline position of $x/D = 2$. Full lines indicate the PSD estimates obtained from the small-scale random fluctuations only, whereas dash-dotted lines indicate the superposition of both—random and coherent—parts.

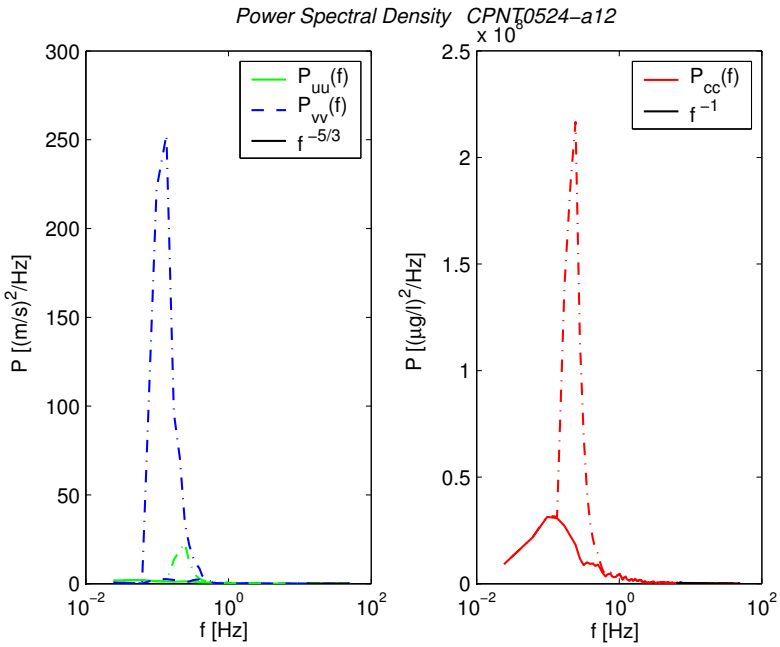

Figure 7.14. Semi-logarithmic plot of the PSD estimates presented in Figure 7.13(a) using a linear scale for the ordinate and a log scale for the abscissa

bulence remains unaffected over the whole spectral range—even at the large scales, where also 2D coherent motions occur. Contrarily, from the moving polynomial fit all the low-frequent fluctuations are extracted whether they belong to the coherent or to the random motion of the flow. This low-pass filtering is clearly reflected in the 1D PSD estimates, as shown in Figure 7.13(b). Also from the spectral density estimates of the turbulence we draw the conclusion that the phase–resolved averaging technique is well suited to extract the coherent part of the flow field.

In Figure 7.14 the data of Figure 7.13(a) has been re-drawn using a linear scaling for the ordinate axis. The magnitude of the narrow peak centered at f_i elucidates the strength of the large-scale coherent vortices forming the vortex street-like wake. On the contrary, the low PSD values of the 3D random turbulence are distributed over a wide range of frequencies. Therefore, the total kinetic energy accumulated in the coherent flow is roughly of the same order of magnitude as the TKE contained in the small-scale random turbulence. Note that the plots of Figure 7.14 display the frequency range on a logarithmic abscissa, which visually increases the width of the narrow peak of 2D turbulence and at the same time shrinks the wide frequency range of 3D turbulence.

8. Integral Model for Shallow Wake Flow

In the following we will derive an *analytical model* to describe the time- and depth-averaged velocity and scalar distributions, $\langle \bar{\boldsymbol{u}} \rangle (x, y)$ and $\langle \bar{c} \rangle (x, y)$, in the *far field of a shallow turbulent wake flow.* We will decompose the main velocity component into an *ambient velocity* u_a well outside the wake and a *deficit (or defect) velocity* u_s, i.e. $u(x, y) = u_a(x) - u_s(x, y)$, as illustrated in the definition sketch of Figure 8.1. Therefore, in the first instance, using subsequent deficit formulations for the momentum and volume fluxes, we derive an *analytical deficit model.* This can be superposed onto the underlying vertically sheared base flow field in order to obtain a non-deficit model to describe the complete flow field of a shallow far wake.

8.1 Basic considerations

8.1.1 Transverse distribution of velocity and mass

Similar to other 2D shear flows, the cross-sectional distributions of $\langle u_s \rangle (x, y)$ and $\langle c \rangle (x, y)$ are almost *self-similar* in the wake flow far downstream of an obstacle. They can then be described employing Gaussian distributions (cf. for instance Hinze (1975); Holley & Jirka (1986); Pope (2000)), although also other functional dependencies, e.g. trigonometrical like $\operatorname{sech} \xi$ or even polynomials, are in use (cf. the review of Negretti (2003a)). In the near field of

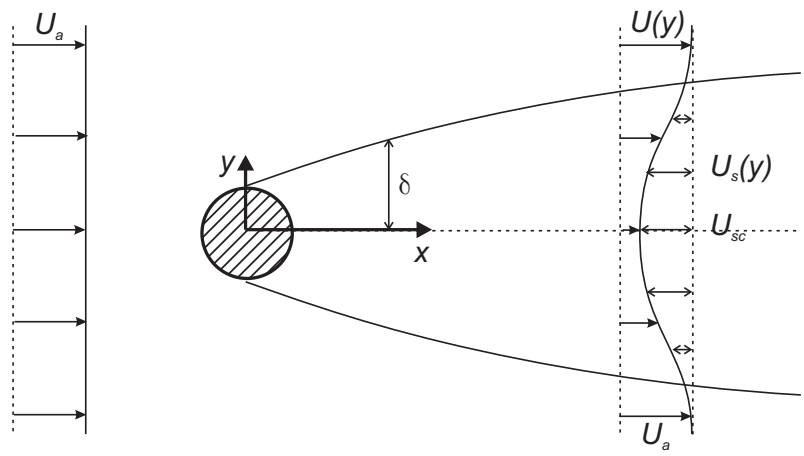

Figure 8.1. Conceptual sketch of the time-mean flow field of the shallow wake downstream of a cylinder.

the wake self-similar profiles have not jet developed. Further detail on the self-similarity and Gaussian transverse distribution of $\langle u_s \rangle$ and $\langle c \rangle$ in shallow turbulent wake flow will be presented in Section 9.1.

Using an appropriate standardization for the transverse direction, $y^+ = y/\delta$, and for the cross-sectionally distributed quantity, $m^+ = m/m_c$, the functionality of the self-similar distribution is found to be Gaussian.

Thus, in the far wake we obtain for the defect velocity,

$$\langle u_s(x,y)\rangle^+ = f_u\left(y^+\right) = \exp\left(-\left(n\,y^+\right)^2\right) \text{ , i.e.} \tag{8.1a}$$

$$\langle u_s(x,y)\rangle = \langle u_{sc}(x)\rangle \exp\left(-\left(n\frac{y}{\delta(x)}\right)^2\right) , \tag{8.1b}$$

and for a mass concentration

$$\langle c(x,y)\rangle^+ = f_c\left(y^+\right) = \exp\left(-\left(n\,\frac{y^+}{r_\gamma}\right)^2\right) \text{ , i.e.} \tag{8.2a}$$

$$\langle c(x,y)\rangle = \langle c_c(x)\rangle \exp\left(-\left(n\frac{y}{r_\gamma\,\delta(x)}\right)^2\right) . \tag{8.2b}$$

Here, δ denotes the wake half width based on the velocity, and r_γ denotes the diffusion ratio of the concentration-based half width to the velocity-base half width $r_\gamma = \delta_c/\delta_u$ expressing the diffusion of a scalar quantity compared to the dissipation of the velocity deficit.[1] The conversion factor n depends on the definition of the wake half width δ.

In general, the *wake half width* δ is defined as the cross-sectional distance from the centerline, for which the main velocity component reaches a certain fraction of the centerline velocity u_{sc}. There are three commonly used definitions of δ and their associated constants n listed in Table 8.1.

When setting up an integral model we will perform cross-sectional integrations of various combinations of u_s and c. The general solution for the integral of a normally distributed variable x is given by

[1] The turbulent Schmidt number $Sc_t = \nu_t/D_t$ is related to the diffusion ratio as $Sc_t = 1/r_\gamma^2 = \delta_u^2/\delta_c^2$ (cf. Pope, 2000, pp. 162).

Table 8.1. Conversion of commonly used definitions of wake half width.

transverse position	value of velocity defect	conversion factor n
$\delta = \delta_{1/2}$	$u_s\left(\delta_{1/2}\right) = \frac{1}{2}u_{sc}$	$n^2 = \ln 2$
$\delta = \delta_{1/e}$	$u_s\left(\delta_{1/e}\right) = \frac{1}{e}u_{sc}$	$n^2 = 1$
$\delta = \delta_{1/e^2}$	$u_s\left(\delta_{1/e^2}\right) = \frac{1}{e^2}u_{sc}$	$n^2 = 2$

$$\int_0^{x_e} \exp\left(-q^2 x^2\right) dx = \frac{\sqrt{\pi}}{2q} \operatorname{erf}(q\, x_e) \ , \tag{8.3}$$

where $\operatorname{erf}(x) = \frac{2}{\sqrt{\pi}} \int_0^x \exp\left(-t^2\right) dt$ is the error function.

Since $\operatorname{erf}(\infty) = 1$, the definite integral of a Gaussian distribution becomes

$$\lim_{x_e \to \infty} \int_0^{x_e} \exp\left(-q^2 x^2\right) dx = \frac{\sqrt{\pi}}{2q} \ . \tag{8.4}$$

Some definite integrals, which we will use for the fluxes of momentum and mass, and their associated integral constants are evaluated below.

$\int_{-\infty}^{\infty} u_s\, dy = i_1\, u_{sc}$ with $i_1 = \sqrt{\pi}\, \frac{\delta}{n}$,
$\int_{-\infty}^{\infty} u_s^2\, dy = i_2\, u_{sc}^2$ with $i_2 = \sqrt{\frac{\pi}{2}}\, \frac{\delta}{n}$,
$\int_{-\infty}^{\infty} c\, dy = i_3\, c_c$ with $i_3 = \sqrt{\pi}\, \frac{r_\gamma\, \delta}{n}$,
$\int_{-\infty}^{\infty} c\, u_s\, dy = i_4\, c_c\, u_{sc}$ with $i_4 = \sqrt{\frac{\pi}{r_\gamma^2+1}}\, \frac{r_\gamma\, \delta}{n}$,

where the subscript $_c$ denotes values at the wake centerline.

8.1.2 Integral volume and momentum equations

For the development of an integral shallow wake model it is convenient to use appropriate integrated variables rather then velocity fields and mass concentration fields, though in Section 8.2 we will deduce the basic differential equations from the 2D shallow flow equations. Although we will primarily use their deficit formulations, also the total fluxes are presented below. The *total volume flux* (or discharge), *specific momentum flux* (i.e. momentum flux per unit mass ρ), and *tracer mass flux*, respectively, are

$$\begin{aligned} Q &= \lim_{y_e \to \infty} \int_{-y_e}^{y_e} \langle u \rangle\, h\, dy \\ &= \lim_{y_e \to \infty} \int_{-y_e}^{y_e} \langle u_a - u_s \rangle\, h\, dy = Q_a - Q_s \ , \end{aligned} \tag{8.5}$$

$$\begin{aligned} M &= \lim_{y_e \to \infty} \int_{-y_e}^{y_e} \left(\langle u \rangle\, h\right) \langle u \rangle\ dy = \lim_{y_e \to \infty} \int_{-y_e}^{y_e} \langle u_a - u_s \rangle^2\, h\, dy \\ &= \lim_{y_e \to \infty} \int_{-y_e}^{y_e} \langle u_a u \rangle\, h\, dy - \lim_{y_e \to \infty} \int_{-y_e}^{y_e} \langle u_s u \rangle\, h\, dy \ , \end{aligned} \tag{8.6}$$

$$\begin{aligned} Q_c &= \lim_{y_e \to \infty} \int_{-y_e}^{y_e} \langle c u \rangle\, h\, dy \\ &= \lim_{y_e \to \infty} \int_{-y_e}^{y_e} \langle c\, (u_a - u_s) \rangle\, h\, dy = Q_{ca} - Q_{cs} \ . \end{aligned} \tag{8.7}$$

Obviously, all integral terms, which only contain powers of $\langle u_a \rangle$, but not of $\langle u_s \rangle$ such as Q_a, can not be integrated definitely with the limits $y_e \to \infty$. However, in Section 8.3.5 we will also present an approximation for those fluxes, leading to an analytical solution for the underlying set of differential equations.

The *deficit fluxes of volume, specific momentum, and mass*, respectively, are defined as

$$Q_s = \lim_{y_e \to \infty} \int_{-y_e}^{y_e} \langle u_s \rangle \, h \, dy \ , \tag{8.8}$$

$$M_s = \lim_{y_e \to \infty} \int_{-y_e}^{y_e} \langle u_s \, u \rangle \, h \, dy = \lim_{y_e \to \infty} \int_{-y_e}^{y_e} \langle u_s \, (u_a - u_s) \rangle \, h \, dy \ , \tag{8.9}$$

$$Q_{cs} = \lim_{y_e \to \infty} \int_{-y_e}^{y_e} \langle c \, u_s \rangle \, h \, dy \ . \tag{8.10}$$

We can solve the definite integrals for Q_s, M_s and Q_c also for $y_e \to \infty$ using the Gaussian integral solutions from Section 8.1.1. For the volume deficit flux, the momentum deficit flux and the total mass flux, respectively, this yields

$$Q_s = i_1 \, h \, \langle u_{sc} \rangle = \sqrt{\pi} \, \frac{\delta}{n} h \, \langle u_{sc} \rangle \ , \tag{8.11}$$

$$\begin{aligned} M_s &= i_1 \, h \, \langle u_a \, u_{sc} \rangle - i_2 \, h \, \langle u_{sc}^2 \rangle \\ &= \sqrt{\pi} \, \frac{\delta}{n} h \, \langle u_a \, u_{sc} \rangle - \sqrt{\frac{\pi}{2}} \, \frac{\delta}{n} h \, \langle u_{sc}^2 \rangle \ , \end{aligned} \tag{8.12}$$

$$\begin{aligned} Q_c &= i_3 \, h \, \langle c_c \, u_a \rangle - i_4 \, h \, \langle c_c \, u_{sc} \rangle \\ &= \sqrt{\pi} \, \frac{r_\gamma \, \delta}{n} h \, \langle c_c \, u_a \rangle - \sqrt{\frac{\pi}{r_\gamma^2 + 1}} \, \frac{r_\gamma \, \delta}{n} h \, \langle c_c \, u_{sc} \rangle \ . \end{aligned} \tag{8.13}$$

8.1.3 Initial conditions for flux quantities

In general, for the inflow conditions we will define an arbitrary cross section where we assume Gaussian distributions of $\langle u_s \rangle$ and c to be valid. These distributions are characterized by initial values (denoted with subscript $_0$) for the wake half width δ_0 and for the centerline values of the velocity defect $\langle u_{sc0} \rangle$ and of the tracer mass concentration $\langle c_{c0} \rangle$. With Equations (8.11) to (8.13) this yields *initial flux values for volume deficit, momentum deficit and for mass*, respectively,

$$Q_{s0} = \sqrt{\pi} \, \frac{\delta_0}{n} h \, \langle u_{sc0} \rangle \ , \tag{8.14}$$

$$M_{s0} = \sqrt{\pi}\,\frac{\delta_0}{n} h \left\langle u_{sc0} \right\rangle \left(\left\langle u_a \right\rangle - \frac{\left\langle u_{sc0} \right\rangle}{\sqrt{2}} \right) \ , \tag{8.15}$$

$$Q_{c0} = \sqrt{\pi}\,\frac{r_\gamma\,\delta}{n} h \left\langle c_{c0} \right\rangle \left(\left\langle u_a \right\rangle - \frac{\left\langle u_{sc0} \right\rangle}{\sqrt{r_\gamma^2 + 1}} \right) \ . \tag{8.16}$$

We could further simplify the integral wake model, if we would choose the initial cross section to be located at the downstream stagnation point at the end of the recirculation zone of the wake, thus $\langle u_{sc0} \rangle = \langle u_a \rangle$. Then the initial fluxes become

$$Q'_{s0} = \sqrt{\pi}\,\frac{\delta_0}{n} h \left\langle u_a \right\rangle \ , \tag{8.17}$$

$$M'_{s0} = \sqrt{\pi}\,\frac{\delta_0}{n} h \left\langle u_a^2 \right\rangle \left(1 - \frac{1}{\sqrt{2}} \right) \ , \tag{8.18}$$

$$Q'_{c0} = \sqrt{\pi}\,\frac{r_\gamma\,\delta}{n} h \left\langle c_c u_a \right\rangle \left(1 - \frac{1}{\sqrt{r_\gamma^2 + 1}} \right) \ . \tag{8.19}$$

8.2 Conservation equations in far field of shallow wake

In this section we will derive the set of equations for the analytical far wake model on the basis of the *2D shallow water equations* (2D SWE). Here, we will present a brief summary on the deduction of the 2D SWE. For more detail the reader is referred to a review by v. Carmer et al. (2000) or to textbooks on hydrodynamics like Hinze (1975); Tennekes & Lumley (1977); Chaudhry (1993). A thorough discussion has been given by Vreugdenhil (1994). Starting from the *Navier-Stokes Equations* and using order–of–magnitude arguments due to the shallowness of the flow, in the vertical momentum equation the local acceleration term, advective terms and stress gradient terms are small compared to the gravitational acceleration term, and can be neglected. Thus, the z-momentum equation consists only of the hydrostatic pressure to balance the gravitational acceleration: $\frac{\partial p}{\partial z} = -\rho g$. Implementation of this hydrostatic pressure distribution into the horizontal momentum equations results in *3D shallow water equations.* A *Reynolds averaging* procedure[2] applied to these

[2] *Reynolds averaging* means, that we decompose the velocity components into temporal mean and fluctuating parts $u = \langle u \rangle + u'$, substitute them into the equation and finally take the temporal average $\langle\,\rangle$ of the equation.

equations provides time-mean equations of continuity and momentum. Furthermore, an integrating over the flow depth h results in the time- and depth-averaged horizontal velocity components, $\overline{\langle u \rangle}$ and $\overline{\langle v \rangle}$, and in the time- and depth-averaged mass concentration, $\overline{\langle c \rangle}$, given by

$$\overline{\langle u_i \rangle} = \frac{1}{h} \int_0^h \langle u_i(z) \rangle \, dz \ , \text{ and } \quad \overline{\langle c \rangle} = \frac{1}{h} \int_0^h \langle c(z) \rangle \, dz \ . \tag{8.20}$$

Vertical local deviations of the time- and depth-averaged values are denoted as

$$\langle u_i \rangle' = \left(\langle u_i \rangle - \overline{\langle u_i \rangle} \right) \text{ and } \langle c \rangle' = \left(\langle c \rangle - \bar{c} \right) \ .$$

Since in the remainder of this chapter we are concerned with depth-averaged quantities solely, we omit the over-bar notation for clarity unless necessary otherwise.

The—time- and depth-averaged—continuity, momentum, and tracer mass conservation equations constitute a set of *2D shallow water equations* given as

$$\frac{\partial h}{\partial t} + \frac{\partial \langle u \rangle h}{\partial x} + \frac{\partial \langle v \rangle h}{\partial y} = 0 \ , \tag{8.21}$$

$$\begin{aligned} &\frac{\partial \langle u \rangle h}{\partial t} + \frac{\partial}{\partial x} \left(\langle u \rangle^2 h + \frac{1}{2} g h^2 \right) + \frac{\partial \langle u \rangle \langle v \rangle h}{\partial y} \\ &= gh \left(S_{0x} - S_{fx} \right) + \frac{\partial}{\partial x} \left(h T_{xx} \right) + \frac{\partial}{\partial y} \left(h T_{xy} \right) \ , \end{aligned} \tag{8.22}$$

$$\begin{aligned} &\frac{\partial \langle v \rangle h}{\partial t} + \frac{\partial}{\partial y} \left(\langle v \rangle^2 h + \frac{1}{2} g h^2 \right) + \frac{\partial \langle u \rangle \langle v \rangle h}{\partial x} \\ &= gh \left(S_{0y} - S_{fy} \right) + \frac{\partial}{\partial x} \left(h T_{yx} \right) + \frac{\partial}{\partial y} \left(h T_{yy} \right) \ , \end{aligned} \tag{8.23}$$

$$\begin{aligned} &\frac{\partial \langle c \rangle h}{\partial t} + \frac{\partial \langle c \rangle \langle u \rangle h}{\partial x} + \frac{\partial \langle c \rangle \langle v \rangle h}{\partial y} \\ &\quad + \frac{\partial}{\partial x} \left(-D_m \frac{\partial \langle c \rangle h}{\partial x} + \langle u' c' \rangle h + \dot{M}_x \right) \\ &\quad + \frac{\partial}{\partial y} \left(-D_m \frac{\partial \langle c \rangle h}{\partial y} + \langle v' c' \rangle h + \dot{M}_y \right) = 0 \ , \end{aligned} \tag{8.24}$$

where S_0 and S_f represent the bottom slope and the energy slope, respectively. T_{ij} denote time- and depth-averaged lateral stress terms, and $\dot{M}_i$ denote mass dispersion tensors. D_m is the molecular diffusivity of a tracer mass in the fluid, and g is the gravitational acceleration.

Since the bottom slope has been assumed to be mild, it is approximated by $S_0 = \sin \vartheta$ with an inclination angle ϑ.

The mean energy dissipation due to time-averaged bottom shear stresses $\langle \tau_{bx_i} \rangle$ will be related to the depth-averaged time-mean flow field by a quadratic friction law,

$$ghS_{fx} = \frac{\langle \tau_{bx} \rangle}{\rho} = \frac{\lambda}{8} \langle u \rangle \sqrt{\langle u \rangle^2 + \langle v \rangle^2} \text{ , and} \tag{8.25a}$$

$$ghS_{fy} = \frac{\langle \tau_{by} \rangle}{\rho} = \frac{\lambda}{8} \langle v \rangle \sqrt{\langle u \rangle^2 + \langle v \rangle^2} \text{ ,} \tag{8.25b}$$

where the bottom friction coefficient is given by the Darcy-Weisbach friction coefficient λ introduced in Section 5.3.1. At this point, we want to draw the reader's attention to the fact that the common hypothesis of (8.25) means that the time-averaged bottom shear stresses are obtained from the time-mean velocity field, instead of averaging the instantaneous shear stresses calculated from the instantaneous velocity fields (cf. Equation (8.91)). We will discuss the validity of this hypothesis in the context of shallow wake flows with predominating 2D LCS in Section 8.4.4.

The depth-averaged lateral stresses T_{ij} include the effects of viscous friction, of turbulent friction, and of momentum dispersion due to depth-averaging:

$$T_{ij} = \frac{1}{h} \int_0^h \nu \left(\frac{\partial \langle u_i \rangle}{\partial x_j} + \frac{\partial \langle u_j \rangle}{\partial x_i} \right) - \langle u_i' u_j' \rangle + \left(\langle u_i \rangle' \langle u_j \rangle' \right) \, dz \text{ ,} \tag{8.26}$$

where ν is the kinematic viscosity of the fluid.

The Taylor analysis of mass dispersion showed that—at asymptotically large times—the longitudinal dispersive flux is proportional to the longitudinal gradient in the depth-averaged concentration. Extension to 2D shear flow (Fischer et al., 1979, pp. 99) leads to the definition of a bulk dispersion tensor,

$$\dot{M}_x = \int_0^h \langle u \rangle' \langle c \rangle' \, dz = \left(-K_{xx} \frac{\partial \overline{\langle c \rangle}}{\partial x} - K_{xy} \frac{\partial \overline{\langle c \rangle}}{\partial y} \right) h \tag{8.27a}$$

$$\dot{M}_y = \int_0^h \langle v \rangle' \langle c \rangle' \, dz = \left(-K_{yx} \frac{\partial \overline{\langle c \rangle}}{\partial x} - K_{yy} \frac{\partial \overline{\langle c \rangle}}{\partial y} \right) h \text{ .} \tag{8.27b}$$

The mass dispersion coefficients K_{ij}—accounting for the effects of depth variations in the horizontal velocity components on the depth-averaged tracer concentration—can be calculated from the velocity deviation components and from the vertical turbulent diffusivity D_{tz},

$$K_{xx} = -\frac{1}{h} \int_0^h \langle u \rangle' \int_0^h \frac{1}{D_{tz}} \int_0^h \langle u \rangle' \, dz \, dz \, dz \text{ ,} \tag{8.28a}$$

$$K_{xy} = -\frac{1}{h} \int_0^h \langle u \rangle' \int_0^h \frac{1}{D_{tz}} \int_0^h \langle v \rangle' \, dz \, dz \, dz \text{ ,} \tag{8.28b}$$

$$K_{yx} = -\frac{1}{h}\int_0^h \langle v\rangle' \int_0^h \frac{1}{D_{tz}} \int_0^h \langle u\rangle' \, dz\, dz\, dz \ , \tag{8.28c}$$

$$K_{yy} = -\frac{1}{h}\int_0^h \langle v\rangle' \int_0^h \frac{1}{D_{tz}} \int_0^h \langle v\rangle' \, dz\, dz\, dz \ . \tag{8.28d}$$

If a logarithmic velocity distribution applies, the vertical turbulent diffusivity can be given as $D_{tz}(z) = \kappa\, u^\star z \left(1 - \frac{z}{h}\right)$, where $\kappa = 0.41$ is the v. Kármán constant, and $u^\star$ is the bed friction velocity defined by (5.5). Since predicted concentration distributions are not very sensitive to the variation of D_{tz} with depth, the depth-averaged value $\overline{D_{tz}} = \frac{\kappa}{6} h u^\star \approx 0.067 h u^\star$ may be employed (Rutherford, 1994).

In the following, additional assumptions will be:

1. The flow is considered to be stationary, and the suspended tracer mass to be conservative, thus all temporal derivatives vanish in Equations (8.21) to (8.24).
2. The x direction of the coordinate system shall be aligned with the gradient of the bottom. Thus, no transverse slope is present, $S_{0y} = 0$, and the transverse gravitational acceleration term vanishes.
3. The time-mean bottom shear stresses will be modelled using the time-mean velocity distributions, (8.25). This widely used model has been employed also by Lee & Jirka (1980) for the analysis of shallow jet flows.
4. Concerning the lateral shear stress terms, in turbulent flow usually the effects of viscous shear are dominated by turbulent shear. Therefore, the first integral term in (8.26) will be neglected. Also, and more questionable, the dispersive effect of the depth-averaging, the so-called 'differential advection' (Vreugdenhil, 1994), will be omitted.[3]
5. The molecular diffusion terms and the bulk mass dispersion terms occurring in the tracer mass conservation equation (8.24) will be neglected.

Employing the above assumptions, and expanding the spatial mean derivatives of the momentum equations (8.22) and (8.23) and of the mass conservation equation (8.24) with the application of the continuity equation (8.21), the set of 2D SWE, Equations (8.21) to (8.24), further simplifies to

$$\frac{\partial \langle u\rangle h}{\partial x} + \frac{\partial \langle v\rangle h}{\partial y} = 0 \ , \tag{8.29}$$

[3] According to Vreugdenhil (1994, pp. 36), besides the (negligibly small) viscous stresses and the turbulent stresses, the differential advection terms may contribute to about 25% to the lateral shear stresses. All attempts to include the dispersive effect of differential advection into the 2D SWE have failed until 1994. Only recently Yulistiyanto et al. (1998) presented calculations of the flow around a cylinder using shallow flow equations including also the dispersive terms, which have been modelled in analogy to the bulk mass dispersion $\dot{M}$, (8.27). They stressed the importance to represent both the turbulent diffusion and dispersion terms of the lateral stresses, (8.26), in a shallow wake flow.

$$\langle u\rangle \frac{\partial \langle u\rangle h}{\partial x} + \langle v\rangle \frac{\partial \langle u\rangle h}{\partial y} + \frac{\partial \left\langle u'^2\right\rangle h}{\partial x} + \frac{\partial \langle u'v'\rangle h}{\partial y} + gh\frac{\partial h}{\partial x} - gh\sin\vartheta_x + \frac{\lambda}{8}\langle u\rangle\sqrt{\langle u\rangle^2 + \langle v\rangle^2} = 0 \ , \tag{8.30}$$

$$\langle u\rangle \frac{\partial \langle v\rangle h}{\partial x} + \langle v\rangle \frac{\partial \langle v\rangle h}{\partial y} + \frac{\partial \langle u'v'\rangle h}{\partial x} + \frac{\partial \left\langle v'^2\right\rangle h}{\partial y} + gh\frac{\partial h}{\partial y} + \frac{\lambda}{8}\langle v\rangle\sqrt{\langle u\rangle^2 + \langle v\rangle^2} = 0 \ , \tag{8.31}$$

$$\langle u\rangle \frac{\partial \langle c\rangle h}{\partial x} + \langle v\rangle \frac{\partial \langle c\rangle h}{\partial y} + \frac{\partial \langle u'c'\rangle h}{\partial x} + \frac{\partial \langle v'c'\rangle h}{\partial y} = 0 \ . \tag{8.32}$$

8.2.1 Momentum deficit flux equation

We will further simplify the 2D momentum equations by adapting them to the far field of a wake flow. Hence, we will make further use of scaling arguments, as was already necessary for the deduction of the 2D SWE from the Navier-Stokes equations in plane shear flow (e.g. Tennekes & Lumley, 1977).

In the time-mean wake far field the transverse velocity component is much smaller than the longitudinal component, $\langle v\rangle \ll \langle u\rangle$, and the longitudinal gradients of the flow field are much smaller than the transverse gradients, $\frac{\partial}{\partial x} \ll \frac{\partial}{\partial y}$. Using these order–of–magnitude arguments we can approximate the transverse momentum equation (8.31) by

$$\frac{\partial \left\langle v'^2\right\rangle h}{\partial y} + gh\frac{\partial h}{\partial y} = 0 \ . \tag{8.33}$$

This equation is integrated over y, differentiated with respect to x, and finally substituted in (8.30), which can now be written as

$$\langle u\rangle \frac{\partial \langle u\rangle h}{\partial x} + \langle v\rangle \frac{\partial \langle u\rangle h}{\partial y} + \frac{\partial}{\partial x}\Big(\left(\left\langle u'^2\right\rangle - \left\langle v'^2\right\rangle\right) h\Big) + \frac{\partial \langle u'v'\rangle h}{\partial y} - gh\sin\vartheta_x + \frac{\lambda}{8}\langle u\rangle\sqrt{\langle u\rangle^2 + \langle v\rangle^2} = 0 \ . \tag{8.34}$$

Again, from scaling reasons we can neglect the third term of (8.34), because in the far wake the turbulence is regarded as horizontally isotropic, i.e. $\left\langle u'^2\right\rangle \sim \left\langle v'^2\right\rangle$. Hence, we obtain a *single momentum equation*,

$$\langle u\rangle \frac{\partial \langle u\rangle h}{\partial x} + \langle v\rangle \frac{\partial \langle u\rangle h}{\partial y} + \frac{\partial \langle u'v'\rangle h}{\partial y} - gh\sin\vartheta_x + \frac{\lambda}{8}\langle u\rangle\sqrt{\langle u\rangle^2 + \langle v\rangle^2} = 0 \ . \tag{8.35}$$

Well outside the wake flow we encounter *uniform flow conditions*, i.e. $\langle u_a \rangle = u_a$ and all horizontal derivatives of flow quantities are zero, $\frac{\partial}{\partial x} = 0$ and $\frac{\partial}{\partial y} = 0$. The main velocity component approaches the ambient velocity u_a. Thus, in the ambient flow (8.35) becomes the balance between gravitational forces and bottom shear,

$$-gh \sin \vartheta_x + \frac{\lambda}{8} u_a \sqrt{u_a^2} = 0 \ . \tag{8.36}$$

Next, we subtract the ambient momentum balance (8.36) from the momentum balance within the wake (8.35), which results in a *momentum deficit equation*

$$\begin{aligned} &\langle u \rangle \frac{\partial \langle u \rangle h}{\partial x} + \langle v \rangle \frac{\partial \langle u \rangle h}{\partial y} + \frac{\partial \langle u'v' \rangle h}{\partial y} \\ &+ \frac{\lambda}{8} \left(\langle u \rangle \sqrt{\langle u \rangle^2 + \langle v \rangle^2} - u_a^2 \right) = 0 \quad . \end{aligned} \tag{8.37}$$

In order to solve (8.37), we decompose $u = u_a - u_s$. Since we assume the ambient velocity to be independent of the x position, i.e. $u_a = const$, its local gradients vanish, and we can substitute

$$\frac{\partial}{\partial x_i} \langle u \rangle = \frac{\partial}{\partial x_i} \langle u_a - u_s \rangle = -\frac{\partial}{\partial x_i} \langle u_s \rangle \ . \tag{8.38}$$

Since continuity holds (Equation (8.29)), the advective terms of (8.37) are

$$-\langle u \rangle \frac{\partial \langle u_s \rangle h}{\partial x} - \langle v \rangle \frac{\partial \langle u_s \rangle h}{\partial y} = -\frac{\partial \langle u \rangle \langle u_s \rangle h}{\partial x} - \frac{\partial \langle v\, u_s \rangle h}{\partial y} \ . \tag{8.39}$$

Now, we substitute the advective terms in (8.37). Hence, the momentum deficit equation results as

$$\begin{aligned} &-\frac{\partial \langle u \rangle \langle u_s \rangle h}{\partial x} - \frac{\partial \langle v \rangle \langle u_s \rangle h}{\partial y} + \frac{\partial \langle u'v' \rangle h}{\partial y} \\ &\qquad + \frac{\lambda}{8} \left(\left(u_a - \langle u_s \rangle \right) \sqrt{\langle u \rangle^2 + \langle v \rangle^2} - u_a^2 \right) = 0 \ . \end{aligned} \tag{8.40}$$

In wake flows the velocity deficit the transverse velocity component $\langle v \rangle$ and the Reynolds stresses $\langle u'v' \rangle$ are anti-symmetric with respect to the wake centerline $(x,\ y = 0)$, i.e. $\langle v\,(-y_u) \rangle = -\langle v\,(y_u) \rangle$ and $\langle u'v'\,(-y_u) \rangle = -\langle u'v'\,(y_u) \rangle$. Therefore, if we perform an integration in the transverse direction on equation (8.40), the second and third integral term will vanish. Transverse integration of (8.40), thus, results in

$$\frac{\partial}{\partial x} \int_{-\infty}^{\infty} \langle u \rangle \langle u_s \rangle h \, dy =$$

$$-\frac{\lambda}{8}\int_{-\infty}^{\infty}\left(u_a-\langle u_s\rangle\right)\sqrt{\langle u\rangle^2+\langle v\rangle^2}-u_a^2\,dy\ . \tag{8.41}$$

Since in the far field $\sqrt{\langle u\rangle^2+\langle v\rangle^2}\approx\langle u\rangle$, the integral term on the right-hand side can be transformed and approximated as

$$\begin{aligned}\left(u_a-\langle u_s\rangle\right)\langle u\rangle-u_a^2&=\langle u_s\rangle\left(2u_a-\langle u_s\rangle\right)\\&\approx 2\langle u_s\rangle\left(u_a-\langle u_s\rangle\right)=2\langle u_s\rangle\langle u\rangle\ .\end{aligned} \tag{8.42}$$

Hence, the above equation (8.41) becomes after expansion of the right-hand side with the flow depth h

$$\frac{\partial}{\partial x}\int_{-\infty}^{\infty}\langle u\rangle\langle u_s\rangle\,h\,dy=-\frac{\lambda}{4h}\int_{-\infty}^{\infty}\langle u_s\rangle\langle u\rangle\,h\,dy\ . \tag{8.43}$$

Here, the integral quantity is exactly the net specific momentum deficit flux, as it has been defined in (8.9). Therefore, the *integral equation for the momentum* finally reads

$$\frac{\partial}{\partial x}M_s=-\frac{\lambda}{4h}\,M_s\ . \tag{8.44}$$

8.2.2 Flux equations for volume and tracer mass

Next, we will derive the conservation equation for the volume deficit flux proceeding from the Reynolds averaged 2D continuity equation (8.29). First, we decompose $u=u_a-u_s$. As noted in the previous section, since we assume the ambient velocity to be a constant, its local gradients vanish. Thus, we substitute the advective terms of (8.29) by (8.38), integrate the equation in the transverse direction, and obtain

$$-\frac{\partial}{\partial x}\lim_{y_u\to\infty}\int_{-y_u}^{y_u}\langle u_s\rangle\,h\,dy+\frac{\partial}{\partial y}\lim_{y_u\to\infty}\int_{-y_u}^{y_u}\langle v\rangle\,h\,dy=0\ . \tag{8.45}$$

Since the first left-hand term of (8.45) is the longitudinal rate of change of the volume deficit flux, we substitute the definition of the volume deficit flux (8.11). Making use of the anti-symmetric behavior of $\langle v\rangle$ with respect to the wake centerline, the second term can be reformulated as

$$\begin{aligned}\frac{\partial}{\partial y}\int_{-y_u}^{y_u}\langle v\rangle\,h\,dy&=\Big[\langle v\rangle\,h\Big]_{-y_u}^{y_u}=\langle v\,(y_u)\rangle\,h-\langle v\,(-y_u)\rangle\,h\\&=\langle v\,(y_u)\rangle\,h-\left(-\langle v\,(y_u)\rangle\right)h=2\langle v\,(y_u)\rangle\,h\ .\end{aligned}$$

Hence, (8.45) results in

$$-\frac{\partial}{\partial x}Q_s + 2h \lim_{y_u \to \infty} \langle v\,(y_u)\rangle = 0\ . \tag{8.46}$$

The second integral term of (8.45) represents an *entrainment rate* into the wake at the wake boundary. Since $\lim_{y_u \to \pm\infty} \langle v\,(y_u)\rangle = 0$, the entrainment of ambient fluid into the wake necessitates an approximation of (8.45) by bounded integrals. Setting the upper bound $y_u = \frac{k}{n}\delta$ relative to the wake half width for both integral terms did not prove particularly helpful.[4] Instead, we use a finite limit y_u only for the second integral term, which leads—analogously to (8.46)—to

$$-\frac{\partial}{\partial x}Q_s + 2h\,\langle v\,(y_u)\rangle = 0\ . \tag{8.47}$$

The transverse velocity at the wake boundary, $v(y_u)$, is called an *entrainment velocity* v_e in order to quantify the specific flux of volume entrained from the high velocity ambient flow into the wake.[5] In jet flows the entrainment velocity is commonly related to the centerline value of the longitudinal excess velocity as the characteristic velocity scale in jets (cf. Morton et al. (1956), Lee & Jirka (1980)). In wake flows the corresponding characteristic velocity is the main velocity deficit, thus, the entrainment velocity is given as $v_e = -\alpha\, u_{sc}$.[6] The entrainment coefficient α is of the order $\mathcal{O}(10^{-1})$ in self-similar shear flows, if the entrainment velocity is evaluated at the $1/e$ half width, following the commonly agreed usage of v_e. Hence, the *volume deficit flux equation* is

$$\frac{\partial}{\partial x}Q_s + 2\,\alpha\,\langle u_{sc}\rangle\, h = 0\ . \tag{8.48}$$

If we introduce the definition of the complete volume flux (8.5) to Equation (8.48), we obtain an equation for the *complete volume flux equation*,

$$\begin{aligned} &\frac{\partial}{\partial x}\left(Q_a - Q\right) + 2\,\alpha\,\langle u_{sc}\rangle\, h = 0 \quad \Leftrightarrow \\ &\frac{\partial}{\partial x}Q - 2\,\alpha\,\langle u_{sc}\rangle\, h = 0\ . \end{aligned} \tag{8.49}$$

The balances of the volume deficit flux and of the complete volume flux through a control volume from the initial cross-section of the wake flow to an arbitrary downstream cross-section are obtained, respectively, as

[4] Employing the Leibniz integral rule results in

$$\int_0^{y_u} \frac{\partial\,\langle u_s\rangle\, h}{\partial x} dy - \langle u_s\,(y_u)\rangle\, h \frac{k}{n}\frac{\partial \delta}{\partial x} = \langle v\,(y_u)\rangle\, h\ .$$

[5] In wake flows the velocity v_e is directed inwards on both sides of the wake.

[6] The negative sign arises from the definition of the velocity defect $u_s = u_a - u$ being a positive quantity in wake flows.

$$Q_s(x) = Q_{s0} - 2\alpha \int_0^x \langle u_{sc} \rangle \, h \, d\tilde{x} \text{ , and} \tag{8.50a}$$

$$Q(x) = Q_0 + 2\alpha \int_0^x \langle u_{sc} \rangle \, h \, d\tilde{x} \text{ .} \tag{8.50b}$$

Finally, we will formally deduce the *equation for the conservation of tracer mass flux* from (8.32). Due to scale arguments, also the longitudinal fluctuating transport can be neglected in (8.32), and the *tracer mass balance* reduces to

$$\langle u \rangle \frac{\partial \langle c \rangle h}{\partial x} + \langle v \rangle \frac{\partial \langle c \rangle h}{\partial y} + \frac{\partial \langle v'c' \rangle h}{\partial y} = 0 \text{ .} \tag{8.51}$$

Now, we integrate (8.51) with respect to y. The first integral term represents the longitudinal change of the mass flux Q_c, as defined in (8.13). Since the time- and depth-averaged mass concentration $\langle c \rangle$ and the transverse velocity $\langle v \rangle$ as well as the transverse turbulent mass flux $\langle v'c' \rangle$ are 0 outside the wake (i.e. $y \to \pm\infty$), the second and third integral terms cancel, so that

$$\frac{\partial}{\partial x} Q_c = 0 \text{ .} \tag{8.52}$$

The tracer mass is conserved, since we consider the tracer to be non-reactive (i.e. conservative).

8.3 Solution of the system of flux equations

In the previous section we deduced a set of ordinary differential equations for integral flux variables of the wake flow. With the solution of this set of flux equations, and making use of characteristic wake properties, namely the self-similarity and transverse Gaussian distribution, we derive a model for the velocity and mass fields in a far wake flow.

In the following discussion we are always concerned with time- and depth-averaged fields of velocity and mass. In order to improve the clarity of the equations we omit the overbar and angular bracket notation unless otherwise necessary.

8.3.1 Auxiliary relations for flux quantities

Before we start to solve the set of differential equations, we will briefly present some relations between these flux variables. We will make use of these auxiliary equations mainly to develop a descriptive model of the wake flow field from the solutions of the flux equations, but also to close the set of flux equations. Again, also because we will conduct integrations of the transverse distributions of u_s and c, as introduced in Section 8.1.1, the derived analytical model is restricted

to flow regions, where self-similarity holds, and the flow field can be described with Gaussian distributions.

Normalizing the fluxes of volume deficit, momentum deficit, and tracer mass, Equations (8.11) to (8.13), with their corresponding initial values, Equations (8.14) to (8.16), we obtain

$$\frac{M_s}{M_{s0}} = \frac{\sqrt{\pi}\frac{\delta}{n} h\, u_{sc}\left(u_a - \frac{u_{sc}}{\sqrt{2}}\right)}{\sqrt{\pi}\frac{\delta_0}{n} h\, u_{sc0}\left(u_a - \frac{u_{sc0}}{\sqrt{2}}\right)} = \frac{\delta}{\delta_0}\frac{u_{sc}}{u_{sc0}}\frac{\left(u_a - \frac{u_{sc}}{\sqrt{2}}\right)}{\left(u_a - \frac{u_{sc0}}{\sqrt{2}}\right)} \ , \tag{8.53}$$

$$\frac{Q_s}{Q_{s0}} = \frac{\sqrt{\pi}\frac{\delta}{n} h\, u_{sc}}{\sqrt{\pi}\frac{\delta_0}{n} h\, u_{sc0}} = \frac{\delta}{\delta_0}\frac{u_{sc}}{u_{sc0}} \ , \tag{8.54}$$

$$\frac{Q_c}{Q_{c0}} = \frac{\sqrt{\pi}\frac{r_\gamma \delta}{n} h\, c_c\left(u_a - \frac{u_{sc}}{\sqrt{r_\gamma^2+1}}\right)}{\sqrt{\pi}\frac{r_\gamma \delta_0}{n} h\, c_{c0}\left(u_a - \frac{u_{sc0}}{\sqrt{r_\gamma^2+1}}\right)} = \frac{\delta}{\delta_0}\frac{c_c}{c_{c0}}\frac{\left(u_a - \frac{u_{sc}}{\sqrt{r_\gamma^2+1}}\right)}{\left(u_a - \frac{u_{sc0}}{\sqrt{r_\gamma^2+1}}\right)} \ . \tag{8.55}$$

The ratio between momentum deficit flux and volume deficit flux reads

$$\frac{M_s}{Q_s} = \frac{\sqrt{\pi}\frac{\delta}{n} h\, u_a\, u_{sc} - \sqrt{\frac{\pi}{2}}\frac{\delta}{n} h\, u_{sc}^2}{\sqrt{\pi}\frac{\delta}{n} h\, u_{sc}} = u_a - \frac{u_{sc}}{\sqrt{2}} \ . \tag{8.56}$$

For arbitrary initial conditions and for initial conditions at the downstream stagnation point (i.e. $u_s = u_a$) we obtain, respectively,

$$\frac{M_{s0}}{Q_{s0}} = u_a - \frac{u_{sc0}}{\sqrt{2}} \ , \tag{8.57}$$

$$\frac{M'_{s0}}{Q'_{s0}} = u_a\left(1 - \frac{1}{\sqrt{2}}\right) \ .$$

In non-dimensional form, this ratio can be written

$$\frac{M_s/M_{s0}}{Q_s/Q_{s0}} = \frac{M_s^*}{Q_s^*} = \frac{M_s/Q_s}{M_{s0}/Q_{s0}} = \frac{\sqrt{2}\, u_a - u_{sc}}{\sqrt{2}\, u_a - u_{sc0}} \ . \tag{8.58}$$

For the ratio between the squared volume deficit flux and the momentum deficit flux we find

$$\frac{Q_s^2}{M_s} = \frac{\sqrt{\pi}\frac{\delta}{n} h\, u_{sc}}{u_a - \frac{u_{sc}}{\sqrt{2}}} \ . \tag{8.59}$$

This yields for initial conditions at an arbitrary cross section and at the downstream stagnation point, respectively,

$$\frac{Q_{s0}^2}{M_{s0}} = \frac{\sqrt{\pi}\frac{\delta_0}{n} h\, u_{sc0}}{u_a - \frac{u_{sc0}}{\sqrt{2}}} \ , \tag{8.60}$$

$$\frac{Q_{s0}'^2}{M_{s0}'} = \frac{\sqrt{\pi}\frac{\delta_0}{n}h}{1-\frac{1}{\sqrt{2}}} \ .$$

8.3.2 Set of flux equations

The set of ordinary differential equations to be solved consists of the *momentum deficit balance* (8.44),

$$\frac{\partial}{\partial x}M_s = -\frac{\lambda}{4h}\,M_s \ ,$$

of the *tracer mass balance* (8.52),

$$\frac{\partial}{\partial x}Q_c = 0 \ ,$$

and of the volume deficit balance (8.48),

$$\frac{\partial}{\partial x}Q_s + 2\,\alpha\,u_{sc}\,h = 0 \ .$$

From the flux relation (8.56) we obtain

$$u_{sc} = \sqrt{2}\left(u_a - \frac{M_s}{Q_s}\right) \ .$$

Substituting u_{sc}, *volume deficit balance* (8.48) becomes

$$\frac{\partial}{\partial x}Q_s + 2\,\sqrt{2}\,\alpha\,h\left(u_a - \frac{M_s}{Q_s}\right) = 0 \ . \tag{8.61}$$

The solution to the momentum deficit equation (8.44) is

$$M_s = c_I\left(-\frac{\lambda}{4h}\right)\exp\left(-\frac{\lambda}{4h}x\right) \ ,$$

Using the boundary condition for the initial cross-section at $x = 0$, i.e. implementing the initial momentum deficit $M_{s0} = -\frac{\lambda}{4h}c_I\exp(0)$, the *momentum deficit flux* becomes

$$M_s = M_{s0}\exp\left(-\frac{\lambda}{4h}x\right) \ . \tag{8.62}$$

Equation (8.62) indicates the longitudinal decay of the momentum deficit due to bottom friction. This recovery of momentum flux is a characteristic feature of shallow wake flows. Obviously, following the above discussion, in unbounded wake flows the momentum deficit flux is preserved, because we do not retain any dissipative term then. Recall that viscous shear terms have already been neglected in the lateral stress terms of Equations (8.30) and (8.31).

As mentioned above, the tracer mass balance (8.52) states that the mass flux of a conservative tracer is conserved, i.e.

$$Q_c = Q_{c0} = const \ . \tag{8.63}$$

Re-arranging the volume deficit balance (8.61), the equation reads

$$Q_s \frac{\partial}{\partial x} Q_s + 2\sqrt{2}\,\alpha\, h\, u_a\, Q_s = 2\sqrt{2}\,\alpha\, h\, M_s \ .$$

Hence, we are concerned with a non-linear, non-homogeneous ordinary differential equation of first order without an analytical solution. Albeit the homogeneous differential equation has been solved, it was found impossible to present also a solution for the full equation (e.g. by variation of variable). Therefore, we will apply an appropriate numerical procedure to solve this equation (e.g. a Runge–Kutta scheme or a predictor-corrector method like Adams–Moulton).

8.3.3 Non-dimensional formulation of the set of conservation equations and their solutions

In order to obtain a general solution for the fluxes of volume deficit, momentum deficit, and tracer mass, we have to rewrite the set of differential equations in non-dimensional form. We will normalize each quantity by its initial value. Normalized quantities are denoted by *, e.g. $Q_s^* = \frac{Q_s}{Q_{s0}}$. The non-dimensional longitudinal coordinate is defined as $x^* = \frac{\lambda\, x}{4h}$.

From (8.44) and (8.62), the *momentum deficit* differential equation and its solution using non-dimensional variables are, respectively,

$$\frac{\partial}{\partial x^*} M_s^* = -M_s^* \ , \tag{8.64}$$

$$M_s^* = \frac{M_s}{M_{s0}} = \exp\left(-x^*\right) \ . \tag{8.65}$$

For the *tracer mass* differential equation (8.52) and its solution (8.63), we obtain in non-dimensional form, respectively,

$$\frac{\partial}{\partial x^*} Q_c^* = 0 \ , \tag{8.66}$$

$$Q_c^* = 1 \ . \tag{8.67}$$

The volume deficit differential equation (8.61), for which no analytical solution exists, requires some additional definitions of non-dimensional parameters, which we define in a manner similar to Jirka et al. (1986). These are related to the *strength of the wake flow*, to the *bottom friction*[7], and to the *entrainment*, respectively,

[7] The bottom friction parameter ϕ_m, Equation (8.68b), resembles a gradient stability number S_g (cf. Equation (2.4)) of the deficit flow field.

$$R_m = u_{sc0}\frac{Q_{s0}}{M_{s0}} = \frac{u_{sc0}}{u_a - \frac{u_{sc0}}{\sqrt{2}}} \ , \tag{8.68a}$$

$$\phi_m = \frac{\lambda}{4h}\,\frac{Q_{s0}^2}{hM_{s0}} = \frac{\lambda}{4h}\,R_m\,\frac{Q_{s0}}{h\,u_{sc0}} = \frac{\lambda}{4h}\,\sqrt{\pi}\frac{\delta_0}{n}R_m \ , \tag{8.68b}$$

$$a_m = 4\sqrt{2}\,\frac{\alpha}{\phi_m} \ . \tag{8.68c}$$

Furthermore, from (8.58) we can deduce the non-dimensionalized centerline defect velocity,

$$u_{sc}^* = \frac{u_{sc}}{u_{sc0}} = \sqrt{2}\frac{u_a}{u_{sc0}} - \frac{M_s^*}{Q_s^*}\left(\sqrt{2}\frac{u_a}{u_{sc0}} - 1\right) \ . \tag{8.69}$$

We now can transfer (8.48) into a preliminary normalized form,

$$\frac{\partial}{\partial x^*}Q_s^* + \frac{2\,\alpha\,h}{\lambda/8h}\,\frac{u_{sc}}{Q_{sc0}} = 0 \ ,$$

where the second term contains the non-dimensional centerline velocity defect u_{sc}^*. With some basic transformations we achieve the normalized *volume deficit* differential equation corresponding to its dimensional form (8.61),

$$\frac{\partial}{\partial x^*}Q_s^* + \frac{a}{2}\left(1 + \frac{R_m}{\sqrt{2}} - \frac{M_s^*}{Q_s^*}\right) = 0 \ , \tag{8.70}$$

where $M_s^* = \exp\left(-x^*\right)$.

Figure 8.2 shows the exponential decay of the log-scaled normalized momentum deficit M_s^*, Equation (8.65), along the roughness–scaled longitudinal distance x^*, depicted by a full line. The development of the volume deficit flux Q_s^* can be predicted by numerically solving Equation (8.70) for specific initial and boundary conditions represented by the non-dimensional parameters ϕ_m, R_m, and α. The downstream decay of Q_s^*, denoted by a dashed line, and thus the recovery of the volume flux, is exemplified in Figure 8.2, as predicted using an explicit Runge–Kutta solver for Equation (8.70) with the parameter set $R_m = 0.226$, $\phi_m = 0.039$, and $\alpha = 0.098$. The parameter values represent the initial and boundary conditions of a simulation of the far wake data of series 18_vs06, where the initial cross-section has been located at $x/D = 18.1$.

8.3.4 Model equations for velocity and mass fields in wake flow

We will now present a set of equations to describe the depth-averaged time-mean velocity and scalar fields of shallow turbulent far wakes. This will consist of two equations to describe the self-similar transverse distribution of the velocity deficit u_s and the scalar concentration c by Equations (8.1) and (8.2). They are complemented by another three equations to calculate the longitudinal development of the main centerline deficit velocity u_{sc}, of the wake half

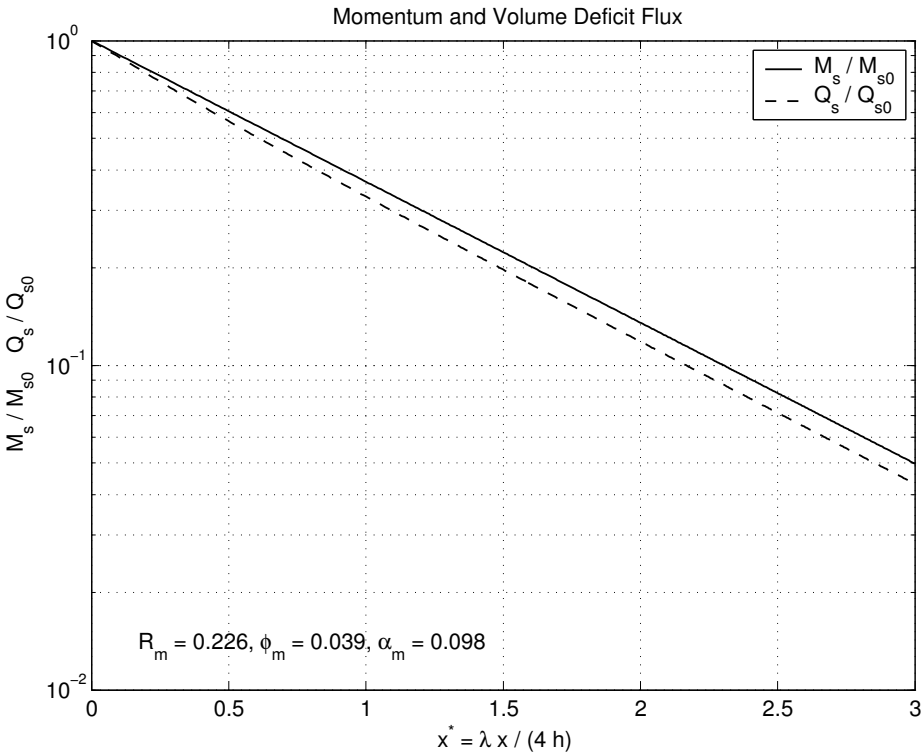

Figure 8.2. The longitudinal decay of the normalized momentum deficit flux M_s^*, given by Equation (8.65) of the integral far wake model, is displayed on a semi-log scale by a full line. The volume deficit flux Q_s^* (dashed line) has been obtained from numerically solving the governing differential equation (8.70) for a given set of initial and boundary parameters $R_m = 0.226$, $\phi_m = 0.039$, and $\alpha = 0.098$, to give an example taken from a simulation of PIV measurement series 18_vs06.

width δ, and of the centerline mass concentration c_c. For this purpose we employ the solutions to the set of conservation equations, and combine them with integral solutions for these fluxes.

For the normalized momentum deficit differential equation (8.64) we gave the analytical solution (8.65) for M_s^*. However, the normalized volume deficit differential equation (8.70) has to be solved numerically for Q_s^*. Now, starting with Equation (8.58) representing the ratio of normalized momentum and volume deficit M_s^*/Q_s^*, we can deduce the *centerline velocity deficit* normalized by its initial value,

$$\begin{aligned}\frac{u_{sc}}{u_{sc0}} &= \sqrt{2}\frac{u_a}{u_{sc0}}\frac{Q_s^* - M_s^*}{Q_s^*} + \frac{M_s^*}{Q_s^*} \\ &= 1 + \frac{\sqrt{2}}{R_m}\left(1 - \frac{M_s^*}{Q_s^*}\right) \ . \end{aligned} \tag{8.71}$$

Using the second characteristic wake flow velocity, the ambient velocity u_a, an alternative formulation for the non-dimensional centerline velocity deficit is

$$\frac{u_{sc}}{u_a} = \frac{u_{sc0}}{u_a}\frac{M_s^*}{Q_s^*} + \sqrt{2}\left(1 - \frac{M_s^*}{Q_s^*}\right)$$
$$= \sqrt{2} - \frac{M_s^*}{Q_s^*}\frac{2}{R_m + \sqrt{2}} \ . \tag{8.72}$$

From (8.54) we obtain the *half width* normalized with its initial value, from substituting u_{sc}^* by (8.71),

$$\frac{\delta}{\delta_0} = Q_s^* \left(\frac{u_{sc}}{u_{sc0}}\right)^{-1} \tag{8.73}$$
$$= \frac{Q_s^{*2}}{\frac{R_m+\sqrt{2}}{R_m}\left(Q_s^* - M_s^*\right) + M_s^*} \ .$$

The non-dimensional *centerline mass concentration* is evaluated from (8.55) by substituting (8.73) as

$$\frac{c_c}{c_{c0}} = \frac{1}{Q_s^*} \cdot \frac{u_a/u_{sc0} - 1\Big/\sqrt{r_\gamma^2 + 1}}{u_a/u_{sc} - 1\Big/\sqrt{r_\gamma^2 + 1}} \ . \tag{8.74}$$

where $\frac{u_a}{u_{sc0}} = \frac{1}{R} + \frac{1}{\sqrt{2}}$, and $\frac{u_a}{u_{sc}}$ is given by (8.72).

In conclusion, the set of equations describing the flow field and scalar field of a shallow turbulent far wake consists of the equations (8.71), (8.73), (8.74), (8.1), and (8.2). They depend on the deficit fluxes of volume and momentum, Q_s^* and M_s^*, and on the initial and boundary conditions parameterized by the model coefficients for wake strength, for bottom friction, for lateral entrainment, and for mass diffusion, R_m, ϕ_m, α, and r_γ.

8.3.5 Continuity equation in non-defect form

Since the volume deficit differential equation has to be solved numerically, we will now derive an approximation, which leads to a differential equation with an existing analytical solution. We will discuss the properties of the subsequent volume deficit flux equation, and demonstrate the restrictions in its applicability to the far field of shallow wake flows.

As already noted, the unbounded transverse integral of the main velocity component does not exist. In this section, we will therefore approximate the complete volume flux (8.5) by introducing a finite integral for the ambient volume flux, so that

$$Q = \int_{-\infty}^{\infty} u\, h\, dy = \int_{-\infty}^{\infty} (u_a - u_s)\, h\, dy$$
$$\approx \int_{-y_e}^{y_e} u_a\, h\, dy - \int_{-\infty}^{\infty} u_s\, h\, dy \ , \tag{8.75}$$

where $y_e = \sqrt{\frac{\pi}{2}}\,\frac{\delta}{n}$ denotes the magnitude of the lower and upper limits of integration for the ambient volume flux. Evaluating the integral terms, we obtain the following approximation[8] for the volume flux,

$$Q \approx \left(\sqrt{2}\,u_a - u_{sc}\right)\sqrt{\pi}\,h\frac{\delta}{n}\ . \tag{8.76}$$

Making use of (8.76), the ratio between the momentum deficit flux and the volume flux becomes

$$\frac{M_s}{Q} \approx \frac{\sqrt{\frac{\pi}{2}}\,\frac{\delta}{n}h\,u_{sc}\,\left(\sqrt{2}\,u_a - u_{sc}\right)}{\sqrt{\pi}\,\frac{\delta}{n}h\,\left(\sqrt{2}\,u_a - u_{sc}\right)} = \frac{u_{sc}}{\sqrt{2}}\ . \tag{8.77}$$

We now substitute the expression for u_{sc} into the complete volume flux differential equation (8.49), which results in a non-linear homogeneous differential equation of first order,

$$\frac{\partial}{\partial x}Q - 2\sqrt{2}\,h\,\alpha\,\frac{M_s}{Q} = 0\ . \tag{8.78}$$

In standardized form, the volume flux equation (8.78) is expressed as

$$\frac{\partial}{\partial x^*}Q^* - \frac{a_m}{2}\,\frac{Q_{s0}^2}{Q_0^2}\,\frac{M_s^*}{Q^*} = 0\ , \tag{8.79}$$

where $Q^* = Q/Q_0$, $M_s^* = M_s/M_{s0}$, $x^* = \lambda/4x/h$, and a_m has been given by (8.68).

Because of its homogeneity we are able to solve this differential equation by separation of variables and subsequent integration. The solution to (8.79) is

$$Q^{*\,2} = -a_m\,\frac{Q_{s0}^2}{Q_0^2}\exp\left(-x^*\right) + C_I\ . \tag{8.80}$$

In order to obtain a finite value for the initial volume flux Q_0, we again employ the volume flux approximation (8.75), which results in

$$\frac{Q_{s0}}{Q_0} \approx \frac{u_{sc0}}{\sqrt{2}\,u_a - u_{sc0}} = \frac{R}{\sqrt{2}}\ . \tag{8.81}$$

---

[8] An alternative and more consistent approximation of the complete volume flux (8.5) can be introduced by

$$Q \approx \tilde{Q} = \int_{-y_e}^{y_e}\left(u_a - u_s\right)h\,dy\ ,$$

where the limits of integration are $y_e = k\,\delta/n$. Using (8.3) in order to evaluate the transverse integral of the Gaussian distribution of u_s, the volume flux approximation results in

$$\tilde{Q} = \left(\sqrt{2}\,u_a - \mathrm{erf}\,(k)\,u_{sc}\right)\sqrt{\pi}\,h\frac{\delta}{n}\ ,$$

which contains an error function in the velocity deficit term. However, for $k = \sqrt{\pi/2}$ and $\mathrm{erf}\left(\sqrt{\pi/2}\right) = 0.9237$ the value of $\tilde{Q}$ is close to the approximation presented in (8.76), which justifies the more handy approximation (8.75).

Hence, Equation (8.80) is approximated by

$$Q^{*\,2} = -\frac{a_m}{2} R_m^2 \exp\left(-x^*\right) + C_I \ . \tag{8.82}$$

The integration constant C_I can be evaluated from the boundary conditions.

Thus, we apply the initial conditions at $x^* = 0$, where $Q^* = 1$. Evaluating (8.82) at $x^* = 0$, the integration constant becomes

$$C_I = 1 + \frac{a_m}{2} R_m^2 \ . \tag{8.83}$$

The complete volume flux finally finally reads

$$Q^* = \sqrt{1 + \frac{a_m}{2} R_m^2 \big(1 - \exp\left(-x^*\right)\big)} \ . \tag{8.84}$$

The limits of Q^* are

$$\lim_{x^* \to 0} Q^* = 1 \text{ and } \lim_{x^* \to \infty} Q^* = \sqrt{1 + \frac{a_m}{2} R_m^2} \ .$$

The latter one represents an absolute upper limit for the complete volume flux, which conflicts with the boundless downstream growth of the wake flow.

Therefore, considering the outflow condition for $x^* \to \infty$ to check for consistency of C_I, we would obtain

$$\lim_{x^* \to \infty} Q^* = \left.\frac{Q_a}{Q_0}\right|_{\infty} = \sqrt{C_I} \ . \tag{8.85}$$

Since the ambient volume flux has to be evaluated at an infinitely far downstream position, also the application of the volume flux approximation using bounds of integration at $\pm y_u$, i.e. (8.75), leads to a limit of Q_a/Q_0 at infinity, because the wake half width δ grows without restraint.

$$\frac{Q_a}{Q_0} \approx \frac{\sqrt{2}\, u_a}{\sqrt{2}\, u_a - u_{sc0}} \frac{\delta}{\delta_0} = \frac{R_m + \sqrt{2}}{\sqrt{2}} \frac{\delta}{\delta_0} \tag{8.86}$$

When we turn to the volume deficit flux, Q_s^* from $Q^* = \left(Q_a - Q_s\right)/Q_0$ becomes

$$Q_s^* = \frac{Q_s}{Q_{s0}} = \frac{Q_0}{Q_{s0}} \left(\frac{Q_a}{Q_0} - Q^* \right) \ . \tag{8.87}$$

The ratio Q_0/Q_{s0} is substituted by (8.81), and using the volume flux approximation (8.75) we find $Q_a/Q_0 \approx \frac{R+\sqrt{2}}{\sqrt{2}} \frac{\delta}{\delta_0}$. Then, Q_s^* can be approximated by

$$Q_s^* = \frac{\sqrt{2}}{R_m} \left(\frac{R_m + \sqrt{2}}{\sqrt{2}} \frac{\delta}{\delta_0} - Q^* \right) \ . \tag{8.88}$$

Inserting the approximate solution for the complete volume flux, Equation (8.82), we obtain an approximation for the volume deficit flux as

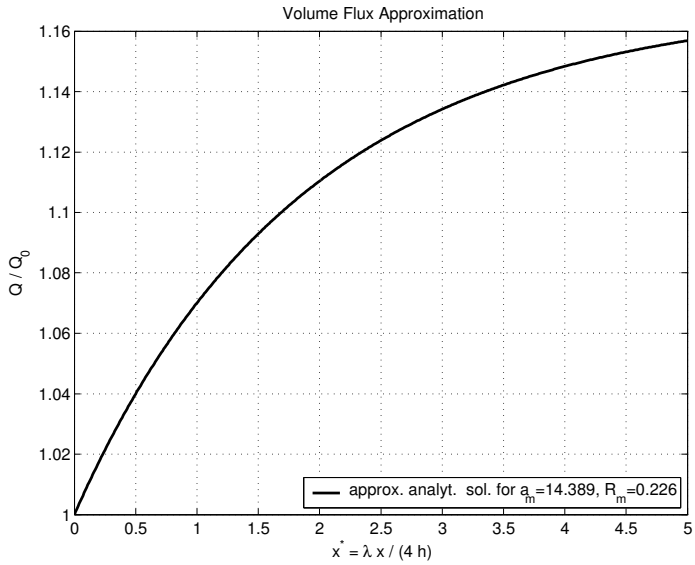

Figure 8.3. An approximated analytical solution for the normalized volume flux Q^*, Equation (8.84), has been obtained from the differential integral flux equation using a volume flux approximation (8.75). For the boundary parameters R_m, ϕ_m, and α, the same values as for Figure 8.2 have been used.

$$Q_s^* = \left(1 + \frac{\sqrt{2}}{R_m}\right) \frac{\delta}{\delta_0} - \sqrt{\frac{2}{R_m^2} + a_m\big(1 - \exp\left(-x^*\right)\big)} \ . \tag{8.89}$$

Both in (8.88) and (8.89) the volume deficit flux depends on the wake half width δ introduced by Q_a, and thus grows without constraint instead of tending to zero.

Figure 8.3 shows the standardized complete volume flux Q^* in the wake computed from Equation (8.84). There are some shortcomings with the employed volume flux approximation (8.75). Firstly, boundary conditions could only be used at the initial cross-section, but not in the outflow. Therefore, secondly, the upper limit of Q^* is not infinite, but bounded. Thirdly, the volume flux approximation that has been employed to obtain the approximative solution does not allow for an explicit solution for the volume deficit flux.

Therefore, in order to receive an appropriate solution to the continuity differential equation (8.58) we have to employ some numerical procedure rather than using an approximated analytical solution. Since the solution of this non-dimensional equation (8.58) depends also on the additional non-dimensional parameters R_m, ϕ_m, and α, Equations (8.68), we need an individual solution for each set of parameters. Hence, it is necessary to employ the numerical solver in each specific flow situation. The set of differential equations for the far wake integral fluxes have been parameterized. However, an analytical solution for the volume or volume deficit differential equations is still missing, and thus, a purely analytical scheme for a far wake integral model.

8.4 Application of integral far wake model

In the following section we want to demonstrate the applicability of the integral model for shallow turbulent far wakes. Firstly, we will show, how the various non-dimensional parameters influence the solutions of the conservation flux equations. Secondly, we will compare the model prediction for the momentum deficit and volume deficit flux to experimental data, which were evaluated from PIV measurements of shallow wake flows conducted in the laboratory. We will, thirdly, show the model solutions for a wake flow field of velocity and tracer mass. Finally, we try to verify the assumptions used to derive the integral model and, thus, deduce some information on the limits of application as well as on promising aspects to further improve the model.

8.4.1 Sensitivity to variation of non-dimensional parameters

From the set of normalized flux conservation equations for the integral model we state that the momentum deficit equation (8.65) and the tracer mass equation (8.67) contain just one dependent variable x^*, whereas the volume deficit differential equation (8.70) features additional non-dimensional parameters characterizing the wake flow. These are ϕ_m, R_m, and a_m (cf. Equations (8.68)) related to the bottom shear, the horizontal shear induced by an obstacle, and the lateral entrainment, respectively. In Figures 8.4 to 8.6 we use a numerical procedure to compute the solution of (8.70) for different values of one the additional non-dimensional parameters ϕ_m, R_m, and α in each figure while keeping default values for the remaining parameters. The default values are $R_m = 0.175$ (i.e $u_{sc0} = 0.2\,u_a$), $\lambda = 0.033$, $\phi_m = 0.04$, $\alpha = 0.098$, and thus $a_m = 3.53$, they are based on measured wake data of series 18_vs06.

The influences of the *bottom friction* on the wake flow field are two-fold, as is obvious from the normalized volume deficit differential equation (8.70). Primarily, we use the longitudinal coordinate $x^* = \frac{\lambda}{4}\frac{x}{h}$ normalized by the frictional length scale to represent the damping and dissipating effect of the vertical shear. Moreover, being part of a_m, the bottom shear is also introduced independently of x^* in the parameter ϕ_m, which compares specific boundary conditions of the wake flow, namely the effects of vertical and transverse shear flow. As mentioned in Section 8.3.3, ϕ_m is closely related to the gradient stability number S_g. Figure 8.4(a) shows the development of $Q_s(x^*)$ for different values of the Darcy–Weisbach friction coefficient λ. Over a smooth bottom the volume deficit decreases much faster with the roughness–scaled downstream distance x^* than over a rough bottom. This apparent contradiction to our intuition can be eliminated, if we take into account that for the friction length scale, which we used to normalize x, we obtain larger values over a rough bottom. With respect to the absolute distance x the volume deficit flux decreases

more slowly for reduced bottom friction, as illustrated in Figure 8.4(b). Here, the same data as used for Figure 8.4(a) is plotted over the lateral–shear–scaled distance x/D, i.e. normalized with the constant cylinder diameter.

The second additional non-dimensional parameter in the volume deficit differential equation concerns the initial *strength of the wake* represented by the ratio of the initial velocity deficit and the ambient velocity $\frac{u_{sc0}}{u_a}$, which is transformed into the strength parameter R_m and also present in the combined factor a_m. Variation of R_m is induced either by different ambient velocities u_a, or by the choice of the position of the initial cross-section, where the initial conditions for the wake model are defined. We can think of the position of the initial cross-section as the shortest distance from the obstacle for the applicability of the integral far wake model. A ratio $\frac{u_{sc0}}{u_a} = 1$ or $R_m = 3.41$ indicates an absolute velocity of 0, as it is found at a stagnation point in the flow field. In wake flows a stagnation point will always occur at the downstream end of the obstacle. Of course, if there exists a recirculation zone downstream of the obstacle, a second stagnation point will be encountered downstream in the wake flow field. Since the assumption of Gaussian distributed values of velocity and scalar does not hold close to the source of the wake (i.e. the obstacle, and eventually, the attached recirculation bubble), it might be necessary for the applicability of the wake model to locate the initial cross-section more downstream, which results in smaller values of $\frac{u_{sc0}}{u_a}$ and of R_m.

In Figure 8.5(a), $Q_s(x^*)$ is plotted for initial velocity ratios of 0.50, 0.25, and 0.10, or wake strength parameters R_m of 0.369, 0.212, and 0.093, respectively. The different values of R_m for the numerical calculations were selected—according to experimental data of an arbitrary wake flow (series 18_vs06)—by choosing different positions of the initial cross-section, and thus by variation of u_{sc0} for constant u_a, instead of varying u_a for a constant u_{sc0}. For higher values of R_m we observe a stronger initial decrease of the volume deficit flux followed downstream by a mild asymptotic approach toward zero deficit. For lower values of R_m we observe a more gradual decrease as the volume deficit flux vanishes. Again we should point out, that Q_s is normalized by its initial value Q_{s0}, which depends on the position of the initial cross-section and is therefore related to the value of R_m.

Hence, a dimensional representation, preserving the absolute values of Q_s, is given in Figure 8.5(b). The downstream distance is given with respect to the obstacle, thus to the origin of x^* at the initial cross-section the off-set distance to the center of the obstacle has been added, i.e. $x^*_{off} + x^* = \lambda/4\,(x_{off} + x)\,/h$. Four different values of u_{sc0}/u_a, 0.5, 0.25, 0.15, 0.1, or values of R_m, 0.369, 0.212, 0.136, 0.093, correspond to different initial cross-sections located at $x/D = 1.9$, 11.6, 23.2, 31.0 in the vortex street-like wake flow, series 18_vs06. For this range of R_m, and keeping all other parameters constant, the volume deficit fluxes have been calculated from the integral far wake model, which

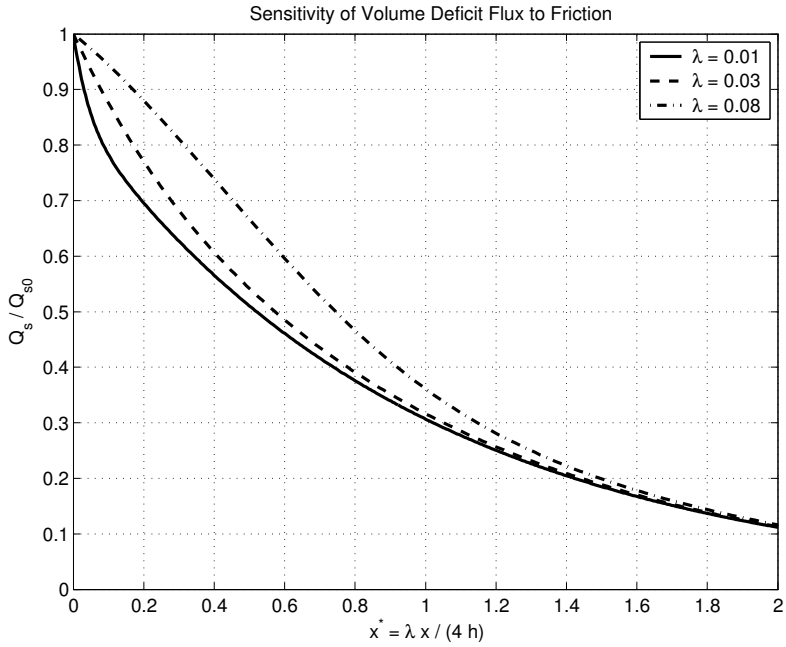

(a) Roughness–scaled downstream distance

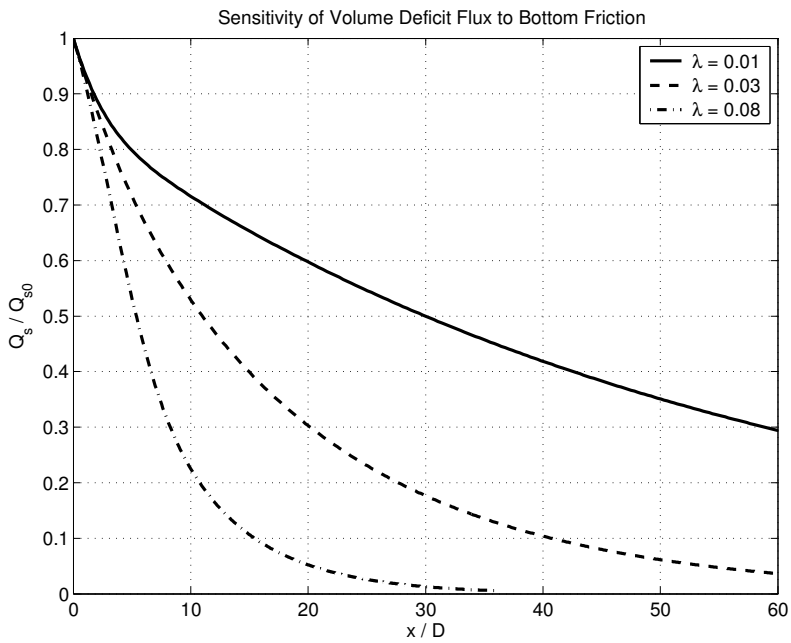

(b) Lateral–shear–scaled downstream distance

Figure 8.4. Sensitivity of volume deficit flux Q_s to variation of bottom friction coefficient λ. We numerically solve the volume deficit flux equation (8.70) for different values of λ between 0.01 and 0.08, inducing a change also in ϕ_m, and in a_m. The other non-dimensional parameters are kept constant at $R_m = 0.175$ (i.e $u_{sc0} = 0.2\,u_a$), and $\alpha = 0.098$. In Figure (a) Q_s^* is plotted over the roughness–scaled downstream distance $\lambda/4\,x/h$ that also varies with the change of λ. In Figure (b) the same values of Q_s^* are associated with the lateral–shear–scaled distance x/D, which is independent of λ.

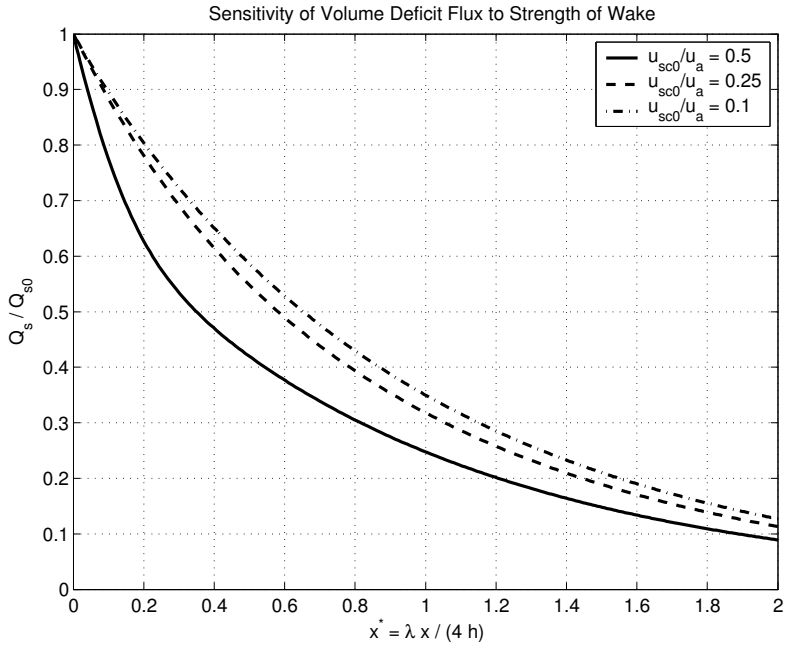

(a) Roughness–scaled downstream distance

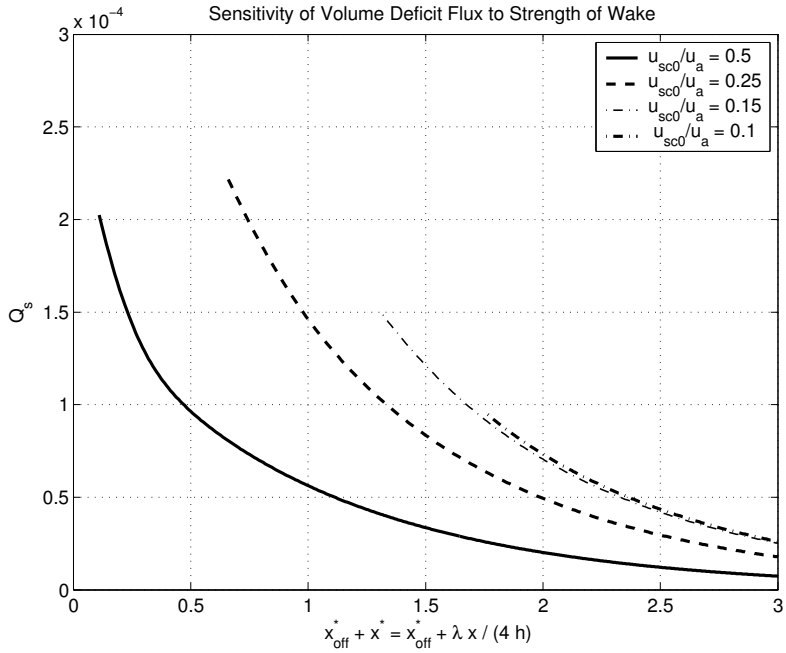

(b) Lateral–shear–scaled downstream distance

Figure 8.5. Sensitivity of volume deficit flux Q_s to variation of wake strength R_m. The volume deficit flux equation (8.70) is numerically solved for different values of R_m between 0.37 and 0.09, inducing a change also in ϕ_m, and in a_m. The other non-dimensional parameters are kept constant at $R_m = 0.175$ (i.e $u_{sc0} = 0.2\,u_a$), and $\alpha = 0.098$. Variation of R_m is realized by changing u_{sc0} and keeping u_a constant. In Figure (a) standardized values $Q_s^* = Q_s/Q_{s0}$ are plotted over the roughness–scaled downstream distance. Since a variation of R_m also changes Q_{s0}, Figure (b) depicts absolute values Q_s plotted over the downstream distance with respect to the center of the obstacle.

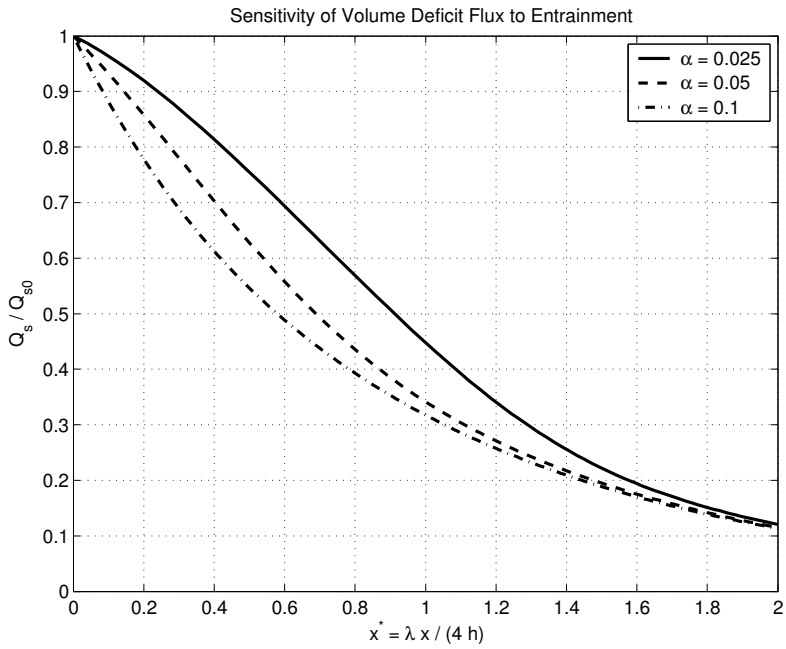

Figure 8.6. Sensitivity of volume deficit flux Q_s to variation of entrainment coefficient α. The volume deficit flux equation (8.70) is numerically solved for different values of α between 0.01 and 0.1, inducing a change also in a_m. The other non-dimensional parameters are kept constant at $R_m = 0.175$ (i.e $u_{sc0} = 0.2\,u_a$), and $\lambda = 0.033$.

implies a self-similar transverse distribution of u_s. Depending on the position of the initial cross-section, i.e. on R_m, a different development of Q_s has been predicted for high values of R_m, as they occur in the near and transitional wake regions of development and decay of 2D LCS. However, for $u_{sc} \lesssim 0.15 u_a$ the predictions become consistent, as indicated by the two dash–dotted lines. This region can be associated with the wake far field below $x/D = 25$, where large-scale vortical structures have disintegrated almost completely.

Additionally, an increase of the initial volume deficit flux Q_{s0} in the near field can be observed from the predictions for $u_{sc0}/u_a = 0.5,\ 0.25$ at $x/D = 1.9,\ 11.6$. This might be addressed on the one hand to detrainment of wake fluid into the ambient flow in the near field of wake development, as is also indicated by the development of the entrainment coefficient α. On the other hand, in the developing near wake velocity profiles are not jet self-similar, and probably steeper than Gaussian.

The *entrainment* of higher velocity fluid from the ambient flow into the wake region is represented by the entrainment coefficient a_m in this model. This is the third additional dependent variable in the volume deficit flux differential equation. Figure 8.6 illustrates the influence of α on the longitudinal development of Q_s^*. As expected, a larger value of the entrainment rate yields a faster reduction of the volume deficit flux, and a faster recovery of the flow.

8.4.2 Prediction of momentum deficit and volume deficit fluxes and comparison to experimental data

For various shallow turbulent wake flows we conducted laboratory experiments, which provide detailed information concerning the properties of the velocity and scalar fields. From our experimental data we are able to compute the same flux quantities, which we also calculate with the integral wake model. The normalized volume deficit flux Q_s^* and the momentum deficit flux M_s^* are presented in Figures 8.7 and 8.8 for two selected flow configurations together with the appropriate analytical and numerical solutions for the given initial and boundary conditions.[9] We have seen before that it takes 1 to 3 frictional length units x^* both for the momentum deficit flux and for the volume deficit flux to vanish, that is for the wake flow to recover. Unfortunately, from the experimental data we have evidence only up to $x^* \approx 0.4$ due to the restrictions in laboratory space. Since the selection of appropriate initial conditions of the wake is essential to the prediction of the further development of the flow, because we have to satisfy the assumptions of the proposed far wake model, it might be necessary to start well downstream of the immediate near field. Even if the experimental data, which cover especially the initial stage of the wake development, provide initial conditions sufficiently far downstream, we still lack data to verify the proper performance of the integral model in the far wake. Nevertheless, we can still increase our confidence in the model observing from the initial stage of the wake. Furthermore, we may gain insight to the transition between near field and far field of the wake.

Figure 8.7 depicts Q_s^* and M_s^* for a wake flow, which does not show any significant recirculation bubble behind the cylindrical obstacle. In this case (series 38_vs01, $S = 0.01$) we observe a vortex-street like wake with the formation of 2D coherent vortical structures, which are very persistent in the wake flow. The maximum value of the ratio u_{sc}/u_a is only about 25%. In order to normalize the data, and also for the initial conditions of the numerical solutions, we locate the initial cross-section at $x/D = 25.1$, where $\frac{u_{sc0}}{u_a} = 0.208$. The measured fluxes both of volume deficit and of momentum deficit increase—through the regions of the developing near wake and of the 2D LCS–dominated intermediate wake—up to a distance of about 20 D, then reach a constant value over some distance, before the disintegration of the wake starts. The initial cross-section is located shortly downstream of the beginning of the decrease at $x/D = 25.1$ corresponding to a frictional distance $x^* = 0.28$. The entrainment coefficient $\alpha = 0.026$ has been adjusted to obtain the most suitable reproduction also of the centerline velocity deficit u_{sc}^* and the wake half width δ_u^*, as

[9] We will continue the comparison for the same flow configurations in the next section with characteristic wake flow quantities.

shown in Figure 8.9. Though α displays a very low value in this wake flow, it has been verified from velocity measurements (cf. Section 8.4.4).

The second wake flow configuration (series 18_vs06) is comparable to the first one with respect to the generation and arrangement of 2D coherent structures in a vortex-street like manner, but these are not as strong and persistent as in the first case ($S = 0.06$). Although also in this case we do not observe a permanent region of flow recirculation behind the cylinder, we have evidence for the development of a recirculation bubble from the centerline velocity deficit approaching zero near the obstacle, i.e. $u_{sc}/u_a \to 1$ for $x/D \to 0.5$. Figure 8.8 again shows the deficit fluxes computed from the PIV data. Both cases display a similar behavior, however, neither the lateral–shear–scale nor the bottom–friction–scale seem to be the proper scaling for the near field development. In this case the initial cross-section has been located well in the region of wake recovery at $x/D = 18.1$, where $\frac{u_{sc0}}{u_a} = 0.195$. The entrainment coefficient was found to be $\alpha = 0.098$—again in gross agreement with appropriate velocity measurements. The decay both of M_s^* and Q_s^* is slightly over-estimated far downstream of the obstacle with the applied set of parameters, though α, R_m, and λ have been obtained or verified from experimental data. Since also M_s^*, depending only on x^*, is affected, decreasing the bed roughness and thus the bottom friction coefficient would be appropriate. However, λ would have to be reduced from 0.0328—a value that corresponds to almost hydraulically smooth flow conditions at the given Re_h—to about 0.024, which is physically impossible because it is clearly lower than the corresponding smooth bottom value. In order to meet the u_{sc}^* and δ^* developments, also the entrainment coefficient would have to be reduced to $\alpha = 0.07$—still in the range of values calculated from velocity data.

8.4.3 Prediction of velocity and scalar fields

Since the main purpose of the integral wake model is the prediction of the wake flow field, in Section 8.2 we derived a set of equations using the solutions of the deficit flux equations to describe the mean wake far fields for the main flow velocity component and a scalar quantity. We will verify now, how well the integral wake model will predict these flow field information for the flow conditions, which we already used to compare the deficit flux predictions.

In Figures 8.9 and 8.10 we compare the predicted longitudinal development of the centerline velocity deficit and of the wake half width to data obtained from wake flow measurements. As for the preceding section, the flow conditions correspond to a pure vortex street-like shallow wake with $S = 0.01$ (series 38_vs01), and to a vortex street-like wake with a tendency to grow a permanent recirculation bubble (series 18_vs06), respectively. Data for the wake half width, δ_u and δ_γ, have been calculated from the time-mean fields of

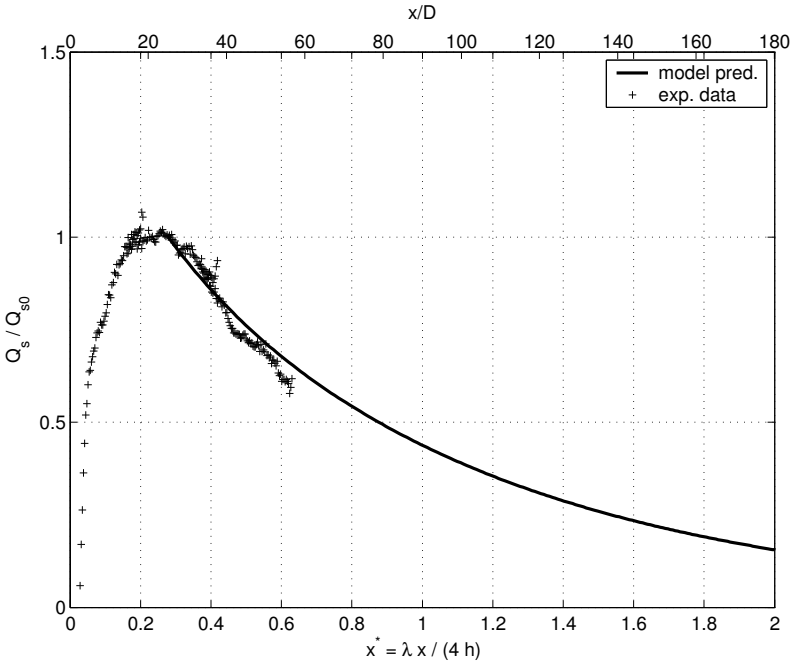

(a) Volume deficit flux Q_s^*

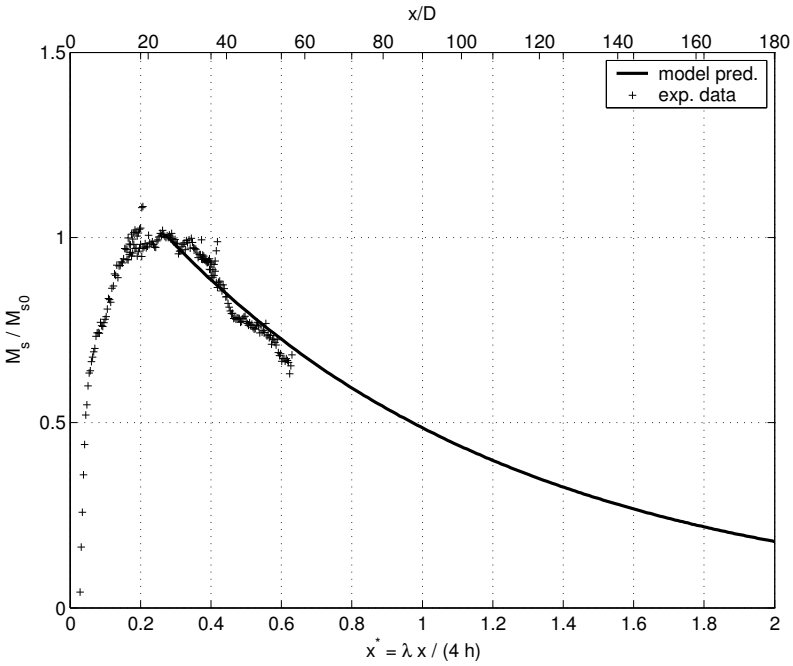

(b) Momentum deficit flux M_s^*

Figure 8.7. Volume and momentum deficit fluxes for a vortex street-like wake flow, $S = 0.01$, (series 38_vs01). Initial conditions for the integral wake model are evaluated from cross-section at $x/D = 25.1$, esp. $\frac{u_{sc0}}{u_a} = 0.208$. The entrainment coefficient adapted for the data is surprisingly low, $\alpha = 0.026$.

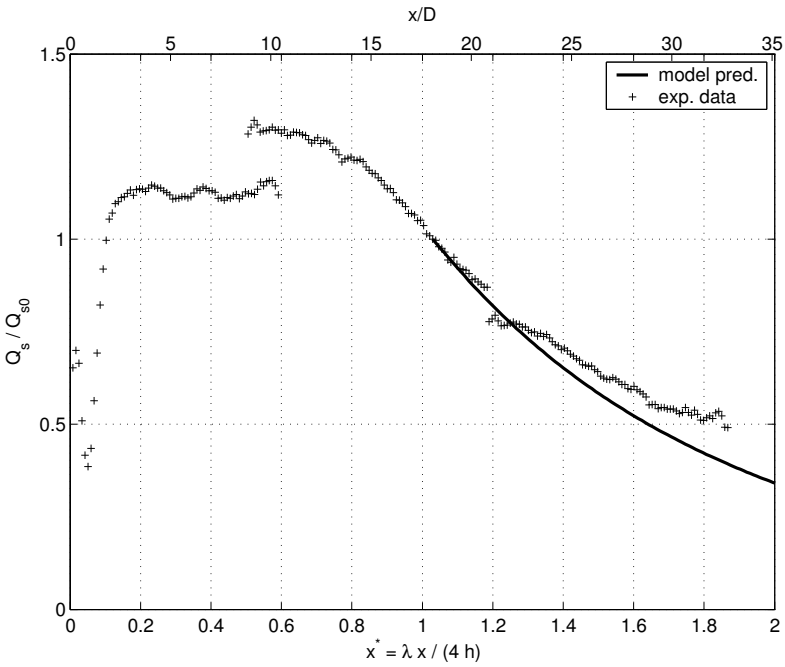

(a) Volume deficit flux Q_s^*

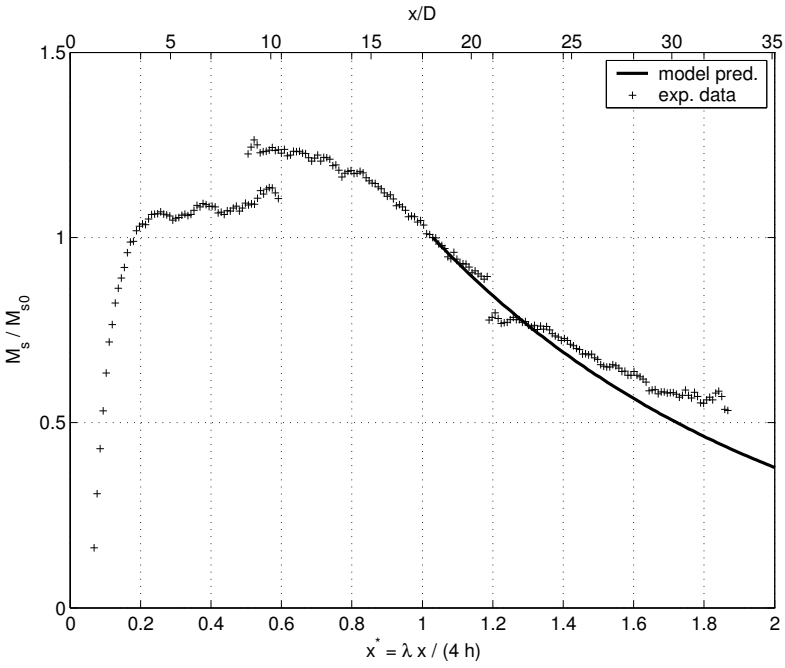

(b) Momentum deficit flux M_s^*

Figure 8.8. Volume and momentum deficit fluxes for a vortex street-like wake flow, $S = 0.06$, tending to maintain a permanent recirculation bubble. (series 18_vs06). Initial conditions for the integral wake model are evaluated from cross-section at $x/\overline{D} = 18.1$, esp. $\frac{u_{sc0}}{u_a} = 0.195$. The entrainment coefficient adapted for the data is $\alpha = 0.098$.

velocity u, and of mass concentration c. In the wake far field the width ratio $r_\gamma = \delta_\gamma/\delta_u$ is found to be independent of the downstream position. For the first case of a pure VS wake shown in Figure 8.9 we observe good agreement of the model predictions with the experimental data both for u^*_{sc} and for δ. In the second VS wake tending to build up a permanent recirculation bubble, shown in Figure 8.10, the decay of u_{sc} and the growth of δ are slightly over-predicted. This corresponds to the findings for the prediction of the deficit fluxes (cf. Figure 8.8).

Figure 8.10 illustrates the flow field behavior for a wake flow with an existing recirculation bubble and weaker (but still very distinct) 2D coherent vortical structures. From Figure 8.8 we know, that for these flow conditions the deficit fluxes of volume and momentum have only a weak tendency to decrease, they are almost preserved after an initial stage up to $x^* \approx 0.2$. This is also visible in the normalized centerline velocity deficit u^*_{sc} being constant over a long range of x^*. As expected we cannot reproduce this behavior with the numerical model with the current values for the non-dimensional parameters α and ϕ_m. The reason, why we still apply these values, is that they lead to a correct prediction of the wake half-width, which is growing despite the constancy of the deficit fluxes and velocity. Though we do not fully understand this specific wake flow development,[10] we can agree that finally the wake will be dissipated by the mechanisms of vertical shear. Also in this case we should therefore not conclude that the integral model would not work properly more downstream in the far field of the wake.

[10] If we would argue about the reasons for this conservation of deficit quantities, we should surely consider the existence of 2D coherent structures. They do not only scale with the roughness length scale $4h/\lambda$, but their life span, until they disintegrate, depends strongly on the length scale related to the generation of the horizontal shear, namely the cylinder diameter D. $x^* = 0.3$ in this case corresponds to $x/D = 8.5$, whereas for the first case with stronger 2D coherent structures the same x^* yields $x/D = 54.0$. As stated in v. Carmer & Jirka (2001) after 10 to 20 x/D the turbulent kinetic energy, extracted from the ambient flow and mainly transferred to the motion of the coherent structures, is dissipated again. After this distance we would thus expect the wake flow to be controlled by the vertical shear again and the integral model to be applicable, whereas the existence of 2D coherent vortical structures involves additional dynamic effects, which are not taken into account in the numerical model. In the first case, $x/D = 20$ corresponds with $x^* \approx 0.11$, by that distance the maximum deficit fluxes are reached and maintained over some distance, so we encounter a similar behavior in both cases. We may distinguish three regions in a shallow wake, namely the immediate near field, where the wake is generated, a transitional region dominated by large-scale coherent structures, and the far field dominated by small-scale bottom induce turbulence. In the first case we can observe the wake passing through all three regions, whereas in the second case we do not enter the third stage of the wake far field, for which the integral model is intended primarily.

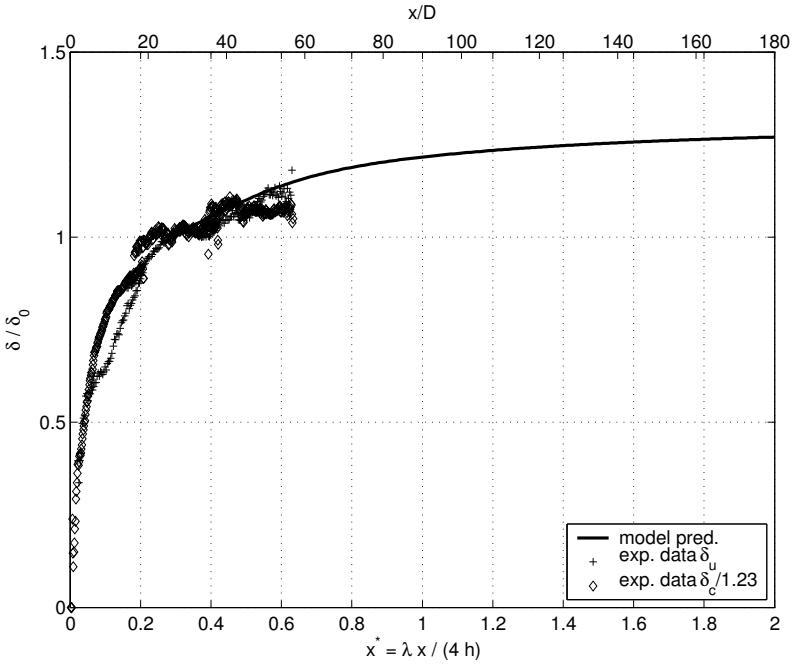

(a) Wake half width $\frac{\delta}{\delta_0}$

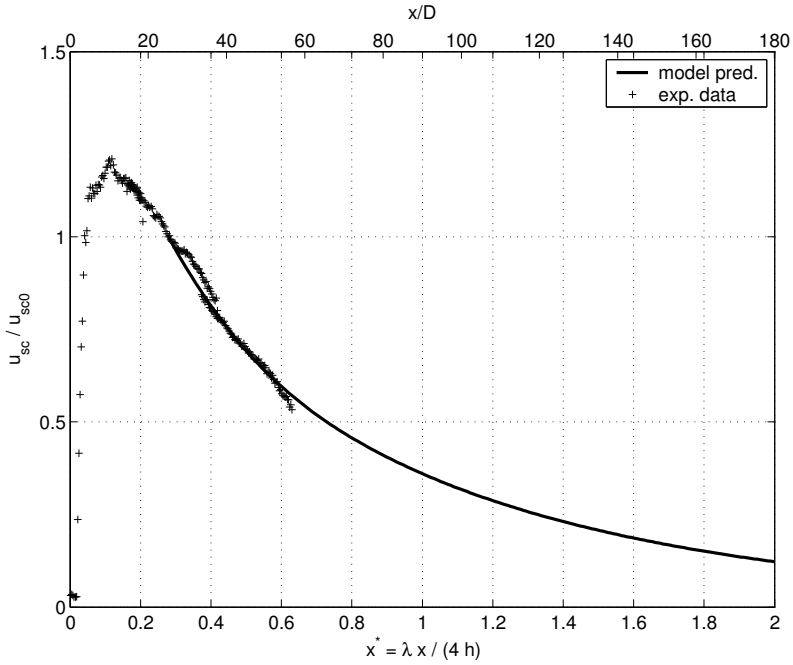

(b) Centerline velocity deficit $\frac{u_{sc}}{u_{sc0}}$

Figure 8.9. Characteristic flow properties for a vortex street-like wake flow, $S = 0.01$, (series 38_vs01). For initial and boundary conditions see Figure 8.7. The wake half width displayed in Figure (a) is computed either from the velocity and mass concentration fields, δ_u and δ_γ. The concentration-based half width δ_γ is reduced by the width ratio $r_\gamma = 1.23$.

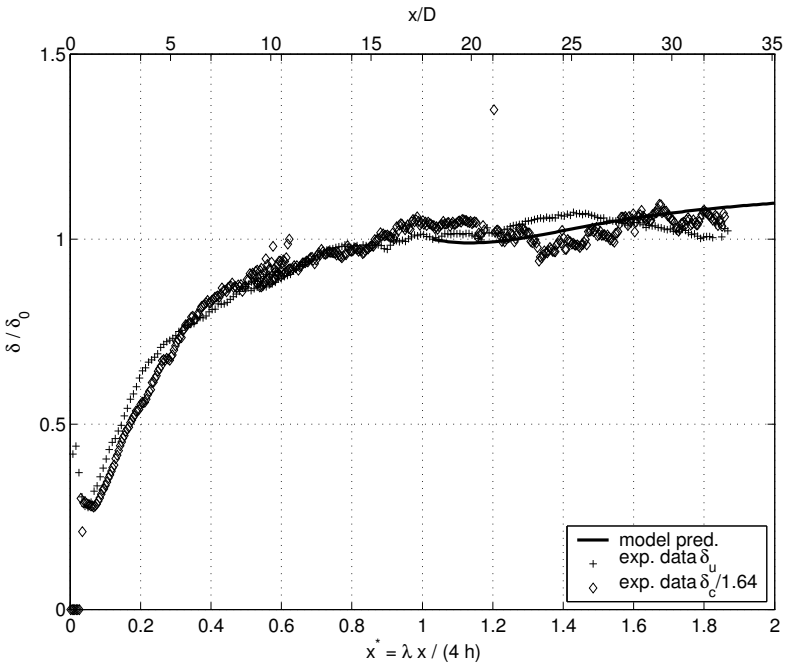

(a) Wake half width $\frac{\delta}{\delta_0}$

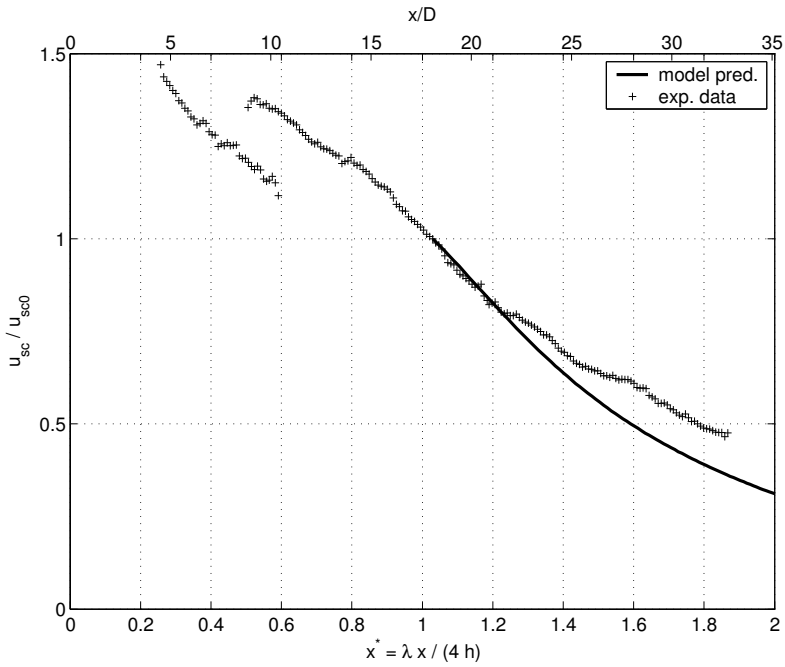

(b) Centerline velocity deficit $\frac{u_{sc}}{u_{sc0}}$

Figure 8.10. Characteristic flow properties for a vortex street-like wake flow, $S = 0.06$, tending to maintain a permanent recirculation bubble. (series 18_vs06). For initial and boundary conditions see Figure 8.8. The wake half width displayed in Figure (a) is computed either from the velocity and mass concentration fields, δ_u and δ_γ. The concentration-based half width δ_γ is reduced by the width ratio $r_\gamma = 1.64$.

8.4.4 Discussion of model assumptions

In this section we will briefly discuss some essential assumptions for the application of the integral wake model. Concerning the physical grounds of the arising questions, further light will be shed throughout Part III.

Transverse distribution of u and c. For the derivation of the integral wake model we presumed the main velocity component as well as a scalar quantity to show a *self-similar development* and to be *normally distributed* in the transverse direction. If we employ appropriate scaling quantities for the standardization—for instance the velocity deficit $u_s^+ = \frac{u_s}{u_{sc}}$ and the transverse distance $y^+ = \frac{y}{\delta_u}$—, self-similarity means that the normalized transverse distribution is independent of the longitudinal distance x, or to be more precise that the dependency on x is incorporated in the scaling variables, thus (cf. Equation (8.1))

$$\begin{aligned} u_s^+ &= f_u\left(y^+\right) \\ \frac{u_s\left(x,y\right)}{u_{sc}\left(x\right)} &= \exp\left(-\left(n\frac{y}{\delta_u\left(x\right)}\right)^2\right) \ . \end{aligned}$$

Analogously, the self-similar transverse distribution of tracer mass becomes (cf. Equation (8.2)),

$$\begin{aligned} c^+ &= f_c\left(y^+\right) \\ \frac{c\left(x,y\right)}{c_c\left(x\right)} &= \exp\left(-\left(n\frac{y}{\delta_\gamma\left(x\right)}\right)^2\right) \ , \end{aligned}$$

where further use can be made of a constant ratio of the wake half widths based on velocity and on mass concentration, $\delta_\gamma = r_\gamma\,\delta_u$.

The second lines of the above equations state, that these self-similarly distributed quantities show a Gaussian distribution in the transverse normalized direction y^+. Figure 8.11 displays the spatial average of several transverse profiles of the normalized velocity deficit for the first case of a shallow wake showing strong 2D coherent structures. Since all transverse distributions, evaluated at different distances downstream of the cylinder between $x/D = 8$ and $x/D = 32$, collapse on a single curve denoted by ♦, this figure confirms the self-similarity and proper normalization of u_s/u_{sc}. In the integral wake model the velocity deficit is assumed to follow a Gaussian distribution (8.1) in the transverse direction, which is confirmed from Figure 8.11, where a bold line indicates the solution of Equation (8.1). The prediction assuming a normal distribution slightly overestimates the experimental data at the outer edges of the wake around $y^+ \approx \pm 1.8$. We will address this fact in Section 9.1, but also refer to Tennekes & Lumley (1977, pp. 117) or Pope (2000, pp. 119, 149). Furthermore, we will demonstrate in Section 9.1 that self-similarity and

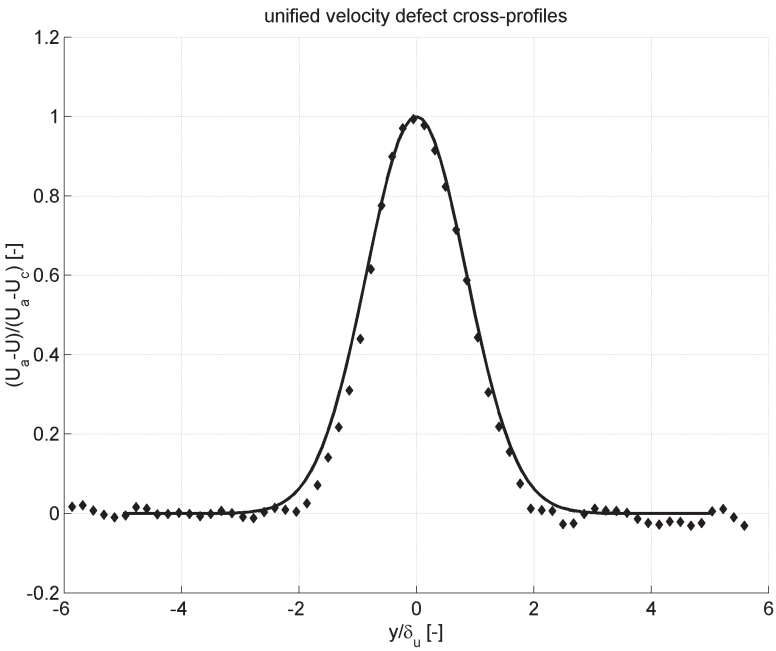

Figure 8.11. Distribution of normalized velocity deficit $u_s^+ = u_s/u_{sc}$ along the normalized transverse direction $y^+ = y/\delta_u$ (v. Carmer et al., 2001). ♦ symbols depict the longitudinal average of measured velocity deficit cross-profiles for different locations at $8 \leq x/D \leq 32$ in the wake of series 38_vs01. Since all normalized profiles collapse on the same distribution, self-similarity holds. The bold full line represents the Gaussian distribution computed from Equation (8.1) and well predicts the measured profiles despite some deviation near the boundary of the wake.

Gaussian distribution in the transverse direction are restricted to a distinct wake region associated mainly with the far field.

Turbulent mixing and lateral entrainment. Another important question concerns the implementation of *transverse spreading* by virtue of mixing and entrainment both of volume deficit and of tracer mass. Throughout this chapter we are concerned with the development and application of an integral wake model. Therefore, we do not need to examine the transverse flux of turbulent x-momentum $\langle u'v' \rangle$ explicitly, because the transverse integration of the Reynolds shear stress yields a net value of zero in the momentum deficit differential equation. Moreover, the Gaussian transverse distribution of u_s/u_{s0} includes a constant–viscosity hypothesis to model the turbulent stresses $\langle u'v' \rangle$ (cf. Section 9.1).

In order to represent the transverse spreading in the differential equation of the volume deficit flux, we used an entrainment hypothesis first presented by G. I. Taylor, as reported by Morton et al. (1956). This is to relate the rate of inflow of ambient fluid into the shear flow to a local property of the shear flow, especially to its local mean velocity difference. Applied to a wake flow, this hypothesis says that the inflow velocity of diluting water into any

wake would be proportional to the maximum mean velocity deficit u_{sc} in the wake at the cross–section of inflow (cf. also FISCHER ET AL. (1979) for jet flows). As a constant of proportionality the entrainment coefficient α has been introduced, for the application of this concept to the volume deficit flux we refer to Section 8.2.2. It is essential to note, that we assume the entrainment coefficient to be a constant value, i.e. $\alpha \neq f(x)$.

In order to empirically prove this assumption, in agreement with the commonly used definition, we evaluated local values $\alpha(x)$ directly at the transverse positions $y^+ = y/\delta_u = 1$. The entrainment rate then depends on the local transverse velocity component $v(x, \delta)$, called the *entrainment velocity* v_e, and thus depends on the definition of the wake half-width. Following the common definition v_e is evaluated at $y = \pm\delta_{1/e}$. Hence the entrainment coefficient is given as

$$\alpha(x) = \frac{v\left(x, \delta_{1/e}\right)}{u_{sc}(x)} = \frac{v_e(x)}{u_{sc}(x)} \ . \tag{8.90}$$

Figure 8.12 shows the downstream development of $\alpha(x)$ for the pure VS wake (series 38_vs01) and for the bubble–tending VS wake (series 18_vs06). Values of α have been calculated from the velocity data separately in both lateral shear layers of the wake. For each downstream position corresponding values have been averaged, i.e. $\alpha(x) = 1/2\left(\alpha_{le}(x) + \alpha_{ri}(x)\right)$. Here, a positive sign of α means entrainment into the wake, while a negative sign denotes detrainment of wake fluid into the ambient flow. Note that x is standardized by the momentum deficit length scale $\ell_m = \sqrt{M_{s0}}/u_a^2$ defined in (9.1). Though care has to be exercised in quantitative analyzing the results[11], we recognize that α does not have a constant value. In the wake near field α rapidly decreases from high initial values with $\alpha > 0.2$ indicating significant entrainment of ambient fluid during the development of the wake and the 2D LCS. After approximately 5 x/D α drops below zero and continues to decrease up to $x/D \approx 7.5$, then increases again. Thus, the transitional region characterized by the advection and decay of large 2D coherent structures even shows a net detrainment of wake fluid into the ambient flow resulting in an increase of the volume deficit flux Q_s, as indicated in Figures 8.7 and 8.8. In the far field the increase stops as the LCS disintegrate. The positive value of α is expected to asymptotically tend to zero far downstream of the obstacle as

[11] We observe significant differences between corresponding α on both sides of the wake that stem from uncertainties in the experimental evaluation of the transverse velocity component v. Time-mean transverse velocities $\langle v \rangle$ are of the order of 1 mm/s in the wake far field. Unfortunately, due to small imperfections of the bed topography revealing minor variations of the bottom elevation transverse flow velocities are induced that for an undisturbed shallow flow are of the same order of magnitude. These errors in the transverse velocities show up more significantly when normalized with the centerline deficit velocity u_{sc}, which acquires diminishing values far downstream of the cylinder.

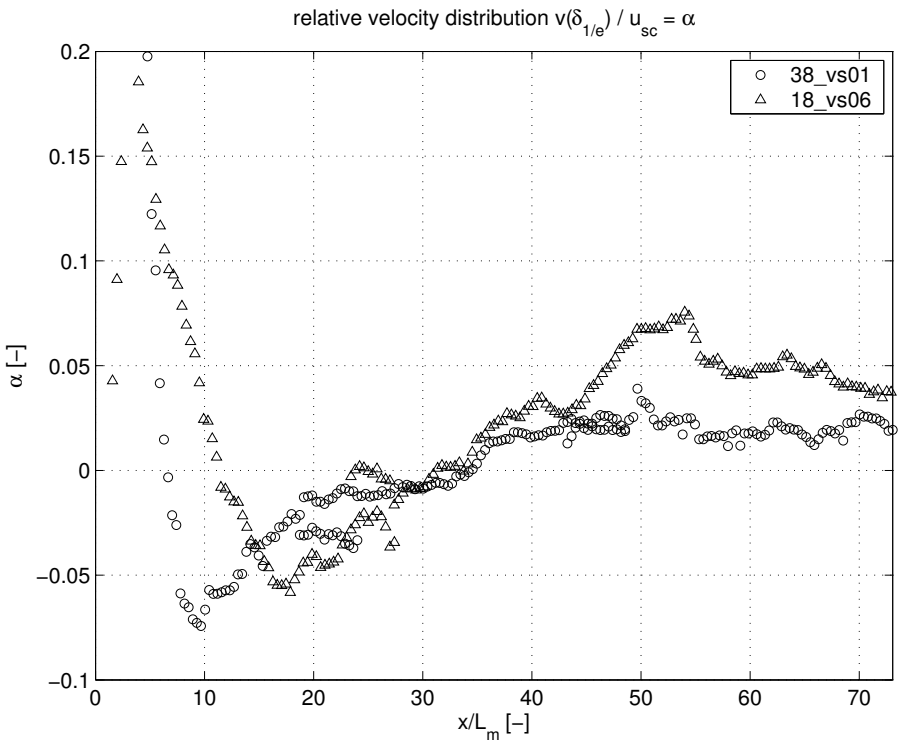

Figure 8.12. Longitudinal development of entrainment coefficient α. From data of measurement series 38_vs01 and 18_vs06 entrainment coefficients have been evaluated separately on both sides of the wake, and averaged for each downstream position. A positive sign denotes entrainment of ambient fluid into the wake flow. Contrary to the entrainment hypothesis, α is not a constant, but varies with the longitudinal distance x. Due to restrictions in the experimental accuracy of v, the results should not be employed to calibrate far field values of α.

the flow deficit constituting the wake flow finally vanishes. However, due to the restricted experimental accuracy in the transverse velocity, it can not be decided whether α remains constant or tends to zero. In the latter case a linear decay law could be given for the far wake development of α in analogy to the asymptotic wake regime of axisymmetric jets (Jirka, 2004) as

$$\alpha = \alpha_1 + \alpha_2 \frac{u_a}{u_a - u_{sc}}$$

which relates α to the local wake strength. Contrarily, in the intermediate wake region, α is inversely proportional to the above ratio, i.e. $\alpha \propto \left(\frac{u_a}{u_a - u_{sc}}\right)^{-1} = \left(\frac{u_a}{u_c}\right)^{-1}$.

Dissipation due to bottom friction. The implementation of the *bottom friction* in the momentum equations of the SWE is another question that demands further attention. In the Reynolds averaged 2D SWE for the x- and y-momentum, Equations (8.30) and (8.31), we expressed the influence of the bottom shear employing Equation (8.25). By doing so we evaluated the bottom

shear from the mean velocity field $\langle \boldsymbol{u} \rangle$ only, which is the usual approach (e.g. Vreugdenhil, 1994) .

Unfortunately, this commonly used approximation for boundary layer flow is valid only for flow without predominant periodic large-scale motions, because the vertical shear stresses are deducted from the mean flow field only. Contrary to plane boundary layer flows, the shallow wake flows examined in this work show significant large-scale coherent vortical structures. These eddies contain a reasonable part of turbulent kinetic energy, which is dissipated mainly at the bottom as they advect downstream. Therefore, by the above approximation the frictional losses will be underestimated severely in the transitional region of the wake due to the neglect of the coherent vortical motion, whereas in the far field this assumption will hold more accurately, since the vortical structures constituting the periodic–advective flow are already dissipated, and thus frictional losses are solely induced by bottom shear due to the mean–advective flow. Especially in the transitional region, the time-resolved averaged representation of the mean shear stresses in the form

$$\frac{\langle \tau_{bx} \rangle}{\rho} = \frac{\lambda}{8} \left\langle u \sqrt{u^2 + v^2} \right\rangle \text{ and } \frac{\langle \tau_{by} \rangle}{\rho} = \frac{\lambda}{8} \left\langle v \sqrt{u^2 + v^2} \right\rangle \ , \tag{8.91}$$

should give better results compared to using only the mean flow field. The difficulty of computing the shear stresses in a vortex street-like shallow wake flow is comparable to modeling tidal stresses. Though there might be possibilities to represent also these slowly fluctuating motions by a stress term of some sort (cf. e.g. Vreugdenhil (1994)), it would still be questionable how to implement it into a quasi-1D model.

The implications of using the time-resolved averaged formulation for the mean shear stress in the SWE are delicate, and of course the derivation of the simple differential equation for the momentum deficit, as presented in Section 8.2.1, would be impossible. Using the simplified Reynolds averaged bottom shear not only leads to an underestimation of the shear stress term in the x–momentum equation, but has further shortcomings. In the transverse momentum equation (8.33), the bottom friction term is completely neglected, as is acceptable for mean transverse velocities $\langle v \rangle \ll \langle u \rangle$. Though in shallow wakes outside the immediate near field, this assumption is always valid for the mean flow field $\langle \boldsymbol{u} \rangle$, the periodic counter-rotating vortices in the vortex street-like transitional wake region induce large additional velocity components—provoking significant periodic fields of bottom shear stress—, which cancel out only when averaging over a whole vortex shedding cycle. For the same argument, the magnitude of the velocity vector might not be approximated by the main velocity component $|\boldsymbol{u}| \approx \sqrt{\langle u \rangle^2 + \langle v \rangle^2} \approx \langle u \rangle$, as applied in (8.37) in flows, where significant variations occur in the time– or phase–resolved velocity fields.

Since on one hand we are not able to sustain the complete Reynolds averaged bottom shear terms in the 2D SWE, on the other hand using the mean shear approximation introduces significant inaccuracies, we try to reduce them by suggesting the following compromise. First, the magnitude of the average velocity vector reads $\langle|\boldsymbol{u}|\rangle = \left\langle\sqrt{u^2+v^2}\right\rangle = \sqrt{\langle u^2\rangle + \langle v^2\rangle}$. Second, when using a velocity component for the evaluation of an averaged shear stress term, we want to consider only its magnitude, but not its direction, as our final interest is to reproduce energy losses. Thus, we propose another approximation of the full shear stress terms in the longitudinal and transverse direction, respectively,

$$\begin{aligned}\frac{\langle\tau_{bx}\rangle}{\rho} &= \frac{\lambda}{8}\,\langle|u|\rangle\,\sqrt{\langle u^2\rangle + \langle v^2\rangle} \text{ and}\\ \frac{\langle\tau_{by}\rangle}{\rho} &= \frac{\lambda}{8}\,\langle|v|\rangle\,\sqrt{\langle u^2\rangle + \langle v^2\rangle}\ .\end{aligned} \tag{8.92}$$

We want to stress the importance of the LCS in the transitional wake region also on the Reynolds averaged flow fields by evaluating the transverse bottom shear stresses from the time–mean, from the phase–resolved, and from the time–resolved velocity fields. In Figure 8.13(a) the magnitude of the phase–resolved transverse velocity component $v(\phi)$ is shown for a given phase angle ϕ in the shedding cycle of the large-scale coherent structures in the wake. Since $v(\phi)$ amounts to more than 30% of the vector magnitude $|\boldsymbol{u}(\phi)|$, and the transverse shear is of the same magnitude compared to the total shear, it is therefore not a negligible quantity. Note, that $v(\phi)$ reveals the large-scale vortices in the alternate change of the flow direction. Obviously, the amount of energy dissipated at the bottom does not depend on the flow direction. If we would take the average of the transverse motion over the full phase retaining the direction and thus the sign of v, this would result in a vanishing v-field due to the periodicity of the flow. In Figure 8.13(b) we compare the average transverse and main shear fields evaluated from absolute values of the phase resolved shear $\langle|\tau_{by}(\phi)|\rangle\,/\,\langle|\tau_{bx}(\phi)|\rangle$ using (8.92). As the dissipation of turbulent kinetic energy is a scalar quantity, which does not depend on the direction of the flow, we computed the average from the absolute values of the phase–resolved velocity. In the presence of the vortex street-like wake we notice a significant amount of absolute shear stress, which shifts downstream during the shedding cycle of the vortical structures. In Figure 8.13(c) we present the evaluation of the absolute bottom shear fields averaged over the whole data set using (8.92), in contrast to the evaluation given in Figure 8.13(b) based on the phase–resolved re-sampled flow fields. We notice, that the process of phase–resolved re-sampling does not alter the qualitative behavior and only slightly underestimates the real shear stresses, since the high-frequent small-scale fluctuations are suppressed. On the contrary, Figure 8.13(d) depicts the

appropriate values computed from the approximative approach using only the mean velocity fields. Due to the vanishing mean transverse component $|\langle v \rangle|$ the mean transverse shear is of minor influence and is not sufficient to represent the dissipation of turbulent kinetic energy stored in the large-scale vortical structures. In conclusion, in periodic flows it is essential to evaluate the average transverse bottom shear stress from the absolute values of a time series. If we do so, we have to take care about the large-scale vortical motions, neglecting the fluctuating part yields a large error. If we do not average over absolute values, we will underestimate the frictional losses regardless, whether we keep the fluctuating velocity fields or not. As a consequence in order to model the frictional losses using time-mean flow fields in predominantly periodic flows or in shallow flows with predominant 2D LCS, the bed friction coefficient λ has to be increased to much higher values than predicted from the bottom roughness.

8.4.5 Concluding remarks

The analytical integral 1D model for shallow wake flows derived in this chapter consists of conservation equations for the standardized fluxes of volume deficit Q_s^*, of momentum deficit M_s^*, and of tracer mass Q_c^*, Equations (8.65), (8.67), and (8.70), respectively. Employing these conservation equations, the downstream development of velocity u_{sc} and tracer mass c_c along the centerline, and of the wake half width δ is represented by Equations (8.71), (8.74), and (8.73), respectively. In order to derive the above set of integral equations, extensive use has been made of the self-similar, and Gaussian transverse distributions of velocity deficit and mass concentration, given by Equations (8.1), and (8.2).

The applicability of the integral model is restricted to the far field of shallow wake flows, since

- self-similarity and Gaussian distribution do not hold in the near and intermediate field,
- the order–of–magnitude arguments used in the derivation of the momentum conservation equation from the 2D SWE are not valid in the near and intermediate field,
- the entrainment of ambient fluid into the wake differs in the near, intermediate and far field. The constant entrainment rate presupposed for the model is a suitable approximation only in the far field,
- in the bed friction model bottom shear stresses are included only as they are induced by the mean–advective flow, bottom stresses induced by the periodic–advective motion of the vortex street-like wake and of its associated 2D LCS have been neglected.

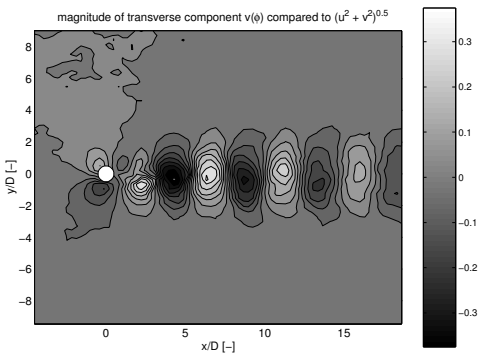

(a) Transverse phase–resolved averaged velocity component for a given phase angle ϕ

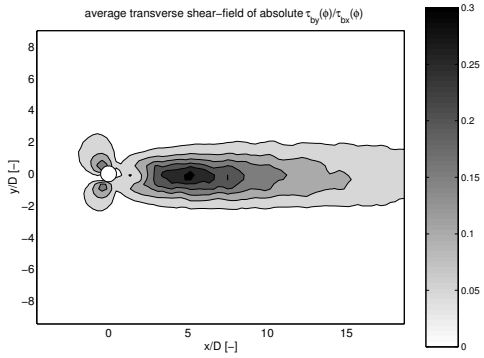

(b) Transverse shear $\langle|\tau_{by}(\phi)|\rangle \,/\, \langle|\tau_{bx}(\phi)|\rangle$ from phase–resolved averaged flow fields

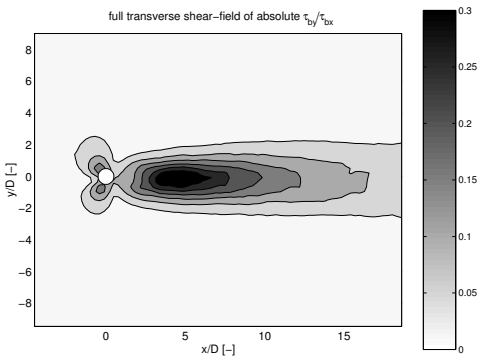

(c) Average transverse shear of whole time series

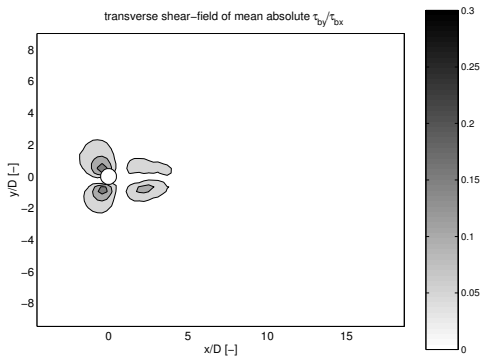

(d) Average transverse shear from mean flow field

Figure 8.13. Normalized transverse bottom shear τ_{by}/τ_{bx} in the transitional wake region. Figure (a) shows the magnitude of the standardized phase–resolved transverse velocity component $v_p(\phi)/\sqrt{\langle u_p\rangle^2 + \langle v_p\rangle^2}$ for a given phase angle, $v(\phi)$ amounts to more than 30% of the vector magnitude $|\boldsymbol{u}(\phi)|$. In Figure (b) we compare the average transverse and longitudinal shear fields approximated by absolute values of the phase–resolved shear $\langle|\tau_{by}(\phi)|\rangle \,/\, \langle|\tau_{bx}(\phi)|\rangle$ computed by adapting (8.92), whereas Figure (c) illustrates the same quantity evaluated by averaging over the whole time-resolved data set using (8.92). Contrary, Figure (d) depicts the appropriate values computed from the common approximative approach using the mean velocity fields only.

9. Time-mean Description of Shallow Wake Flow

Especially in the far field of shallow wake flows, where large-scale vortical structures are no longer present, time-averaged flow quantities allow for a complete description of the wake flow—together with the statistical description of turbulence presented in Chapter 7. In this chapter only those quantities are examined, which have already been used to develop an integral wake model in Chapter 8. All data have been obtained from field-wise PIV and PCA measurements of surface velocity fields and of depth–averaged mass concentrations. Further analyses of these measurements concerning the quasi-periodic flow and the large-scale coherent vortical structures will be presented in Part III of this study.

The data obtained from various shallow wake flows will also be compared to recent results of theoretical studies on unbounded and shallow wakes using linear stability analysis.

9.1 Time-mean evaluation of planar measurements

9.1.1 Transverse distribution of velocity and mass

In the far field of shallow turbulent wake flows we expect the distributions of the velocity deficit and the tracer mass to be *self-similar*, when standardized by appropriate scales (cf. Section 8.1.1). Here, the transverse direction is non-dimensionalized by the local wake half width, $y^+ = y/\delta$, and the ordinates by their centerline values, $u_s^+ = u_s/u_{sc}$ and $c^+ = c/c_c$. For an unbounded plane wake it has been shown (see e.g. (Pope, 2000) for more detail) that solving the x-momentum equation (cf. Section 8.2.1) the self-similarity of $u_s\,(x, y)$—which has been employed to derive the momentum deficit equation—requires that the deficit velocity follows a *Gaussian distribution* (8.1). This also implies the *turbulent–viscosity hypothesis* using a constant value of the normalized eddy viscosity $\nu_t^+ = \nu_t/\left(u_{sc}\,\delta\right)$ (cf. Hinze (1975, pp. 489), Pope (2000, pp. 119, 147)). Hence, in 2D shear flows the transverse flux of turbulent x momentum is approximated by

$$\left\langle u'v' \right\rangle = -\widehat{\nu_t}\,\langle u_{sc}\rangle\,\delta\frac{\partial\,\langle u_s\rangle}{\partial y}\ .$$

Analogously, the turbulent transverse mass flux in 2D shear flow becomes with the *gradient–diffusion hypothesis*

$$\langle v'c' \rangle = -D_t \frac{\partial \langle c \rangle}{\partial y} \ .$$

Using a constant dispersion ratio r_γ in the Gaussian scalar distribution (8.2) related to the turbulent Schmidt number by $r_\gamma \propto Sc_t^{-1/2}$ (Pope, 2000, pp.161) implies that we also assume a constant turbulent diffusivity $D_t = \nu_t/Sc_t$ throughout a wake cross–section.

Transverse distributions of the velocity deficit u_s/u_{sc} and of the mass concentration c/c_c in a shallow turbulent wake are presented in Figure 9.1 for a vortex street-like wake flow of series 38_vs01. They represent the characteristic behavior observed in shallow wake flows of stability classes VS and UB. Cross–sectional distributions of experimental data (• symbols) obtained from PIV and PCA measurements are compared to the analytical far field solutions (8.1) and (8.2) indicated by bold full lines. Figures 9.1(a) and 9.1(b) show distributions of u_s^+ and c^+, respectively, for cross–sections at $x/D = 1.75$, 2.25, 3, 4 in the wake near field. The velocity deficit distribution u_s^+ reveals a strong initial deviation not only from self-similarity, but—probably more important—also from a Gaussian distribution. At the outer edges of the wake u_s^+ takes negative values with the minima located at $\pm y^+ \approx 2.5$ and approaches the ambient velocity u_a from negative values, i.e. $\lim_{y^+ \to \pm\infty} u_s/u_{sc} = 0^-$. Hence, in the immediate vicinity of the obstacle, the flow velocity takes lower values relative to u_a in the wake core, but along the edges of the wake becomes faster than u_a.[1] Compared to the Gaussian far field distribution a second inflection point occurs at the outer edge of the wake close to the cross–sectional minimum of u_s^+. Tachie & Balachandar (2001) reported similar transverse distributions of u_s in the shallow near wake generated by a flat plate placed normal to the flow. LIF measurements of plate–generated wakes of varying shallowness showed similar transverse concentration distributions (Balachandar et al., 1999).

Figures 9.1(c) and 9.1(d) depict the transverse distributions of velocity deficit and mass concentration, respectively, in the transitional and far field at $x/D = 5$, 15, to 55. Both u_s^+ and c^+ show self-similarity, and follow a Gaussian distribution given by Equations (8.1) and (8.2). Near the wake boundaries at $\pm y^+ \approx 1.8$ the wake flow quantities decrease faster than predicted by

[1] Closer to the obstacle even the centerline velocity exceeds the ambient velocity, $u_c > u_a$. Taking into account that from the PIV measurements we obtain *surface* velocity fields, we may conclude that this accelerated flow can be addressed to 3D flow up-welling in the lee of the cylindrical obstacle.

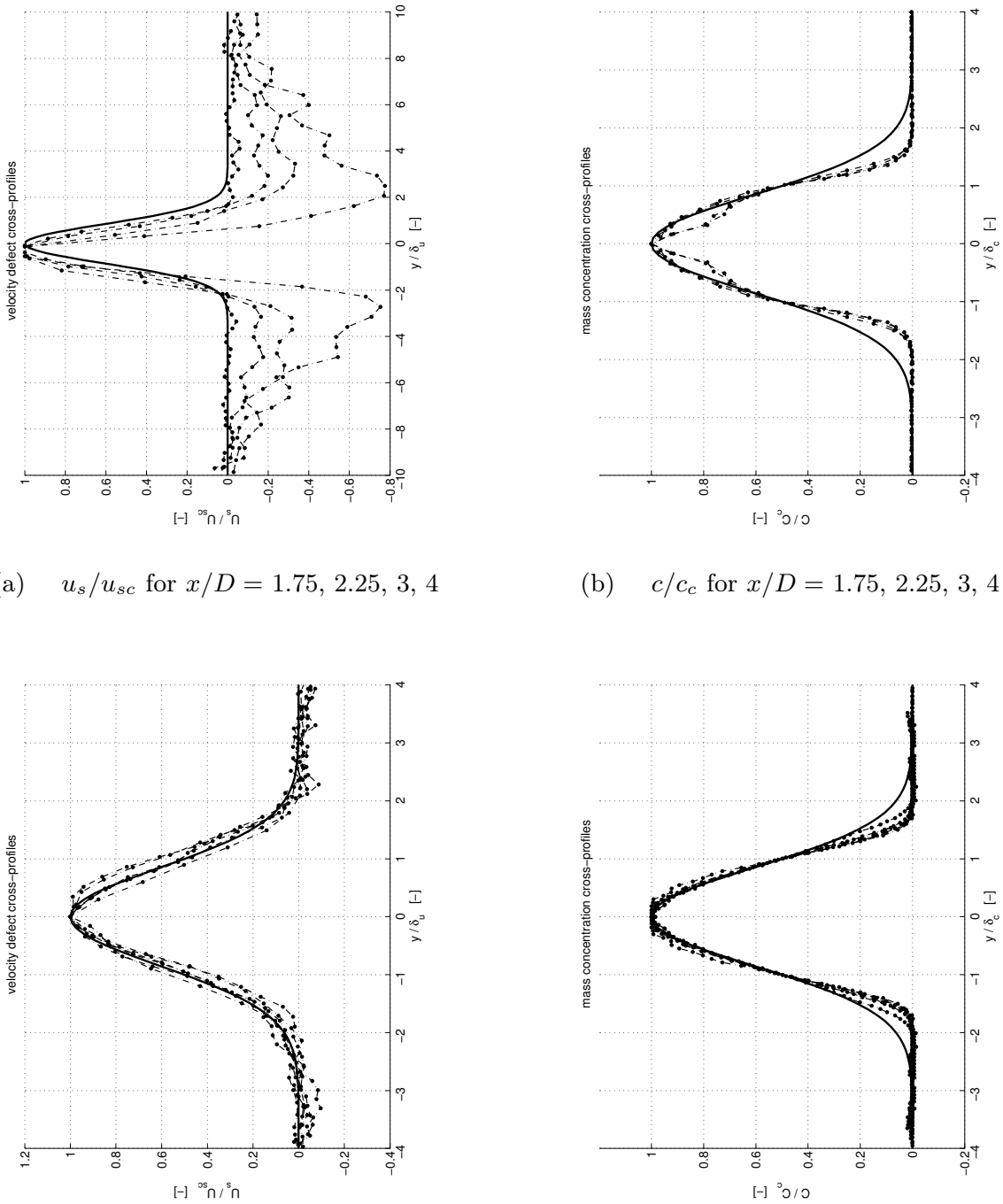

(a) u_s/u_{sc} for $x/D = 1.75$, 2.25, 3, 4

(b) c/c_c for $x/D = 1.75$, 2.25, 3, 4

(c) u_s/u_{sc} for $x/D = 5$, 15, to 55

(d) c/c_c for $x/D = 5$, 15, to 55

Figure 9.1. Transverse distributions of the velocity deficit u_s/u_{sc} and of the mass concentration c/c_c in a shallow turbulent wake are presented for a vortex street-like wake flow of series 38_vs01. Experimental data (• symbols), extracted at specific cross–sections from PIV and PCA measurements, are compared to the analytical far field solutions (8.1) and (8.2) indicated by a bold full line. Figures (a) and (b) show cross–sections at $x/D = 1.75$, 2.25, 3, 4 in the wake near field, revealing a strong initial deviation from self-similarity in u_s^+. In the transitional and far field at $x/D = 5$, 15, to 55 both u_s^+ and c^+ follow a Gaussian distribution that slightly over-predicts the data near the wake boundaries at $y^+ \approx 1.8$.

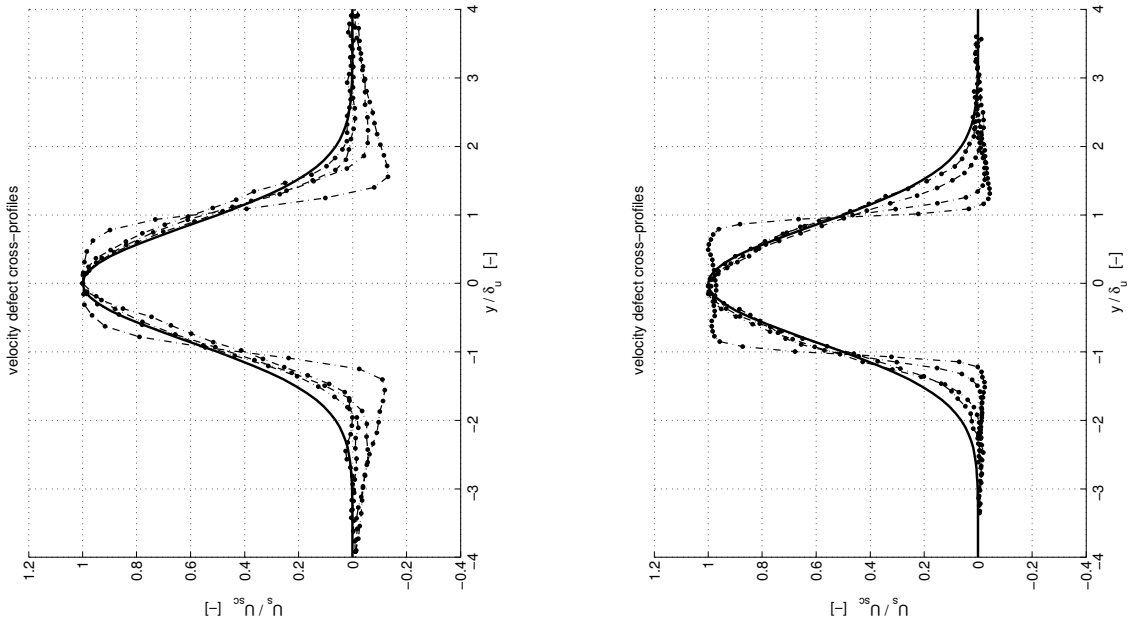

(a) vortex street-like shallow wake (b) unsteady bubble shallow wake

Figure 9.2. Transverse distributions of the velocity deficit u_s/u_{sc} in the near field of shallow wakes are presented for a vortex street-like wake flow of series 25_vs07 in Figure (a) and for a unsteady bubble wake of series 17_ub25 in Figure (b). Experimental data (• symbols), extracted at cross–sections $x/D = 0.5$, 1, 1.5, 2 from PIV measurements, are compared to the analytic far field solutions (8.1) indicated by a bold full line. The initial deviation of u_s^+ from self-similarity and Gaussian distribution occurs regardless of the wake stability class.

a Gaussian distribution.[2] As has also been observed in other 2D shear flows Pope (2000, pp. 105), the constant turbulent viscosity hypothesis—employed for the deduction of the Gaussian distribution—will not hold near the boundaries of a shallow wake, but $\widehat{\nu_t}$ will decrease to zero near the edges.

In the intermediate and far wake the transverse distributions of u_s^+ and c^+ show the same characteristic properties, namely self-similarity and Gaussian distribution, independently of the wake stability and of the presence of 2D LCS. Also in the near field of a shallow wake the transverse distributions behave similar regardless of the wake stability. This is illustrated in Figure 9.2 from the velocity deficit distributions of a VS wake (series 25_vs07) and of an UB wake (series 17_ub25), plotted at cross–sections at $x/D = 0.5$, 1, 1.5, 2. For both stability classes the profiles are neither self-similar nor Gaussian. As also demonstrated in Figure 9.1(a), u_s^+ initially takes negative values at the

[2] This deviation is quite obvious in c^+, but also usually encountered in u_s^+. In the PIV measurements of series 38_vs01 a coarse spatial resolution with respect to the diameter of the obstacle ($\Delta y/D \approx 0.\overline{3}$) leads to an inaccuracy in determining the centerline position.

wake boundaries involving a second inflection point, and shows steeper flanks. This shape form gradually changes into the self-similar Gaussian distribution at more downstream positions.

9.1.2 Downstream development of velocity and mass

Shallow turbulent wake flows—vertically sheared due to the bottom, and horizontally sheared due to an large-scale obstacle—like other shallow shear flows display a characteristic duality of the macro length scales. Lengths can be normalized by a transverse macro scale e.g. by the initial wake width or by the diameter of the obstacle, or by a vertical macro scale related to the flow depth. The standardized downstream distance then becomes x/D using a transverse shear–scale, or $c_f\, x/h$ using a bottom friction–scale. The former is applicable primarily in the near and intermediate wake fields, where stronger transverse shear is present. The latter applies to the far field, where bottom friction–induced shear prevails. In order to locate the transition between near and far field for wake flows of different strength, an integral length scale can be introduced based on the initial momentum deficit, which conceptually corresponds to a jet/crossflow length scale comparing the strength of a jet to the ambient flow (Jirka, 2004). This *wake length scale* will be defined as

$$\ell_M = \frac{M_{s0}^{1/2}}{u_a} \ . \tag{9.1}$$

Assuming a Gaussian distribution of the velocity deficit in the initial cross–section, M_{s0} can be obtained from Equation (8.15). Locating the initial cross–section at the downstream stagnation point, where $u_{c0} = 0$, i.e. $u_{sc0} = u_a$, and assuming $\delta_0 = D/2$, the initial momentum deficit can be approximated by $\tilde{M}_{s0} = \sqrt{\pi/2}\, D/2\, h\, u_a^2$, and the wake length scale becomes $\ell_M = \left(\sqrt{\pi/8}\, hD\right)^{1/2}$. If we assume an initial top–hat velocity profile, where $u = 0$ inside the wake (initial width $\delta_0 = D/2$), then from $\tilde{M}_{s0} = h\, D\, u_a^2$ the wake length scale becomes $\ell_M = \sqrt{hD}$.

Since in this section we compare the downstream development of flow quantities of various wake flows that differ with respect to their initial momentum deficit, we normalize the downstream distance with the wake length scale as $x/\sqrt{hD}$ approximating the initial velocity distribution by a top–hat profile. Note that the origin of the x axis remains in the center of the obstacle.

In Figure 9.3 the downstream development of the *wake half width* δ_u based on the velocity deficit is compared to the *wake half width* δ_γ based on the mass concentration for a vortex street-like wake flow (series 18_vs06). The half width have been evaluated as the transverse distance from the centerline up to the location of $u_s/u_{sc} = 1/2$, or $c/c_c = 1/2$, respectively. The upper, logarithmic

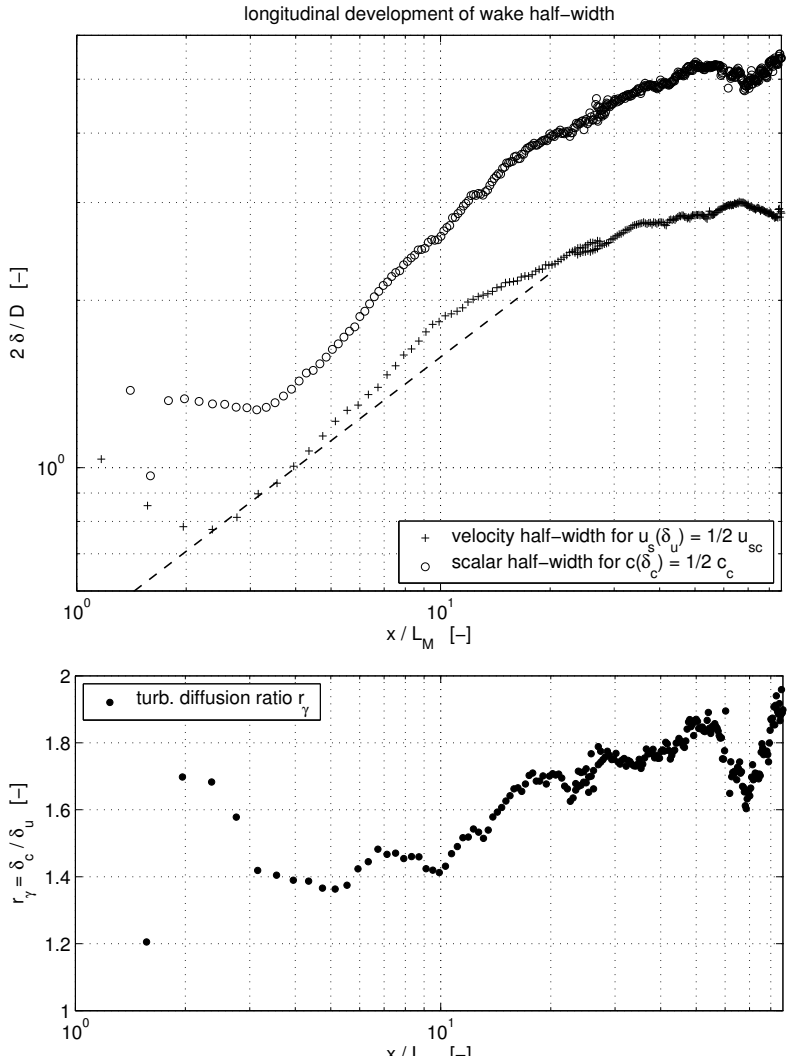

Figure 9.3. For a vortex street-like wake (series 18_vs06) the wake half width $\delta_{1/2}$ to the 1/2–value has been calculated from the fields of velocity deficit and of mass concentration to obtain δ_u and δ_γ. In the upper plot the downstream spreading of the wake is compared in the near and intermediate field to the $x^{1/2}$ growth of an unbounded plane wake (dashed line). The lower plot presents the downstream development of the turbulent diffusion ratio $r_\gamma = \delta_\gamma/\delta_u$.

plot shows the wake half width normalized by the radius of the obstacle, δ_u and δ_γ are denoted by + and ∘ symbols, respectively. The spreading of an unbounded plane wake follows a $x^{1/2}$ dependency, which is indicated by a dashed line up to $\ell_M = 20$. We may expect also shallow wakes to show the same dependency in the near and intermediate fields as long as the transverse horizontal shear dominates the bottom friction. For the given shallow wake flow the spreading of the wake displays such an increase, i.e. $\delta_u \propto x^{1/2}$, in the region of wake generation and 2D LCS development up to $\ell_M = \mathcal{O}(10)$. Farther downstream in the bottom friction dominated far field without predominating 2D LCS the growth rate obtains significantly lower values.

The spreading of a tracer mass introduced into the developing wake is illustrated from the concentration–based wake half width δ_γ. Compared to the velocity deficit based half width δ_γ is always larger, but qualitatively displays the same downstream growth rates in the near and far wake fields. The *width ratio* $r_\gamma = \delta_\gamma/\delta_u$ is presented in the semi-logarithmic lower plot of Figure 9.3. For the given wake flow r_γ takes values between 1.4 in the near field and 1.8

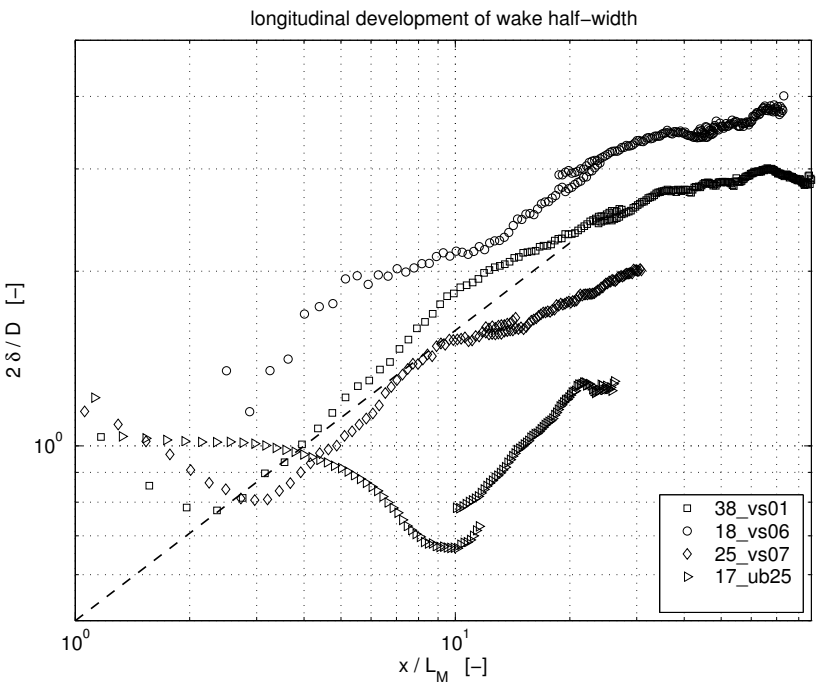

(a) wake half width δ_u/δ_{u0}

Figure 9.4. The downstream development of flow quantities have been collocated for three VS wakes ($S = 0.01,\ 0.06,\ 0.07$) and one UB wake ($S = 0.25$). Data obtained from the measurement series 38_vs01, 18_vs06, 25_vs07, and 17_ub25 are denoted by □, ∘, ◊, and ▷ symbols, respectively. The data is plotted on a logarithmic scale over the downstream distance normalized by the integral wake length scale ℓ_M, cf. (9.1). Figure (a) displays the velocity deficit based–wake half width $\delta_u/(D/2)$. A dashed line indicates a $x^{1/2}$ power law growth encountered in unbounded plane wakes.

in the far field. This behavior has been observed also in other shallow wake flows of increased wake stability—with a stability parameter $S \gtrsim 0.05$. However, for the case of a highly unstable VS wake ($S = 0.01$) r_γ takes lower values around 1.25, which have also been observed in an unbounded plane wake. Since $r_\gamma = Sc_t^{-1/2}$ using the turbulent–viscosity and gradient–diffusion hypotheses, the *turbulent diffusivity* is related to the eddy viscosity by $D_t = \nu_t\, r_\gamma^2$, and becomes 2 or 3 times the eddy viscosity in shallow wake flows.

In order to compare the time-mean flow fields of different shallow turbulent wakes, four flow configurations with wake stability parameters S ranging from 0.01 to 0.25 have been selected. Series of PIV and PCA measurements have been sequentially conducted with the overlapping fields of observation located at different downstream positions. Thus, velocity and mass fields have been obtained over a maximum of downstream distance. In Figures 9.4(a) to 9.4(c) flow quantities evaluated from measurement series 38_vs01, 18_vs06, 25_vs07, and 17_ub25 are denoted by □, ∘, ◊, and ▷ symbols, respectively. The last series represents a UB wake with $S = 0.25$, the recirculation zone attached to the

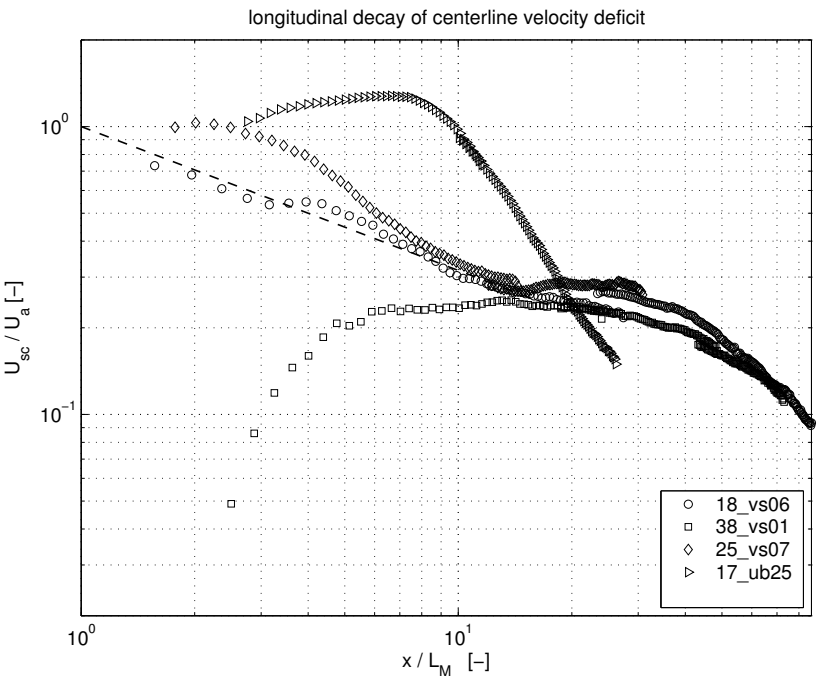

(b) centerline velocity deficit u_{sc}/u_a

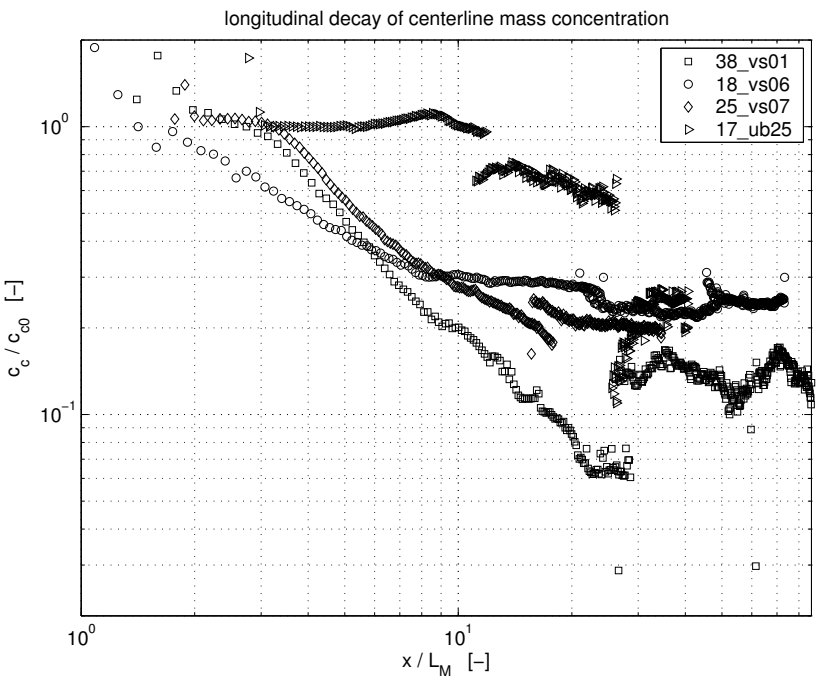

(c) centerline concentration c_c/c_{c0}

Figure 9.4. (con't) Figure (b) depicts the downstream evolution of the centerline velocity deficit u_{sc} normalized by an initial value $u_{sc0} = u_a$ at an initial cross–section at the downstream stagnation point. A dashed line indicates a $x^{-1/2}$ power law decay of unbounded plane wakes. Figure (c) displays the normalized centerline concentration c_c/c_{c0}.

obstacle ends at about $x/D = 1.8$. The stability class of the other three series is VS with stability numbers of $S = 0.01,\ 0.06,\ 0.07$, respectively. To allow for comparison between the different wake flows, the downstream distance is standardized by the integral wake length scale, x/ℓ_M, the flow quantities are standardized by appropriate initial values.

Figure 9.4(a) shows the downstream development of the velocity deficit–based *wake half width* normalized with the obstacle radius, $\delta_u/\left(D/2\right)$, obtained from the different wake flow configurations listed above. As also shown in the previous Figure 9.3, the VS wakes roughly follow a $x^{1/2}$ growth in the near field, continued in a reduced growth in the intermediate and far field. For the UB wake the half width initially decreases from $2\delta_u/D = 1$ at the obstacle to about 0.65 at the end of the recirculation bubble, then increases in the near field with roughly the same growth rate as observed from the VS wakes, finally transits to a reduced growth farther downstream.

The *centerline velocity deficit*, displayed in Figure 9.4(b), is normalized by an initial value $u_{sc0} = u_a$, as the initial cross–section is located at the downstream stagnation point. The weaker VS wakes with $S = 0.06$ and 0.07 initially show a decay of the velocity deficit with $u_{sc}/u_a \propto x^{-1/2}$ (indicated by a dashed line) that also occurs in unbounded plane wakes. Beyond $x/\ell_M \approx 20$ a transition takes place toward an increased recovery of the velocity deficit. The highly unstable VS case ($S = 0.01$) does not start from $u_{sc}^+ = 1$ at the rear stagnation point, but from $u_{sc}^+ < 0$ as already discussed with Figure 9.1. As a result, it increases in the near field, but after $x/\ell_M = 20$ shows the same deficit decay as observed from the other VS wakes. In contrast, the UB wake takes values of $u_{sc}^+ > 1$ in the recirculation bubble, then decreases at a higher rate than the VS wakes.

The longitudinal decay of the *centerline mass concentration* normalized by its initial value in a cross–section close to the obstacle and shortly downstream of the injection point is presented in Figure 9.4(c). For all wake flows we observe a power law decay in the near field, followed by a transition to a strongly reduced decay in the far field.[3] In the case of the UB wake we observe a constant concentration within the recirculation bubble—even slightly increasing toward the end of the bubble, where the 2D LCS are shed off—, then c_c^+ decays with a reduced rate compared to the VS wakes.

The transitions from a near field behavior to an intermediate and far field behavior can be grossly associated with a downstream distance of $x/\ell_M = 10$ to 20, regardless of the flow quantity and of the stability of the wake flow. A transitional distance of 10 ℓ_M corresponds to 7.8 D, 3.8 D, 3.2 D, and 1.8 D

[3] Due to a lack of quality and color resolution of the available PCA camera the effective depth of the concentration measurements is 6 bit or 7 bit. The quantitative evaluation of the very low concentrations in the far field is therefore regarded as less reliable.

for the four different wake flows of series 38_vs01, 18_vs06, 25_vs07, and 17_ub25 presented in Figure 9.4(a) to (c).

9.2 Linear stability analysis

9.2.1 Introduction to linear stability analysis

In the general case of a plane viscous shear flow, a *small-amplitude* (e.g. sinusoidal) perturbation in space and time is superimposed on the predominately parallel base flow $\boldsymbol{U} = [U(y), 0, 0]$, the total flow field decomposed into base flow plus the perturbation reads:

$$\tilde{\boldsymbol{u}} = [U + u, v, w] \qquad \text{and} \qquad \tilde{p} = P + p.$$

Both the base flow and the total flow satisfy the Navier-Stokes equations. Subtracting the x-, y-, z-momentum, and continuity equation of the base flow from the appropriate total equations leaves - after neglecting all terms nonlinear in the perturbation variables and their derivatives - the perturbation equations. Making use of *Squire's theorem*[4], only the 2D perturbation equations have to be considered, which allows to define a streamfunction $\psi(x, y, t)$ for the perturbation field:

$$u = \frac{\partial \psi}{\partial y} \qquad \text{and} \qquad v = -\frac{\partial \psi}{\partial x}.$$

We assume normal modes for the perturbation variables, i.e.

$$[u, v, \psi] = [\hat{u}(y), \hat{v}(y), \phi(y)]\, e^{i(kx - \omega t)}, \tag{9.2}$$

where k is the wave number, c is the wave speed, the wave frequency is $\omega = kc$. $\hat{u}$, $\hat{v}$, and ϕ denote the amplitudes of the perturbation variables u, v, and ψ depending on the transverse coordinate y. Then we must have

$$\hat{u} = \phi_y \qquad \text{and} \qquad \hat{v} = -ik\phi.$$

From the Navier-Stokes equations, which according to Squire's theorem we can now simplify in a 2D depth-averaged way, we end up with a single forth-order ordinary differential equation

$$(U - c)\left(\phi_{yy} - k^2\phi\right) - U_{yy}\phi = \frac{1}{i\,k\,Re}\left(\phi_{yyyy} - 2k^2\phi_{yy} + k^4\phi\right), \tag{9.3}$$

where the subscripts denote derivatives with respect to y. All variables have been non-dimensionalized by a characteristic length scale L and a characteristic velocity scale U_0; time is scaled by L/U_0, the molecular Reynolds number is

[4] Squire showed in 1933, that in a plan flow to each unstable three-dimensional disturbance there corresponds a more unstable two-dimensional one.

$Re = U_0 L/\nu$. The boundary conditions at the walls are the no-slip conditions for the flow perturbations

$$u = v = 0, \qquad \text{which require} \qquad \phi = \phi_y = 0. \tag{9.4}$$

Equation (9.3) is the well-known *Orr-Sommerfeld equation*, which governs the stability of nearly parallel viscous flows. In general, the velocity perturbations $\boldsymbol{u}$ occur in x, t, i.e. both in space and time. Therefore both the wavenumber $k = k_r + i\,k_i$ and the wave speed $c = c_r + i\,c_i$ may be complex, where the imaginary parts k_i and c_i denote a spatial and atemporal amplification rate, respectively. If $k_i = 0$, disturbances will only grow with time; if $c_i = 0$, their growth only occurs in space. Solutions of the eigenvalue problem of the perturbation differential equation (9.3) for k and ω are difficult to obtain, and in general require the use of numerical methods. Instead of solving (9.3) for both complex k and ω, i.e. for the general case of a spatiotemporal perturbation with both spatial and temporal amplification rates k_i and ω_i, we can solve the eigenvalue problem for either k or ω being real. We then conduct a temporal or spatial linear stability analysis, respectively. Since (9.3) is linear with respect to ω, the temporal solution for $k = k_r$ is easier to obtain than the spatial solution.

For a given base flow $U(y)$, in (9.3) also Re is determined. Thus, (9.3) defines the eigenvalue problem with ϕ as the eigenfunction and $c(k)$ as the complex eigenvalue depending on k. For simplicity, we choose $k = k_r$, i.e. with $k_i = 0$ we assume no spatial growth of the disturbance to occur, we thus apply the temporal stability analysis. Now the real part c_r represents the phase velocity of the perturbation. For $Re \to \infty$, i.e. for inviscid dynamics of the disturbed flow[5], the sign of the imaginary part c_i characterizes the *temporal* stability regime of the disturbance. For $c_i > 0$ we have a growing instability, for $c_i < 0$ the disturbance is damped.

So far, we briefly recalled the fundamental approach to analyze the stability of a plane viscous shear flow. For a thorough discussion on hydrodynamic stability the reader is referred to classic textbooks like Betchov & Criminale Jr. (1967); Drazin & Reid (1981); Drazin (2002), or Oertel Jr. & Delfs (1996).

In order to carry out linear stability analyses of shallow turbulent shear flows, which are horizontally bounded by a solid bottom and a free surface, Chu et al. (1983, 1991) implemented a bottom friction term in the inviscid depth-averaged shallow-water equations (2D SWE). Chen & Jirka (1997, 1998) and Socolofsky et al. (2003) extended the analysis by including also viscosity and combined the set of equations into a single *modified Orr-*

[5] For $Re \to \infty$, the right-hand side of the Orr-Sommerfeld equation (9.3) tends toward zero, the resulting inviscid perturbation equation is called the *Rayleigh equation*.

Sommerfeld equation. Substituting small-amplitude 2D normal mode perturbations (9.2) into the equations of motion, after eliminating the pressure and $\hat{u}$ the *shallow-water perturbation equation* becomes

$$(U-c)\,\hat{v}_{yy} - \left[(U-c)\,k^2 + U_{yy}\right]\hat{v} = D_{bf} + D_{tv} \tag{9.5}$$

with

$$D_{bf} = \frac{c_f U}{ikh}\left(-\hat{v}_{yy} - \frac{U_y}{U}\hat{v}_y + \frac{k^2}{2}\hat{v}\right),$$
$$D_{tv} = \frac{\nu_t}{ik}\left(\hat{v}_{yyyy} - 2k^2\hat{v}_{yy} + k^4\hat{v}\right).$$

Equation (9.5) constitutes a modified form of the Orr-Sommerfeld equation with the added effect of bottom friction. Whereas the left side of the above equation remains unchanged compared to Equation (9.3), the viscous terms on the right side take a different form. The viscosity term D_{tv} utilizes the turbulent viscosity ν_t to represent the stabilizing effect of small-scale turbulent fluctuating motions, which dominate the molecular viscosity ν relevant in laminar flows. The second term D_{bf} representing the damping effect due to bottom friction was added by Chu et al. (1983); it was implemented into the shallow water perturbation equation by Chen & Jirka (1997), and is presented here in a revised form (Socolofsky et al., 2003; van Prooijen & Uijttewaal, 2002).

In order to derive Equation (9.5) the *rigid-lid assumption* was applied, i.e. a variation of the water depth h is expressed only in terms of pressure variation, thus a perturbation of the base flow is not represented in a wave-like depth perturbation. According to Ghidaoui & Kolyshkin (1999), for small local Froude numbers $Fr \to 0$ the rigid-lid assumption works well for all turbulent Reynolds numbers $Re = \sqrt{gL}\,L/\nu_t$.[6]

9.2.2 Stability regimes and flow classes

In the previous subsection, we discussed either the temporal *or* the spatial evolution of small perturbations, regardless whether these disturbances are physically meaningful or impossible. In reality, such disturbances are introduced into the flow at a certain time and in a finite area, then they develop *both in time and space.* We will now consider spatially local perturbations, which are temporally instantaneous. In this case, initially the unstable base flow receives a perturbation impulse generating a wave-packet, which then develops in the base flow. As the perturbation impulse can be concentrated locally at a point or along a line, this will result in a 3D wave-packet or in a 2D wave-packet,

[6] For instance, the result for $Fr = 0.5$ deviates by less than 1% from the result for $Fr = 0$ for $Re \in [100; 1000]$. (Ghidaoui & Kolyshkin, 1999, p. 877)

which contains the perturbation energy and covers a limited area. The wave-packet generated by this spatially and temporally local disturbance (and so the area of perturbation) now will either be advected downstream with the main flow, while the area of its origin recovers its undisturbed state, or it will influence the area of the initial perturbation permanently.

When we investigate the spatiotemporal development of a small-amplitude perturbation, introduced into an unstable[7] plane shear flow at a time $t = 0$ over a limited duration T and at a position $x = 0$ over a limited transverse extent, we are interested in the *temporally asymptotic* behavior of such a perturbation. We can identify two substantially different spatiotemporal scenarios for the development of an induced perturbation wave-packet:

> The amplified perturbation leaves the location of its origin irreversibly. We call this behavior *locally convectively unstable.*

> The amplified perturbation does not leave the location of its origin, but grows continuously at this place. We call this behavior *locally absolutely unstable.*

We can therefore discriminate regions of the unstable base flow, where a local perturbation impulse leads to a permanent destabilization of the flow at the the initial location, from those regions, where the flow re-stabilizes again. We call them *absolutely unstable regions* and *convectively unstable regions*, respectively. Figure 9.5 shows the principles of shear flow instability. The top plot sketches the classical unstable flow of a free mixing layer behind a splitter plate, where wave-packets travelling downstream indicate a locally convectively unstable flow. Introducing a second obstacle in the shear flow (middle plot) may lead to resonance, so that self-sustained oscillations can be obtained; but the instability is still locally convective. The bottom sketch shows the transition between two different regions of local instability for an unstable wake flow. Figure 9.6 clarifies the definitions of local instability regions also in the (x, t)-plane again for the case of a plane shear flow in the wake of a cylindrical obstacle.

This distinction is essential for the active control of shear flows, because only in absolutely unstable regions it is possible to effectively manipulate the flow field. Only in these regions the flow field can be influenced globally, i.e. also in the upstream direction. For more details on local spatiotemporal perturbations the reader is referred to Huerre & Monkewitz (1985) and to Oertel Jr. (1990), concerning mixing layers and wakes, respectively.

In shallow turbulent wake flows linear stability analysis aims to associate the instability regimes to the wake flow classes VS (vortex street-like wake),

[7] The instability of the base flow has to be ascertained from a previous temporal stability analysis.

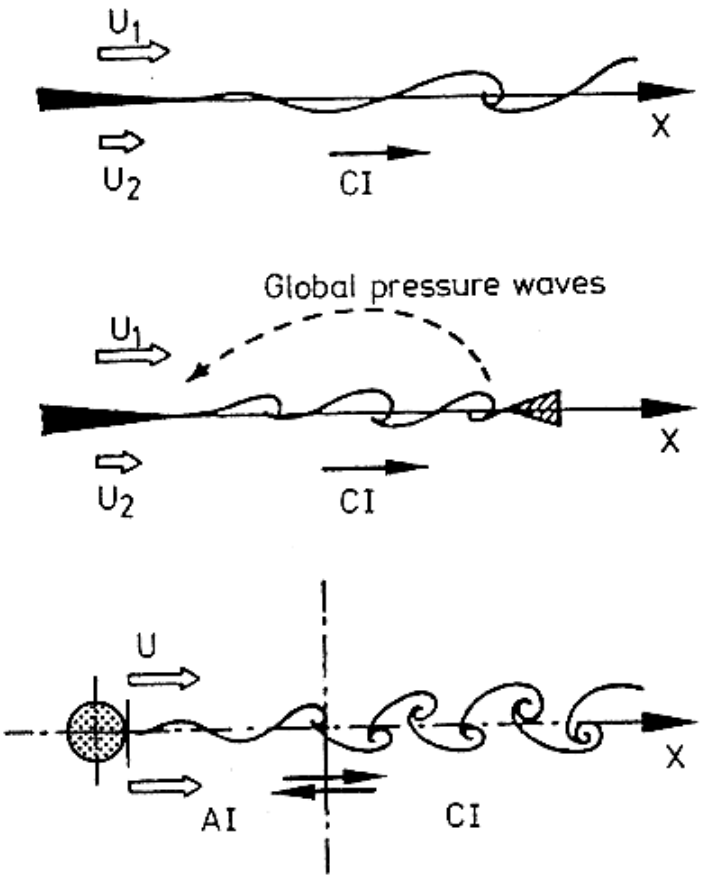

Figure 9.5. Absolutely and convectively unstable regions in shear flows: Chomaz et al. (1987) (from Oertel Jr., 1990, p. 540) illustrated the principle of shear flow instability. The classical plane shear flow behind a splitter plate (top plot) is locally convectively unstable (CI), even if an additional obstacle (middle plot) excites resonance oscillations. In the wake downstream of a blunt body (bottom plot) a locally absolutely unstable region (AI) exists in the near field, more downstream the wake flow is locally convectively unstable.

UB (unsteady bubble wake), and SB (steady bubble wake). If we would follow a suggestion of Oertel Jr. & Delfs (1996) to call a perturbed flow, that contains a locally absolutely unstable flow region, an absolutely unstable flow, then we would have to classify every shallow wake flow to be absolutely unstable, because every unstable wake flow contains a region of local absolute instability.

Contrarily, Chen & Jirka (1997) identified a critical return velocity in the recirculation zone to separate absolutely and convectively unstable flow regions. From the maximum return velocities observed in the different wake flow cases, they concluded that UB wake flows with lower return velocity would be convectively unstable, whereas VS wakes with sufficiently high return velocities should be called absolutely unstable. Obviously, and with respect to the same wave frequency $f_{wake} = 2\pi/T$ (i.e. the global wake frequency belonging to the low frequent instability with cycle period T of the whole wake), both VS and UB wakes are absolutely unstable, since both contain an absolutely unstable flow region. Otherwise, starting with an initially steady flow around the obstacle, an initial small-amplitude perturbation could not temporarily grow and time-asymptotically create the pattern of a locally fixed low-frequency perturbation of the wake. So, if we would like to use a single term to characterize

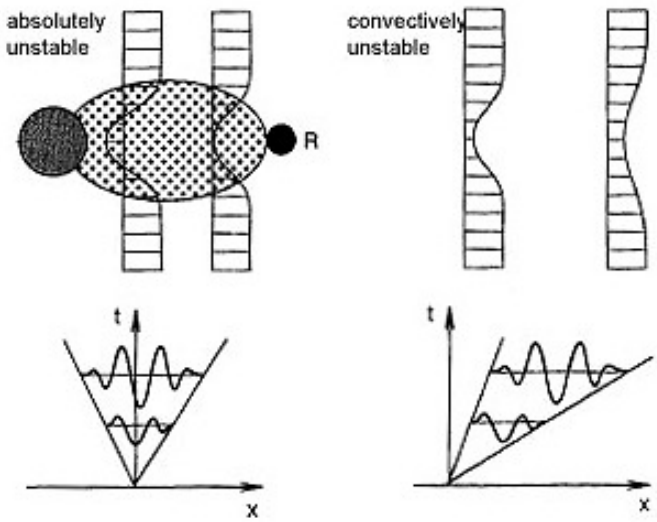

Figure 9.6. Absolutely and convectively unstable regions in wake flow: The definition sketch after Oertel Jr. & Delfs (1996) shows regions of absolute and convective local instability in the wake of a cylinder. The plan shear flow has to be classified as unstable from a foregoing temporal instability analysis. In the lee of the obstacle the dotted area denotes the absolutely unstable region, which is surrounded by the convectively unstable region. As explained in the (x, t)- plane, an initial disturbance introduced in the absolutely unstable region grows in time (i.e. temporal instability), and permanently influences this area. Point R denotes the most downstream point, for which an initial disturbance still leads to the change and permanent de-stabilization of the wake flow. In the convectively unstable region more downstream, an initial perturbation is advected downstream, but does not spread upstream or stay at its origin.

the stability of the whole wake, we should call both the VS and UB wakes to be *globally absolutely unstable*, the SB wake to be *globally convectively unstable*, and for even higher S to find *globally stable* wakes. We want to stress, that speaking of global instability, we refer to the whole wake instability with f_{wake}. For higher wave number perturbations, i.e. $f > f_{wake}$, also a globally stable wake will be convectively unstable, since it essentially is a shallow shear flow comparable to a mixing layer.

For the instability analysis of shallow turbulent wakes, Chen & Jirka (1997) employed a far-field transverse distribution of the main flow component to analyze also the near-field of the wake. Besides the non-linear effects in the near-field especially induced by the periodic (i.e. coherent) flow, also the time-mean $U(y)$ distribution differs significantly in the near-field, since it involves a second inflection point. We know that inflection points, where $\partial^2 u/\partial y^2 = 0$, are crucial for the stability of shear flows.

In this work we will focus on the *local* stability of shallow wake flows. We will identify regions of local absolute and local convective instability, i.e. regions that are sensitive to absolute or convective instability, for the different types of shallow wakes. We will use the results of far-wake linear stability analyses of Chen & Jirka (1997); Socolofsky et al. (2003), and, although there

remain some doubts about the applicability of this technique, we will extend the results also to the near-wake.

9.3 Local instability of shallow wake flows

9.3.1 Comparison of measurement and linear stability analysis

The modified Orr-Sommerfeld equation (9.5)—the governing equation of linear stability analysis in shallow shear flow—is non-dimensionalized using the characteristic local scales of length and velocity, $\mathcal{L}$ and $\mathcal{U}$, based on the half width $\delta(x)$ and on the centerline velocity deficit $u_{sc}(x)$. Then on the right-hand side of (9.5), the bottom friction term D_{bf} and the turbulent shear stress term $D_{t\nu}$ can be standardized using a local stability parameter $S_f = c_f\,\mathcal{L}/h$ and a local turbulent Reynolds number $Re = \mathcal{U}\mathcal{L}/\nu_t$.

In order to compute the stability regimes in the far field of shallow turbulent wakes, the flow field is described using a self-similar transverse distribution of the velocity deficit, which is approximated by a classic hyperbolic-secant profile (Chen & Jirka, 1997; Socolofsky et al., 2003),

$$U(y) = \bar{U}\left(1 - R_w + R_w \operatorname{sech}^2\left(\frac{y}{l}\right)\right) \quad . \tag{9.6}$$

Here, $R_w = (u_c - u_a)/(u_c + u_a)$ is an expression for the velocity deficit, i.e. for the wake strength, $\bar{U} = 1/2\,(u_c + u_a)$ is the cross–sectional averaged velocity, l is a transverse length scale related to the width by $2\delta_{1/e} = \sinh^{-1}(l) = 0.881\,l$. The hyperbolic-secant profile (9.6) is a special case of a more general hyperbolic-sine wake profile (Monkewitz, 1988), where the 'shape' factor is $N = 1$, whereas $N > 1$ leads to steeper profiles near the wake boundaries (cf. Section 9.1.1).

The modified Orr-Sommerfeld equation for a self-similar shallow wake flow, (9.5), constitutes an eigenvalue problem with the eigenfunction $\hat{v}$ for the eigenvalues k, ω, R_w, Re, and S_f, where both k and ω are complex. Chen & Jirka (1997) showed that shallow wake flows in the laboratory and in environmental flows take values $Re = \mathcal{O}\left(10^3 \text{ to } 10^4\right)$, and that the corresponding results of stability analyses are independent of Re in this range. Thus, for stability analyses of shallow wakes the turbulent shear stress term $D_{t\nu}$ is neglected.

To numerically solve the perturbation equation, a pseudo-spectral collocation method employing Chebyshev polynomials mapped to an infinite domain has been employed (Socolofsky et al., 2003); a finite Chebyshev polynomial method has been employed by Chen & Jirka (1997). The search procedure of Chen & Jirka (1997) allowed to identify the transitions among the different local stability regions. Transition from absolutely unstable to convectively unstable flow occurs for a saddle–point in the $(k_r,\, k_i,\, \omega_r)$ domain, where

for a given S_f the saddle–point occurs for a critical value of R_w. Transition from convectively unstable to stable flow occurs for vanishing k_i, where for a given R_w the critical value of S_f is the maximum value of S_f in the (k_r, S_f) plane. Hence, using the critical transition values of S_f and R_w, the different stability regions can be localized in the (R_w, S_f) plane.

The downstream development of the wake half width $\delta_u(x)$ and of the centerline velocity deficit $u_{sc}(x)$ has been obtained from experimental data of various shallow wake flows (Section 9.1.2). The observed $\delta_u(x)$ and $u_{sc}(x)$ are re-arranged in terms of

$$S_f = c_f \frac{2\delta_{1/e}}{h} = \frac{2n\, c_f}{h}\, \delta \ , \tag{9.7a}$$

$$R_w = \frac{u_c - u_a}{u_c + u_a} = \frac{-u_{sc}}{2u_a - u_{sc}} \ , \tag{9.7b}$$

where the width conversion factor is $n = \sqrt{\ln 2}$ (cf. Table 8.1) for $\delta_{1/2}$ as evaluated from the measurements.

As the stability parameter S_f of a shallow wake flow tends to zero, the influence of bottom friction vanishes, and the flow can be regarded as an unbounded plane wake, also called a 'deep' wake. The standardized velocity deficit R_w takes values related to specific flow situations, which can be distinguished as follows:

$R_w < -1$	i.e. $u_c < 0$	reversed flow (recirculation),
$R_w = -1$	i.e. $u_c = 0$	stagnation point,
$-1 < R_w < 0$	i.e. $0 < u_c < u_a$	co-flowing wake,
$R_w = 0$	i.e. $u_c = u_a$	uniform flow (wake vanished),
$R_w > 0$	i.e. $u_c > u_a$	jet flow.

The maximum return velocity corresponding to $R_w = -2.07$ has been observed to be constant in recirculation zones of UB wakes ($S < 0.5$); in steady bubble wakes ($S > 0.5$) the minimum R_w increased (Chen & Jirka, 1997). Our measurements of UB wakes with $S = 0.25$ yield minimum R_w values of -1.9 to -1.8, which may indicate a tendency toward VS wakes at this global stability number.

The downstream development of δ_u and u_{sc} is presented in terms of S_f and R_w in Figures 9.7 for different wake flows (denoted by • symbols) starting at $x/D = 0.5$ immediately behind the cylindrical obstacle. The laboratory shallow wake flow configurations cover global stability parameters in the range $0.01 \leq S \leq 0.25$, and represent the stability class of vortex street-like wakes and its transition to unsteady bubble wakes. The local stability parameter S_f, Equation (9.7a), is in the range $0 < S_f < 0.4$. Values of the standardized velocity deficit R_w, Equation (9.7b), are in the range $-1.9 \leq R_w \leq 0$. The transitions between locally absolutely unstable regions (AU), locally convec-

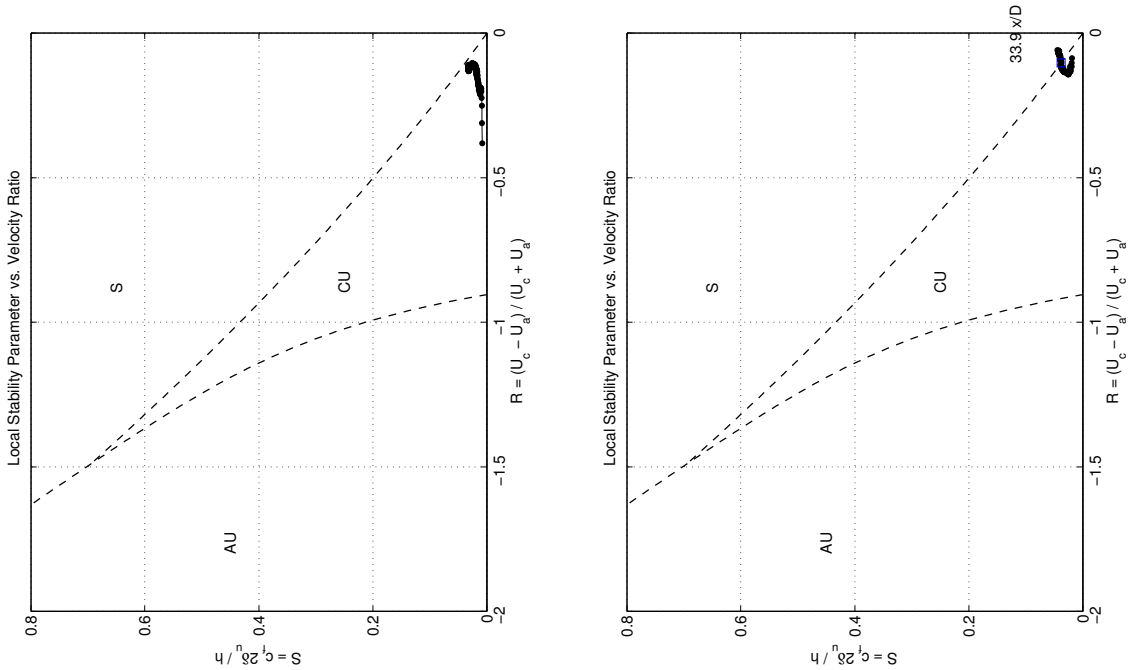

(a) VS wake, $S = 0.01$ (series 80_vs01) (b) VS wake, $S = 0.01$ (series 38_vs01)

Figure 9.7. The downstream development of the wake half width δ and of the centerline velocity deficit u_{sc}, evaluated from PIV measurements of laboratory shallow wake flows, are represented in the plane of a local wake strength parameter $R_w = (u_c - u_a)/(u_c + u_a)$ and of a local stability number $S_f = c_f\, 2\delta/h$, Equations (9.7a) and (9.7b), respectively. In this plane also the local transitions between absolutely unstable regions (AU), convectively unstable regions (CU), and stable regions (S) are indicated by dashed lines, as obtained by Socolofsky et al. (2003) from a linear stability analysis.

tively unstable regions (CU), and locally stable regions (S), resulting from linear stability analysis (Socolofsky et al., 2003), are indicated by dashed lines. The location of the first measurement cross–section downstream of a transition into a different stability region is indicated by a □ symbol, and the corresponding x/D value is displayed (cf. Table 9.1).

Figures 9.7(a) to 9.7(c) show vortex street-like wake flows with a low global stability number indicating the transition to 'deep' or unbounded plane wakes. The measurement series are 80_vs01, 38_vs01, and 38_vs03 with $S = 0.01$, 0.01, 0.03 given in plots (a), (b), and (c), respectively. As reported in Section 9.1, the second wake shows a jet-like behavior immediately downstream of the cylinder even at the centerline. Data are given for $x/D > 3$ in this case, closer to the obstacle the velocity deficit becomes $R_w > 0$. Figures 9.7(d) and 9.7(e) show ideal shallow VS wakes (series 18_vs06 and 25_vs07_2) with similar values of the wake stability parameter $S = 0.06$ and 0.07. The corresponding values of the cylinder diameter–to–depth ratio D/h are 7 and 10.

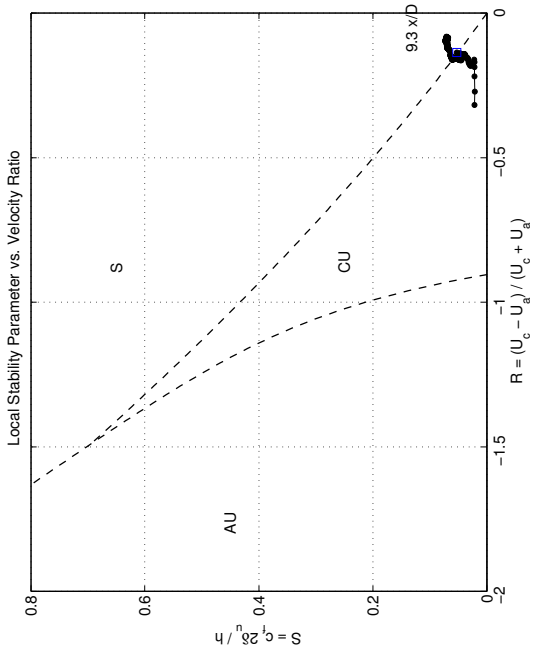

(c) VS wake, $S = 0.03$ (series 38_vs03)

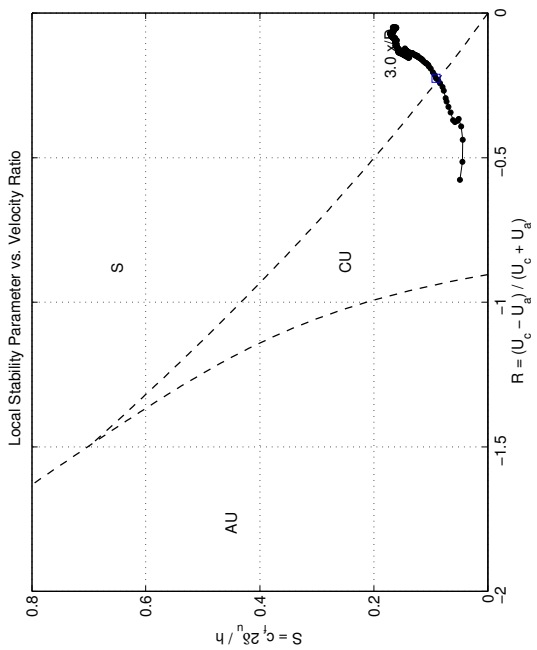

(d) VS wake, $S = 0.06$ (series 18_vs06)

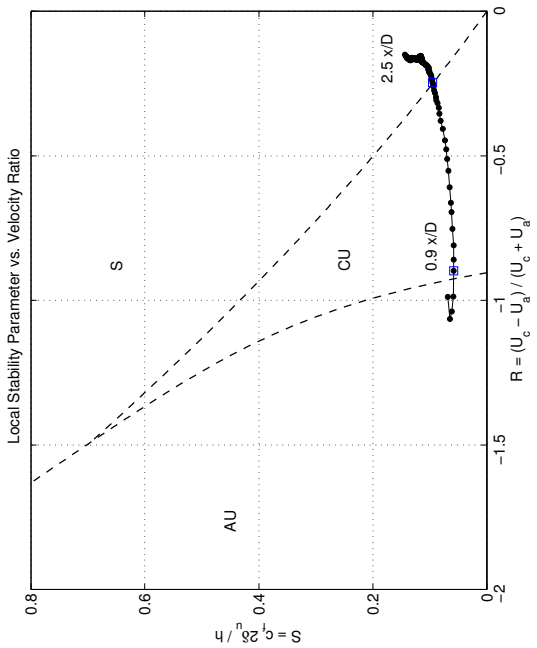

(e) VS wake, $S = 0.07$ (series 25_vs07_2)

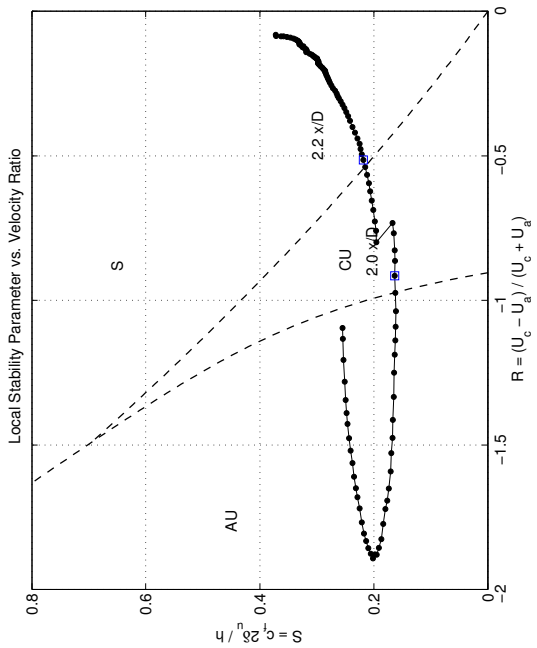

(f) UB wake, $S = 0.25$ (series 17_ub25_3)

Figure 9.7. (con't)

Figure 9.7(f) shows an unsteady bubble wake (series 17_ub25) with $S = 0.25$, thus near to the transition from the VS wake stability class.

In VS wake flows large-scale vortices are shed off the cylinder perimeter directly, and form a double–row of staggered counter-rotating eddies. Since no recirculation zone exists, the centerline velocity u_c becomes zero, and $R_w = -1$, at the cylinder boundary only. The velocity deficit takes values of $R_w \geq -1$ in VS wakes. The smallest value of the wake half width δ occurs at the location of the vortex separation, i.e. at $x/D \leq 0.5$, and monotonically increases with downstream distance. Therefore, the minimum value of S_f is found at the cylinder boundary ($x/D = 0.5$). Since the transition among the absolutely unstable (AU) and convectively unstable (CU) regions occurs at critical values of R_w between -0.904 and -0.993 for S_f between 0 and 0.2, in VS wakes the absolutely unstable region is small, and the transition to the convectively unstable region occurs almost immediately behind the obstacle. The transition between the convectively unstable and the stable region, however, occurs at $R_w \to 0^-$ for small S_f of deep VS wakes; in such flows the CU region lasts almost until the wake completely vanishes.

In the VS wake flows a few values within the AU region can be observed only in the case presented in Figure 9.7(e). On the one hand, surface PIV measurements of the low S cases had a reduced spatial resolution relative to the cylinder diameter, and the small AU region very close to the cylinder probably was not resolved accurately. On the other hand, the hyperbolic–secant transverse profile, Equation (9.6), does not approximate the observed near field distribution of u_{sc}. A steeper and over-shooting profile with a second inflection point at the wake boundary can lead to different critical R_w for the AU–CU transition for given S_f.

For VS wakes close to deep or unbounded plane wakes the transition from locally convectively unstable to stable flow occurs at large downstream distances, where the wake has almost disappeared. In the case presented in Figure 9.7(a) the field of observation reached down to $x/D = 35.5$, still no CU–S transition can be observed. For the same global stability number $S = 0.01$ in the wake of Figure 9.7(b) this transition occurs at $x/D = 33.9$.

UB wakes form a short recirculation zone in the lee of the cylinder. The cylinder boundary layers, unsteadily separating from both sides the cylinder, do not roll-up immediately, but enclose the recirculation bubble, and merge and roll-up at the downstream end of the bubble. From the bubble end alternately shed counter-rotating 2D LCS advect downstream as in the case of VS wakes. Negretti (2003b) presents details on the vortex growth in the detached shear layers and on its merging and separation for shallow UB wakes. Along the wake centerline two stagnation points ($u_c = 0$, i.e. $R_w = -1$) are encountered at both ends of the recirculation zone—at the cylinder boundary at $x/D = 0.5$ as for VS wakes, but additionally at the downstream bubble end

where the vortex street is shed. Within the recirculation bubble the velocity deficit takes values $R_w < -1$. Since the wake half width decreases along the bubble, and reaches its smallest value at the downstream bubble end, also the local stability parameter S_f decreases until $R_w = -1$. The UB wake presented in Figure 9.7(f) shows a decrease in S_f from 0.25 at the cylinder (i.e. the global stability parameter S) to 0.16 at the bubble end. Since in the bubble of UB wakes R_w values occur significantly smaller than -1, in the (R_w, S_f) plane the possible AU area is much larger than for VS wakes. Contrarily, the CU regime is significantly smaller, because the CU–S transition occurs much earlier. For instance for a critical $S_f = 0.2$ the transition is at $R_w = -0.502$, where the wake deficit is still large ($u_{sc}/u_a = 0.668$). The AU–CU transition in UB wakes occurs slightly within the recirculation zone, for critical S_f between 0.2 and 0.4 the corresponding R_w are found between -0.993 and -1.141. The expression 'unsteady bubble' wake mirrors the fact that the predominant large-scale perturbations are advected downstream from within the time-mean recirculation zone.

For even higher values of S_f the SB wake class is encountered, which does not show any large-scale vortical structures at all. Though in this case the AU regime ends at even smaller values of R_w compared to UB wakes, the CU regime is vanishingly small. 2D LCS that may form at the end of the recirculation zone, reach well into the locally stable region of the SB wake; hence, they are stabilized before they shed off.

Table 9.1 lists the downstream distances where the transitions among different local stability regions take place for the various wake flows. Distances are standardized by the cylinder diameter and by the integral wake length scale, x/D and x/ℓ_M. Note the decreasing downstream distance of the CU–S transition as the global stability parameter increases. The convectively unstable region has a length of 1.6 D in the VS wake with $S = 0.07$, and a length of only 0.2 D in the UB wake.

In conclusion, in shallow wakes the absolutely unstable and convectively unstable regions are short, shallow wakes are predicted to stabilize a short distance downstream of the obstacle. The transition to the stable flow region roughly correlates with the transition between near and intermediate wake fields for $x/\ell_M = \mathcal{O}(10)$ (cf. Section 9.1.2). The extent of the locally stable region—as obtained from a linear stability analysis of shallow wake flows—does not appear to be closely related to the existence of 2D LCS. Large-scale vortical structures resulting from the low-frequent perturbations, which are dominant in the intermediate wake field, are found to be present in the stable wake region. As demonstrated in Section 7.1.4, such large-scale coherent structures contain a predominant amount of the TKE in wake flow, until they are dissipated after 20 to 30 x/D. In Chapter 10 of this study we will show from structure identification that 2D LCS are active in wake regions, where the flow is regarded

as locally stable with respect to low-frequent perturbations from linear stability analysis.

9.3.2 Control of wake instability

The stability of wake flows can be controlled only by flow manipulations in wake regions of local absolute or convective instability. For a general discussion of flow control in shear flows the reader is referred to Huerre & Monkewitz (1990); Fiedler (1998), to Oertel Jr. (1990) for wakes, and to Delville et al. (1998) for the effect of large-scale vortical structures.

In shallow wakes absolutely unstable flow regions are located directly at the obstacle boundaries and downstream in the recirculation bubble attached to the obstacle. Statically or passively controlling the absolute unstable wake region is exercised by different methods. To suppress the vortex shedding the 'feedback information' between both sides of the cylinder can be disrupted e.g. by a splitter plate or by base bleeding or suction. Oertel Jr. (1990) numerically analyzed stabilization of blunt body wakes by base bleeding. Chen & Jirka (1997) employed porous obstacles introducing a base bleed into the wake. For shallow UB wakes this base bleeding also results in weakening of the detached shear layers of the recirculation zone. Negretti (2003b) enhanced the bottom roughness along the unsteady bubble lateral shear layers, and thus also stabilized UB wakes. Also the surface roughness of the obstacle can be manipulated. Also the well-known 'Scruton Spiral' found on many industrial chimneys brakes up the coherence of the vortex shedding by introducing a 3D distortion to the plane vortices.

Dynamic control of the convectively unstable flow region is difficult in wake flows being a modification of a predominant ambient base flow by vortical

Table 9.1. Downstream distances for the local transition between absolutely unstable (AU) and convectively unstable (CU) and stable (S) flow regions are obtained from experimental data of different shallow turbulent wake flows presented in Figures 9.7(a) to 9.7(f).

series	**stability no.**	***AU–CU* transition**		***CU–S* transition**	
	S	x/D	x/ℓ_M	x/D	x/ℓ_M
80_vs01	0.01	–	–	> 35.5	> 44.4
38_vs01	0.01	–	–	33.9	43.6
38_vs03	0.03	–	–	9.3	16.8
18_vs06	0.06	–	–	3.0	7.9
25_vs07_2	0.07	0.9	2.7	2.5	8.0
17_ub25_3	0.25	2.0	10.7	2.2	11.9

structures that memorize the initial conditions of the wake generation. Dynamic control can therefore be done by periodical perturbations of the base flow (by distributed macro roughness elements) or by (vibrational or rotational) perturbation of the wake generator. Since the convectively unstable region of shallow wake flows is short, the possibilities for a shallow wake control through manipulation of the ambient flow are restricted.

Also the interaction of different shallow wakes can lead to stabilization of the individual wake flows. This has been demonstrated for shallow wake flows by Heinrich (1999); v. Carmer et al. (2000) for two cylinders in different arrangements. Rows of cylinders positioned normal to a shallow base flow have been used to study shallow grid–generated turbulence (Uijttewaal & Jirka, 2003), and mass diffusion in enhanced turbulence of shallow base flows (Rummel, 2002; Rummel et al., 2004). An early break down of large-scale 2D vortices in such multiply interacting wakes has been shown compared to a single wake.

Summary of Part II

Spectral description of turbulence. The turbulence field in shallow turbulent wake flow can be regarded as isotropic 'locally' at the small-scale range of random turbulent fluctuations. The concept of a universal equilibrium range may apply, in which the spectral transfer and the dissipation of TKE are independent of distinct flow conditions, but solely depend on 'inner' variables, namely on the viscosity ν and on the dissipation rate ϵ. In the inertial subrange the transfer of TKE is unaffected by viscosity and follows the energy cascade of Kolmogorov's -5/3 power law toward higher wave numbers. In the large-scale energy-containing range the production of TKE is non-universal, but depends on the specific flow conditions (for instance, of a double-sheared shallow wake flow) given by macro flow scales $\boldsymbol{u}_0$ and ℓ_0.

The spectral distribution of the fluctuation of a passive scalar component displays a range of isotropic fluctuations at high wave numbers depending only on the diffusivity D_m and the scalar dissipation rate ϵ_γ, corresponding to the universal equilibrium range of the velocity field. In the inertial–convective subrange at moderate wave numbers also the scalar is spectrally transferred without being molecularly diffused. The spectral density estimates of the scalar variance, then, cascade to higher wave numbers as $S_\gamma \propto k_w^{-5/3}$. For high Schmidt–number flows, i.e. $\nu \gg D_m$, there exist a range of wave numbers, at which TKE is dissipated, but the scalar is still unaffected by diffusion. In this dissipative–convective subrange the scalar fluctuations cascade toward higher wave numbers following a -1 power law.

Large-scale fluctuations of the horizontal wake flow field with length scales significantly larger than the water depth, $\ell > h$, are likely to show characteristics of 2D turbulence. The concept of the double cascade of forced 2D turbulence may be applicable locally in the large-scale range. Energy introduced at a wave number $k_{w,i}$ will be spectrally re-distributed toward higher wave numbers, $k_w > k_{w,i}$, following the k_w^{-3} enstrophy cascade, which also applies to freely decaying turbulence. Complementary, TKE is also transferred toward lower wave numbers, $k_w < k_{w,i}$, along the inverse energy cascade, $S(k_w) \propto k_w^{-5/3}$. Scalar fluctuations introduced in the range of the enstrophy cascade will be spectrally transferred through an inertial–convective subrange with $S_\gamma \propto k_w^{-1}$, and for high Schmidt numbers enter a viscous–convective subrange, for which $S_\gamma \propto k_w^{-1}$ still holds. Scalar fluctuations in the range $k_w < k_{w,i}$ of the inverse energy cascade will, nevertheless, follow a direct -5/3 cascade toward higher wave numbers.

Characteristic scales of length and time are used to describe the turbulence field. Macro scales reflect the specific flow conditions, for instance in a turbulent uniform open-channel flow the macro scales of length and velocity can be given as $\ell_0 = h$ and $u_0 = \bar{U}$. The large-scale 2D motion of the double-

sheared flow is characterized by its own set of global macro scales of time $\mathcal{T}_0$ and length $\mathcal{L}_0$. Integral length and time scales, ℓ_I and τ_I, are commonly used to characterize the range of energy–containing eddies. Despite they have no physical equivalent, the Taylor scales of length and time, ℓ_λ and τ_λ, derived from the correlation coefficients are often employed to describe the range of small-scale fluctuations. The Kolmogorov micro scales of turbulence, ℓ_η and τ_η, indicate the beginning of the dissipative subrange. Furthermore, the small-scale scalar fluctuations are characterized by scalar Taylor scales, $\ell_{\lambda,\gamma}$ and $\tau_{\lambda,\gamma}$, or—corresponding to the Kolmogorov scales—by the Batchelor scales of scalar fluctuation, $\ell_{\eta,\gamma}$ and $\tau_{\eta,\gamma}$.

Turbulence in shallow wake flow. Instead of employing a Reynolds decomposition, velocity and mass concentration data of point-wise (and planar) measurements in shallow wake flow can be triple-decomposed into large-scale coherent and small-scale random flow fields. A phase–resolved averaging procedure based on the mean cycle period T_P is superior to low-pass filtering techniques in separating the coherent and random turbulence fields. An adaptive phase–resolved averaging based on individual cycle periods $T_{P,i}$ is well suited also for more unstable wake flows showing a distinct variation in T_P.

Based on the auto-correlation coefficients $r_{ii}(\tau)$ the global macro time scales given by the mean cycle periods, $\mathcal{T}_0 = T_P$, have been calculated as well as the integral time scales τ_I. It has been shown that—though calculated from the non-decomposed data—τ_I is a macro time scale only of the small-scale random turbulence, whereas $\mathcal{T}_0$ represents the large-scale coherent motion. Using the appropriate scale relations, the Taylor, Kolmogorov, and Batchelor time scales have been computed.

From the triple-decomposed data the large-scale coherent and the small-scale random parts of kinetic energy and mass concentration as well as of the mass fluxes have been obtained. The large-scale coherent motion is of crucial importance in the transfer of momentum and mass. In the first instance, and especially when interested in averaged quantities, the coherent and random fluctuations can be regarded as completely de-correlated. Anisotropy of the turbulence field is due to the large-scale fluctuations only, in the high wave number range isotropic turbulence applies.

The structural duality of double-sheared shallow turbulent wake flows can be described as a dual spectral structure of 2D turbulence at the large scales and 3D isotropic turbulence at the small scales. In the low wave number ranges of the PSD estimates the transfer of kinetic energy follows a -3 enstrophy cascade toward higher k_w, though a significant amount of TKE seems to be dissipated directly due to bottom friction instead of being transferred through the spectral ranges. Also, the complementary inverse energy cascade of 2D turbulence is absent in shallow bottom friction–exposed wake flows. Corresponding

to the enstrophy cascade, the mass variance is spectrally transferred toward higher k_w with a -1 power law, thereby being unaffected by influences of bottom friction. On the small scales the spectral structure can be described by the concepts of locally isotropic turbulence. Energy and mass are transferred through the inertial–convective subrange following the Kolmogorov and Batchelor -5/3 power laws, cascading further down to the dissipative and diffusive scales inaccessible to the present LDV-LIF measurements.

Analytical wake flow model. The analytical integral 1D model for shallow wake flows consists of conservation equations for the standardized fluxes of volume deficit Q_s^*, of momentum deficit M_s^*, and of tracer mass Q_c^*, Equations (8.65), (8.67), and (8.70), respectively. Employing these conservation equations, the downstream development of velocity $\langle u_{sc} \rangle$ and tracer mass $\langle c_c \rangle$ along the centerline, and of the wake half width δ is represented by Equations (8.71), (8.74), and (8.73), respectively. In order to derive the above set of integral equations, extensive use has been made of the self-similar, Gaussian transverse distributions of velocity deficit and mass concentration, given by Equations (8.1), and (8.2).

In contrast to unbounded plane wakes, where the momentum deficit is conserved, in shallow wakes the bottom shear–induced dissipation of TKE leads to a decrease of the initial momentum deficit. Moreover, the existence of a periodic–advective part of the flow with predominant large-scale vortical motion results in different rates of mixing and entrainment and of frictional losses. The proposed integral wake model is applicable only in the far field of shallow wake flows, since the assumptions of self-similar Gaussian transverse distributions of $\langle u_s \rangle$ and $\langle c \rangle$, and of a constant entrainment coefficient α do not hold in the near and intermediate fields. Furthermore, the order–of–magnitude arguments used to deduce the momentum conservation equation from the 2D SWE as well as the model to incorporate the bottom shear stresses are valid in the far field only.

Time-mean fields and local stability regions of shallow wake flows. The time-mean description of shallow turbulent wake flows have been obtained in terms of the downstream development of the centerline velocity deficit u_{sc}^*, of the centerline mass concentration c_c^*, and of the wake half widths δ_u and δ_γ, as well as of the transverse distributions of the velocity deficit u_s^+, and of the mass concentration c^+. A transition from the wake near field, where in the first instance the laws of unbounded plane wakes apply, to intermediate and far wake regions, where the rates of growth and decay diminish with downstream distance, occurs after $x/\ell_M \approx 10$ to 20.

Experimental data of wake flow measurements have been related to results of linear stability analysis. The local stability regions of shallow wake flows, as predicted by linear stability analysis, have been identified. In shallow wakes the

absolutely unstable and convectively unstable regions are short, shallow wakes are predicted to be stabilized a short distance downstream of the obstacle. The transition to the stable flow region at $x/\ell_M = \mathcal{O}(10)$ roughly correlates with the transition between near and intermediate fields of shallow wakes. The extent of the locally stable region—as obtained from a linear stability analysis of shallow wake flows—does not appear to be closely related to the existence of 2D LCS. Large-scale vortical structures resulting from the low-frequent perturbations, which are dominant in the intermediate wake field, are found to be present in the stable wake region.

Part III

Large-Scale Coherent Vortical Structures in Shallow Wakes

10. Large-Scale Coherent Vortical Structures in Shallow Wakes

One of the most interesting phenomena in almost all turbulent shear flows is the existence of organized vortical motions embedded in a turbulent base flow of rather disordered and weak vorticity. Such phenomena are often referred to as *coherent structures* and usually associated with regions of concentrated vorticity. Since these coherent structures greatly influence the transport of momentum and scalar quantities (e.g. mass or heat), the entrainment of ambient fluid, and the mixing and advection in the mean flow, they are of great interest in engineering applications, for instance effective mixing of industrial discharges in the environment, drag reduction, combustion processes, vibration and resonance in structural design, or noise reduction in acoustics. Understanding of the mechanisms of the generation and decay of coherent structures is the basis for their prediction and even their control and, thus, can help solving practical engineering problems.

An essential feature of shallow wake flows behind cylindrical obstacles is the formation of vortical structures, whose horizontal extend is many times larger than the water depth h, but scales with the initial half-width of the wake δ_0 and, thus, with the radius of the obstacle $D/2$. Arranged in a shallow wake similar to a von Kármán vortex street, counterrotating large-scale coherent structures (LCS) shed alternately from both sides of the obstacle or from the attached recirculation zone. As long as they exist, LCS have a great impact on the transfer of momentum and mass within the wake flow. The knowledge of the conditions for the generation of these LCS as well as of their fate while they advect downstream, is crucial for the processes in the transitional region of the shallow wake.

In this chapter firstly the methodology will be presented, how large-scale coherent vortical structures are detected in wake flow fields, as observed in laboratory experiments. Secondly, LCS in shallow wakes will be characterized by identifying and quantifying their main properties.

10.1 Identification of large coherent structures

As the importance of coherent vortical motions in turbulent shear flows is now widely recognized both in fundamental and applied research, there exists a huge and rapidly growing body of literature concerning their identification and characterization. This literature will not be discussed in detail here, but references will be restricted to those papers, which have had an immediate impact on the present study on large coherent structures in shallow wake flows. For a review of the recent significant literature, the reader is referred to Bonnet et al. (1998) and the references given herein. Holmes et al. (1996) is mainly devoted to this topic, but many of the recent textbooks also discuss coherent structures to a limited extent.

10.1.1 Definition of coherent structures

Although their is still no general agreement on a single definition of coherent structures, a working definition has to be stated before discussing their identification. A definition, which is often referred to, was given by Hussain (1986):

> "A coherent structure is a connected [, large-scale] turbulent fluid mass with a instantaneously phase-correlated vorticity over its spatial extend."
>
> Hussain (1986, p. 307), Hussain (1983, p. 2818)

This definition contains all the essential information for the identification of LCS at least in the case of shallow turbulent wakes. The flow quantity, which constitutes the basis for the eduction of LCS, is the *vorticity* $\boldsymbol{\omega}$. Obviously, from kinematic grounds, vortical motions, whose typical length scale greatly exceed the flow depth, can be treated as a 2D flow. Thus, in order to extract large-scale coherent structures in shallow flow, it is sufficient to observe the horizontal vortical motions, i.e. the vertical component ω_z of the vorticity vector. Though our intuition is to connect coherent flow structures to their vorticity, since we understand them as vortical motions, we could also try to use other measures. An example, which sometimes led to misinterpretation in flow visualization, is to relate the structure identification to a scalar quantity like a dye concentration. Here it was presumed, that the regions of high tracer concentration should be identical to regions of high connected vorticity significant for LCS. This was exemplified by Holmes et al. (1996, pp. 40) using the interesting far wake visualizations of Cimbala et al. (1988). From shallow wake flows it is quite obvious, that even though in the near field a LCS has been marked with tracer dye, in the far field a blob of high tracer concentration

is still advected downstream, while the underlying coherent vortical structure has already dissipated its kinetic energy and disintegrated.[1]

From the above definition the flow field can be decomposed into coherent vortical structures and an incoherent base flow, which is characterized by small-scale 3D random turbulent velocity fluctuations. To discriminate the coherent part of the flow from the incoherent background, an appropriate *phase–resolved averaging* procedure can be employed to evaluate the average history or life of coherent vortical structures from a series of individual large-scale eddies. This averaged rotational fluid motion will be called the large coherent structure. So, the requirement of phase correlation for LCS implies that they show connected vorticity not only in space, but also in the phase–resolved temporal domain.

Finally, the size of the LCS has to be addressed. In turbulent shear flow it is well known that coherent flow structures of various sizes co-exist (e.g. 'ribs', 'hairpins', 'typical eddies' of Taylor length-scale).[2] In contrast, by *large* coherent structures those structures will be understood that have a length scale, which is of the order of the transverse shear flow. How do large-scale coherent vortical structures interact with the small-scale incoherent turbulence of the surrounding ambient (or time-mean) flow? The answer to this question, crucial for all turbulent shear flows, also contributes to the solution for many aspects of momentum and mass transfer in shallow turbulent flow.

There is much discussion, whether such a definition is sufficient for the detection of LCS in different flow configurations or not, but there might be consensus that at least it is necessary. For example, Jeong & Hussain (1995) examine the general applicability of different definitions in order to develop a common criterion for the eduction of LCS.

10.1.2 Eduction scheme for LCS in shallow wake flow

To elucidate the role of coherent structures in diverse flow configurations, various methodologies to identify and extract LCS have been developed since the 1970s. The proposed techniques always reflect the flow data to be analyzed, which in turn was (and still is) strongly depending on the available measurement techniques. Obviously, there is a great difference between the data records obtained from a single hot-wire anemometer and the information buried in the

[1] See Figure 10.7 for a comparison of ω_{core} and c_{core} depending on x/D. In the wake far field for $x/D > 30$ the LCS have disintegrated and their vorticity vanished, but mass still prevails in the former LCS. Due to the vertical dispersion resulting from the bottom–induced shear, this discrepancy is far less obvious in shallow wake flows compared to unbounded plane wakes.

[2] Since viscous dissipation occurs below the Kolmogorov length-scale ℓ_η, no fluctuations with higher frequency exist. Thus, in the spectral range of order $\mathcal{O}(l_K)$ all fluctuations finally tend to be coherent. (cf. also Chapter 6)

raw data of a 3D PIV or combined PIV/PLIF system. So, progress in measurement techniques, and today also in computer power and numerical methods, allows for and sometimes also needs development of more sophisticated methods to analyze and extract the essential data. It is beyond the scope of this work to review the recent developments and the currently available structure identification schemes. The reader is referred to Bonnet et al. (1998) for an overview and an extended recent bibliography. Following Camussi (2002), we briefly categorize the methods frequently used nowadays to educe LCS from 2D velocity fields:

- *Galileian or Reynolds decomposition*: one of the most used methods for coherent structure identification from 2D velocity fields consists in translating the velocity vector field by an amount equal to the structure advection velocity. When the translation velocity is evaluated locally, the method is usually denoted as a Galileian transformation. Similarly, a Reynolds decomposition is applied when the translation is based on the global mean advection velocity. Vortical structures are identified in the transformed vector fields or streamlines.
- *Direct analysis of the vorticity vector field*: because of the vortical motion of the flow field in the vicinity of coherent structures, it is straight forward to identify the LCS by regions of concentrated vorticity. Since the vorticity is solely associated with spatial derivatives, which are available from 2D velocity fields, the vorticity fields allows for the same temporal resolution as the velocity data. Besides the enhancement of small-scale turbulence and noise by applying a finite difference algorithm to the unsmoothed data, also regions of high local shear cannot be separated from actual vortical structures.
- *Analysis of the velocity gradient tensor evaluated locally*: Refined definitions for coherent vortical structures are based on properties of the velocity gradient tensor $\nabla \boldsymbol{u}$, e.g. a positive second invariant, or complex eigenvalues of $\nabla \boldsymbol{u}$. For a detailed discussion see e.g. Jeong & Hussain (1995).
- *Large eddy simulations filtering*: Analogous to the numerical large eddy simulations (LES) the velocity vector data is low-pass filtered here to suppress the high-frequency small-scale fluctuations. This is contrary to the above eduction schemes, which imply a high-pass filtering with a low (Reynolds decomposition) or higher cut-off frequency (vorticity, or velocity gradient).

Further structure identification methods employ for instance proper orthogonal decomposition (POD), linear stochastic estimation (LSE), or maybe most promising wavelet analysis.

Prerequisites. For the reasonable choice of a methodology to educe LCS in shallow wake flows, whether an existing method has to be employed or to be improved, or a new one has to be developed, the individual prepositions have to be clarified, which are twofold at least: technical measurement conditions,

and physical flow conditions. On the one hand, denoted as *technical measurement conditions*, the kind, quality and quantity of the data provided by the employed measurement techniques request and restrict the eduction scheme. In the framework of this research study, both point-wise and planar measurements of 2D velocity vectors and tracer concentrations were conducted. For the identification of LCS we will use the horizontal velocity fields obtained from a 2D Particle Image Velocimetry (PIV) system, which is adapted to the observation of LCS in shallow flows. The temporal and spatial resolution of the data is optimized to record a series of individual large-scale eddies interacting with each other and with the vertical shear flow. Because of the restricted resolution both in time and space, however, fluctuations are resolved only down to intermediate scales, so effectively the employed PIV technique works as a low-pass filter with an intermediate cut-off frequency.

On the other hand, the *physical flow conditions* of a shallow wake flow induced by a cylindrical obstacle differ from other turbulent shear flows. Depending on the class of wake instability, we will encounter LCS organized in a vortex street-like formation generated at or near the obstacle (called 'topographical forcing'), or more or less monopolar eddies in the shallow mixing layers of the initially stable wake flow (i.e. 'internal transverse shear instability'). The latter ones are not covered by the present LCS identification methodology[3]. Topographically forced flow instabilities reveal a much better spatial and temporal predictability than those internally induce by transverse shear. Their 'place of birth' is fixed, since they are generated by separation near the obstacle, as well as their 'date of birth', since the shedding cycle shows a distinct periodicity for a strong forcing. Because of these initial conditions and the axisymmetric mean flow, also the travelling paths of the large-scale eddies do not vary much.

In conclusion, for the structure identification a methodology will be employed, which makes use of the local evaluation of horizontal velocity gradients, to benefit most from the 2D PIV data. Since these methods suffer from noise

[3] Because of the smaller transverse main velocity gradients compared to topographical forcing at an obstacle, shallow mixing layers bear a weaker forcing mechanism for LCS. In order to provide this forcing, one has to control the ambient flow to prevent separation near the cylindrical obstacle, but nevertheless produce and maintain enough shear for the growth of LCS in the mixing layers of the wake. This task might be impossible, unless other geometrical shapes of obstacles like a porous plate are used. Since for this kind of instability an equilibrium shear flow is needed, which provides sufficient length for the development of large-scale structures, other facilities might be better suited than the Karlsruhe shallow water facility. Contrarily to our eduction scheme, to extract large-scale coherent structures from mixing layer flows we first have to identify individual eddies, which are then phase–aligned averaged to educe their underlying coherent structure. The general feasibility of structure identification in such shallow turbulent shear flow was demonstrated by Dietz (2001), who conducted and evaluated experiments on large-scale structures in a shallow mixing layer introduced by the confluence of two streams initially separated by a splitter plate.

arising from the finite differences algorithm approximating the velocity gradients, we will employ some preprocessing to smooth the discrete data. Since the LCS are related to their "phase-correlated vorticity", a phase–resolved averaging procedure has to be applied to the detected individual realizations of the large-scale eddies. Here, we will take advantage of the physical flow conditions, namely the high spatial predictability of the occurrence of vortical structures. Instead of applying the structure identification directly on the time history of the flow field, at first a phase averaging procedure will be employed on the data in order to filter them. Afterwards the *coherent* vortical structures will be educed directly instead of individual eddy structures, which still would have to be phase-correlated.

A quick overview of the exact procedures is given in v. Carmer et al. (2001, 2002), in the remainder of this section we will discuss our method in more detail.

Phase–resolved averaging procedure. The purpose of the phase–resolved averaging procedure is to educe the *coherent flow*[4] from a sequence of instantaneous flow fields. Therefore, the data has to be post-processed to provide sets of phase–resolved ave-raged vector (and scalar) fields. The general procedure of phase–resolved averaging makes use of the evident periodicity of the wake flow and implies the following steps. At first, the individual periods for each shedding cycle are determined for the velocity fields as well as for the concentration fields using an auto-correlation approach. Next, based on the individual cycle periods, the time histories of the vector and scalar fields are re-organized by assigning each field of a time series to its appropriate phase angle ϕ. The cycle period is split into a number of phase intervals, and all fields belonging to a certain phase interval are then averaged, which leads to phase–resolved averaged fields for discretized phase angles ϕ_i. Using phase–resolved averaged instead of ensemble–averaged data, means to adopt a triple decomposition into mean, periodic and random parts, instead of a classical Reynolds decomposition into mean and fluctuating parts. So, effectively the phase–resolved averaging procedure works like a narrow adaptive low-frequency bandpass–filter, which is adjusted to the individual frequency of each shedding cycle.

Structure identification. In order to separate large eddy structures from the surrounding small-scale turbulence, use is made of the *Weiss function Q* (Weiss, 1981, 1991), which was first applied by McWilliams (1984) to educe vortical structures in numerically simulated quasi-2D geostrophic turbulence. This method is based on the comparison of the magnitudes of rate–of–strain

[4] In optics coherency of light terms light of the same frequency and phase. In the case of a shallow vortex street-like wake in turbulent bottom shear flow we address the repetitive, quasi-periodic low-frequent part of the flow as the coherent flow.

and vorticity, what makes it a very comprehensive criterion, which satisfies the definition of a LCS. The *Weiss function* is given as

$$\begin{aligned} Q &\equiv \left(\frac{\partial u}{\partial x} - \frac{\partial v}{\partial y}\right)^2 + \left(\frac{\partial v}{\partial x} + \frac{\partial u}{\partial y}\right)^2 - \left(\frac{\partial v}{\partial x} - \frac{\partial u}{\partial y}\right)^2 \\ &= \theta_1^2 \, + \, \theta_2^2 \, - \, \omega_z^2 \, , \end{aligned} \tag{10.1}$$

which is the difference between a squared combination of the normal strain rates in θ_1, the squared doubled shear strain terms $(2\,s_{xy})^2 = 1/4\,(\partial u/\partial y + \partial v/\partial x)^2$ in θ_2^2, and the squared vertical vorticity ω_z^2. For the situation of a shallow turbulent wake flow the horizontal linear strain rate terms in θ_1 are small compared to the shear strain term θ_2, and therefore not of significance for the identification of vortical structures.[5] If θ_1 is discarded from Q, then the remainder would be proportional to the second invariant of the tensor ∇u defined as $II_{\nabla \boldsymbol{u}} \equiv \frac{1}{2}\left(u_{i,i}^2 - u_{i,j}\,u_{j,i}\right) = -\frac{1}{2}u_{i,j}\,u_{j,i}$. Therefore, also the approximation

$$Q \approx -2\,II_{\nabla u} = \left(\frac{\partial v}{\partial x} + \frac{\partial u}{\partial y}\right)^2 - \left(\frac{\partial v}{\partial x} - \frac{\partial u}{\partial y}\right)^2 = \frac{\partial u}{\partial y} \cdot \frac{\partial v}{\partial x} \tag{10.2}$$

could be employed. Hence, it can be noted that regions of negative Q could be approximated by regions of a positive second invariant $II_{\nabla u}$, which is the main criterion for structure identification introduced by Hunt et al. (1988), cited and fundamentally improved by Jeong & Hussain (1995).

However, in the present study on shallow wake flow the original definition of Q given in (10.1) is employed. From the horizontal velocity fields obtained from the PIV system, the planar distributions of Q are computed. For the identification of large eddy structures use is made of the physical explanation of $Q(x, y)$. Flow regions, which are dominated by vorticity, i.e. $|\omega| > |\theta_1| + |\theta_2|$, are associated with negative values of Q.[6] On the contrary, regions where $Q > 0$ are dominated by (especially shear) strain. It can easily be shown that Q must vanish in the area integral in axisymmetric shear flows as is a shallow turbulent wake. Due to small-scale turbulence and noise, and amplified by the finite differences scheme, small irregular pattern of low negative and positive Q values occur in every turbulent flow.

Large-scale vortical structures concentrate a high amount of vorticity in their cores, and can therefore be characterized by their significantly higher magnitude of negative Q. Thus, depending on small-scale turbulence intensity,

[5] The shear strain term θ_2^2 and the vorticity term ω^2 are of the same order of magnitude, whereas the term containing the normal components of the rate-of-strain θ_1^2 was evaluated to be less than 10 % of θ_2^2 on average.

[6] For vanishing or equal normal strain components, $\theta_1 \to 0$, and $|\omega| > |\theta|$ is exactly equivalent to $Q < 0$.

noise, and data post-processing, a fixed absolute Q value can be established as a *static threshold*, $Q_{eddy} = const$, to separate large-scale vortices. On the other hand a threshold can be defined *dynamically* with respect to a local reference value, e.g. $Q_{eddy}/Q_{ref} = const = e^{-1}$. The latter kind of definition is already employed to compute the half-width δ_u of the wake from the time-averaged flow field, this definition allows to use δ_u as a length scale in the integral model in order to establish self-similarity of the transverse velocity distribution.

For the eduction of vortices being spatially connected 2D structures in the time-dependent flow field, a time-dependent reference value has to be employed instead of using a time-averaged one. In consequence regarding the space-domain, the time-dependent reference value is localized at a fixed point in the time-dependent flow field, instead of a reference line in the time-mean flow. In order to implement a dynamic threshold criterion for the identification of vortices, for each value $Q(\boldsymbol{x}, t)$ depending on time and space one has to associate a reference value, which is the local maximum of negative Q occurring in the core of each vortical structure. Computing the length scale of a vortex in this dynamical way allows for self-similarly normalize the vortex properties in a Lagrangian frame. The most benefit from this dynamic threshold definition can be obtained in those regions of the flow, where (i) self-similarity really holds for the vortices, and (ii) the dynamic threshold really applies.

The motivation for preposition (i) is, that without assuming self-similarity one cannot conclude from the spatial extent and strength of a vortex to its magnitude of further properties integrated over the vortex area (e.g. total kinetic energy). Without a self-similar distribution the same peak values and widths would not result in identical area–integrated properties of eddy structures. Thus, in the region of vortex generation and growth, it might be misleading to apply a dynamic threshold, since one still could not predict the contents of further properties for the whole vortex area. Preposition (ii) results from the fact, that due to 3D turbulence, measurement and numerical noises, we always have to apply a certain absolute threshold, below which no unambiguous attribution to the vortex is possible. How far downstream of the obstacle the dynamic threshold will drop below the static threshold and thus will become inappropriate, will depend on the flow conditions characterized by the stability number $S = c_f\ D/h$, and on the noise level. Any doubt has to be avoided about which criterion was applied at each spatiotemporal position in the wake flow, as well as any mixing of criteria, otherwise the final disappearance of the vortex cannot be observed. Therefore, the application of a dynamic threshold is restricted to the wake region where the established vortices are in an early stage of decay, it prevents the observation of the vortex generation as well as the final disintegration.

In conclusion, a singular large-scale eddy will be identified by its Q value falling below a specific absolute threshold in a connected region. The detected

area covered by such a large vortical structure will depend on the chosen threshold value of Q_{eddy}. Besides the measurement and data processing techniques, the necessary threshold level reflects the scale difference between large quasi-2D structures and the small-scale 3D turbulence.[7] A proper choice of the Q threshold guarantees for a correct evaluation of the vortex area over the whole wake flow field.

Finally, it should be mentioned again that regarding the structure identification scheme there is no difference, whether we apply the scheme on time–resolved data or first run a phase–resolved averaging procedure and then apply the scheme to the phase–resolved re-sampled data. In the former case individual vortices are identified which have to be phase–aligned to extract the underlying coherent vortical structure. In the latter case using the coherent flow field the LCS are educed directly. So far, the methodology to identify LCS in shallow wake flows has been introduced by more general reasoning, but without justifying the procedures. This will be demonstrated in the following section, where the eduction techniques is applied to a set of experimental data from a vortex street-like shallow wake flow. The topography of the large-scale coherent wake flow, and the decomposition of various flow properties into coherent and incoherent parts provide strong support for our schemes being appropriate to educe LCS in shallow wake flow.

10.2 Characteristic flow properties of large coherent structures

10.2.1 Topography of large coherent structures

Since our eduction method for LCS in shallow wake flow involves a phase–resolved averaging procedure in a fixed (Eulerian) frame without making use of the Taylor hypothesis, we obtain topographical information on LCS not only in the phase-domain, but also in space. In other words, we are able to observe both the local variations of LCS during the phase cycle, and the spatial changes of the LCS while they advect downstream, thus we obtain both local and advective rates of change for the LCS.[8] Resolving also the advective derivatives is a crucial precondition for the understanding of all kinds of shallow flows, which are continuously influenced by bottom friction over their spatial extent.

Shedding cycle of LCS in fixed frame. We start the discussion on the topography of LCS in the shallow wake of a cylindrical obstacle by presenting

[7] When using the phase–resolved averaged flow field to extract LCS instead of single vortices, the threshold value Q_{LCS} can be reduced significantly, because the high-frequency fluctuations of the shear flow do not contribute to the periodic flow field.

[8] As mentioned above, this results from the appropriately selected combination of technical measurement conditions and physical flow conditions.

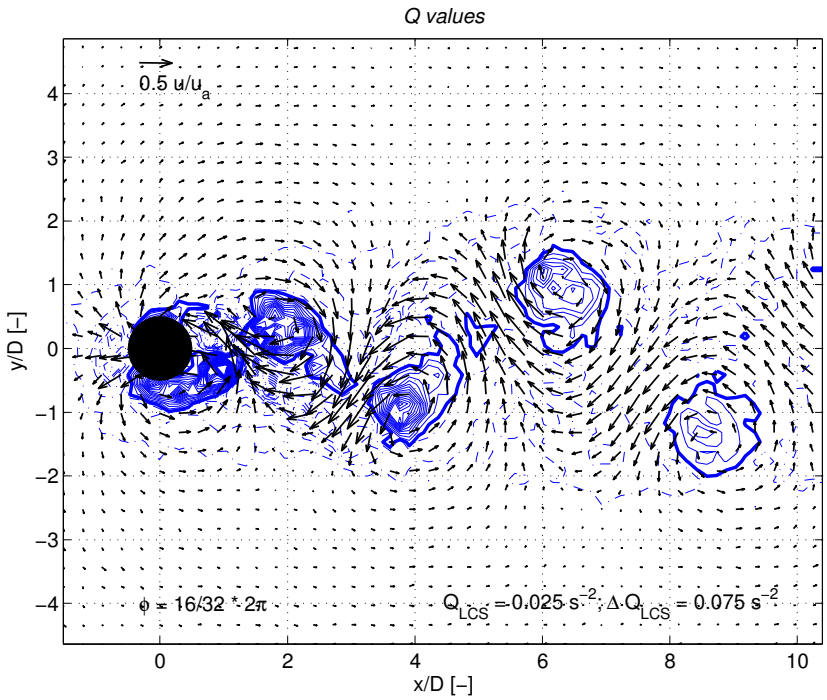
Q values
0.5 u/u_a
y/D [–]
x/D [–]
ϕ = 16/32 * 2π
Q_LCS = 0.025 s^-2; ΔQ_LCS = 0.075 s^-2

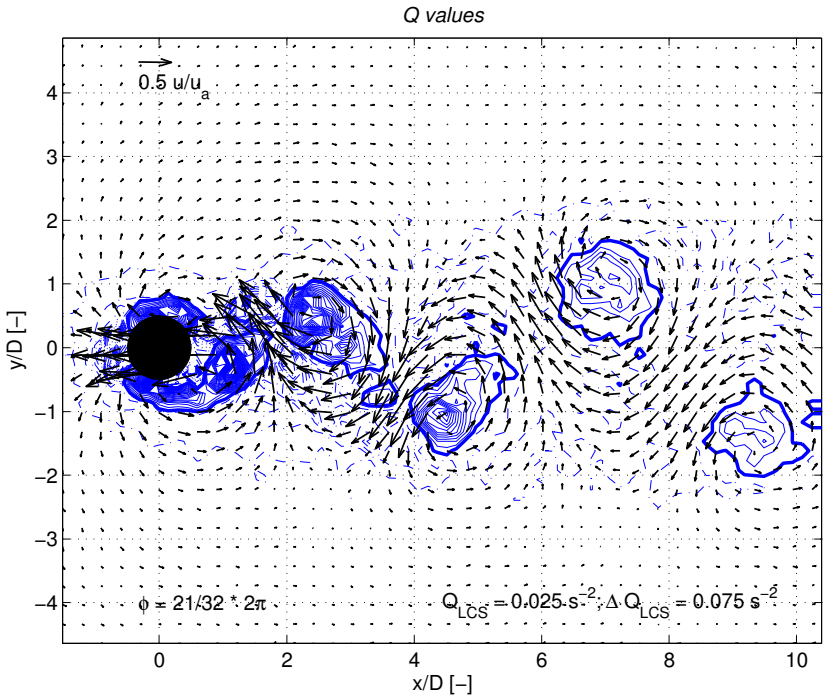
Q values
0.5 u/u_a
y/D [–]
x/D [–]
ϕ = 21/32 * 2π
Q_LCS = 0.025 s^-2; ΔQ_LCS = 0.075 s^-2

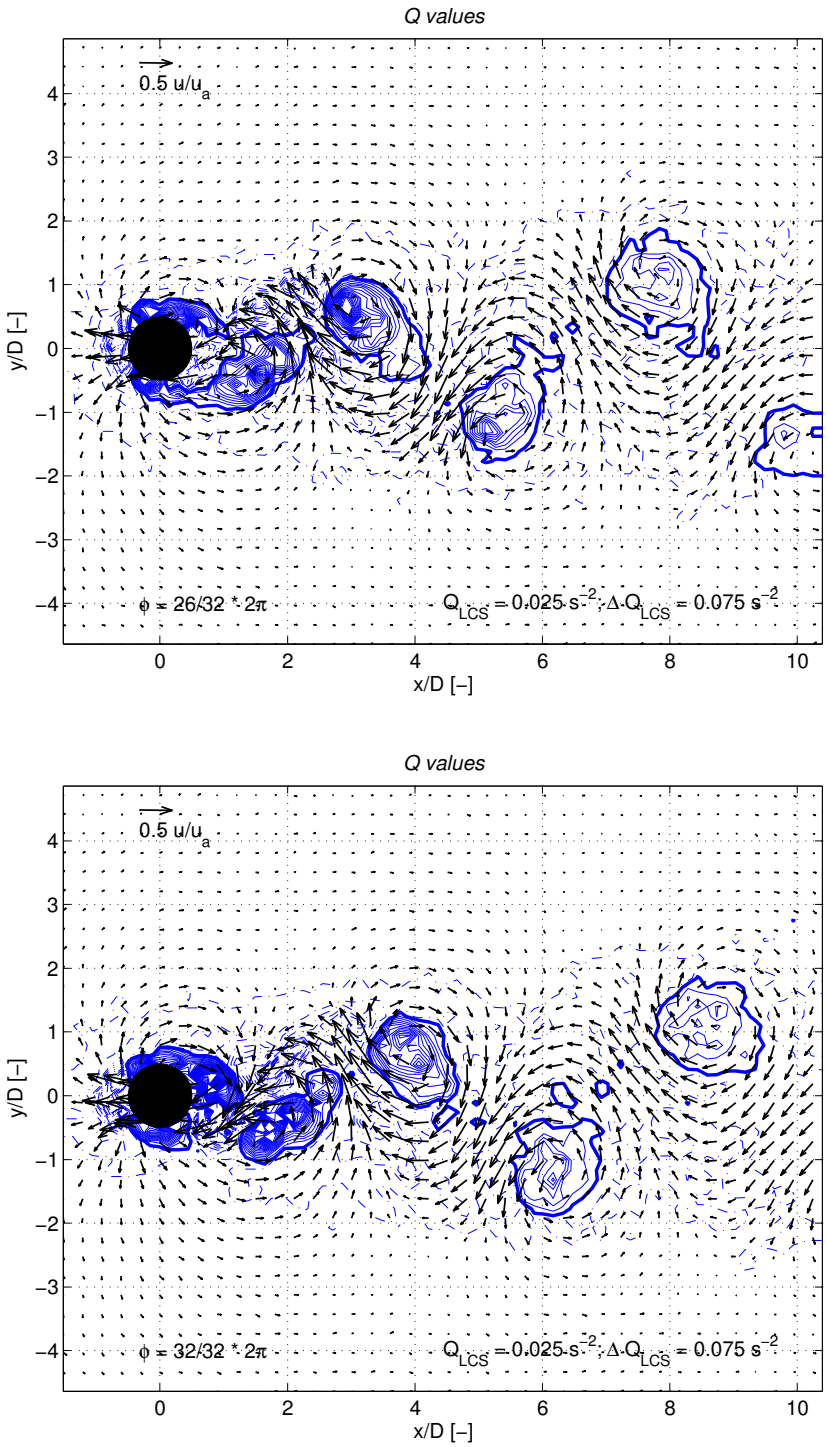

Figure 10.1. Phase-resolved averaged flow fields for a vortex street-like shallow wake (series 18_vs06, run 1, cf. Table 5.2) are displayed for 4 different discrete phase angles ϕ_i showing the generation of LCS in the right shear layer of the wake. The horizontal velocity vectors are reduced by the mean undisturbed (ambient) flow field, thus the deviation of the flow field induced by the cylindrical obstacle is depicted. Contours show phase-averaged values of the Weiss function Q defined by (10.1). Full lines show negative Q related to vorticity-dominated flow regions, the bold full line indicates the threshold level of small negative Q used to distinguish LCS from the surrounding water body and from background noise. Dotted lines show strain-dominated regions of positive Q values.

phase–resolved averaged horizontal velocity fields $\{\boldsymbol{u}\}$ and distributions of Q values, which were computed from $\{\boldsymbol{u}\}$. As an example, we use the data of a vortex street-like wake flow (series 18_vs06, run 1, cf. Table 5.2) with $D/h = 7$, where the ratio of the horizontal and vertical length scales of the shear flow is a geometrical measure for the shallowness of the flow. So, this flow is characterized by a high shallowness, and we therefore expect the kinematic and dynamic effects of the vertical shear flow to significantly influence the development of the LCS.

In Figure 10.1 we use a geophysical coordinate system having its origin in the center of the cylindrical obstacle (filled in black), where distances are normalized by a macro length scale of the transverse shear flow, namely the cylinder diameter D. The phase-time in this case is discretized into 32 phase angles ϕ_i. Since the phase-time is repetitive per definitionem, the first time segment following a full cycle is identically equal to the first time segment, or in general $\phi_i = \frac{t_i}{T}\,2\pi \equiv \frac{T+t_i}{T}\,2\pi = \phi_{i+n}$ with $i = 1 \ldots n$. The 4 phase angles depicted in Figure 10.1 are $\phi_i = \frac{16}{16}\pi$, $\frac{21}{16}\pi$, $\frac{26}{16}\pi$, and $\frac{32}{16}\pi$ spanning half the shedding cycle in 3 approximately equal increments. Here we can follow the generation of LCS in the right wake shear layer, i.e. we observe the average shedding process of individual large eddies into the right-hand side of the wake flow. Displayed in the plots of this figure are the phase-averages of the *horizontal surface velocity fields*, which for better perceptibility are reduced by the mean undisturbed flow field $\boldsymbol{u_a}$ (i.e. without obstacle). Also, though we only displayed a quarter of the calculated velocity vectors, we used the full velocity data set for the deduction of further flow quantities. Here, this is the Q *value* computed from (10.1) comparing the strength of strain and vorticity, which enables us to identify vorticity dominated flow regions. Dash-dotted line contours indicate positive Q values and strain-dominated regions, whereas full lines indicate negative values of Q, which is related to areas dominated by vortical motion. The bold full line shows the negative Q contour closest to zero, indicating the static threshold level Q_{LCS}, which separates the vorticity of the 3D small-scale turbulence from the higher vorticity magnitudes contained in the large-scale vortical structures. Here, the threshold level is given as $Q_{LCS} = -0.025\,s^{-2}$, or non-dimenisonalized by ambient flow variables as $Q_{LCS}\,h^2/u_a^2 = 4.2\;10^{-4}$.[9] Contour levels are distributed linearly with a step size of $\Delta Q_{LCS} = 0.075\,s^{-2}$ or $\Delta Q_{LCS}\,h^2/u_a^2 = 12.7\;10^{-4}$, where on the one hand linear levels were chosen to allow the reader also to recognize the gradients of Q, but on the other hand the high variability of the Q values demanded also higher step sizes.

[9] The vertical enstrophy from the instantaneous surface velocity fields of the ambient flow was computed as $\omega_z \cdot \omega_z \approx 0.006$ for the present measurement run. This value corresponds to about 25% of the magnitude of the given Q_{LCS}.

The evaluations presented in Figure 10.1 exemplify, what a shallow turbulent wake flow can look like, and what the importance of large-scale vortices may be. Large patches associated with connected negative Q values are alternately aligned in the wake of the obstacle. Their length scale is of the order of magnitude of the transverse shear layers, which in turn is roughly $\mathcal{O}(D)$. From the vector representations it becomes clear that the connected vorticity–dominated regions exhibit a strong rotational motion, as expected. We can easily see the counter-rotating staggered arrangement, which resembles a von Kármán vortex street. Also the centers of rotation coincide remarkably well with the local minima of negative Q, when we use a Lagrangian frame moving with the ambient velocity. This question will be addressed in more detail in the following. We can surely state that the applied eduction scheme identifies *connected regions of phase–correlated vorticity*, which we associate with large-scale coherent vortical structures. These LCS are embedded in an area with large lumps of positive Q, where the phase–averaged flow is dominated by straining motions mainly due to shear. In the immediate vicinity of the obstacle this strain–dominated region really surrounds the LCS, more downstream we find that also those regions show connected patterns, which are arranged anti-symmetrically with the LCS along the wake centerline A less shallow case (series 38_vs01, runs 1 and 2, cf. Table 5.2) is presented in Figure 10.2. The area in toto covered either by significant vortical or straining motion can therefore be regarded as the wake flow induced by transverse shear at the obstacle. Outside the wake region in the ambient flow, where solely the bottom–induced vertical shear is acting, neither negative Q below the negative threshold value nor positive Q above the positive threshold can be found. There exist no strong horizontal structures neither in the coherent flow field nor in the time–resolved fields.

Because the reduced velocity vector field may lead to misinterpretation at first sight, we want to mention that vectors pointing upstream indicate that the flow is slower than the ambient flow. But of course this does not mean per se that the flow direction reverses in the wake. In fact, in this flow configuration only a very short zone of flow recirculation can be found (cf. also Figure 9.4(b)). The less shallow VS wake flow presented in Figure 10.2 does not develop a recirculation zone at all. On the other hand, since the flow is forced around the obstacle and also around the large-scale vortices, due to the displacement it is accelerated to velocities even higher than the ambient flow. The regions of accelerated flow in the immediate vicinity of the obstacle have been addressed in Sections 9.1.1 and 9.1.2.

The *generation of LCS* is captured very well in the full series of phase–resolved Q fields, which cannot be presented here in their entirety due to the limited space. Around $\pm 75°$ from the upstream stagnation point we observe two regions of very high vorticity, which might be identified as the nuclei of

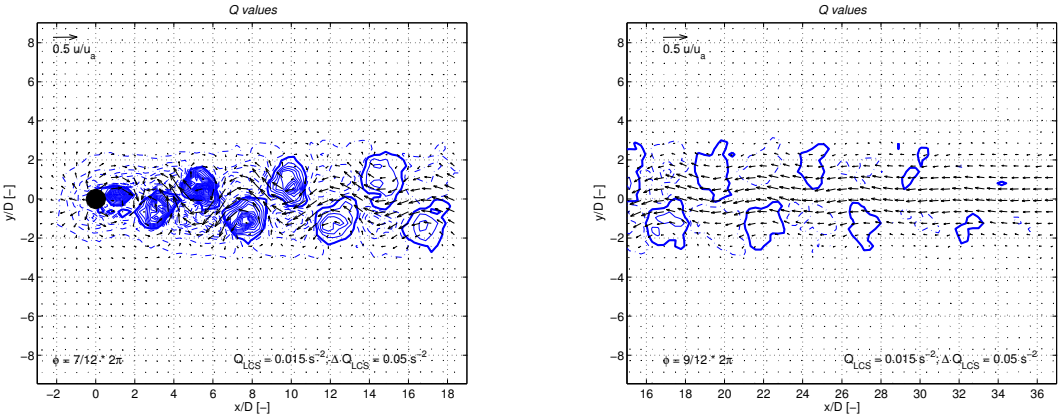

Figure 10.2. Phase-resolved averaged flow fields of a vortex street-like shallow wake (series 38_vs01, runs 1 and 2, cf. Table 5.2) illustrate the downstream development of the wake flow carrying LCS. The shallowness is only $D/h = 1.7$, the wake is less shallow. The phase-angles ϕ of the plots for the different runs are selected as to present a continuous coherent flow field. The threshold level is given as $Q_{LCS} = -0.015\,s^{-2}$, or non-dimenisonalized as $Q_{LCS}\,h^2/u_a^2 = 8.0\;10^{-4}$. Contour levels are distributed linearly with a step size of $\Delta Q_{LCS} = 0.05\,s^{-2}$ or $\Delta Q_{LCS}\,h^2/u_a^2 = 26.8\;10^{-4}$. Refer to Figure 10.1 for further detail.

the LCS. Due to feedback they show an alternate behavior, e.g. while the right-hand region moves to the back some degrees, the left-side region moves forward. While the vortical region is moving towards the lee side it is firstly stretched and secondly continuously fed by more vorticity. This soon gives rise to a second maximum located also close to the cylinder perimeter, but downstream of the first one. Figure 10.1 shows the beginning of this process for the left shear layer side in plot 2 for ϕ_{21}. For ϕ_{26} and ϕ_{32} the stretching of the attached vortical region and growth of the second maximum can be recognized. The end of this tearing process is depicted in ϕ_{16} for the right shear layer, now this second maximum becomes separated from the obstacle due a shear–dominated flow intrusion along the leeward cylinder boundary. As can be seen for the right side at ϕ_{26}, the second maximum is now moving into the detached shear layer, but remains connected to its nucleus. Finally at ϕ_{32}, the second maximum completely separates from the first one, and can now be understood as a single LCS. In this stage it contains an extremely high amount of negative Q, which as a result of the tearing process is found to be located in an elliptical shape with its major axis inclined by 45° against the centerline.

As a LCS advects downstream, it gradually reshapes toward a circular geometry. Its core remains located in the former position of the outward focus of the elliptical shape. The steep gradients clearly indicate the circular circumference. A braid of lower vorticity is directed from its downstream end toward

the upstream end of its adjoining LCS travelling ahead.[10] This braid, which can be observed clearly in flow visualizations (cf. Figure 11.1 or Figure 11.2(b)), influences the transverse mass exchange across the wake and the entrainment and mixing of fresh fluid. We will discuss this aspect during the next chapter. While downstream of the cylinder the LCS acquire their circular shape, also the organization of the strain–dominated regions of positive Q becomes more pronounced. As can be seen more clearly in Figure 10.2, centers of strain (i.e. maxima of positive Q) are anti-symmetrically located opposite of the vortex cores. They effectively separate LCS of the same sign (i.e. the same sense of rotation) and prevent them from merging.[11] At least in this sense the strain–dominated regions also sustain the LCS, but in the following we will add more to the importance of these regions in shallow wake flows.

We now have a first impression of large-scale coherent vortices existing in shallow wake flows. In the next paragraphs we will gain more insight into the topography of LCS by examining their streakline and streamline pattern, and into their decay as they advect downstream over a bottom of given roughness.

Streaklines of the coherent flow field. From the phase–resolved averaged surface flow fields also streaklines can be computed to further elucidate the large scale periodic motion in the wake flow. In anticipation of Section 11.2.2 a numerical particle tracking procedure is applied that allows to observe virtual kinematic floats continuously released into the coherent quasi-periodic velocity fields extracted from PIV measurements. The turbulent diffusive transport of the small-scale random part of the wake flow, which is induced by the small-scale Reynolds shear $\{u_r\, v_r\}$, is only poorly resolved by the employed PIV system. These random turbulent fluctuations are excluded by the filtering effect of the phase–resolved averaging procedure, as is the influence due to variations

[10] Only LCS of opposite sign, which therefore cannot merge, are involved in this kind of interaction. Since no exchange of large-scale vorticity is involved in this process, we will not call it a partial pairing of different LCS (cf. also Hussain, 1986, p. 311), but a tearing or straining process of an individual LCS. Nevertheless, as a concept we could look at a monopolar vortex, which has to be surrounded by a ring of opposite vorticity in order to balance the vorticity of the core, and assume that this vorticity should be organized in smaller eddies. For instance Lugt (1979, p. 187, p. 360) reported laboratory visualizations by Weske of steady secondary vortices in the boundary layer of a primary vortex. As a second monopolar of opposite sign would approach the first one, we could think of an interaction, that would include the transfer of ring vorticity from the first monopolar to the core of the adjoining second vortex. In the end this would lead to an vortex street like arrangement rather than a bipolar vortex. But concluding, we do not have any experimental evidence of such an vorticity exchange, and whether or not we would be able to observe the appropriate small scales, there is some indication from streamline fields that such interactions are not possible.

[11] Whether these strain-dominated regions prevent the LCS even from interaction, or on the contrary they result from interaction of the LCS, is an open question. The generation not only of LCS, but also of strain regions has to be examined as well as their sustaining interaction.

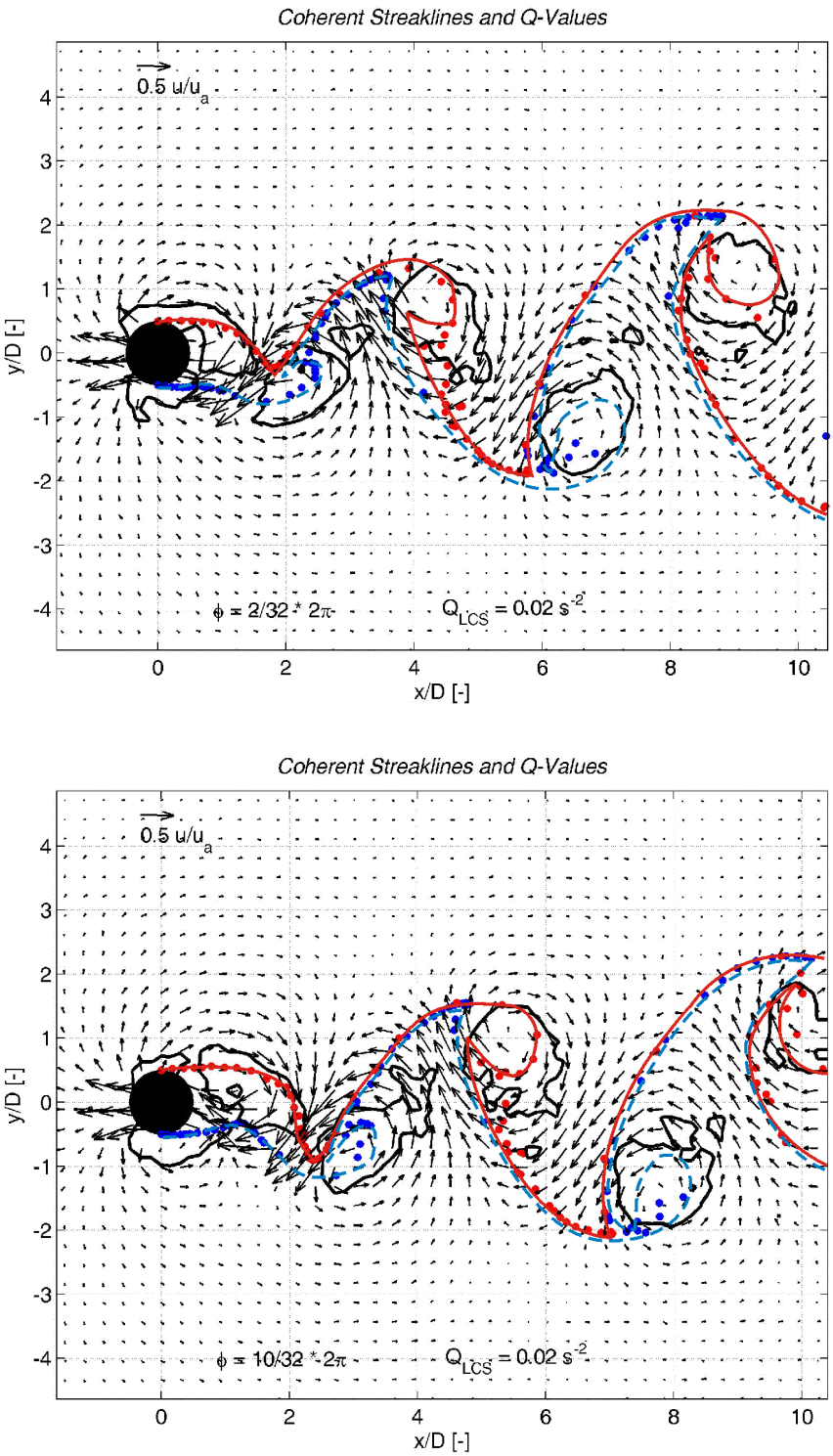

Figure 10.3. Coherent streaklines are computed from the phase–resolved averaged flow fields of a vortex street-like shallow wake flow (series 18_vs06, run 1). Here, numerical tracers are continuously released into the left and right cylinder boundary layers, the sources are located at $x/D = 0$ and $y/D = \pm 0.5$. Additionally, bold contour lines show the LCS indicated by their threshold value Q_{LCS}. Vectors depict the horizontal velocity field reduced by the undisturbed (ambient) flow field. The phase interval of the lower plot follows the upper one with a phase difference of $\pi/2$.

of the individual large eddies with respect to the LCS. In Figure 10.3 we show streaklines in a vortex street-like shallow wake (series 18_vs06, run 1) emerging from two point-sources located at both sides of the cylindrical body ($x/D = 0$ and $y/D = \pm 0.5$). The LCS are indicated by bold contour lines of a threshold value Q_{LCS} superimposed on the vector field of the periodic horizontal flow $\{\boldsymbol{u}\} - \boldsymbol{u_a}$. Also from the streaklines we can observe clearly the intrusion of ambient fluid across the whole wake and its final entrainment at the downstream ends of the LCS, where the strained braids connecting the LCS are rolled-up into the coherent eddies. We can observe that a streakline is usually rotated around the outer side of the LCS, when the origin of the streakline is located in the same shear layer as the LCS, whereas it is strained along the inner side of the LCS, when its origin is in the opposite shear layer.

Since the streaklines can be regarded as continuous releases of small tracer floats from point–sources, they can also provide an estimate for the mass transport solely by the LCS dominated low-frequency wake flow. Since the floats are released at a constant rate, we even have an impression of the concentrations of the tracer mass. For example we notice a significant agglomeration of floats, where the braids are connected to the LCS. We will address these aspects again in Section 11.2 in more detail.

Coherent streamlines for different moving observers. From the phase–aligned averaged surface flow fields we can also compute streamlines, i.e. curves that are parallel to the velocity vectors everywhere in the flow. We use a common definition of a *streamfuction* ψ,

$$u \equiv \frac{\partial \psi}{\partial y} \qquad \text{and} \qquad v \equiv -\frac{\partial \psi}{\partial x} \ , \tag{10.3}$$

based on the assumption that the vertical component of the flow $w = 0$, and therefore, continuity satisfies $\partial u/\partial x + \partial v/\partial y = 0$. Contrary to velocity gradients and its derived quantities like vorticity or a scalar quantity, streamlines are not Galilean invariant, but they vary in different moving frames. Displaying streamlines in a fixed Eulerian frame is useful in the immediate vicinity of the obstacle inducing a shallow wake in the flow region, which is associated with an absolute flow instability. In case of predominantly convectively unstable flow—as observed in a vortex street-like shallow wake—we get more insight from an analysis in a Lagrangian frame.

In an introductory video to the Karlsruhe shallow flow facility (cf. v. Carmer & Deutsch, 2001, 2002) we present a camera flight following a tracer dye–tagged large-scale eddy with its advection speed. This gives a good impression both of the fate of the structure and of an observation in a Lagrangian frame.

Perry et al. (1982) used some of the classical movies by L. Prandtl to extract streamlines in a two-dimensional bluff body flow in order to exam-

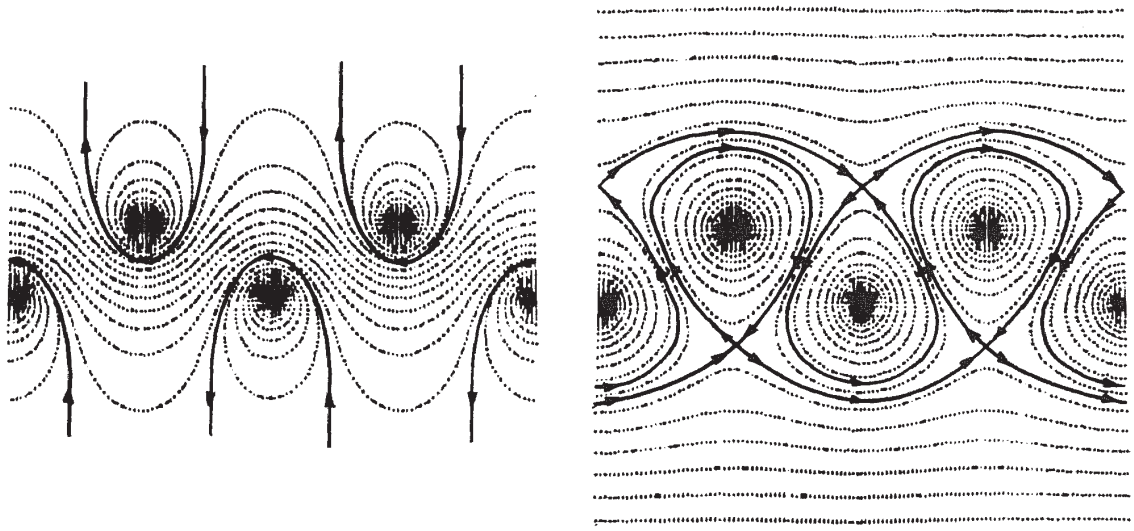

(a) Lagrangian frame moving with U_a (b) Lagrangian frame moving with U_{LCS}

Figure 10.4. Streamlines obtained from far wake calculations using a classical von Kármán vortex street model were shown by Perry et al. (1982) in a Lagragian frame moving with the ambient flow velocity U_a (on the left) and with the advection speed U_{LCS} of the eddies (on the right). A bold line indicates a dividing streamline or 'separatrix'. Contrary to a vortex street-like shallow turbulent wake flow, the eddies were treated as irrotational point vortices in an unbounded ambient flow. (from Perry et al., 1982)

ine the vortex-shedding process. They realized that in the far wake it is not of much help to use a fixed frame of observation, and therefore they added calculations of a von Kármán vortex street in unbounded ambient flow to support the Eulerian visualization. Following von Kármán's model the eddies were approximated by irrotational potential vortices, in the first instance the streamlines from this calculation can be regarded as an idealization also for a vortex street-like shallow turbulent wake. In Figure 10.4 we reproduce the far wake streamlines shown by Perry et al. (1982) in a Lagragian frame moving with the ambient flow velocity U_a (on the left) and with the advection speed U_{LCS} of the eddies (on the right). A bold line indicates a dividing streamline or 'separatrix'. The touching separatrices of adjacent vortices (they actually do not cross) indicate a saddle point in the velocity vector field. If we vary the longitudinal traversing speed of the observational frame, the saddle-points move laterally; moving the frame with the ambient velocity (on the left), the saddle-points tend toward infinity. On the contrary, the centers of closed streamlines, which coincide with the cores of the eddies, do not vary their lateral position, because being irrotational vortices they have infinite velocity and velocity gradients at their centers regardless of the finite traversing velocity of the frame. Employing a different model approximation for the vortices, like an Oseen

or RANKINE vortex, resulted in improved predictions of a von Kármán vortex street (cf. e.g. the review of CHEN (1973) for further references).

In Figure 10.5 streamlines computed from the phase–resolved averaged velocity fields (series 18_vs06, run 1) are shown for different traversing speed of the frame of observation. Observing this vortex street-like shallow wake flow in a fixed Eulerian frame (cf. Figure 10.5(a)), no closed streamlines attached to the cylinder can be found, i.e. no recirculation zone related to an absolutely unstable flow region exists (or only a very small zone that could not be resolved). Concluding that this wake flow is dominated by convective instability associated with the LCS, the frame of observation is advected with the large-scale vortices. In the next two plots of Figure 10.5 we display the streamline pattern with respect to a frame moving with the mean ambient velocity U_a (Figure 10.5(b)), and moving with the mean advection speed U_{LCS} of the LCS[12] (Figure 10.5(c)). Bold lines indicate threshold values Q_{LCS} to educe the coherent structures. Both streamline figures are comparable to the schematized plots in Figure 10.4 from PERRY ET AL. (1982). When moving with U_a, the velocity gradients tend toward zero outside of the wake, thus the streamlines become indifferent and sensitive to small deviations from U_a outside of the wake.[13] Contrary to Figure 10.4, in Figure 10.5 the centers of closed streamlines are not fixed in frame space, but also shift laterally for different frame traversing speed. This results from the velocity distribution in the cores of the shallow vortical structures, which is not like an irrotational vortex, but closer to a solid-body rotation (cf. also Figure 10.7). Furthermore, the shape of the closed cavity (following a 'separatrix' not displayed here) is slightly tilted toward the centerline. This can clearly be seen in Figure 10.5(c) moving with U_{LCS}, where the associated centers and saddle-points are not located at the same downstream position, but the saddle-points are located a little more downstream. So, compared to the idealized computation, we have a loss of symmetry in the shallow wake, which might be attributed to the presence of the cylinder.

Comparing the streamline pattern with the Q value distribution, local minimum Q values of the vorticity–dominated regions coincide with the centers of the closed streamlines, when moving with U_{LCS}. The saddle-points are characterized by high positive Q values and are located amid the shear-dominated

[12] For the streamlines in Figure 10.5(c) the traversing speed of the Lagrangian frame has been chosen to $0.88\,U_{LCS}/U_a$, which was found to be appropriate for a downstream position of about $x/D = 8$. The general dependence of the core velocity U_{LCS} on x/D is displayed in Figure 10.7 in terms of the standardized slip velocity $(U_a - U_{LCS})/U_a$.

[13] We expect PERRY ET AL. (1982) having encountered the same problem resulting from numerical noise instead of geometric imperfections and measurement noise of the PIV system. No streamlines are computed further away from the wake in the undisturbed ambient flow.

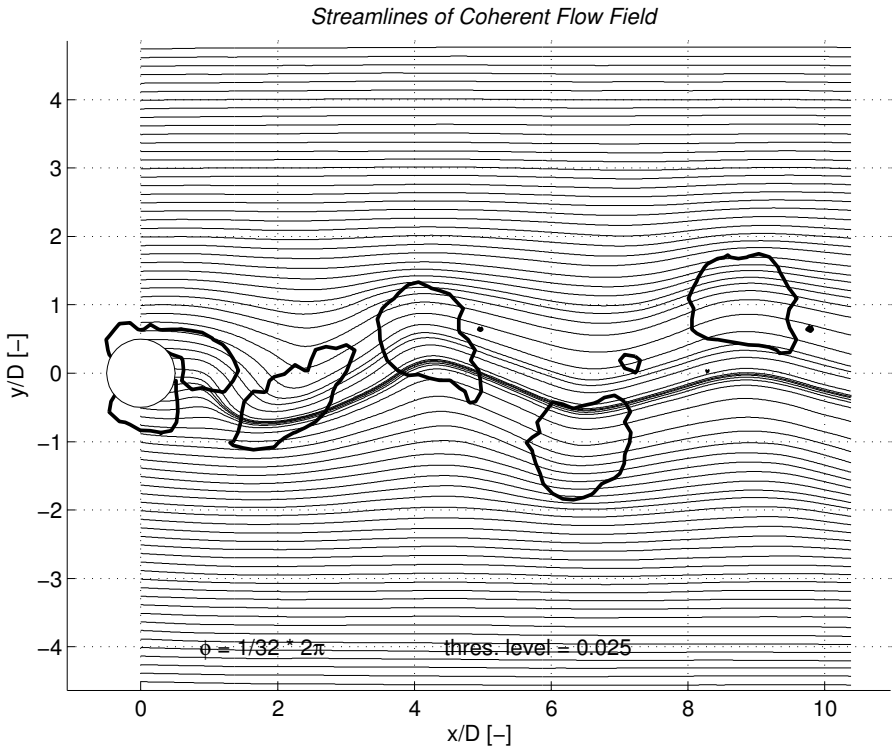

(a) Streamlines in fixed frame

Figure 10.5. Streamlines were computed from the phase–resolved averaged velocity fields for a vortex street-like shallow turbulent wake flow (series 18_vs06, run 1) for different traversing speed values of the Lagrangian frame. The thin lined streamline pattern is displayed together with the bold iso-lines of threshold value Q_{LCS} indicating the LCS. The streamlines are computed in a Eulerian frame in plot (a), and for a frame moving downstream with the traversing speed equal to the mean ambient velocity U_a and equal to the mean advection speed $U_{LCS} = 0.88\,U_a$ of the large-scale vortices in plots (b) and (c), respectively.

regions for an observer moving with the eddies. We can also compare the coherent streamlines to the streaklines in the coherent flow field, as e.g. for a Eulerian frame of observation represented in Figure 10.5(a) and in the top plot of Figure 10.3, respectively. Unlike the hypothesis of Perry et al. (1982), the streaklines emerging from the cylinder boundary do not coincide with the dividing (or any other) streamlines, regardless which traversing speed for the moving frame we choose. Since we reduce the velocity vectors by a given longitudinal velocity like U_a or U_{LCS} instead of really applying a moving frame of observation, we do not obtain a steady flow field, but still retain a periodic field.[14]

[14] The generation and fate of the large-scale vortical structures as they advect downstream, makes it difficult to obtain steady solutions when following a single structure. We would have to normalize the fields by characteristic scales depending on the downstream position (e.g. the velocity field $u(x, y)$ by the core velocity defect $u_{s,core}(x)$). Because in shallow

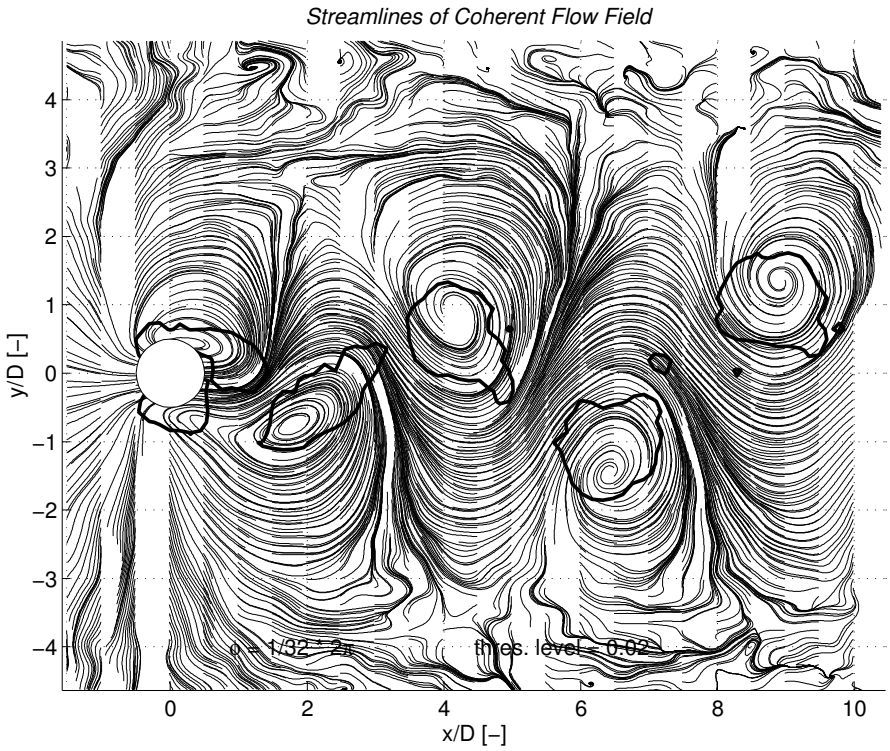

(b) Frame moving downstream with mean ambient velocity U_a

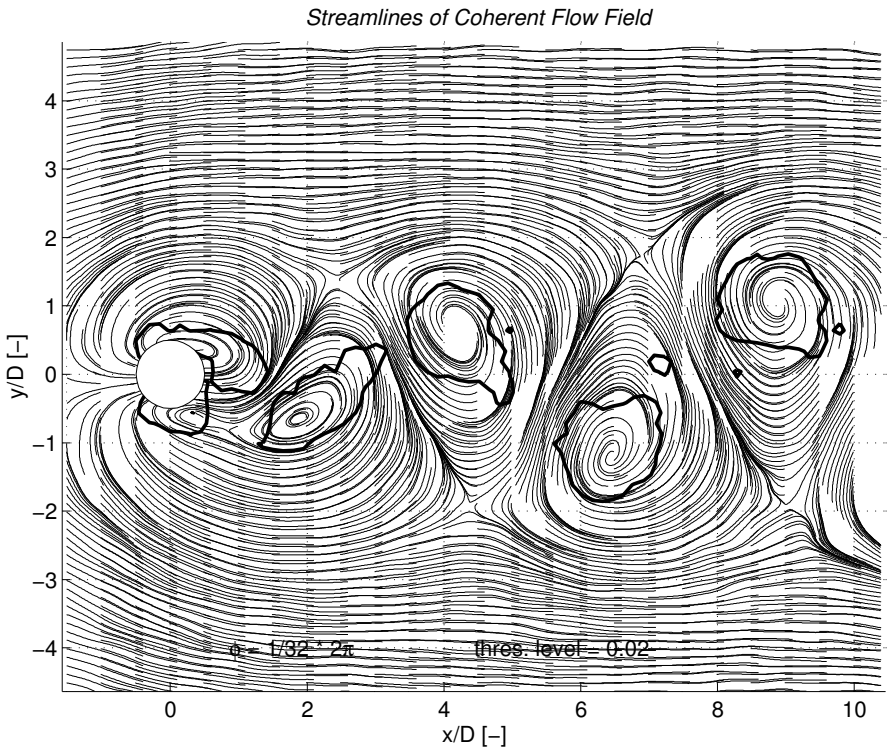

(c) Frame moving downstream with mean advection speed U_{LCS} of LCS

Figure 10.5. Continued, for caption see facing page.

10.2.2 Transient behavior of large coherent structures

In the case of vortex street-like shallow wakes, large-scale coherent vortical structures are an essential part of the low-frequency periodic flow field, and thus they also influence the time-mean flow field. We already showed various flow properties of time-averaged wake flow fields in Chapter 9. Decomposed into coherent and random part, distributions of flow properties over the whole wake field will be addressed later in this section. In the following subsection we will focus on the LCS themselves, and briefly discuss their gross features and its variation as the LCS advect downstream suffering from bottom-induced shear.

We educe LCS from the periodic wake flow field by means of the Q value given by (10.1). The center or core of the LCS is characterized by a local maximum of the negative Q value. The horizontal extent of a single LCS can either be evaluated statically by a constant threshold value Q_{LCS} or dynamically using a threshold relative to the local minimum, e.g. $Q_{LCS}/min(Q) = e^{-1}$, as discussed in Section 10.1.2. Throughout this work we prefer the prior definition to discriminate the LCS from numerical noise also far downstream from the obstacle, where Q tends toward zero.

Figure 10.6 shows a single LCS in the right shear layer of a vortex street-like shallow wake (series 18_vs06) at different downstream positions $x/D = 7$, 15, 23, 31. Based on the Q distribution, a bold + marks the core position of the LCS, and a bold full line indicates the boundary of the LCS based on a static threshold value Q_{LCS}. The low-frequency surface velocity field $\boldsymbol{u_p}$ is reduced by the velocity at the core position, which we call the structure's advection speed $\boldsymbol{u_{LCS}}$. Thus, the reduced velocity vectors centered around the single vortex are essentially the same as observed within a Lagrangian frame moving with $\boldsymbol{u_{LCS}}$. The vector field is underlaid in gray scale with the vertical vorticity $\omega_{p,z}$ calculated from the low-frequency quasi-periodic surface velocity fields. Light and dark areas indicate high positive and negative vorticity, respectively. Note that velocity and vorticity are given in dimensional form here, and that the vorticity scale changes with downstream position, whereas the velocity scale is retained.

Figure 10.6(a) shows a single LCS at $x/D = 7$ in its mature stage and beginning to decay again. The shape is roughly circular and symmetric with respect to the LCS core. Since $\boldsymbol{u_{LCS}}$ varies with the downstream position

---

wakes two controlling mechanisms act simultaneously, namely the local lateral shear due to the obstacle and the continuous vertical shear due to bottom friction, two characteristic velocities would be of relevance: $u_{s,core}(x)$ and the friction velocity $u^*(x, y)$. Within the far wake the dependency of both forces is analyzed analytically (cf. Chapter 8), but an important part of the wake shows a transient behavior, which reveals a complex interaction of both mechanisms.

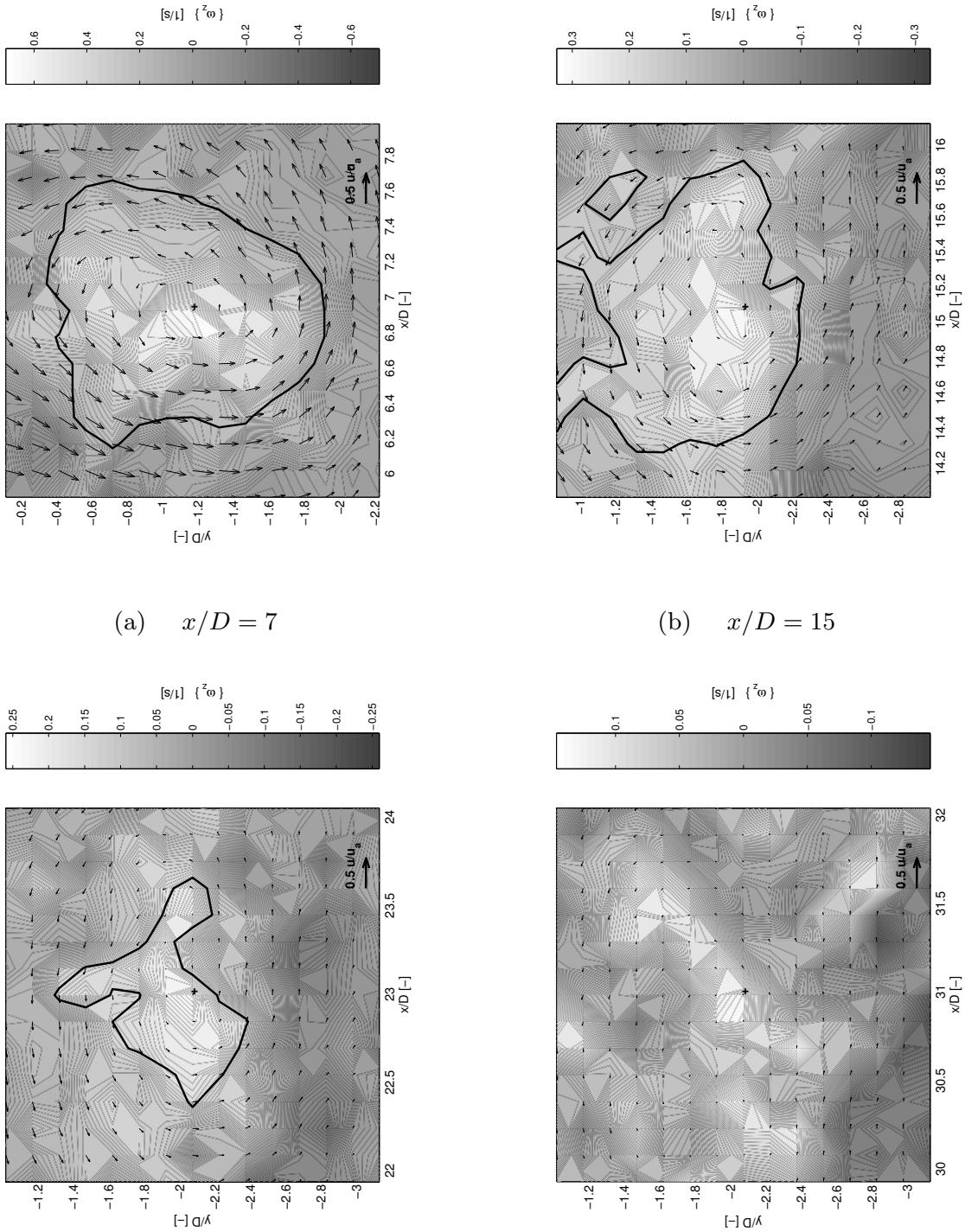

(a) $x/D = 7$

(b) $x/D = 15$

(c) $x/D = 23$

(d) $x/D = 31$

Figure 10.6. A moving observer follows a single LCS in the right shear layer of a vortex street-like shallow wake (series 18_vs06). The core positions in the four plots from upper left to lower right are $x/D = 7$, 15, 23, 31. A + marks the position of a local minimum of the Q value being the center of the LCS. A bold full line shows the boundary of the LCS as calculated with a constant absolute threshold Q_{LCS}. Vectors indicate the flow velocity relative to the velocity in the core called the LCS' advection speed $\boldsymbol{u_{LCS}}$. Light and dark areas show large positive and negative magnitudes of the coherent vertical vorticity $\omega_{p,z}$, a medium gray indicates $\omega_{p,z} = 0$.

(cf. the relative vortex slip velocity $(u_a - u_{LCS})/u_a$ in Figure 10.7(b)), the Lagrangian frame of observation accelerates with $u_{LCS}/u_a \to 1$. Therefore, the reduced flow velocity $(u - u_{LCS})$ changes in each plot as does the core advection speed. Comparing the flow velocities of the rotational motion of the vortex displayed at different positions in the consecutive plots gives an impression how the strength of the vortex varies as it advects downstream. As illustrated in Figures 10.6(b) and 10.6(c), with increasing downstream distance the vortex looses its symmetry, it becomes skewed toward the outside of the wake and shows a more erratic shape. At $x/D = 31$ in Figure 10.6(d) the LCS has disintegrated, though we still find its core from the local minimum of Q. But its strength is not sufficient anymore to unambiguously identify the whole structure by its Q value. Also the area of significant vorticity has lost its spatial connection. $\omega_{p,z}$ shows a patchy distribution of low values resulting from the velocities, which indicate only a weak circulation.

The local minima of Q indicate the centers of vorticity–dominated flow regions. The transient behavior of the LCS with downstream distance can be characterized by its core magnitude of Q, which in turn is strongly dominated by $\omega_{p,z}$ near the core. In the sequence of plots in Figure 10.6 (cf. also Figure 10.7 (b)) we can observe the decrease of the vorticity values both in the core of the LCS and over its whole area, whereas the values outside the LCS remain roughly constant and close to zero.

The plots of Figure 10.7 shed more light on the longitudinally transient characteristic of large-scale coherent structures in a shallow turbulent wake (series 18_vs06). The positions $y/D = \delta_{core}$ of the vortex cores within the coherent wake flow field $\boldsymbol{u_p}$ (marked with $\circ$ symbols) are shown for both wake shear layers in Figure 10.7(a). The distance δ_{core} of the core from the wake centerline is an additional measure for the width of the wake. The LCS trajectory follows the development of the wake half width δ_u defined by the time-mean defect velocity as $\langle u_s(x, \delta_u)\rangle / \langle u_{s,c}(x)\rangle = 1/2$. Beyond $x/D \approx 12$ the longitudinal change diminishes both in the mean wake width and in the lateral LCS core position for this wake flow configuration. Note that the minor asymmetry occurs in the core positions of both shear layers. This results from the velocity field not being uniform—neither in the longitudinal nor in the lateral direction—due the imperfect topography of the horizontal bottom, and amplified by very shallow flow conditions in this series. Figure 10.7(b) visualizes the longitudinal development of velocity defect of the LCS advection speed $u_s(\delta_{core}) = (u_a - u_{LCS})$ normalized with the ambient velocity of the undisturbed flow u_a (indicated by a bold full line, and plotted with respect to the second y-axis). When the LCS have reached their mature stage at $x/D \approx 5$, the advection speed deviates by roughly 10% from the base velocity. As the LCS decay while travelling further downstream, they accelerate until their advection speed approaches the ambient velocity after $x/D \approx 20$. Indicated by a dash-dotted line also the core

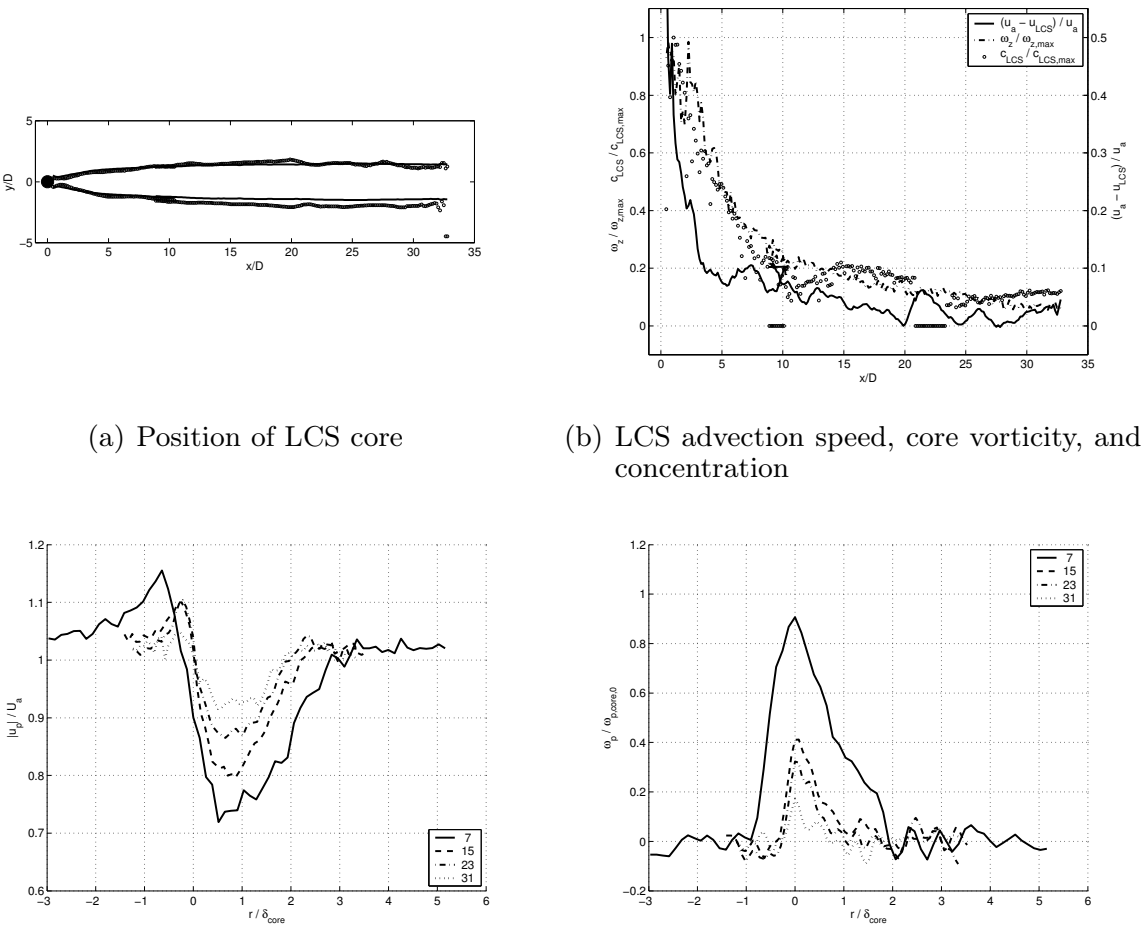

(a) Position of LCS core

(b) LCS advection speed, core vorticity, and concentration

(c) Velocity profiles within LCS

(d) Vorticity profiles within LCS

Figure 10.7. The transient behavior of LCS advecting downstream is illustrated by evaluations of the coherent wake flow fields. (a) The position of the LCS core δ_{core} in both wake boundary layers (i.e. phase–resolved averaged pathline indicated by •) is compared to the time-mean growth of the wake (full lines show location of wake half width δ_u, where $\langle u_s(x, \delta_u)\rangle \,/\, \langle u_s(x, 0)\rangle = 1/2$). (b) The development of the deficit of the core velocity $(u_a - u_{LCS})/u_a$ is marked with •. The vertical vorticity $\omega_{p,z}$, indicated by a full line, is also decreasing rapidly. (c) For different downstream positions the relative velocity $(u_p)/u_a$ is plotted transversely over the relative distance from the LCS core r/δ_{core}. (d) Analogously the transverse distribution of the vorticity $\omega_{p,z}(r/\delta_{core})$ is shown for $x/D = 7$, 15, 23, 31.

vorticity $\omega_{p,z}(\delta_{core})$, normalized by its initial maximum value, is evaluated over the downstream distance in Figure 10.7(b). Compared to the velocity defect the decrease of the vorticity is more gradual; at $x/D = 5$ $\omega_{p,z}$ still amounts to 50%, and at $x/D = 20$ to 15%. For an unbounded wake the decrease between these two downstream positions is around 50% (Hussain & Hayakawa, 1987, p. 212), whereas in the present shallow wake flow we observe a less rapid decrease $\omega_{p,z,core}(x/D = 20) = 0.35\,\omega_{p,z,core}(x/D = 5)$. Denoted by ∘ symbols the mass concentration at the vortex core position, resulting from a continuous injection into the cylinder boundary layer, is non-dimensionalized by its initial

maximum value. The downstream decrease of $c_{LCS}/c_{LCS,max}$ corresponds very closely to the decay of the core vorticity.

In Figure 10.7(c) and 10.7(d) we show transverse profiles of the main coherent velocity and of the coherent vertical vorticity with respect to the distance $r = y - \delta_{LCS}$ from the vortex core in the right shear layer. Although we do not intend to give a self-similar description of the LCS here, we normalize r with the local core distance from the centerline $\delta_{core}(x)$.[15] The magnitude of the coherent velocity $\boldsymbol{u_p}$, normalized by the undisturbed ambient velocity u_a, is display in transverse cross–sections at different downstream positions. In general, we observe velocities, which are significantly higher than the ambient, at the outer side of the wake ($r/\delta_{core} < 0$). Inside the wake the flow is slower than the ambient velocity showing its minimum values close to the wake centerline ($r/\delta_{core} = 1$). The distribution at $x/D = 7$ (denoted by a full line) is stretched when compared to the more downstream profiles, which indicates that self-similarity of the LCS does not hold at this donwstream position (cf. footnote 15). At the more downstream positions $x/D = 15$, 23, 31 a self-similar velocity distribution can be obtained for a normalization with a local maximum value, i.e. with $u_{LCS}\,(x/D)$. The distribution of the coherent vertical vorticity $\omega_{p,z}$ in Figure 10.7(d) also shows a skewed distribution, but a more gradual decrease as demonstrated in Figure 10.7(b). The same stretching depending on the lateral scale can be observed. A self-similar vorticity distribution across the LCS can be expected when employing proper local scales, i.e. a dynamic $\delta_{LCS}\,(x)$ and $\omega_{p,z}\,(\delta_{LCS})$.

What kind of descriptive model do we expect for the LCS in shallow wake flow? As the LCS is initially generated due to severe horizontal shear, the initial vortex might be approximated by a potential vortex, which is irrotational save the center with its vorticity singularity. The tangential velocity in such a vortex is inversely proportional to the radial distance $u_\vartheta \propto 1/r$. Initially having a core of finite vorticity, which does not necessarily has to be a solid-body rotation with constant vorticity and $u_\vartheta \propto r$, this rotational core will spread into the surrounding irrotational flow. The combination of a solid-body core rotation with a potential outer vortex is called a Rankine vortex model, which has a discontinuous transition in u_ϑ and a jump in ω_z. An idealized model, which omits discontinuities, is the so-called Oseen vortex. As derived

[15] The planar measurements conducted for this study were designed to get more insight into the wake flow dynamics over the whole spatial extend. Special emphasis laid on its longitudinal development. In order to observe the behavior of a single eddy or LCS more closely, we need a higher spatial resolution in order to reduce measurement noise, and to access also the wake far field characterized by only weakly energetic large-scale structures. We would expect the decaying LCS to behave in a self-similar way. Making use of a dynamic threshold definition for Q_{LCS}, a more appropriate length scale for the LCS could be evaluated.

also by TRUCKENBRODT (1980, pp. 265) this model is capable of reproducing the time-dependent spreading of the vortex in an unbounded flow.

We should not hope to be able to fully describe the LCS in a vortex street-like shallow wake using the above mentioned model, because here we are concerned with vortices in a continuous and variable horizontal shear flow combined with a vertical plane shear flow and its dissipating effect due to bottom friction. Comparing the velocity and vorticity distributions in Figures 10.7(c) and 10.7(d), we can state that in the vicinity of the vortex, where $u_\vartheta \to u_a$, the flow is irrotational ($\omega_{p,z} \approx 0$) and strain–dominated. This seems to be true in the outer regions of the wake as the normalized velocity defect approaches unity. In the central part of the wake we encounter a significant amount of vorticity, which can therefore be addressed as the LCS region. Not surprisingly, the maximum $\omega_{p,z}$ value is always located at the vortex center defined by Q. Note the distinct vorticity peak over all downstream positions. Also further downstream the core vorticity cannot be regarded as constant over the width of the LCS, i.e. the vortex core should not be approximated by solid–body rotation. Furthermore, we observe significant skewness especially in the lower values of the vorticity distribution. This asymmetry in the low vorticity region results from the braids connecting adjacent LCS of opposite sense of rotation. We also observe a significant strain rate in this area. From the evaluation of the Q values tending to zero and even obtaining positive values in the other wake shear layer, we do not classify this area neither as a vorticity–dominated region nor as strain–dominated, but as insignificant, and not to belong to the primary LCS.

10.2.3 Two–length–scale decomposition of velocity fields

When examining shallow turbulent wake flows, we are confronted with fluctuating velocity fields of clearly *two different length scales*, namely the low frequency periodic vortical motion of the quasi 2D large-scale structures and, by contrast, the high frequency random fluctuation of the turbulent vertically sheared basic flow. In order to explore the interaction and mutual dependency of the fluctuations of both length scales, it is appropriate to decompose the time-resolved velocity data into low and high frequency parts $\boldsymbol{u_p}$ and $\boldsymbol{u_r}$.

$$\begin{aligned} \boldsymbol{u} &= \boldsymbol{u_p} + \boldsymbol{u_r} \\ &= \{\boldsymbol{u}\} + (\boldsymbol{u} - \{\boldsymbol{u}\}) \end{aligned} \tag{10.4}$$

A Reynolds decomposition into mean and turbulent parts obviously can not cope with a two-length-scale problem of turbulence. But we can combine both the Reynolds and the *two–length–scale decomposition* (10.4) into a *triple decomposition* (cf. e.g. HUSSAIN, 1983)

$$\begin{aligned} \boldsymbol{u} &= \boldsymbol{U} + \boldsymbol{u}_{\boldsymbol{p}}^{*} + \boldsymbol{u}_{\boldsymbol{r}} \\ &= \langle \boldsymbol{u} \rangle + \{\boldsymbol{u} - \langle \boldsymbol{u} \rangle\} + (\boldsymbol{u} - \langle \boldsymbol{u} \rangle - \{\boldsymbol{u} - \langle \boldsymbol{u} \rangle\}) \end{aligned} \tag{10.5}$$

Note, that in (10.5) for the time-mean of the phase–resolved averaged flow field $\left\langle \boldsymbol{u}_{\boldsymbol{p}}^{*} \right\rangle = 0$, whereas for the double decomposition (10.4) $\langle \boldsymbol{u}_{\boldsymbol{p}} \rangle = \boldsymbol{U}$.

In (10.5), we distinguish between the mean advective flow $\boldsymbol{U}$ and the low frequency periodic flow field $\boldsymbol{u}_{\boldsymbol{p}}^{*}$, which implies that the coherent structures are only small perturbations of a mean flow. But in accordance with Hussain (1986),

> "in many cases the coherent structures are highly dominant. That is, in many cases they are not perturbations of the time-mean flow: they are the flow."
>
> Hussain (1986, p. 351)

Regarding the mechanism for the generation of a shallow shear instability, this surely applies for the strongest mechanism, the topographical forcing for example in the case of a vortex street-like wake flow. Here, the time-mean flow can be considered the result of many such structures and their interactions. In a region occupied by a structure, the entire non-random motion is the coherent structure, and a vortex street-like instability consists of a closed pattern of interfering LCS. Therefore, we prefer to use a two–length–scale decomposition (10.4) into low and high frequency parts throughout this work. However, also this double–decomposition has some constraints, e.g. it cannot address the evolution of coherent structures with respect to a driving flow or the extraction of energy by coherent structures from the flow which advects the structures. Especially when we examine the transport of a scalar quantity like a solute mass, the triple decomposition leads to fluxes of negative coherent scalar magnitudes. This behavior does merely elucidate, but obscure the physics of the transport processes. Also from the analytical aspects, there are no benefits from the triple decomposition of scalar fluxes.

Sometimes we still find it useful and desirable to use a kind of triple decomposition. To avoid the artificial separation between time-mean and coherent flow parts, we prefer to divide the flow into the undisturbed base flow and its deviation due to a perturbation. This decomposition proves especially useful when investigating the generation and fate of LCS, which are disturbances of a base flow, e.g. a vortex street-like wake instability induced by an obstacle. But this distinction is only possible because an undisturbed flow exists and is known.

To discriminate between both frequency parts a broad variety of signal analysis techniques can be applied. The phase–resolved averaging procedure provides an appropriate post-processing scheme to extract the large-scale coherent vortical structures from the instantaneous flow based on their individual

cycle periods. The deviation of an instantaneous flow field from its corresponding phase–aligned averaged field is called the *random turbulent fluctuation* of the flow. Thus, we set up a narrow, but variable band-pass filter for the coherent flow field. The incoherent fluctuating fields result effectively from a high-pass filtering, since the low-frequency variations are already included in the phase–resolved averages.

Characterization of coherent flow fields from decomposed data. We will decompose the velocity vectors with a two-length-scale algorithm. In the following we will benefit from the analytical properties of the decomposition, that (i) the time-mean and the phase average of the random fluctuations are zero $\langle \boldsymbol{u_r} \rangle = \{\boldsymbol{u_r}\} = 0$, (ii) the time-mean of the coherent (phase averaged) flow fields are $\langle \boldsymbol{u_p} \rangle = \boldsymbol{U}$ or $\left\langle \boldsymbol{u_p^*} \right\rangle = 0$, (iii) vice versa the phase average of the time-mean fields are just the time-mean fields, and (iv) the low- and high-frequency fluctuations are completely decorrelated, i.e. $\langle \boldsymbol{u_p}\, \boldsymbol{u_r} \rangle = 0$. For brevity we make use of the Einstein summation convention[16] for all indices except for p and r denoting the coherent and random parts. Furthermore, we use

$$\frac{\tilde{D}}{Dt} = \frac{\partial}{\partial t} + u_{pj} \frac{\partial}{\partial x_j} \tag{10.6}$$

for the substantial derivative of a fluid element in the coherent flow field. Of course the local rate–of–change equals 0 in steady flow, and though the coherent flow field containing the large-scale wake instability is periodic, the overall flow is steady.

Applying a double decomposition (10.4) to the Navier-Stokes equations, yields after taking the phase–average for the coherent and random parts of continuity and momentum, respectively, (Hussain, 1977, 1983)

$$\frac{\partial u_{pi}}{\partial x_i} = \frac{\partial u_{ri}}{\partial x_i} = 0 \ , \tag{10.7a}$$

$$\frac{\tilde{D}}{Dt} u_{pi} = -\frac{\partial p_p}{\partial x_i} + \frac{1}{\mathrm{Re}} \frac{\partial^2 u_{pi}}{\partial x_k^2} - \frac{\partial}{\partial x_j} \left\{ u_{ri}\, u_{rj} \right\} \ , \tag{10.7b}$$

$$\begin{aligned} \frac{\tilde{D}}{Dt} u_{ri} = & -\frac{\partial p_r}{\partial x_i} + \frac{1}{\mathrm{Re}} \frac{\partial^2 u_{ri}}{\partial x_k^2} - u_{rj} \frac{\partial u_{pi}}{\partial x_j} \\ & - \frac{\partial}{\partial x_j} \left(u_{ri}\, u_{rj} - \left\{ u_{ri}\, u_{rj} \right\} \right) \ . \end{aligned} \tag{10.7c}$$

For vorticity and turbulent kinetic energy, the coherent and random parts are, respectively,

[16] The *Einstein summation convention* concerns summation over repeated indices, i.e. whenever an index occurs twice in a term, a summation over the repeated index is implied, albeit no summation sign is explicitly written.

$$\frac{\tilde{D}}{Dt}\omega_{pi} = \omega_{pj}\frac{\partial u_{ri}}{\partial x_j} + \frac{1}{\mathrm{Re}}\frac{\partial^2 \omega_{pi}}{\partial x_k^2} + \frac{\partial}{\partial x_j}\left(\{u_{ri}\,\omega_{rj}\} - \{u_{rj}\,\omega_{ri}\}\right) \ , \tag{10.8a}$$

$$\frac{\tilde{D}}{Dt}\omega_{ri} = \omega_{pj}\frac{\partial u_{ri}}{\partial x_j} + \omega_{rj}\frac{\partial u_{pi}}{\partial x_j} + \frac{1}{\mathrm{Re}}\frac{\partial^2 \omega_{ri}}{\partial x_k^2} - u_{rj}\frac{\partial \omega_{pi}}{\partial x_j} - \frac{\partial}{\partial x_j}\left(u_{rj}\,\omega_{ri} - \{u_{rj}\,\omega_{ri}\}\right) + \frac{\partial}{\partial x_j}\left(u_{ri}\,\omega_{rj} - \{u_{ri}\,\omega_{rj}\}\right) \ , \tag{10.8b}$$

and

$$\frac{\tilde{D}}{Dt}\frac{\left\{u_{pi}^2\right\}}{2} = -\frac{\partial}{\partial x_j}\left(p_p\,u_{pi}\right) + \{u_{ri}\,u_{rj}\}\frac{\partial u_{pi}}{\partial x_j} - \frac{\partial}{\partial x_j}\left(u_{pi}\,\{u_{ri}\,u_{rj}\}\right) + \frac{1}{\mathrm{Re}}\frac{\partial}{\partial x_j}\left\{u_{pi}\left(\frac{\partial u_{pi}}{\partial x_j} + \frac{\partial u_{pj}}{\partial x_i}\right)\right\} - \frac{1}{2\mathrm{Re}}\left\{\left(\frac{\partial u_{pi}}{\partial x_j} + \frac{\partial u_{pj}}{\partial x_i}\right)^2\right\} \ , \tag{10.9a}$$

$$\frac{\tilde{D}}{Dt}\frac{\left\{u_{ri}^2\right\}}{2} = -\frac{\partial}{\partial x_j}\left\{u_{rj}\left(p_r + \frac{1}{2}u_{ri}^2\right)\right\} - \{u_{ri}\,u_{rj}\}\frac{\partial u_{pi}}{\partial x_j} + \frac{1}{\mathrm{Re}}\frac{\partial}{\partial x_j}\left\{u_{ri}\left(\frac{\partial u_{ri}}{\partial x_j} + \frac{\partial u_{rj}}{\partial x_i}\right)\right\} - \frac{1}{2\mathrm{Re}}\left\{\left(\frac{\partial u_{ri}}{\partial x_j} + \frac{\partial u_{rj}}{\partial x_i}\right)^2\right\} \ . \tag{10.9b}$$

In the above equations we find various phase–resolved averaged energy transport terms. These comprise advection terms like $u_p\left(\partial\left\{u_r^2\right\}/\partial x\right)$, $v_p\left(\partial\left\{u_r^2\right\}/\partial y\right)$, $u_p\left(\partial\left\{v_r^2\right\}/\partial x\right)$, and $v_p\left(\partial\left\{v_r^2\right\}/\partial y\right)$, coherent energy transport terms of incoherent kinetic energy like $(\partial/\partial y)\left(u_p\,\langle u_r\,v_r\rangle\right)$, coherent production terms like $-\left\{u_r^2\right\}(\partial u_p/\partial x)$ or dissipation terms like $\left\langle(\partial u_r/\partial x)^2\right\rangle$, and $\langle(\partial u_r/\partial y\;\partial v_r/\partial x)\rangle$. Their spatial distribution over the coherent flow of (or at least containing) the LCS can be evaluated to get more insight into the physics of two-length-scale flows. In the following section we will discuss some of these terms in more detail.

In the kinetic energy equations the second right-hand term denotes the coherent production of incoherent turbulence, therefore it appears as a source for the coherent kinetic energy and as a sink for the random kinetic energy.

More detail on this set of double decomposed equations can be found in Hussain (1983). Hussain (1977, pp. 590) also presented the deduction of the corresponding triple decomposed equations, which are also briefly discussed in Hussain (1983).

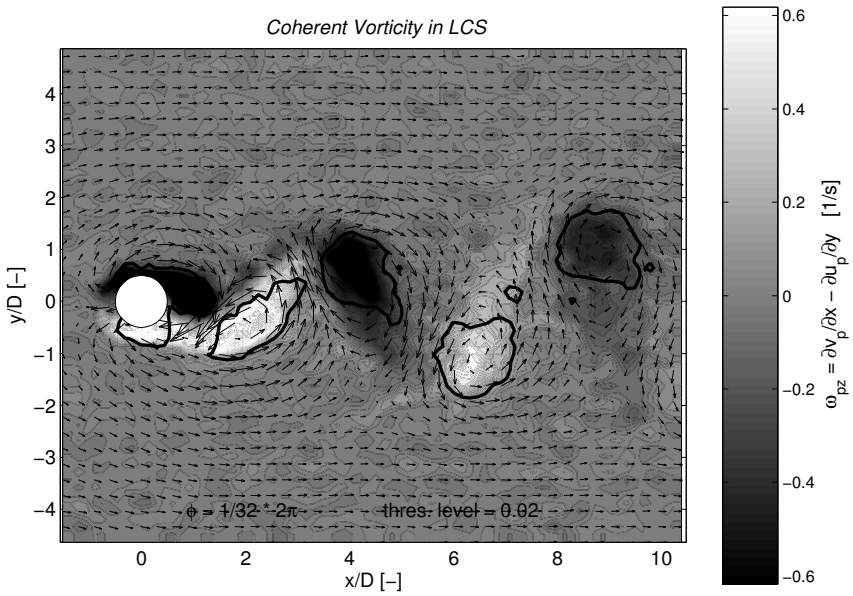

Figure 10.8. The vorticity computed from a coherent surface velocity field of a vortex street-like shallow wake flow (series 18_vs06, runs 1) is depicted in gray-scale together with the threshold value of Q (bold lines) and the velocity vectors reduced by the mean vortex advection speed. White and black areas indicate high magnitudes of vorticity exceeding the maximum value noted at the color bar. Local peak values of vorticity coincide with the cores of the LCS. The vorticity of the mature LCS is torn toward the wake centerline.

10.2.4 Dynamics of shallow wakes — fields of coherent and incoherent properties

Since, in general, properties of wake flows like turbulent kinetic energy, vorticity, divergence, strain, or further derivatives like their production or dissipation terms are derived from the appropriate velocity fields, we also obtain the coherent parts of these properties not from a phase–aligned averaged decomposition of these quantities themselves, but we calculate them from the coherent velocity fields. In the same way, the incoherent or random turbulent parts of these properties are deducted from the randomly fluctuating velocity fields.

Vorticity. For the identification of large-scale coherent vortical structures from the phase–aligned re-sampled flow field we apply an eduction scheme based on the Q value to discriminate the vorticity–dominated flow regions from the strain–dominated ones. Thus, when we presented the Q distribution in the coherent flow field, we inherently showed distributions related to the coherent vorticity and to the coherent normal and shear strain rates (cf. Equation (10.1)).

The *vertical component of the coherent vorticity* is

$$\omega_{p,z} = \frac{\partial v_p}{\partial x} - \frac{\partial u_p}{\partial y} \ . \tag{10.10}$$

Note that like all derived flow properties the coherent vertical vorticity is evaluated from the phase–resolved averaged velocity components. It is not meant to be the phase–resolved average of the instantaneous vertical vorticity field.

Since the Q value is closely related to the vertical vorticity, we omit to display distributions of coherent vertical vorticity here extensively, but show just one example distribution in Figure 10.8. Obviously, the loci of maximum Q coincide with the maxima of the absolute coherent vorticity, regions of high vorticity magnitude are per definitionem areas of high negative Q. In the outward direction of the wake the vorticity rapidly decreases toward the ambient coherent vorticity, which is zero on spatial average. Since only small-scale fluctuations exist outside the wake in the bottom shear flow, which are not represented in the coherent flow field, coherent vorticity has to vanish completely in the ambient flow. From the LCS cores directed toward the wake centerline, we find a region of lower vorticity with less steep gradients, which is oriented in the direction of stretching of the LCS, as they are still developing. When the LCS have established and achieved their final circular shape, the low vorticity region is oriented normal to the wake centerline, but clearly not in the direction of the braids. As we can observe from the vector field, vorticity stretches out from the LCS cores toward the saddlepoints in the shear-dominated regions.

Shear strain rate. Another term adding to the Q value is the horizontal rate of shear strain $s_{p,xy}$, which is represented by θ_2^2 in (10.1). The *coherent horizontal shear strain rate* is expressed as

$$s_{p,xy} = \frac{\tau_{xy}}{\mu} = \frac{\theta_{p2}}{2} = \frac{1}{2}\left(\frac{\partial u_p}{\partial y} + \frac{\partial v_p}{\partial x}\right) \ . \tag{10.11}$$

We illustrate the distribution of this quantity in Figure 10.9 for the same conditions as used to display $\omega_{p,z}$ in Figure 10.8. Pure black or white areas indicate regions of high rates of shear strain beyond values marked at the color bar. The local maxima of the shear strain are located in the shear-dominated wake regions close to the LCS between the vortex cores and the saddlepoints in the stream lines indicated by the velocity vectors. Here, we find dominating longitudinal gradients of transverse velocity $\partial v_p/\partial x$. These high intensity regions coincide with the areas of lower vorticity torn away from the LCS toward the wake centerline. Although also the squared shear strain rates θ_2^2 are weak near the saddlepoints, they still dominate the squared vorticity ω^2, which is almost zero there, and thus, they establish shear–dominated regions centered at the saddlepoints.

A second, but weaker maximum of shear strain is located near the outer boundary of the LCS. This results primarily from the displacement of fluid

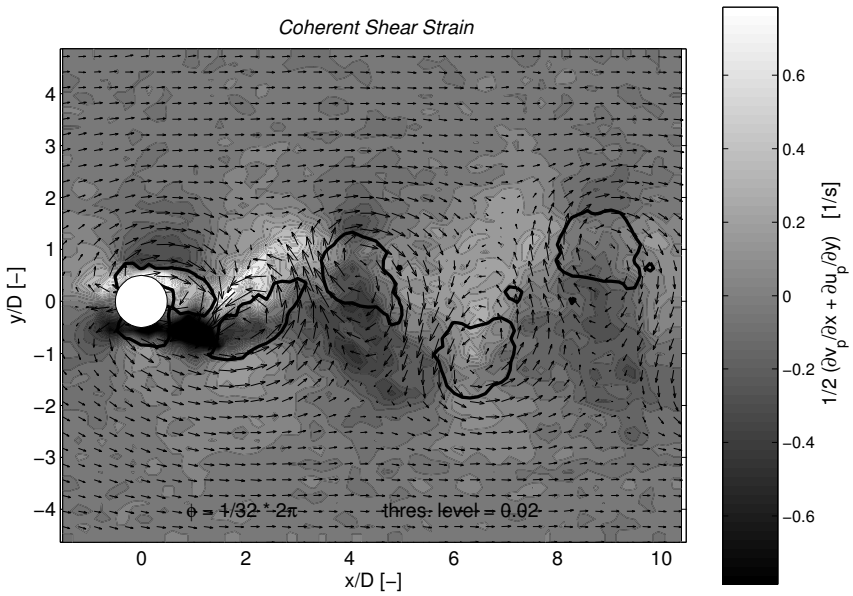

Figure 10.9. The coherent rate of shear strain is displayed in gray-scale for the same flow conditions as in Figure 10.8. Regions of high magnitude of shear strain coincide with the regions of low magnitude of vorticity, which is torn away from the vortex cores toward the saddlepoints.

due to the vortical structure, which gives rise to transverse gradients of main velocity $\partial u_p/\partial y$.

Divergence. The *divergence* of the flow field is defined as

$$\nabla \cdot \boldsymbol{u} = \frac{\partial u_i}{\partial x_i} = \frac{\partial u}{\partial x} + \frac{\partial v}{\partial y} + \frac{\partial w}{\partial z} \ . \tag{10.12}$$

From the two-dimensional PIV measurement system we obtain horizontal surface velocity fields, thus they only enable us to compute the horizontal parts of $\nabla \cdot \boldsymbol{u}$.

For incompressible flow without external sources from continuity reasons we have $\nabla \cdot \boldsymbol{u} = 0$. Therefore we can conclude from the divergence of the horizontal velocity field to the vertical gradient of the vertical velocity component, albeit we are not able to measure the magnitude of this gradient directly. Knowledge of the flow also in the vertical direction is essential, if we are interested in the question, whether flow pattern of these LCS are two-dimensional or three-dimensional. From the coherent velocity fields $\boldsymbol{u}_p$ we obtain the *coherent horizontal divergence* of the wake flow close to the water surface,

$$\nabla_H \cdot \boldsymbol{u}_p = \frac{\partial u_p}{\partial x} + \frac{\partial v_p}{\partial y} \ . \tag{10.13}$$

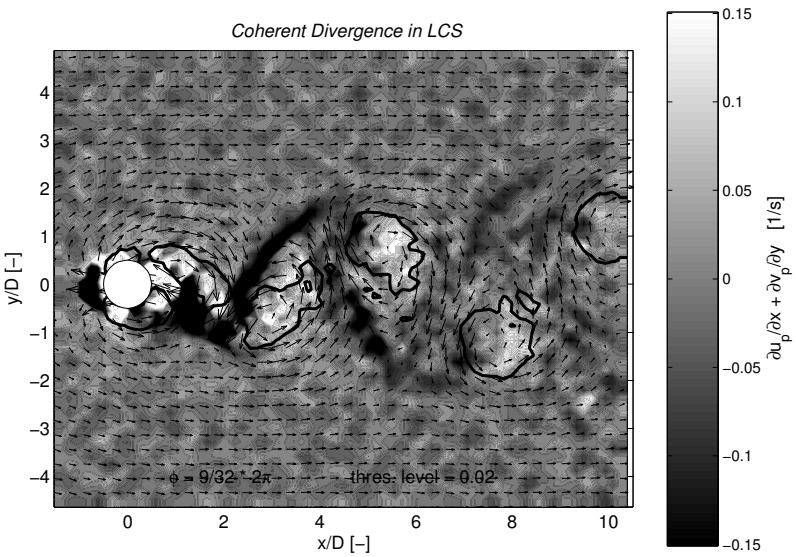

(a) Coherent divergence in flow field with developing LCS up to 10 x/D

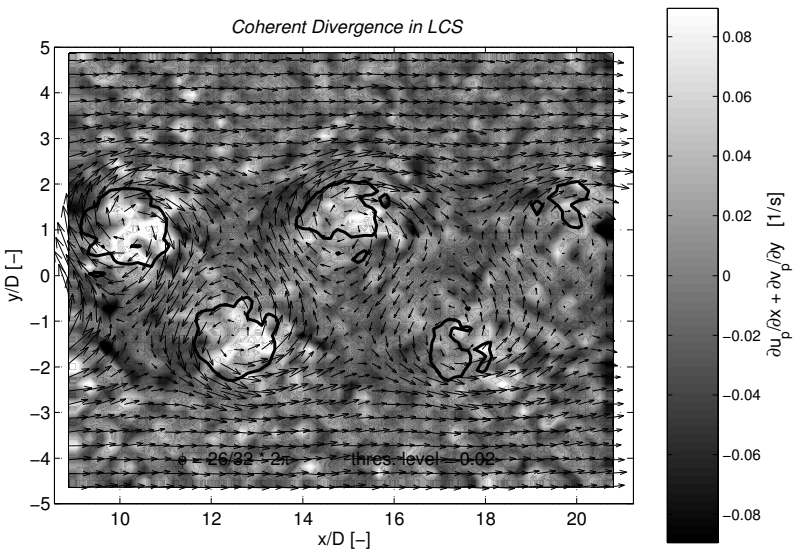

(b) Coherent divergence in flow field with decaying LCS up to 21 x/D

Figure 10.10. The large-scale horizontal divergence (10.13) computed from the coherent horizontal velocity fields is displayed gray scale-coded for a vortex street-like shallow wake instability (series 18_vs06, runs 1). White indicates divergent regions with a magnitude greater than the maximum gray scale denoted at the color bar, black stands for convergent regions. In the vortex cores we clearly observe divergence zones at the surface, corresponding to upwelling flow in the LCS cores. In the region up to 5 D downstream of the obstacle, where the generation and growth of the LCS takes place, convergence zones are located in the shear-dominated regions along the braids connecting the LCS. In (b) the mature LCS decay due to dissipation induced by bottom friction, while they advect further downstream. Convergence zones outside the LCS now concentrate at the upstream onset of the braids to the LCS and around the streamline saddle-points of the wake flow vector field, which is adjusted to the advection speed of the structures here.

The large-scale horizontal divergence computed from the coherent horizontal velocity fields using (10.13) is displayed gray scale–coded in Figure 10.10 for a vortex street-like shallow wake instability (series 18_vs06, runs 1). In the coherent divergence fields light shading indicates divergent regions with a magnitude greater than the maximum gray scale denoted at the color bar, whereas dark shading stands for convergent regions. Figure 10.10(a) shows the region up to 5 D downstream of the obstacle, where the generation and growth of the LCS takes place. As expected, we encounter regions of high positive or negative divergence in the immediate vicinity of the cylinder, which arise from the distinct 3D motion of the large-scale secondary flow around the cylinder. In the lee of the obstacle the growing vortical structures in both detached cylinder shear layers show a divergent surface flow field corresponding to a source of volume in this plane. Between the alternately separating vortices fluid is intruding, which establishes a strongly convergent region. As the vortical structures develop, they maintain their characteristic divergent surface flow field. Thus, divergent zones are associated with vorticity-dominated regions of the coherent wake flow. Furthermore, convergence zones are located in the strain-dominated areas, they are aligned with the braids connecting vortices of opposite sense of rotation. In the region of developing LCS the convergence zones form line sinks of near surface volume. Divergent and convergent regions in the surface flow fields are related to up- and down-welling flows associated with large-scale vortices; they are a strong indication for the tornado-like secondary motion of the LCS.

Figure 10.10(b) illustrates, how the mature LCS decay due to dissipation induced by bottom friction, while they advect further downstream. In the vortex cores we still observe divergence zones at the surface, corresponding to sources of volume, i.e. upwelling flow in the LCS cores. Convergence zones, again, are located outside the LCS along their braids. But now they clearly reshape and concentrate near the LCS at the upstream onset of the braid and at the streamline saddle points of the wake flow vector field, which is adjusted to the advection speed of the structures in Figure 10.10. As the LCS disintegrate, also the regions of pronounced positive and negative divergence fade away in the coherent flow field, leaving only the numerical jitter of the finite differences scheme.

Divergent surface flow fields due to up- and down-welling motion associated with large-scale vortices are visualized by floating particles evenly distributed over the whole upstream flow width as they are used for the PIV measurements. In Figure 10.11 the accumulation of particles in the convergent regions and their displacement in divergent regions is obvious. Such secondary flow of large-scale vortical structures is not restricted to shallow wake flow, but it is a rather common feature of large eddies in shallow flows. For instance, Dietz (2001, p. 25) observed the same secondary motions in large eddies generated

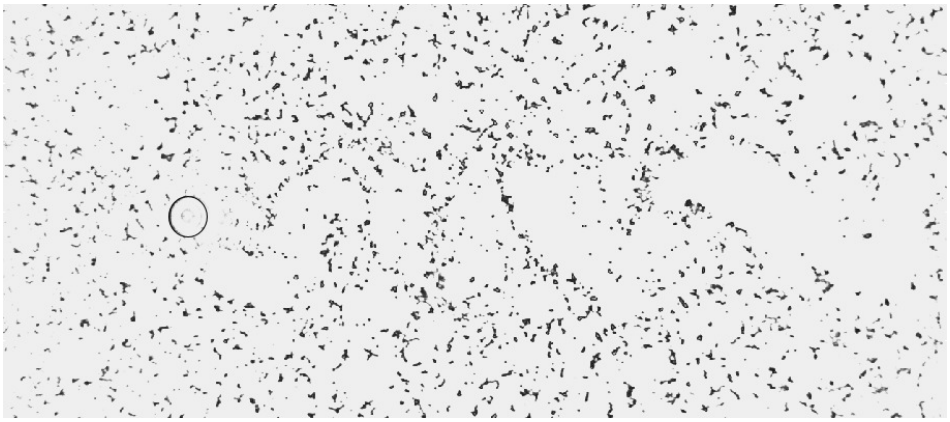

Figure 10.11. An example images (series 38_vs01), also to be evaluated by the PIV measurement system, illustrates that particles floating near the surface are rearranged by secondary motion of the flow, though initially they were evenly spread over the whole width of the upstream flow. Divergent zones within the large eddies are lacking particles, whereas in the convergent zones the particles cluster.

in a shallow mixing layer. Besides the implications of applying a 2D data acquisition to evaluate a 3D flow, also technically it is not trivial just to get high-quality information of the surface flow field (esp. an appropriate density and uniformity in the particle distribution also in the downstream part of the area of observation).

If we compare the above coherent divergence fields to the time-mean divergence $\nabla \cdot \boldsymbol{U}$, we find the coherent divergence being much more pronounced than the time-mean values. The peak magnitude of divergence occurring in the core of a LCS exceeds the local time-mean value by far; for the series reported above, we observe of factor of 20. Obviously the secondary currents, associated to the LCS of the quasi-periodic flow, are more significant in the phase–resolved averaged coherent flow field than in the time-mean flow, because such mean secondary currents, which were also observed by Ohmoto et al. (2002) in a similar shallow shear instability, are induced by the large-scale coherent vortical structures of the shallow wake flow. On one hand, this illustrates again that it is often not useful to distinguish the time-mean flow from the low-frequency coherent flow. A vortex street-like shallow wake flow is not a steady wake flow disturbed by large-scale vortices, but it is a periodically fluctuating flow, whose low-frequency fluctuations is essential to the mean flow.

On the other hand, this secondary motion of the LCS (being a tertiary motion to the mean flow) has a certain impact on the analysis of the planar measurements in shallow wake flow. With the presupposition of 2D flow at the large scales, i.e. no significant alteration of the horizontal flow field depending on the vertical position, firstly, we are allowed to directly conclude from the near-surface velocity field to the flow field at an arbitrary depth and also to the depth-averaged coherent flow. Secondly, from depth-averaged horizon-

tal distributions of mass concentration we characterize the coherent transport mechanisms, ascribing all deviations to small-scale random processes. Both of these conclusions we draw from the PIV measurements and from the PCA measurements, respectively. When analyzing the flow pattern and transport processes, especially when modelling parts of the transport, it has to be taken into account that, from the employed planar measuring systems, we tend to neglect secondary (vertical) motions of the predominantly horizontal coherent flow.

Turbulent kinetic energy. The *turbulent kinetic energy* is usually defined to be half the trace of the Reynolds stress tensor,

$$k \equiv \frac{1}{2} \left\langle \boldsymbol{u'}\, \boldsymbol{u'} \right\rangle = \frac{1}{2} \left\langle u_i'\, u_i' \right\rangle \ . \tag{10.14}$$

It is the mean kinetic energy per unit mass of a fluctuating velocity field. In Section 7.1.4 longitudinal TKE distributions have been presented for shallow wake flows. With a two–length–scale decomposition we can divide k into its coherent and random parts k_p and k_r. Based on a triple decomposition we have

$$\begin{aligned} k &= k_p^* + k_r \\ &= \frac{1}{2} \left\langle u_{p,i}^*\, u_{p,i}^* \right\rangle + \frac{1}{2} \left\langle u_{r,i}\, u_{r,i} \right\rangle \end{aligned} \tag{10.15}$$

The total mean kinetic energy also covers the mean advective kinetic energy, and yields

$$\begin{aligned} k_{tot} &= K + k_p^* + k_r \\ &= \frac{1}{2} \left\langle U_i\, U_i \right\rangle + \frac{1}{2} \left\langle u_{p,i}^*\, u_{p,i}^* \right\rangle + \frac{1}{2} \left\langle u_{r,i}\, u_{r,i} \right\rangle \\ &= k_p + k_r \end{aligned} \tag{10.16}$$

As indicated by the third line of the above equation, this quantity can also be computed immediately from the double-decomposed velocity data.[17] Detailed information about the spectral distribution of TKE along the low- and high-frequent ranges has been reported in Chapter 7 from LDV measurements. From PIV measurements—restricted in temporal resolution—it was found that for a vortex street-like wake instability in the region of fully developed LCS the mean coherent kinetic energy $k_p = K + k_p^*$ is much larger than the mean random kinetic energy, $k_p/k_r \approx \mathcal{O}\left(10^2\right)$. The triple–decomposed mean coherent kinetic energy k_p^* is still one order–of–magnitude larger and amounts to 10% to 25% of the mean advective energy $1/2 \left\langle U_i\, U_i \right\rangle$. These facts illustrate again that the kinetic energy, which is extracted from the mean flow due to its strong lateral

[17] The simplified relation between double– and triple–decomposed kinetic energy, i.e. $k_p = K + k_p^*$, is valid only for the *mean* kinetic energy, as we benefited from properties of the decomposition mentioned earlier in this section on page 311.

shearing by the obstacle, is primarily transferred to the large-scale coherent motion of the LCS.

The phase–resolved averages of the triple–decomposed coherent kinetic energy $\tilde{k}_p^* = 1/2 \left\{ u_{p,i}^* \, u_{p,i}^* \right\}$ offer a closer look on the spatial energy distribution in the wake flow. In Figure 10.12(a) we present the phase–aligned coherent kinetic energy computed from triple–decomposed velocity fields, where we subtracted the mean undisturbed flow instead of the mean actual flow. That is, in this figure the coherent kinetic energy is shown with respect to the undisturbed base flow, which is reasonable, since coherent kinetic energy is extracted from the base flow near the obstacle. Of course, the highest values of $\tilde{k}_p^*$ occur in regions with high coherent velocity $\boldsymbol{u_p^*}$, which are located in the shear dominated regions between adjacent LCS. The maximum value are roughly 10% of the undisturbed advective kinetic energy for mature LCS, but can be more than 50% closer to the cylinder in the near wake, where the LCS are generated. Inside the LCS the coherent kinetic energy has to be smaller and tending toward zero. Note that the exact location with $\tilde{k}_p^* = 0$ depends on the definition of the reference mean velocity for the triple–decomposition. Since in Figure 10.12(a) we use a reference frame moving with the ambient undisturbed velocity U_a (also for the displayed velocity vectors), vanishing $\tilde{k}_p^*$ are located a bit outward from the centers of the LCS.

The incoherent or random kinetic energy k_r from the high-frequency 3D fluctuations does not depend on whether we apply a double– or triple–decomposition, nor on the definition of a mean advection velocity. In Figure 10.12(b) we show the phase–resolved averaged random kinetic energy $\tilde{k}_r = 1/2 \left\{ u_{r,i} \, u_{r,i} \right\}$ for the same conditions as for the coherent kinetic energy. As for the mean kinetic energy, also for the phase–resolved averages we observe significantly lower values of the incoherent part. But contrary to the coherent kinetic energy, the local maximum intensity is now located close to the center of the LCS amounting to below 2% of the undisturbed mean advective energy also in agreement with Hussain & Hayakawa (1987). The highest values of around 35% decreasing rapidly are found in the generation region of the LCS, but closer to the obstacle than the highest coherent values. Furthermore, a comparison of the mean coherent and incoherent parts reveals that the mean coherent kinetic energy $\tilde{k}_p^*$ is more than ten times larger. Highest ratios are found in the developing region of the LCS.

Reynolds shear stress. The phase–resolved averaged *coherent Reynolds shear stress* obtained from a triple-decomposed velocity field $\boldsymbol{u_p^*}$ is given by

$$\frac{\tilde{\tau}_{xy,p^*}}{\rho} = - \left\{ u_p^* \, v_p^* \right\} \ . \tag{10.17}$$

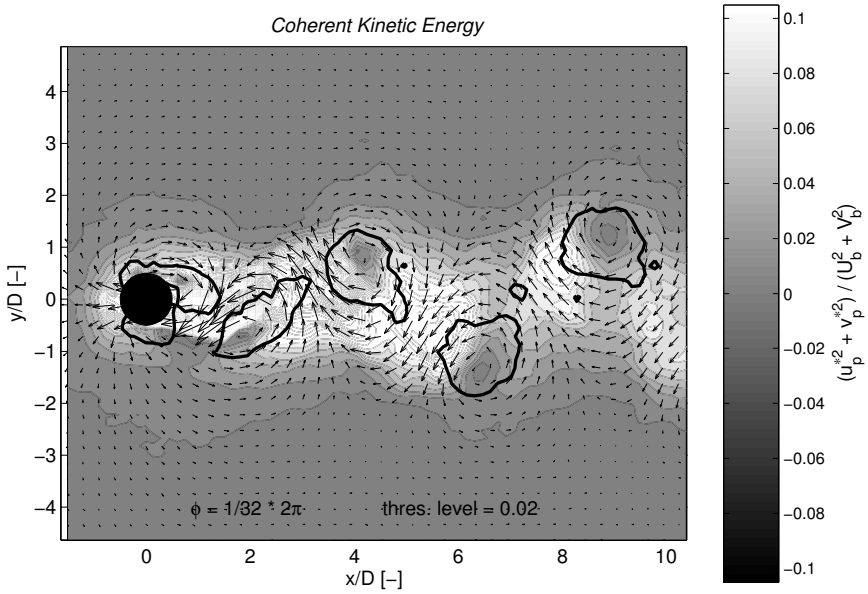

(a) Coherent kinetic energy $\tilde{k}_p^*$ from triple-decomposed flow field

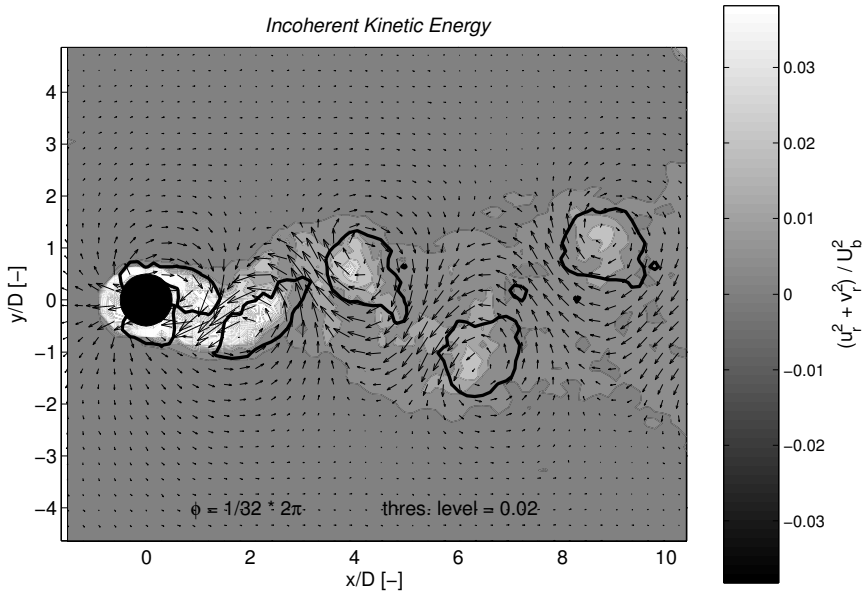

(b) Incoherent kinetic energy k_r

Figure 10.12. The phase–resolved averages of the turbulent kinetic energy is divided into the coherent and random parts using a triple-decomposition. For the coherent kinetic energy $\tilde{k}_p^* = 1/2 \left\{ u_{p,i}^* \; u_{p,i}^* \right\}$ displayed in Figure 10.12(a), the mean advective part not of the actual flow, but of the undisturbed flow was subtracted. Thus, the coherent kinetic energy is related here to the mean advective undisturbed flow, from which it is extracted. In Figure 10.12(b), the incoherent or random kinetic energy $\tilde{k}_r = 1/2 \left\{ u_{r,i} \; u_{r,i} \right\}$ is normalized in the same way. This small-scale turbulent kinetic energy is concentrated near the cores of the LCS, and it is usually one order–of–magnitude smaller than the coherent kinetic energy.

Areas of high magnitudes of $-\left\{u_p^* \, v_p^*\right\}$ are arranged symmetrically about the center of the LCS in a clover–leaf like pattern, which is a straightforward consequence of the coherent velocity field associated with a vortical motion in a frame advected at U_{LCS}. In Figure 10.13(a) gray–scales indicate the horizontal coherent Reynolds shear stress normalized by the mean advective energy. Underlying vectors show the flow velocity in a frame following the LCS, bold isolines of the threshold value Q_{LCS} mark the large-scale coherent eddies. The triple–decomposed coherent shear stresses amount to up to 5% of the mean kinetic energy, once the LCS have established. By contrast and not presented here, the double–decomposed coherent shear stresses $-\{u_p \, v_p\}$ (containing also the mean flow components) peak to 40% of the mean advective energy, where the longitudinal velocity component u_p produces the larger absolute values and the transverse component v_p controls the sign.

Figure 10.13(b) shows phase–aligned the incoherent Reynolds shear stress $-\{u_r \, v_r\}$ normalized and presented in the same way as Figure 10.13(a). Compared to the coherent stresses, the values of the incoherent stresses are a full order–of–magnitude smaller, and peak at 0.5% of the mean advective energy. Though not very clearly visible, areas of intense random shear stress are aligned with the braids in the shear–dominated flow regions. Additionally, absolute peak values of $-\{u_r \, v_r\}$ coincide with the LCS.

Hussain & Hayakawa (1987) observed larger magnitudes of random shear stress in an unbounded wake flow, e.g. twice as high at the cross–section $x/D = 10$. Furthermore, their wind–tunnel measurements indicated the peaks in $-\{u_r \, v_r\}$ occurring near the saddle-points of the streamlines moving with the LCS, but did not reveal the high core intensities observed in shallow wake flows. Eventually, this feature of bounded wakes is associated with the secondary motion of the coherent flow, which results in an up-welling flow in the LCS centers. At the water surface, the redirection of the upward flow should be related to higher small-scale turbulence intensities confirmed earlier in this section (cf. Figure 10.12), and should therefore also produce higher random shear stresses in the cores.

Turbulence production. In the equations for the mean advective kinetic energy $\frac{1}{2}\langle \boldsymbol{U}\rangle\langle \boldsymbol{U}\rangle$ and for the turbulent kinetic energy defined in (10.14), we encounter a term

$$P \equiv -\left\langle u_i' \, u_j'\right\rangle \frac{\partial \langle u_i\rangle}{\partial x_j} \, , \tag{10.18}$$

which is called *production of turbulent kinetic energy.* It describes the extraction of mean-flow kinetic energy by the mean velocity gradient working against the Reynolds stresses and its transformation into turbulent kinetic energy of the fluctuating velocity field. We can distinguish *normal production* and *shear production*, and yield in the horizontal plane, respectively

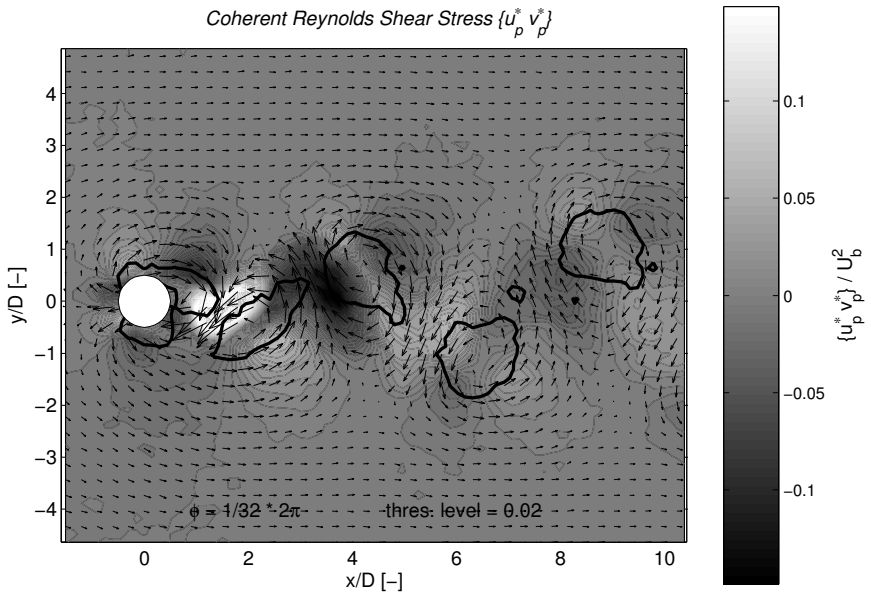

(a) Coherent Reynolds shear stresses $-\left\{u_p^* \; v_p^*\right\}$ from triple-decomposed flow

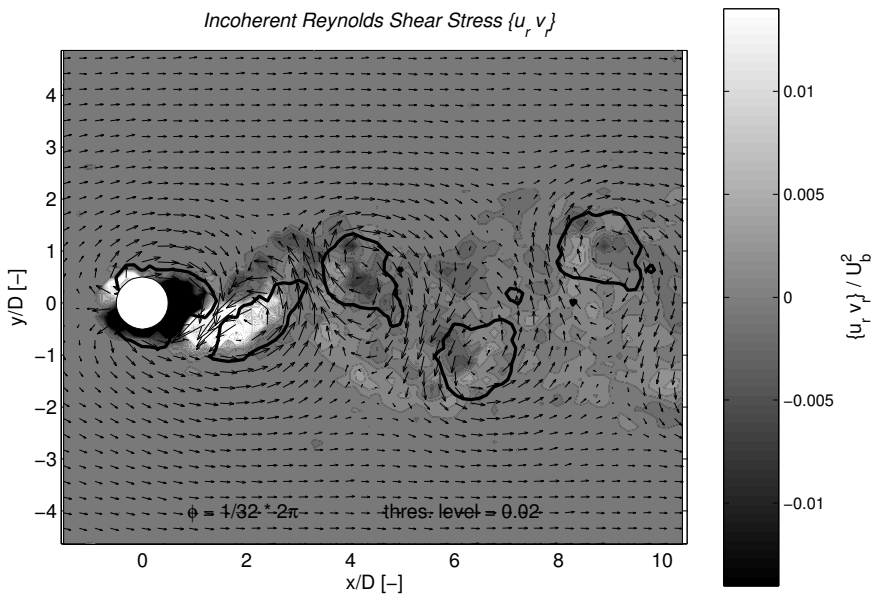

(b) Incoherent Reynolds shear stresses $-\{u_r \; v_r\}$

Figure 10.13. The coherent and incoherent Reynolds shear stress distributions calculated from the phase–aligned velocity fields of series 18_vs06, run 1 using a triple decomposition, are displayed gray-scale coded in Figures (a) and (b), respectively. Vector velocities are reduced by the mean advection speed U_{LCS} of the coherent eddies indicated by bold lines of Q_{LCS}. Compared to unbounded wake flow, the coherent values are significantly higher, and the incoherent stresses show additional peak values in the cores of the LCS.

$$P_n = -\left\langle u'\ u'\right\rangle \frac{\partial \left\langle u\right\rangle}{\partial x} - \left\langle v'\ v'\right\rangle \frac{\partial \left\langle v\right\rangle}{\partial y}\ , \tag{10.19a}$$

$$P_s = -\ \left\langle u'\ v'\right\rangle \left(\frac{\partial \left\langle u\right\rangle}{\partial y} + \frac{\partial \left\langle v\right\rangle}{\partial x}\right)\ . \tag{10.19b}$$

We can use a two–length–scale decomposition of the flow velocity components. Employing a double–decomposition into mean-coherent and random parts, we obtain the phase–resolved averaged production of random turbulent kinetic energy by mean-coherent strain, or *coherent production of incoherent kinetic energy*,

$$\tilde{P} = -\ \left\{u_{r,i}\ u_{r,j}\right\} \frac{\partial \left\{u_i\right\}}{\partial x_j} = -\ \left\{u_{r,i}\ u_{r,j}\right\} \frac{\partial u_{p,i}}{\partial x_j}\ . \tag{10.20}$$

In the double–decomposed energy equations the coherent production appears as a sink term for the large-scale periodic kinetic energy, Equation (10.9a), and consequently as a source term for the small-scale random kinetic energy, Equation (10.9b).

When using a triple–decomposition into mean, coherent, and incoherent parts, this results in two production terms,

$$P_p^* = -\ \left\langle u_{p,i}^*\ u_{p,j}^*\right\rangle \frac{\partial U_i}{\partial x_j}\ , \tag{10.21a}$$

$$\tilde{P}_r = -\ \left\{u_{r,i}\ u_{r,j}\right\} \frac{\partial u_{p,i}^*}{\partial x_j}\ . \tag{10.21b}$$

Here, P_p^* denotes the *mean production of coherent kinetic energy* due to the mean strain field, whereas $\tilde{P}_r$ stands for the *coherent production of random kinetic energy* from the phase–resolved averaged flow field. Both of these quantities are shown in Figure 10.15 for a vortex street-like shallow wake flow (series 18_vs06, run 1). For their normalization we make use of the mean ambient velocity U_a and the longitudinal distribution of the maximum transverse gradient of the mean longitudinal flow component $S_{max}(x) = max_y(\partial \left\langle u\right\rangle / \partial y)$. Since S_{max} provides high values immediately downstream of the obstacle, quickly decreasing toward an almost constant small pedestal value beyond $x/D = 5$, this non-linear way to scale the energy production allows to present a wide range of absolute values down to very low production rates in the area of established LCS decaying due to bottom friction.

Looking at the coherent production of incoherent kinetic energy $\tilde{P}_r$ for a given phase-interval in Figure 10.14, this quantity seems to be aligned with the braids connecting adjacent LCS. More precisely, at the centerline of the braid we observe an area of negative production, which is flanked on both sides by regular positive production with a peak area near the onset of the braid at the LCS. In the surface velocity fields evaluated in this work, the braids are areas of convergent flow (cf. Figure 10.10), but they are not strictly related to the shear

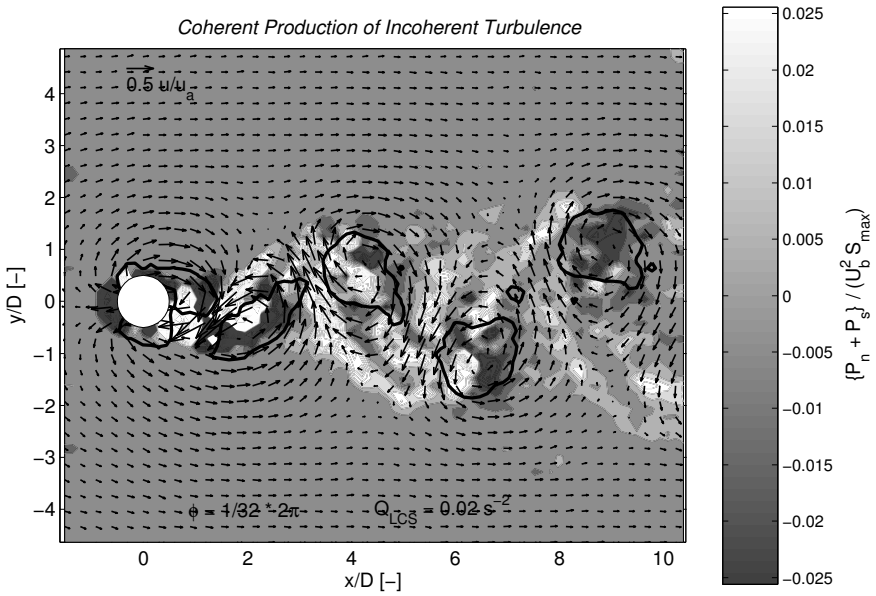

Figure 10.14. The coherent production of random turbulence $\tilde{P}_r$ using (10.21b) is shown for a distinct phase–interval (cf. caption of Figure 10.15 for details).

strain rate (cf. Figure 10.9). Assuming the small-scale incoherent turbulence to be horizontally isotropic, i.e. $\langle u_r u_r \rangle = \langle v_r v_r \rangle$, it is obvious, that the horizontal divergence (10.13) influences the normal production P_n, Equation (10.19a). Evaluated from the given planar measurements in vortex street-like shallow wakes, the normal part of the coherent production $\tilde{P}_{r,n}$ dominates the shear production $\tilde{P}_{r,s}$ by far. In the distribution of incoherent kinetic energy we find high intensities near the cores of the LCS (cf. Figure 10.12), strongly divergent flow occurs at the same locations. The combination of both effects results in areas of significant values of negative coherent production $\tilde{P}_r$ within the LCS. Similarly, additional positive coherent production of incoherent kinetic energy can be introduced in the convergent regions upstream of the braids. The phenomenon of transfer of turbulent kinetic energy back to the coherent flow field has also been observed in large-scale periodic unbounded wake flows (see Pope, 2000, pp. 179), and was assumed to be related to pairing processes. However, as suggested by the correlation of the divergence and the negative values of turbulence production, in the present study on shallow wakes this should be ascribed to the secondary motion of the LCS. Also, no incident of vortex pairing of large-scale coherent structures has been observed in the examined shallow wake flows. Since we only obtained measurements of the surface velocity fields, we do not recommend to expand the observed surface pattern of negative coherent production to a 2D depth–averaged view without prior verification. The generation of small-scale turbulence in the LCS cores may well be

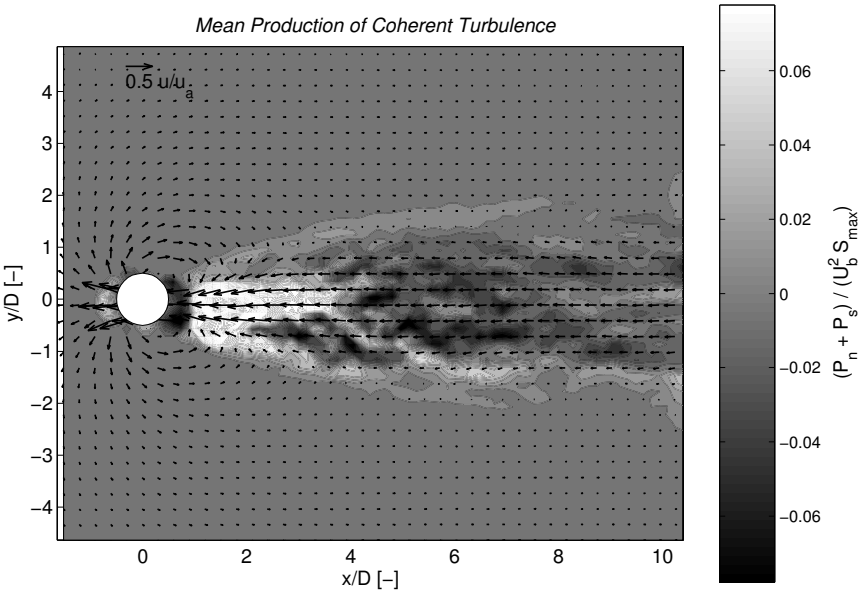

(a) Mean production of coherent kinetic energy

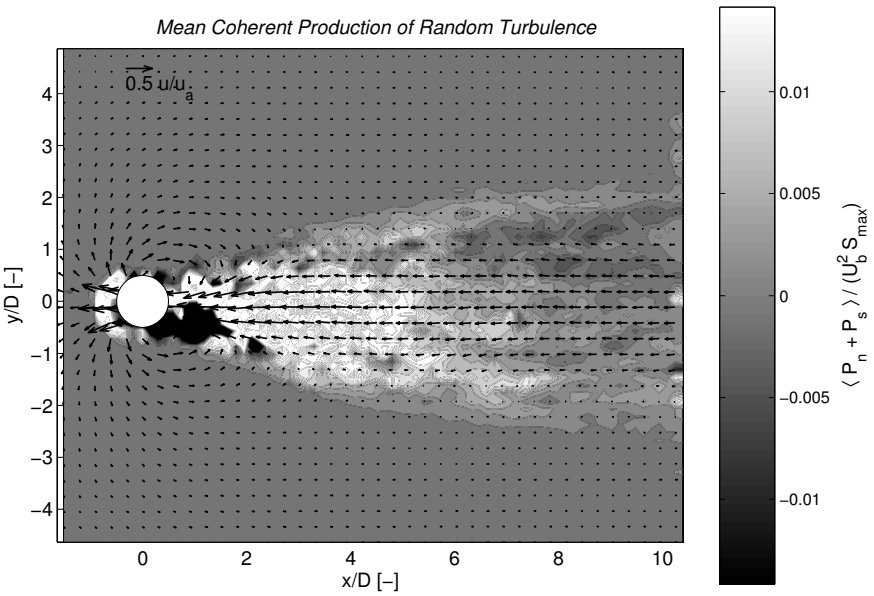

(b) Mean coherent production of incoherent kinetic energy

Figure 10.15. Using a triple–decomposition of the velocity fields, the mean production terms for coherent and for incoherent kinetic energy, P_p^* and P_r obtained by applying Equations (10.21a) and (10.21b) respectively, are displayed gray scale–coded for a vortex street-like shallow wake (series 18_vs06, run 1). The values of the production terms are normalized nonlinearly by the mean ambient velocity U_a and the longitudinal distribution of the maximum transverse gradient of the mean longitudinal flow component $S_{max}(x) = max_y(\partial \langle u \rangle / \partial y)$.

a local surface–related phenomenon as may be the subsequent transfer of this random kinetic energy into the coherent flow. Finally, note again, that the cut-off frequency of 7 Hz as well as the dimensions and mass of the tracer particles prevent a sufficiently high resolution of the small-scale high-frequency fluctuations. All this might explain, why, in contrast to our observations, HUSSAIN & HAYAKAWA (1987) found in an unbounded wake ($Re_D = 1.3 \cdot 10^4$) that the coherent shear production $P_{r,s}$, combined of Equations (10.19b) and (10.21b), contributes to about 80% to the total coherent production $P_r = P_{r,n} + P_{r,s}$. They also located areas of high coherent production around the saddle-points in the strain–dominated regions, zero production inside the vortical structures, and did not observe areas of negative production.

The mean production of coherent kinetic energy, as defined in (10.21a), is displayed in Figure 10.15 (b). The wake region immediately behind the obstacle, where large-scale coherent structures are born and grow, is characterized by high production rates of coherent turbulence. In contrast, we observe an area of significant negative production further downstream of the obstacle, where the LCS have already established and are decaying. If we separate the normal and shear components of this production term (not shown graphically here), we find that the maximum values of both components are of the same order–of–magnitude. The shear component $P^*_{p,s}$ contributes to the production of coherent energy only in the area, where the LCS shed from the cylinder shear layers. Since $P^*_{p,s}$ is anti-symmetric to the wake centerline, it is responsible for the asymmetry of the distribution of P^*_p in this area. The normal component $P^*_{p,n}$ on the other hand is distributed directly axisymmetric along the wake centerline. It gives raise to negative production in the area of decaying LCS, which is aligned in streamwise filaments embedded in positive production. So $P^*_{p,n}$ also redistributes coherent kinetic energy back to the mean flow via mean normal strain rates, which can only be explained by secondary motions providing vertical flow to satisfy continuity in horizontally divergent flow fields.

Taking the average of (10.21b) results in the mean coherent production of random kinetic energy $\left\langle \tilde{P}_r \right\rangle = P_r$, which is displayed gray scale–coded in Figure 10.15(a). It reaches values of the order of about 20% compared to the mean production of coherent turbulence discussed above. We observe a significant production around $1.5 \leq x/D \leq 5$ downstream of the obstacle in the area of growing LCS, which is generally the dynamically most active region of the shallow wake flow. In the area of established decaying LCS $\left\langle \tilde{P}_r \right\rangle$ decreases toward zero. Although not explicitly shown here, beyond the immediate vicinity of the obstacle, the mean coherent production of incoherent turbulence is mainly induced by its mean normal component. Both the random Reynolds shear stress $\{u_r\ v_r\}$ and the coherent shear strain rate $\partial u^*_p/\partial y + \partial v_p/\partial x$ change their sign

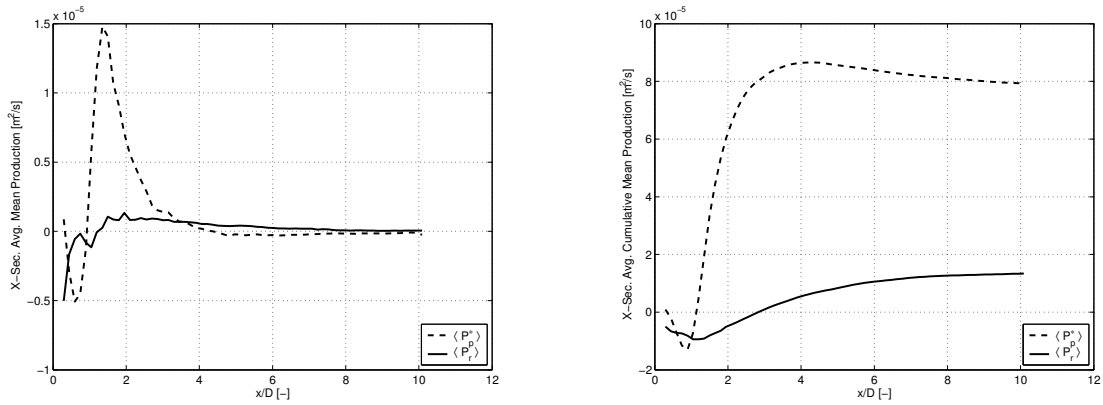

(a) Cross-sectional averaged production terms P_p^* and P_r

(b) Cumulative sums of P_p^* and P_r

Figure 10.16. The cross-sectional averaged mean production of the coherent kinetic energy P_p^* (dashed line), and the coherent production of the random kinetic energy P_r (full line) are displayed in their downstream variation in plot (a). Plot (b) shows the cumulative sums of both quantities starting at $x/D = 0$. In their non-normalized forms it is obvious, that a prominent part of the turbulent kinetic energy of the flow is extracted from the mean advective flow and incorporated into the LCS during their generation.

during the LCS cycle period (cf. Figures 10.13 and 10.9), and eliminate each other on average.

In order to clarify the characteristic distribution of the production terms of both coherent and random kinetic energy, we further evaluate their *cross–sectional averaged distributions* shown in Figure 10.16(a). In Figure 10.16(b) we display the *cumulative sum* of both quantities, which is for the coherent and random kinetic energy, respectively,

$$\int_0^x \frac{1}{B} \int_{-B/2}^{B/2} P_p^* dy\, ds \quad \text{and} \quad \int_0^x \frac{1}{B} \int_{-B/2}^{B/2} \langle P_r \rangle\, dy\, ds\ .$$

For the mean production of coherent turbulence P_p^* marked with a dashed line we observe a strong peak at $x/D \approx 1.5$, where the LCS separate from the cylinder shear layers. Up to a distance $x/D = 3$ from the obstacle most of the kinetic energy is extracted from the mean flow and transferred to the LCS, as we can also see in the cumulative production. Further downstream the averaged mean production becomes negative, so we observe a decrease of P_p^* in its cumulative plot. Around $x/D = 5$ we have the highest magnitude of negative production, then it tends toward zero. The mean coherent production of random turbulence $\left\langle \tilde{P}_r \right\rangle$, indicated by a full line, also reveals its highest values in the area of growing LCS, then decreasing toward zero, as the mature LCS decay. In general, the production of random kinetic energy is significantly smaller than the production of coherent kinetic energy, e.g. we obtain a factor of 10 for the peak values and a factor of 5 for the cumulative values at $x/D = 10$.

Finally, we see, that both mean production components vanish, as the LCS disintegrate. Thus independently of the scale of turbulence, the production of turbulent kinetic energy is closely related to the existence of large-scale coherent vortical structures.

11. Mass Transport due to Large Coherent Structures

In the previous chapter we used the horizontal surface velocity fields obtained from a PIV measurement system in order to identify LCS, and to describe their topography during their life from generation to disintegration. We also elucidated the dynamical behavior of LCS while they advect downstream influenced by bottom friction. Since in all kinds of flow not only the transfer of momentum has to be known, but also the transfer of arbitrary scalar quantities, we will provide additional information on the transfer of soluble tracer mass (as an example for a passive and conservative scalar) in a shallow turbulent wake flow in this chapter.

11.1 Topography indicated by mass concentration

Obviously, since tracer mass concentration has no dynamical significance, it cannot be used for the identification of large-scale coherent vortical structures, which were defined in a dynamical manner in Section 10.1.1. Since mass tends to become trapped in the vortex cores of LCS, high concentration might be an indicator for LCS, thus such structures are often visualized by introducing a tracer dye into the flow. In shallow turbulent wake flows, LCS generated locally near the obstacle dissipate rapidly due to the shallowness-enhanced influence of the bottom friction. Since these LCS exist only over a short flow distance, turbulent diffusion, though prominent due to the 2D turbulent Schmidt number being of order of unity[1], is not sufficient to completely mix high concentration LCS fluid into the ambient flow. So, a tracer dye may still show a connected pattern whereas the vortical motion has long dissipated away. Because of the high molecular Schmidt number $Sc = \nu/D$, this would even be more pronounced for a laminar plane shear flow. Instead of utilizing mass concentration for the structure identification, we will clarify, how the transfer of tracer mass is related to LCS as long as they exist. Thus, we show the influence of the LCS not only on the mean flow field, but also on the mass transport.

[1] $Sc_t = \nu_t/D_t$ has been evaluated to be roughly 0.5 in the present shallow wake flows (cf. Section 9.1), and has been reported to be about 0.7 in unbounded wake flows (Pope, 2000).

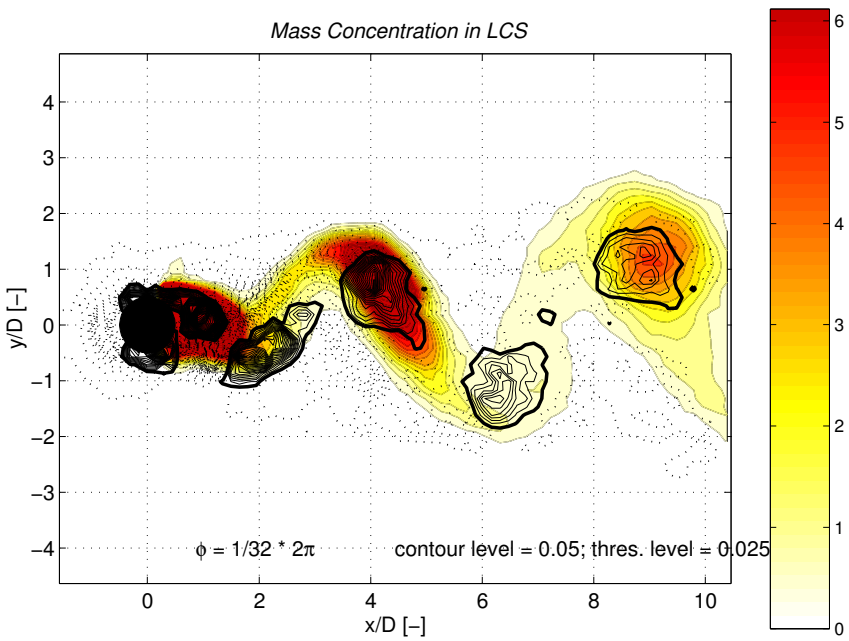
Mass Concentration in LCS
y/D [–]
x/D [–]
ϕ = 1/32 * 2π
contour level = 0.05; thres. level = 0.025

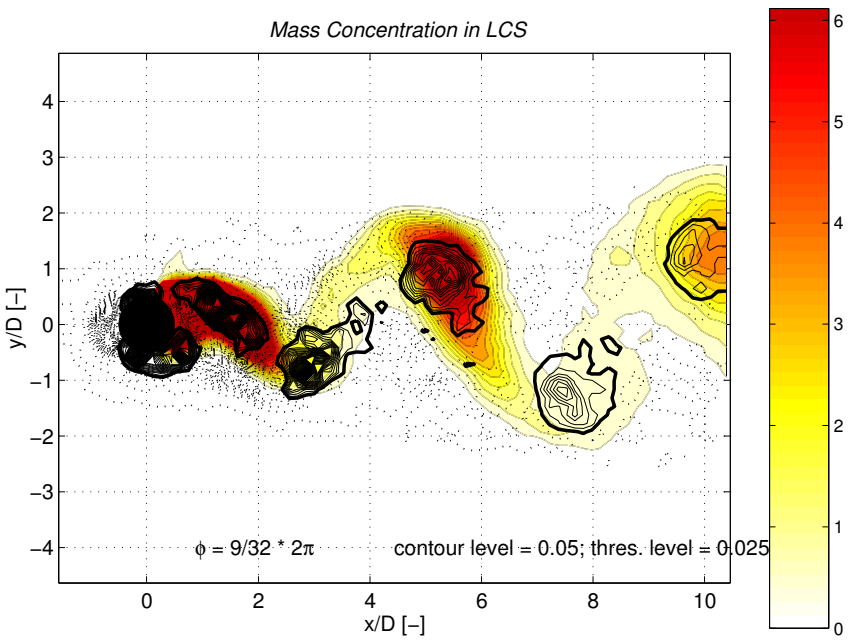
Mass Concentration in LCS
y/D [–]
x/D [–]
ϕ = 9/32 * 2π
contour level = 0.05; thres. level = 0.025

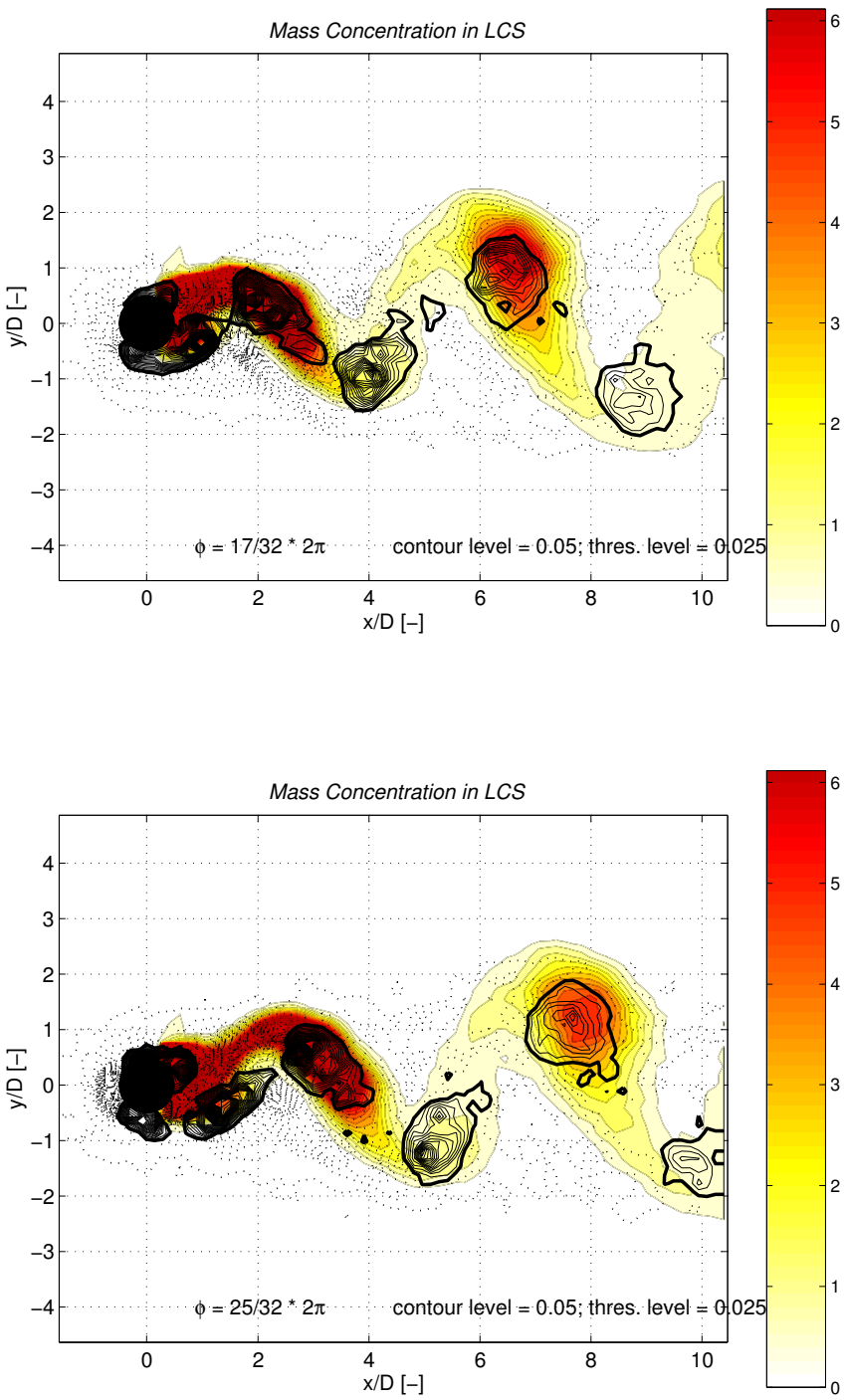

Figure 11.1. Phase-resolved averaged mass concentration fields $c_p\,(x, y, \phi)$ for a vortex street-like shallow wake (series 18_vs06, run 1) are displayed for 4 discrete phase angles ϕ_i showing the transport of mass during the generation of LCS. Tracer dye is continuously injected into the left boundary layer of the obstacle. Its main part becomes trapped inside the separating LCS, local maxima of concentration are found in the vortex cores. As the LCS advect downstream, the tracer mixes transversely over the whole wake along the braids connecting the LCS. During this transfer process the tracer is subjected to small-scale turbulent diffusion.
Color-coded mass concentration in mg/l; contoured Q-values, bold lines indicating LCS.

11.1.1 Coherent concentration fields

Analogously to velocity vector fields, scalar fields can be triple–decomposed or preferably double–decomposed into a large-scale coherent and a small-scale turbulent part. We obtain the large-scale coherent concentration part $c_p = \{c\}$ by conducting the phase–resolved averaging procedure described in Section 10.1.2. Although no coincidentally sampled velocity and mass data is available from the planar measurements[2], we also want to study the mass transfer in the periodic, 'coherent' wake flow and the mass transport capacity of the LCS. Therefore, after adjusting the phase lag, both phase–resolved averaged fields of velocity and of tracer mass are finally cross-correlated.

In order to access the mass fluxes, we will display the coherent concentration fields together with the appropriate Q value distributions. At this point we note again that the Q values are computed using the phase–resolved averaged velocity fields $\{\boldsymbol{u}\}$, which represent the large-scale periodic motion of the wake flow.

Figure 11.1 shows results of the Planar Concentration Analysis (PCA) of a vortex-street like instability of a shallow turbulent wake up to $x/D = 10$. A dye tracer was continuously injected from a point source at mid-depth at the left upstream shoulder of the obstacle co-flowing into the boundary layer. With respect to direction and velocity the dye injection was adjusted locally to the receiving flow to prevent any additional momentum input, thus providing an iso-kinetic source. Due to the high turbulence intensities in the separating turbulent boundary layer, the tracer rapidly mixed over the full vertical extent. The color–coded plots show the phase–resolved averaged concentration fields c_p for four phase–times ϕ_i spanning the full cycle in equal intervals of $\pi/2$ each. Additionally, full line contours denote negative Q values indicating vorticity–dominated regions, where the threshold value Q_{LCS} close to 0, marked by a bold line, divides the LCS from the ambient flow. Shear–dominated regions, which separate the adjacent LCS of the same orientation, are contoured with dotted lines. From the combined illustration of mass concentrations and Q values it becomes obvious that on the left side of the wake the local maximum values of c_p coincide with the local highest negative magnitudes of Q, i.e. the

[2] We address this point in more detail in Chapter 3 in the first part of this work dedicated to measurement techniques, which we developed with the intention of evaluating the large-scale mass transport in shallow turbulent flows. There we also discuss further improvements of the joint PIV-PCA measurement technique.

highest mass concentration occurs in the *cores* of the large coherent vortices.[3] The decrease of the concentration within the LCS, as they advect downstream, has been depicted in Figure 10.6 together with the development of Q and other characteristic dynamical properties of the LCS. The core concentration c/c_0 has roughly the same decay behavior as the core vorticity $\omega_z/\omega_{z,0}$.

Concerning the mass exchange between both sides of the wake flow it can be stated that tracer mass injected into the left side of the cylinder boundary layer is predominately staying in the left shear layer of the wake. In the immediate lee of the obstacle mass is incorporated into the emerging LCS solely on the left side of the vortex street. Only a vanishing small amount of mass is advected by LCS of the opposite shear layer. Still there is a transverse transfer of tracer mass across the whole wake flow. We already observed the strong stretching of the LCS in the early stage of its individual life, which is an artifact of the roll-up and separation process. In the direction of this tearing motion also mass is torn away from the LCS, and thus, the *braids* connecting an LCS to the previous counter-rotating eddy are visualized. These braids do not really connect the cores of counter-rotating eddies, but they surround the opposite LCS and span further on to the next adjacent LCS. So the braids connect LCS of the same sign, thereby bridging the whole vortex street to pass on the outer side of counter-rotating LCS aligned in between in the other wake shear layer. Due to this tearing mechanism tracer mass is distributed across the wake. This is enforced by the bottom friction, which in general acts stronger in the braids than in the vortex cores because of the higher transverse flow velocities. From the coherent flow fields obtained from PIV measurements we know that both the turbulent kinetic energy $\tilde{k}_p$ and the Reynolds shear stresses $-\{u_p\, v_p\}$ are stronger in the strain–dominated regions, especially in the high velocity regions between counter–rotating vortices (cf. Section 10.2.4, note that we presented triple–decomposed values in the associated figures). Also from the incoherent distributions of turbulent kinetic energy and Reynolds shear stresses we gain further insight about the mutual dependence of strain– and vorticity–dominated regions. Both employed velocity measurement systems inherently bear disadvantages for the examination of incoherent turbulence fields, i.e. the planar PIV data suffer from their low temporal resolution and their restriction to the free water surface, whereas the point-wise LDV measurements at discrete locations on the centerline are lacking the instantaneous spatial correlation. In

[3] Note that by linking the phase–resolved averaged fields of depth–averaged concentration and surface velocity via cross–correlations, we *a priori* hypothesized the temporal co-incidence of the local peak values. It has to be proven with simultaneous c and $\boldsymbol{u}$ measurements that there exists neither a phase-lag nor a phase dilation of one quantity with respect to the other. In this work there is some justification from the pointwise LDV-LIF measurements. Still we recommend to examine this question again using an improved PIV-PCA technique allowing for *simultaneous* data acquisition.

order to elucidate the small-scale turbulence and its interaction with the large-scale coherent flow, a more appropriate measurement set-up would have to be employed.

The concept of the braids can be further clarified, when one imagines a point source *continuously* issuing dye tracer into the flow. As the dye is advected in the flow field, the temporal continuity is translated in a spatial continuity in a Eulerian frame. So, a connected thread of dye in the wake flow results from the continuous injection, which can not be broken. As it will be influenced by diffusive processes (and much more in turbulent flow than in laminar flow), the threads will tend to diffuse into the ambient and may even be undetectable, but conceptually they stay connected. Perry et al. (1982) worked on the topography of von Kármán vortex streets in unbounded wake flows using a streamline argumentation. They took a beautiful photograph of a wake flow reproduced here as Figure 11.2(a), which because of the laminar flow illustrates very clearly the connected dye threads in a vortex street. In Figure 11.2(b) we present a view of a vortex street-like shallow turbulent wake, which—despite the strong diffusivity of this kind of flow—still shows the same threads rolling up around the outer side of counter–rotating eddies. Using a numerical particle tracking algorithm we are able also to compute streaklines from the phase-averaged velocity fields evaluated from laboratory experiments. If the incoherent random velocity fluctuation and thus the small-scale turbulent diffusion is neglected, streaklines resulting only from the coherent quasi-periodic motion of the LCS can be obtained, as was already illustrated in Figure 10.3.

11.1.2 Incoherent concentration fields

In order to get information about the mixing and entrainment of ambient fluid into the wake we could analyze the ensemble rms values of the whole time series of instantaneous concentration fields. But these are strongly dominated by the large-scale periodic motions, which we associate with advective transport rather than mixing processes. More insight into the structural mechanisms of mixing can be obtained, if we evaluate the *incoherent fluctuating concentration fields* c_r separately. As a characteristic property of c_r we compute its standard deviations based on the phase–resolved averaged concentration fields. We obtain the *root phase-mean square values (rpms)* c_{rpms} of the measured concentration as

$$\begin{aligned} c_{rpms} &= \sigma_{\{c_r\}} = \sqrt{\{c_r^2\}} \\ &= \sqrt{\left\{(c-c_p)^2\right\}} = \sqrt{\left\{(c-\{c\})^2\right\}} = \sqrt{\{c^2\}-\{c\}^2}\ , \end{aligned} \tag{11.1}$$

since

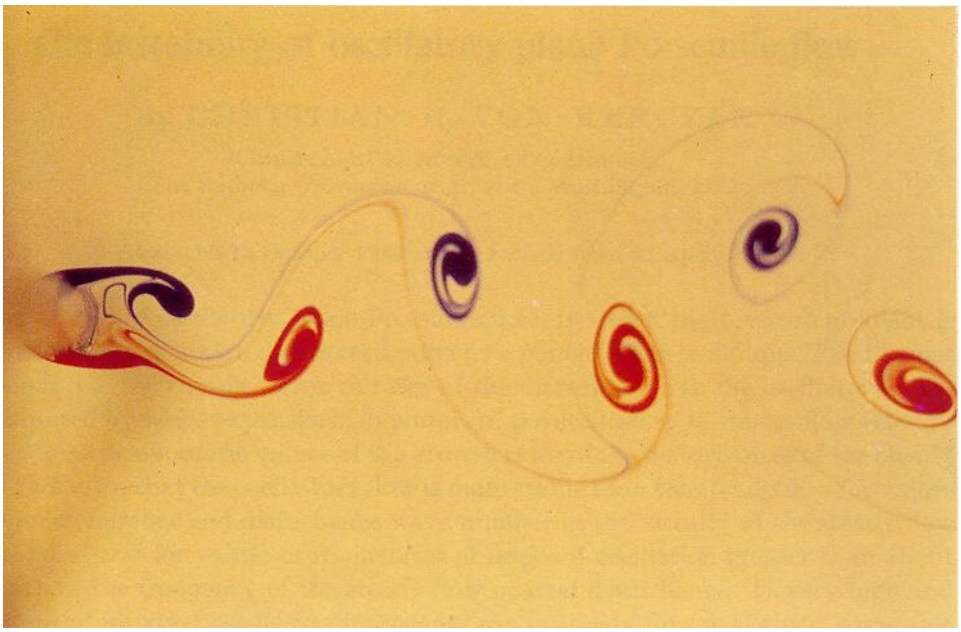

(a) Vortex street in plane laminar wake from Perry et al. (1982)

(b) Vortex street-like instability in shallow turbulent wake

Figure 11.2. The topography of LCS in wake flows can be elucidated by continuous dye injection into the right and left upstream cylinder boundary layers. The top view (a) of a vortex street in an unbounded plane laminar wake visualized by Perry et al. (1982) clearly shows streaklines marked by the threads of blue and red dye. Also in turbulent shallow wake flows the same flow pattern can be observed, as illustrated in figure (b) distorted by an oblique camera angle inclined against the downstream direction. In contrast to the laminar wake affected only by molecular diffusion, in the turbulent shallow flow the effect of combined bottom friction and horizontal shear results in a wide turbulence spectrum which effectively diffuses the dye tracer and blurs the streaklines. If an infinitely thin thread of tracer could be visualized, so that we would resolve also the smallest turbulent wiggles, this thread would not be broken, but remain connected.

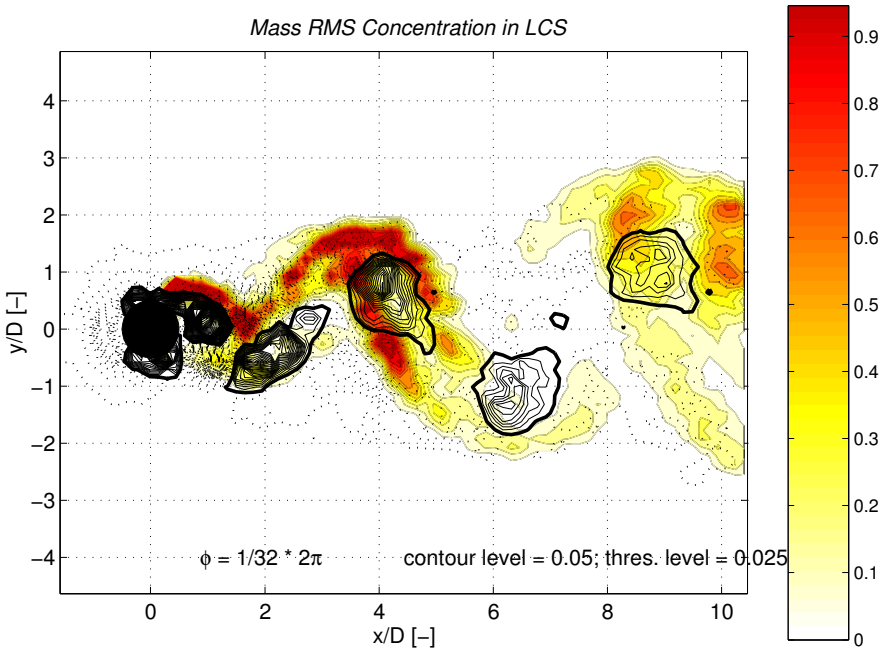
Mass RMS Concentration in LCS
y/D [–]
x/D [–]
ϕ = 1/32 * 2π
contour level = 0.05; thres. level = 0.025

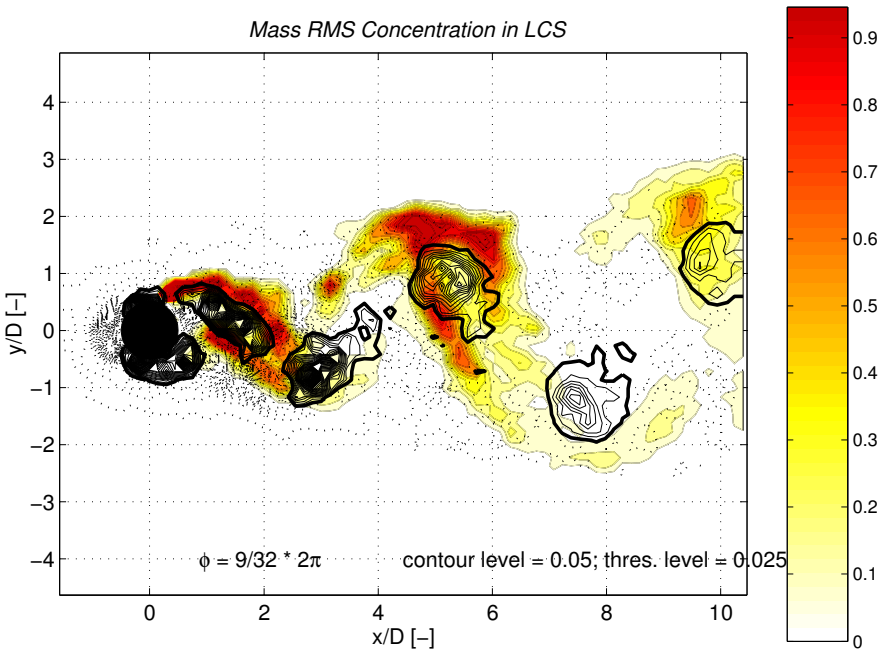
Mass RMS Concentration in LCS
y/D [–]
x/D [–]
ϕ = 9/32 * 2π
contour level = 0.05; thres. level = 0.025

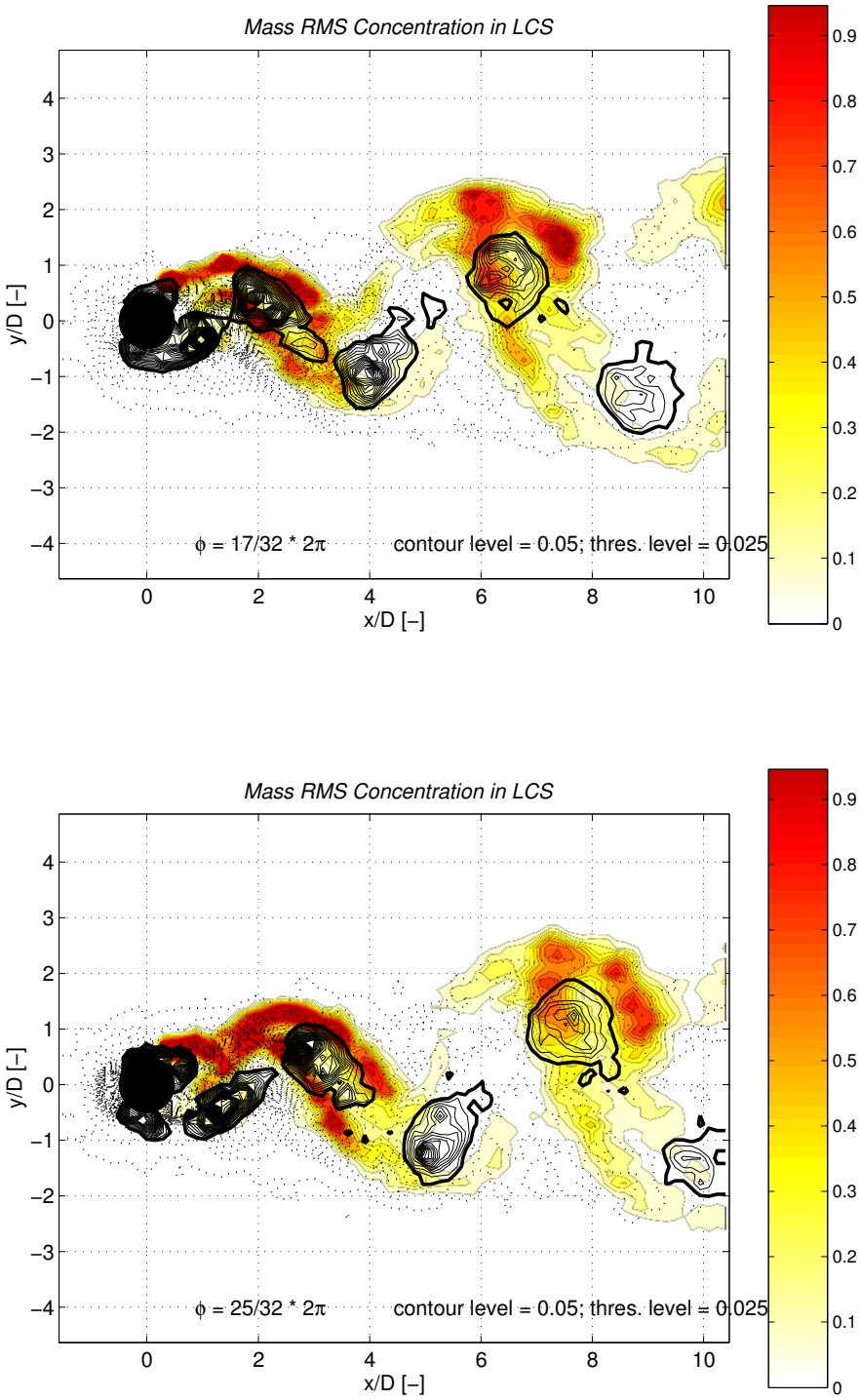

Figure 11.3. Phase–resolved averaged rms mass concentration fields $\{c\}_{rpms}$ for the same flow conditions as Figure 11.1 are displayed for 4 discrete phase angles ϕ_i spanning a full cycle at equal phase interval of $\pi/2$, and thus show the mixing of mass during the generation of LCS. Tracer dye is continuously injected into the left boundary layer of the obstacle. Color–coded standard deviation of mass concentration in mg/l, contoured Q values, bold lines indicating LCS.

$$\left\{(c-c_p)^2\right\} = \left\{c^2 - 2\,c\,c_p + c_p^2\right\} = \left\{c^2\right\} - 2\left\{c\,c_p\right\} + \left\{c_p^2\right\}$$
$$= \left\{c^2\right\} - 2\left\{c\right\}\,c_p + c_p^2 = \left\{c^2\right\} - c_p^2 = \left\{c^2\right\} - \left\{c\right\}^2 \ .$$

In (11.1) we used a double–decomposition of the concentration data into periodic and random parts $c = c_p + c_r$, where we associate the periodic 'coherent' large-scale fluctuations with the phase–resolved averaged concentration fields. The random 'incoherent' fluctuations due to the 3D small-scale turbulence are captured within the deviations of the phase–resolved averaged concentrations. However, the temporal resolution of the measuring device (e.g. 25 Hz for the employed video camera) works as a low-pass filter and prevents the access of higher frequency fluctuations up to the micro scales. Therefore the rpms value of the measured concentration covers only the low-frequency part of the small-scale turbulence. This low-frequency part, in turn, contains most of the energy of the fluctuations, therefore the rpms value is suggested at least as a strong indicator for the random 'incoherent' fluctuations.

Figure 11.3 exemplifies such phase–resolved rms values of mass concentrations for the same physical conditions and phase angles as used in Figure 11.1. The concentration fluctuations are cross-correlated to the LCS indicated by contour lines of Q values. In these plots we can identify regions of intense mixing, which are connected to the LCS. The most important mixing region is located near the outer side of the LCS just at the onset of the braid, where also the opposite coherent streakline folds back. Recalling the velocity fields we can state, that in this mixing region fresh fluid entraining from the other side of the wake is engulfed and incorporated into the LCS. A second region of high mixing is found upstream of the first one also near the outer boundary of the LCS. While the LCS is travelling downstream, this second region follows the rotation of the vortex core and moves in front of the vortex toward the wake centerline. Another filament of intense mixing is encountered, as fresh fluid intrudes into the wake along the concentration-charged braid close to the downstream part of the LCS. Besides the identification of these mixing regions we also recognize areas showing almost no fluctuations. These are the cores of the LCS as well as the region in the immediate lee of the obstacle, which are also regions with the highest local magnitudes of mass concentration. The regions of intense mixing are included in the conceptual model for shallow vortex street-like wake flows in Section 11.1.4.

11.1.3 Gradient of coherent concentration

The local gradients $\partial c_p/\partial x_i$ of the coherent distribution of the mass concentration shown in Figure 11.1 are presented in Figure 11.4 for the phase–interval $1/32 \cdot 2\pi$. Gray scales indicate the magnitude of the gradient vector ranging

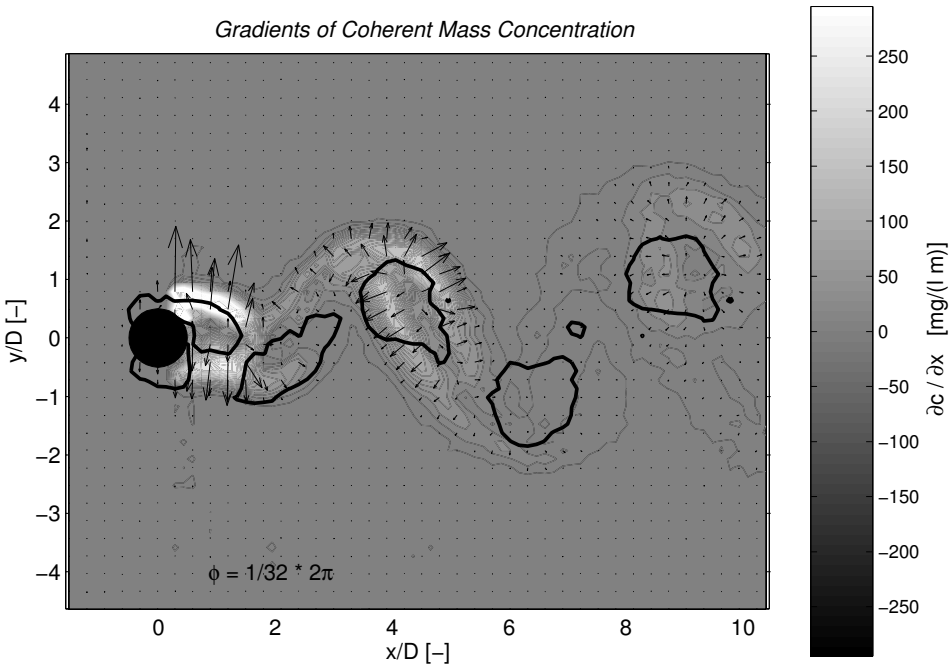

Figure 11.4. The phase–resolved averaged distributions of the magnitude of the coherent mass concentration gradients for the same flow conditions as in Figure 11.1 are displayed gray scale-coded in g/m^4 for a phase angle $1/32 \cdot 2\pi$. Vectors are orientated down the maximum gradient, and bold lines denote Q_{LCS} values to identify the LCS. Also compare this plot to the appropriate coherent distribution of the incoherent concentration fluctuation characterized by c_{rpms} in Figure 11.1.

from gray (zero) to white (> 50 % of maximum value in field). At every 4th nodal point a vector points in the direction of the maximum decrease of the tracer mass concentration. Thus, the vectors also give the direction of the diffusive mass flow rate, since for the gradient–diffusion hypothesis (cf. Section 11.3) one postulates $c_p \boldsymbol{u_p} \propto \partial c_p / \partial \boldsymbol{x}$. Bold isolines indicate the LCS separated from the shear flow by a threshold value Q_{LCS}.

As expected, the maximum values of the gradient $\partial c_p / \partial x_i$ occur around the cores of the LCS near the LCS boundaries. Since the decrease of the gradient vector is directed out of the tracer-charged LCS into the fresh ambient, we can assume the spreading of tracer due to the turbulent diffusive mass flux also to be orientated outward. Comparing the distributions of the concentration gradients to planar distributions of further properties, we gain more insight into the advective mass transport and turbulent mixing in shallow wakes. Large values of the coherent concentration gradient generally occur at locations, where also the coherent intensity of incoherent concentration fluctuations reaches its maximum. In Figure 11.1 the distribution of the root phase-mean square concentrations c_{rpms} indicates this scalar fluctuation intensity, maximum gradients and

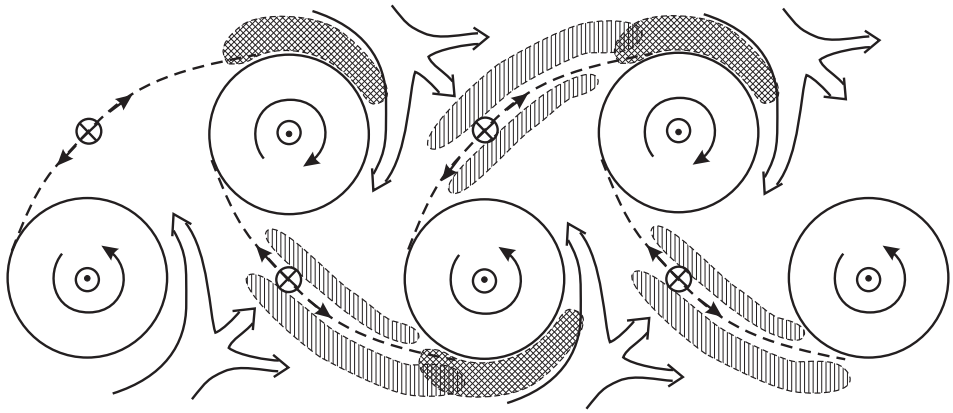

Figure 11.5. A conceptual sketch of a vortex street-like shallow wake flow with predominant 2D LCS. The vortex cores are denoted by $\odot$ symbols, saddle points of the streamlines are denoted by $\otimes$ symbols. Dashed lines indicate the braids connecting counter-rotating LCS across the wake. Double-lined arrows show the entrainment of fresh ambient fluid into the wake. Vertically hatched areas on both sides of the braids indicate regions production of turbulent kinetic energy. Cross-hatched areas indicate regions of intense mass mixing.

maximum intensities coincide remarkably well. Regarding the coherent rate of shear strain (10.11), we also observe good agreement between areas of high $\partial c_p/\partial x_i$, i.e. possibly high diffusive mass flow rates, and areas of high absolute values of ϑ_2^2 (cf. Figure 10.9). This coincidence can also be considered as an indication that at least for the mean and coherent flow fields the gradient–diffusion hypothesis may hold[4], which we will employ to derive an algebraic diffusion model in Section 11.2 and to parameterize the coherent mass transfer rates in Section 11.3.

11.1.4 Conceptual model for a vortex street-like shallow wake

A conceptual model that characterizes the dynamics of shallow wakes dominated by 2D LCS can be developed from the flow quantities evaluated from the laboratory surface velocity and depth–averaged concentration data throughout Part III of the present study. Two rows of counter-rotating eddies in staggered arrangement advect downstream to the right in Figure 11.5. The vortex cores are denoted by $\odot$ symbols, and arrows indicate the sense of rotation. The vortices of approximately circular shape are regions of large positive or negative vorticity values, where the sign reverses among the left and right wake boundary layers. Neighboring vortices of the same sense of rotation, i.e. located in the same vortex row, are separated by shear–dominated regions. Therefore, any merging of large-scale vortices is prevented in vortex street-like wakes. The

[4] As shown in Section 11.3 for 2D shear flows, the turbulent–viscosity hypothesis (11.20) and the gradient–diffusion hypothesis (11.19) can be linked through the Reynolds analogy $\nu_t \approx D_t$, i.e. $Sc_t \approx 1$.

centers of the shear regions are the saddle points of the streamlines—denoted by $\otimes$ symbols—located nearly symmetrically to the vortex cores relative to the wake axis.

The vortices in each wake shear layer are connected serially with each other by so-called 'braids' indicated by dashed lines. These braids are torn all across the wake to the back of the counter-rotating eddies and rolled-up into them, as has clearly been demonstrated by visualization in laboratory flows (cf. Figure 10.4) and by numerical transport simulations (cf. Figure 10.3). With the braids mass can be transferred between the wake shear layers and can be incorporated in LCS of the opposite shear layer. This result is in contrast to Hussain & Hayakawa (1987) who excluded cross–centerline exchange in unbounded plane wakes. In front of the eddies fresh ambient fluid is entrained into the wake and transferred between two counter-rotating eddies to the their back sides, as indicated by double-lined arrows. Hence, also fresh fluid is entrained across the wake centerline.

Regions of high coherent production of incoherent TKE are located on both sides of the braids, but clearly separated by the stretched braids themselves. Coherent counter-flows of ambient fluid entrained from both sides of the wake frontally collide, thus they firstly sustain the stretching of the braids, and secondly nourish the small-scale random TKE from dissipation of their coherent kinetic energy. The production region located along the braid to the outside of the wake is comparably more active than the inner production region. The stretched braids show a significantly converging flow near the free surface indicating a down-welling secondary motion in the braids to the backs of the large-scale eddies. Contrarily, in the cores of the LCS the near-surface flow is diverging as the result of an up-welling current in the vortex centers similar to a tornado vortex structure.

Regions of high scalar variance associated with intense mixing are primarily located close to the LCS in the strain–dominated region. They are found from the onset of the braids along the vortex boundary to the outside of the wake, but reaching also in front of the LCS. In these regions the mass-loaded braids are rolled-up along the outside of the LCS, and provide high gradients of mass concentration. Here, fresh fluid is entrained tangentially along the outside and in front of the LCS into the wake. A second, but weaker mixing region is found at the vortex boundary at the inner onset of the braids.

11.2 Coherent mass transport

11.2.1 Experimental evaluation of coherent mass transport

In the previous sections we presented low-frequency periodic distributions both of horizontal surface velocities obtained from PIV measurements and of depth-

averaged mass concentrations from PCA for a vortex street-like shallow wake flow. Though the measurement techniques were not applied simultaneously and did not even span the same time history of the flow, the characteristic periodic flow pattern was extracted from the velocity fields and from the concentration fields by phase–resolved average re-sampling of the time-resolved data. Subsequent cross–correlation enabled us to elucidate the flow topography of LCS and the associated mixing and entrainment. From the information obtained from the phase–resolved analysis, we can readily quantify the transfer of tracer mass within the wake flow. The double–decomposition of u and c into coherent and incoherent parts, for example, yields the *mean specific longitudinal mass flux*

$$\langle c\,u\rangle = \langle c_p\,u_p\rangle + \langle c_r\,u_r\rangle + \langle c_p\,u_r\rangle + \langle c_r\,u_p\rangle \ . \tag{11.2}$$

A triple–decomposition of the longitudinal mass flux has been given by Equation (7.8) in the context of the combined LDV-LIF measurements.

The first two right-hand terms of Equation (11.2) are the large-scale periodic, and small-scale turbulent parts, respectively. Though the small-scale turbulent mass flux is not accessible by the PIV-PCA technique, as applied in the present study, we know from the combined LDV-LIF measurements on the wake centerline that the small-scale turbulent axial mass transport rate is two orders–of–magnitude smaller than the large-scale periodic transport (cf. Section 7.1.4). As we can observe from the incoherent mass concentration fields in Figure 11.3, we might encounter regions of high turbulent mass transport off the wake centerline. In these combined phase–resolved averaged velocity fields and rms concentration fields, we can identify regions of high incoherent mass fluctuations, i.e. intense mixing, which are located in strain–dominated regions of the wake flow, where also coherent production of random turbulence takes place. Still, this does not mean that both these fluctuations are correlated as to induce a 3D turbulent mass flux in the coherent flow field, and that such a small-scale turbulent flux is significant also for the mean wake flow. Furthermore, the cross–correlated fluctuating parts in Equation (11.2) are small compared to the large-scale transport, as demonstrated from combined LDV-LIF measurements along the wake centerline in Section 7.1.4. Nevertheless, the low- and high-frequency parts do not always have to be de-correlated in vortex street-like shallow wake instability. However, these questions should be addressed in more detail using a truly synoptic PIV-PCA with a higher temporal resolution.

In Figure 11.6 the color-code indicates phase–resolved averaged distributions of the magnitude of the total mean and large-scale mass flux for two phase angles with a phase difference of $\pi/2$. Underlaid bold lines of Q_{LCS} values and vector fields of phase–resolved averaged velocities, reduced by the mean LCS advection speed U_{LCS}, show the coherent wake flow. It is obvious again that the mass transport within the wake is related to the LCS, and mass

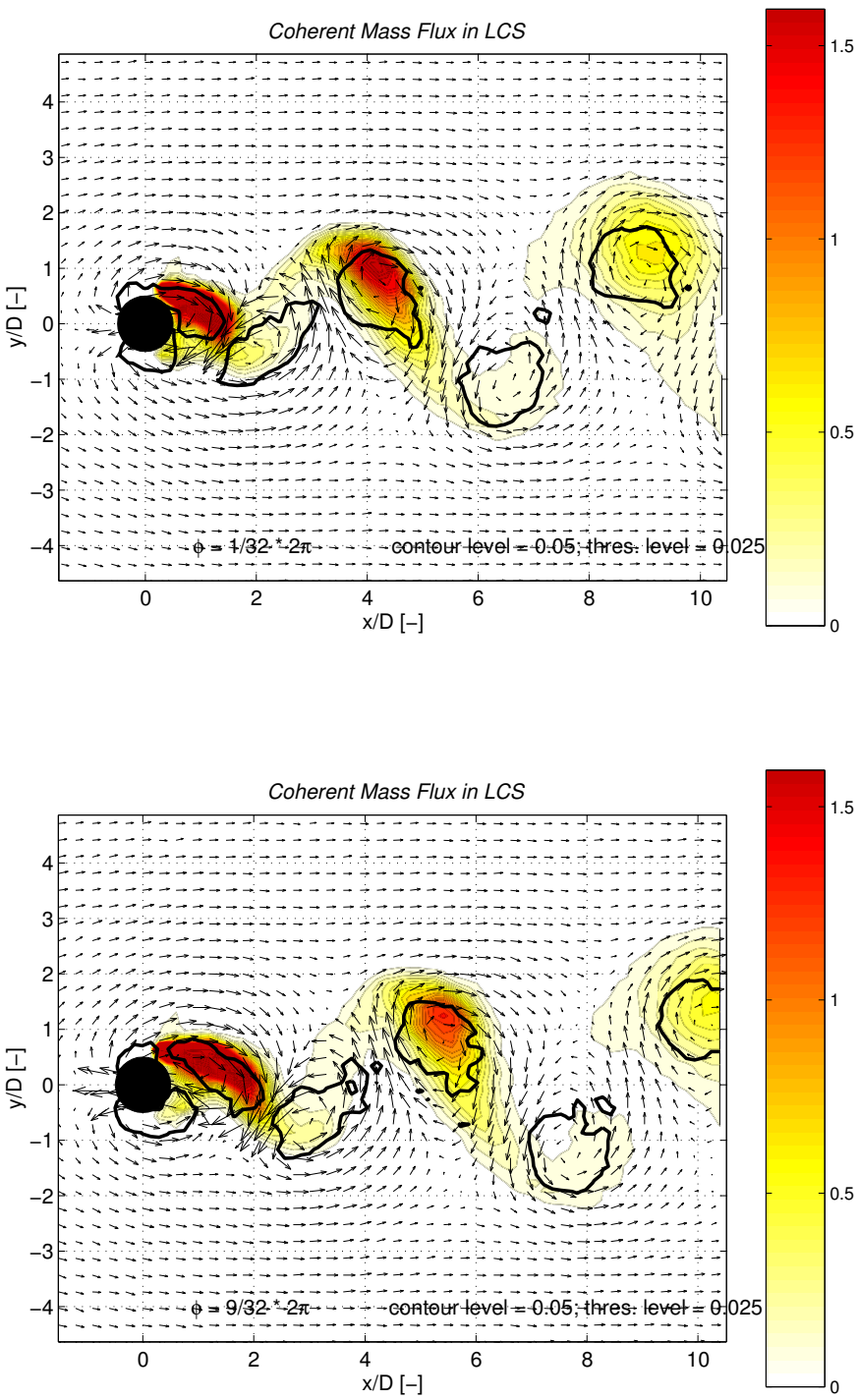

Figure 11.6. The phase–resolved averaged distributions of absolute values of the coherent specific mass flux $\{c_p\ |\boldsymbol{u_p}|\}$ for the same flow conditions as in Figure 11.1 are displayed color-coded in $g/(m^2\ s)$ for two phase angles $\pi/2$ apart. The appropriate velocity vector fields are reduced by the mean eddy advection velocity U_{LCS} and bold lines denote Q_{LCS} values to identify the LCS.

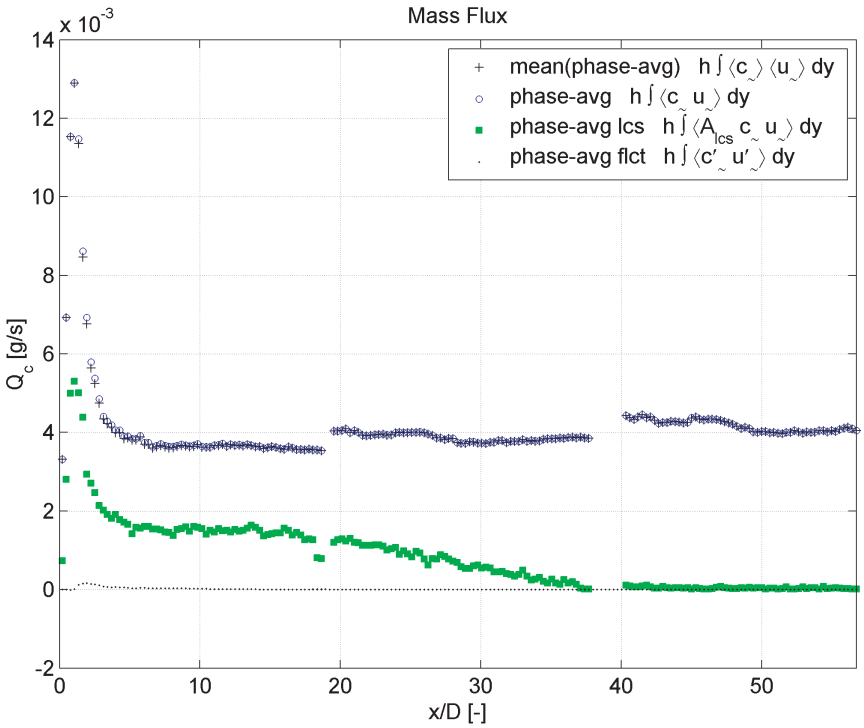

Figure 11.7. The total longitudinal coherent mass flux is obtained from the phase–resolved averaged combined fields (series 38_vs01) of velocity and mass by lateral integration of the local longitudinal flux $\{c_p\ u_p\}$. Blue circles and black crosses show the results of two different evaluation procedures. If only the area covered by the LCS is taken into account (green squares), the transport within the LCS initially amounts to almost 50%, and decreases over a distance of about 25 x/D as the LCS disintegrate.

is mainly transferred within or close to the LCS. Also in the vortex cores, where the rotational velocity is small, a high mass flux is observed due to the mean vortex advection speed U_{LCS}.

The total longitudinal mass transport rate from the phase–resolved averaged flow fields, evaluated by cross-sectionally integrating the specific longitudinal mass flux $\{c_p\ u_p\}$, is given in Figure 11.7 for a similar vortex street-like wake (series 38_vs01). The mean large-scale periodic mass flux is denoted by blue circles and black crosses in Figure 11.7. Green squares show the same mass flux evaluated only from the LCS areas. In the wake near field almost 50% of the flux takes place inside the LCS, which comprise a fluid volume of about 5% to 10% of the total wake fluid volume—depending on the definition of the wake half width δ_u.

As the LCS advect downstream and decay, the flux fraction within the LCS decreases, whereas the total flux has to remain constant also far downstream. This demonstrates the restriction not only of the kinematic effects, but also of the dynamic influence of the LCS to a downstream distance of 20 to 30 diame-

ters.[5] As the LCS are dissipated, their mass is still transported in the coherent flow field, which is no longer dominated by large-scale vortical motions, but can now be described by its ensemble mean values.

11.2.2 Numerical Particle Tracking

In the previous section we evaluated the distribution of a solute tracer mass in a vortex street-like shallow wake. After phase–resolved averaging of the concentration fields, and cross-correlating them to the appropriate coherent flow fields, we calculated the coherent mass fluxes. Instead of employing a rather complicated combined PIV-PCA measurement technique, which is restricted to the low frequency coherent flow with the current set-up, we can also think of using only the velocity fields as obtained by PIV to calculate the associated mass transport, and consequently to access also higher frequency 3D fluctuations with the aid of an appropriate turbulence model.

Procedure. A *numerical particle tracking* scheme is introduced (v. Carmer et al., 2003), in which the wake flow is given by the measured surface velocity fields instead of numerically solving the equations of motion. In the instantaneous velocity fields massless artificial tracer floats are introduced, which are passive to the flow and treated as conservative substances in the mass transport simulation. Nevertheless, they do not necessarily need to be conservative, but we can also implement time-dependent decay or a reactive model e.g. depending on the local mass concentration. For more detail the reader is referred to environmental fluid mechanics textbooks like Fischer et al. (1979) or Chapra (1996). These artificial floats can be released into the flow in arbitrary spatial and temporal configurations. We can simulate point sources or even discretized line or plane sources located somewhere in the flow field, we can model an instantaneous mass pulse as well as a continuous mass release at a constant or variable rate.

The objectives of a numerical particle tracking are twofold in the framework of the present study. On the one hand, we want to elucidate the influences of different turbulent scales on the mass transport, which—technically speaking—addresses the influence of different filter bands. Here, we also include dispersive effects due to depth–averaging. On the other hand, we want to evaluate the general possibility of inferring the depth–averaged flow fields of momentum and mass from given surface velocity fields. This question arises from the fact that especially in the near field of a vortex street-like wake we observed large-scale flow structures revealing significant secondary currents. Since such structures

[5] Over this distance the LCS directly dissipate their kinetic energy, extracted from the mean flow at the obstacle, due to bottom friction. No down-cascading could be observed performing spectral analysis of LDV-LIF data.

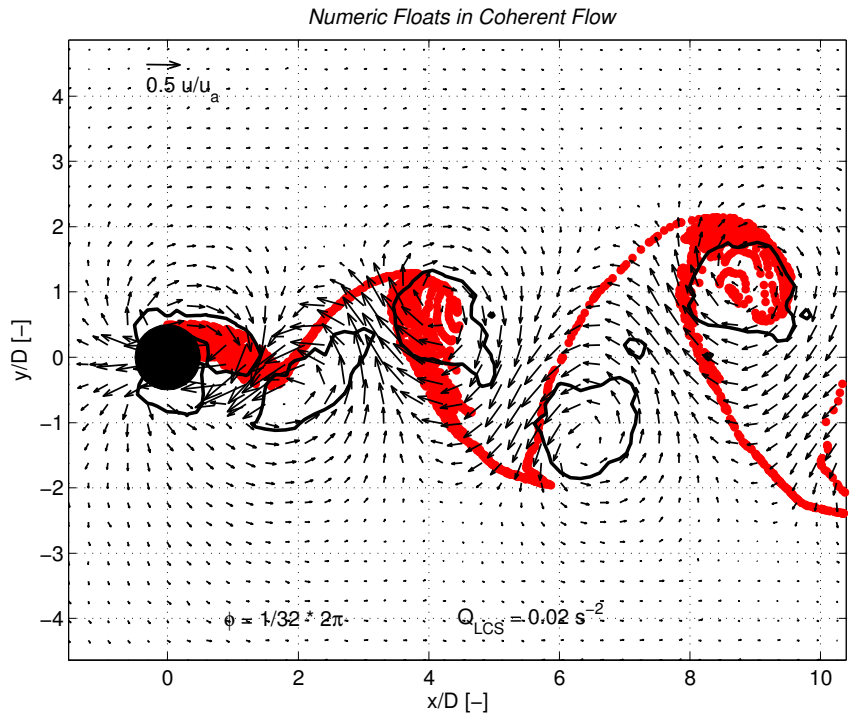
Numeric Floats in Coherent Flow
0.5 u/u_a
y/D [–]
x/D [–]
ϕ = 1/32 * 2π
Q_LCS = 0.02 s^-2

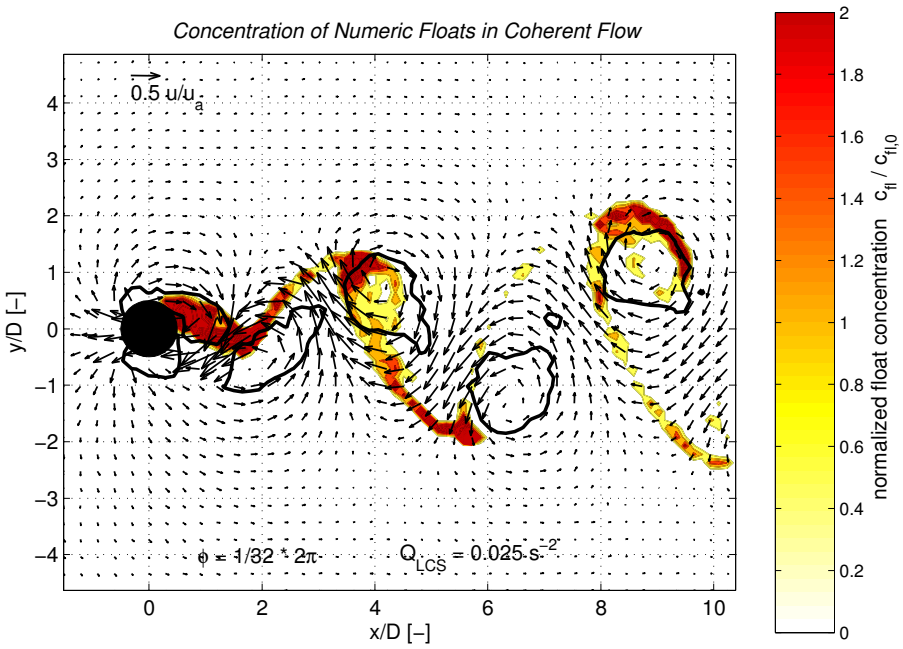
Concentration of Numeric Floats in Coherent Flow
0.5 u/u_a
y/D [–]
x/D [–]
ϕ = 1/32 * 2π
Q_LCS = 0.025 s^-2
normalized float concentration c_fl / c_fl,0

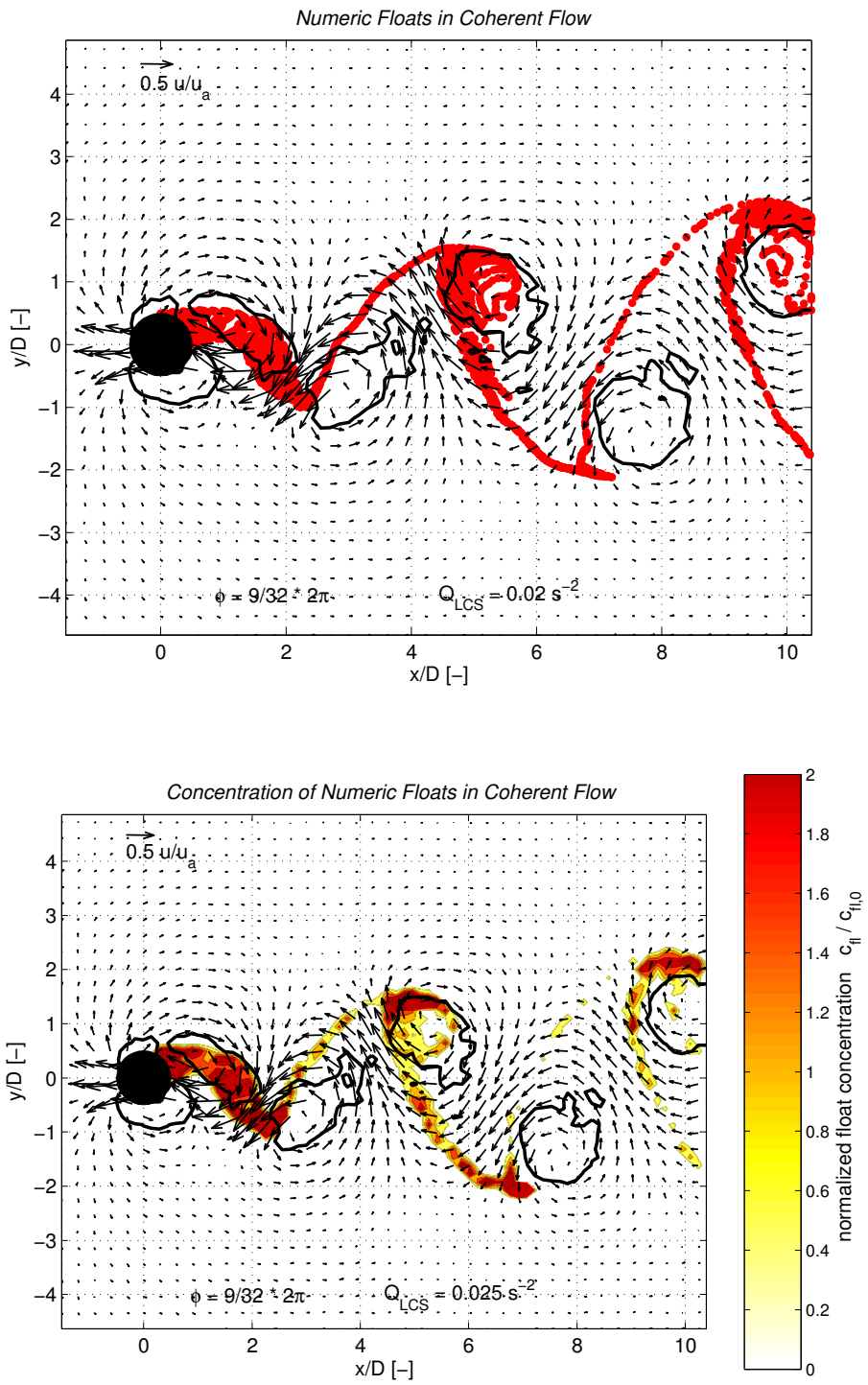

Figure 11.8. A numerical particle tracking procedure is applied to the phase–resolved averaged periodic wake flow field for the same flow conditions as in Figure 11.1. The diffusive transport and spreading due to small-scale turbulent fluctuations is therefore excluded from this computation. Numerical floats are continuously released at the downstream left section of the cylinder perimeter. The upper plots visualize the large-scale advective transport of these particles for two phase angles ϕ_i separated by a quarter of a cycle period. The lower plots show color-coded the particle concentration discretized to the grid of the flow field and normalized with the mean initial concentration of the releasing line source.

that induce additional depth-dependent low-frequency motions can also occur in other shallow shear flow configurations, this question is of general interest.

Calculation of coherent transport. Since we want to compare the results of numerical particle tracking simulations to experimental results from the PCA, we use the *phase–resolved averaged* flow fields $\boldsymbol{u_p}$ as the basis for the mass transport simulation. Consequently, the diffusive transport and spreading due to small-scale turbulent fluctuations is excluded from this computation. For instance, Figure 11.8 shows results from a numerical particle tracking procedure applied to the phase–resolved averaged periodic wake flow field for the same flow conditions as in Figure 11.1. Numerical floats are continuously released at the downstream left section of the cylinder perimeter at a constant mass flow rate $\dot{m}_{in}$. Since the periodic flow field is repetitive, contrary to the instantaneous velocity data we are not restricted in the time domain with the phase–resolved re-sampled data. Thus, we are able to continuously release mass into the flow, until a steady state or equilibrium mass transport is established, i.e. until $\dot{m}_{in} = \dot{m}_{out}$.

The upper plots of Figure 11.8 visualize the large-scale advective transport of the artificial particles for two phase angles $\pi/2$ apart. The lower plots show color-coded the particle concentration discretized to the grid of the flow field and normalized with the mean initial concentration $c_{fl,0}$ due to the releasing line source. Dark red indicates normalized float concentrations $c_{fl}/c_{fl,0}$ of more than twice the mean initial concentration.[6]

Since the tracer material is introduced only into the leeward left cylinder boundary layer, only the LCS of the left wake shear layer are charged with floats, as we already know from the phase–resolved mass concentration measurements. The numerical floats are not subjected to small-scale turbulent diffusive processes, so we can observe the remnants of the condensed streaklines in the wake flow very clearly. The transverse spreading of floats across the wake within the braids is a prominent feature of the large-scale periodic vortex street-like flow, as is obvious from these numerical particle tracking experiments. Despite the omnipresent small-scale turbulent diffusion in shallow turbulent flow, large coherent structures induce a significant amount of transverse mass transfer, which is associated with the periodic, advective motion. In the numerical experiments this transverse spreading along the braids

[6] For example, a line source releasing 33 artificial floats into an area spanning 4 cells has a mean initial concentration $c_{fl,0} = 8.25$. Due to the representation of the curvilinear source on an orthonormal grid the initial float concentrations vary slightly at the different cells containing the source. If the floats, released from a continuous transverse line source, would be advected by a uniform base flow, the initial concentration of floats would be maintained (disregarding transverse diffusion). In shallow vortex street-like wake flows the released floats are concentrated at small areas of the coherent flow field associated with the LCS.

also leads to high concentrations in the opposite shear layer at the onset of the braids behind the LCS. Since this behavior is not found in the laboratory experiments, where also turbulent diffusion acts, we can ascribe it either to the small-scale diffusivity, to bottom friction-induced dispersion due to depth-averaging, or, at larger scales, to some secondary currents of the coherent flow. The relatively thin braids show strong concentration gradients, along which the turbulent diffusion can work. Due to this turbulent diffusivity mass is distributed perpendicular to the braids and transported out of the advective periodic flow motion. This mechanism may also contribute to prevent accumulation of tracer mass behind opposite LCS.

Small-scale turbulence modelling. Although the large-scale coherent motion in the wake flow dominates the mass transfer in the near field, it is not sufficient to fully explain the redistribution and spreading of mass. To cover also the small-scale 3D turbulent transport introduced by the incoherent fluid motion we have to employ an *additional small-scale transport model* for the phase–adjusted averaged fluctuations $\{u_r\}$ and $\{v_r\}$, which should also satisfy the small-scale shear stress distribution $\{u_r\, v_r\}$. There is a broad variety of more or less sophisticated models available, in the present study we exemplify their application for two simple stochastic and algebraic models.

As a *stochastic* approach we implemented a Monte Carlo simulation. Here we assume the 3D turbulent fluctuations to show a Gaussian distribution characterized by its mean and standard deviation. Since the 3D turbulence intensities are not constant, but depend on the coherent flow, we extract the coherent distributions of $\{u_{ri}\}$ resolved in the phase-time and spatial domain from the measured velocity fields. Whereas the mean value per definitionem equals zero everywhere and at all times, we computed the coherent fields of the standard deviations $\sigma_{\{u_{ri}\}}(\phi, x, y)$. So, for the numerical floats depending on position and phase angle we randomly assign an additional small-scale turbulent velocity fluctuation and an associated displacement from a Gaussian distribution $1/\sqrt{2\pi}\,\sigma_{\{u_{ri}\}}\; exp\left(-1/2\left(\{u_{ri}\}/\sigma_{\{u_{ri}\}}\right)^2\right)$. Since we used the experimental data to configure the stochastic model, we expect the Monte Carlo simulation from the coherent flow field to give the same results as the direct transport simulation from the time-resolved flow fields provided that the Gaussian distributions hold.

The small-scale fluctuations of each tracer particle are determined independently in both the longitudinal and transverse direction, with the above stochastic model by drawing randomly from Gaussian distributions. Since the fluctuations in both directions are not independent, but correlated through the small-scale shear stress $\{u_r\, v_r\}$, a turbulence model has to capture them. In general, the easiest way is to satisfy the phase–resolved local shear stress for each individual particle, and not only for the whole ensemble of particles. Thus,

we can model the $\{u_r\}$ fluctuation, e.g. from a stochastic approach, then determine the transverse fluctuation $\{v_r\}$ from the cross-correlated phase–resolved averaged fluctuations given by $\{v_r\} = \{u_r\, v_r\} \,/\, \{u_r\}$.

If we think of *algebraic* models for the turbulent transport, a simple way would involve a uniform–turbulent–viscosity approach

$$-\{u_r\, v_r\} = \nu_t \, \frac{\partial u_p}{\partial y}, \tag{11.3}$$

which is in general an appropriate model in 2D turbulent boundary layer flows with a predominant main flow and a strong lateral gradient. Obviously, in shallow wake flow $\nu_t = const$ does not hold in the near field. Instead we follow the Reynolds analogy in turbulent flow, i.e. $Sc_t = \nu_t / D_t = \mathcal{O}(1)$. If we assume a turbulent Schmidt number of 0.5 for a shallow VS wake concluded from time-mean evaluations in Section 9.1, the turbulent viscosity yields $\nu_t = 0.5\, D_t$.[7] We close this equation by employing a common model for the depth–averaged turbulent diffusivity, now also including the dispersive effects due to depth–averaging,

$$D_t = \alpha\, u_{p*}\, h = \alpha \sqrt{\frac{c_f}{2}}\, u_p\, h \ , \tag{11.4}$$

where $\left(\frac{u_{p*}}{u_p}\right)^2 = \frac{c_f}{2}$ defines the shear velocity, and α is a constant, which depends on the geometrical boundary conditions.

The turbulent viscosity thus becomes

$$\nu_t = Sc_t\, D_t = Sc_t\, \alpha \sqrt{\frac{c_f}{2}}\, u_p\, h \ . \tag{11.5}$$

Following Rutherford (1994) we can estimate the transverse spreading coefficient D_{ty} using $0.15 < \alpha < 0.3$ in straight channels, $0.3 < \alpha < 0.9$ in rivers, and $1 < \alpha < 3$ in meandering rivers. D_{ty} now includes both diffusion due to 3D turbulence and dispersion due to depth-averaged secondary currents on the transverse spreading of the wake. Though the dispersive spreading is more related to the bathymetry and morphology of the flow than to bottom friction (represented in (11.4) by u_{p*}), (11.4) is still commonly used to estimate the transverse dispersion. For the near field of a vortex street-like shallow turbulent wake we choose $\alpha \approx 1$, we could decrease this value further downstream, since the LCS disintegrate.

In order to model the displacement of a numerical float due to small-scale turbulent velocity fluctuations, we can define the deviations from the coherent flow field as

[7] We will confirm this estimate in Section 11.3 for the large-scale coherent fluctuations. In unbounded plane wakes $Sc_t \approx 0.7$ has been reported (Pope, 2000).

$$\{u_r\} = sign\left(\frac{\partial u_p}{\partial y}\right)\sqrt{\nu_t\left|\frac{\partial u_p}{\partial y}\right|}\,, \tag{11.6a}$$

$$\{v_r\} = sign\left(\frac{\partial v_p}{\partial x}\right)\sqrt{\nu_t\left|\frac{\partial v_p}{\partial x}\right|}\,. \tag{11.6b}$$

These definitions for the turbulent displacement of numeric tracer particles reflect the local and phase–time dependent variations of the horizontal flow field. Obviously, this set of equations, (11.6a) and (11.6b) closed with (11.5), does not exactly reproduce the random Reynolds shear stress distribution. Satisfying Equation (11.3) would require $\{v_r\} = \{u_r\}$ instead of (11.6b); different weights for both directions could be implemented in addition to represent horizontal anisotrophy of the small-scale turbulence and diffusivity.

In order to cover the more 2D characteristic of the large-scale periodic wake flow field, instead of (11.3) we can implement another small-scale turbulence model. In analogy to the viscous shear stress, the Reynolds shear stress is related to the shear strain rate via the turbulent viscosity (cf. e.g. Vreugdenhil, 1994; Schlichting & Gersten, 1997)

$$-\{u_r\,v_r\} = \nu_t\left(\frac{\partial u_p}{\partial y} + \frac{\partial v_p}{\partial x}\right)\,. \tag{11.7}$$

The implementation of the above shear stress definition (11.7) is illustrated for two approaches resulting in two different algebraic models.

For the first solution we start with a definition of the main turbulent velocity fluctuation given by Equation (11.6a). For this definition the flow is assumed to be a predominantly longitudinal flow. The easiest implementation of (11.7) in a numerical transport model is to meet this requirement for the displacement of each float in each phase interval, then

$$\{v_r\} = -\frac{\nu_t\left(\frac{\partial u_p}{\partial y} + \frac{\partial v_p}{\partial x}\right)}{\{u_r\}}\,. \tag{11.8}$$

An algebraic model for the displacement of the artificial floats, which is included in the numerical particle tracking algorithms, therefore consists of the equations (11.6a), (11.8), and (11.5).

For the second implementation, following Vreugdenhil (1994, p. 37), in two-dimensional flow the full Reynolds stresses can be described similar to the viscous stresses as

$$\overline{u_r\,u_r} = \nu_t\left(\frac{\partial \overline{u}}{\partial x} - \frac{\partial \overline{v}}{\partial y}\right)\,, \quad \overline{v_r\,v_r} = -\overline{u_r\,u_r} \quad \text{and}$$

$$\overline{u_r\,v_r} = -\nu_t\left(\frac{\partial \overline{u}}{\partial y} + \frac{\partial \overline{v}}{\partial x}\right) \tag{11.9}$$

Using the normal stresses we can derive another formulation for the random velocity fluctuations in the phase–resolved averaged flow field, which also satisfies the shear stress definition (11.7),

$$\{u_r\} = sign\left(\frac{\partial u_p}{\partial x} - \frac{\partial v_p}{\partial y}\right)\sqrt{\nu_t\left|\frac{\partial u_p}{\partial x} - \frac{\partial v_p}{\partial y}\right|} \quad \text{, and} \tag{11.10a}$$

$$\{v_r\} = -\{u_r\} \ . \tag{11.10b}$$

For the closure of (11.10a) and (11.10b) again we use the turbulent viscosity evaluated by (11.5).

Comparison of different turbulence closure models. Figure 11.9 shows the effect of various small-scale turbulence models on the numerical particle tracking scheme of the coherent surface flow fields. For a fixed phase angle of a vortex street-like turbulent shallow wake flow (series 18_vs06, run 1) the horizontal velocities $\boldsymbol{u_p}$ reduced by the mean LCS advection speed $u_{LCS} = 0.917u_a$ are indicated by vector arrows; bold full contour lines indicate the threshold of the Q value to identify the LCS. Figure 11.9(a) shows the depth–averaged distribution of tracer mass experimentally obtained from the PCA system (cf. also Figure 11.1). The solute tracer is injected continuously into the upstream left cylinder boundary at mid-depth. Values of the coherent mass concentration are reproduced color-coded using a standardization with its initial value, i.e. c_p/c_{p0}.

For the same phase angle, all the remaining plots show results of the numerical particle tracking procedure. Numerical floats are continuously released at the downstream left cylinder boundary, as shown in Figure 11.10. Instead of a single point source it was necessary to introduce the floats from a discretized line source of length $\pi D/4$ to realize initial conditions as observed from the laboratory experiments (cf. also Figure 11.8). Since the surface PIV is not capable of resolving the strong 3D flow and the intense high-frequency fluctuations in the immediate vicinity of the obstacle, the numerical floats do not spread into the unsteady bubble attached to the cylinder. The transfer of artificial floats released from a single point source in the cylinder boundary layer into the large-scale coherent wake flow is depicted in Figure 10.3. Moreover, floats were released all along the downstream perimeter of the cylinder to simulate two point sources. From this arrangement no significant differences in the time–mean mass distribution arose compared to a single source release, followed by an a posteriori superposition of a mirror source. For the mass transport simulations presented in Figures 11.9(b) to 11.9(f) 33 artificial floats were continuously released per time step from the line source; about 2,000 to 3,000 floats then had to be tracked simultaneously in the flow field. On a color scale we show the surface area concentrations c_{fl} (intended to be a measure for the depth–averaged volume concentrations) of the numerical floats, the field

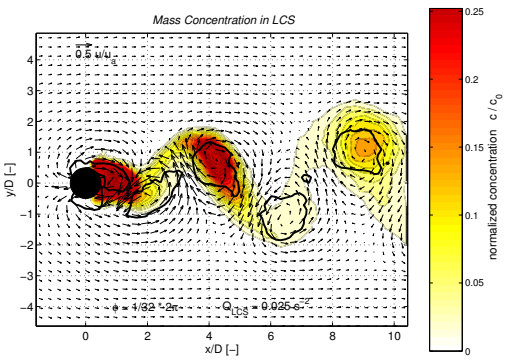

(a) Depth–averaged coherent concentration field obtained from PCA

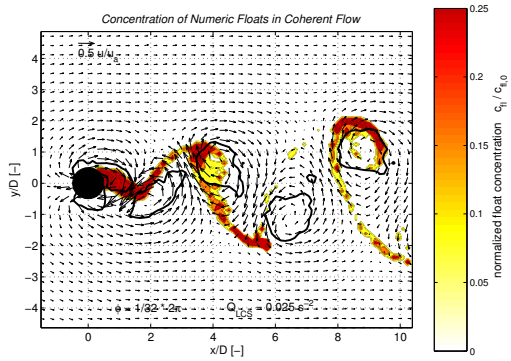

(b) Numerical particle tracking without a small-scale turbulence model

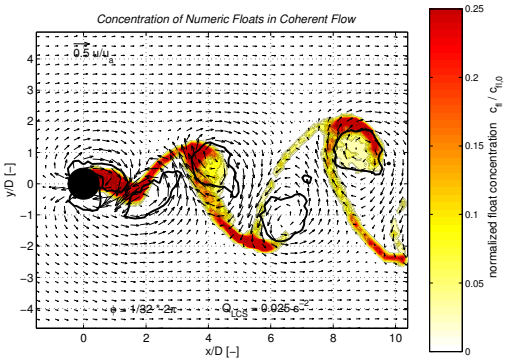

(c) Independent stochastic turbulence models for u_r and v_r

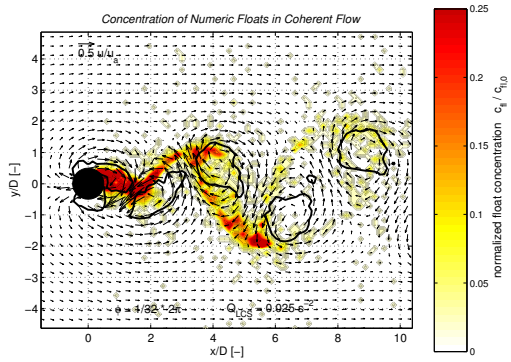

(d) Stochastic turbulence model for u_r and v_r using $\{u_r v_r\}$

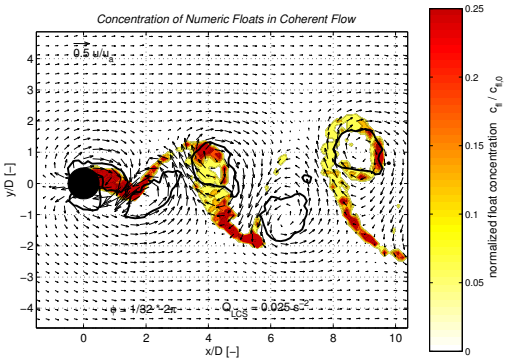

(e) Algebraic model (11.6a), (11.6b), (11.5)

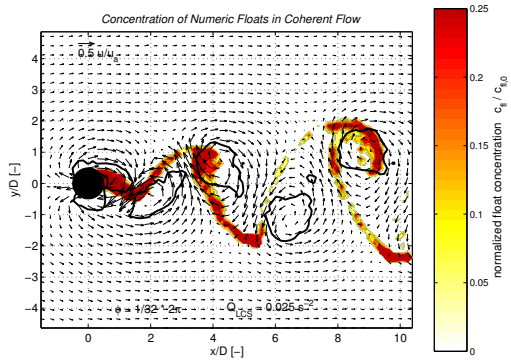

(f) Algebraic model (11.10a), (11.10b), (11.5)

Figure 11.9. Artificial floats are continuously released into the left cylinder boundary layer of the phase–resolved averaged surface velocity fields. Together with the numerical particle tracking in the coherent flow we employ different small-scale turbulence models to realize high-frequency fluctuations of the floats. Plot (a) shows the measured concentration distribution (series 18_vs06, run 1), (b) a result of the numerical particle tracking solely of the coherent flow fields, (c) and (d) a result of the numerical particle tracking using a stochastic 3D turbulence model for u_r and v_r—in (d) also accounting for $\{u_r v_r\}$—, (e) and (f) using different algebraic turbulence models.

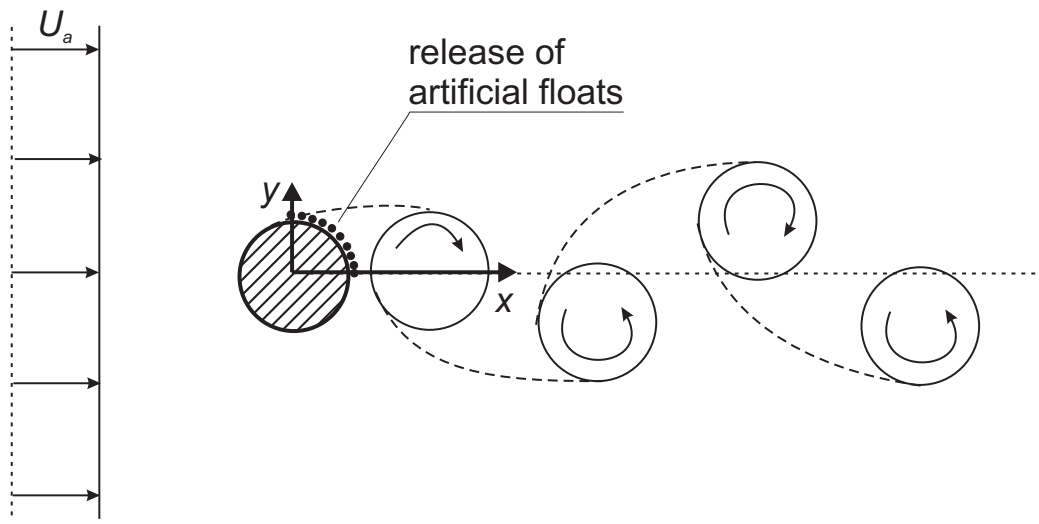

Figure 11.10. For the mass transfer simulations using the numerical particle tracking the artificial tracer floats are continuously released from a discretized line source along the leeward left cylinder boundary. This ensures an initial mass distribution in the left detached wake boundary layer similar to the experimental observations.

concentrations are normalized with the equivalent point source concentration $c_{fl,0}$.[8]

Figure 11.9(b) shows the result of the numerical transport simulation solely of the coherent flow field without any additional small-scale turbulence model, as discussed in the previous paragraphs related to Figure 11.8. While the numerical floats advect within the low-frequency periodic surface flow fields (neglecting the turbulent diffusive transport also at the surface as well as the dispersive effect due to depth-averaging), they tend to accumulate in the convergent surface regions of the wake flow in the braids and especially at the onset of the braids at the LCS. In Figures 11.9(c) and 11.9(d) with a stochastic turbulence model we also capture the random turbulent fluctuation of the surface flow to the extent, to which they could be observed with the employed PIV system. Note that the stochastic model assumes a normal distribution for the small-scale fluctuations adjusted to the observed phase–resolved averaged fluctuations $\sigma_{\{uu\}}$ and $\sigma_{\{vv\}}$; thus, no further parametrization is needed. The obtained phase–resolved averaged distribution of floats is expected to be essentially the same as the distributions we would achieve from a numerical particle tracking relying directly on the time–resolved velocity fields when afterwards applying a phase–resolved re-sampling procedure to them. Compared to the independent stochastic modelling of u_r and v_r in Figure 11.9(c), the correlated

[8] The total number of artificial floats released from the line source simulating a single point source is called the 'equivalent point source concentration'. Float concentrations due to a line source releasing 33 floats per time step to simulate one point source are thus normalized by an equivalent point source concentration of 33. Contrarily, in Figure 11.1 concentrations are normalized by the mean initial concentration.

evaluation incorporating $\{u_r v_r\}$ isotropically for each particle displacement results in only a small increase of the turbulent diffusion in Figure 11.9(d). Albeit we can state some improvement toward the experimental results compared to the solely coherent transport simulation, it is obvious that the measured surface velocity fields do not allow to conclude for the depth–averaged mass transport of a shallow turbulent wake flow. Especially in the convectively unstable region there are effects, which we associate with the secondary currents of the LCS, that prevent to derive the mass transport dynamics from the surface flow fields, regardless whether we use the low-frequency periodic fields or the information of the time–resolved fields.

To overcome this problem, we have to use other turbulence models covering also these dispersive effects of the secondary motions in the wake flow. In Figures 11.9(e) and 11.9(f) we present results gained from surface transport simulations involving the three algebraic models described earlier in this subsection. These rather simple approaches aim toward simulating the small-scale turbulent transport together with the dispersive effects captured in the α coefficient of ν_t in (11.5). For the transport simulations presented in Figures 11.9(e) and 11.9(f) ν_t was estimated using $Sc_t = 0.5$ and $\alpha = 1.0$. As we can conclude from the presented figures, these algebraic models do not suffice to incorporate dispersion due to the strongly anisotropic and inhomogeneous secondary currents, although they might be able to cover dispersion of a plane near equilibrium shear flow. If we intend to improve the algebraic models, it is reasonable to evaluate one further approach. Additionally to a 3D turbulent transport model, we recommend to cover the dispersive effects especially of the secondary flow induced by the LCS for instance by relating the secondary transport to the gradients of the surface divergence fields analogously to a gradient–diffusion model.[9] A detailed discussion of the parametrization of the turbulent diffusivity and the turbulent viscosity via α and Sc_t is omitted here for brevity. The value of the turbulent Schmidt number has been obtained experimentally. Since both parameters appear as factors to the same Equation (11.5) it would be sufficient to adjust α. Increasing α results in isotropic enhancement of the small-scale fluctuations and enhanced mass spreading into the flow. A concentration of floats in the cores of the LCS, as required from experimental observations, can not be achieved this way.

Comparison of time–mean distributions. Since we also need to quantify the capabilities of the numerical particle tracking from the coherent wake flow

[9] We could also employ a common gradient–diffusion model in a simple two–step serial algorithm, where we first compute the mass concentration from the coherent transport simulation, then apply a gradient-diffusion algorithm to include further (primarily 3D turbulent diffusive) transport processes. But we do not expect to solve the difficulties arising from the secondary currents of the LCS with such an approach.

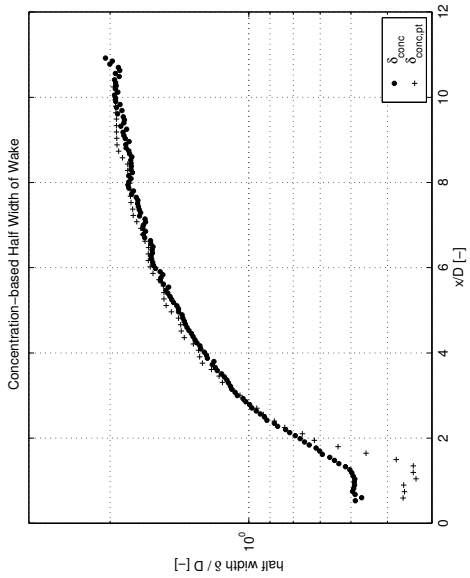

(a) Half width $\delta_{conc}(x)$

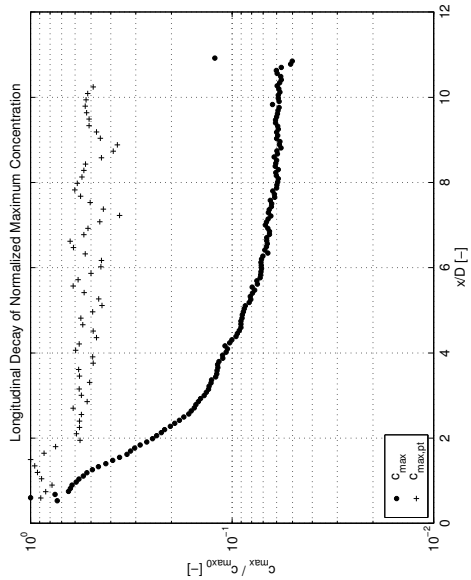

(b) Peak concentration $c_{max}(x)$

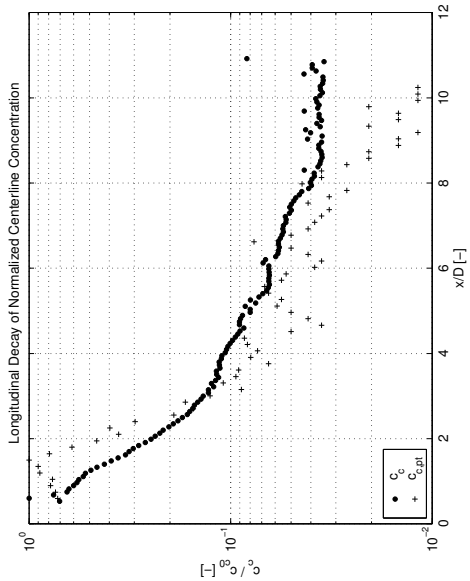

(c) Centerline Concentration $c_c(x)$

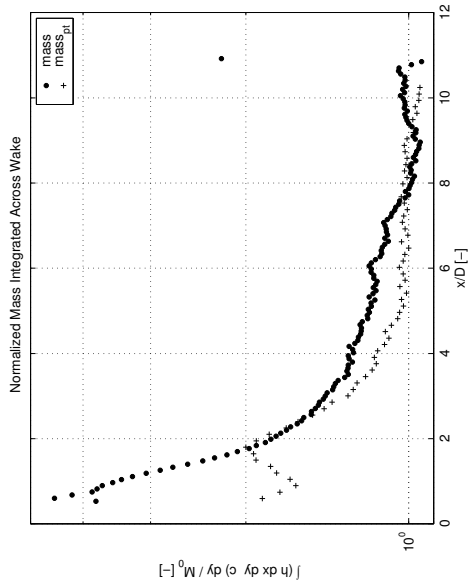

(d) Laterally integrated mass distribution $M(x)/M_{out}$

Figure 11.11. The distribution of artificial floats calculated from the numerical particle tracking, based on the coherent surface flow field and employing a stochastic small-scale turbulence model, is compared to the depth–averaged measured distributions of solute tracer mass (series 18_vs06, run 1). Plots (a) to (e) illustrate the longitudinal development of the wake half-width δ/D, the maximum concentration $c_{max}/c_{max,0}$, the centerline concentration $c_c/c_{c,0}$, the laterally integrated mass M/M_{out}, and the shape of the transverse concentration distribution c/c_0 normalized with initial scales. ∘ symbols denote results evaluated from laboratory data, whereas + symbols denote results derived from the numerical particle tracking. The ordinate is scaled logarithmically. For the transverse profiles bold full lines show experimental data, and dotted lines show numerical data.

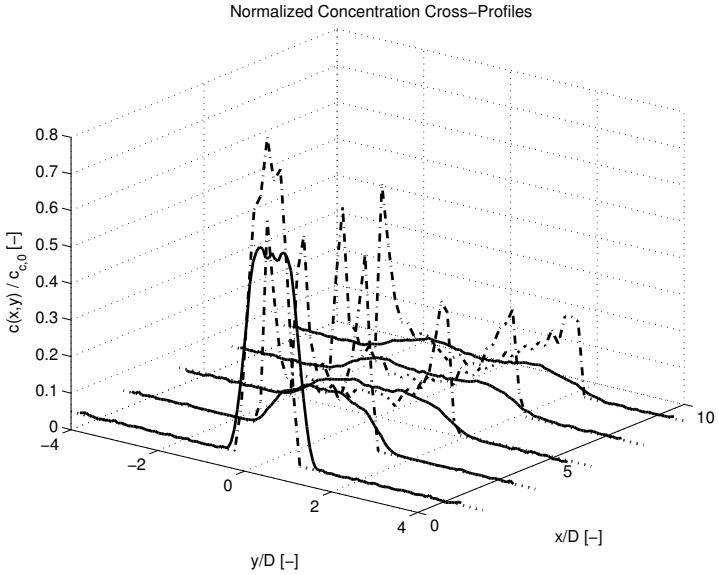

(e) Transverse concentration distribution $c\,(x, y)\,/c_{c0}$

Figure 11.11. For caption see previous page.

obtained of surface velocity measurements, we compare characteristic values of the float distribution with appropriate quantities of measured depth–averaged mass distributions. Instead of analyzing the phase–resolved averaged concentrations, as presented in Figure 11.9, we use the *time–mean* distributions here. To characterize the spreading of mass in the wake depending on the downstream distance x/D we compute the wake half-width δ, the maximum concentration c_{max}, the centerline concentration c_c, the cross–sectional mass M, and the shape of the transverse distribution. Figure 11.11 visualizes results of the numerical particle tracking on the basis of the surface velocity fields of a vortex street-like shallow wake (series 18_vs06, run 1); to predict the phase–resolved random turbulence we apply the previously described stochastic approach, where the longitudinal and transverse small-scale fluctuations are modelled independently. Contrary to Figure 11.9, the release of artificial floats is realized from a line source along the whole lee-ward perimeter of the obstacle as to simulate the effect of a symmetric mass injection from two point sources into both cylinder shear layers. A mirror source of equal strength was added to the measured time–mean concentration fields, in order to compare the numerical simulations to PCA measurement data.

In Figure 11.11(a) the *half-width* δ_{conc} of the wake is defined to be the transverse centerline distance, for which the time-mean concentration in a given cross–section reaches $1/e$ of its maximum value, i.e. $c(x, \delta_{conc}) = 1/e\, c_{max}(x)$. In general, the half width derived from the concentration of the numerical floats perfectly agrees with the measured depth–averaged distributions. In the

intermediate wake field where LCS are predominant the increase of the wake half width is mainly due to the 2D coherent flow field, the small-scale turbulent fluctuations are less important. In the region immediately downstream of the cylinder (roughly $x/D \leq 2$), where the LCS are generated, the flow in the cylinder wake is 3D, and the transverse spreading is underestimated by the surface velocity–based numerical particle tracking.

The *peak concentration* c_{max}, which is normalized by its maximum initial value $c_{max,0}$ at $x/D = 0.5$, shows a significantly slower decay than the measured maximum concentration in Figure 11.11(b). Regardless of the random turbulence model or even if any is used, the normalized peak float concentrations reveal the same decrease and and the same deviation from experimental values. For instance, at $x/D = 8$ the maximum concentration of the numerical floats is still about 23% of its initial value, whereas the observed tracer concentration has already dropped to $c_{max}/c_{max,0} = 6\%$. We can also observe this overestimation of the peak concentrations due to the surface particle tracking in the transverse distributions (cf. Figure 11.11(e)). Consequently and on the contrary, the normalized *centerline concentrations* $c_c/c_{c,0}$ are underestimated in the region of decaying LCS. Due to the restricted resolution of the numerical particle tracking, which is based on the resolution of the PIV algorithm resulting in a $(80 * 64)$ grid and in 32 phase–intervals ϕ_i, considerable scatter and numerical artifacts occur for low concentrations.

The downstream development of the *transversely integrated mass distribution*, $M(x) = \int (c(x,y)\, dx\, dy\, h)\, dy$, is depicted in Figure 11.11(d). M is standardized by the average mass in the outflow that is equal to the mass input, $M_1 = M(x_{out}) = M_0$, because of stationarity and assuming no mass retardation anymore at x_{out}. In general, both the depth–averaged PCA measurements and the numerical particle tracking simulation agree well in the time–mean concentration fields. The mean mass retardation in the near wake of the obstacle, obtained from depth–averaged measurements, is represented also in the simulation using the surface velocity field. However, in the immediate lee of the obstacle a strong retardation, $M > 4M_0$, is observed, whereas the modelled mass tends to its initial value, $M \to M_0$. This discrepancy demonstrates the limitations of both analysis techniques: on the one hand the tracer dye injected from a point source may not yet be vertically mixed resulting in an over-estimation of the actual concentration, and on the other hand 3D flow effects near the cylinder lead to surface wake velocities that over-estimate the depth–averaged wake flow.

For the *transverse distribution of the concentration* in Figure 11.11(e) we use a normalization of the concentration distribution with its characteristic initial values. The transverse distance is scaled with the cylinder diameter, i.e. y/D, and the concentration with its initial centerline value (which is essentially the same as its initial maximum value), i.e. $c(x,y)/c_{c,0}$. For clar-

ity we extract concentration cross-profiles only at the downstream positions $x/D = 1, 3, 5, 7, 9$. From the transverse distributions it is obvious that despite the first profile at $x/D = 1$ in the LCS generation region, the numerical float distributions show a much more pronounced bifurcation compared to the mass distributions. Because of the strong bifurcation, self-similarity can not be maintained in the simulated transverse concentration profiles of the near wake, since the transverse concentration distribution not only scales with its maximum value c_{max}, but also with its centerline value c_c. As already discussed in Chapter 9, downstream of the LCS generation region in the intermediate and far wake the concentration cross–profiles provide a self-similar behavior and a Gaussian distribution scaled with the wake half-width δ_{conc} and the centerline concentration c_c. With the numerical particle tracking the peaks of maximum concentration are predicted to occur more toward the outer edge of the wake. Furthermore, the transverse gradients $\partial c/\partial y$ are much steeper near the boundary of the wake than observed in the experiments. Also the peak values $c/c_{c,0}$ are strongly overestimated.

In conclusion, employing a numerical particle tracking scheme to the surface velocity fields obtained from PIV measurements is a straight-forward choice in order to access the mass transport in turbulent shallow flows without conducting synoptic PCA mass concentration measurements. The numerical particle tracking can only be applied to the low-frequency coherent flow field with the given PIV equipment. For the 3D random turbulent fields we have to employ a turbulence model, since we are not able to directly observe the high-frequency turbulent fluctuations due to lacking temporal resolution of the available PIV system. It has been shown, that making use of a simple turbulence model covering the 3D turbulent diffusion and vertical dispersion influences, does not enable us to correctly derive the spreading of mass within the wake flow field from the surface velocity fields. The main reason for this is regarded to be the existence of significant secondary currents associated with the LCS, which cause surface flow fields to differ distinctly from the depth-averaged flow fields. Modelling these secondary circulations requires an additional dispersive approach, which should be addressed in further research.

11.3 Parametrization of large-scale coherent fluctuations

Also for shallow turbulent shear flows we often use a time–mean representation to describe the main features of such flows. This implies that a standard Reynolds decomposition of the time–resolved flow fields is appropriate to cover the turbulence characteristics of the flow. The unstable near fields of shallow wake flows, and especially of vortex street-like shallow wakes, exhibit a predominately low-frequency periodic flow pattern superimposed by high-

frequency random turbulent fluctuations. As discussed in Chapter 10, instead of a Reynolds decomposition it is more convenient to apply a two–length–scale decomposition using a triple–decomposition (10.5) into time–mean, periodic and random parts. Since we are interested in the mass transfer $\boldsymbol{u}\,c$, which is not directly accessible with the available planar measurement systems, we use the phase–resolved re-sampling technique to obtain at least the time–mean and low-frequency mass fluxes $\boldsymbol{u_p}\,c$. From that, we will explore the possibility to present a descriptive model for the periodic fluxes based on the time-mean fields of flow velocity and mass concentration. Especially in the LCS dominated near field this might still be beneficial, since it clarifies and quantifies the influence of LCS.

11.3.1 Mean scalar equation

When we employ a triple–decomposition of the velocity and mass concentration fields, the coherent fields $u_{p,i}$ and c_p can be written analogously to the Reynolds decomposition of the time-resolved flow,

$$u_{p,i} = \langle u_i \rangle + \{u_{p,i} - \langle u_i \rangle\} = U_i + u^*_{p,i} \ , \tag{11.11}$$

and

$$c_p = \langle c \rangle + \{c_p - \langle c \rangle\} = C + c^*_p \ . \tag{11.12}$$

The mean mass flux thus can be decomposed into

$$\langle u_i\, c \rangle = \left\langle \left(U_i + u^*_{p,i}\right)\ \left(C + c^*_p\right) \right\rangle = U_i\, C + \left\langle u^*_{p,i}\, c^*_p \right\rangle \ , \tag{11.13}$$

where the first right-hand term denotes the mean advective flux, and the second term denotes the low-frequency periodic flux, i.e. it represents the flow rate per unit area of the mass concentration (or mass per infinitely small volume) due to the periodically fluctuating velocity field. Here again, the mass concentration c can be considered as an example for an arbitrary scalar quantity.

The transport equation for mass, or conservation equation for $c(\boldsymbol{x}, t)$, is written as

$$\begin{aligned} \frac{Dc}{Dt} &= D_m \nabla^2 c \\ \frac{\partial c}{\partial t} + \nabla\left(\boldsymbol{u}c\right) &= D_m \nabla^2 c \\ \frac{\partial c}{\partial t} + u_j \frac{\partial c}{\partial x_j} &= D_m \frac{\partial^2 c}{\partial x_j^2} \ . \end{aligned} \tag{11.14}$$

Neglecting the small-scale random fluctuation and thus using the triple–decomposition (11.13) yields after taking the time– and depth–mean (cf. also the tracer mass conservation (8.24) in the 2D SWE)

$$\frac{\partial \langle c \rangle}{\partial t} + \nabla \left(\langle \boldsymbol{u} \rangle \langle c \rangle + \left\langle \boldsymbol{u}_{\boldsymbol{p}}^{*} c_p^{*} \right\rangle \right) = D_m \nabla^2 \langle c \rangle$$
$$\frac{\bar{D} \langle c \rangle}{\bar{D} t} = \nabla \left(D_m \nabla \langle c \rangle - \left\langle \boldsymbol{u}_{\boldsymbol{p}}^{*} c_p^{*} \right\rangle \right) \ . \tag{11.15}$$

As is evident from the expression for the mean substantial derivative, the coherent mass fluxes influence the mean mass conservation in a way analogous to that of the Reynolds shear stresses in the Reynolds equations. Also, the decomposition results in a similar closure problem. To solve (11.15) we need to know a priori the coherent mass fluxes $\left\langle \boldsymbol{u}_{\boldsymbol{p}}^{*} c_p^{*} \right\rangle$.

We can close the transport equations by making use of a model to describe the large-scale turbulent fluxes of mass and momentum, $\left\langle \boldsymbol{u}_{\boldsymbol{p}}^{*} c_p^{*} \right\rangle$ and $\left\langle u_{p,i}^{*} u_{p,j}^{*} \right\rangle$ respectively. Simple algebraic models involve the *gradient–diffusion hypothesis* and the *turbulent–viscosity hypothesis*, which despite their limitations are valuable concepts discussed in various textbooks (e.g. Pope, 2000, pp. 358).

The mass flux vector $\left\langle \boldsymbol{u}_{\boldsymbol{p}}^{*} c_p^{*} \right\rangle$ gives both the direction and the magnitude of the large-scale turbulent transport of the conserved tracer mass. According to the gradient–diffusion hypothesis, this transport is down the mean concentration gradient in the direction of $-\nabla \langle c \rangle$. According to this hypothesis, the mean *turbulent diffusivity* $D_t(\boldsymbol{x})$ due to large-scale coherent fluctuation is defined as

$$\left\langle \boldsymbol{u}_{\boldsymbol{p}}^{*} c_p^{*} \right\rangle = -D_t \nabla \langle c \rangle \ . \tag{11.16}$$

Thus, the mean mass conservation equation (11.15) incorporating the gradient–diffusion hypothesis (11.16) becomes

$$\frac{D \langle c \rangle}{D t} = \nabla \left(\left(D_m + D_t \right) \nabla \langle c \rangle \right) \ . \tag{11.17}$$

Similarly, the mean rate–of–strain tensor is related to the Reynolds shear stress via the *turbulent viscosity* or *eddy viscosity* $\nu_t(\boldsymbol{x})$ given as

$$-\left\langle u_{p,i}^{*} u_{p,j}^{*} \right\rangle + \frac{2}{3} k_p^{*} \delta_{ij} = \nu_t \left(\frac{\partial \langle u_i \rangle}{\partial x_j} + \frac{\partial \langle u_j \rangle}{\partial x_i} \right) \ . \tag{11.18}$$

Again, applying the turbulent–viscosity model allows for the closure of the mean momentum equations, i.e. the RANS equations.

In the 2D SWE (cf. e.g. Equation (8.32)) both the horizontal mass flux terms of (11.16) have yet to be modelled in order to solve the mass conservation equation. Also the evaluation of the turbulent viscosity, albeit easier than for 3D flow, involves three unknowns both in the mean rate–of–strain tensor and the Reynolds shear tensor. We can approximate the description of the flow by the 2D turbulent boundary layer equations in some cases, for instance in unbounded turbulent jets and wakes. These flows are characterized by a mean

velocity predominately in the x direction and variations of the mean quantities predominately in the y direction. Using an appropriate model for the bottom friction, this may also apply to shallow turbulent wakes. Thus, the gradient–diffusion hypothesis reduces to

$$\left\langle v_p^* \, c_p^* \right\rangle = -D_t \frac{\partial \left\langle c \right\rangle}{\partial y} \tag{11.19}$$

and the turbulent-viscosity hypothesis to

$$\left\langle u_p^* \, v_p^* \right\rangle = -\nu_t \frac{\partial \left\langle u \right\rangle}{\partial y} \tag{11.20}$$

These equations, which relate a single covariance to a single gradient, are in essence definitions of D_t and ν_t.

11.3.2 Mean fields of coherent mass flux

We want to illustrate the above mass flux model by applying it to the transverse transport within a vortex street-like shallow turbulent wake. Based on a flow configuration of series 18_vs06 we continuously introduce solute tracer mass into the left cylinder boundary layer. Regarding the mean transverse mass flux, according to (11.13) we can separate the mean advective part VC and the coherent part $\left\{v_p^* \, c_p^*\right\}$, which are shown in Figure 11.12. Especially in the region of LCS generation, where the wake width is still small, we observe a rapid lateral coherent transfer, which is counteracted in part by the mean transverse spreading. As the mean cross velocity component becomes insignificant more downstream of the cylinder, the mean transverse mass flux also ceases. Except for the very vicinity of the obstacle, mass effectively spreads from the left boundary layer over the whole wake exclusively due to the large-scale coherent flow. Therefore, the transverse spreading has to be associated to the LCS, that are generated and decay in this region of the wake flow.

Note that the mass flux is a vector quantity depending on the direction of the reference frame. Thus, negative values of the transverse mean advective and coherent flux parts in Figure 11.12 just indicate, that this mass flux is orientated against the positive y direction. We use a thin full isoline delineating approximately the zero value to separate regions of positive and negative transfer rates, i.e. to clarify the direction of the transfer rates.

11.3.3 Turbulent diffusivity and turbulent viscosity

Based on its definition in Equation (11.19) we compute the *transverse turbulent diffusivity* D_{ty} from the coherent transverse mass flow rates and the mean transverse concentration gradient. Figure 11.13 exemplifies the horizontal distribution of D_{ty} in a shallow wake flow. For this flow configuration (series

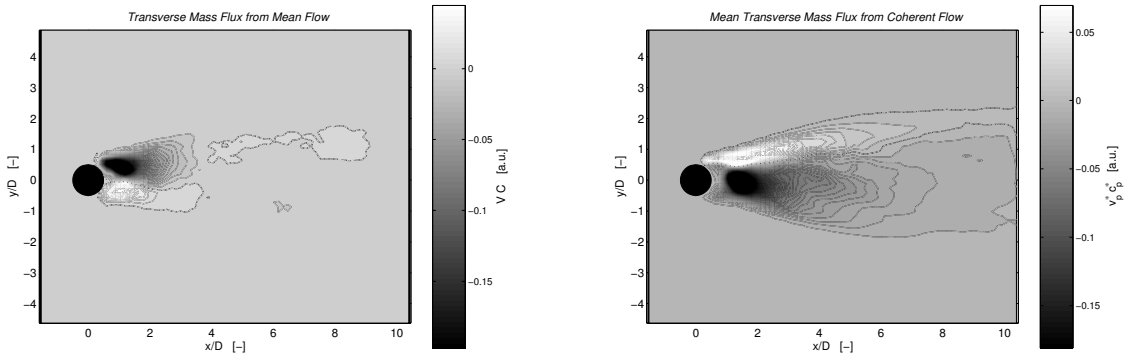

(a) VC (b) $\{v_p^* \, c_p^*\}$

Figure 11.12. The transverse mass transfer rates VC and $\{v_p^* \, c_p^*\}$ of a vortex street-like shallow wake (series 18_vs06, run 1) are calculated from the mean and large-scale periodic flow, respectively. Downstream of the immediate near field of the obstacle the mean mass flux is negligible, as there is no significant cross stream velocity. The existing mass transfer across the wake arises from the low frequency fluctuations associated with the LCS.

18_vs06) D_{ty} is of the order $\mathcal{O}(10^{-3} \; m^2/s)$. When we apply the common estimate (11.4) for the mean flow conditions using $\alpha = 1$, this results in a value of the order $\mathcal{O}(10^{-4} \; m^2/s)$. So we strongly underestimate the turbulent diffusion in the near field of the wake, if we use a mean flow approximation in the presence of LCS. The distribution of the transverse diffusivity is neither homogeneous nor isotropic (not shown here). Ideally, for a symmetric flow also D_{ty} should be symmetrically distributed. In particular, symmetry does not hold further downstream of the obstacle, but D_{ty} is skewed toward the right side of the wake. From the current situation of a point source issuing tracer dye only into the left cylinder boundary layer, the concentrations and its transverse gradients are lower on the right side, which should also be covered by (11.16). For the gradient–diffusion hypothesis it is assumed, that the directions of the mass flux and of the mean concentration gradient coincide. But as cited by Pope (2000), even for homogeneous turbulent shear flow this assumption does not always hold. From the present planar measurements we can state, that there are strong deviations from this prerequisite also for the case of a vortex street-like shallow turbulent wake flow.

Furthermore, we can also observe regions of negative D_{ty}, which is contradictious to its physical meaning of a spreading rate with the dimension $L^2 \, T^{-1}$. As these negative values primarily occur in regions, where the transverse gradient of the mean concentration $\partial C / \partial y$ is close to zero, this should be ascribed

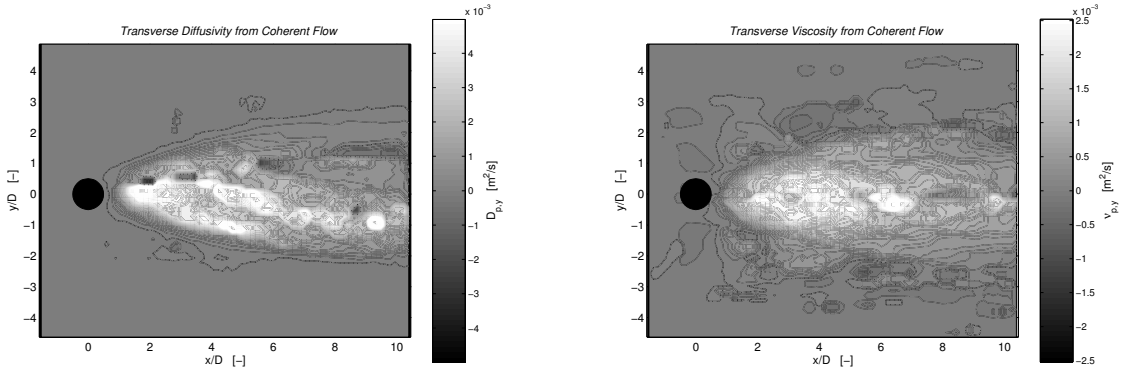

(a) Transverse turbulent diffusivity (b) Transverse turbulent viscosity

Figure 11.13. The transverse turbulent diffusivity of the coherent flow field is evaluated using (11.19). For the turbulent viscosity we apply the unbounded shear flow approximation (11.20).

both to physical noise of the PIV-PCA measurements and to numerical noise of the data processing.[10]

For the right-side plot of Figure 11.13 the *turbulent viscosity* is calculated from (11.20) using the transverse gradient of the main velocity component $\partial U/\partial y$. Also ν_{ty} is not homogeneously distributed, but compared to D_{ty} it reveals more symmetry with respect to the centerline. ν_{ty} is of the same order–of–magnitude than the transverse turbulent diffusivity, though the values of ν_{ty} are slightly below D_{ty}. In the near field of the wake, a turbulent Schmidt number $Sc = \nu_{ty}/D_{ty} \approx 0.5$ appears to be a suitable estimate. Passing through the far field downstream and approaching the plane equilibrium shear flow, i.e. the shallow base flow again, we can make another estimate for Sc_t. The distribution of the eddy viscosity across the shear layer can be described as (Nezu & Nakagawa, 1993)

$$\hat{\nu}_t = \kappa\, u_*\, h\, \frac{z}{h}\left(1 - \frac{z}{h}\right) \ ,$$

which after depth–averaging yields

$$\nu_t = \frac{\kappa}{6}\, u_*\, h \ .$$

As confirmed by Rummel et al. (2002), the depth–averaged turbulent diffusivity of a plane shear flow can be evaluated using

$$D_t = 0.15\, u_*\, h$$

[10] Small gradients $\partial C/\partial y$ result in large D_{ty}, additionally for small gradients, physically unreasonable changes of sign can occur due to noise. Altogether, this can result in large negative values of D_{ty}.

Thus, using the above approximations the turbulent Schmidt number is $Sc_t = 0.46$ in a turbulent plane equilibrium shear flow.

Summary of Part III

Identification of large coherent vortical structures. From field-wise PIV and PCA measurements the spatial coherence of shallow wake flows has been investigated. Using an adaptive *phase–resolved averaging procedure*, based on the time periods of the individual vortex shedding cycles, the surface velocity fields and the depth–averaged concentration fields have been decomposed into large-scale quasi-periodic and small-scale turbulent components. A *structure identification scheme* based on the Q values, Equation (10.1), discriminates vorticity–dominated from shear–dominated flow regions, which allows to educe large vortical structures from instantaneous flow fields. In the present study this structure identification scheme has been applied to the quasi-periodic low-frequent part of the horizontal velocity fields. Hence, the identified large-scale coherent vortical structures (LCS) are ensemble averages of all individual large-scale vortical structures observed at a given downstream position in the left or right wake shear layer. The LCS educed from this procedure ensure a high degree of both spatial and temporal coherence.

Dynamics of shallow wake flows. The educed 2D LCS in the context of the large-scale periodic flow field allowed to elucidate the *generation and decay* processes of large-scale coherent vortical structures in the near and intermediate fields of shallow turbulent wake flows. The flow field of vortex street-like shallow wakes have been examined in an Eulerian and in a Lagrangian frame moving with the LCS advection speed. The downstream development of the decaying LCS has been illustrated from flow fields, and quantified in terms of core position, core vorticity, and advection speed. The *dynamic behavior* of VS wakes, namely the interaction of large-scale coherent motion and of random turbulence, has also been demonstrated from the coherent and incoherent parts of flow properties like vorticity, shear strain, divergence, TKE, Reynolds shear stress, and turbulence production. From the surface velocity fields, convergent fronts have been identified upstream of the braids connecting the LCS, and convergent regions occurred around the saddle-points. The cores of the LCS show substantial divergent surface flow fields that clearly indicate the secondary tornado-like motion of the LCS. It has been demonstrated that a prominent part of the turbulent kinetic energy of the flow is extracted from the mean advective flow and incorporated into the LCS during their generation. This mean production of coherent kinetic energy is restricted to the immediate near field of the wake, whereas the coherent production of random turbulent kinetic energy is associated to the interaction of the established and decaying LCS in the intermediate wake field. Regions of significant coherent production of TKE have been located at the onsets of the braids and along the downstream flank of the braids. The *topography of shallow VS wakes* has been deduced from the synopsis of the distributions of these flow properties.

Mass transfer due to large coherent structures. Depth–averaged fields of tracer mass concentrations have been quantified employing the PCA technique. The *coherent and incoherent parts of the depth–averaged mass concentrations* have been related to the flow dynamics of the large-scale quasi-periodic wake flow. From the combined phase–resolved averaged velocity and mass fields, the *coherent mass transport* of shallow wakes could be evaluated, though not measured directly. The important role of the LCS also on the transfer of mass has been illustrated. As much as 50% of the mass transfer took place within areas associated to LCS, which cover approximately 5% to 10% of the wake area. Regions of intense mixing have been identified in the vortex street-like wake flow, and associated with the interaction of the LCS and their self-induced shear–dominated regions. A conceptual model has been set-up for the region of mature and decaying LCS in shallow vortex street-like wake flows. The mechanism of mass exchange among both wake shear layers and the entrainment of ambient fluid across the wake have been demonstrated. The parametrization of the large-scale coherent wake flow in terms of constant values of the coherent diffusivity and coherent eddy viscosity, as employed for the analytical wake model in Chapter 8, has been elucidated.

Numerical particle tracking. A *numerical particle tracking* has been developed to infer the depth–averaged mass transport from surface velocity fields obtained by PIV measurements. Therefore, the large-scale coherent flow has been extracted from the data, and was used to predict the coherent mass distributions, which did not sufficiently agree with mass concentrations obtained from PCA measurements in laboratory wakes. Stochastic and algebraic small-scale turbulence models have been implemented in the numerical particle tracking calculations without satisfactorily improving the results. The transport simulations in the near and intermediate VS wake field with predominant LCS showed reasonable agreement in terms of the wake half width and the bulk mass transfer. However, the detailed concentration distribution could not be modelled accurately; the local maximum concentrations were over-estimated by far, and did not occur at the cores of the LCS, but at the outer onset of the braids, where the artificial floats accumulated. This behavior has been explained by convergent and divergent wake flow regions present in the surface velocity fields. From the coherent divergence fields *secondary motions* associated with the LCS have be concluded that significantly contribute to the lateral mass transport. The influence of the tornado–like motion on the depth–averaged mass spreading strongly differs from the spreading resulting from the representation of the secondary motion in the surface flow fields.

12. Conclusions and Recommendations

The purpose of this project was to characterize the mean flow and turbulence properties of shallow turbulent wakes induced by a single cylindrical obstacle. The global and local stability had to be further elucidated and quantified. Special emphasis was on the mechanisms of generation and decay of 2D large-scale coherent vortical structures, as well as on their role in the transport of turbulent kinetic energy and of mass.

12.1 Measurement techniques

To experimentally investigate shallow turbulent wake flows a new *shallow flow facility* has been installed at the Institute for Hydromechanics, University of Karlsruhe. Plane near-equilibrium bottom friction–induced shear flows can be realized with a horizontal extent of 5.5 m times 13.5 m and with a flow depth of about 20 mm to 30 mm. Fully automated flow controls and a 3-axial traversing system ensured the necessary accuracy, stability, and repeatability for the experimental programs.

Due to the large horizontal and small vertical dimensions of the shallow flow field non-invasive measurements of flow velocities and mass concentrations could only be conducted from above the flow facility through the free water surface. Shallow wake flows are multi–scale flows with length scales ranging from the dissipative scales of random turbulence induced by vertical bottom shear up to the large scales of quasi-periodic motion of the horizontal wake flow. In order to satisfy this duality two different optical flow measurement systems have been employed. The measurement devices for the flow velocities were commonly available scientific systems, whereas the mass concentrations were obtained by specially designed or developed systems.

A two-dimensional *Laser Doppler Velocimetry* (LDV) system has been employed to observe the horizontal flow velocity components point-wise with high spatial and temporal resolution as to access also the small-scale 3D turbulent fluctuations. The monochromatic LDV laser light also excited a fluorescent dye tracer in order to allow for additional *Laser Induced Fluorescence* (LIF) measurements. The optical probe head of the LDV system also received the flu-

orescent radiation, thus, the LIF was operated in an on–axis mode, which has never been reported before. An extended LIF attenuation model, ranging well into the non-linear concentration–irradiance dependency, has been parameterized in order to capture the wide and dynamic spectrum of concentrations occurring in the wake near– and far–field. The optical arrangement guaranteed for a spatial correlation of the LDV and LIF measurements, the temporal coincidence was ensured by an additional data linking device. The *combined LDV-LIF* system allowed for the synchronous measurement of velocity and mass, and hence, made available also the horizontal mass transport.

The spatial correlation of the low-frequent quasi-periodic wake flow had to be observed by field-wise optical flow measurements. A standard *Particle Image Velocimetry* (PIV) system has been adapted to obtain horizontal velocity fields close to the free surface (Weitbrecht et al., 2002) with a spatial and temporal resolution that allowed to access the large-scale motion, but not the inertial range of small-scale turbulent fluctuations. In order to observe the field-wise concentrations of a tracer mass a *Planar Concentration Analysis* (PCA) has been realized. A hydro–optical model for the light scattering and absorption has been formulated, and has been translated into a conversion algorithm to obtain depth–averaged mass concentrations from irradiance distributions observed with a digital video camera. Though PIV and PCA could not be operated simultaneously, a *phase–resolved averaging* technique has been implemented which allowed to observe the mass transport in the low-frequent periodic flow field associated with the large-scale vortical structures.

A set of complementary measurement series provided detailed information of a variety of shallow wake flows of the vortex street (VS), unsteady bubble (UB), and steady bubble (SB) shallow wake stability classes. Hence, a data base has been provided that can be employed for further data analyses, but also to validate numerical analysis tools and simulation models.

12.2 Mean characteristics of shallow wakes

A review of the theoretical concepts of the *spectral description of turbulence* has been given for classical homogeneous 3D turbulence as well as for quasi-2D turbulence. The spectral transfer both of turbulent kinetic energy and of a passive scalar tracer have been addressed in detail. Characteristic scales of length and time have been stated that delineate the spectral ranges of production and of diffusion and dissipation.

To analyze the *turbulence in shallow wake flows* the velocity and mass fields obtained from LDV–LIF measurements have been triple-decomposed into the time-mean, large-scale coherent and small-scale turbulent parts using an adaptive phase–resolved averaging instead of a low-pass filtering. From the triple-

decomposed data it has been concluded that the large-scale coherent motion plays a crucial role in the transfer of momentum and mass. Spectral distributions of TKE and of mass variance have been calculated from the turbulence measurements in shallow wake flows, which demonstrated the dual spectral structure of 2D turbulence at large scales and 3D isotropic turbulence at small scales. The -3 enstrophy cascade of 2D turbulence toward smaller wave numbers could be verified, though the complementary inverse energy cascade to larger wave numbers was absent. Corresponding to the -3 enstrophy cascade, scalar variance has been shown to cascade down to smaller wave numbers following a -1 power law. On the small scales of 3D turbulence both energy and mass were found to be transferred through the inertial–convective subrange following the Kolmogorov and Batchelor -5/3 power laws.

An *analytical integral 1D model*—including also the effect of bottom shear stress—has been derived for the self-similar far field of shallow wake flows. Conservation equations for the standardized fluxes of momentum deficit M_s^*, of volume deficit Q_s^*, and of tracer mass Q_c^* have been solved analytically and numerically. Employing these solutions the downstream development of velocity deficit u_{sc}^* and tracer mass c_c^* along the wake centerline, and of the wake half widths δ_u and δ_γ have been solved. Then, the self-similar transverse distributions of the velocity deficit u_s^+ and of the mass c^+ followed a Gaussian distribution. The employed models for the bottom shear stress and for the lateral entrainment have turned out to be valid only for diminished large-scale periodic motions. The solutions obtained from the integral far wake model have been validated by experimental data of integral deficit fluxes of shallow wake flows.

From the *time-mean wake flow fields* of various shallow wakes transverse distributions of the velocity deficit u_s^+ and of the mass concentration c^+ have been extracted. The mass concentration showed a self-similar and Gaussian distribution over the full extent of the wake as did the velocity deficit for most part of the wake. In the immediate wake near-field u_s^+ deviated from self-similarity and from Gaussian distribution, and revealed a jet-like flow at the wake boundaries accompanied by a second inflection point in the outer transverse profile. From the longitudinal development of the centerline velocity deficit, of the centerline mass concentration, and of the wake half width, a wake near field could be distinguished over a downstream distance—normalized by the integral wake length scale ℓ_M—of $x/\ell_M = 10$ to 20. In the *wake near field* the wake could be described using the proportionalities of unbounded plane wakes, whereas in the *intermediate wake field* with predominant 2D LCS and in the passive *wake far field* the wake spreading diminished.

Experimental data of wake flow measurements have been related to results of linear stability analysis, and the *local stability regions* of shallow wake flows, as predicted by linear stability analysis (Chen & Jirka, 1997; Socolofsky

ET AL., 2003), have been identified. In shallow wakes the absolutely unstable and convectively unstable regions were found to be short, shallow wakes were predicted to be stabilized a short distance downstream of the obstacle. The transition to the stable flow region at $x/\ell_M = \mathcal{O}(10)$ roughly correlated with the transition between near and intermediate wake fields. Large-scale vortical structures resulting from the low-frequent perturbations, which are dominant in the intermediate wake field, were found to be present in the stable wake region.

12.3 Large-scale coherent vortical structures in shallow wakes

From field-wise PIV and PCA measurements the spatial coherence of shallow wake flows has been investigated. Using an adaptive *phase–resolved averaging procedure*, based on the time periods of the individual vortex shedding cycles, the surface velocity fields and the depth–averaged concentration fields have been decomposed into large-scale quasi-periodic and small-scale turbulent components. To identify the large-scale coherent vortical structures (LCS) a *structure identification scheme*, which discriminates vorticity–dominated from shear–dominated flow regions, has been applied to the quasi-periodic low-frequent part of the horizontal velocity fields. The educed 2D LCS in the context of the large-scale periodic flow field allowed to elucidate the generation and decay processes of large-scale coherent vortical structures in the near and intermediate fields of shallow turbulent wake flows. The *dynamic behavior* of VS wakes, namely the interaction of large-scale coherent motion and of random turbulence, has also been demonstrated from the coherent and incoherent parts of flow properties like vorticity, shear strain, divergence, TKE, Reynolds shear stress, and turbulence production. The *topography of shallow VS wakes* has been deduced from the synopsis of the distributions of these flow properties.

The *coherent and incoherent parts of the depth–averaged mass concentrations* have been related to the flow dynamics of the large-scale quasi-periodic wake flow. From the combined phase–resolved averaged velocity and mass fields, the *coherent mass transport* of shallow wakes could be evaluated, though not measured directly. The important role of the LCS also on the transfer of mass has been illustrated. Regions of intense mixing have been identified in the vortex street-like wake flow, and associated with the interaction of the LCS and their self-induced shear–dominated regions.

A *numerical particle tracking* has been developed to infer the depth–averaged mass transport from surface velocity fields obtained by PIV measurements. Therefore, the large-scale coherent flow has been extracted from the data, and was used to predict the coherent mass distributions, which did not sufficiently agree with mass concentrations obtained from PCA measure-

ments in laboratory wakes. Different small-scale turbulence models have been implemented in the numerical particle tracking calculations without satisfactorily improving the results. From the coherent divergence obtained from the surface velocity fields *secondary motions of the LCS* have be concluded that significantly contribute to the lateral mass transport. The influence of the tornado–like motion on the depth–averaged mass spreading strongly differs from the spreading resulting from the representation of the secondary motion in the surface flow fields.

12.4 Further perspectives

Albeit a number of fundamental questions were not addressed in depth in the framework of this study—either owe to a lack of time or of finance—, and remain challenging topics in fluid dynamics research, we want to raise some points that seem to be of relevance for the transfer of the improved basic knowledge to applied sciences and engineering applications.

So far, shallow wakes have been treated as disturbances of a uniform base flow. *Global acceleration and deceleration* of the base flow is expected to significantly alter the stability of shallow wake flows. Due to deceleration of the ambient flow the wake will be de-stabilized, the generation of large-scale coherent structures can be stimulated, its decay can be diminished. Local deceleration occurs in tidal flows in the coastal environments, advective deceleration is encountered, for instance, with the gradual expansion of the river banks in estuaries.

The stability of wake flows can be controlled by manipulating the base flow advecting the initial disturbance introduced by a single island. Random or selective enhancement of the turbulence spectrum may stabilize the wake flow. *Random or regular distributions of macro roughness elements*, which can be understood as ripples and dunes at the bottom of riverine or coastal flows, may stimulate a wake stabilization.

The important role of the 2D LCS on the transport of mass has been demonstrated in this study. The influence of these large-scale vortices on the *sediment transport* and on the *bottom erosion* has to be further elucidated. The tornado–like secondary motion of the LCS may further enhance the mobilization of sediments and the re-suspension of adhesive constituents. *Mixing and entrainment* of fresh fluid, which are of special interest for the transport of reactive constituents, may change due to the secondary motion of the LCS.

In order to improve the numerical particle tracking for the transport simulation in shallow wake flows, the effect of the secondary motion of the LCS should be included in a *divergence–based closure* of the model. The mass transport of reactive constituents may be implemented in the numerical particle tracking.

Decay laws may include the time-dependent decay, and the decay depending on the concentration of the tracer or on the concentration of another constituent.

A. Calculation procedure for spectral density estimates

In Section 6.1.4 a recipe-like summary of the procedure to calculate spectral density estimates of random processes was presented briefly. In the following section this procedure will be applied to the LDV-LIF turbulence measurements in shallow turbulent wake flows.

A.1 Preparation of time series

According to step 1 of the PSD estimation procedure one has to specify the particular parameter values for the computation of the spectral density distributions for the actual flow configurations and experimental restrictions.

To begin with, we have to estimate the *frequency range of interest* in shallow turbulent wake flows as obtained in our laboratory experiments. Using an estimate for the Strouhal number $St = Df/U$ of the large-scale wake instability to be $St \approx 0.3 \pm 0.05$, the frequency f_D of this global wake instability is expected to be of the order-of-magnitude $\mathcal{O}(10^{-1} Hz)$. Since we are interested in the energy distribution in the spectral domain to elucidate the turbulent energy cascading processes, we aim for a frequency band ranging from one order-of-magnitude below f_D up to two orders-of-magnitude above f_D, i.e. $f \in \left[\mathcal{O}(10^{-2} Hz)\ \mathcal{O}(10^{1} Hz)\right]$.

During the LDV-LIF measurements we ensured a data sampling rate of significantly more than 100 Hz for all measurement series, which enabled us to resample all the data with a *time increment* $\triangle t = 0.01\ s$. The Nyquist frequency, being the highest frequency obtained from the PSD, thus becomes $f_N = 50\ Hz$, reliable estimates of the spectral density will range up to maybe half the Nyquist frequency. So we expect our frequency band to range up to $f_{high} \approx 25\ Hz$.

Since the lowest frequency within the frequency range of the PSD should be significantly lower than the frequency of the wake instability, for example $f_{low}/f_D \lesssim 1/2$, we choose the required *length T^* of each re-sampled data sequence* to be the reciprocal of half the lowest frequency. Excluding any padded zeros, the length of a single re-sampled data block yields $T^* \approx 1/\left(0.5^2 f_D\right) = 40\ s$, if we assume $f_D = 0.1\ Hz$.

We set the maximum effective band width to $B_e = 0.5\, f_D$ in order also to resolve a downstream frequency variation of the global wake instability due to merging of large-scale vortical structures. For a $0.1\, Hz$ wake instability the *required frequency resolution of the PSD* is $B_e = 0.05\, Hz$. Assuming a maximum turbulence intensity of 25 % or 50 %, the required length T_{res} of the re-sampled data blocks becomes $T_{res} \approx (\sigma_u/\langle u \rangle)^{-2}/0.05\, Hz \approx 320\, s$ or $T_{res} \approx 80\, s$, respectively. To ensure the required low frequency resolution in the PSD, we realize a block length $T = \max(T^*, T_{res}) = T_{res}$.

In order to perform the FFT of the re-sampled data sequences, the number of data points contained in each data block has to be an integer power of 2. Instead of adding an appropriate number of zero values to the data blocks, we elongate the time T of each block to such a duration, that the FFT requirement

$$\lg_2(T/\,\Delta t) = n, \qquad n \in \mathbb{N}$$

is met. For a global wake frequency $f_D = 0.1\, Hz$ we would extend T from $80\, s$ to $81.92\, s$ making use of $N = 2^{13}$ observations in each data sequence.

Finally, we determine the *width of the band-averages* applied to the block-averaged PSD. Therefore, an odd number $(2n+1)$ of adjacent spectral estimates has to be averaged in such a way that the required frequency resolution B_e is still satisfied. The width of band-averaging is given by $(2n+1) = B_e T = 40.96 \approx 39$.

A.2 Windowing and smoothing

In order to increase the statistical reliability of spectral estimates (i.e. their degrees of freedom), we have to conduct some sort of averaging or smoothing with the spectral estimates. The smoothing can be applied directly to the time series data (*time domain weighting*), but is most commonly applied to the spectral estimates (*frequency domain smoothing*). Smoothing can be applied to the entire record to slightly increase the number of degrees of freedom per spectral estimate. Here, as in most practical applications, smoothing by *band-averaging* is applied to a series of short overlapping blocks partitioned from the full time series. We then ensemble average the smoothed spectra from each segment (i.e. *block averaging*) to increase the number of degrees of freedom per spectral estimate. The more smoothing we do, the narrower the confidence limits and the greater the reliability of any observed spectral peaks. The trade-off is a loss of spectral resolution and longer processing time.

A.2.1 Time domain weighting

In step 2 of the PSD computation procedure we split the full time series of the re-sampled data into several shorter block employing a filter window. Instead

of using a rectangular window, we choose a more appropriate filter function with respect to the FFT conducted with the shorter data segments.

A window is a convolution function applied to finite observations or their Fourier transforms to minimize so-called leakage in the spectral domain. Weighting in the time domain and smoothing in the frequency domain are adjoint Fourier functions. A window is applied to the finite data series to reduce the effect of the discontinuities at the boundaries of the observational period, since few harmonics will fit exactly into the partitioned data blocks. Such discontinuities are responsible for spectral contributions or leakage over the entire estimates, since spectral energy at frequencies higher than the Nyquist frequency is folded back into the spectral estimates of the lower frequencies. In the time domain, the windows $w(t)$ are applied to the data as a multiplicative weighting; the windowed data $\phi_w(t)$ are attenuated to zero smoothly at the boundaries, so that the periodic extensions of the data are continuous. In the frequency domain, the value $\Phi_w(f)$ in the convolution (generally denoted by $*$) at a particular frequency f is the sum of all the spectral contributions $\Phi(f)$ at each f weighted by the window $W(f)$ centered at f_0 and measured at f.

$$\begin{aligned}
&\phi_w(t) = \phi(t)\, w(t) \\
&\Longleftrightarrow \quad \Phi_w(f) = \Phi(f)\, W(f) = \int \Phi(\nu) W(f-\nu) d\nu,
\end{aligned}$$

and for finite discrete time series

$$\begin{aligned}
&\phi_w(t_k) = \phi(t_k)\, w(t_k) \\
&\Longleftrightarrow \quad \Phi_w(f_k) = \Phi(f_k)\, W(f_k) = \sum_{i=0}^{N-1} \Phi(f_i) W(f_k - f_i).
\end{aligned}$$

Concerning the shape of the window function the simplest function is the rectangular (or box-car) window $w(t_k) = 1$ for $0 < t_k < T$ and $w(t_k) = 0$ otherwise. The rectangular window extracts a data block of length T from a longer, even indefinite time series. Due to the discontinuous boundaries leakage of spectral energy poisons the spectral estimates. In this sense the FFT of a finite time series is the result of a convolution of the FFT's from the indefinite data series and from the rectangular window function. Beside this omnipresent basic window, there exist various data windows or tapers ranging from the classic Bartlett, Hann or Hamming window, to more sophisticated windows such as Kaiser-Bessel or Dolph-Chebyshev. The variety of these windows is discussed in text-books on digital signal analysis, see for instance Brigham (1997, pp. 280) and Kammeyer & Kroschel (2002, pp. 201) for more detail.

Applying a weighting function to a data time series means to dampen part of the fluctuations especially near the edges of the filter, i.e. part of the energy contained in the fluctuations is dampened away. Since we want to retain the

true amplitudes of the Fourier transformed windowed data Φ_w in order to get its true energy distribution in the frequency domain, the Fourier transformed windowed data has to be amplified. This amplification factor depends on the chosen window function and is given by

$$a_{wndw} = \left(\frac{1}{N} \sum_{k=0}^{N-1} w_k^2 \right)^{1/2} \tag{A.1}$$

Since we are interested in the spectral densities, we can simply multiply the PSD by the squared amplification factor a_{wndw}^2.

Depending on the particular objectives of the examination, we apply one out of two selected weighting functions for the spectral analysis of the pointwise LDV-LIF data throughout this work. We will briefly discuss both functions, the cosine window and the Kaiser-Bessel window, in comparison to a box-car or rectangular window.

The so-called *cosine taper* is given here by

$$w\left(k\ \triangle t\right) = \begin{cases} \frac{1}{2}\left(1 - \cos\frac{10\pi k \triangle t}{T}\right) & , 0 \leq k\ \triangle t \leq T/10 \\ 1 & , T/10 < k\ \triangle t < 9T/10 \\ \frac{1}{2}\left(1 + \cos\frac{10\pi(k \triangle t - 9T/10)}{T}\right) & , 9T/10 \leq k\ \triangle t \leq T \end{cases} \tag{A.2}$$

The main purpose of this kind of window is to reduce the effects of the boundary discontinuities of the rectangular window. Therefore, the end parts of a rectangular weighting functions are smoothly brought to zero using cosine functions (cf. Figure A.1(a), left plot). In Fourier space, with increasing frequency shift the cosine window shows a significant attenuation in the side-lobes compared to the rectangular window (cf. Figure A.1(a), right plot). As can be clarified from the convolution of both the Fourier transformed window and data series, less energy is folded back into the finite spectral domain located near the main-lobe. Indicated by the -3 dB bandwidth of the main-lobe, from the rectangular window the advantage of a narrow main-lobe is retained, as is the drawback of an only weak attenuation of the first side-lobe (of only -13 dB).

The *Kaiser-Bessel window* was rated the "top performer" in a comparative study of many different classical types of windows reported by Emery & Thomson (1998, pp. 448). Its main advantage among others is, that it has a high equivalent noise bandwidth, since the first side-lobes are greatly attenuated and the amplitudes of the farther side-lobes asymptotically decrease. The trade-off is an increased main-lobe width for reduced side-lobe levels. In the time-domain the weighting function is defined as the zeroth-order modified Bessel-function I_0 of the first kind normalized by its center value.

$$w\left(k\ \triangle t\right) = \frac{I_0\left(\pi\alpha\Omega\right)}{I_0\left(\pi\alpha\right)}, \qquad \text{for} \quad 0 \leq |k\ \triangle t| \leq T/2 \tag{A.3}$$

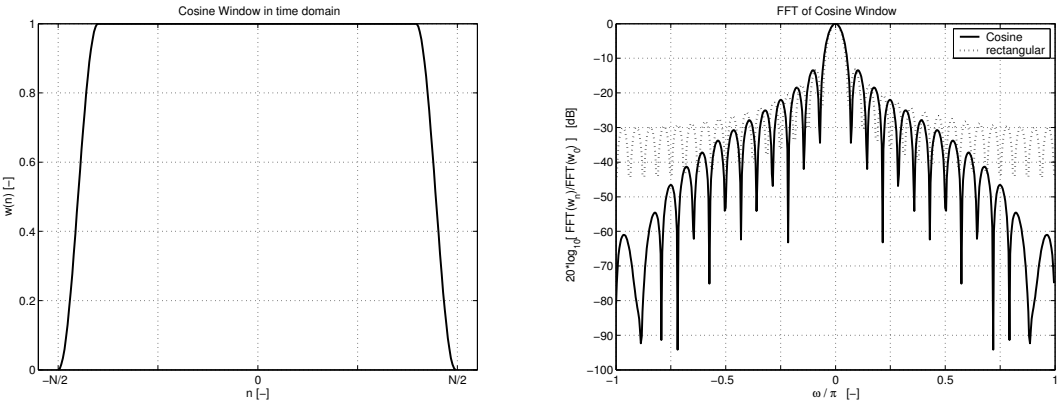

(a) Cosine window function (A.2)

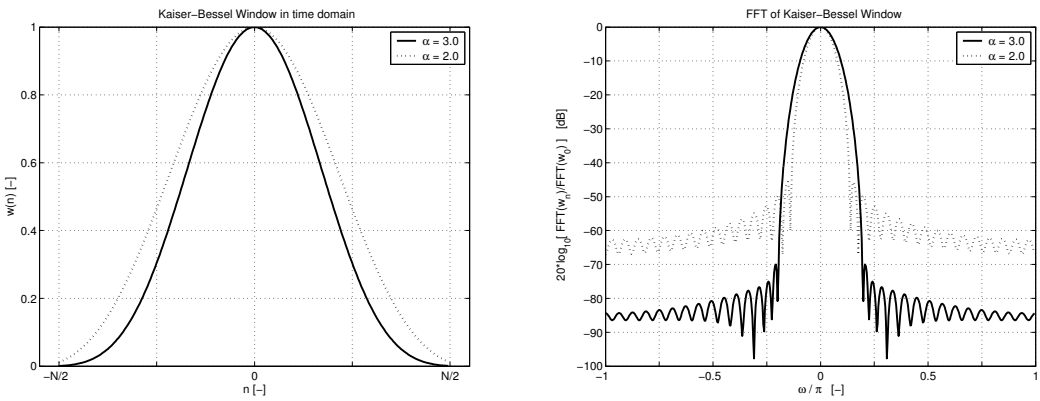

(b) Kaiser-Bessel window function (A.3) for $\alpha = 2.0$ and 3.0

Figure A.1. The window functions, as they are implemented in the spectral analyses presented here, are exemplified for $N = 32$ weights. On the left-hand side the multiplicative filters $w(k\,\triangle t)$ are shown in the time domain. The plots on the right-hand side illustrate their normalized Fourier transforms $|W(\omega_k)|/W(\omega_0)$ for the convolution with the Fourier transformed data series. (a) The *cosine window* function using (A.2) resembles a rectangular filter window, whose edges show a smooth fall-off to zero. In Fourier space, the cosine window shows a significant attenuation in the side-lobes with increasing frequency shift compared to the rectangular window. - (b) The *Kaiser-Bessel window* function (A.3) shows steeper flanks and a more narrow filter for the higher Bessel parameter $\alpha = 3.0$ in the time domain. In the frequency domain, compared to the weights with $\alpha = 2.0$ this results in an even more reduced level of the first side-lobe at the cost of an even broader bandwidth of the main-lobe.

where $\Omega = \sqrt{1-(2k\,\triangle t/T)^2}$ in the argument of the Bessel function, and $I_0(x) = \sum_{n=0}^{\infty}\left[\frac{(x/2)^n}{n!}\right]^2$ is the Bessel function with $\pi\alpha$ the parameter in the Bessel argument with typical values $2.0 \le \alpha \le 3.5$.

The modified Bessel function can be approximated for $|x| \le 3.75$ with $Z = (x/3.75)^2$ by

$$I_0(x) = \left[\left(\left\{\left[\left(4.5813\times10^{-3}Z + 3.60768\times10^{-2}\right)Z\right.\right.\right.\right.$$

$$
\begin{aligned}
&+ 2.659732 \times 10^{-1}\big]\, Z + 1.2067492\big\}\, Z \\
&+ 3.0899424)\, Z + 3.5156229]\, Z + 1.0
\end{aligned}
\tag{A.4}
$$

and for $|x| > 3.75$ with $Z = 3.75/|x|$ by

$$
\begin{aligned}
I_0(x) = \frac{\exp|x|}{\sqrt{|x|}}\, \big[\big(\big\{\big[\big(\big\{\big[\big(&3.92377 \times 10^{-3} Z \\
&- 1.647633 \times 10^{-2}\big)\, Z + 2.635537 \times 10^{-2}\big]\, Z \\
&- 2.057706 \times 10^{-2}\big\}\, Z + 9.16281 \times 10^{-3}\big)\, Z \\
&- 1.57565 \times 10^{-3}\big]\, Z + 2.25319 \times 10^{-3}\big\}\, Z \\
&+ 1.328592 \times 10^{-2}\big)\, Z + 3.9894228 \times 10^{-1}\big]
\end{aligned}
\tag{A.5}
$$

Figure A.1(b) illustrates the Kaiser-Bessel weighting function for $\alpha = 2.0$ and 3.0 for $N = 32$ weights; the dampening effect near the edges of the filter is much more gradually than for the cosine taper. In the frequency domain the Kaiser-Bessel window provides a strong attenuation of the first side-lobe of -45 dB and -70 dB, respectively, and also a further decrease of the side-lobes with the growing frequency shift (cf. right plot of Figure A.1(b)). Thus, compared to the box-car window or to the cosine window, the leakage of energy into the side-lobes is dramatically reduced, the representation of the energy cascading processes in the spectral density distribution can be expected to be more reliable than in the case of a cosine taper. The main drawback of the Kaiser-Bessel window is its increased frequency bandwidth of the main-lobe in terms of frequency bins. Therefore, we loose spectral resolution of predominating frequencies in the data also for a high signal-to-noise ratio.

In conclusion, the spectral density distribution of cosine tapered data may still carry a significant amount of energy in the higher frequencies, which for an inadequately low Nyquist-frequency is folded back into the PSD. The side-lobe attenuation of the Kaiser-Bessel window can provide much better performance in the higher frequencies. Contrarily, due to the extended width of the main-lobe the Kaiser-Bessel weighting function tends to smear out lower frequencies, whereas the cosine taper offers a distinct representation of a pronounced main frequency in the frequency spectrum of a data series.

A.2.2 Frequency domain smoothing

After having transformed the partitioned data into Fourier space in step 3 of the PSD computation procedure, in step 4 we evaluate their spectral estimates and apply further smoothing to the PSD.

Instead of computing the Fourier transform of a whole time series with N' elements, the time series can be divided into k_{bl} shorter blocks of N elements each. Using the Fourier transforms of these data blocks, the spectral estimates

of the whole series can be evaluated by averaging the corresponding frequency bins of the PSD of each short data series. This kind of smoothing of the spectral density is usually called *block-averaging*. Because of the shorter time intervals of the individual data blocks, the lowest available frequency f_{low} of the signal FFT increases compared to f_{low} of the FFT from the full data series. On the other hand, if we are able to obtain the same frequency range also from the shorter data blocks, than as a trade-off we will lack frequency resolution, when Fourier transforming only the partitioned blocks.

When we apply a window function like a Kaiser-Bessel window (A.3) to the (partitioned) data series prior to the FFT, data points at the edges of the filter will have less impact on the spectral estimates than points near the center of the filter. In order to compensate for this filter effect and give a more uniform weighting to all data points, usually the data blocks are extracted from the full time series with an *overlap* of 30% to 50%, i.e. the last $0.3\,N$ to $0.5\,N$ data points of a data block are identically equal to the first data points of the consecutive block. To select an appropriate overlap percentage, we have to consider the fact that due to the overlap we induce some correlation among the spectral estimates of the individual blocks. For a filter window with a pronounced central weighting (e.g. Hann, Hamming, or Kaiser-Bessel), adjoining data blocks with an overlap of 0.5 or even higher can be regarded as independent time series for spectral analysis. The LDV-LIF data processed for this examination are weighted either with a cosine taper (A.2) and an overlap of 10% or using a Kaiser-Bessel window (A.3 with $\alpha = 3.0$) and an overlap of 50% before calculating the spectral estimates.

Another way of smoothing in Fourier space is to apply a so-called *band-averaging* procedure. In individual or block-averaged spectral density distributions, adjacent frequency bands are averaged together, for instance a band-average of width 3 of the spectral estimate is defined as $\bar{S}_{\phi\phi}(f_i) = 1/3\,[S(f_{i-1}) + S(f_i) + S(f_{i+1})]$, $\bar{S}_{\phi\phi}(f_{i+3}) = 1/3\,[S(f_{i+2}) + S(f_{i+3}) + S(f_{i+4})]$, and so on. Obviously, the band-averaging procedure reduces the frequency resolution of the PSD, since adjoining frequency bins are combined. Therefore, the required band width B_e has to be lower than the initial frequency resolution of the FFT from the individual data series.

Bibliography

Adrian R.J. (1991). 'Particle-imaging techniques for experimental fluid mechanics.' *Ann. Rev. Fluid Mech.*, **23**:261–304.

Adrian R.J. & Yao C.S. (1987). 'Power spectra of fluid velocities measured by Laser Doppler Velocimetry.' *Exp. Fluids*, **5**:17–28.

Albrecht H.E., Borys M., Damaschke N., & Tropea C. (2003). *Laser Doppler and Phase Doppler Measurement Techniques*. Springer, Berlin, Heidelberg.

Andresen P. (2001). 'Laser induced fluorescence.' In Mayinger & Feldmann (2001), pp. 195–226.

Arcoumanis C., McGuirk J.J., & Palma J.M.L.M. (1990). 'On the use of fluorescent dyes for concentration measurements in water flows.' *Exp. Fluids*, **10**:177–180.

Arst H. (2003). *Optical Properties and Remote Sensing of Multicomponental Water Bodies*. Springer-Verlag, Berlin Heidelberg New York.

Aubrun S., Boisson H.C., & Bonnet J.P. (2002). 'Further characterization of large-scale coherent structure signatures in a turbulent-plane mixing layer.' *Exp. Fluids*, **32**:136–142.

Babarutsi S. & Chu V.H. (1991). 'A two-length-scale model for quasi-two-dimensional turbulent shear flows.' *Proc. 24th IAHR Congress*, pp. C–53 – C–60.

Babarutsi S. & Chu V.H. (1998). 'Modeling transverse mixing layer in shallow open-channel flows.' *J. Hydr. Eng.*, **124**(7):718–727.

Balachandar R., Chu V.H., & Zhang J. (1997). 'Experimental study of turbulent concentration flow field in the wake of a bluff body.' *ASME J. Fluids Eng.*, **119**:263–270.

Balachandar R., Tachie M.F., & Chu V.H. (1999). 'Concentration profiles in shallow turbulent wakes.' *ASME J. Fluids Eng.*, **121**:34–43.

Balu M., Balachandar R., & Wood H. (2001). 'Concentration estimation in two-dimensional bluff body wakes using image processing and neural networks.' *J. Flow Viz. Image Proc.*, **8**(2/3):121–139.

BASF (1996). 'Analytical tests for the Sicovit and Sicomet colorants.' Technical Information ME 342 e, BASF Fine Chemicals, Ludwigshafen.

BASF (1997). 'Sicovit(R) - colorants for foods, drugs, and cosmetics. Sicomet(R) - colorants for cosmetics only.' Technical Information ME 341 e, BASF Fine Chemicals, Ludwigshafen.

Batchelor G.K. (1959). 'Small scale variation of convected quantities like temperature in turbulent fluid. part 1: General discussion and the case of small conductivity.' *J. Fluid Mech.*, **5**:135–139.

Batchelor G.K. (1967). *An Introduction Into Fluid Dynamics*. Cambridge University Press.

Batchelor G.K. (1969). 'Computation of the energy spectrum in homogeneous two-dimensinal turbulence.' *Phys. Fluids Suppl., II*, **12**:233–239.

Berger E. & Wille R. (1972). 'Periodic flow phenomena.' *Annual Review of Fluid Mechanics*, **4**:313–340.

Bergmann L. & Schaefer C. (1987). *Lehrbuch der Experimentalphysik*, volume 3. Optik. de Gruyter, New York, 8th edition. In german.

Betchov R. & Criminale Jr. W. (1967). *Stability of Parallel Flows*. Academic Press, New York.

Betchov R. & Criminale, Jr. W.O. (1966). 'Spatial instability of the inviscid jet and wake.' *Phys. Fluids*, **9**(2):359–362.

Bimberg D., ed. (1993). *Meßtechniken mit Lasern*. expert-Verlag, Ehningen. In German.

Bonnet J.P., Delville J., Glauser M.N., Antonia R.A., Bisset D.K., Cole D.R., Fiedler H.E., Garem J.H., Hilberg D., Jeong J., Kevlahan N.K.R., Ukeiley L.S., & Vincendeau E. (1998). 'Collaborative testing of eddy structure identification methods in free turbulent shear flows.' *Exp. Fluids*, **25**:197–225.

Born M. & Wolf E. (1964). *Principles of Optics*. Pergamon-Press, Oxford.

Bradshaw P., Ferriss D.H., & Atwell N.P. (1967). 'Calculation of boundary layer development using the turbulent energy equation.' *J. Fluid Mech.*, **28**:593–616.

Brigham E.O. (1995). *FFT - Schnelle Fourier Transformation*. Oldenbourg Verlag, München, 6. corr. edition.

Brigham E.O. (1997). *FFT-Anwendungen*. Oldenbourg Verlag, München.

Bukata R.P., Jerome J.H., Kondratyev K.Y., & Pozdnyakov D.V. (1995). *Optical Properties and Remote Sensing of Inland and Coastal Waters*. CRC Press, Boca Raton, FL.

Camussi R. (2002). 'Coherent structure identification from wavelet analysis of particle image velocimetry data.' *Exp. Fluids*, **32**:76–86.

v. Carmer C.F. (1998). 'Geschwindigkeitsverteilung im breiten Gerinne: Theorie, Messung, Prognose.' In Pohl H., ed., 'Wasserbaukolloquium 1998 "Hydraulische und Numerische Modelle im Wasserbau. Entwicklung und Perspektiven". Mitteilungen des Instituts für Wasserbau und Technische Hydromechanik, Heft 13,' pp. 193–204. Dresden. In German.

v. Carmer C.F. (2000). 'LDA-LIF System zur Untersuchung großräumiger kohärenter Strukturen in flacher turbulenter Strömung.' In Delgado A., Werner F., Ruck B., Leder A., & Dopheide D., eds., 'Lasermethoden in der Strömungsmesstechnik, 8. GALA-Fachtagung,' pp. 18.1–18.9. Shaker Verlag, Aachen.

v. Carmer C.F. & Deutsch H. (2001). 'Karlsruher Flachwasser-Versuchsstand. Stofftransport in ebener turbulenter Scherströmung.' Präsentations-Videofilm IfH, Univ. Karlsruhe. 10 min, german language.

v. Carmer C.F. & Deutsch H. (2002). 'Karlsruhe shallow flow facility. Mass transport in turbulent plane shearflow.' video presentation IfH, Univ. Karlsruhe. 12 min, extended english version.

v. Carmer C.F. & Jirka G.H. (2001). 'On turbulence and transport in shallow wake flow.' *Proc. 29th IAHR Congress Beijing, China*, **B**:80–86.

v. Carmer C.F., Koch T., & Jirka G.H. (2000). 'Großräumige wirbelstrukturen in turbulenter flachwasserströmung.' Technical Report 766, Institut für Hydromechanik, Universität Karlsruhe.

v. Carmer C.F., Rummel A.C., & Jirka G.H. (2002). 'Combined planar measurements of flow velocity and mass concentration in shallow turbulent flow - Part 2: Application of coupled PIV-PCA technique to turbulent shallow wake flows.' *Proc. ASCE/IAHR Int. Symp. Hydr. Meas. & Exp. Meth. Estes Park, Co., USA.*

v. Carmer C.F., Rummel A.C., & Jirka G.H. (2003). 'Influence of secondary motion in large-scale coherent structures on the mass transport in a shallow turbulent wake.' *Proc. Int. Symp. Shallow Flows, Delft, NL.*

v. Carmer C.F., Weitbrecht V., & Jirka G.H. (2001). 'On the genesis and fate of large coherent vortical structures in turbulent shallow wake flows.' *Proc. 3rd Int. Symp. Env. Hydr. Tempe, USA.*

Chanson H. (2002). 'Whirlpools. experiencing naruto whirlpools.' *IAHR Newsletter*, **19**:28–29.

Chapra S. (1996). *Surface Water-Quality Modeling*. McGraw-Hill.

Chaudhry M.H. (1993). *Open-Channel Flow*. Prentice-Hall, Englewood Cliffs, US.

Chen D. & Jirka G.H. (1995). 'Experimental study of plane turbulent wakes in a shallow water layer.' *Fluid Dynamics Research*, **16**:11–41.

Chen D. & Jirka G.H. (1997). 'Absolute and convective instabilities of plan turbulent wakes in a shallow water layer.' *J. Fluid Mech.*, **338**:157–172.

Chen D. & Jirka G.H. (1998). 'Linear stability analysis of turbulent mixing layers and jets in shallow water layers.' *J. Hydr. Research*, **36**(5):815–830.

Chen D. & Jirka G.H. (1999). 'LIF study of plane jet bounded in shallow water layer.' *J. Hydr. Eng.*, **125**:817–826.

Chen Y.N. (1973). '60 Jahre Forschung über die Kármánschen Wirbelstrassen – Ein Rückblick.' *Schweizerische Bauzeitung*, **91**(44):1079–1096. In German.

Chopra K.P. (1973). 'Atmospheric and oceanic flow problems introduced by islands.' *Advances in Geophysics*, **16**:297–421.

Chu V.H., Wu J.H., & Khayat R.E. (1983). 'Stability of turbulent shear flows in shallow channel.' *Proc. 20th IAHR Congress, Moscow*, **3**:128–133.

Chu V.H., Wu J.H., & Khayat R.E. (1991). 'Stability of transverse shear flows in shallow open channels.' *J. Hydr. Eng.*, **117**(10):1370–1388.

Cimbala J.M., Nagib H.M., & Roshko A. (1988). 'Large structure in the far wakes of two-dimensional bluff bodies.' *J. Fluid Mech.*, **190**:265–298.

Coles D. (1956). 'The law of the wake in the turbulent boundary layer.' *J. Hydr. Eng.*, **1**:191–226.

Coppeta J. & Rogers C. (1998). 'Dual emission laser induced fluorescence for direct planar scalar behavior measurements.' *Exp. Fluids*, **25**:1–15.

Corrsin S. (1951). 'On the spectrum of isotropic temperature fluctuations in an isotropic turbulence.' *J. Appl. Phys.*, **22**:469–473.

Cowen E.A., Chang K.A., & Liao Q. (2001). 'A single-camera coupled PTV-LIF technique.' *Exp. Fluids*, **31**:63–73.

Cowen E.A. & Monismith S.G. (1997). 'A hybrid digital particle tracking velocimetry technique.' *Exp. Fluids*, **22**:199–211.

Cramp A., Coulson M., James A., & Berry J. (1991). 'A note on the observed and predicted flow patterns around islands - flat holm, the bristol channel.' *Int. J. Remote Sensing*, **12**:1111–1118.

Crimaldi J.P. (1997). 'The effect of photobleaching and velocity fluctuations on single-point LIF measurements.' *Exp. Fluids*, **23**:325–330.

Crimaldi J.P. & Koseff J.R. (2001). 'High-resolution measurements of the spatial and temporal scalar structure of a turbulent plume.' *Exp. Fluids*, **31**:90–102.

Davies P.A., Dakin J.M., & Falconer R.A. (1995). 'Eddy formation behind a coastal headland.' *J. Coastal Research*, **11**:154–167.

DeFelice T.P., Meyer D.J., Xian G., Christopherson J., & Cahalan R. (2000). 'Landsat-7 reveals more than just surface features in remote areas of the globe.' *Bulletin of the American Meteorological Society*, **81**:1047–1049.

Delville J., Cordier L., & Bonnet J.P. (1998). *Large-Scale-Structure Identification and Control in Turbulent Shear Flows*, pp. 199–274. In Gadel Hak et al. (1998).

Deusch S., Dracos T., & Rys P. (1996). 'Establishment of a tomographic laser induced fluorescence system.' In Dracos T., ed., 'Tree-Dimensional Velocity and Vorticity Measuring and Image Analysis Techniques,' pp. 277–297. Kluwer Academic Publishers, Dordrecht.

Dietz P. (2001). *Entwicklung großräumiger Wirbelstrukturen in einer flachen Mischungsschicht*. Vertieferarbeit, Universität Karlsruhe, Technische Universiteit Delft.

Dietz P., Kurzke M., & Carmer C.F.v. (2002). 'STUMTRA - eine Mess- und Steuer-Software für den Flachwasser-Versuchsstand. Bedienungsanleitung, Programmdokumentation, Betriebshinweise.' Technical Report 790, Institut für Hydromechanik, Universität Karlsruhe.

Donges A. & Noll R. (1993). *Lasermesstechnik*. Hüthig, Heidelberg.

Dracos T., Giger M., & Jirka G.H. (1992). 'Plane turbulent jets in a bounded fluid layer.' *J. Fluid Mech.*, **241**:587–614.

Drazin P.G. (2002). *Introduction to Hydrodynamic Stability*. Cambridge University Press, Cambridge, UK.

Drazin P.G. & Reid W.H. (1981). *Hydrodynamic Stability*. Cambridge University Press, Cambridge.

Durst F., Melling A., & Whitelaw J.H. (1981). *Principles and Practice of Laser-Doppler Anemometry*. Academic Press, London, 2nd edition.

van Dyke M. (1982). *An Album of Fluid Motion*. Parabolic Press, Stanford, Ca.

Eder A., Durst B., & Jordan M. (2001). 'Laser-doppler velocimetry - principle and application to turbulence measurements.' In Mayinger & Feldmann (2001), pp. 113–134.

Emery W.J. & Thomson R.E. (1998). *Data Analysis Methods in Physical Oceanography*. Pergamon.

Etling D. (1989). 'On atmospheric vortex streets in the wake of large islands.' *Meteorol. Atmos. Phys.*, **41**:157–164.

Etling D. (1990). 'Kármánsche Wirbelstraßen im Lee großer Inseln.' *Die Geowissenschaften*, **8**:91–95.

Ferrier G., Davies P.A., & Anderson J.M. (1996). 'Remote sensing observations of a vortex street downstream of an obstacle in an estuarine flow.' *Int. J. Remote Sensing*, **17**:1–8.

Fiedler H.E. (1998). *Control of Free Turbulent Shear Flows*, pp. 335–430. In Gad-el Hak et al. (1998).

Fischer H.B., List E.J., Koh R.C.Y., Imberger J., & Brooks N.H. (1979). *Mixing in Inland and Coastal Waters*. Academic Press, San Diego.

Fjortoft R. (1953). 'On the changes in the spectral distribution of kinetic energy for two-dimensional non-divergent flow.' *Tellus*, **5**:225–230.

Frette Ø., Erga S.R., Stamnes J.J., & Stamnes K. (2001). 'Optical remote sensing of waters with vertical structure.' *Applied Optics*, **40**:1478–1487.

Fujita I., Muste M., & Kruger A. (1998). 'Large scale particle image velocimetry for flow analysis in hydraulic engineering applications.' *J. Hydr. Res.*, **36**:397–414.

Fukushima C., Aanen L., & Westerweel J. (2000). 'Investigation of the mixing process in an axisymmetric turbulent jet using PIV and LIF.' *Proc. 10th Int. Symp. Appl. Laser Techn. Fluid Mech.*.

Furukawa K. & Wolanski E. (1998). 'Shallow-water frictional effects in island wakes.' *Estuarine, Coastal and Shelf Science*, **46**:599–608.

Geyer W.R. (1993). 'Three-dimensional tidal flow around headlands.' *J. Geophysical Research*, **98**:955–966.

Geyer W.R. & Signell R. (1990). 'Measurements of tidal flow around a headland with a shipboard acoustic doppler current profiler.' *J. Geophysical Research*, **95**:3189–3197.

Gharib M., Kremers D., Koochesfahani M.M., & Kemp M. (2002). 'Leonardo's vision of flow visualization.' *Exp. Fluids*, **33**:219–223.

Ghidaoui M.S. & Kolyshkin A.A. (1999). 'Linear stability analysis of lateral motions in compound open channels.' *J. Hydr. Eng.*, **125**(8):871–880.

Giger M., Dracos T., & Jirka G.H. (1991). 'Entrainment and mixing in plane turbulent jets in shallow water.' *J. Hydr. Research*, **29**:615–642.

Green F.J. (1990). *The Sigma-Aldrich Handbook of Stains, Dyes, and Indicators*. Aldrich Chemical Company Inc., Milwaukee.

Guilbault G.G. (1973). *Practical Fluorescence*. Dekker, New York.

Gad-el Hak M., Pollard A., & Bonnet J.P., eds. (1998). *Flow Control. Fundamentals and Practices*. Springer, Berlin Heidelberg.

Hannemann K. & Oertel Jr. H. (1989). 'Numerical simulation of the absolutely and convectively unstable wake.' *J. Fluid Mech.*, **199**:55–88.

Hecht E. (2002). *Optics*. Addison-Wesley, San Francisco, 4th international edition.

Heinrich K.E. (1999). *Umströmung eines Kreiszylinderpaares in flacher turbulenter Grundströmung*. Master's thesis, Univ. Karlsruhe. In German.

Herring J.R. (1974). 'Approch of an axisymmetric turbulence to isotropy.' *Phys. Fluids*, **17**:859–872.

Hesse M., Meier H., & Zeeh B. (1995). *Spektroskopische Methoden in der organischen Chemie*. Thieme, Stuttgart, 5th rev. enl. edition. In german.

Hinterberger C. (2004). *Dreidimensionale und tiefengemittelte Large-Eddy-Simulation von Flachwasserströmungen*, volume 2004/2 of *Dissertationsreihe am Institut für Hydromechanik der Universität Karlsruhe*. Universitätsverlag, Karlsruhe. ISBN 3-937300-18-X. In German.

Hinze J.O. (1975). *Turbulence*. McGraw-Hill, New York, 2nd edition.

Hockney R.W. & Eastwood J.W. (1988). *Computer Simulation Using Particles*. Adam Hilger, Bristol.

Holley E.R. & Jirka G.H. (1986). 'Mixing in rivers.' Technical Report E-86-II, US Army Waterways Experiment Station, Vicksburg, US.

Holmes P., Lumley J.L., & Berkooz G. (1996). *Turbulence, Coherent Structures, Dynamical Systems and Symmetry*. Cambridge University Press.

Huerre P. & Monkewitz P. (1985). 'Absolute and convective instabilities in free shear layers.' *J. Fluid Mech.*, **159**:151–168.

Huerre P. & Monkewitz P. (1990). 'Local and global instabilities in spatially developing flows.' *Ann. Rev. Fluid Mech.*, **22**:473–537.

Hunt J.C.R., Wray A.A., & Moin P. (1988). 'Eddies, stream, and convergence zones in turbulent flows.' Report CTR-S88, Center for Turbulence Research.

Hussain A.K.M.F. (1977). 'Mechanics of pulsatile flows of relevance to the cardiovascular system.' In Hwang N.H.C. & Normann N.A., eds., 'Cardiovascular Flow Dynamics and Measurements,' pp. 541–632. University Park Press, Baltimore.

Hussain A.K.M.F. (1983). 'Coherent structures - reality and myth.' *Phys. Fluids*, **26**(10):2816–2850.

Hussain A.K.M.F. (1986). 'Coherent structures and turbulence.' *J. Fluid Mech.*, **173**:303–356.

Hussain A.K.M.F. & Hayakawa M. (1987). 'Eduction of large-scale organized structures in a turbulent plane wake.' *J. Fluid Mech.*, **180**:193–220.

Ingram R.G. & Chu V.H. (1987). 'Flow around islands in rupert bay: An investigation of the bottom friction effect.' *J. Geophysical Research*, **92**:14521–14533.

Jähne B. (2002). *Digital Image Processing*. Springer Verlag, Berlin, Heidelberg, New York, 5th rev. ext. edition.

Jeong J., Grinstein F.F., & Hussain F. (1994). 'Eduction of coherent structures in a numerically simulated plane wake.' *Applied Scientific Research*, **53**:227–236.

Jeong J. & Hussain F. (1995). 'On the identification of a vortex.' *J. Fluid Mech.*, **285**:69–94.

Jirka G.H. (1998). 'Large scale flow structures and mixing processes in shallow flows.' *Proc. 2nd Int. Symp. Env. Hydr., Hong Kong*.

Jirka G.H. (1999). 'Environmental fluid mechanics - Its role in solving problems of pollution in lakes, rivers and coastal waters.' In Bianchi G., ed., 'Environmental Applications of Mechanics and Computer Science. CISM Courses and Lectures, No 409,' pp. 49–98. Springer, Berlin.

Jirka G.H. (2001). 'Large scale flow structures and mixing processes in shallow flows.' *J. Hydr. Research*, **39**:567–573.

Jirka G.H. (2004). 'Integral model for turbulent buoyant jets in unbounded stratified flows. part 1: Single round jet.' *Env. Fluid Mech.*, **4**(1):1–56.

Jirka G.H., Colonell J.M., & Douglas J. (1986). 'Outfall mixing design in shallow coastal water under arctic ice cover.' *MTS Journal*, **20**(3):44–53.

Jirka G.H. & Uijttewaal W.S.J. (2004). 'Shallow flows: A definition.' In Jirka G. & Uijttewaal W.S.J., eds., 'Shallow Flows,' pp. 3–11. Balkema, Leiden, NL.

Kammeyer K.D. & Kroschel K. (2002). *Digitale Signalverarbeitung. Filterung und Spektralanalyse mit MATLAB-Übungen*. Teubner, Stuttgart, 5. durchges. erg. edition.

Käss W. (1992). *Geohydrologische Markierungstechnik*. Borntraeger, Berlin.

Khatibi R.H., Williams J.J.R., & Wormleaton P.R. (2001). 'Friction parameters for flows in nearly flat tidal channels.' *J. Hydr. Eng.*, **126**:741–749.

Kirkgöz M.S. & Ardiçlioğlu M. (1997). 'Velocity profiles of developing and developed open channel flow.' *J. Hydr. Eng.*, **123**(12):1099–1105.

Klingholz R. (1997). 'Fotografie, Die rasenden Reporter.' *GEO*, (4):16–45.

Koch W. (1985). 'Local instability characteristics and frequency determination of self-excited wake flows.' *J. Sound Vibr.*, **99**(1):53–83.

Kolyshkin A.A. & Ghidaoui M.S. (2002). 'Gravitational and shear instabilities in compound and composite channels.' *J. Hydr. Eng.*, **128**(12):1076–1086.

Kondratyev K.Y. & Filatov N.N., eds. (1999). *Limnology and Remote Sensing*. Springer, Berlin Heidelberg New York.

Kraichnan R.H. (1967). 'Inertial ranges in two-dimensional turbulence.' *Phys. Fluids*, **10**:1417–1423.

Kraichnan R.H. & Montgomery D. (1980). 'Two-dimensional turbulence.' *Reports Progr. Phys.*, **43**:547–619.

Kruppa B., Strube G., & Gerlach C. (2001). 'Light scattering.' In Mayinger & Feldmann (2001), pp. 95–112.

Kühn G. (2000). *PIV und PTV im Strömungslabor: Erfassung von Oberflächengeschwindigkeiten mit Ganzfeldmessverfahren*. Master's thesis, University of Karlsruhe. In German.

Kundu P.K. & Cohen I.M. (2002). *Fluid Mechanics*. Academic Press, San Diego, Ca., 2nd edition.

Kurzke M. (2002). *Auswirkung des Buhnenneigungswinkels auf den Stofftransport in Flüssen*. diploma thesis, University of Karlsruhe. German language.

Kurzke M., Weitbrecht V., & Jirka G.H. (2002). 'Laboratory concentration measurements for determination of mass exchange between groin fields and main stream.' *Proc. IAHR conf. Riverflow, Louvain-de-la-Neuve, Belgium*.

Lass H.U. (2002). private communication, Süddeutsche Zeitung 10.28.2002.

Leder A. (1990). 'Windkanalmessungen mit LDA-Systemen.' In Ruck B., ed., 'Lasermethoden in der Strömungsmesstechik,' pp. 319–365. AT-Fachverlag.

Leder A. (1992). *Abgelöste Strömungen*. Vieweg.

Lee J.H. & Jirka G.H. (1980). 'Multiport diffuser as line source of momentum in shallow water.' *Water Resources Research*, **16**(4):695–708.

Lemoine F., Antoine Y., Wolff M., & Lebouche M. (1999). 'Simultaneous temperature and 2D velocity measurements in a turbulent heated jet using combined laser-induced fluorescence and LDA.' *Exp. Fluids*, **26**:315–323.

Lemoine F., Wolff M., & Lebouche M. (1996). 'Simultaneous concentration and velocity measurements using combined laser-induced fluorescence and laser Doppler velocimetry: Application to turbulent transport.' *Exp. Fluids*, **20**:319–327.

Lemoine F., Wolff M., & Lebouché M. (1997). 'Experimental investigation of mass transfer in a grid-generated turbulent flow using combined optical methods.' *Int. J. Heat Mass Transfer*, **40**:3255–3266.

Lesieur M. (1997). *Turbulence in Fluids*. Kluwer Academic Publishers, Dordrecht, NL, 3rd rev. edition.

Lesieur M. & Herring J.R. (1985). 'Diffusion of a passive scalar in tow-dimensional turbulence.' *J. Fluid Mech.*, **161**:77–95.

Lloyd P.M. & Stansby P.K. (1997a). 'Shallow-water flow around model conical islands of small side slope. i: Surface piercing.' *J. Hydr. Eng.*, **123**(12):1057–1067.

Lloyd P.M. & Stansby P.K. (1997b). 'Shallow-water flow around model conical islands of small side slope. ii: Submerged.' *J. Hydr. Eng.*, **123**(12):1068–1077.

Lugt H.J. (1979). *Wirbelströmung in Natur und Technik*. Braun, Karlsruhe. German language.

Ma X., Karamanos G.S., & Karniadakis G.E. (2000). 'Dynamics and low-dimensionality of a turbulent near wake.' *J. Fluid Mech.*, **410**:29–65.

Maassen S.R. (2000). *Self-organization of confined two-dimensional flows*. Thesis, Technische Universiteit Eindhoven.

Maassen S.R., Clercx H.J.H., & van Heijst G.J.F. (2002). 'Self-organization of quasi-two-dimensional turbulence in stratified fluids in square and circular containers.' *Phys. Fluids*, **14**(7):2150–2169.

Marple Jr. S.L. (1987). *Digital Spectral Analysis with Applications*. Prentice-Hall, Englewood Cliffs, NJ.

Mayinger F. & Feldmann O., eds. (2001). *Optical Measurements. Techniques and Applications*. Springer, Berlin, 2nd corr. edition.

McWilliams J.C. (1984). 'The emergence of isloated coherent vortices in turbulent flow.' *J. Fluid Mech.*, **146**:21–43.

McWilliams J.C. (1990). 'The vortices of two-dimensional turbulence.' *J. Fluid Mech.*, **219**:361–385.

Meyer K.E., Özcan O., Larsen P.S., Gjelstrup P., & Westergaard C.H. (2000). 'Point and planar LIF for velocity-concentration correlation in a jet in cross flow.' *Proc. 10th Int. Symp. Appl. Laser Techn. Fluid Mech.*.

Monkewitz P.A. (1988). 'The absolute and convective nature of instability in two-dimensional wakes at low Reynolds numbers.' *Phys. Fluids*, **31**(5):999–1006.

Morton B., Taylor G.I., & Turner J.S. (1956). 'Turbulent gravitational convection from maintained and instantaneous sources.' *Proc. R. Soc.*, **A**(234):1–23.

Moser R.D., Kim J., & Mansour N.N. (1999). 'Direct numerical simulation of turbulent channel flow up to $Re_\tau = 590$.' *Phys. Fluids*, **11**:943–945.

Müller G., Bruce T., & Kauppert K. (2002). 'Particle Image Velocimetry: A simple technique for complex surface flows.' *Proc. Riverflow Conf., Louvain-la-Neuve, Belgium*.

Münsterer T. & Jähne B. (1998). 'LIF measurements of concentration profiles in the aqueous mass boundary layer.' *Exp. Fluids*, **25**:190–196.

Muste M., Xiong Z., Schöne J., & Li Z. (2004). 'Validation and extension of image velocimetry capabilities for flow diagnostics in hydraulic modeling.' *J. Hydr. Eng.*, **130**:175–185.

Nadaoka K. & Yagi H. (1998). 'Shallow-water turbulence modeling and horizontal large-eddy computation of river flow.' *J. Hydr. Eng.*, **124**(5):493–500.

NASA (2002). 'NASA eyes intricate pattern on cloud street.' `http://eob.gsfc.nasa.gov/Newsroom/NasaNews/`.

Nash J.D., Jirka G.H., & Chen D. (1995). 'Large scale planar laser induced fluorescence in turbulent density-stratified flows.' *Exp. Fluids*, **19**:297–304.

Negretti M.E. (2003a). *Analysis of the Wake Behind a Circular Cylinder in Shallow Water Flow*. Master's thesis, Universita' delgi studi di Trento.

Negretti M.E. (2003b). *Entwicklung von kohärenten 2D Strukturen im Nachlauf eines Kreiszylinders im turbulenter Flachwasserströmung*. Master's thesis, University of Karlsruhe. In German.

Newland D.E. (1993). *An Introduction to Random Vibrations, Spectral and Wavelet Analysis*. Longman Scientific & Technical, Harlow, Essex, 3rd edition.

Nezu I. & Nakagawa H. (1993). *Turbulence in Open-Channel Flows*. Balkema, Rotterdam.

Nezu I. & Rodi W. (1986). 'Open-channel flow measurements with a laser Doppler anemometer.' *J. Hydr. Eng.*, **112**:335–355.

Oboukhov A.M. (1949). 'Structure of the temperature field in turbulent flows.' *Isv. Akad. Nauk SSSR, Ser. Geogr. Geophys.*, **13**:58–69. In Russian.

Oertel Jr. H. (1990). 'Wakes behind blunt bodies.' *Ann. Rev. Fluid Mech.*, **22**:539–564.

Oertel Jr. H. & Delfs J. (1995). 'Mathematische Analyse der Bereiche reibungsbehafteter Strömungen.' *ZAMM - Z. angew. Math. Mech.*, **75**:491–505.

Oertel Jr. H. & Delfs J. (1996). *Strömungsmechanische Instabilitäten*. Springer, Berlin.

Ohmoto T., Okamoto T., & Nakashima T. (2002). 'Three-dimensional flow structure in an open channel with a flexible vegetation zone.' *Proc. 1st Int. Symp. Hydr. Meas. & Exp. Meth. Estes Park, Co., USA*.

Oppenheim A.V. & Schafer R.W. (1989). *Discrete-Time Signal Processing*. Prentice-Hall, Inc., Englewood Cliffs, New Jersey.

Panofsky H.A. & Dutton J.A. (1984). *Atmospheric Turbulence. Models and Methods for Engineering Applications*. John Wiley & Sons, New York.

Papanicolaou P.N. & List J.E. (1988). 'Investigation of round vertical turbulent buoyant jets.' *J. Fluid Mech.*, **195**:341–391.

Pattiaratchi C., James A., & Collins M.B. (1986). 'Island wakes and headland eddies: A comparison between remotely-sensed data and laboratory experiments.' *J. Geophysical Research*, **92**:783–794.

Perry A.E., Chong M.S., & Lim T.T. (1982). 'The vortex-shedding process behind two-dimensional bluff bodies.' *J. Fluid Mech.*, **116**:77–90.

Pope S.B. (2000). *Turbulent Flows*. University Press, Cambridge.

Pozdnyakov D. & Grassl H. (2003). *Colour of Inland and Coastal Waters. A Methodology for its Interpretation*. Springer-Verlag, Berlin Heidelberg New York.

van Prooijen B.C. & Uijttewaal W.S.J. (2002). 'A linear approach for the evolution of coherent structures in shallow mixing layers.' *Phys. Fluids*, **14**(12):4105–4114.

Raffel M., Willert C.E., & Kompenhans J. (1998). *Paricle Image Velocimetry. A Practical Guide*. Springer-Verlag, Berlin Heidelberg New York.

Rehab H., Antonia R.A., & Djenidi L. (2001). 'Streamwise evolution of a high-Schmidt-number passive scalar in a turbulent plane wake.' *Exp. Fluids*, **31**:186–192.

van Rijn L.C. (1994). *Principles of Fluid Flow and Surface Waves in Rivers, Estuaries, Seas, and Oceans*. Aqua Publications, Amsterdam, 2. edition.

Ruck B. (1987). *Laser-Doppler-Anemometrie*. AT-Fachverlag, Stuttgart.

Ruck B. (1990a). 'Laser-Doppler-Anemometrie.' In Ruck B., ed., 'Lasermethoden in der Strömungsmesstechnik,' pp. 99–150. AT-Fachverlag.

Ruck B., ed. (1990b). *Lasermethoden in der Strömungsmesstechnik*. AT-Fachverlag, Stuttgart.

Rummel A. (2002). *Auswertung des Stofftransportes in turbulenter Flachwasserströmung mit Hilfe eines Ganzfeld-Bildanalyse-Verfahrens*. diploma thesis, University of Karlsruhe. German language.

Rummel A.C., Socolofsky S.A., v. Carmer C.F., & Jirka G.H. (2004). 'Enhanced diffusion from a continuous point source in shallow flow with grid turbulence.' *Phys. Fluids*. In print.

Rummel A.C., v. Carmer C.F., & Jirka G.H. (2002). 'Combined planar measurements of flow velocity and mass concentration in shallow turbulent flow - Part 1: Development of a planar concentration analysis (PCA) system.' *Proc. ASCE/IAHR Int. Symp. Hydr. Meas. & Exp. Meth. Estes Park, Co., USA.*

Rutgers M.A., Wu X.L., & Daniel W.B. (2001). 'Conducting fluid dynamics experiments with vertically falling soap films.' *Rev. Sci. Ins.*, **72**:3025–3037.

Rutherford J.C. (1994). *River Mixing*. John Wiley, Chichester.

Sakakibara J. & Adrian R.J. (1999). 'Whole field measurement of temperature in water using two-color laser induced fluorescence.' *Exp. Fluids*, **26**:7–15.

Schlichting H. & Gersten K. (1997). *Grenzschicht-Theorie*. Springer, Berlin, 9. überarb. u. erweit. edition. German language.

Scorer R. (1986). *Cloud Investigation by Satellite*. Ellis Horwood, Chichester.

Seuntiëns H.J., Kieft R.N., Rindt C.C.M., & Van Steenhoven A.A. (2001). '2D temperature measurements in the wake of a heated cylinder using LIF.' *Exp. Fluids*, **31**:588–595.

Slavik J. (1994). *Fluorescent Probes in Cellular and Molecular Biology*. CRC Press, Boca Raton, FL.

Smart P.L. & Laidlaw I.M.S. (1977). 'An evaluation of some fluorescent dyes for water tracing.' *Water Resources Research*, **13**:15–33.

Socolofsky S.A. & Jirka G.H. (2001). *Environmental Fluid Mechanics - Part I: Mixing, Transport, and Transformation*. Institute for Hydromechanics, University of Karlsruhe, 1. edition.

Socolofsky S.A., v. Carmer C.F., & Jirka G.H. (2003). 'Shallow turbulent wakes: Linear stability analysis compared to experimental data.' *Proc. Int. Symp. Shallow Flows, Delft, NL.*

Sommeria J. (2002). 'Two-dimensional turbulence.' In Lesieur M., Yaglom A., & David F., eds., 'New Trends in Turbulence,' EDP/Springer.

Spiegel Online (2002). 'Vulkan verwirbelt die Wolken.' `http://www.spiegel.de/wissenschaft/erde/`.

Stansby P.K. (1997). 'Semi-implicit finite volume shallow-water flow and solute transport solver with $k - \epsilon$ turbulence model.' *Int. J. Num. Methods Fluids*, **25**:285–313.

Strube G. (2001). 'Raman scattering.' In Mayinger & Feldmann (2001), pp. 169–194.

Stull R.B. (1988). *An Introduction to Boundary Layer Meteorology*. Kluwer Acad. Publ., Dordrecht, NL.

Swamee P.K. & Jain A.K. (1976). 'Explicit equation for pipe-flow problems.' *J. Hydr. Div. ASCE*, **102**(HY5):657–664.

Tachie M.F. & Balachandar R. (2001). 'Shallow wakes generated on smooth and rough surfaces.' *Exp. Fluids*, **30**:467–474.

Taylor G.I. (1935). 'Statistical theory of turbulence: Parts I–III.' *Proc. R. Soc. London Ser. A*, **151**:421–464.

Tennekes H. & Lumley J.L. (1977). *A First Course in Turbulence*. MIT Press, Cambridge, 4. edition.

Thomson R.E., Gower J.F.R., & Bowker N.W. (1977). 'Vortex streets in the wake of the aleutian islands.' *Monthly Weather Review*, **105**:873–884.

Tropea C. (1993). 'Laser-Doppler-Anemometrie.' In Bimberg (1993), pp. 67–102. In German.

Truckenbrodt E. (1980). *Fluidmechanik, Bd. 2 Elementare Strömungsvorgänge dichteveränderlicher Fluide sowie Potential- und Grenzschichtströmungen*. Springer, Heidelberg, 2. edition. German language.

Truckenbrodt E. (1996). *Fluidmechanik - Bd. 1, Grundlagen und elementare Strömungsvorgänge dichtebeständiger Fluide*. Springer, Heidelberg, 4. überarb. u. erweit. edition. German language.

TSI (1996). *Instruction Manual for Model IFA 655 Digital Burst Correlator*. TSI Inc.

Tukker J. (1997). *Turbulence Structures in Shallow Free-Surface Mixing Layers*. Ph.D. thesis, Delft University of Technology, Delft, The Netherlands.

Uijttewaal W.S.J. & Booij R. (2000). 'Effects of shallowness on the development of free-surface mixing layers.' *Phys. Fluids*, **12**(2):392–402.

Uijttewaal W.S.J. & Jirka G.H. (2003). 'Grid turbulence in shallow flows.' *J. Fluid Mech.*, **489**:325–344.

Uijttewaal W.S.J. & Tukker J. (1998). 'Development of quasi two-dimensional structures in a shallow free-surface mixing layer.' *Exp. Fluids*, **24**:192–200.

Vreugdenhil C.B. (1994). *Numerical Methods for Shallow-water Flow*. Kluwer Academic Publishers, Dordrecht, NL.

Walker D.A. (1987). 'A fluorescence technique for measurements of concentration in mixing liquids.' *J. Phys. E: Sci. Instrum.*, **20**:217–224.

Wang G.R. & Fiedler H.E. (2000a). 'On high spatial resolution scalar measurement with LIF. part 1: Photobleaching and thermal blooming.' *Exp. Fluids*, **29**:257–264.

Wang G.R. & Fiedler H.E. (2000b). 'On high spatial resolution scalar measurement with LIF. part 2: The noise characteristic.' *Exp. Fluids*, **29**:265–274.

Webster D.R., Roberts P.J.W., & Ra'ad L. (2001). 'Simultaneous DPTV/PLIF measurements of a turbulent jet.' *Exp. Fluids*, **30**:65–72.

Weiss J. (1981). 'The dynamics of enstrophy transfer in two-dimensional hydrodynamics.' Technical Report LJI-TN-81-121, La Jolla Inst.

Weiss J. (1991). 'The dynamics of enstrophy transfer in two-dimensional hydrodynamics.' *Physica D*, **48**:273–294.

Weitbrecht V. (2004). *Influence of dead-water zones on the dispersive mass transport in rivers*, volume 2004/1 of *Dissertationsreihe am Institut für Hydromechanik der Universität Karlsruhe*. Universitätsverlag, Karlsruhe. ISBN 3-937300-07-4.

Weitbrecht V. & Jirka G.H. (2001). 'Flow patterns in dead zones of rivers and their effect on exchange processes.' *Proc. 3rd Int. Symp. Env. Hydr. Tempe, USA*.

Weitbrecht V., Kühn G., & Jirka G. (2002). 'Large scale piv-measurements at the surface of shallow water flows.' *J. Flow Meas. & Instrum.*, **13**(5-6):237–245.

Wolanski E., Asaeda T., Tanaka A., & Deleersnijder E. (1996). 'Three-dimensional island wakes in the field, laboratory experiments and numerical models.' *Continental Shelf Research*, **16**:1437–1452.

Wolanski E., Imberger J., & Heron M.L. (1984). 'Island wakes in shallow coastal waters.' *J. Geophysical Research*, **89**:10553–10569.

Wolfbeis O.S. (1993). *Fluorescence Spectroscopy. New Methods and Applications*. Springer, Berlin, Heidelberg.

Yulistiyanto B., Zech Y., & Graf W.H. (1998). 'Flow around a cylinder: Shallow-water modelling with diffusion-dispersion.' *J. Hydr. Eng.*, **124**(4):419–429.

Zdravkovich M.M. (1997). *Flow Around Circular Cylinders, Volume 1: Fundamentals*. Oxford University Press, Oxford.

Zhou T., Antonia R.A., Danaila L., & Anselmet F. (2000). 'Transport equations for the mean energy and temperature dissipation rates in grid turbulence.' *Exp. Fluids*, **28**:143–151.